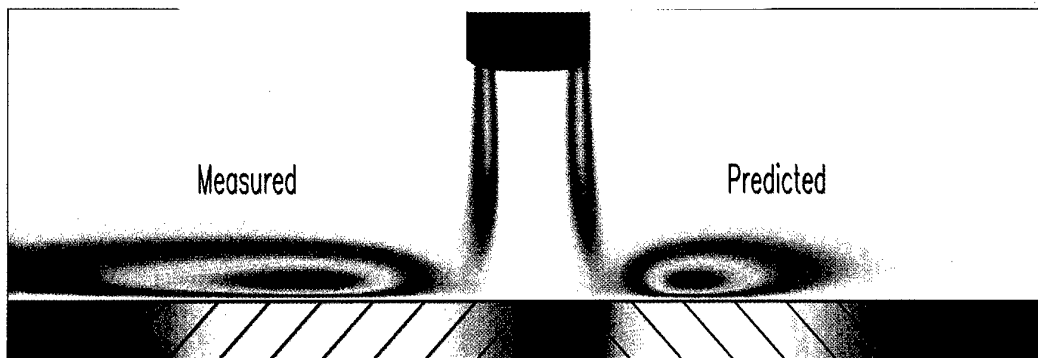


*2nd EF Conference in*  
**TURBULENT HEAT  
TRANSFER**

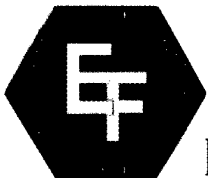
Manchester, UK 1998

**DISTRIBUTION STATEMENT A**

Approved for public release;  
Distribution Unlimited



**Volume II**



**ENGINEERING FOUNDATION**

**2nd International Conference**

**on**

**TURBULENT HEAT TRANSFER**

**Manchester**

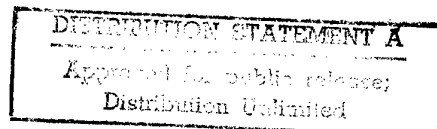
**May 31 - June 4, 1998**

**Organized by UMIST and the University of Manchester**

**In collaboration with**

**ASME Heat Transfer Division**

**The Engineering Foundation**



**Volume II**

19980617 084

## **Sponsorship of THT-2**

The Organizing Committee expresses its sincere appreciation to the following organizations for their support of this conference:

UK Health & Safety Executive

US Air Force

US Army

ABB

Electricité de France

Magnox Electric

Nuclear Electric

Shell Research, Amsterdam

## **Organizing Committee**

Brian Launder, Chairman  
Derek Jackson, Co-Chairman  
Pepe Humphrey, Nobu Kasagi  
Al Ortega, Frank Schmidt

## **Local Arrangements Committee**

Pei An, Brian Axcell, John Byrne  
Tim Craft, Shui-Sheng He,  
Hector Iacovides, David Jackson  
Derek Jackson, Catherine King,  
Brian Launder

## **Scientific Committee**

G Bergeles, K Bremhorst, J Coupland  
J K Eaton, M Fiebig, K Hanjalic, J Hannis  
B V Johnson, T V Jones, D Laurence,  
Y Nagano, J M Owen, S Sarkar, A M Savill,  
R M C So, K Suzuki, R Viskanta



# CONTENTS

## VOLUME I

### **Session 1: Heat Transfer Under Simple Shearing** **(Chairmen: B. E. Launder and T. J. Hanratty)**

- Y. Na, D. V. Papavassiliou and T. J. Hanratty  
Use of Direct Numerical Simulation to Study the Effect of Prandtl Number on Temperature Fields 1 - 3
- H. Kawamura and H. Abe  
DNS of Turbulent Heat Transfer in Channel Flow with Respect to Reynolds-Number Effect 1 - 15
- K. Matsubara, M. Kobayashi, H. Maekawa and K. Suzuki  
DNS of Spanwise Turbulent Heat Transfer in a Channel 1 - 23
- D. M. McEligot, A. Mohsen Shehata and T. Kunugi  
Prediction of Strongly-Heated Internal Gas Flows 1 - 33
- Y. Hagiwara, T. Okuda, M. Tanaka and S. Murai  
The Modification of Quasi-Streamwise Vortices in Liquid Turbulent Flow in a Duct by the Injection of Polymer Solution 1 - 48
- C. B. Lee  
New Observations in Transitional Flat Plate Boundary Layers: Measurement and Visualisation 1 - 54

### **Session 2: Vertical Mixed and Natural Convection** **(Chairman: A. Ortega)**

- P. Poškas, B. Jazbutis  
Experimental Investigation of Turbulent Mixed Convection Heat Transfer in a Vertical Annulus for Aiding Flows 2 - 3
- Y. S. Chumakov and S. B. Nikolskaja  
Features of Dynamic and Heat Structure of Free Convection Boundary Layer near Vertical Heated Surface. 2 - 9
- M. A. Cotton, J. O. Ismael and P.J. Kirwin  
Variable Property Mixed Convection: Low-Reynolds-Number and Strain Parameter Eddy Viscosity Model Results 2 - 20
- J. Li and J. D. Jackson  
Buoyancy-Influenced Turbulent Heat Transfer to Air Flowing in a Uniformly Heated Vertical Tube 2 - 31

### **Session 3: Flows with Interfaces** **(Chairman: N. Kasagi)**

- V. De Angelis and S. Banerjee  
Turbulent Transport Processes Across Fluid-Fluid Interfaces 3 - 3

**Session 4: Separating, Impinging and Recovering Flows**  
**(Chairmen: G. Hammond and K. Bremhorst)**

K. Inaoka, J. Yamamoto and K. Suzuki Dissimilarity Between Heat Transfer and Momentum Transfer in a Disturbed Turbulent Boundary Layer with Insertion of a Rod	4 - 3
T. J. Craft Prediction of Heat Transfer in Turbulent Stagnation Flow with a New Second-Moment Closure	4 - 15
K. Bremhorst and N. D. Agnew Surface Heat Transfer and Flow Structures of Steady and Fully Pulsed Radial Reattaching Jets	4 - 26
W. B. Tsai, W. W. Lin, C. C. Chieng Computation of Enhanced Turbulent Heat Transfer in a Channel With Periodic Ribs	4 - 39
E. Ya. Epik, L. E. Yushyna and T. T. Suprun Heat Transfer in Relaxation Zone after a Local Closed Separation of Various Types	4 - 49
S. He, Z. Xu and J. D. Jackson Buoyancy-Opposed Turbulent Wall Jet Flow down a Vertical Plane Surface	4 - 59

**Session 5: Horizontal, Stratified Flows**  
**(Chairmen: M. A. Leschziner and K. Hanjalić)**

X. Chavanne, F. Chillà, B. Castaing, B. Chabaud, B. Hébral and P. Roche A Cryogenic Experiment for the Rayleigh-Bénard Convection Study	5 - 3
S. Kenjereš and K. Hanjalić Transient Analysis of Rayleigh-Bénard Convection over Flat and Wavy Walls with a RANS Model	5 - 9
S-H. Peng and L. Davidson Comparison of Subgrid-Scale Models in LES for Turbulent Convection Flow with Heat Transfer.	5 - 24
C. A. Armitage, B. E. Launder and M. A. Leschziner Second-Moment Modelling of Combined Turbulent Heat and Species Transfer in Multiply Stratified Fluid Bodies	5 - 36
B. B. Ilyushin Modelling the Non-Local Turbulent Transport of Momentum, Heat and Substance in the Convective PBL	5 - 48
S. Tsujimura, O. Iida and Y. Nagano Effects of Rotation on Unstably Stratified Turbulence	5 - 58

**Session 6: Engineering Turbulence Models**  
**(Chairmen: Y. Nagano and K. Suzuki)**

D. E. Musielak Numerical Simulation of Transverse Hydrogen Injection into Mach 6.3. Airflow and its Effect on Surface Cooling	6 - 3
C. B. Hwang and C. A. Lin Low-Reynolds Number Modelling of Transpired Flows	6 - 9
T. V. Jones Theory for the Use of Foreign Gas in Simulating Film Cooling	6 - 22
D. Giebert, R. Koch, A. Schulz and S. Wittig Evaluation of Advanced Low-Reynolds Number $k-\epsilon$ Turbulence Models for Predicting Convective Heat Transfer	6 - 30
P. M. Wikström and A. V. Johansson DNS and Scalar-Flux Transport Modelling in a Turbulent Channel Flow	6 - 46
S. Fu and C. Wang A Proposal for Anisotropic Eddy-Diffusivity Model for Scalar Fluxes	6 - 52

**VOLUME II**

**Session 7: Measurement and Modelling of 3D Separated Flows**  
**(Chairmen: D. Laurence and T. V. Jones)**

X. Cheng, H. J. Neitzel Heat Transfer of Naturally Induced Turbulent Convection in Advanced Reactor Containment	7 - 3
H. Iacovides, D. C. Jackson, G. Kelemenis, B. E. Launder and Y-M. Yuan Recent Progress in the Experimental Investigation of Flow and Local Wall Heat Transfer in Internal Cooling Passages of Gas-Turbine Blades	7 - 14
B. Bonhoff, S. Parneix, J. Leusch, B. V. Johnson, J. Schabacker, A. Bölcş Experimental and Numerical Study of Developed Flow and Heat Transfer in Coolant Channels with 45 and 90 Degree Ribs	7 - 29
H. Iacovides and M. Raisee Recent Progress in the Computation of Flow and Heat Transfer in Internal Cooling Passages of Turbine Blades	7 - 42
E. R. Meinders and K. Hanjalić Vortex Structure and Heat Transfer in Turbulent Flow over a Wall-Mounted Matrix of Cubes	7 - 58
B. P. Axcell, C. Tianpong and J.E. Byrne Convective Heat Transfer to a Rotating Disk with Roughened Surfaces	7 - 72

**Session 8: Large-Eddy Simulation for Industrial Flows**  
**(Chairman: J. D. Jackson)**

P. R. Voke Large-Eddy Simulation of Aeronautical Flows	8 - 3
K. Abe and K. Suga Large-Eddy Simulation of Passive Scalar Fields under Several Strain Conditions	8 - 15
G. Grötzbach, M. Wörner Direct Numerical and Large Eddy Simulations in Nuclear Applications	8 - 31

**Poster Papers**

D. J. Bergstrom and X. Huang Large Eddy Simulation of Natural Convection in a Vertical Slot	P - 3
L. Bogusławski Influence of the Round Jet Flow Structure on the Distribution of Local Heat Transfer and its Fluctuations on Impinged Surface	P - 15
P. W. Li, H. Daisaka, Y. Kawaguchi, A. Yabe, K. Hishida, M. Maeda Experimental Investigation of Heat Transfer Enhancement for Turbulence Drag-Reducing Flow in a Two-Dimensional Channel	P - 21
T. G. Karayiannis and Y. S. Tian An Experimental Estimation of Turbulence Kinetic Energy in Low Turbulence Buoyant Flow	P - 30
J-P. Moro, M. Saez and E. Hopfinger An Experimental Study of Mixed Convection	P - 39
A. F. Kurbatskii and S. V. Poroseva Modelling Turbulent Diffusion in a Rotating Cylindrical Pipe Flow	P - 46
S. A. M. Said, A. Al-Farayedhi, M. Habib, S. A. Gbadebo, A. Asghar, S. Al-Dini Experimental Investigation of Heat Transfer in Pulsating Turbulent Pipe Flow	P - 54
A. V. Gorin and D. Ph. Sikovsky On the Ability of Turbulence Models to Predict the Complex Turbulent Flows: the Application of Scaling Analysis	P - 63
V. G. Sviridov, N. G. Razuvanov, A. V. Ustinov The Effect of Natural Convection of Local Heat Transfer for a Liquid Metal Flow in a Heated Horizontal Tube under a Longitudinal Magnetic Field	P - 73
N. F. Yurchenko Optimization of Heat Transfer Control Based on a Receptivity Approach	P - 77
R. W. Hill and K. S. Ball Direct Numerical Simulations of Turbulent Forced Convection Between Counter-Rotating Disks	P - 83
P. Diamessis, D. Bouris and G. Bergeles Prediction of Grid Turbulence Evolution with a Simple Multifractal Cascade Model	P - 99
T. J. Craft Second-Moment Computations of the Three-Dimensional Thermal Wall Jet	P - 115

R. Bridon, G. P. Hammond and G. D Lock Application of Thermal Imaging to Determine the Heat Transfer Characteristics of Three-Dimensional, Turbulent Wall Jets	P - 123
A. V. Starchenko, A. M. Bubenchikov, E. S. Burlutsky Mathematical Modelling of Heat Exchange by Turbulent Flow of Suspension in a Pipe	P - 131
V. V. Ram, S. Lau and M. Kaniewski A Visualisation Study of the Flow Patterns of Longitudinal Vortices Generated by Winglets in a Channel	P - 141
P. Ya. Cherepanov and V. A. Babenko Dissipative Properties of a Dynamic and Thermal Flat Wake with Negative Net Excessive Momentum in Stratified Flow	P - 152

### **Author Index**

**Session 7**

**Measurement and Modelling of 3D Separated Flows**



# HEAT TRANSFER OF NATURALLY INDUCED TURBULENT CONVECTION IN ADVANCED REACTOR CONTAINMENT

X. Cheng, H.J. Neitzel

Research Center Karlsruhe  
Institute of Applied Thermo- and Fluidynamics  
Postfach 3640, D-76021 Karlsruhe, Germany  
Fax: +49-7247-824837, email: xu.cheng@iatf.fzk.de

## ABSTRACT

The use of passive safety features in a nuclear power plant is a desirable method of achieving simplification, increasing the reliability of safety functions and promoting an improved public acceptance of nuclear energy. One essential of the new containment concept proposed by the Research Center Karlsruhe and the Technical University Karlsruhe is its potential to remove the decay heat by turbulent natural air convection. Due to asymmetric heating the flow inside the test channel is 3-dimensional with a strong coupling of convection with thermal radiation. To determine the coolability of such a passive cooling system and to study the physical phenomena involved, experimental separate-effects investigations are performed in the PASCO test facility. In addition numerical studies are performed by using the 3-D code FLUTAN. The tests performed have generated a broad and generic data base for the development of physical models and for the validation of computer codes. In the flow channel considered thermal radiation contributes significantly to the total heat transfer.

## 1 INTRODUCTION

For next generation water cooled reactors the use of passive safety features should be investigated in respect to their feasibility and functional performance. Passive containment cooling by natural air convection and thermal radiation has been proposed in the past for several innovative reactor concepts.

The composite containment, shown in fig. 1, proposed by the Research Center Karlsruhe and the Technical University Karlsruhe is to cope with beyond-design basis accidents [1]. One essential of this new containment concept is its potential to remove the decay heat by natural air convection coupled with thermal radiation. The containment consists of an inner steel shell of about 60 m diameter and an outer reinforced concrete shell. The annulus of approx. 80 cm radial gap width is bridged by longitudinal support ribs fixed in the concrete shell. The ribs are placed on the circumference with approx. 50 cm spacing, so that many individual cooling channels are formed in the gap. In a core meltdown accident the decay heat is converted into steam by direct contact of the melt with the water. The steam produced condenses on the inner surface of the externally cooled containment shell. The increase in the temperature of the steel shell results in natural convection of air in the individual channels formed by the support ribs in the annular gap. Moreover, radiative heat transfer takes

place between the steel shell, the support ribs and the concrete shell. Decay heat is thus removed by natural air convection coupled with thermal radiation to the ambient atmosphere in a passive way. Due to asymmetric heating the flow inside the test channel is 3-dimensional with a strong coupling of turbulent convection with thermal radiation.

Natural convection heat transfer in an open-ended vertical flow channel has been widely investigated in the past several decades owing to its important applications in electronic cooling, solar energy collectors and nuclear engineering [2-4]. Most of the studies consider two-dimensional laminar flow. The first numerical study concerning turbulent natural convection in an open-ended two-dimensional channel was performed by Borgers et al. [3]. The turbulent flow characteristics of air are predicted by a mixing length model. Pica et al. [5] performed experimental investigations on turbulent natural convection of air in a large vertical channel with the channel height 2.6 m and the channel width 1.2 m. The channel depth was varied from 7.5 cm to 17 cm. One of the wall is heated with uniform heat flux, while the other walls are made of glass plates and kept adiabatic. Because of the low emissivity of the glass plates the effect of thermal radiation was neglected. Combined natural convection and thermal radiation heat transfer between vertical flat plates was first of all numerically investigated by Carpenter et al. [6]. It was found that at high Rayleigh



number thermal radiation reduces significantly the heated wall temperature by keeping heat flux uniform and constant. However, this work has been restricted to two-dimensional laminar flow conditions.

The above bibliographic survey underlines the deficiency in experimental as well as in theoretical studies on turbulent natural convection heat transfer coupled with thermal radiation in a three-dimensional vertical channel with asymmetrical heating. Therefore, the separate-effects test program PASCO (acronym for passive containment cooling) is presently under way at the Research Center Karlsruhe. The general aim of this program is to determine the coolability of such a passive cooling system and to study the physical phenomena involved. In the PASCO experiments

different effects, e.g. the effect of flow channel geometries and wall emissivity on heat transfer are studied. Moreover, generic informations and a broad data base will be provided for validation of advanced multi-dimensional computer codes and for developing models of heat transfer for the system considered.

This work is partially supported by the European Commission in the 4th Framework Programme. Nine European institutions have agreed on a common research programme with the main purpose to provide a generic data base for containment thermal-hydraulic analysis (DABASCO-project [7]). The PASCO programme is one of the eight work packages involved in the DABASCO-project.

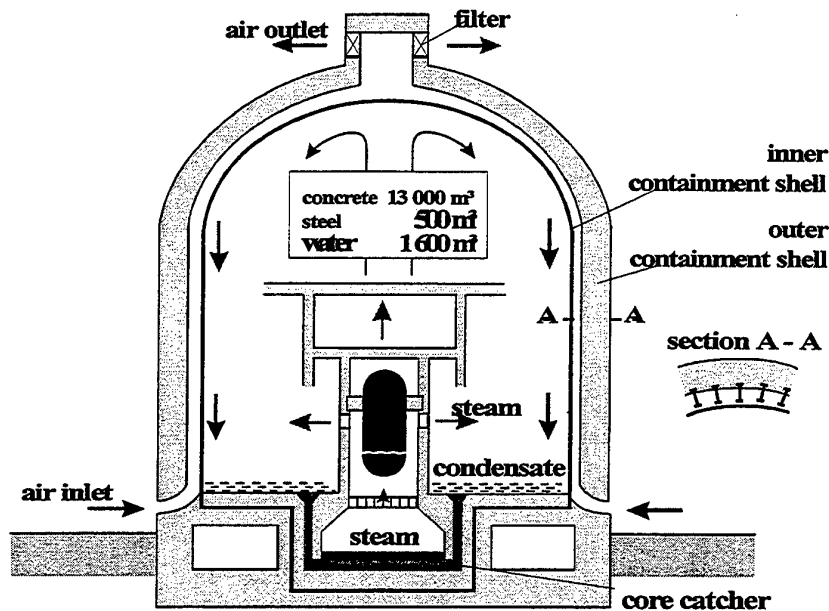


Figure 1: Composite containment

## 2 TEST FACILITY PASCO

The PASCO test facility shown in fig.2 simulates one cooling channel in the annular gap of the composite containment proposed. The test section consists of a vertical rectangular channel of which one wall is electrically heated. The channel is open to the atmosphere at its inlet and outlet. The width of the channel is 0.5 m. The maximum channel depth is 1.0 m which can be changed. The maximum heated height is 8.0 m consisting of four individually heatable plates made of steel, so that four different values of channel height can be realized, i.e. 2, 4, 6 and 8 m. By changing the channel depth and the channel height the effect of the channel geometry will be studied. In each steel plate nine heater wires are embedded which are uniformly

distributed over the plate. At both ends of the heated plates an additional heater is inserted to achieve a more uniform distribution of the heated wall temperature. The electric power fed to each heated plate as well as to the additional heaters is separately controlled according to local temperature values. In this way, a well uniform distribution of the heated wall temperature can be achieved.

All the walls are thermally insulated from the ambient surroundings. The main heat loss is resulted by the heat conduction from the heated plates to the peripheric structure material. To determine the heat loss a thermal calibration has been performed at different temperature levels. The thermal calibration was made by putting an insulating layer directly onto the heated wall. The

temperature of the heated wall was set at a predefined value with a well uniform distribution. During experiments the heat power transferred via air convection inside the flow channel is obtained by subtracting the total electrical power by the heat loss determined by the calibration.

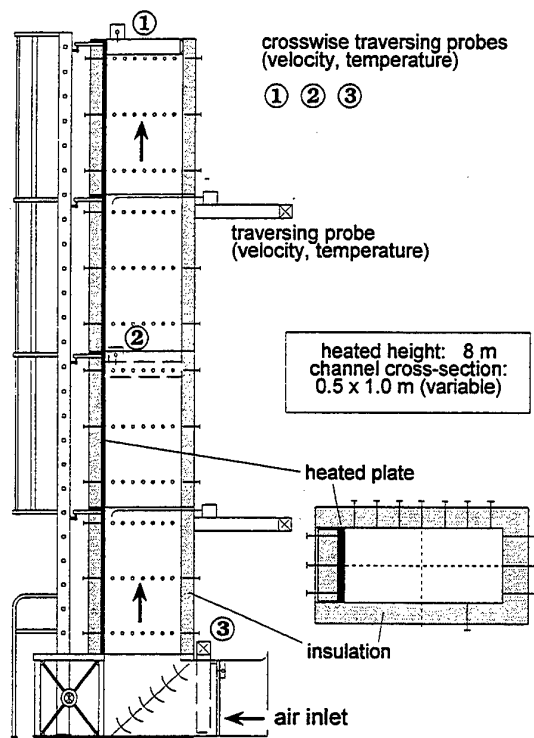


Fig.2: PASCO test facility

Table 1 summarizes the test parameters performed. In the present experiments the temperature of the heated wall is controlled to be constant and uniform. The heated wall temperature varies from 100°C to 175°C, which corresponds to a saturation pressure range of steam from 0.1 to about 0.9 MPa which covers the reactor conditions. Preliminary calculations with a 1-D code showed that thermal radiation contributes significantly to the decay heat removal in the composite containment. With high emissivities of 0.9 of the walls the heat transferred by radiation equals approximately to the amount transferred by convection. To investigate the effect of thermal radiation on the total heat transfer, experiments with two different values of wall emissivity (0.4 and 0.9) are performed.

Table 1: Test matrix

Heated wall temperature $T_h$ , °C	100 - 175
Wall emissivity $\epsilon$	0.4, 0.9
Heated height $H$ , m	4.0, 8.0
Channel depth $L$ , m	0.25 - 1.0

The maximum height of the test channel is limited to 8 m. Because of the reduced height the results could not be directly extrapolated to a reactor containment of about 40 m height. Nevertheless, with a heated height of 8 m a turbulent air flow inside the PASCO test channel is expected. The Grashof number of the flow in the PASCO test channel

$$Gr = \frac{g \beta H^3 \Delta T}{\nu^2} \quad (1)$$

is ranging from  $7 \cdot 10^{11}$  to  $8 \cdot 10^{12}$ .

The test facility is equipped among others with approx. 170 thermocouples to measure the distribution of wall temperatures. Traversing probes for recording the air temperature and the air velocity are installed at five different elevations. Cross-wise traversing probes at the inlet, in the mid-plane and at the outlet measure the temperature- and velocity distributions over each individual channel cross-section. Calibrations were performed to determine the heat loss from the heated wall to the ambient surroundings at different values of the heated wall temperature. Moreover, temperatures of the ambient air, the pressure at the channel inlet, the air humidity and the heating power at four different heated plates are recorded. The measurement accuracy of different parameters are summarized in table 2.

Table 2: Measurement accuracy

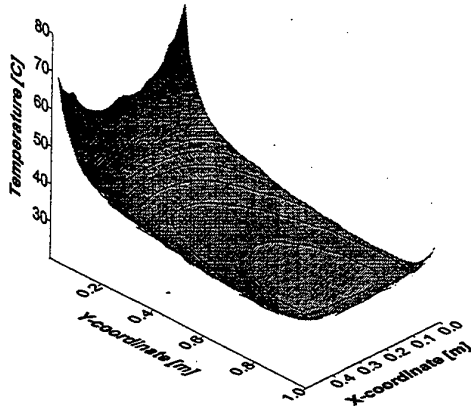
Temperature, °C	± 0.75
Air velocity, %	± 2.0
Pressure, %	± 0.5
Heating power, %	± 1.0

With this comprehensive instrumentation experimental data are generated for the development of physical models and for the validation of multi-dimensional computer codes.

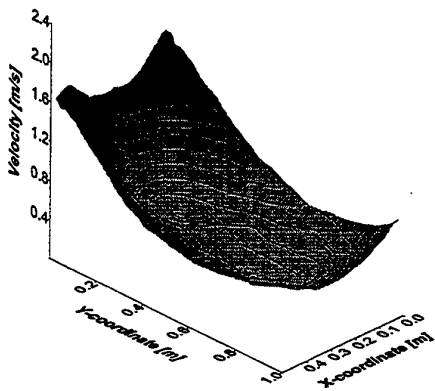
### 3 EXPERIMENTAL RESULTS

Figures 3a and 3b show an example of the measured profile of the air temperature and the air velocity at the test channel outlet. It can be seen that the air temperature decreases rapidly with the distance from the heated wall. The maximum temperature locates in the corner where the heated wall connects the side wall. Due to thermal radiation the air temperature increases again by approaching to the side wall and the back wall. The minimum value of the air temperature appears in the central region. Similar results have also been obtained for the air velocity distribution (fig. 3b). As expected for natural convection, the maximum air velocity is observed close to the wall surface. Again,

due to thermal radiation a minimum of the air velocity is found in the central region.



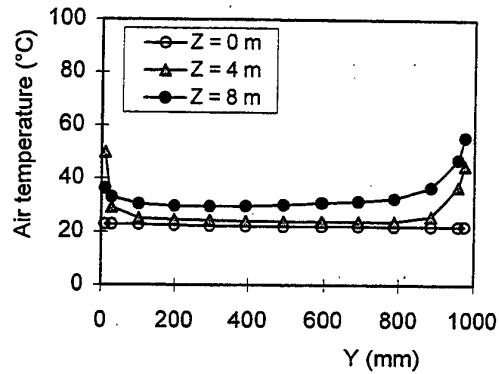
(3a) air temperature



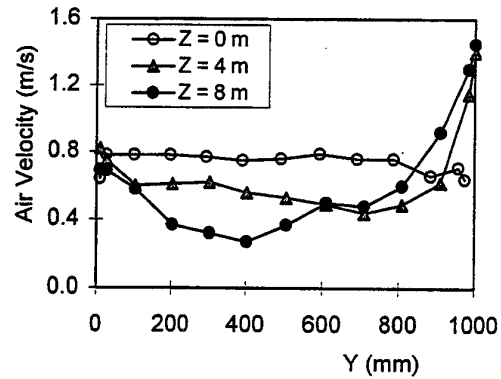
(3b) air velocity

Fig. 3: Measured distribution of air temperature (3a) and air velocity (3b) at the channel outlet  
 $T_h = 150^\circ\text{C}$ ,  $\varepsilon = 0.9$ ,  $L = 1.0\text{ m}$ ,  $H = 8.0\text{ m}$

Figures 4a and 4b show the air temperature and the air velocity along the mid-line ( $X = 0.25\text{ m}$ ) versus the distance from the back wall ( $Y$ ) at different axial levels. Near the inlet cross-section ( $Z = 0\text{ m}$ ) the air temperature distribution is uniform (about  $20^\circ\text{C}$ ) over the entire channel depth. At higher axial levels the temperature near the walls increases and the region affected by the higher wall temperature enlarges. Near the outlet cross-section this affected region spreads over the entire cross section, so that the air temperature in the central region is clearly higher than the inlet air temperature. The air velocity has a well uniform distribution in the central region in the lower part of the channel. At higher axial levels the air velocity near the walls increases, whereas it decreases in the central region.



(4a)



(4b)

Fig. 4: Air temperature (4a) and air velocity (4b) along the middle line ( $X = 0.25\text{ m}$ )  
 $T_h = 150^\circ\text{C}$ ,  $\varepsilon = 0.9$ ,  $L = 0.5\text{ m}$ ,  $H = 8.0\text{ m}$

Figure 5 shows the air velocity at the outlet cross-section along the mid-line ( $X = 0.25\text{ m}$ ) versus the distance from the back wall ( $Y$ ) at different values of the channel depth  $L$  and the wall emissivity. By decreasing the wall emissivity from 0.9 down to 0.4 the effect of thermal radiation and, consequently, the temperature on the back wall reduces. This leads to a reduction in the air velocity near the back wall. In the region near the heated wall the flow condition remains nearly unchanged. Reducing the channel depth enhances the radiative heat exchange between the heated wall and the back wall, so that the air velocity increases.

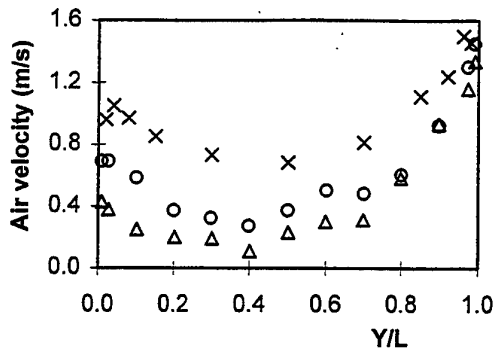


Fig. 5: Air velocity at the outlet cross-section and  $X=0.25$  m

o:  $T_h = 150^\circ\text{C}$ ,  $\varepsilon = 0.9$ ,  $L = 1.0$  m,  $H = 8.0$  m

$\Delta$ :  $T_h = 150^\circ\text{C}$ ,  $\varepsilon = 0.4$ ,  $L = 1.0$  m,  $H = 8.0$  m

x:  $T_h = 150^\circ\text{C}$ ,  $\varepsilon = 0.9$ ,  $L = 0.5$  m,  $H = 8.0$  m

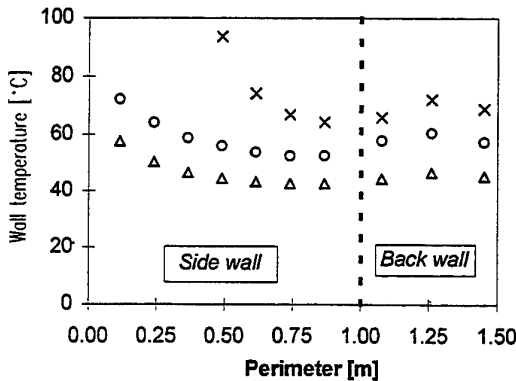


Fig. 6: Temperature profile on the side wall and the back wall at  $Z = 3.8$  m

o:  $L = 1.0$  m,  $\varepsilon = 0.9$ ,  $T_h = 150^\circ\text{C}$ ,  $H = 8.0$  m

x:  $L = 0.5$  m,  $\varepsilon = 0.9$ ,  $T_h = 150^\circ\text{C}$ ,  $H = 8.0$  m

$\Delta$ :  $L = 1.0$  m,  $\varepsilon = 0.4$ ,  $T_h = 150^\circ\text{C}$ ,  $H = 8.0$  m

Figure 6 illustrates the measured temperatures on the side wall and on the back wall at the middle elevation ( $Z = 3.8$  m) for three tests with different values of the channel depth and the wall emissivity. The temperature on the side wall decreases with increasing the distance from the heated wall. Due to thermal radiation the temperature on all the unheated walls is much higher than the average air temperature at the same elevation (about  $25^\circ\text{C}$ ). These results emphasize the strong influence of thermal radiation on the total heat transfer. By reducing the channel depth the temperature on the back wall increases due to a larger view factor between the heated wall and the back wall. Decreasing the wall emissivity from 0.9 down to 0.4 leads to a reduction in the temperature of the unheated walls more than  $10^\circ\text{C}$ .

Figure 7 shows the measured heating power versus the heated wall temperature at different values of the channel depth and the wall emissivity. It is found that the channel depth affects only slightly the heating power, whereas the heat power depends strongly on the temperature of the heated wall and on the wall emissivity. At high wall emissivity 0.9, a total heat power of about 6.5 kW is removed at a heated wall temperature of  $150^\circ\text{C}$ . This indicates that the passive containment cooling system with air natural convection and thermal radiation is a very promising concept. By reducing the wall emissivity from 0.9 down to 0.4, the total heating power decreases more than 30%. Increasing the heated wall temperature from  $100^\circ\text{C}$  to  $175^\circ\text{C}$  leads to an increase in the heating power about 150%.

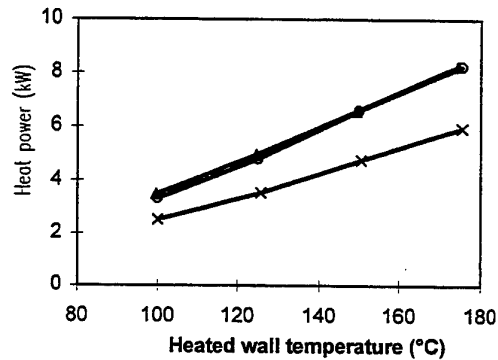


Fig. 7: Measured heating power versus the heated wall temperature at different conditions

o:  $\varepsilon = 0.9$ ,  $L = 1.0$  m,  $H = 8.0$  m

$\Delta$ :  $\varepsilon = 0.9$ ,  $L = 0.5$  m,  $H = 8.0$  m

x:  $\varepsilon = 0.4$ ,  $L = 1.0$  m,  $H = 8.0$  m

#### 4 NUMERICAL SIMULATIONS

In addition to the experimental work numerical simulation is performed to investigate the flow and heat transfer behaviour. The flow in the PASCO test channel is 3-D turbulent natural convection with a strong interaction between convective and radiative heat transfer. Numerical simulation of such a system requires high capabilities of a computer code. In the present study the FLUTAN code is used which is developed at the Research Center Karlsruhe [8]. For the turbulence modeling the standard  $k-\varepsilon$  model is used with logarithmic wall functions for velocity- and temperature distribution near the wall. More details about the code and the physical models used can be found in [9].

##### 4.1 Basic equations

The channel geometry considered is a rectangular, vertical channel, as indicated in fig. 8. One of the walls ( $Y = L$ ) is heated and kept at a constant temperature  $T_h$ .

All the walls are thermally insulated against the ambient surroundings. The heat conduction inside the walls is neglected. The air entering the flow channel has a uniform temperature  $T_{in}$ . The basic equations for the turbulent flow under stationary conditions are summarized as following:

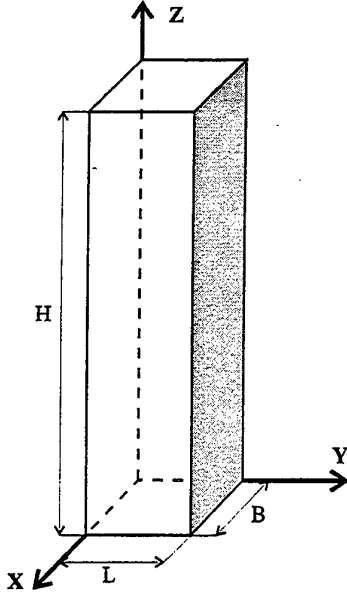


Figure 8: Flow channel and coordinate system

Mass conservation:

$$\frac{\partial(\rho u_i)}{\partial x_i} = 0 \quad (2)$$

Momentum conservation:

$$\frac{\partial(\rho u_i u_j)}{\partial x_j} = -\frac{\partial P}{\partial x_i} + \frac{\partial}{\partial x_i} \left[ (\mu + \mu_t) \frac{\partial u_i}{\partial x_i} - \frac{2}{3} \rho k \right] + \rho g_i \quad (3)$$

Energy conservation:

$$\frac{\partial(\rho u_j T)}{\partial x_j} = \frac{\partial}{\partial x_i} \left[ \left( \frac{\mu}{Pr} + \frac{\mu_t}{\sigma_t} \right) \frac{\partial T}{\partial x_i} \right] \quad (4)$$

Transport equation of the kinetic energy of turbulence  $k$ :

$$\frac{\partial(\rho u_j k)}{\partial x_j} = P_k + G_k - \rho \varepsilon + \frac{\partial}{\partial x_j} \left[ \left( \frac{\mu + \mu_t}{\sigma_k} \right) \frac{\partial k}{\partial x_j} \right] \quad (5)$$

Transport equation of the dissipation rate of the kinetic energy  $\varepsilon$ :

$$\frac{\partial(\rho u_j \varepsilon)}{\partial x_j} = C_1 \frac{\varepsilon}{k} (P_k + G_k) \left( 1 - C_3 \frac{G_k}{P_k} \right) - C_2 \frac{\rho \varepsilon^2}{k} + \frac{\partial}{\partial x_j} \left[ \left( \frac{\mu + \mu_t}{\sigma_\varepsilon} \right) \frac{\partial \varepsilon}{\partial x_j} \right] \quad (6)$$

with

$$\mu_t = \frac{C_\mu \rho k^2}{\varepsilon} \quad (7)$$

$$P_k = \mu_t \left[ \frac{\partial u_i}{\partial x_j} \left( \frac{\partial u_i}{\partial x_j} + \frac{\partial u_j}{\partial x_i} \right) \right] \quad (8)$$

$$G_k = -\frac{\mu_t}{\rho \sigma_t} \frac{\partial \rho}{\partial T} \left( \frac{\partial T}{\partial x_j} g_j \right) \quad (9)$$

In the immediate vicinity of a solid wall where large variation in the values of turbulent properties exists, the so-called wall-function treatment is applied to compute wall shear stress

$$\tau_w = \frac{\kappa \rho k^{1/2} u C_\mu^{1/4}}{\ln(E y C_\mu^{1/4} k^{1/2} / \nu)} \quad (10)$$

and convective heat flux

$$q_c = \frac{\kappa \rho k^{1/2} C_\mu^{1/4} C_p (T_w - T)}{\ln(E y C_\mu^{1/4} k^{1/2} / \nu) + 9.24 \kappa (Pr / \sigma_t - 1) (\sigma_t / Pr)^{1/4}} \quad (11)$$

Here  $y$  is the distance from the wall. The constants in the basic equations above are summarized in table 3.

Table 3: Constants in the basic equations

$C_1$	$C_2$	$C_3$	$C_\mu$	$\kappa$
0.09	1.44	1.92	0.8	0.4
$\sigma_k$	$\sigma_\varepsilon$	$\sigma_t$	$E$	
1.0	1.3	0.9	9	

## 4.2 Thermal radiation model

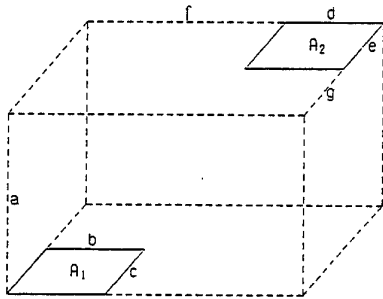
The convective heat transfer is coupled with thermal radiation by the thermal boundary condition at unheated walls, where the net radiative heat must be transferred by natural convection of air. A thermal radiation model with high numerical efficiency has been developed to determine the radiative heat transfer. The fluid (air) is

considered radiatively non-participating and the walls are grey and diffuse. The net radiative heat power of a surface element  $Q_{r,i}$  is computed by the net-radiation method for enclosures [10]:

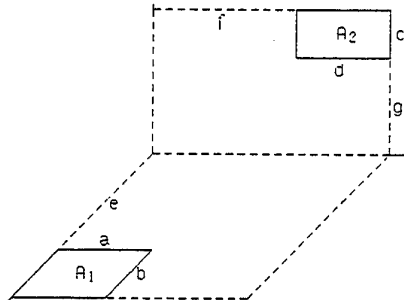
$$\left(\frac{Q_{r,i}}{\varepsilon_i}\right) = \left(\frac{E_i}{\varepsilon_i}\right) - \sum_j \left(\frac{E_j}{\varepsilon_j}\right) \varphi_{j,i} + \sum_j (1 - \varepsilon_j) \varphi_{j,i} \left(\frac{Q_{r,j}}{\varepsilon_j}\right) \quad (12)$$

The above radiation equation can be solved either directly or iteratively. The direct solution is exact and usually needs larger computing expenditure. An iterative solution, e.g. the Gauß-Seidel iteration, requires only a few iterations for intermediate or high wall emissivities. Nevertheless, at low emissivities the direct solution method is more efficient than the iterative method.

The radiative heat power can be easily computed by solving eq. (12), as long as the view factors  $\varphi_{ij}$  are known. Generally, view factor can only be obtained numerically. For a flow channel in the Cartesian coordinate system where boundary walls are either parallel or perpendicular to each other, the view factor between any two surface elements has been derived analytically. Figure 9 shows two different cases: (9a) two parallel surface elements and (9b) two perpendicular surface elements.



(9a) two parallel surface elements



(9b) two perpendicular surface elements

Figure 9: Geometrical parameters of two surface elements in a Cartesian coordinate system

To specify the dimensions of any two surface elements and their relative positions, seven geometric parameters are needed, indicated as  $a, b, c, d, e, f, g$  in fig. 9.

The view factor for two parallel surface elements (fig. 9a) is derived as following:

$$\begin{aligned} \frac{\varphi_{12} \cdot \pi \cdot A_1}{a^2} &= \sum_{i=1}^4 Z_i \sum_{j=1}^4 S_j \cdot \left\{ \frac{1}{2} \cdot X_j \cdot \sqrt{1 + Y_i^2} \cdot \arctan \left( \frac{X_j}{\sqrt{1 + Y_i^2}} \right) \right\} \\ &+ \sum_{i=1}^4 Z_i \sum_{j=1}^4 S_j \cdot \left\{ \frac{1}{2} \cdot Y_i \cdot \sqrt{1 + X_j^2} \cdot \arctan \left( \frac{Y_i}{\sqrt{1 + X_j^2}} \right) \right\} \\ &- \sum_{i=1}^4 Z_i \sum_{j=1}^4 S_j \cdot \left\{ \frac{1}{4} \cdot \ln(1 + X_j^2 + Y_i^2) \right\} \quad (13) \end{aligned}$$

For two perpendicular surface elements (fig. 9b) the view factor can be calculated by:

$$\begin{aligned} \frac{\varphi_{12} \cdot \pi \cdot A_1}{a^2} &= \sum_{i=1}^4 Z_i \sum_{j=1}^4 S_j \cdot \left\{ \frac{1}{8} \cdot (X_i^2 - Y_j) \cdot \ln(X_i^2 + Y_j) \right\} \\ &+ \sum_{i=1}^4 Z_i \sum_{j=1}^4 S_j \cdot \left\{ \frac{1}{2} \cdot \sqrt{Y_j} \cdot X_i \cdot \arctan \left( \frac{X_i}{\sqrt{Y_j}} \right) \right\} \quad (14) \end{aligned}$$

The parameters  $X_i, Y_i, Z_i$  and  $S_i$  in eq.(13) and in eq.(14) are summarized in table 4 and table 5, respectively.

Table 4: Parameters in equation (13)

	$X_i$	$Y_i$	$Z_i$	$S_i$
$i = 1$	$(f+d)/a$	$(g+e)/a$	+1	+1
$i = 2$	$(b-f)/a$	$g/a$	-1	+1
$i = 3$	$(b-f-d)/a$	$(c-g-e)/a$	-1	-1
$i = 4$	$f/a$	$(c-g)/a$	+1	-1

Table 5: Parameters in equation (14)

	$X_i$	$Y_i$	$Z_i$	$S_i$
$i = 1$	$(f+d)/a$	$[g^2 + (e+b)^2]/a^2$	+1	+1
$i = 2$	$(a-f)/a$	$[e^2 + (g+c)^2]/a^2$	+1	+1
$i = 3$	$(a-f-d)/a$	$[g^2 + e^2]/a^2$	-1	-1
$i = 4$	$f/a$	$[(g+c)^2 + (e+b)^2]/a^2$	-1	-1

For computing flow conditions accurately, the computational domain has to be divided into sufficiently small sub-zones. The fine discretization

results in a large number of surface elements. If the radiation equation, eq.(12), is applied to all the surface elements, a large storage capacity and a huge computing time are needed. Therefore, the so-called **macro-elements method** has been developed in this study, to improve the numerical efficiency.

The basic idea of the macro-elements method is to combine a few surface elements (micro-elements) to form one macro-element. The emissivity of all the surface elements which belong to the same macro-element is identical. The effective surface temperature of a macro-element is computed by the following equation:

$$T_i^4 = \frac{1}{A_i} \left[ \sum_{i \in I} A_i \cdot T_i^4 \right] \quad (15)$$

The subscripts 'i' and 'I' stand for micro-elements and macro-elements, respectively. After solving the radiation equation for the macro-elements, the net radiative heat flux of a micro-element can be determined by:

$$q_{r,i} = q_{r,I} + e_i - e_a \quad (16)$$

Numerical analysis shows that by a suitable selection of the macro-elements the additional error resulted by introducing the macro-elements method can be kept negligible small, whereas the storage needs and the computing time can be reduced significantly.

### 4.3 Numerical results

Figures 10a and 10b illustrate the calculated profiles of the air temperature and the air velocity at the channel outlet cross-section for the same condition as in figure 3. It can be seen that the calculated results agree well with the measured data.

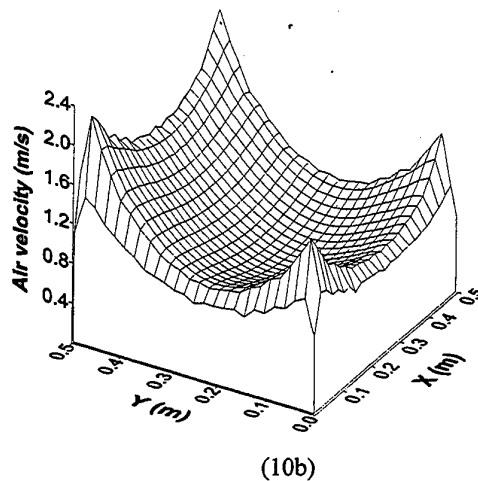
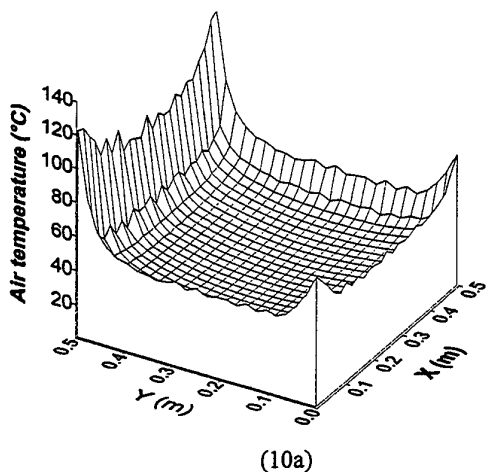
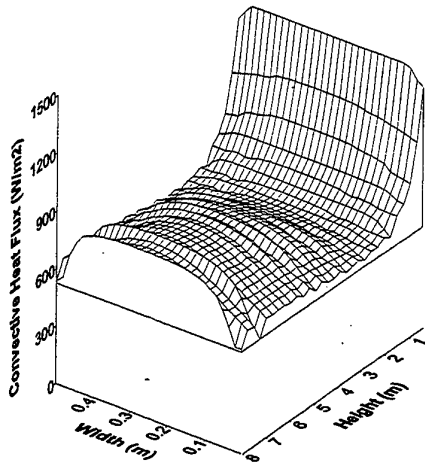


Figure 10: Profiles of the air temperature (10a) and air velocity (10b)

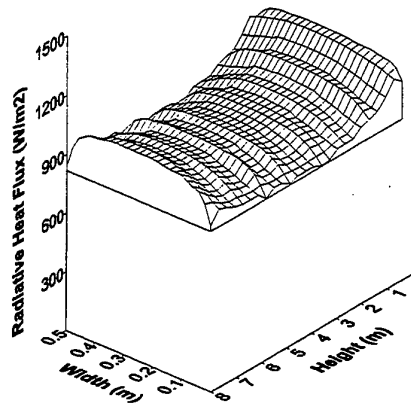
$$T_h = 150^\circ\text{C}, \varepsilon = 0.9, L = 0.5 \text{ m}, H = 8.0 \text{ m}$$

Figure 11 presents the profiles of the convective heat flux and the radiative heat flux at the heated wall. Due to the development of the boundary layer the convective heat flux in the inlet region is much higher than in the other regions, where the convective heat flux remains nearly uniform. Due to the radiative heat loss to the ambient surroundings the radiative heat flux in the inlet as well as in the outlet region is higher than in the middle region where the radiative heat flux has a well uniform distribution. It is also clearly seen that for the condition considered the heat power transferred from the heated wall by radiation is comparable to that transferred directly by natural convection.

Figure 12 shows the ratio of the heat power transferred from the heated wall by thermal radiation to the heat power transferred directly by convection versus the heated wall temperature for two different values of wall emissivity. At high wall emissivity ( $\varepsilon = 0.9$ ) the power ratio is larger than 1. In this case more heat is transferred from the heated wall by thermal radiation than by convection. The minimum value of the ratio is found by a heated wall temperature of about  $80^\circ\text{C}$ . At low wall emissivity ( $\varepsilon = 0.4$ ) the ratio of the radiative heat power to the convective heat power is still larger than 50%. The minimum of the ratio is also found by a heated wall temperature of about  $80^\circ\text{C}$ . This emphasizes the strong effect of thermal radiation on the overall heat transfer even at low values of wall emissivity and at low wall temperatures.



(11a) convective heat flux



(11b) radiative heat flux

Figure 11: Calculated convective and radiative heat flux at the heated wall

$$T_h = 150^\circ\text{C}, L = 1.0 \text{ m}, H = 8.0 \text{ m}, \varepsilon = 0.9$$

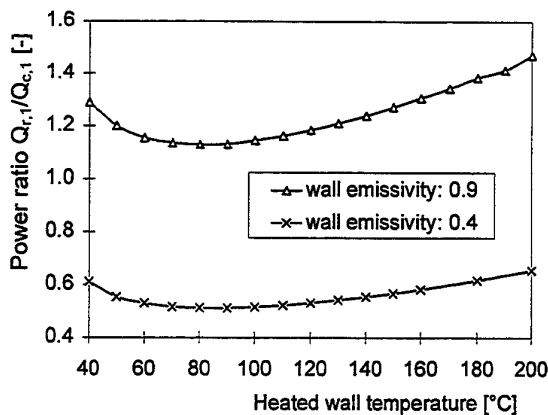


Figure 12: Power ratio versus the heated wall temperature

$$T_h = 150^\circ\text{C}, L = 0.5 \text{ m}, H = 8.0 \text{ m}$$

#### 4.4 Comparison with experimental data

Figure 13 compares the calculated air temperature and air velocity at the channel outlet cross-section along the middle line ( $X = 0.25 \text{ m}$ ) with experimental data. A good agreement between the numerical results and the experimental data has been obtained.

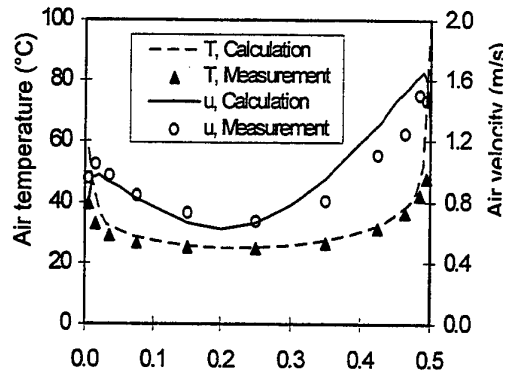


Figure 13: Comparison of the calculated air temperature and air velocity with the test data:

$$T_h = 150^\circ\text{C}, \varepsilon = 0.9, L = 0.5 \text{ m}, H = 8.0 \text{ m}$$

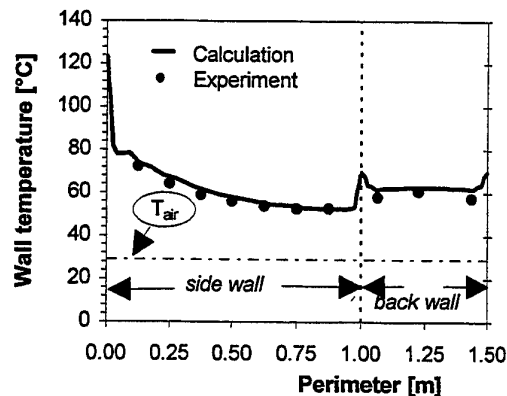


Figure 14: Temperature distribution on the back wall and on the side wall ( $Z = 3.8 \text{ m}$ ):

$$T_l = 150^\circ\text{C}, \varepsilon = 0.9, L = 0.5 \text{ m}, H = 8.0 \text{ m}$$

Figure 14 illustrates the measured and the calculated temperature on the side wall and on the back wall at the middle elevation. An excellent agreement between the experimental data and the numerical results has been found. The temperature on the side wall decreases with increasing the distance from the heated wall. Due to thermal radiation the temperature on all the unheated walls is much higher than the average air temperature at the same elevation.

Figure 15 compares the measured heat power with the calculated results for all test points obtained up to now. It is seen that for all test conditions the deviation between the measured and the calculated heat power is



less than 10%. Further analysis shows that the average heat flux at each individual heated plate can also be well reproduced by the FLUTAN code. The comparison above shows that the CFD code FLUTAN combined with the radiation model developed reproduces the experimental results accurately and is proven to be successfully verified for turbulent natural convection coupled with thermal radiation in a vertical, rectangular channel with asymmetric heating.

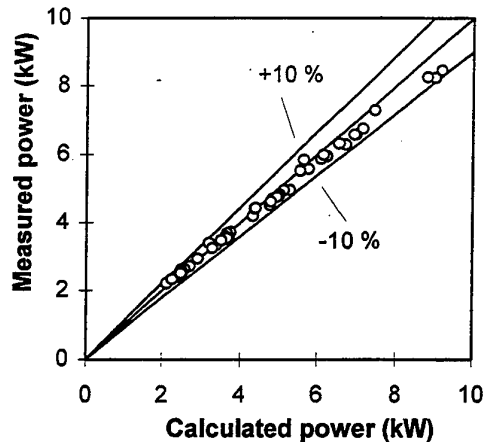


Fig. 15: Comparison of the measured with the calculated heating power

## 5 CONCLUSIONS

For future nuclear power plants the consequences of severe accidents must be limited to the near vicinity of the plant. To meet this new safety goal, the use of new innovative features, e.g. passive decay heat removal, is required in advanced water cooled reactors to ensure the containment integrity. One essential of the composite containment is its potential to remove the decay heat by turbulent natural convection of air coupled with thermal radiation. A thorough bibliographic survey underlines the deficiency in experimental as well as in theoretical studies on turbulent natural convection heat transfer coupled with thermal radiation in a three-dimensional vertical channel with asymmetrical heating. In the present study investigations have been performed for a better understanding and for looking insight of the flow and heat transfer behaviour in the system considered. The effect of the heated wall temperature, the wall emissivity and the channel geometry on the flow and heat transfer behaviour has been studied. A broad and detailed data base has been generated for the validation of computer codes and for development of physical models. A radiation model with high numerical efficiency has been developed. Analytical equations have been derived for calculating the view factor between any two surface elements. The so-called macro-elements method has been developed to improve

the numerical efficiency. The FLUTAN code combined with the radiation model developed has been proven to be an accurate and efficient numerical tool to investigate the flow and heat transfer behaviour of turbulent natural air convection coupled with thermal radiation in a vertical, rectangular channel with asymmetric heating. The present experimental and analytical research work within the PASCO program has shown that the passive containment cooling by natural air convection coupled with thermal radiation is a promising concept. At intermediate and high wall emissivities thermal radiation contributes significantly to the total heat transfer, even at low temperatures of the heated wall.

Future test series in the PASCO separate-effects program deal mainly with methods to improve heat transfer using turbulent promoters. Efforts will be continued to develop heat transfer correlations of turbulent natural convection coupled with thermal radiation in a vertical, rectangular channel with asymmetric heating.

## ACKNOWLEDGEMENT

This work was executed under the multi-partners research contract DABASCO (contract No. FI4S-CT96-0042) co-financed by the European Commission under the Euratom specific Nuclear Fission Safety programme 1994-1998.

## Nomenclature

A	: surface area, $m^2$
B	: channel width, $m$
$C_p$	: specific heat, $J/kg K$
E	: emitted heat power, $W$
e	: emitted heat flux defined as $\sigma \cdot \varepsilon \cdot T^4$ , $W/m^2$
g	: gravitational acceleration, $m/s^2$
H	: channel height, $m$
k	: kinetic energy of turbulence, $m^2/s^2$
L	: channel depth, $m$
O	: outgoing heat power, $W$
P	: pressure, $Pa$
Q	: heat power, $W$
q	: heat flux, $W/m^2$
Ra	: Rayleigh-number
T	: temperature, $^{\circ}C$
u	: velocity, $m/s$
X, Y, Z	: coordinates, $m$
$\beta$	: thermal expansion coefficient, $1/K$
$\varepsilon$	: emissivity or dissipation rate of kinetic energy, $m^2/s^3$
$\phi$	: view factor
$\lambda$	: thermal conductivity, $W/m K$
$\mu$	: dynamic viscosity, $kg/m s$

$\nu$  : kinetic viscosity,  $m^2/s$   
 $\rho$  : density,  $kg/m^3$   
 $\tau$  : shear stress,  $N/m^2$

Subscripts:

c : convection  
h : heated wall  
in : inlet cross-section  
r : radiation

References

- [1] Hennies, H.H., Kessler, G., Eibl, J., Improved Containment Concept for Future Pressurized Water Reactors, *International Workshop on Safety of Nuclear Installations of the Next Generation and Beyond, Chicago, IL, USA, August 28-31, 1989*
- [2] Peterson, G.P., Ortega, A., Thermal Control of Electronic Equipment and Devices, *Advances Heat Transfer, Vol.20 (1990), pp.281-310*
- [3] Borgers, T.R., Akbari, H., Free Convection Turbulent Flow within the Trombe Wall Channel, *Solar Energy, Vol.33, No.3/4, pp253-264*
- [4] Nishi, Y., Kinoshita, I., Study on Reactor Vessel Auxiliary Cooling System with High-Performance Heat Collector, *Proc. of Int. Conference on Fast Reactors and Related Fuel Cycles, Kyoto, Japan, October 1995, pp.12.6-1 - 12.6-9*
- [5] La Pica, A., Rodono, G., Volpes, R., An Experimental Investigation on Natural Convection of Air in a Vertical Channel, *Int. J. Heat Mass Transfer, Vol.36, No.3 (1993), pp.611-616*
- [6] Carpenter, R.J., Briggs, D.G., Sernas, V., Combined Radiation and Developing Laminar Free Convection between Vertical Flat Plates with Asymmetric Heating, *Journal of Heat Transfer, February 1976, pp.95-100*
- [7] Cheng, X., et al., Common Experimental Data Base for the Development of Physical Models and Correlations for Thermal-Hydraulic Containment Analysis (DABASCO), *FISA-97, Luxembourg, November 1997*
- [8] Grötzbach, G., Cheng, X., Development progress of the FLUTAN code for modelling heat transfer in LWR-systems (in german), *Proc. of Annual Meeting on Nuclear Technology '96, Mannheim, May 1996, pp.168-171*
- [9] Shah, V.L., et al., "COMMIX-1B: A Three-Dimensional Transient Single-Phase Computer Program for Thermal Hydraulic Analysis of Single and Multicomponent Systems", *NUREG/CR-4348 Vol.1 and Vol.2, 1985*
- [10] Hottel, H.C., Sarofim, A.F., *Radiative Transfer, McGraw-Hill, New York, 1964*

# RECENT PROGRESS IN THE EXPERIMENTAL INVESTIGATION OF FLOW AND LOCAL WALL HEAT TRANSFER IN INTERNAL COOLING PASSAGES OF GAS-TURBINE BLADES

H. Iacovides, D.C. Jackson, G. Kelemenis, B.E. Launder and Y-M Yuan

Department of Mechanical Engineering  
UMIST, Manchester, UK

## ABSTRACT

This paper reviews our recent experimental investigations of flow and heat transfer through passages relevant to gas-turbine blade-cooling applications. These are internal flows influenced by the presence of strong-curvature U-bends, surface rib-roughness and orthogonal rotation. The adaptation of LDA and the liquid-crystal techniques for the measurement of the detailed flow development and local wall heat transfer respectively, inside rotating passages of complex geometries is first presented. A series of data sets are then presented and discussed which show how strong curvature, rib-roughness and orthogonal rotation influence the mean and turbulent motion and their resulting effects on wall heat transfer. Tightly curved, round-ended U-bends generate strong secondary motion and cause flow separation at the bend exit, which substantially raise turbulence levels. Wall heat transfer is significantly increased, especially immediately downstream of the U-bend. The local heat-transfer around the perimeter of the passage is also found to vary considerably. In square-ended U-bends additional flow separation regions are found within the bend, while the size of flow separation at the bend exit is reduced. The enhancement of wall heat transfer is similar to that of the round-ended U-bend, but there are differences in the local variation. Orthogonal rotation, about an axis normal to that of the bend, further complicates the flow development in a square-ended U-bend by inducing additional flow features within and downstream of the bend. These additional features produce noticeable differences in wall heat transfer between the leading and trailing sides of the rotating passages. The introduction of surface ribs, results in a considerable increase in turbulence levels, a reduction in the size of the curvature induced separation bubble and a complex flow development after the bend exit with additional separation regions along the outer wall. Heat-transfer levels in the straight sections are more than doubled by the introduction of ribs. The effects of the bend on the overall levels of Nusselt number are not as strong as in the smooth U-bend, but are still significant. The effects of the bend on the variation of local heat-transfer coefficients within the ribbed downstream section are also substantial.

## 1. INTRODUCTION

The demand for improvements in the efficiency and power output of gas-turbines, has led engine designers to

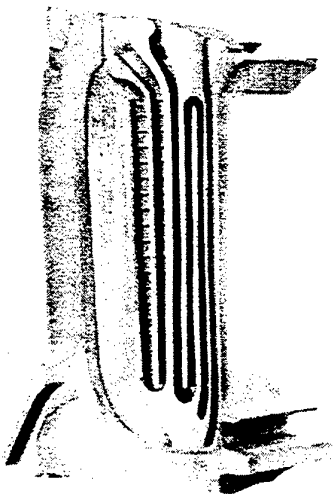


Figure 1. Sectioned turbine blade (courtesy of Rolls-Royce plc)

continuously seek to raise operating temperatures. In order to preserve the structural integrity of rotating blades, elaborate cooling systems have evolved in which relatively cool air is extracted from the compressor and, through the central shaft, is fed to cooling passages inside the turbine blades and nozzle guide vanes. As may be inferred from the sectioned high-pressure turbine blade, shown in Figure 1, the flow inside these cooling passages is complex and highly three-dimensional, influenced by the presence of sharp U-bends, artificial rib-roughness and also by the rotation of the blades. In order to optimise the cooling process, the engine designer needs to have accurate information on the detailed flow development and on its effects on local wall heat transfer. Because of the geometrical complexities of the cooling passages and the presence of rotation, most of the experimental heat-transfer data available until recently, though of considerable value, were nevertheless confined to averaged values. Due to the lack of detailed data on local flow and heat transfer, it has neither been possible to gain a clear understanding of the hydrodynamic and thermal behaviour in such passages, nor to develop and validate numerical flow solvers that can be reliably used for the simulation of blade cooling flows and the consequent thermal stresses that arise.

One of the main reasons for the lack of detailed flow measurements has been the fact that in order to reproduce

the engine operating conditions, while using air as the working fluid, experimental models have to rotate at high rotational speeds, thousands of revolutions per minute, which inevitably limits the size of the experimental models. For this reason, a rotating flow facility has been developed at UMIST, Figure 2, which uses water as the working fluid. As a result, engine conditions can be reproduced at

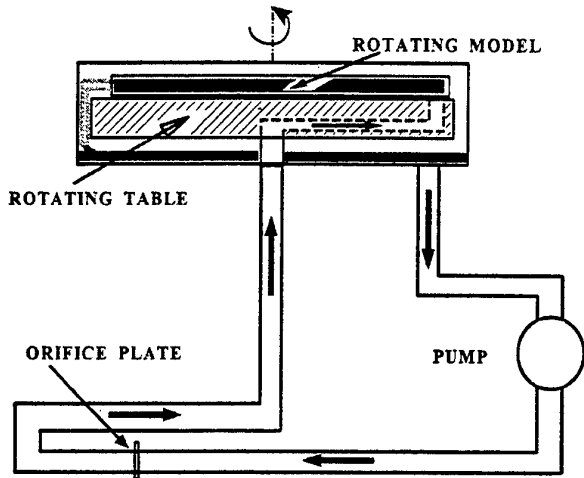


Figure 2. Rotating flow water rig

considerably lower rotational speeds, allowing the use of larger experimental models, with model cooling passages typically 50mm in diameter. This in turn, enables the collection of detailed flow and thermal data.

In this paper we provide an overview of our efforts to produce local flow and thermal data using this rotating flow facility. The methods developed will be described and the resulting measurements presented and discussed.

## 2. APPARATUS AND PROCEDURE

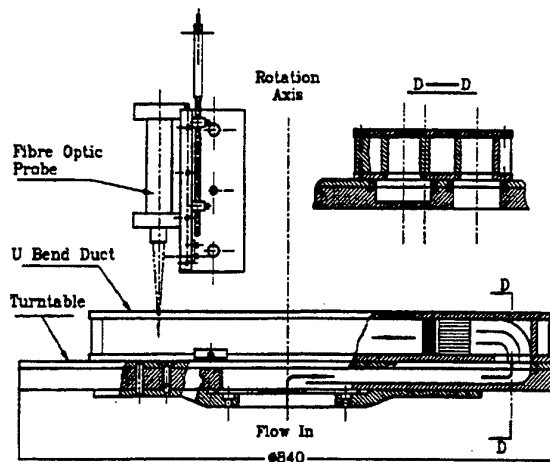
### 2.1 Apparatus

As shown in Figures 2 and 3, the rig consists of a motor-driven turntable mounted in a 1.22m diameter water tank. Experimental models of blade cooling passages are mounted on the turntable so that the axis of rotation is normal to the main flow direction, resulting in an orthogonal-mode rotation. Water is circulated in a closed loop system, where it is first pumped through a long orifice plate section. It then arrives, through a vertical pipe, below the centre of the rotating turntable and enters an internal passage built into the rotating turntable, through which it enters the experimental model mounted on the turntable. The outflow is exhausted into the open water tank. A combination of fine wire meshes and a honeycomb section is located at the entrance to the experimental model, to ensure uniform and symmetric entry conditions.

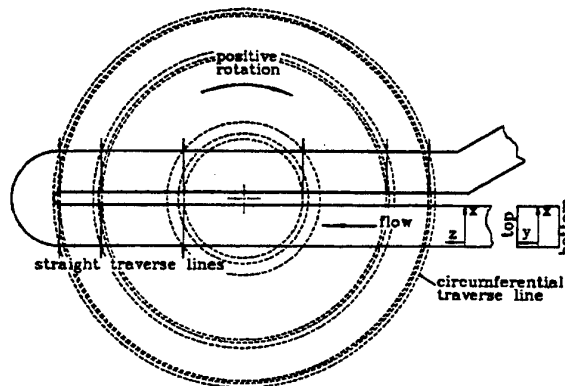
The turntable can be driven at any required speed, up to 250rpm in either direction. A feedback control circuit utilises the input from a rotary encoder on the drive shaft to control precisely the rotational speed.

### 2.1 Flow Measurements

The main problem that had to be addressed was how to gather data on the mean and fluctuating motions from a rotating model. As shown in Figure 3(b), this was accomplished through the use of a fibre-optic LDA system.



(a) Side View



(b) Top View with traverse lines

Figure 3. Rotating turntable

The system used is a TSI two-channel, four-beam fibre-optic system, with frequency shifting on both channels. A four watt Argon-ion laser was used to power the system and two counter processors (TSI 1980B) were initially used for signal validation, which were later replaced by a TSI IFA 655, digital burst correlator. Subsequent processing was done through a Zech data acquisition card on a PC. A stationary fibre-optic probe, of focal length 0.135m, positioned above the rotating model of a cooling passage, collected measurements of two components of the instantaneous velocity vector, with a coincidence window of 20 $\mu$ s, along circular traverse lines, as the experimental model rotated past it.

The circumferential location of each data point was indexed by an incremental rotary encoder mounted on the rotating drive shaft and, as more data points were collected with each rotation, an ensemble average was constructed

along each traverse line. An 1/8-degree resolution produced 2880 data bins per traverse line. A total of 60k-80k data points was gathered in each traverse. To obtain profiles along straight line traverse lines across each passage, either three, as shown in Figure 3(b), or two circumferential traverses were performed along close radial positions, so as to envelop the required straight line. The corresponding straight-line profiles were then obtained by interpolating the data of the enveloping circumferential traverses. For stationary models manual traverses were carried out. Further details of the LDA method can be found in [1] and [2].

## 2.2 Heat Transfer Measurements

For the heat-transfer investigations, it was decided that the liquid-crystal technique would be the most suitable for the mapping of the local Nusselt number along the walls of the rotating models. As it well documented [3] and [4], the molecular structure of thermochromic liquid crystals, over a certain temperature range, depends on temperature. Changes in molecular structure in turn affect the wavelength of visible light absorbed by the liquid crystals and hence, over a certain temperature range, the colour of the liquid crystals can be used to determine their temperature. In heat transfer experiments where air is the working fluid, most groups have adopted the transient liquid-crystal technique, in which the surface under investigation is covered with a layer of liquid crystals and is exposed to a hot air stream. As the surface temperature gradually rises from the initial ambient conditions, the movement of the colour contours of the liquid crystals along the surface is monitored. Then, at each location along the surface, from the time needed for the wall temperature to rise from its initial value to that of the crystal-colour-change temperature, the solution of the one-dimensional transient heat-conduction equation produces the value of the coefficient of wall heat flux,  $h$ .

In the case of water, the higher coefficients of heat transfer involved, lead to a substantially shorter thermal time constant ( $\tau = \rho_w c_{pw} k_w / h^2$ ). Surface temperatures thus rise too rapidly to measure accurately. The steady-state liquid crystal technique has therefore been adopted for our investigations and was used with both air and water as the working fluids. The surfaces of the experimental model are covered with a thin, electrically heated stainless steel foil, which provides a constant heat-flux thermal boundary condition. A thin layer of liquid crystals is then applied over the surface of the heating foil. Once steady thermal conditions are reached, the resulting colour contours are also contours of known wall temperature, determined through a prior calibration, under conditions of uniform wall heat flux. Electrical measurements provide the wall heat flux,  $q_w$  and, from the overall energy balance, the fluid bulk temperature,  $T_B$ , can also be determined.

$$m c_p (dT_B/dx) = A q_w \quad (1)$$

The local Nusselt number along each colour contour can then be calculated, since :

$$Nu \equiv (q_w D_h) / [k (T_w - T_B)] \quad (2)$$

By repeating the above procedure for a number of heating rates, detailed mapping of the local Nusselt number over each heated wall can be constructed.

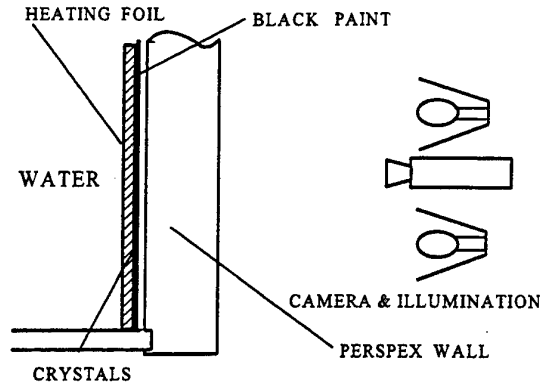


Figure 4. Arrangement of liquid crystals in water-cooled passages.

First a number of cases involving heat transfer in stationary passages, with air as the working fluid, were investigated. These enabled the software necessary for the digital processing of the images of the heated surfaces to be developed. In all cases, the liquid crystals employed, were micro-encapsulated crystals manufactured by Merck, with a nominal colour-change band between 29.5°C and 31°C, for the entire visible spectrum, and a nominal change of 0.1°C across the yellow colour, which was used to determine the wall temperature. At each heating rate, the image of the resulting colour contours was recorded using a CCD camera, digitized and stored on a PC. The digitized image was then converted into a hue-saturation-and-intensity format and the pixels with a hue value corresponding to that of the yellow colour were identified. Software developed for this study then corrected the co-ordinates of the selected pixels, accounting for distortions caused by the camera lens and angle. The information from each image was thus reduced to provide the co-ordinates of the constant-wall-temperature contour. The value of  $h$  along the contour line was then calculated, using equations (1) and (2). Finally, the contour lines produced by different heating rates were brought together and, through interpolation, the continuous variation of the Nusselt number over the heated surface was produced.

With water as the working fluid, because of the higher heat fluxes involved, the time required for thermally steady conditions to be reached is greatly reduced, but considerably higher power levels are needed. Moreover, the nominally waterproof liquid crystals employed, were found to absorb water, which made the resulting images unclear. The 15µm thick stainless-steel foil selected for these investigations was able to produce power density levels up to 80kW/m<sup>2</sup>, which preliminary calculations showed to be necessary. In order to prevent exposure of the liquid

crystals to the water, the arrangement shown in Figure 4 was employed, in which the liquid crystals were enveloped between the stainless steel foil and the perspex wall of the passage. The colour contours were viewed through the perspex wall, by a camera located opposite to the heated wall. As can also be seen in Figure 4, illumination, necessary for the colour contours to become visible, was provided by two power efficient halogen lamps on either side of the camera. This arrangement was first tested for water flow through a heated stationary passage.

For the rotating passages the additional problems of supplying the electrical power and recording the resulting images in a rotating frame of reference had to be addressed. As can be seen in Figure 5, six power slip rings were used to transmit the electrical power to different sections of the heated model, each one capable of transmitting up to

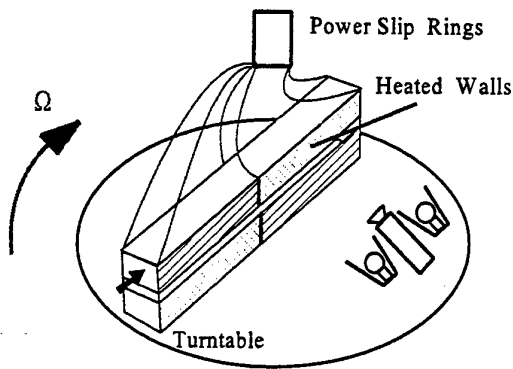


Figure 5. Heating and monitoring arrangements for rotating passages.

2.5kW. The camera was also mounted on the rotating turntable and its signal was fed to a PC through separate slip rings. The illumination lamps were powered through slip rings, from a heavy duty battery.

### 2.3 Cases Examined

All the idealised blade-cooling passages examined so far are of a square cross-section. As shown in Figure 6, Cases I, II and III, passages with round-ended U-bends with and without ribs were first investigated. In these passages, the axis of rotation was parallel to the curvature axis of the U-bend, thereby producing a symmetry plane at the mid-plane of the passage. More recent investigations have focused on square-ended U-bends, Cases V and VI in Figure 6, in which the axis of rotation is normal to that of the bend curvature.

LDA measurements have been obtained for Cases I, II and III under stationary and also for the rotating conditions indicated in Figure 6, for a flow Reynolds number of 100,000 and a rotation number ( $Ro = \Omega D / W_b$ ) of 0.2, and also, for Cases V and VI, under both stationary and rotating conditions for the same Reynolds and rotation numbers.

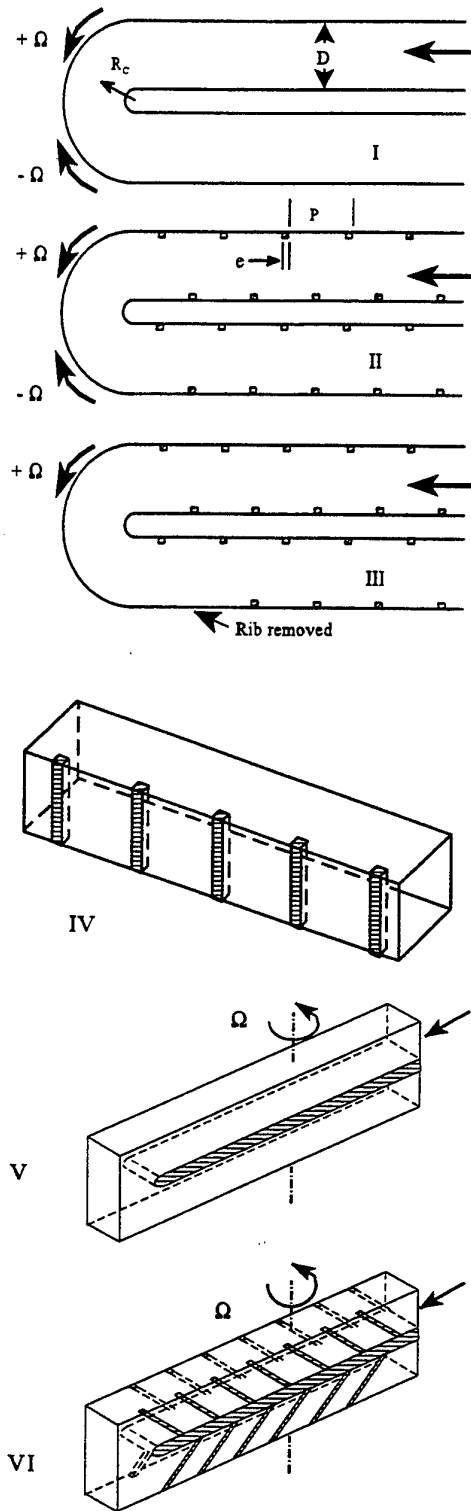


Figure 6. Cases Examined

Heat-transfer measurements have been obtained for Cases I, II and III under stationary conditions only, using air as the working fluid, for Case IV, again, only under

stationary conditions using water and for cases V and VI under both stationary and rotating conditions, using water. In Cases I to III only the inner and outer walls were heated. In case IV only the ribbed wall was heated, while in cases V and VI only the two vertical walls, as shown in Figure 6, were heated.

For all U-bends the curvature ratio at the inner wall,  $R_{in}/D$ , was 0.15. In all cases, the ribs used were of a square cross section. The ratio between the rib height and the duct diameter  $e/D$  was 0.1 and the ratio between the distance between adjacent ribs and the rib height,  $P/e$  was 10. In case VI, the ribs were inclined at an angle of  $45^\circ$  to the main flow direction.

In addition to the LDA and the thermal measurements, flow visualisation tests were also carried out and for some cases static pressure measurements were also obtained.

### 3. PRESENTATION AND DISCUSSION OF RESULTS

Due to space limitations only a representative sample of the results obtained can be presented here.

#### 3.1 Flow Measurements

The vector plots of Figure 7 show the flow development for Case I under stationary conditions. The primary influence on the flow development is exerted by the strong streamwise pressure gradients that develop at the bend entry and exit planes. At the bend entry there is a strong acceleration along the inner wall, while along the outer wall the flow is decelerated, with the deceleration becoming stronger near the corner between the flat, top, and the outer walls. As the flow progresses through the bend, the flow along the outer wall becomes faster. Along the inner wall, the strong adverse pressure gradient at the bend exit influences the upstream flow development and by the  $90^\circ$  location the flow

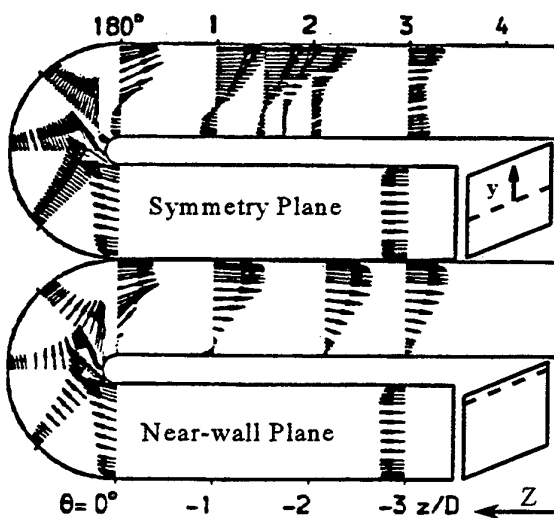


Figure 7. Mean flow development for Case I, under stationary conditions.

along the symmetry plane begins to separate. Because of the strong secondary motion generated by curvature, the flow

within the bend becomes strongly three-dimensional. Along the flat walls, fluid is convected from the outer to the inner side of the bend, which, as can be seen in Figure 7, delays flow separation along the inner side. The separation bubble along the inner wall reaches its maximum width at the bend exit and, along the symmetry plane, persists up to approximately two diameters downstream of the bend exit. The outer wall fluid is strongly accelerated at the bend exit. Along the top wall, due to the effects of the secondary motion, reattachment occurs earlier, but after reattachment the flow recovers more slowly.

The flow development along the symmetry plane for Cases II and III, also under stationary conditions, is shown in Figure 8. This shows how the presence of ribs normal to the flow direction, placed in a staggered arrangement along

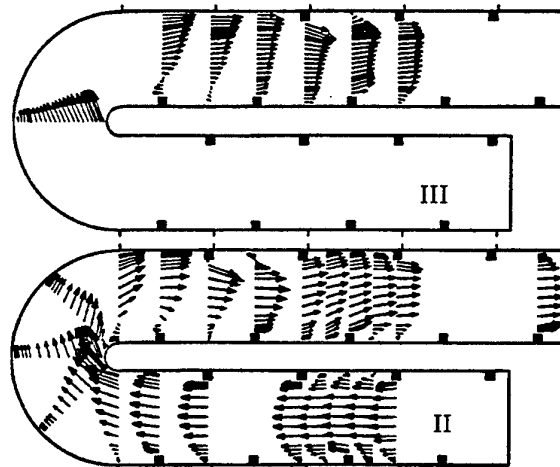


Figure 8. Mean flow development along the symmetry plane for Cases II and III, under stationary conditions.

the inner and outer walls of the straight sections, influences the flow development. The vector plots for Case II show that the presence of ribs along the upstream section delays the flow separation along the inner wall of the bend, while the ribs in the downstream section promote earlier reattachment, at about one diameter downstream of the bend exit. The first rib along the outer wall after the bend exit also appears to be especially influential. As the high momentum fluid along the outer wall encounters this first downstream rib, a large separation bubble is formed downstream thereof, extending over the entire rib interval. The measurements for Case III reveal that removal of this first downstream rib displaces this separation bubble one diameter further downstream, and also reduces its size. But along the inner wall the curvature-induced separation bubble is lengthened, extending as far as the second downstream rib.

The additional effects of orthogonal rotation about an axis parallel to that of the bend can be seen in Figure 9, for

both positive and negative rotation. For the former, Coriolis and curvature forces re-enforce each other while, for negative rotation, they oppose each other. For both directions of rotation the vectors along the first traverse line

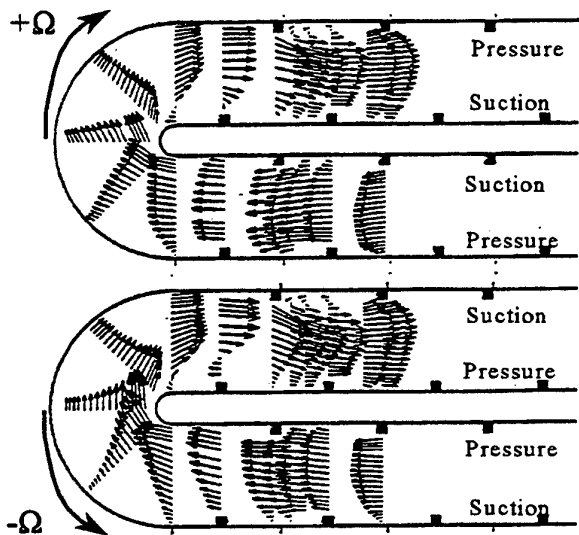


Figure 9. Mean flow development along the symmetry plane for Case II, under rotating conditions.

in the upstream section, about two diameters before the bend, show that, along the symmetry plane, the faster fluid is transported to the pressure side of the rotating passage. As earlier work on rotating passages with smooth walls has shown, [5] and [6], this is the result of the Coriolis-driven secondary motion. It consequently appears that even in straight passages with ribbed surfaces, the effects of orthogonal rotation cannot be ignored. The flow development within the bend is also strongly affected by rotation. Because positive rotation displaces the faster fluid towards the outer wall, it leads to a more uniform velocity distribution within the bend, while negative rotation has the opposite effect. Figure 9 also shows that positive rotation causes a reduction in the size of the curvature-induced separation bubble along the inner wall. The slower fluid that positive rotation causes to be convected to the inner wall is better able to follow the wall curvature. Negative rotation on the other hand, has the opposite effect. Consequently, even when the curvature and rotation axes are parallel, the interaction between curvature and rotation is still influential.

The effects of rib roughness and rotation on turbulence can be seen in the profiles of streamwise turbulence intensities for Case II, in Figure 10. The profiles at the upstream location,  $z/D=0.45$ , reveal that the presence of ribs generates turbulence levels that are substantially higher than those encountered in smooth passages. This is, of course, the reason why ribs are introduced to blade cooling passages. The high turbulence levels upstream of the bend are responsible for the delayed flow separation along the inner wall. Within and downstream of the bend, turbulence levels increase even further, especially in regions

of flow separation. On the whole, rotation does not exert a strong influence on turbulence intensities in these ribbed passages. Both positive and negative rotation enhance turbulence levels in the core of the U-bend. Downstream of

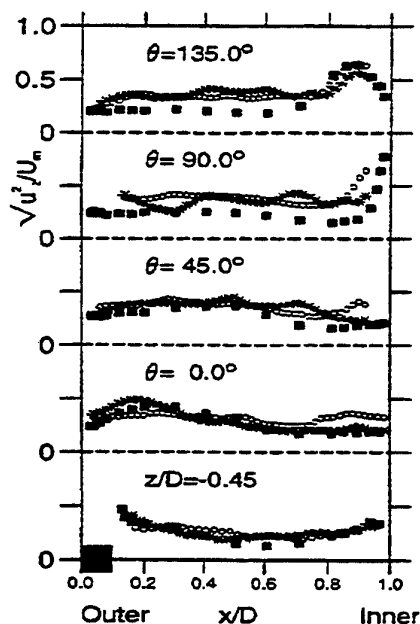
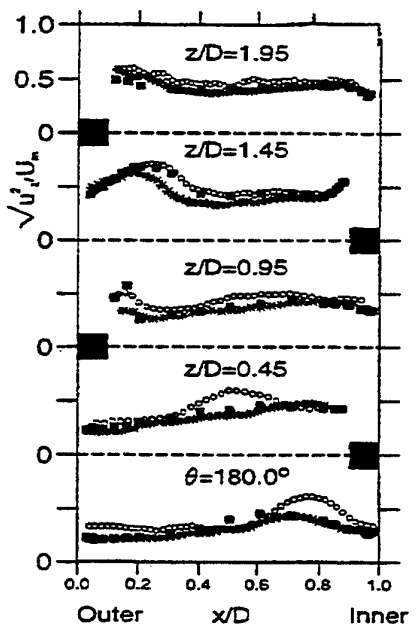


Figure 10. Streamwise turbulent intensities along the symmetry plane for Case II.

■ ■ ■ :  $Ro=0$ , \* \* \* :  $Ro=0.2$ , ○ ○ ○ :  $Ro=-0.2$

the bend, negative rotation increases turbulence levels in certain regions, while with positive rotation, turbulence intensities are somewhat reduced. These trends are broadly in agreement with what has been reported for U-bends with smooth walls [1], though, in the absence of ribs, the effects of rotation on turbulence are stronger.



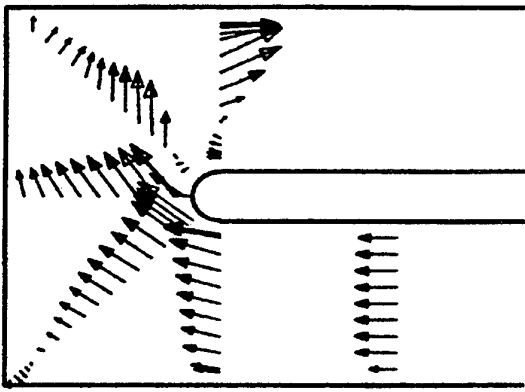


Figure 11. Mean flow development along the geometrical symmetry plane for Case V.

second half of the bend, imposing an overall acceleration on the flow.

Vector plots on a plane normal to the geometric symmetry plane, half-way between the inner and outer walls, shown in Figure 12, reveal that within the bend the flow becomes non-symmetric. Flow visualisation tests, using dye injection, revealed that the corner separation bubbles make the flow within the square-ended U-bend unstable, which destroys the flow symmetry. Downstream of the bend, however, flow symmetry is restored. The curvature-induced secondary motion transports the faster fluid to the near-wall (vertical wall) regions, leaving the slower fluid in the duct centre. Measurements of turbulence levels, not shown here, reveal that in the exit region of the square-ended U-bend, turbulence levels are higher than those found in a round-ended U-bend [1].

When the passage rotates orthogonally about an axis

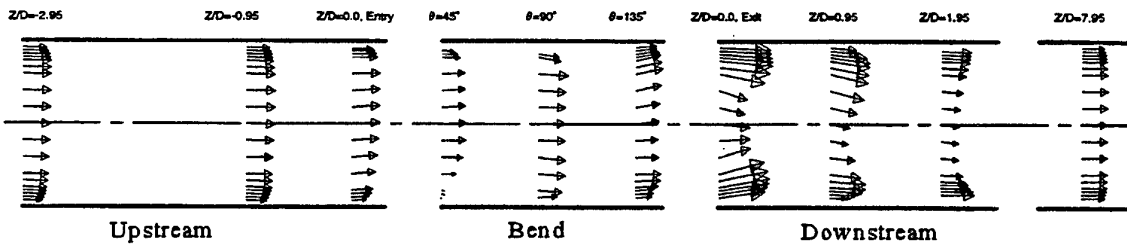


Figure 12. Mean flow development along circumferential mid-plane for Case V

The geometry and mode of rotation of real blade cooling passages are closer to those shown in Cases V and VI, where the U-bend is square-ended and the axis of rotation is normal to that of curvature. Figure 11, shows the mean flow development along the geometrical symmetry plane of such a smooth passage, under stationary conditions. Additional separation bubbles are formed at the corners. The curvature-induced separation bubble along the inner wall, is considerably smaller than that observed in the smooth round-ended U-bend in Figure 7, because in this geometry, the effective cross-sectional area reduces over the

normal to that of curvature, the geometrical symmetry plane is no longer (even ideally) a plane of flow symmetry. Vector plots obtained at the 90° location of the bend, shown in Figure 13, indicate that a strong vortex is formed along the leading side of the rotating passage, which, as far as the upstream flow is concerned, is the high suction side. Dye injection tests have also confirmed the presence of this vortex, which starts near the leading side (which for the upstream flow is the suction side) of the rotating passage, but over the second half of the bend, as also shown in Figure 13, it crosses to the trailing side, which in the downstream

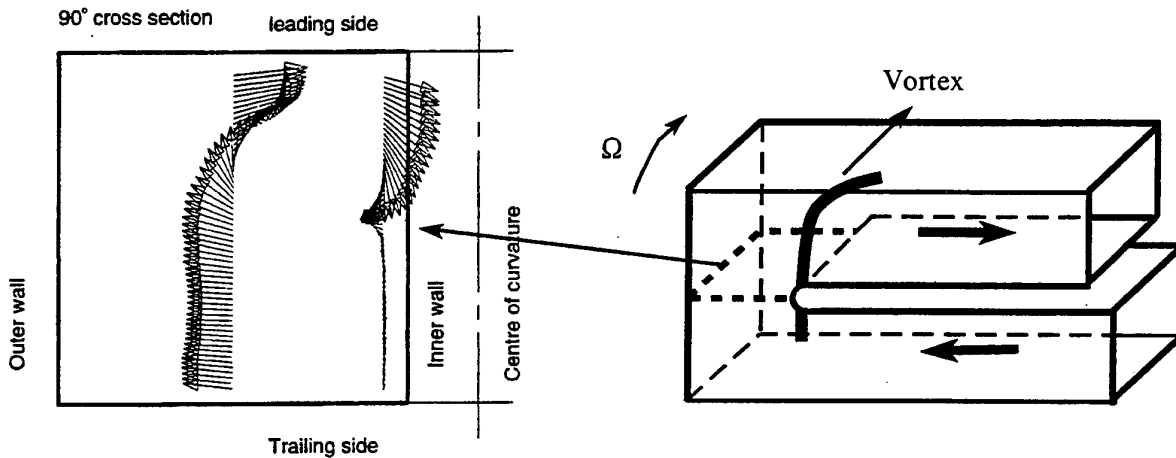


Figure 13. Secondary motion at the 90° plane of a rotating square-ended U-bend, Case V

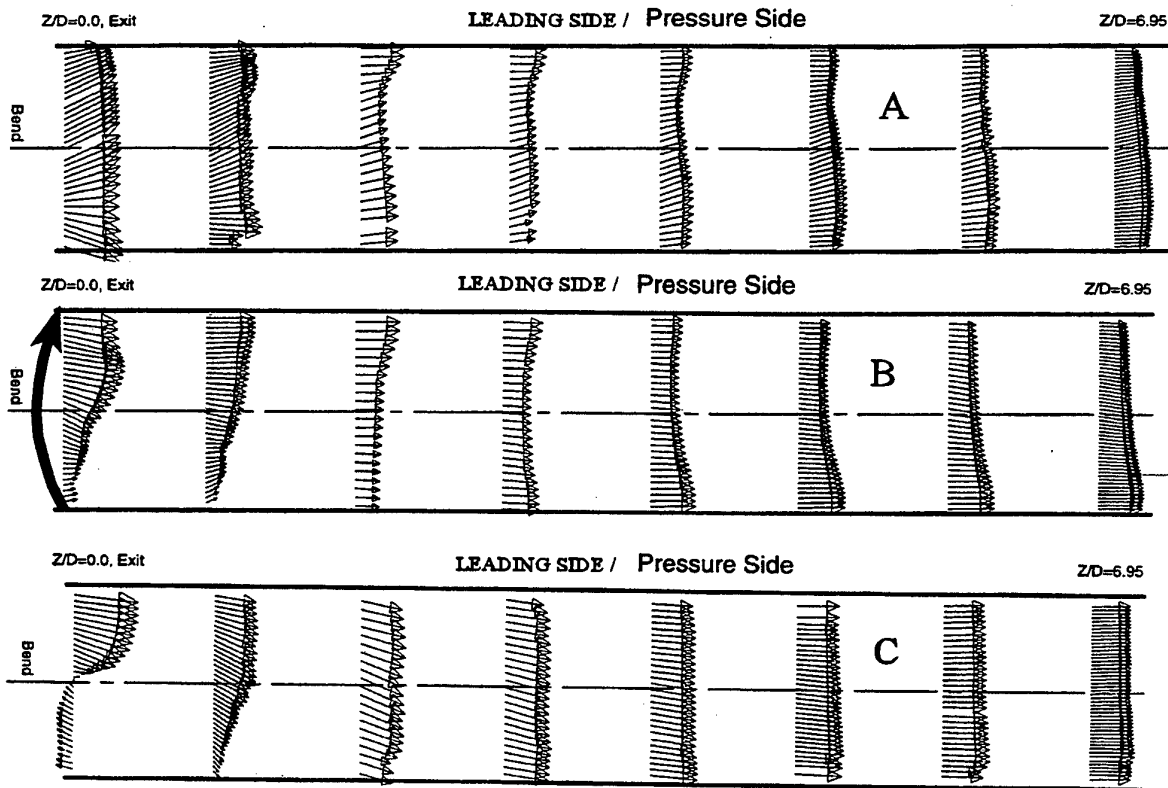
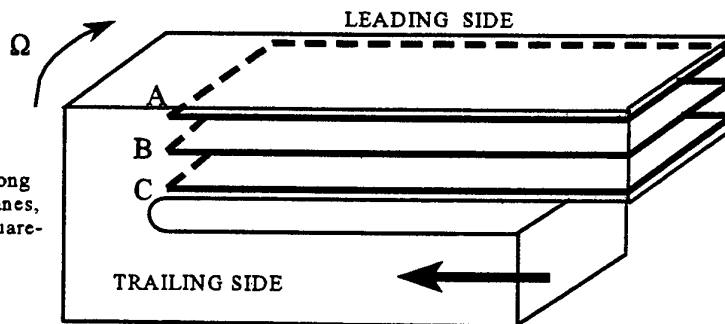


Figure 14. Mean flow development along indicated circumferential planes, downstream of a rotating square-ended U-bend, Case V.



region becomes the suction side.

The flow development in the downstream region, is mapped in detail in the vector plots of Figure 14. At the exit plane along the inner wall the flow separates along the trailing (now the suction) side, while along the leading side the flow is strongly accelerated. At the middle of the exit plane there is no flow separation along the trailing side, though there is still a considerable increase in velocity across the duct, from the trailing to the leading side. Near the outer wall, the velocity is uniformly high across the duct. The cross-duct motion at the exit plane indicates that a single streamwise vortex is present, which along the inner wall and the duct centre convects the fluid from the leading to the trailing side, and along the outer wall returns the fluid to the leading side. This is consistent with the single vortex found at the  $90^\circ$  plane. Because of this secondary motion,

the flow along the leading side re-attaches in less than one diameter downstream of the bend exit and further downstream the faster fluid is transported from the leading to the trailing side which, in the downstream section is the suction side. Even after seven diameters from the bend exit, the faster fluid is still along the suction side, which is the opposite from what is found in fully developed flow in a rotating straight duct. It may thus be concluded that when the Coriolis and curvature forces are normal to each other, the resulting flow is not only more complex than when the two forces are in the same direction, but that the effects of the bend on the flow persist further downstream.

The LDA investigations have thus shown the effects of strong curvature and rib-roughness on the flow development through cooling passages. the influence of orthogonal rotation (with the Coriolis and curvature forces both parallel and normal to each other) and also the effects

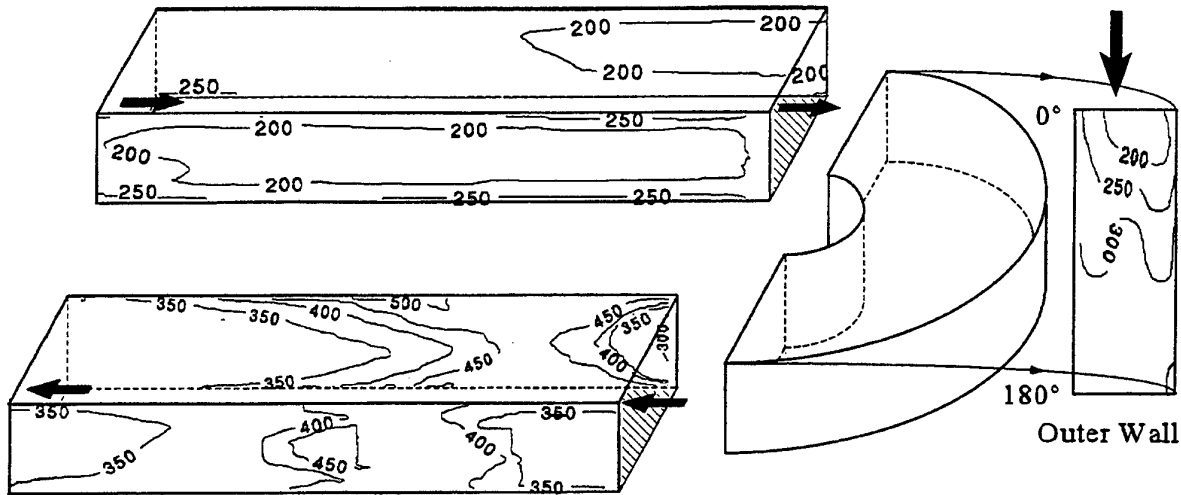


Figure 15. Nusselt number contours for air flow in a stationary round-ended U-bend, Case I.  $Re=95,000$  and  $Pr=0.71$

of round- and square-ended U-bends. The next question to be addressed is how these flow features influence the local wall heat transfer.

### 3.2 Heat-Transfer Measurements

The influence of strong curvature on local wall heat transfer can be seen in the Nusselt number contours for Case I, under stationary conditions using air as the working fluid, Figure 15. Only the inner and outer walls were heated. In the upstream section, Nusselt-number levels along both walls are fairly uniform and close to the value returned by the Dittus Boelter correlation:

$$Nu=0.023 Re^{0.8} Pr^{0.4} \quad (3)$$

Within the U-bend heat transfer levels rise along the outer wall, with the maximum level at each axial location

occurring at the centre line of the outer wall. The general rise in Nusselt number is consistent with the flow acceleration along the outer wall, as shown in Figure 7. The higher heat transfer levels along the centre line of the outer wall, are most probably caused by the secondary motion, which in the centre of the passage convects cool fluid to the outer wall. As the fluid near the outer wall is heated, it is transported to the corner regions, leading to a reduction in the heat transfer coefficient in the two corners. Downstream of the bend, along the outer wall, heat-transfer coefficients continue to rise reaching a maximum value more than twice that prevailing upstream, at about three diameters after the bend exit. As can be seen in [1], the location of the maximum wall heat transfer coincides with the region where the highest turbulence levels along the outer wall have been measured. Beyond this point, as the flow along the outer wall starts to slow down and the turbulence levels begin to reduce, Nusselt numbers also start to diminish.

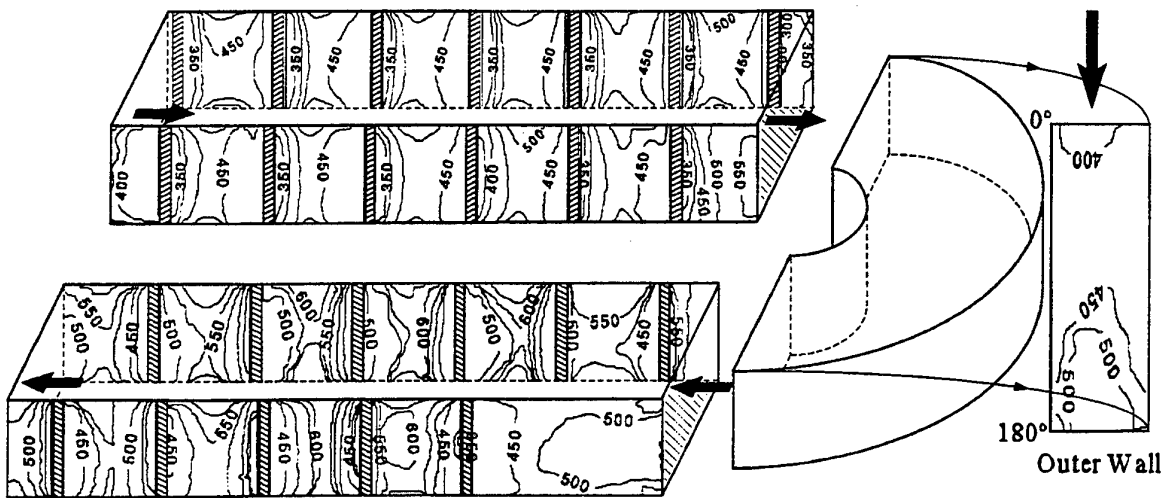


Figure 16. Nusselt number contours for air flow in a stationary round-ended, ribbed U-bend, Case III.  $Re=95,000$  and  $Pr=0.71$

Even after six diameters from the bend exit, however, the Nusselt number is still more than 50% higher than that upstream. Along the inner wall, Nusselt number levels rise very rapidly after the bend exit, reaching their maximum values, similar to those along the outer wall, about two diameters after the exit, which is very close to the reattachment point, Figure 7. In contrast to the measured distribution along the outer wall, along the inner wall, the Nusselt numbers in the corner regions are higher than those on the centre line. This is also consistent with the curvature-induced secondary motion which, along the thermally insulated top and bottom walls, transports relatively cool fluid to the corner regions of the inner wall. As this fluid is heated by the inner wall it moves towards the duct centre, causing a strong reduction in wall heat transfer. At about three diameters downstream of the bend, the variation in Nusselt number between the centre line and the corner regions, at the inner wall, is about 60%. As the flow begins to recover after re-attachment Nusselt number levels along the inner wall begin to decrease, though, as for the outer wall, even after six diameters from the bend exit, they are still significantly higher than those of the upstream region. The strong streamwise changes in the mean flow and the rise in turbulence levels caused by the tight U-bend thus lead to substantial increases in wall heat transfer. Moreover, curvature-induced secondary motion, as well as contributing to the increase in wall heat transfer, also influences the distribution of the local Nusselt number on the inner and outer walls. The influence of the bend on heat transfer is still significant after six diameters from the bend exit.

The effects of rib-roughness on heat transfer can be seen in the Nusselt number contours of Figure 16, for Case II, under stationary conditions, using air as the working fluid. Again, only the inner and outer (now ribbed) surfaces were heated. The ribs were made of perspex and the heating foil underneath the ribs was short circuited. The rib surfaces could thus be considered as thermally insulated. In the upstream section, there appear to be enough rib intervals for thermal conditions to repeat themselves over each interval. Nusselt numbers become highest in the middle of each rib interval, by which point, according to the LDA data of Figure 8, the flow has re-attached, after separating behind the upstream rib. Nusselt number levels in the corner regions are higher than in the centre of each wall, probably because the top and bottom walls are thermally insulated. The actual levels of wall heat transfer are two to three times higher than those in the smooth U-bend (Case I). This substantial increase in heat transfer must be related to the high levels of turbulence caused by the presence of ribs, as shown in Figure 10. Within the bend, heat-transfer levels display a monotonic rise along the outer wall but, in contrast to the smooth U-bend, Nusselt number levels along the centerline are higher than those in the corners. The levels of heat transfer along the outer wall are higher than the corresponding levels for the smooth U-bend, but not as high as the highest levels encountered in the ribbed upstream sections. Downstream of the bend, along the outer wall, heat-transfer levels fall after the first diameter, where, as

shown in Figure 8, the flow along the outer wall starts to decelerate. Over the first downstream rib interval along the outer wall, where a large separation bubble is generated, the Nusselt number rises to levels higher than those encountered upstream of the bend. Heat transfer levels gradually fall, over the subsequent rib intervals, tending towards the levels measured in the upstream section. Along the inner wall, over the first downstream rib interval, which is partially within the bend-induced separation region, heat-transfer levels are especially high in the corner regions. Over the two subsequent rib intervals, the Nusselt number rises even further, to levels higher than those along the outer downstream wall. Beyond the third downstream rib, heat-transfer coefficients begin to fall towards those of the upstream sections.

The overall effect of the U-bend and of the ribs on wall heat transfer, can be more easily assessed through the plots of the side-averaged Nusselt numbers, shown in

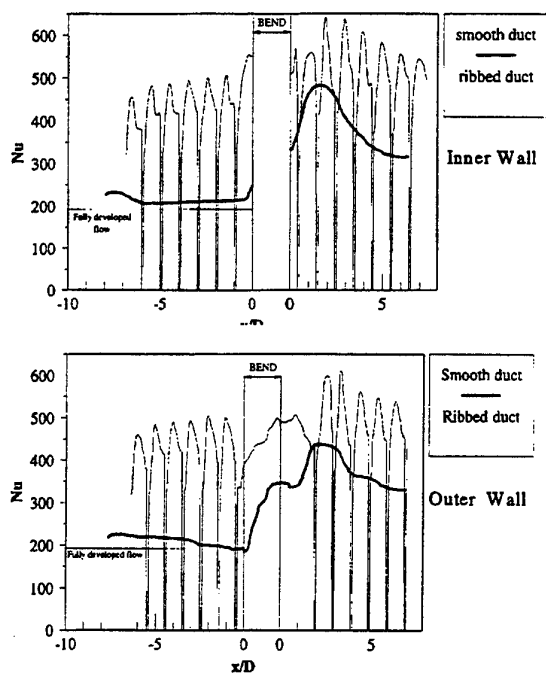


Figure 17. Development of the side averaged Nusselt numbers along inner and outer walls, for the round-ended U-bend with and without ribs, Cases I and III

Figure 17. As expected, the introduction of ribs raises the levels of the heat-transfer coefficient in the upstream section by more than a factor of 2. The round-ended U-bend still influences heat transfer levels downstream of the bend, especially along the inner wall, but its effects are not as strong as in the smooth U-bend.

Attention is now turned to the use of water as the working fluid. The first case examined, Case IV, was that of flow through a straight duct, with only one ribbed wall. The ribbed wall was also the only heated wall. The ribs were made of pure copper and were affixed to the duct

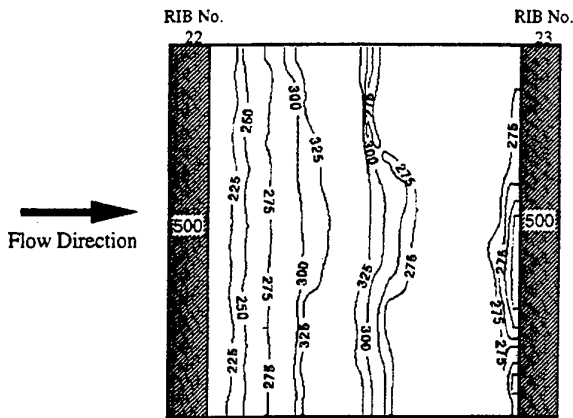


Figure 18. Nusselt number contours for water flow in a stationary, straight channel, case IV.  $Re=40,000$ ,  $Pr=5.45$

walls, over the heating foil. The ribs were electrically isolated from the heating foil, with a layer thin enough to introduce only a small thermal resistance. The rib can thus be considered to provide constant temperature surfaces, given the high thermal conductivity of copper. The total rate of heat transfer from the surfaces of each rib exposed to the water may be considered the same as the heat generated by the area of the heating foil underneath each rib. Because the passage was long enough for repeating flow and thermal conditions to develop over each rib interval, measurements are presented for only one, in the form of Nusselt number contours, shown in Figure 18. These contours show that, as in Case III, the Nusselt number rises from the rib corner at the upstream end of the rib interval, to a maximum value at about  $0.4D$  from the rib corner. After a minor reduction the Nusselt number remains constant over the second half of the rib interval, showing a further, moderate rise near the downstream rib. Thermocouples embedded in the copper ribs, reveal that the average Nusselt number over the rib surfaces, with a value of 500, is about 60% higher than the average Nusselt number over the inter-rib surface.

The distribution of the side-averaged Nusselt number over the rib interval is also compared with one produced at Rolls-Royce Bristol [7] using a passage of identical geometry but with air as the working fluid, at a Reynolds number of 122,000. The Dittus-Boelter equation has been used to scale the results of the Rolls-Royce study, to account for the differences in Prandtl and Reynolds numbers. As can be seen in Figure 19, the scaled results are in close agreement.

The method was subsequently applied to the square-ended U-bend with smooth walls, Case V. Only the two vertical walls, as shown in Figure 6, were heated. Because of the heating arrangements, a thin strip in the middle of the bend remained unheated. The resulting Nusselt-number contours for stationary and rotating conditions, at a Reynolds number of 30,000, are displayed in Figure 20. Under stationary conditions, they show that, as also seen in the round-ended U-bend, in the upstream section, the

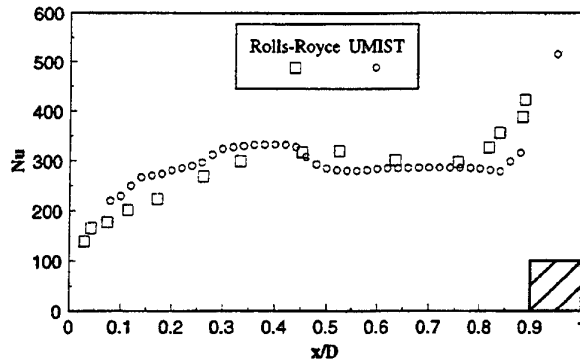


Figure 19. Comparison of profiles of the side-averaged Nusselt numbers for Case IV, with water (UMIST) and air (Rolls-Royce) as the working fluids.

Nusselt number is uniform. Its level is about 25% higher than that returned by the experimental correlation recommended by Kays [8] for fluids with Prandtl numbers between 1 and 20, Equation (4), for fully-developed flow at this Reynolds and Prandtl numbers.

$$Nu = 0.0155 Re^{0.83} Pr^{0.5} \quad (4)$$

The turbulence levels measured in the upstream section are, however, also higher than those encountered in fully-developed flow in a straight duct.

Nusselt numbers rise within the U-bend. Over the first half of the bend, the highest levels being along the end-wall corner. Higher turbulence levels due to flow separation at the corner are the most probable cause. The levels of Nusselt number rise even further over the second half of the U-bend, especially at the bend exit where peak levels are twice as high as the upstream values. These high values persist for the first downstream diameter, where the LDA measurements have shown that the secondary motion transports the high momentum fluid to the heated walls, and then they gradually reduce. Even after four diameters, however, they are still higher than the upstream values.

Under rotating conditions, along the leading side, ( $Ro=-0.2$ ), heat transfer levels in the upstream section (which for the leading side is the suction side), are found to increase in the corner regions. This is consistent with the expected, Coriolis-driven, secondary motion, which, along the unheated walls, would transport cooler fluid to the corner regions of the leading side, as shown in Figure 20. At the bend entry, there is an abrupt rise in heat-transfer coefficient, which is markedly stronger than that observed in the stationary case. Two regions of local maxima are formed over the first half of the U-bend, one near the inner wall and one along the end-wall corner. These higher levels of  $Nu$  in the bend entry region of the leading side, are consistent with the strong vortex that was found in the LDA and flow-visualisation experiments in this region, shown Figure 13.

Over the second half of the bend region, where the

vortex is observed to turn away from the leading the high levels of heat transfer near the inner wall disappear and the higher heat transfer regions are now along the end-wall and outer-wall corners. The region of low Nusselt number near the inner-wall corner, at and downstream of the bend exit, coincides with the region over which, according to the LDA

measurements in Figure 14, the cross-duct motion is directed away from the leading side. Similarly, the higher Nusselt number levels measured along the outer wall corners over the same region, appear to be caused by the fact that near the outer wall, the cross-duct motion is directed towards the leading side. Further downstream of the

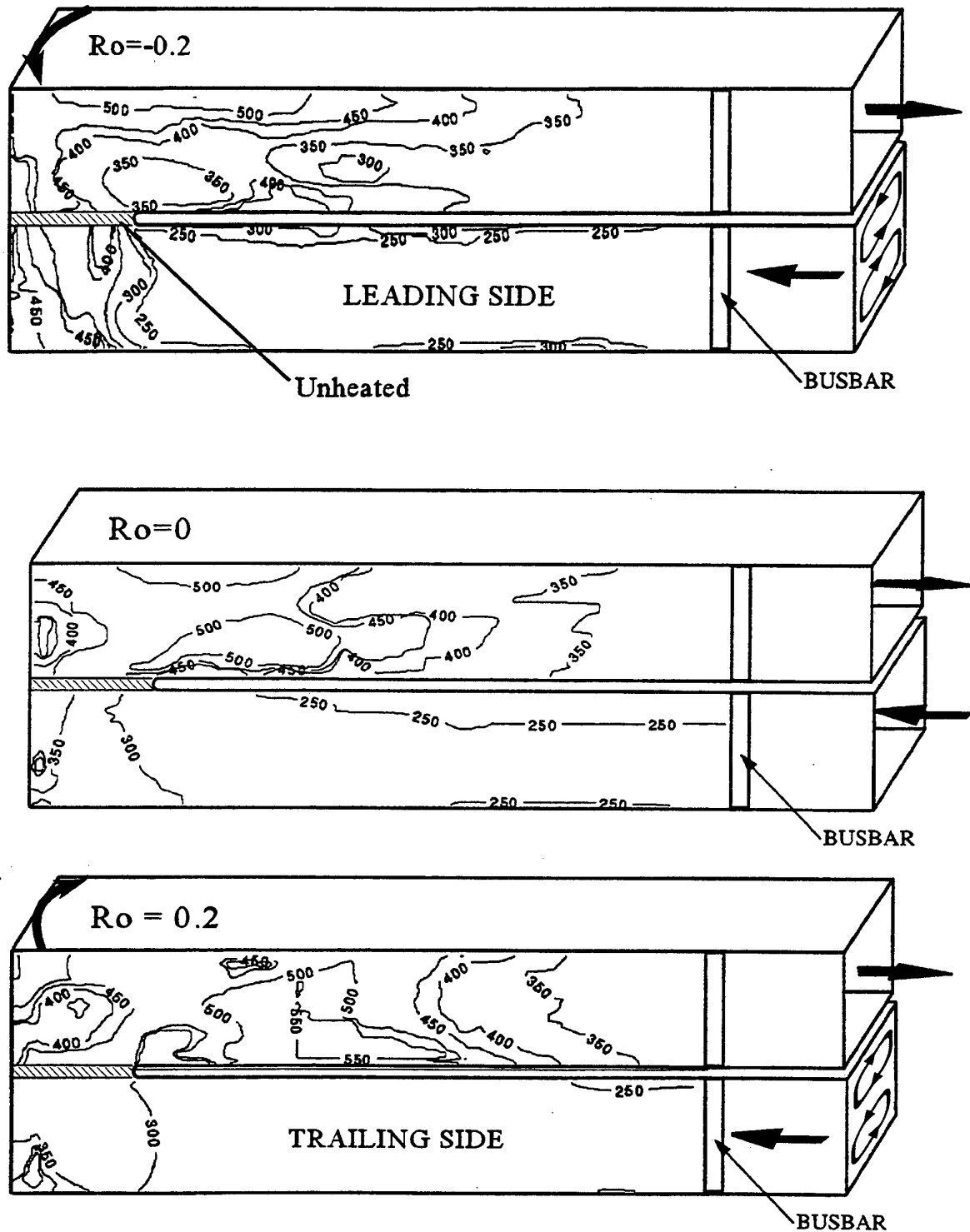


Figure 20. Nusselt number contours for Case V.  $Re=30,000$  and  $Pr=5.9$

bend exit, beyond the first two diameters, in contrast to the stationary case, Nusselt number levels in the middle of the leading side are lower from those in the corner regions. As can be seen in Figure 14, along the leading side, after the first two downstream diameters, the flow along the inner wall is faster than that along the mid-plane. While the flow near the outer wall, over the same region, does not appear to be faster than that along the mid-plane, LDA data, not presented here, show that near the outer wall, the turbulence intensities along the cross-duct direction are higher than those near the mid-plane.

Along the trailing side, heat-transfer levels in the upstream section (for which the trailing side is the pressure side) are uniform and, over the first half of the bend, the increase in Nusselt number is not as strong as that observed at the leading side (or even in the absence of rotation). This is also consistent with the LDA measurements and flow visualisation observations within the U-bend, shown in Figure 13. Over the second half of the bend, there is a

trailing side appears to be similar to that on the stationary side, though the actual levels are different. This is probably because the flow development along the trailing side of the rotating square-ended U-bend is similar to that for the stationary case. One notable difference is, of course, the larger curvature-induced separation bubble at the bend exit, for the trailing side which causes the higher Nusselt number levels in the downstream region. The distribution of the local Nusselt number along the leading side of the rotating U-bend is, on the other hand, different from that of the stationary case for two reasons in particular: the formation of the strong vortex at the bend entry and the fact that, at the bend exit, instead of flow separation, there is strong flow acceleration along the inner wall.

The variation of the side-averaged value of the Nusselt number along the square-ended U-bend, under both stationary and rotating conditions, presented in Figure 21, enable us to quantify more easily the effects of curvature and rotation on wall heat transfer. For the stationary case, the

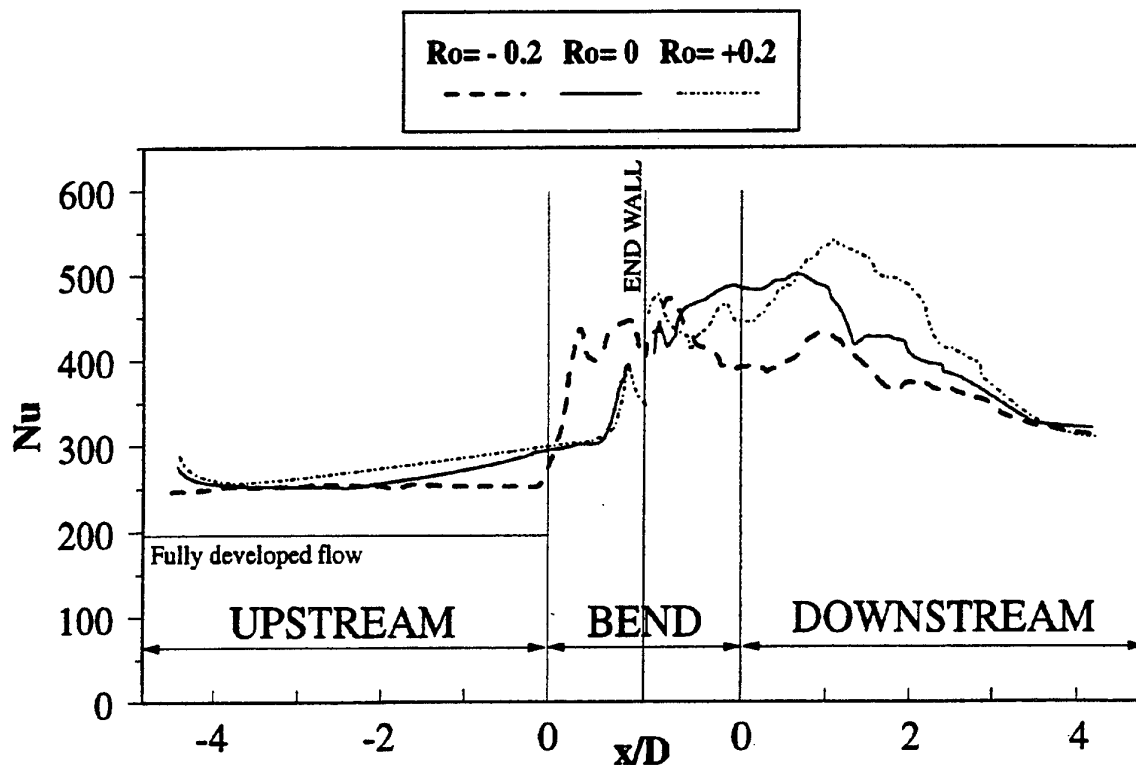


Figure 21. Side-averaged Nusselt number for Case V.  $Re=30,000$  and  $Pr=5.9$

marked rise in Nusselt number as the vortex turns from the leading to the trailing side. At, and immediately downstream of, the bend exit the effects of the separation bubble along the inner wall, shown in the measured vector plots in Figure 14, are clearly evident. When the flow re-attaches, at about one diameter from the bend exit, a further increase in local Nusselt number takes place, resulting in values higher than those measured either along the leading or the stationary sides.

The variation of local Nusselt number along the

U-bend raises the Nusselt number levels by a factor of two, compared to the upstream values. This maximum level is reached at about 0.6 diameters after the bend exit. Even after four diameters downstream of the bend exit, Nusselt numbers are about 20% higher than those upstream. Rotation effects on the Nusselt number upstream of the bend appear to be small, though, as expected, heat-transfer coefficients are augmented along the pressure side ( $Ro=0.2$ ) and attenuated along the suction side ( $Ro=-0.2$ ). The reason for this apparently weak influence of rotation on wall heat

transfer is the short length of flow development upstream of the bend, about  $10D$  in total, and the uniform velocity distribution produced by the honeycomb section and wire meshes. Consequently, the boundary layers do not have a sufficient length of flow development. The Coriolis-induced secondary motion therefore, which arises from the non-uniformity of velocity across the duct, does not become as strong as in fully-developed flow in a rotating duct. Within the first half of the U-bend, as noted in the local Nu contours of Figure 20, heat-transfer coefficients along the leading side show a rapid rise, 35% higher than for the stationary case, while along the trailing side the Nu levels follow those of the stationary case. Over the second half of the U-bend and over the first diameter downstream, Nusselt-number levels along the trailing side become lower than those of the stationary case by about 20% because of the absence of flow separation. Along the trailing side over the second half of the duct and the first four diameters downstream (as noted earlier) the thermal development is similar to that of the stationary case. However, because of the larger separation bubble at the inner wall, the peak heat-transfer coefficient occurs further downstream (after one diameter from the bend exit) and is about 10% higher than that of the stationary case.

These comparisons for the square-ended U-bends with smooth walls, have shown how the local flow features caused by strong curvature and orthogonal rotation directly influence the local Nusselt number. The primary influence appears to be that of curvature, increasing the coefficient of local wall heat flux by as much as a factor of 2. Even with a short length of upstream flow development, which does not allow the Coriolis-driven secondary motion to reach its full strength, the effects of orthogonal rotation on the local wall heat transfer within and downstream of the square-ended U-bend cannot be ignored. Differences between the Nusselt number levels along the leading and trailing sides are as high as +45% within the U-bend and -25% downstream.

#### 4. CONCLUDING REMARKS

The rotating flow test facility described, can uniquely produce data on the local flow and thermal development in rotating passages of complex geometries. The resulting measurements provide a series of data sets suitable for the validation of numerical flow solvers used in the computation of flow and convective heat transfer through blade-cooling passages, reveal the mean and turbulent flow features that develop under the influence of strong curvature, rib-roughness and orthogonal rotation and also how the fluid motion determines the local thermal behaviour.

In smooth passages, strong curvature, in addition to generating strong secondary motion, also leads to regions of strong favourable and adverse pressure gradients, most notably at the bend exit, where flow separates along the inner wall and strongly accelerates along the outer wall. Flow separation causes a substantial increase in turbulence levels, especially over the first three downstream diameters. The secondary motion and the higher turbulence levels

increase the Nusselt number through the bend, with the peak values, along both the inner and outer walls, reached between two and three diameters after the bend exit. Moreover, the secondary motion induces strong perimetral variations in Nusselt number along both the inner and outer walls. Bend effects on heat transfer remain appreciable even after seven diameters from the exit. In a square-ended U-bend, additional separation regions are formed in the bend corners, but separation along the inner wall at the bend exit is reduced because of the flow acceleration caused by the effective reduction in cross-sectional area. The effects of the square-ended U-bend on heat transfer along the continuous flat walls are equally as strong as those of the round-ended U-bend on the inner and outer walls. Because of the smaller separation bubble at the bend exit, the Nusselt number reaches its peak level closer to the bend exit, though still in the downstream region. Orthogonal rotation, about an axis normal to that of the bend, leads to significant modifications in the flow development through the square-ended U-bend. A strong axial vortex is formed near the leading side at the bend entry which subsequently crosses to the trailing side at the bend exit. As a result, a single, rather than a symmetric double vortex structure appears at the bend exit, increasing the size of the inner-wall separation bubble along the trailing side and flow along the leading side not only suppressing separation but also accelerating the inner. These rotation-induced features have a notable effect on local wall heat transfer. Along the leading side, the strong vortex produced within the bend by rotation raises wall heat transfer at the bend entry, while the suppression of flow separation at the bend exit reduces the Nusselt number in the downstream region.

The introduction of ribs substantially raises turbulence levels which, for the case of the round-ended U-bend, reduce the size of the separation bubble along the inner wall. The flow development downstream of the bend becomes very complex, as the flow, highly distorted by the bend, encounters ribs along the inner and outer walls, and is also found to be sensitive to the distance of the first downstream ribs to the bend exit. Wall heat transfer is substantially raised within the bend and also within the upstream and downstream sections. While the effects of the U-bend on heat transfer levels are not as strong as in the case with smooth walls, they are nevertheless still significant. Furthermore, the effects of the bend on the perimetral variation in Nusselt number after the bend exit are also highly evident.

The non-linear nature of the laws that govern the fluid motion lead to the development of complex flow patterns in blade cooling passages, which can neither be anticipated nor deduced by simply combining the separate effects of rotation, strong curvature and rib roughness. Detailed experimental data, or use of reliable flow solvers is thus necessary. Further work is currently in progress providing data for flow and heat transfer through U-bend with angled ribs, Case VI in Figure 6.



## Acknowledgements

Funding for the work presented has been provided by the EPSRC, ABB(Switzerland), EDF(France), EGT, and Rolls-Royce plc. The authors gratefully acknowledge both the financial and technical support received. The authors also acknowledge technical support provided by Mr D. Cooper, Mr J Hosker and Mr M. Jackson. Finally the contribution of the authors' former colleagues Drs S.C. Cheah and H H Ji is gratefully acknowledged.

Authors' names are listed alphabetically.

## References

1. Cheah S C, Iacovides H, Jackson D C, Ji H H and Launder B E, 1996, "LDA Investigation of the Flow Development Through Rotating U-ducts", ASME Journal of Turbomachinery, **118**, 590-596.
2. Iacovides H, Jackson D C, Ji H, Kelemenis G, Launder B E and Nikas K, 1998, "LDA Study of the Flow Development Through an Orthogonally Rotating U-Bend of Strong Curvature and Rib-Roughened Walls.", ASME Journal of Turbomachinery, 120, 366-391.
3. Baughn J W and Yan X, 1992, "Local Heat Transfer Measurements in Square Ducts with Transverse Ribs", ASME HTD-Enhanced Heat Transfer, **202**, 1-7
4. Jones T V, Wang Z and Ireland P T, 1992, "Liquid Crystal Techniques", ICHMT, Int Symp. on Heat Transfer in Turbomachinery, Athens, Greece.
5. Hart J E, 1971, "instability and Secondary Motion in a Rotating Channel Flow.", J Fluid Mechanics, **45**,341-351
6. Iacovides H and Launder B E, 1991, "Parametric and numerical study of fully-developed flow and heat transfer in rotating rectangular ducts.", ASME Journal of Turbomachinery, **113**, 331-338, .
7. G Purchase 1991, Personal Communication.
8. Kays W M, Convective Heat and Mass Transfer, McGraw-Hill.

# EXPERIMENTAL AND NUMERICAL STUDY OF DEVELOPED FLOW AND HEAT TRANSFER IN COOLANT CHANNELS WITH 45 AND 90 DEGREE RIBS

B. Bonhoff  
S. Parneix  
J. Leusch  
B. V. Johnson

ABB Corporate Research Ltd  
Baden- Dättwil, Switzerland

J. Schabacker  
A. Böls

Swiss Federal Institute of Technology  
EPFL-LTT  
Lausanne, Switzerland

## ABSTRACT

The flow characteristics within coolant channels, typical of those employed in coolant channels of airfoils in large gas turbines, were investigated experimentally and numerically to assess current capability of Navier-Stokes codes to predict flow and heat transfer in coolant passages. The assessment was made for developed flows in a stationary square coolant channel with square ribs at 45 and 90 degrees to the duct centerline, with rib heights of 10 percent of the channel height and with a Reynolds number of 50,000. A stereoscopic digital PIV measurement system was assembled to simultaneously measure all three-velocity components in narrow sheets. The stereoscopic arrangement was chosen because of the highly three-dimensional turbulent nature of the flow in the coolant channels. The instantaneous PIV data were averaged to obtain the three mean velocities and the six Reynolds stresses. Velocity and heat transfer distributions were calculated for developed flow in one segment of the ribbed channels by applying cyclic boundary conditions. The calculations were made with three sets of wall and turbulence models: 1) a standard  $k-\epsilon$  turbulence model with wall functions, 2) a differential-Reynolds-stress turbulence model with wall functions and 3) a standard  $k-\epsilon$  turbulence model with a two-layer wall model. The comparison between the measurements and predictions for the 90-degree rib configuration showed that the flow predictions were within the accuracy of the measurements for all turbulence models. The comparison for the 45-degree rib configuration showed differences greater than the measurement uncertainty. It was suspected that the flow was not fully developed at the comparison location in the experiment. The heat transfer and friction predictions for the selected numerical boundary conditions were compared to correlations for a similar configuration found in the literature. The comparison showed that the RSM results were more consistent than the  $k-\epsilon$  results with and without wall functions.

## 1 INTRODUCTION

Advanced gas turbines are designed to operate with high efficiency to decrease fuel consumption as well as the pollution of the environment. The theoretical efficiency of the gas turbine cycle rises with higher turbine pressure ratios and more importantly with higher turbine inlet temperatures. The maximum turbine inlet temperature is limited by the availability of blade material that can withstand such high temperatures and stresses. During the last 50 years a considerable increase of the turbine inlet temperature has been achieved, e.g. Lakshminarayana (1). Modern materials can withstand temperatures of 1100 to 1300K. Present gas turbines operate at turbine inlet temperatures of approximately 1500 to 2000K or more. Effective cooling is applied to the turbine components that are exposed to the hot stream. For this, a combination of internal and external cooling methods is typically employed to lower the mean blade temperature to allowable values.

For the internal cooling of the blades, the coolant is passed through a multi-pass circuit from hub to tip and ejected at the trailing edge or the blade tip. The straight sections of these coolant passages are connected by 180° bends. To enhance heat transfer, the walls are

roughened by ribs or pin fins that lead to complicated flow patterns in the passage. Numerical heat transfer predictions are not yet sufficiently accurate for design purposes that are dominated by complex turbulent transport processes. This is especially true for the complicated heat transfer patterns in the turning region of stationary or rotating coolant passages with rib roughened walls. To improve the performance of the CFD codes that will be used to evaluate a cooling configuration, a validation of the predictions is necessary and detailed measurements of the flow structure in the passages are required for comparison. The studies described in this paper support one gas turbine developer's efforts to understand and model the internal cooling with the expectation that better mathematical modeling will decrease airfoil design time and produce an airfoil that uses an optimally small amount of coolant flow.

### 1.1 Background information for Numerical Heat Transfer and modeling of internal coolant passages

Thus, far most of the published numerical effort has been directed toward obtaining heat transfer predictions in smooth stationary and rotating coolant channels.

Reviews of the efforts to predict heat transfer in these channels were presented by Iacovides and Launder (2) and by Prakash and Zerkle (3). The reader is referred to their reviews for details of previous work and to Bo et al. (4) for a general discussion of the code algorithms and turbulence models. Most of these predictions have been compared to averaged heat transfer results without accompanying flow velocity and turbulent transport data.

Less data has been available for the comparison of the velocity and turbulent transport characteristics for flow in coolant channels with ribs. The data available was generally obtained with LDV or hot wires and was limited to traverse locations along the centerline of the passage and a limited number of other locations. Previous experiments to define the flow characteristics and to provide data for CFD evaluation have included LDV measurements in rotating and stationary two-pass passages by Cheah et al. (5) and Iacovides et al. (6). Liou and Chen (7) recently performed LDV measurements of the developing flow through a smooth duct with a 180° straight-corner turn. Tse and Steuber (8) reported 3D LDV measurements in rotating square serpentine coolant passage with skewed ribs.

Mixed numerical and experimental investigations were presented by Abuaf and Kercher (9) for a large scale model of a gas turbine blade containing a three-pass serpentine with ribs normal to the flow direction. The computations were performed using a  $k-\epsilon$  turbulence model with standard wall functions. Prakash and Zerkle (10) predicted flow and heat transfer in a ribbed rectangular duct with and without rotation, using a high Re number  $k-\epsilon$  turbulence model with standard wall functions. Selected comparisons with correlations from the literature for stationary passages and with results from proprietary rotating experiments for rotation numbers of 0.0, 0.06 and 0.12 were satisfactory.

Bonhoff et al. (11) and (12) presented a numerical / experimental comparison of the heat transfer in a two pass serpentine. These investigations included flow and heat transfer in the straight sections and the bend regions of cooling channels with smooth walls and walls with rounded ribs at an angle 45 degree to the flow direction. The results for stationary and rotating mode were compared to experiments presented by Wagner et al. (13) and Johnson et al. (14). For the calculations, the FLUENT code was used with the  $k-\epsilon$  model, the RNG variation of the  $k-\epsilon$  model and the differential Reynolds stress model. One important conclusion from these papers was that results using the differential Reynolds stress model were consistently closer to the experimental data than those obtained using the standard or the RNG  $k-\epsilon$  models. This was especially true for the turn region where the flow separates.

The velocity and turbulent transport characteristics, and therefore the heat transfer characteristics, in coolant passages with ribs are also believed to be influenced by the shape of the ribs, especially the curvature at the root and crown of the rib

and the angle of the rib to the mean flow direction. The present investigation is limited to ribs with sharp corners that are typical of those in large electrical producing gas turbines.

## 1.2 Background information on the PIV Measurement technique

In the present study, the particle-image-velocimetry (PIV) method was employed for the investigation of the flow field in a model of a stationary coolant passage. PIV was chosen because of the high data acquisition rate and the good spatial resolution of the measured flow fields. These advantages, compared to LDV, are obtained because the PIV measurement obtains data from a plane in the flowfield rather than a point. The reader is referred to Grant (15) for a more references on the PIV measurement technology and a detailed discussion of the requirements for the setup of PIV experiments.

The PIV measurement technology has limitations and operational difficulties. The measurements of highly three-dimensional flow with a single-camera PIV system could have substantial errors because the out-of-plane motion of a particles perpendicular to the light sheet plane produces a systematic measurement error that increases with increasing distance from the optical axis, e.g., Lourenco (16). An error correction for the in-plane components is feasible if the out-of-plane component of the flow is known. Schabacker and Böls (17) applied the correction to single-camera 3D PIV velocity measurements and showed that the effect of the out-of-plane motion can not be corrected completely, although the correction improves the measurement accuracy.

Several measurement uncertainties can be avoided with a stereoscopic PIV optical arrangement. Prasad and Adrian (18) describe several optical and operational arrangements. Westerweel and Nieuwstadt (19) have reported performance tests on three-dimensional velocity measurements with a digital two-camera stereoscopic PIV system.

For the present investigation, a stereoscopic digital PIV system that employs the angular displacement method and commercially available devices was assembled. No modifications to the cameras were made. The small amount of defocusing of the images towards the edges was found to have a minor influence and was tolerated. The system is capable of measuring simultaneously all three velocity components. Subsequently, an ensemble average of the velocity data in identical spatial windows is calculated leading to the mean and fluctuating velocity field.

## 2 DESCRIPTION OF EXPERIMENT

A sketch of the test section is shown in Figure 1. Air was chosen as the working medium because heat transfer experiments will be conducted in the same facility in the near future. A continuously running

compressor supplies the air to the test rig. Upstream of the test-rig, the mass flow rate is measured by means of an orifice meter. The air enters the settling chamber with an inner diameter of 600 mm via a 150-mm tube and a conical entrance section with an angle of 30°. The settling chamber is equipped with a combination of perforated plates, honeycombs and meshes to reduce unsteadiness and swirl in the flow. For the PIV experiments, 1-3  $\mu\text{m}$  oil droplets generated by a Polytec L2F-A-1000 Aerosol Generator are injected upstream of the settling chamber to guarantee a homogeneous seeding density in the test section.

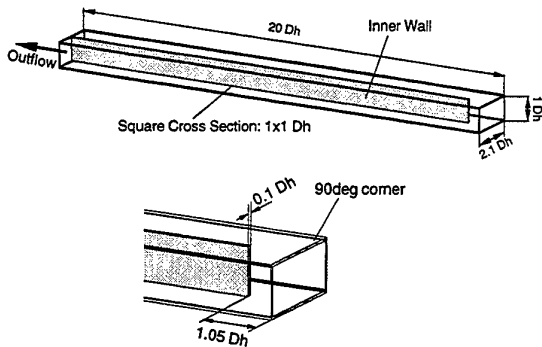


Figure 1 The internal coolant passage test facility

A modular concept was chosen for the test section design that allows an easy exchange of the components. Presently, the test rig is equipped with a model of a two-pass cooling passage of a gas turbine blade. The flow path in the downstream and upstream leg has a cross-section of  $100 \times 100 \text{ mm}^2$  with a corresponding hydraulic diameter  $D_h = 100 \text{ mm}$  and a length of  $19 D_h$ . The test section is made of 5-mm thick float glass to obtain good optical properties for the PIV experiment. The thickness of the divider plate is  $0.1 D_h$ . The total section including the section entrance can be turned  $90^\circ$  around the x-axis without changing the flow conditions in the duct. This allows an easy optical access to the positions of interest for the PIV measurements.

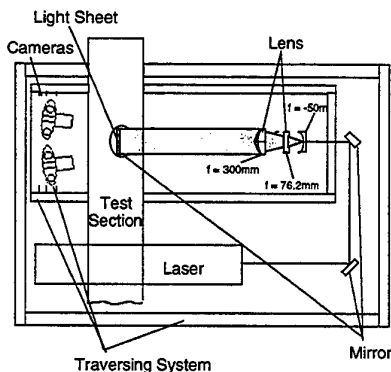


Figure 2 PIV setup

A Quantel TwinsB Nd-Yag double oscillator pulsed laser provides light pulses having a maximum energy of 320 mJ at a wavelength of 532 nm. The time

delay between a pair of pulses can be adjusted from  $1 \mu\text{s}$  to 1s with pulse duration of 5 ns. A plano-concave lens (-30 mm focal length) combined with two plano-cylindrical lenses (76.2 and 300 mm focal length) transform the beam into a thin vertical light sheet. By adjusting the distance between these lenses, the desired thickness and width of the light sheet can be obtained. All lenses have an anti-reflection coating. The complete system including laser, light sheet optics and camera is mounted on a traversing system shown in Figure 2 that allows an easy traverse to the position of interest.

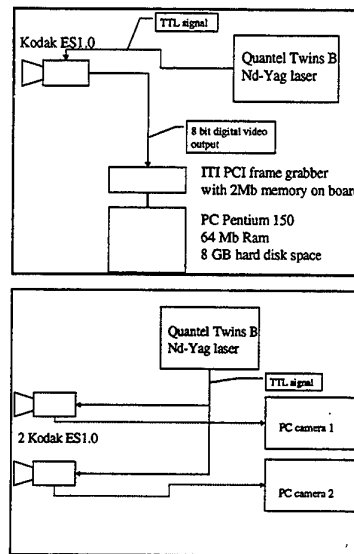


Figure 3 Digital PIV system

A sketch of the digital PIV system is shown in Figure 3. The system consists of two independent Kodak ES1.0 cameras each having its own PC. The ES1.0 has a CCD interline transfer sensor, which has a pixels array of 1008(H) by 1018(V) pixels. Each pixel measures nine microns square with a 60% fill factor using a micro lens. The camera outputs 8 bit digital images with 256 gray levels. The camera is used in a special double exposure frame triggering mode which allows the capture of two images separated by a delay ranging from 2 ms to 66 ms. Nikkor 55-mm micro lenses are mounted on the cameras. For a typical recording situation, the cameras are placed with an oblique angle of 5 deg. at a distance of 0.7 m from the light sheet plane.

The PIV image acquisition starts with a signal from the laser. Two images are captured in rapid succession by capturing the first image in the photo diode array, transferring this image to the CCD array and then capturing a second image in the photo diode array. The first image is transferred from the CCD to the frame grabber while the second image is being captured by the photo diode array. The second image is then transferred into the CCD array and subsequently onto the frame grabber's second image buffer. The frame grabber is an Imaging Technology PCI frame grabber with 2 MB memory onboard. The PCs are equipped with 64 MB RAM and 8 GB hard disk space.

During the PIV measurement series, 50 images are written in real time into the PC's RAM memory after which the acquisition is stopped and the images are saved on the hard disk.

The PIV recordings from the right and left camera are interrogated independently with the PIV software package VISIFLOW. A cross-correlation analysis method is used with an interrogation window size of 64 by 64 pixels and 50 percent overlap between the interrogation windows. The camera acquires images with a resolution of 1008 by 1018 pixels. Each recording results in a 30 by 30 vector field of the instantaneous velocity. Usually the data contains a small number of spurious vectors (<2%). The vector field is therefore validated with predefined thresholds for the vector continuity and velocity magnitude. Vectors that do not fall within the thresholds are removed and the remaining gaps are filled by a weighted average of surrounding vectors.

From the processed vector fields, the instantaneous three-dimensional velocity field can be reconstructed. For angular PIV systems, where both cameras observe the light sheet from the same side, the corresponding interrogation positions for the two images in the plane of the light sheet do not match in general. Therefore, a calibration of the camera system is performed that also corrects for the distortion of the images in the lenses and the glass walls of the passage.

For the evaluation of time-averaged turbulent transport models, the engineers require the mean-velocity field and the turbulence quantities of the flow. The statistical distribution of the velocity components is obtained from identical spatial windows in a series of instantaneous PIV measurements. From these statistical distributions the desired mean-velocity field and Reynolds stresses are obtained. The data requirements, uncertainty estimates and system limitations for these results are discussed further by Schabacker et al. (20).

### 3 DESCRIPTION OF ANALYTICAL MODEL

The focus of the present analysis is on a periodic-developed flow condition which assumes that the flow repeats itself cyclically from one rib to the next. This assumption allows the calculation domain to be limited to the region between two adjacent ribs and the computational grid contains a reasonable number of nodes. The calculation domains for the two cases investigated are shown in Figure 4.

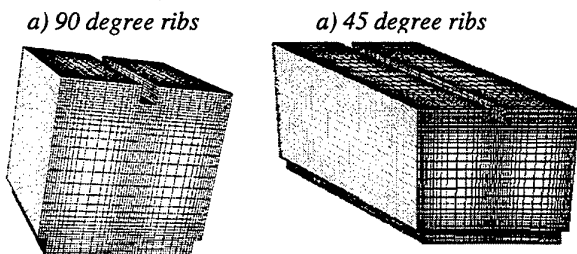


Figure 4 Computational domain

### 3.1 Mathematical and numerical methods

The structured FLUENT code V 4.4.7 was used for all calculations. This program is a finite volume code using a cell centered, nonstaggered grid. The Reynolds-averaged Navier-Stokes equations and the transport equations of the turbulent quantities are solved by the pressure correction algorithm SIMPLE.

During the iteration process, the sparse large linear systems of equations were solved by an iterative Line-Gauß-Seidel algorithm (LGS). When solving the pressure correction equation, a multigrid technique in combination with a one-dimensional block correction was used in order to increase the rate of convergence of the LGS algorithm.

The fluid is considered as incompressible. The fluid properties are assumed as constant. For time scales much larger than the largest turbulent time scale, the flow is considered stationary. To account for turbulent effects, the Reynolds-averaged Navier-Stokes equations are considered to be the governing equations of the flow field.

### 3.2 Turbulence modeling

The main characteristics of the three semi-empirical turbulence models, used for the flow predictions, are outlined below.

#### *The standard k-ε model:*

In this model two entities that are used for describing turbulence are introduced: the specific kinetic turbulent energy  $k$  and its dissipation  $\epsilon$ . For both entities, differential transport equations are introduced which are solved in addition to the other equations. The Reynolds-stress tensor is calculated according to the Boussinesq hypothesis and the dynamic viscosity is replaced by an effective viscosity  $\mu_{eff} = \mu + \mu_t$  with  $\mu_t = \rho C_\mu k^2 / \epsilon$ .  $C_\mu$  is a modeling constant. A detailed description of this model can be found in Launder and Spalding (21).

#### *The differential Reynolds stress model (RSM):*

For the auto- and cross-correlations of the turbulent velocities differential transport equations are introduced as well as for the entity which has the same function as in the  $k$ - $\epsilon$  turbulence model above. More details can be found in Launder, Reece and Rodi (22).

Both the  $k$ - $\epsilon$  and the RSM turbulence models are used in combination with the logarithmic wall function to treat the wall boundary layer. The theory of turbulence modeling and a detailed description of the implementation can be found in the FLUENT manual (23).

#### *Two layer k-ε model:*

In the two layer model, the whole domain is subdivided into a viscosity-affected region and a fully-turbulent region. The demarcation of the two regions is based on a wall-distance-based Reynolds number.

$$Re_y \equiv \frac{\rho \cdot y}{\mu} \sqrt{k} \quad (1)$$

In the fully turbulent region ( $Re_y > 200$ ), the standard k- $\epsilon$  model is employed. In the viscosity-affected near-wall region, the one equation model of Wolfstein (24) is employed. In this model the k equation is solved as in the standard k- $\epsilon$  model and the turbulent viscosity is computed from  $\mu_t = \rho C_\mu k^{1/2} l_\mu$ . The length scale  $l_\mu$  is computed from

$$l_\mu = c_l y \left[ 1 - \exp\left(-\frac{Re_y}{A_\mu}\right) \right] \quad (2)$$

In this equation  $c_l$  and  $A_\mu$  are model constants found in Chen and Patel (25).

### 3.3 Configuration

The integration domain is shown in Figure 4. The grid consists of about 56,000 computational cells for the calculations with wall functions and of about 260,000 cell for the two layer approach. For the present calculations with cyclic boundary conditions the only boundary conditions that are needed are the mass flow through the channel and the wall temperatures. With the constant density and viscosity the mass flow was calculated for adjusting the Re number. The wall temperature was set to a constant value of 100 K above the bulk inlet temperature.

## 4 COMPUTATIONAL RESULTS

The computational results of the flow field are compared first to the experimental data of the PIV measurements for the channel with 90 degree ribs and then for the channel with 45 degree ribs. The calculated heat transfer results for both cases are compared to correlations found in the literature. Reference locations for the rib modules are  $x=0$  at the downstream corner of the bottom rib and  $y=0$  is located at the bottom of the channel (Fig. 5).

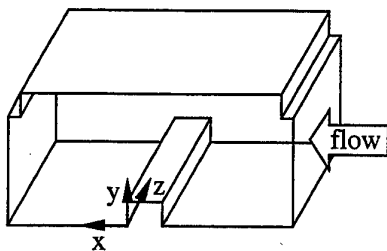


Figure 5 Definition of coordinate system

### 4.1 The 90-degree ribbed channel

The developed flow solution was obtained with periodic boundary conditions and will be compared with the experimental data for the 10<sup>th</sup> rib module. Fig. 6a shows the streamwise velocity profiles one rib height downstream of a rib, in the mid-span of the channel. Note that all three models reproduce the shape of the U-profile. Compared to a smooth channel, this profile

is more parabolic-like with a maximal velocity of about 1.5 times the bulk velocity. The presence of the recirculation zone is also predicted. The rearward velocity of this recirculation zone is over-predicted by the k- $\epsilon$  model (with both wall-functions or the 2-layer approach), whereas the RSM model predicts the measured level of reverse flow. On the upper-wall, the measurement-location is at 5 rib heights downstream of the rib where the flow has reattached. Note a kink in the RSM-profile. Additional calculations were made at a higher Reynolds number ( $Re = 100,000$ ) with the same grid, allowing therefore a greater  $y^+$ -value at the first discretization point. However, the same anomalous pattern was obtained. The latter has been observed in previous studies dealing with backstep flows by Obi (26), Lasher & Talbee (27), Basara (28). The anomaly was attributed to the LRR model used for the pressure-strain correlations. This finding has been confirmed by Hanjalic & Jakirlic (29), who managed to get rid of it by introducing a correction term, based on a generalization of the Yap correction (30). Unfortunately, this turbulence model correction is not available in Fluent or UNS and could not be used for the calculations. Fig. 6b shows that the computed levels of turbulence are in good agreement with the experimental data, both qualitatively and quantitatively. Note the high levels of turbulence (about 14%) in the center of the channel due to the build-up of the shear layers on both roughened walls. The RSM model shows an overall better prediction.

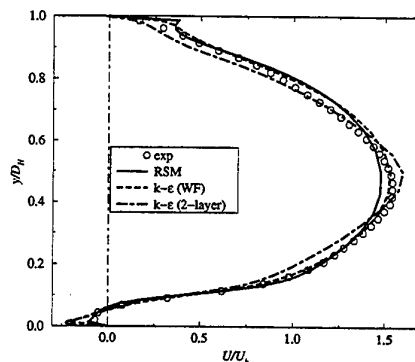


Figure 6a Streamwise velocity profiles

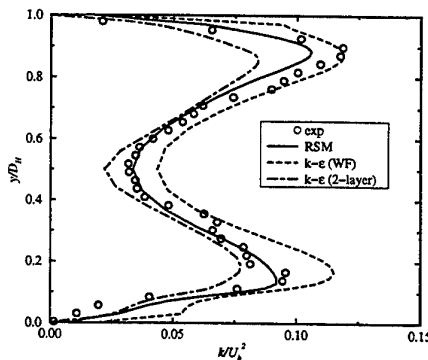


Figure 6b Turbulent kinetic energy profiles

Figure 6 Velocity and turbulent energy profiles for 90 deg ribs at  $x/h = 1$  and  $z/D = 0.5$

The next comparison concerns the velocity profiles along a line in the streamwise direction, along the mid-span of the channel, and located at 0.2 rib heights from the bottom. The measured and predicted streamwise velocity and turbulent kinetic energy are compared in Figs. 7a and b. Note that this location is very close to the wall, which makes the measurements a little uncertain, especially for the k-profiles. Results from all three turbulence and wall models predict the qualitative character of the U-profiles. Negative velocity values correspond to the recirculation zone. The negative velocities of this recirculation zone are over-predicted by the k- $\epsilon$  model (as shown in the previous station). In the inter-rib region after reattachment, the streamwise velocities of the flow are better predicted by the 2-layer model. Both wall-function models over-predict the streamwise velocity. To ensure a sufficiently high  $y^+$ -value, the first discretization point was placed at about 0.15 rib heights from the bottom of the channel where,  $y^+$  was around 10. Unfortunately, this value is less than the required minimal value of 15-30 and might explain the over predictions with the wall functions. The same characteristic resulted for the turbulent kinetic energy, the 2-layer approach giving a better quantitative answer. This result indicates the limits of the wall-function approach for the coolant passage applications. Thus, if the Reynolds number or the rib height are too small, then wall functions are likely to produce erroneous results due to the required minimum  $y^+$  value of the first discretization point.

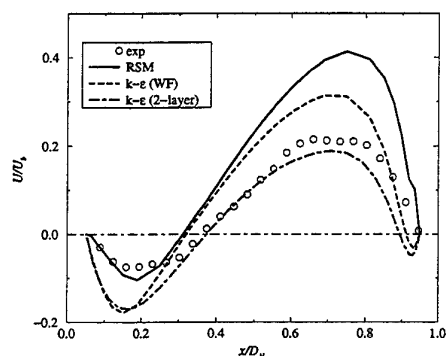


Figure 7a Streamwise velocity profiles

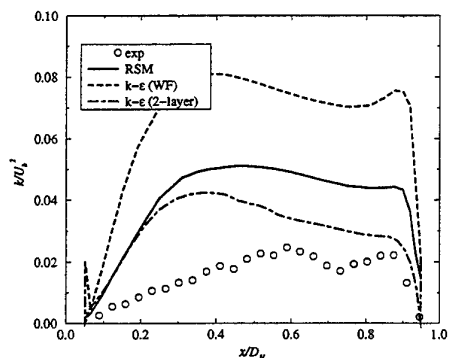


Figure 7b Turbulent kinetic energy profiles

Figure 7 Velocity and turbulent energy profiles for 90 deg ribs at  $y/h = 0.2$  and  $z/D = 0.5$

Several measured and predicted flow characteristics are compared in the mid-span plane of the channel. The RSM computation was chosen for the prediction. Because of symmetry of the present configuration, the spanwise average velocity is 0 in this plane. The average normal (Figure 8b) and streamwise (Figure 8a) velocity distributions are well predicted, both quantitatively and qualitatively. Although the RSM anomalous pattern of the U-profiles after reattachment occurred, the size and intensity of the recirculation zone is well predicted. Upstream of the rib, the RSM computations over-predict the normal velocity of the flow (see the maximum levels of the V-contours at the upper-left corner of the rib) as was shown in Fig. 7.

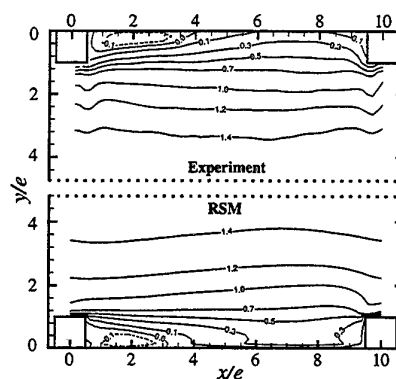


Figure 8a: Streamwise velocity

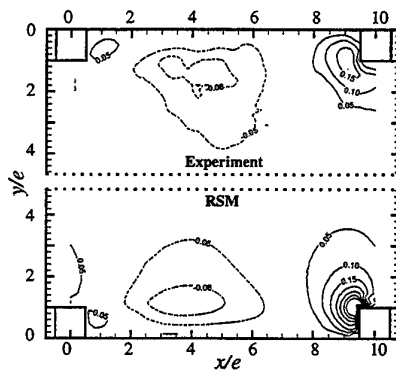


Figure 8b Vertical velocity

Figs. 8c & d present the turbulence quantities. Note that the overall flow characteristics predicted by the RSM model is fairly close to the experiment. The levels of turbulence in the channel core, as well as in the inter-rib spacing are well predicted. Note also that the uv-Reynolds stress prediction is in a fair agreement with the experimental data. The level of accuracy in the Reynolds stresses was estimated to be lower for the Reynolds stresses than for the velocities or the kinetic energy.

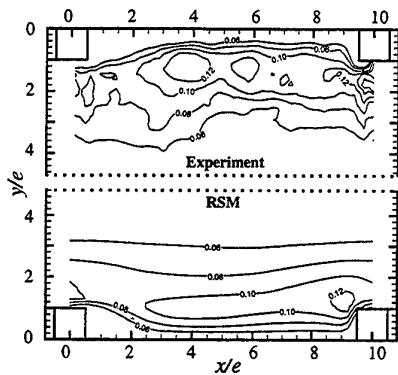


Figure 8c Turbulent kinetic energy iso-contours

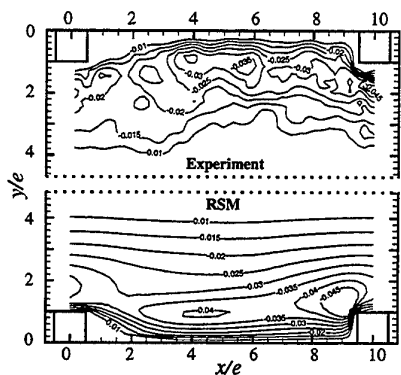


Figure 8d Reynolds-stress  $uv$  iso-contours

Figure 8 Comparison of measured and predicted flow characteristics for 90 deg ribs at the midspan of the channel

#### 4.2 The 45-degree ribbed channel

The flow in the 45 degree ribbed configuration is more complex than for the 90 degree ribbed configuration. The 45 degree ribbed configuration has no symmetry plane and the inclination of the ribs causes a complex 3D-vortex where the fluid is driven towards one side (called "trailing") wall by the ribs, and returns towards the opposite side wall (called "leading") in the center of the channel. This secondary motion is expected to enhance the heat transfer performance and therefore, an accurate computation of the vortex structure is important. The ribbed wall configuration is shown on Fig. 9.

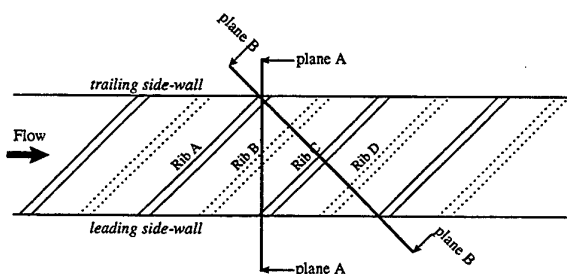
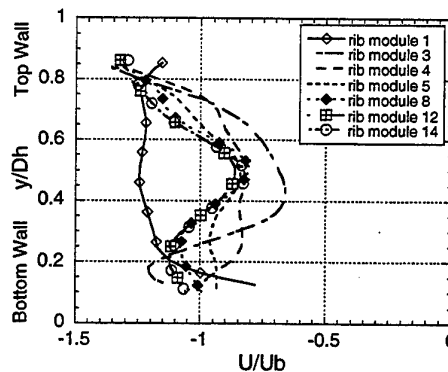
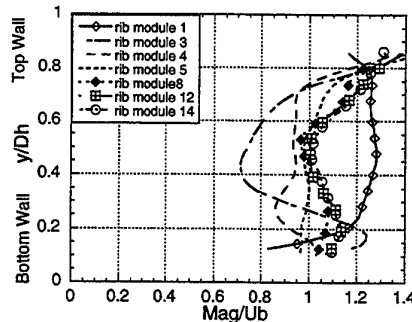


Figure 9: Configuration of the 45-degree arrangement and location of slices

Mean measured velocity profiles at selected distances from the inlet along the mid-plane of the channel are presented in Fig 10. The profiles have been plotted at streamwise locations corresponding to the center of the rib on the top wall. The experimental data measured between the 8<sup>th</sup> and 9<sup>th</sup> rib of the apparatus was used for comparison with the numerical predicted results. A longer channel length was required to obtain a developed flow than was necessary for the 90-degree rib configuration. Because the experiment consisted of measurements in the first leg of a U-duct, the measurements from the last ribs of this leg were too close to the U-turn to be considered for our comparison purposes.



10a Streamwise velocity profiles



10b Total velocity magnitude profiles

Figure 10 Velocity profiles at selected locations in the coolant passage

The development of the secondary motion with the 45 degree ribs produces complex velocity profiles. The streamwise velocity profiles have two maxima and one minimum at the center of the duct. The profile is different than that from the 90-degree configuration where the maximum velocity occurred in the center of the channel. This can be explained by the presence of two secondary vortices, shown later in Fig 12, with maximal cross flow velocities in their center.

The calculations reproduce the complex flow characteristics as shown by the velocity profiles in Figure 11. Note that the maximal streamwise velocities are over-predicted (Fig. 11a). However, the flow may not be fully-developed at these locations (see Fig. 10b).



The spanwise velocity profiles, shown in Fig. 11b, indicate the strong three-dimensionality of this flow. The flow is driven along the bottom and top walls along the ribs with a positive spanwise velocity and then returns towards the opposite side wall in the core of the channel with a negative spanwise velocity. The intensity of this movement is reproduced by all the turbulence and wall models. The vertical velocity profiles are presented in Fig. 11c. The qualitative behavior of the vertical velocities is reproduced by the calculations with negative velocities close to the bottom wall and the top rib. In the core of the channel, there is an upwards flow. Although the three models capture this feature, they under-predict the magnitude in the center section. Note that calculations with either the RSM with wall-functions or the k- $\epsilon$  model with a 2-layer approach produce the experimentally measured levels of downwards velocity. The velocity magnitude profiles in Figure 11d show one effect of the ribs inclination, namely that there is less velocity defect along the walls for the 45-degree configuration which is good for mixing and heat transfer performances. Also the maximal velocity magnitudes are located closer to the ribbed walls instead of being in the core of the channel.

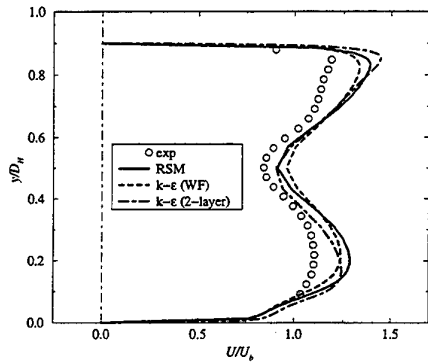


Figure 11a Streamwise velocity profiles

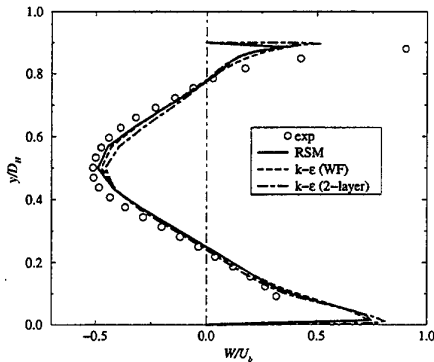


Figure 11b Spanwise velocity profiles

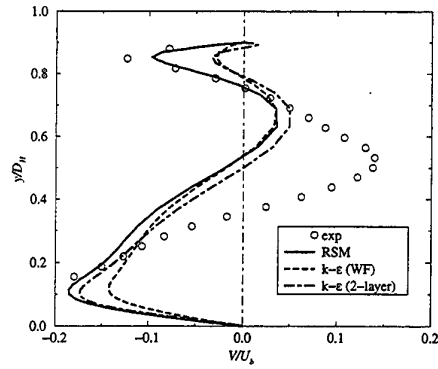


Figure 11c Vertical velocity profiles

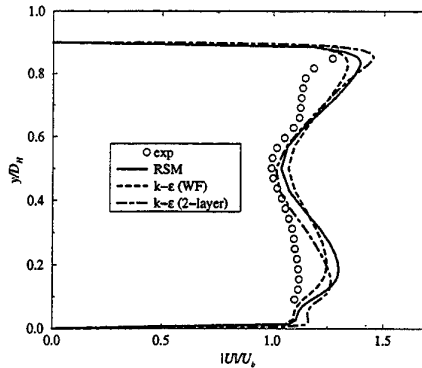


Figure 11d Velocity magnitude profiles

Figure 11 Velocity profiles at  $z/D=0.5$  and a streamwise location corresponding to the middle of the top rib, Plane A, Rib B

The enhancement of heat transfer performances with a 45-degree inclined ribs configuration is due to the creation of secondary motions in the channel. The 2D-contours of the spanwise velocity in plane A is shown in Fig. 12. The RSM predictions are able to reproduce the secondary flow motion, both quantitatively and qualitatively (cf. Figs. 12b). The shapes and locations of the secondary vortices are well predicted.

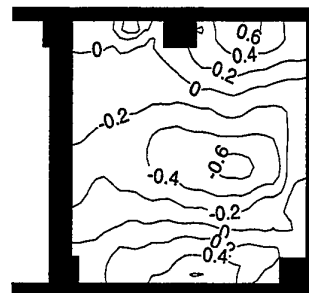


Figure 12a Experimentally measured

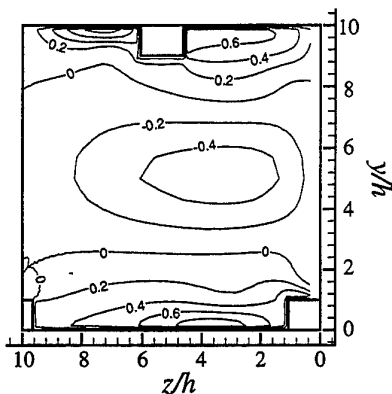
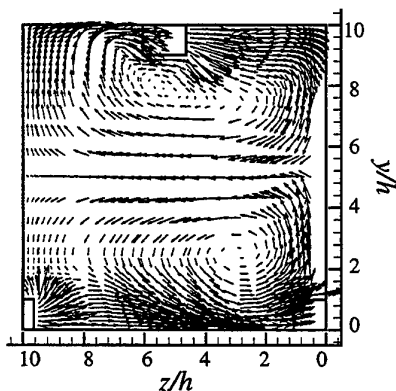


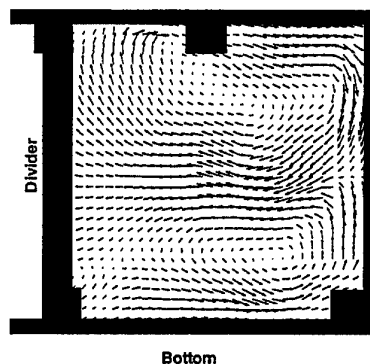
Figure 12b Predicted with RSM model

Figure 12 Secondary motion in plane A; the flow is coming out of the plane

A comparison between the measured and predicted secondary flow vectors in a plane orthogonal to the streamwise direction are shown in figure 13. The plane through the channel is  $1/2\sqrt{2}$  rib heights downstream of the onset of the rib on the side walls, plane A. The fluid is driven along the ribs close to the bottom and top walls, and in the opposite direction in the center of the channel. Coolant is convected towards the roughened walls along the side walls, thereby enhancing the mixing process and the heat transfer performances. The predictions with the RSM model reproduce this motion both quantitatively and qualitatively. Note that both the shapes and locations of the secondary vortices are fairly well predicted.



13a Predicted with RSM model

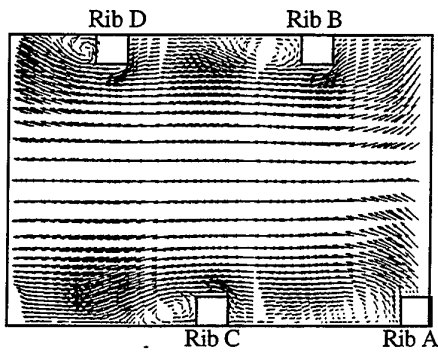


13b Experimentally measured

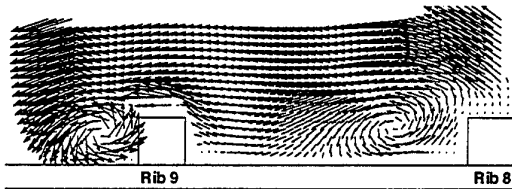
Figure 13 Comparison of predicted and measured secondary motions in plane A, (the flow is coming out of the plane)

The development of the flow in plane B is shown in Figure 14. Plane B is perpendicular to the rib axes. Note that the pitch to height ratio in this plane, is smaller than for the 90-degree configuration (i.e.,  $10/\sqrt{2}$  instead of 10). The recirculation zone or vortex behind each rib is small in the "leading" side-wall (about one rib height behind rib D). The size of the recirculation zone or vortex increases when the flow approaches the "trailing" side-wall. In Fig. 14 the flow behind rib A (resp. C) from the prediction is compared to the flow behind rib 8 (resp. 9) from the experiment. On the "leading" side-wall downstream of the rib, the recirculation is small and the angle of the flow at reattachment is bigger than in a standard "backstep" configuration. This is thought to be due to the secondary motion which is driving fluid along the leading side-wall towards the roughened wall.

The vertical velocity contours in a plane between the ribs at the 50 percent rib height level are shown in Figure 15. An increase of downwards velocity can be observed. As far as comparison is concerned, these qualitative features of the flow in this local region are well reproduced by the numerical predictions. Downstream of Rib A, the bubble appears narrower in the prediction than in the experiment. Also the measured vorticity in this vortex is higher than in the RSM-computation. Nevertheless, the contours of the downwards velocity in this plane are well predicted with vertical velocities as much as 40 percent of the bulk velocity behind the ribs on the leading side-wall.

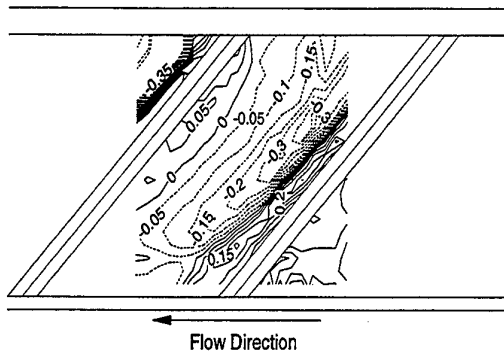
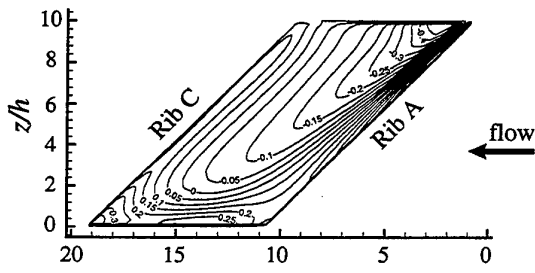


14a Predicted with RSM model



14b Experimentally measured

Figure 14 Comparison of the projected flow in plane B



15b Experimentally measured

Figure 15 Comparison of Experimental and predicted Iso-contours of the vertical velocity in an horizontal plane located at 50% rib height from the roughened wall

The average flow is also well predicted by calculations with either k-ε model ( wall functions or the 2-layer approach). The secondary flow was predicted at approximately the measured values. This

secondary motion is strongly driven by the rib geometry with the flow-wall interactions. In addition, the turbulence model has not much space to act on this secondary flow because of the presence of repeated ribs. Therefore, the standard "too-rapid-diffusion-of-secondary-motions" observed with the k-ε model, was expected to have less influence in the present configuration than usual.

### 4.3 Heat transfer and pressure losses

Important information for the design of a cooling system are the average heat transfer coefficients (characterized by the non-dimensional Nusselt number) and the average pressure losses (characterized by the non-dimensional friction factor) of a cooling channel. The Nusselt number has been evaluated with the volume averaged temperature as a reference temperature. The cooling efficiency is a third important parameter for cooling designs with a low pressure loss constraint. Following previous experimental studies, Gee and Webb (31), Han et al. (32), one way of evaluating the performance or efficiency of a cooling system is to evaluate the ratio  $(Nu/Nu_s)/(f/f_s)^{1/3}$ , indicating the values obtained for a smooth channel. Standard correlations are usually chosen for the smooth wall correlation, e.g., Han et al. (32).

For comparison of the predicted heat transfer results, the Han et al. (32) correlation for similar configurations but with non-staggered ribs (inclination angles between 30 and 90 degrees) has been chosen. Staggering the ribs is expected to show similar trends. The Han et al. correlation was established with a confidence of 5% for the friction factor and 10% for the Nusselt number. The predicted results for pressure drop, heat transfer coefficient and cooling efficiency obtained by the three turbulence models are tabulated in Tables 1 to 3.

The predicted results for the three models bracket the Han et al. correlation for the 90-deg configuration. In particular, the efficiency seems to be quite well predicted. However, no definitive quantitative conclusion can be drawn here because the Han et al. correlation is for non-staggered ribs. There are differences between the predicted results with the 2-layer approach and the wall-function models. The former predicts a heat transfer coefficient and pressure losses about 20 to 30% smaller than the latter. The conclusion is that the turbulence model, especially close to the heated wall, influences the quantitative heat transfer predictions.

	Han et al. correlation	RSM WF	k-ε WF	k-ε 2 layer
90 deg.	$4.5 \cdot 10^{-2}$	$5.9 \cdot 10^{-2}$	$5.3 \cdot 10^{-2}$	$3.8 \cdot 10^{-2}$
45 deg.	$4.6 \cdot 10^{-2}$	$6.0 \cdot 10^{-2}$	$6.5 \cdot 10^{-2}$	$6.4 \cdot 10^{-2}$
Increase	2.2 %	1.7 %	22.5 %	68.5 %

Table 1 Friction factor for one roughened-channel period

	Han et al. correlation	RSM WF	k-ε WF	k-ε 2 layer
90 deg.	210.5	233	253	201
45 deg.	256.2	290	350.5	377.5
increase	22 %	24 %	38.5 %	88 %

Table 2 Nusselt number for one roughened-channel period

	Han et al. correlation	RSM WF	k-ε WF	k-ε 2 layer
90 deg.	1.01	1.02	1.15	1.02
45 deg.	1.23	1.27	1.50	1.62
increase	22 %	24.5 %	30.5 %	59 %

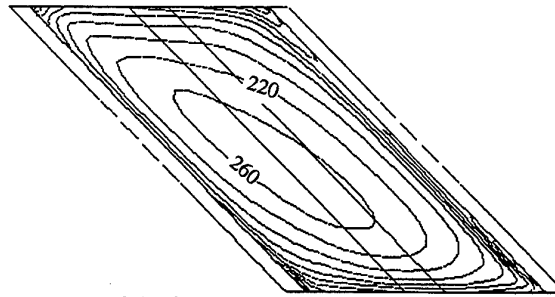
Table 3 Efficiency of the cooling system

For the 45-degree configuration, the conclusion is different. Although the predicted heat transfer and pressure drop are greater than the values from the correlation, the increase in cooling efficiency (about 22-24%) is well predicted with the RSM model. The qualitative enhancement of heat transfer between the 90 deg and the 45 deg rib configurations is predicted by the k-ε model but the heat transfer increase of 60% for the k-ε with the 2-layer model is greater than expected from the Han et al. correlation. This over-prediction is confusing because the mean flow, and the secondary vortex system, which are responsible for the heat transfer enhancement are well predicted by this model (cf. Figs. 11).

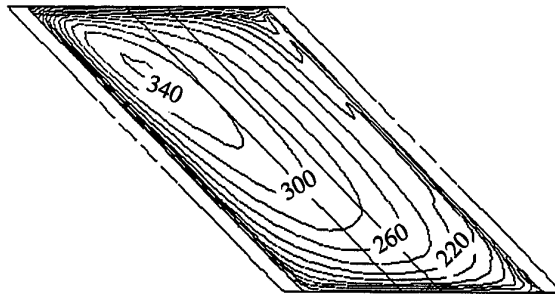
Fig. 16 shows the distribution of local Nusselt number iso-lines on the roughened wall with both RSM and k-ε models, both with the wall function approach. A smoother distribution occurred for the RSM-prediction. In particular, in the k-ε results there is an area of high heat transfer immediately downstream of the rib, along the "leading" side-wall. This area is located in the reattachment region, described previously. Here the flow toward the wall is high (40 percent of the bulk velocity), the bubble is small and its intensity is enhanced by the presence of the secondary motion in the channel. Thus, the impingement of the flow on the wall is stronger than predicted for the 90-degree configuration or for the 45 deg. configuration on the other side of the channel.

Fig. 17 shows a comparison of the dimensionless turbulent kinetic energy close to the wall (15 percent of rib height away from the wall). One can observe the similar phenomena for the 2 models, the k-ε model produces a local high turbulence spot in the same region. The same observation can be made with the 2-layer approach for the k-ε model. Previously, k-ε models have predicted higher than measured levels of turbulence in impingement regions, e.g., Craft et al (33), Behnia et al (34). This characteristic of the model may explain the difference in heat transfer even if the mean average flow is quite well reproduced by all the models. Note also that the anisotropy of near-wall turbulence increases in the inclined rib configuration, which weakens the assumed isotropic k-ε condition. Local

heat transfer experiments will be necessary for a better assessment and more definitive conclusions regarding this coolant passage.

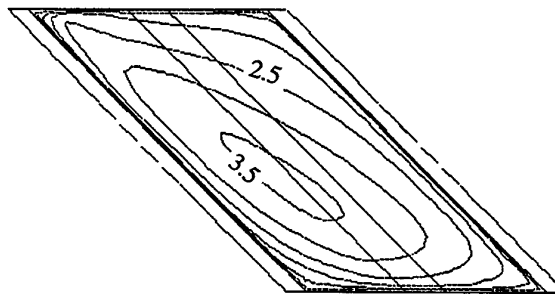


16a) RSM near wall Nusselt numbers

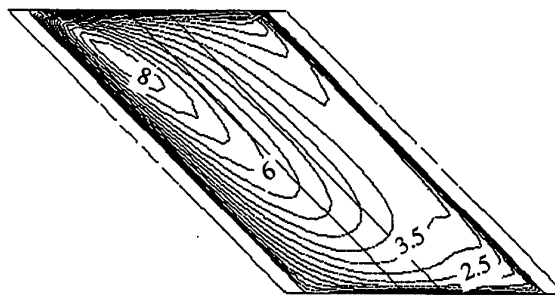


16b) k-ε near wall Nusselt numbers

Figure 16 Nusselt numbers on wall with 45 degree ribs



17a) RSM turbulence model



17b) kε turbulence model

Figure 16 Iso contours of  $k/U_b^2 (*10^{-2})$  distribution at distance equal 15 percent rib height from the wall with 45 deg ribs

## 5 CONCLUDING REMARKS

In the present paper, a stereoscopic PIV system has been employed for the measurement of the turbulent flow characteristics in a model of a gas turbine coolant passage. The PIV technique was shown to be capable of obtaining velocity measurements with a high spatial resolution and a reasonably small uncertainty of the results. The data acquisition rate was high and thus allowed for a fuller investigation of the flow in a complex geometry where many measurement planes are required to obtain a comprehensive understanding of the flow phenomena and a large database for the evaluation of turbulence models for CFD codes. From the statistical distribution of the velocity components, the mean-velocity field and turbulent transport of the flow were calculated. The velocity fields were arranged on a regular grid and can therefore ideally be used to evaluate CFD simulations.

Computations have been performed for the experimental flow and geometric conditions with three different turbulence models: i) the  $k-\epsilon$  model with both wall functions and ii) a two-layer approach, and iii) the RSM model with wall functions and with two rib configurations: i) 90 and ii) 45 degrees to the mean flow direction. Comparison of the predicted flows with measurements showed a generally good agreement. The complex flow features like the recirculation zones and vortices behind the ribs and the secondary motion through the channel were predicted. A global analysis of the results showed a slight preference for the RSM model (see for example the intensity of the bubble in the 90-degree case), although the differences are not as high as what could have been expected, especially for the 45-degree configuration. The grid for the 45 degree configuration represented the limit of the applicability range of the wall function with regard to resolving the near wall flow. A smaller  $Re$  number or smaller rib heights would lead to too small  $y^+$  - values near the wall. Some larger differences in the predicted results between the models were found close to the solid boundaries, especially in predicted turbulence levels. These differences lead to different wall heat transfer distributions and pressure losses. The RSM velocity distributions predictions were consistent with the experimental data, returned reasonable ratios of heat transfer efficiency and predicted the relative influence of the ribs inclination. The  $k-\epsilon$  model, with both wall functions and a two layer model, over-predicted the increase of heat transfer efficiency with 45-degree configuration. For the 45 degree rib configurations, near-wall anisotropy of turbulence and impingement zones are expected to be important and may explain the  $k-\epsilon$  model results.

A combined two layer wall model and a Reynolds stress model could provide the physical modeling required to reproduce the qualitative accuracy desired for the design and evaluation of complex coolant passages. For further investigations, near-wall velocity data and heat transfer data from the same test

section are needed to make a better assessment of numerical heat transfer prediction methods for complex coolant channels.

## 6 Acknowledgement

This study was supported by ABB Corporate Research, Ltd., Switzerland.

## 7 Nomenclature

$A_\mu$	turbulence model constant
$C_\mu$	turbulence model constant
$D$	Height and width of passage legs, $D=100$ mm
$D_h$	Hydraulic diameter $D_h = D$
$h$	rib height
$k$	Turbulent kinetic energy
$l_\mu$	turbulence model constant
$Re$	Reynolds number
$Re_y$	wall-distance based Reynolds number
$Nu$	Nusselt number
$u'v'$	Cartesian component of turbulent shear stress
$u'w'$	Cartesian component of turbulent shear stress
$u'$	Fluctuating velocity component in axial direction
$U$	Mean velocity component in x direction
$U_b$	Bulk mean-velocity
$v'$	Fluctuating velocity component in vertical direction
$V$	Mean velocity component in y direction
$w'$	Fluctuating velocity component in spanwise direction
$W$	Mean velocity component in z direction
$x$	Cartesian coordinate in axial duct direction
$y$	Cartesian coordinate in vertical duct direction
$z$	Cartesian coordinate in spanwise duct direction
$\mu$	dynamic viscosity of the fluid
$\mu_t$	turbulent dynamic viscosity
$\mu_{eff}$	effective dynamic viscosity
$\rho$	density
$\epsilon$	dissipation rate

## 8 References

- (1) B. Lakshminarayana, "Fluid Dynamics and Heat Transfer of Turbomachinery", 1996, John Wiley and Sons, Inc.
- (2) Iacovides, H. and Launder, B. E., "Computational Fluid Dynamics Applied to Internal Gas-Turbine Cooling: A Review", 1995, Inter. J. Heat and Fluid Flow, Vol. 16, pp. 454-470
- (3) Prakash, C. and Zerkle, R., "Prediction of Turbulent Flow and Heat Transfer in a Radial Rotating Square Duct", 1992, ASME Journal of Turbomachinery, Vol. 114, pp. 835-846
- (4) Bo, T., Iacovides, H. and Launder, B. E., "Convective Discretisation Schemes for the Turbulence transport Equations in Flow Predictions Through Sharp U-Bends", 1995, Int. J. of Num. Methods for Heat and Fluid Flow, Vol. 5, pp. 33-48

- (5) S.C. Cheah, H. Iacovides, D.C. Jackson, H. Li, B. E. Launder, "LDA Investigation of the Flow Development Through Rotating U-Ducts", 1994, ASME paper 94-GT-226
- (6) H. Iacovides, D.C. Jackson, H. Li, G. Kelemenis, B. E. Launder and K. Nikas, "LDA Study of the Flow Development through an Orthogonally Rotating U-Bend of Strong Curvature and Rib Roughened Walls," 1996, ASME paper 96-GT-476
- (7) Liou, T and Chen, C., "LDV Study of Developing Flows Through a Smooth Duct with a 180 Deg Straight-Corner Turn", 1997, ASME paper 97-GT-283
- (8) Tse, D. G. N. and Steuber, G. D., "Flow in a Rotating Square Serpentine Coolant Passage with Skewed Trips", 1997, ASME paper 97-GT-529
- (9) Abuaf, N and Kercher, D. M., "Heat Transfer and Turbulence in a Turbulated Blade Cooling Circuit", 1994, ASME Journal of Turbomachinery, Vol. 116, pp. 169-177.
- (10) Prakash, C. and Zerkle, R., "Prediction of Turbulent Flow and Heat Transfer in a Ribbed Rectangular Duct with and without Rotation", 1993, ASME preprint 93-GT-206.
- (11) Bonhoff, B., Tomm, U. and Johnson, B. V., "Heat Transfer Predictions for U-Shaped Coolant Channels with Skewed Ribs and with Smooth Walls", 1996, ASME 96-TA-007, ASME Turbo Asia, Jakarta, Indonesia
- (12) Bonhoff, B., Tomm, U., Johnson, B. V. and Jennions I., "Heat Transfer Predictions for Rotating U-Shaped Coolant Channels with Skewed Ribs and with Smooth Walls", 1997, ASME paper 97-GT-162
- (13) Wagner, J. H., Johnson, B. V., and F. C. Kopper, "Heat Transfer in Rotating Serpentine Passages With Smooth Walls", 1991, ASME Journal of Turbomachinery, Vol. 113, pp. 321-330.
- (14) Johnson, B. V., Wagner, J. H., Steuber, G. D., and Yeh, F. C., "Heat Transfer in Rotating Serpentine Passages with Trips Skewed to the Flow", 1994, ASME Journal of Turbomachinery, Vol. 116, pp. 113-123.
- (15) Ian Grant (editor), "Selected Papers on Particle Image Velocimetry", 1994, Spie Milestone Series, Vol. MS 99
- (16) Lourenco, L. M., "Some Comments on Particle Image Displacement Velocimetry", 1988, Von Karman Institute for Fluid Dynamics, Lecture Series 1988-06
- (17) Schabacker, J. and Bölcs, A., "Investigation of Turbulent Flow by Means of the PIV Method," 1996, Paper presented at the 13th Symposium on Measuring Techniques for Transonic and Supersonic Flows in Cascades and Turbomachines, Zurich, Switzerland, September 5-6
- (18) Prasad, A. K and Adrian, R. J, "Stereoscopic Particle Image Velocimetry Applied to Liquid Flows" 1993, Experiments in Fluids, Vol. 15, pp. 49-60
- (19) Westerweel, J. and Nieuwstadt, F. T., "Performance Tests on 3-Dimensional Velocity Measurements with a Two-Camera Digital Particle-Image-Velocimeter", 1991, Laser Anemometry, Vol. 1, pp. 349-355
- (20) J. Schabacker, A. Bölcs and B.V. Johnson, "PIV Investigation of the Flow Characteristics in an Internal Coolant Passage with two Ducts Connected by a Sharp 180° Bend", To be presented at ASME IGTI Gas Turbine Conference, Stockholm Sweden, June 1998.
- (21) Launder, B. E. and Spalding, D. R., "The Numerical Computation of Turbulent Flows", 1974, Computer Methods in Applied Mechanics and Engineering, V. 3, pp. 269-289
- (22) Launder, B. E., Reece, G. J., and Rodi, W., "Progress in the Development of a Reynolds Stress Turbulence Closure", 1975, J. Fluid Mech., Vol. 68 (part 3), pp. 537-566
- (23) FLUENT User's Guide, 1995, Version 4.3, Vol. I-IV, Fluent Deutschland GmbH
- (24) Wolfstein, M., "The velocity and temperature distribution of one-dimensional flow with turbulence augmentation and pressure gradient", 1969, Int. J. Heat Mass Transfer, V. 12, pp. 301-318
- (25) Chen, H. C. and Patel, V. C., "Near-wall turbulence models for complex flows including separation", 1988, AIAA J., Vol. 26, pp. 641-648
- (26) Obi, S. "Berechnung komplexer turbulenter Strömungen mit einem Reynolds-Spannungs-Modell", 1991, PhD Thesis, University of Erlangen
- (27) Lasher, W. C. and Taulbee, D. B., "On the computation of turbulent back-step flow", 1992, Int. J. Heat and Fluid Flow, Vol. 13, pp 30-??
- (28) Basara, B. "A numerical study into the effects of turbulent flows around full-scale buildings", 1987, PhD Thesis, Faculty of Technology, University of Manchester
- (29) Hanjalic, K. and Jakirlic, S. "Contribution towards the second-moment closure modeling for separating and reattaching turbulent flows", 1998, Computers and Fluids, Vol. 27, No 2, pp. 137-156.
- (30) Yap, C. "Turbulent heat and momentum transfer in recirculating and impinging flows", 1993, PhD Thesis, City Univ. London
- (31) Gee, D. L. and Webb, R. L. "Forced convection heat transfer in helically rib-roughened tubes", 1980, Int. J. Heat and Mass Transfer, Vol. 23, pp. 1127-1136
- (32) Han, J. C., Park, J. S. and Lei, C. K., "Heat transfer enhancement in channels with turbulence promoters", 1985, J. for Engineering for gas turbines and power, Vol. 107, pp. 628-635
- (33) Craft, T., Graham, L. and Launder, B. "Impinging jet studies for turbulence model assessment - II. An examination of the performance of four turbulence models", 1993, Int. J. Heat and Mass Transfer, Vol. 36, No 10, pp. 2685-2697
- (34) Behnia, M., Parneix, S. and Durbin, P. "Prediction of heat transfer in an axisymmetric turbulent jet impinging on a flat plate", 1998, Int. J. Heat and Mass Transfer, Vol. 41, No 10, pp. 1845-1855

# RECENT PROGRESS IN THE COMPUTATION OF FLOW AND HEAT TRANSFER IN INTERNAL COOLING PASSAGES OF TURBINE BLADES.

H. Iacovides and M Raisee

Department of Mechanical Engineering  
UMIST, Manchester, UK

## ABSTRACT

This paper describes our efforts to develop numerical flow solvers capable of reliably predicting convective heat transfer through gas-turbine blade-cooling passages. The influences on the mean and turbulent flow due to strong curvature, orthogonal rotation and surface rib-roughness are first presented and their implications for the modelling of turbulence are discussed. A number of turbulence models, of effective viscosity (EVM) and second-moment type, are then applied to the computation of flow and heat transfer through passages in which one or more of the three main influences, curvature, orthogonal rotation and rib-roughness, are present. As far as numerical aspects are concerned, it is shown that in flows through, passages of complex ribbed geometries, it is found that the use of body fitted grids can substantially reduce grid requirements. The presence of secondary motion, induced by rotation or curvature, is shown to necessitate the use of low-Re or zonal closures, while the introduction of second-moment closures, arising from the basic stress transport model, also improves computations of flows influenced by curvature. The prediction of curvature-induced is greatly improved by the introduction of near-wall second-moment closures. Low-Reynolds-number second-moment closures also become necessary in the prediction of flow through heated rotating ducts, when rotational buoyancy is important. Heat transfer computations through two- and also three-dimensional ribbed passages reveal that low-Re turbulence models are necessary and that a low-Re differential stress closure yields thermal predictions that are superior to those of the low-Re EVM model. Two non-linear  $k-\epsilon$  models tested in flows through ribbed passages have been found to be in need of further refinement, while for some of the simpler cases more advanced, realisable models of stress transport have been shown to be promising. The conclusion that emerges from all the cases tested is that the low-Re second-moment closures produce the most reliable flow and heat transfer predictions.

## 1. INTRODUCTION

The design of effective internal cooling passages within the rotating blades of gas-turbines has been exercising the minds of engine designers for a number of decades. As can

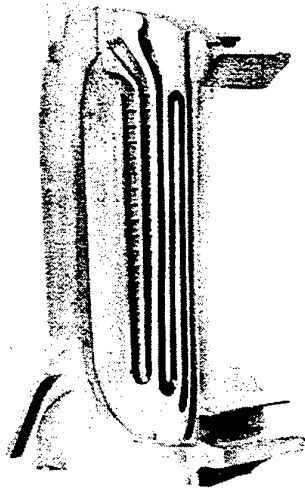


Figure 1. Sectioned gas-turbine blade.

these passages is not only affected by the rotation of the blade, but also by the presence of sharp U-bends and heat-transfer-enhancing ribs. The resulting flow field is consequently complex and highly three-dimensional, containing regions of strong acceleration, flow separation and secondary motion. Wall heat transfer is highly non-uniform and even mean values cannot be accounted for by existing correlations. The development of numerical methods that can reliably predict wall heat transfer in such passages thus can greatly facilitate the design process.

Flow solvers used for the computation of such flows, need to be able to resolve the complex three-dimensional features of the mean motion with numerical accuracy and also to employ mathematical models of turbulence that reproduce the effects of separation, streamline curvature and rotation on the turbulence field. Moreover, since the main interest is in the computation of wall heat transfer, an additional and more challenging requirement is that the near-wall turbulence must also be faithfully reproduced. Progress in the development of suitable numerical techniques has been difficult, because of the heavy computational demands involved and also because of, until recently, the lack of detailed experimental data, against which turbulence models could be validated. This paper reviews recent efforts of the UMIST group to address some of the issues related to the computation of blade cooling flows.

be seen from the sectioned blade shown in Figure 1, flow in

The main flow features that develop inside blade

cooling passages are first presented, together with a discussion of their effects on turbulence and wall heat transfer and of the implications for the modelling of turbulence of these flows. The turbulence models employed are then presented and some numerical aspects are also mentioned. A brief review of the earlier computational work of the UMIST group is then presented, followed by the main focal point of this paper, the presentation of our more recent efforts to simulate the heat and fluid flow inside blade cooling passages.

## 2. BLADE COOLING FLOWS

As can be seen in Figure 1, the two main geometrical features influencing the flow through blade cooling passages are the presence of sharp U-bends and of artificial rib-roughness. A third influence is introduced by the blade rotation. The rotation axis is normal to both the flow direction and the curvature axes of the U-bends. Before embarking on any simulations of blade cooling flows, it would therefore be sensible to have some idea of how each of these features would, on its own, influence the flow and thermal development.

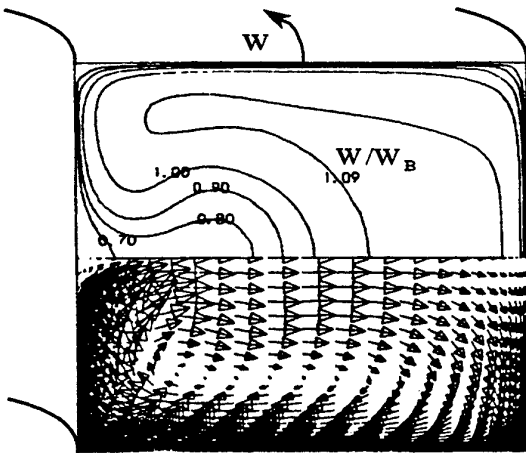


Figure 2. Cross-duct flow in a curved duct.

As far as curvature effects are concerned, in flows through curved ducts, local imbalances between the curvature-induced centrifugal force and the opposing centripetal pressure gradient, lead to secondary motion, which, as shown in Figure 2, transports fluid from the outer to the inner side of the curved duct, which is then returned to the outer wall through the duct centre. As a result, the faster fluid is convected to the outer side of the curved passage. The distribution of the local coefficient of wall heat transfer will consequently be complex, with the higher levels encountered along the outer side. Moreover, the secondary velocities are strongest at the near-wall regions. Thus in order to accurately predict the secondary motion, the near-wall regions and perhaps even the viscous sub-layer regions would need to be adequately resolved. In U-bends of strong curvature, as documented in the

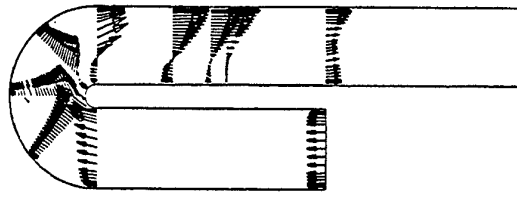


Figure 3. Mean flow development in a U-bend of strong curvature. LDA data [1].

measurements of Cheah et al [1], the streamwise pressure gradients that develop at both ends of the bend exert the strongest influence. Within and downstream of the bend, as shown in Figure 3, there is a sizeable separation region along the inner wall and strong flow acceleration the outer wall. Flow separation would of course increase turbulence levels and this would enhance the rate of wall heat transfer. The turbulence models employed should therefore also be able to reproduce the effects of flow separation and also those of strong acceleration on turbulence. Transport-based models are therefore essential.

In addition to the above effects on the mean motion, streamline curvature also has a direct effect on turbulence. As identified by Bradshaw [2], the effective viscosity approximation is unable to reproduce this effect. Consequently, as shown by numerous researchers, such as Iacovides and Li [3], the non-symmetric velocity profiles that develop across curved channels [4], cannot be reproduced by effective viscosity models.

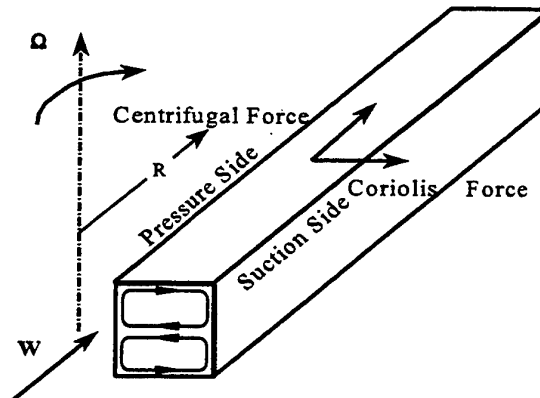


Figure 4. Orthogonally rotating duct.

Orthogonal rotation, generates two types of body forces within the fluid. The Coriolis force and the centrifugal force. The effects of the Coriolis force are not entirely unlike those of curvature. The Coriolis force, with magnitude  $-2\rho\Omega W$ , is normal to the main flow direction and consequently gives rise to an opposing cross-duct pressure gradient. As in a curved duct, local imbalances between the Coriolis and the pressure-gradient forces, again strongest in the boundary layer regions, generate a secondary motion similar to that in a curved duct. The consequences are thus similar for both the flow and thermal



development and also the subsequent numerical modelling.

The centrifugal force,  $\rho\Omega^2R$ , in constant density flows, is simply counteracted by an equal and opposite pressure-gradient force. In flows through strongly heated passages, rotational buoyancy effects can arise. When the flow moves away from the centre of rotation, as is the case in Figure 4, then in a heated duct, rotational buoyancy would slow down the lighter near-wall fluid and speed up the heavier core fluid. The increase in boundary-layer thickness is then expected to further influence the Coriolis-driven secondary motion, as well as the levels of near-wall turbulence. Data for the somewhat analogous case of mixed convection in strongly heated vertical (stationary) tubes by Cotton and Jackson [5], also suggest that in outward flows rotational buoyancy is expected to enhance turbulence transport. For inward motion, the above effects of rotational buoyancy are reversed. One of the characteristics of buoyant flows, is their departure from the semi-logarithmic near-wall distribution. Use of the wall function approximation, though numerically attractive, becomes inappropriate.

In addition to the effects on the mean flow, both the Coriolis force and rotational buoyancy also have a direct influence on turbulence, through the generation rate,  $P_{ij}$ :

$$\begin{aligned}
 P_{ij} = & - \left[ \overline{u_i u_k} \frac{\partial U_j}{\partial x_k} + \overline{u_j u_k} \frac{\partial U_i}{\partial x_k} \right] \\
 & - 2\Omega_p (\epsilon_{ipq} \overline{u_q u_j} + \epsilon_{jpr} \overline{u_r u_i}) \\
 & - \frac{\overline{u_i \rho'}}{\rho} (\Omega_k X_k \Omega_j - \Omega_k \Omega_k X_j) \\
 & - \frac{\overline{u_j \rho'}}{\rho} (\Omega_k X_k \Omega_i - \Omega_k \Omega_k X_i) \quad (1)
 \end{aligned}$$

The Coriolis terms do not, however, contribute to the generation rate of the turbulent kinetic energy,  $P_{kk}$ . Effective viscosity models are consequently unable to account for this process. The buoyancy contribution, on the other hand, is present in  $P_{kk}$ . While the preceding discussion implies that in the computation of flows through curved and rotating passages the use of non-isotropic stress closures is essential, the fact that in three-dimensional passages the primary effect of rotation and curvature is the development of secondary motion, suggests that, provided that they can correctly resolve the secondary motion, EVM models should be able to reproduce the main flow features.

Finally rib roughness, by causing flow separation, as can be seen in the data of Iacovides et al [6], leads to a substantial enhancement of turbulence levels. As reported in another article in this proceedings [7], the resulting levels of wall heat transfer can be more than twice as high as those of a smooth passage. Turbulence models must therefore be able to return the correct levels of near-wall turbulence in the presence of flow separation.

The variety of flow features present in blade cooling

passages pose severe challenges to turbulence models. The wall function approximation and the effective viscosity approach, though numerically efficient, become questionable. Moreover the geometrical complexity of the real passages, makes the use of terms that include the wall distance and direction undesirable.

### 3. FLOW EQUATIONS

All the equations are presented in Cartesian tensor notation.

#### 3.1 Mean Flow Equations

$$\text{Continuity} \quad \frac{\partial}{\partial x_i} (\rho U_i) = 0 \quad (2)$$

Momentum Transport

$$\begin{aligned}
 \frac{\partial}{\partial x_j} (\rho U_i U_j) = & - \frac{\partial P}{\partial x_i} \\
 & + \frac{\partial}{\partial x_j} \left[ \mu \left( \frac{\partial U_i}{\partial x_j} + \frac{\partial U_j}{\partial x_i} \right) - \rho \overline{u_i u_j} \right] - 2\rho \epsilon_{ijp} \Omega_p U_j \\
 & - \rho [\Omega_j X_j \Omega_i - \Omega_j \Omega_j X_i] \quad (3)
 \end{aligned}$$

$$\text{Enthalpy} \quad \frac{\partial}{\partial x_j} (\rho U_j T) = \frac{\partial}{\partial x_j} \left[ \frac{\mu}{Pr} \frac{\partial T}{\partial x_j} - \rho \overline{u_j t} \right] \quad (4)$$

#### 3.2 Turbulence Modelling Equations

The discussion of Section 2, suggests that in the simulation of blade cooling flows, different approaches to near-wall modelling and also second-moment closures must also be included. The closures employed therefore ranged from eddy-viscosity  $k$ - $\epsilon$  to algebraic (ASM) and differential (DSM) stress closures, while more recently, non-linear  $k$ - $\epsilon$  models have also been tested.

As far as the modelling of near-wall turbulence is concerned, initially a zonal approach was adopted, in which the flow domain is sub-divided into two regions, the fully turbulent, core, region and the near-wall region. A high-Re turbulence transport model is then employed in the core region, ( $k$ - $\epsilon$ , ASM, etc) which is then matched to simpler low-Re models within the near-wall region. The near-wall models employed, included the Van-Driest mixing length hypothesis, Wolfstein's [8] one-equation model of  $k$ -transport and simplified second-moment closures in which, as in the one-equation model, the near-wall dissipation rate of turbulence is obtained from the wall distance. In addition to the zonal models, low-Re variants, in which the dissipation rate equation was solved across the near-wall

regions, of the k- $\epsilon$  [9], the non-linear k- $\epsilon$  [10] and of second-moment closures have also been used.

As far as second-moment closures are concerned, most of the computations have so far been performed using variants of the basic second-moment closure, which uses the linear pressure-strain redistribution term, and reproduces the wall-echo effects on turbulence by employing the "wall reflection" terms that rely on the wall distance and wall normal direction. While some evidence has emerged that realisable closures offer a promising route for the computation of convective heat transfer in curved passages, these, more elaborate, closures have not yet been incorporated in our most commonly used codes.

Of the models used only those that either have been extensively tested, or are not easily accessible in the literature are presented here.

### 3.1.1 High-Re Models

#### High-Re k- $\epsilon$ Model

$$\overline{\rho u_i u_j} = \frac{2}{3} k \delta_{ij} - \mu_t \left( \frac{\partial U_i}{\partial x_j} + \frac{\partial U_j}{\partial x_i} \right) \quad \mu_t = \rho c_\mu \frac{k^2}{\epsilon}$$

$$\frac{\partial}{\partial x_j} (\rho U_j k) = \frac{\partial}{\partial x_j} \left[ \left( \mu + \frac{\mu_t}{\sigma_k} \right) \frac{\partial k}{\partial x_j} \right] + P_k - \rho \epsilon \quad (5)$$

$$P_k = -\rho \overline{u_i u_j} \left( \frac{\partial U_i}{\partial x_j} \right)$$

$$\frac{\partial}{\partial x_j} (\rho U_j \epsilon) = \frac{\partial}{\partial x_j} \left[ \left( \mu + \frac{\mu_t}{\sigma_\epsilon} \right) \frac{\partial \epsilon}{\partial x_j} \right] - c_{\epsilon 1} \frac{\epsilon}{k} P_k - \rho c_{\epsilon 2} \frac{\epsilon^2}{k} \quad (6)$$

#### Basic Second-Moment Closure

$$\frac{\partial}{\partial x_k} (\rho U_k \overline{u_i u_j}) = \frac{\partial}{\partial x_k} \left[ \left( \mu + \frac{\mu_t}{\sigma_k} \right) \frac{\partial \overline{u_i u_j}}{\partial x_k} \right] + P_{ij} - \rho \epsilon_{ij} + \Phi_{ij} \quad (7)$$

Where  $P_{ij}$  as in equation (1), and the dissipation rate and  $\Phi_{ij}$ , are obtained from equations (9) and (10) respectively.

$$\epsilon_{ij} = 2\delta_{ij} \epsilon / 3 \quad (8)$$

$$\Phi_{ij} = -c_1 \frac{\epsilon}{k} \left( \overline{u_i u_j} - \frac{2}{3} k \delta_{ij} \right) - c_2 \left( P_{ij} - \frac{2}{3} P_k \delta_{ij} \right) + (\Phi_{ij1}^w + \Phi_{ij2}^w) \quad (9)$$

The conventional wall reflection terms are used, which rely on the wall distance  $x_n$  and the unit vector normal to the wall  $n$ .

$$\Phi_{ij,1}^w = c_1^w \frac{\epsilon}{k} \left( \overline{u_k u_m n_k n_m} \delta_{ij} - \frac{3}{2} \overline{u_k u_i n_k n_j} - \frac{3}{2} \overline{u_k u_j n_k n_i} \right) \left\{ \frac{k^{1.5}}{\epsilon c_\epsilon x_n} \right\} \quad (10)$$

$$\Phi_{ij,2}^w = c_2^w \frac{\epsilon}{k} \left( \Phi_{km2} n_k n_m \delta_{ij} - \frac{3}{2} \Phi_{ik2} n_k n_j - \frac{3}{2} \Phi_{jk2} n_k n_i \right) \left\{ \frac{k^{1.5}}{\epsilon c_\epsilon x_n} \right\} \quad (11)$$

### 3.2.2 Low-Re Models

#### Wolfshtein's Model of k-Transport

The k-transport equation is the same as equation (5) for the high-Re k- $\epsilon$ .

The dissipation rate,  $\epsilon$ , and the turbulent viscosity,  $\mu_t$ , are obtained from:

$$\epsilon = \frac{k^{3/2}}{\ell_c} \quad \text{and} \quad \mu_t = \rho c_\mu \ell_\mu \sqrt{k} \quad (13)$$

The length scales  $\ell_c$  and  $\ell_\mu$  are obtained from the near-wall distance  $Y$ , according to:

$$\Phi_{ij2} = -c_2 \left( P_{ij} - \frac{2}{3} P_k \delta_{ij} \right) \quad (12)$$

$$\ell_c = 2.55 Y [ 1 - \exp(-0.263 y^*) ] \quad (14)$$

$$\ell_\mu = 2.55 Y [ 1 - \exp(-0.016 y^*) ] \quad (15)$$

#### Launder-Sharma [9] k- $\epsilon$

$$\frac{\partial}{\partial x_j} (\rho U_j k) = \frac{\partial}{\partial x_j} \left[ \left( \mu + \mu_t \right) \frac{\partial k}{\partial x_j} \right] + P_k - \rho \epsilon - 2\rho \nu \left( \frac{\partial \sqrt{k}}{\partial x_j} \right)^2 \quad (16)$$

$$\frac{\partial}{\partial x_j} (\rho U_j \epsilon) = \frac{\partial}{\partial x_j} \left[ (\mu + \mu_t) \frac{\partial \epsilon}{\partial x_j} \right] + c_{c1} \frac{\epsilon}{k} P_k - \rho c_{c2} f_2 \frac{\epsilon^2}{k} + 2 \rho \nu v_i \left[ \frac{\partial^2 U_i}{\partial x_i \partial x_i} \right]^2 \quad (17)$$

Where :  $\mu_t = \rho c_\mu f_\mu k^2 / \epsilon$   
 $f_2 = 1 - 0.3 \exp(-R_t^2)$ ,  $f_\mu = \exp[-3.4 / (1 + 0.02 R_t)]$   
 $R_t = k^2 / (\nu \epsilon)$

### Zonal Differential Stress Model (DSM)

Stress Transport Equations :

$$\frac{\partial}{\partial x_k} (\rho U_k \overline{u_i u_j}) = \frac{\partial}{\partial x_k} \left[ \left( \mu + \frac{\mu_t}{\sigma_k} \right) \frac{\partial \overline{u_i u_j}}{\partial x_k} \right] + P_{ij} - \rho \epsilon_{ij} + \Phi_{ij} - \left[ H_{ij} - \frac{1}{3} H_{kk} \delta_{ij} \right] + J_{ij} \quad (18)$$

With  $P_{ij}$  as in equation (1) and  $\epsilon_{ij}$  now obtained from The redistribution term  $\Phi_{ij}$  is similar to that of the basic model, but with the wall reflection terms including a sub-

$$\epsilon_{ij} = \frac{2}{3} (1 - f_c) \epsilon \delta_{ij} + f_c \frac{\overline{u_i u_k}}{k} \epsilon \quad (19)$$

layer dumping function :

$$\Phi_{ij}^w = f_w (\Phi_{ij}^w + \Phi_{ij}^w) \quad (20)$$

The role of the wall reflection terms within the sub-layer is partly fulfilled by the additional low-Re term  $H_{ij}$ . The low-Re terms are as follows :

$$H_{ij} = f_H \frac{\nu}{k} \left( \frac{\overline{u_i u_k}}{k} \frac{\partial \sqrt{k}}{\partial x_k} \frac{\partial \sqrt{k}}{\partial x_j} + \frac{\overline{u_j u_k}}{k} \frac{\partial \sqrt{k}}{\partial x_k} \frac{\partial \sqrt{k}}{\partial x_i} \right) \quad (21)$$

$$J_{ij} = f_J k \left( \frac{\partial U_i}{\partial x_j} + \frac{\partial U_j}{\partial x_i} \right) \quad (22)$$

The damping functions that appear in the above terms have the following expressions :

$$f_c = \exp(-y^*/3) \quad f_w = [1 - \exp(-0.12y^*)] [1 + \exp(-0.03y^*)]$$

$$f_J = 0.06 \exp(-y^*/3) \quad f_H = (10.2 + 7.5y^*) \exp(-y^*/20)$$

In the fully turbulent region, the  $\epsilon$  transport equation is the same as that of the high-Re  $k$ - $\epsilon$  model, equation (7).

In the near-wall regions, the dissipation rate,  $\epsilon$ , is also obtained from a prescribed length scale  $\ell_c$ , obtained from :

$$\ell_c = 2.55 Y [1 - \exp(-0.236 y^*)]$$

### Low-Re Differential Stress Model (DSM)

The stress transport equations are the same as those of the Zonal DSM, equations (18) to (22). The damping functions, however, depend on the local Reynolds number of turbulence,  $R_t$ .

$$f_c = \exp(-R_t/8) \quad f_w = [1 - \exp(-R_t/20)] [1 - \exp(-R_t/100)]$$

$$f_J = 0.06 \exp(-R_t/8) \quad f_H = (10 + 2.6R_t) \exp(-R_t/20)$$

The dissipation rate equation used is the same as equation (17) for the low-Re Launder-Sharma  $k$ - $\epsilon$ . The damping function,  $f_\mu$ , which still appears in the stress and  $\epsilon$  transport equations is now obtained from :

$$f_\mu = \exp[-4 / (1 + 0.01 R_t)^2]$$

### Non-Linear $k$ - $\epsilon$ Models [10]

The stresses are obtained from the algebraic expressions that are non-linear in terms of  $S_{ij}$  and  $\Omega_{ij}$ :

$$S_{ij} \equiv \frac{\partial U_i}{\partial x_j} + \frac{\partial U_j}{\partial x_i} \quad \text{and} \quad \Omega_{ij} \equiv \frac{\partial U_i}{\partial x_j} - \frac{\partial U_j}{\partial x_i}$$

$$S \equiv \frac{k}{\epsilon} \sqrt{S_{ij} S_{ij}/2}, \quad \Omega \equiv \frac{k}{\epsilon} \sqrt{\Omega_{ij} \Omega_{ij}/2}$$

The  $k$  and  $\epsilon$  transport equations are similar to those of the Launder-Sharma model.

A 3-equation version of this model, involving a transport equation for  $A_2$  ( $\equiv a_{ij} a_{ij}$ ), details of which can be found in [10] has also been tested.

### Length Scale Correction Terms

It is well known, that in separated flows, the Launder-Sharma version of the  $\epsilon$  equation returns excessively high levels of near-wall turbulence. To address this problem, Yap [11] proposed the addition of a correction term to the  $\epsilon$  equation, YC, based on the wall distance, Y.

$$YC = \max \left[ 0.83 \frac{\epsilon^2}{k} \left( \frac{k^{1.5}/\epsilon}{2.55Y} - 1 \right) \left( \frac{k^{1.5}/\epsilon}{2.55Y} \right)^2, 0 \right] \quad (23)$$

In a recent proposal by Hanjalic [12], the wall distance

in the above term is eliminated by using the gradient of the length scale normal to the wall surface. Here, these ideas are further developed, by (a) introducing the resultant of the length scale gradient vector and (b) by also taking into account the effects of wall damping across the sub-layer.

From Woolfshtein :  $\ell_c = 2.55 Y [ 1 - \exp(-0.263 y^*) ]$

Differentiating  $\ell_c$  and then replacing  $y^*$  by  $R_\tau$ , as proposed by Yap (11), produces the following expression for the gradient of the equilibrium length scale,  $(d\ell_c/dY)$ :

$$(d\ell_c/dY) = c_t [ 1 - \exp(-B_c R_t) ] + B_c c_t R_t \exp(-B_c R_t)$$

With  $c_t = 2.55$  and  $B_c = 0.1069$

From the resultant gradient,  $D\ell$ , of turbulent length scale  $\ell = k^{3/2}/\epsilon$ , a correction factor  $F$  is defined according to :

$$D\ell = \{ (d\ell/dx_i) (d\ell/dx_j) \}^{1/2}$$

$$F = [ (D\ell - (d\ell_c/dY)) / c_t ]$$

A new version of the Yap term, NYC, is then developed:

$$NYC = \max [ 0.83 F (F+1)^2 \rho \epsilon^2 / k, 0. ] \quad (24)$$

#### Algebraic Stress Models. ASM

In addition to the closures described above, algebraic stress closures have also been employed. These can be obtained from the high-Re, zonal and low-Re DSM closures, by modelling the transport of the stresses using the transport of  $k$ , according to Rodi's proposal [13] :

$$\frac{D}{Dt} \overline{(u_i u_j)} = \frac{\overline{u_i u_j}}{k} \frac{Dk}{Dt} \quad (25)$$

### 3.3 Modelling of Turbulent Heat Fluxes

In all EVM and some second-moment computations the turbulent heat fluxes have been modelled through the effective diffusivity approximation:

$$\rho \overline{u_i t} = - \frac{\mu_t}{\sigma_T} \frac{\partial T}{\partial x_i} \quad (26)$$

In most of the second-moment computations the generalised gradient diffusion hypothesis has been employed.

$$\overline{u_i t} = - \rho c_T \frac{k}{\epsilon} \overline{u_i u_j} \frac{\partial T}{\partial x_j} \quad (27)$$

### 3.4 Numerical Issues

The calculations presented here were carried out with a number of finite volume solvers. For the initial studies and also most current two-dimensional computations fixed, orthogonal co-ordinate methods were used. Recent three-dimensional computation have been obtained using the STREAM code, which employs general non-orthogonal co-ordinates, with a Cartesian velocity decomposition. For the fully-elliptic, three-dimensional computations, for the discretization of convection bounded version of the upstream quadratic interpolation scheme, QUICK [14], were employed such as those described in [15] and [16]. Grid issues are discussed during the presentation of results.

## 4. EARLIER WORK

Our group's computations initially focussed on flow and heat transfer through passages with smooth surfaces.

While in practice U-bends encountered in blade cooling passages have a strong curvature, the radius of curvature is less than passage diameter, flows through U-bends of less severe curvature were first examined, in which separation does not occur and consequently the flow development is mainly influenced by the secondary motion. One of the cases that was extensively examined was flow through a U-bend of square cross-section and of a moderate curvature ratio of  $R_c/D=3.38$ , at Reynolds number,  $Re$ , of 67,000, because of the availability of both flow and thermal data, references [17] and [18].

The predicted vector plots of Figure 5, produced by Choi et al [19], reveal that curvature induces a complex secondary motion, certainly more complex than the single vortex in each symmetric half of the cross-section, normally expected. Moreover, the predicted secondary flow pattern depends on the modelling strategy adopted. A k- $\epsilon$  EVM with wall functions, produces a double cell, for each

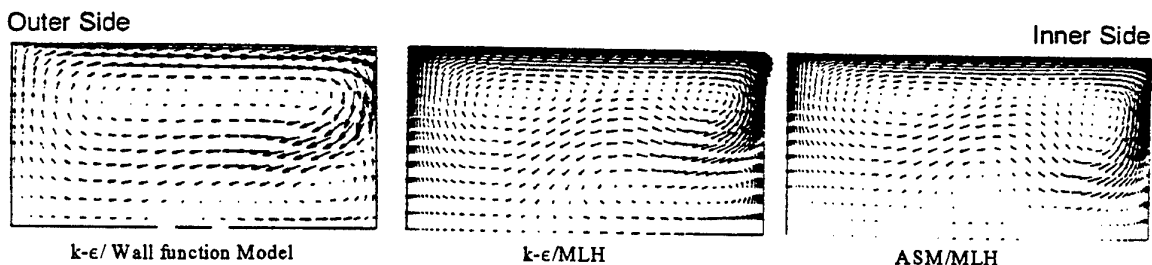


Figure 5. Predicted secondary motion at the 135-degree plane of the U-duct of moderate curvature.

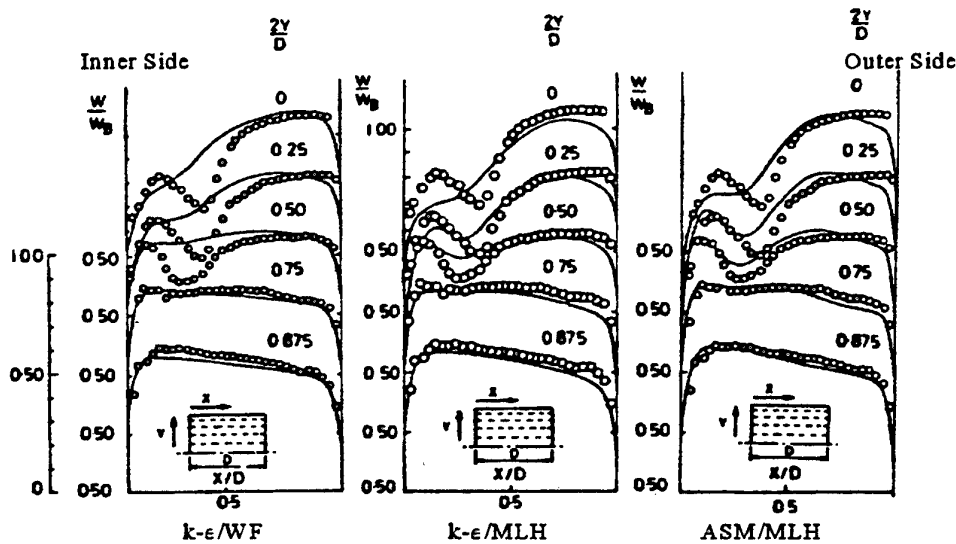


Figure 6. Comparisons of streamwise velocity at the 90-degree plane of the U-duct of moderate curvature.

symmetric half, arrangement. When instead of the wall function approximation a fine near-wall grid is employed, using the mixing length hypothesis across the viscous sub-layer, an additional discrete vortex appears. Refinement of the core turbulence model from an EVM to an ASM, produces a further vortex and also noticeable changes to the shape of the vortices. These changes in the secondary motion result in successive clear-cut improvements in the agreement with the measured streamwise mean velocity field, as demonstrated in Figure 6. As a subsequent study by Besserman and Tanricut [20], focussed on heat transfer computations through a U-bend of stronger curvature, provided further evidence that replacing the wall function approximation with a zonal near-wall modelling approach, results in emphatically better agreement with the measured Nusselt number distribution. The U-bend of moderate curvature has been more recently revisited by Iacovides et al [21], with heat transfer being the main focal point. In addition to ASM closures differential stress closures were also included in the core, including one of the new differential closures that do not require wall reflection terms. Clear-cut improvements over the best Choi et al dynamic field results were found and also, as shown in Figure 7, significant improvements in the resultant heat transfer predictions.

The U-bends found in blade cooling passages, however, are of a curvature strong enough to cause flow separation, as shown in Figure 3. Attempts to compute the flow development through a U-bend of curvature ratio  $R_c/D$  of 0.65, focussed first, Bo et al [22], on the question of securing grid independence. It emerged that it was essential to employ a higher order treatment of convection like LODA [15], even on the turbulence variables  $k$  and  $\epsilon$ . As revealed in Figure 8, agreement is also satisfactory with the measured heat transfer coefficient along the along the flat (top) wall of the U-bend. However, agreement between

the zonal EVM computations and the measurements of the heat transfer coefficient is less satisfactory along the inner and outer walls, especially in and immediately downstream

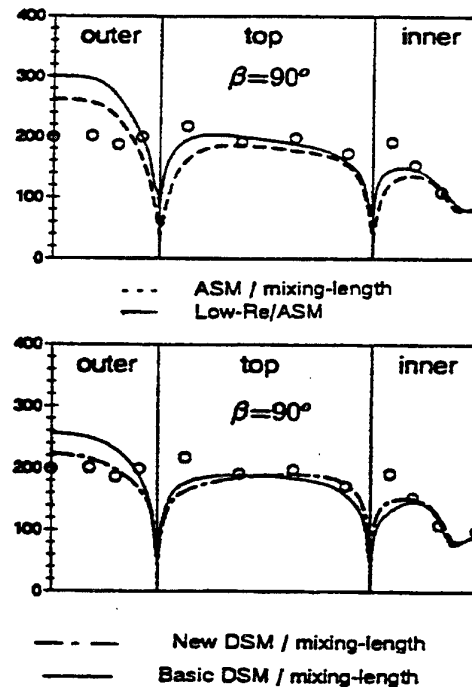


Figure 7. Comparisons of local Nusselt number for a heated U-bend of moderate curvature..

of regions where the near-wall flow is rapidly accelerated. From simpler two-dimensional boundary layers, it is well known that in such regions, a thickening of the viscous sub-layer occurs and this suggests that solving a transport

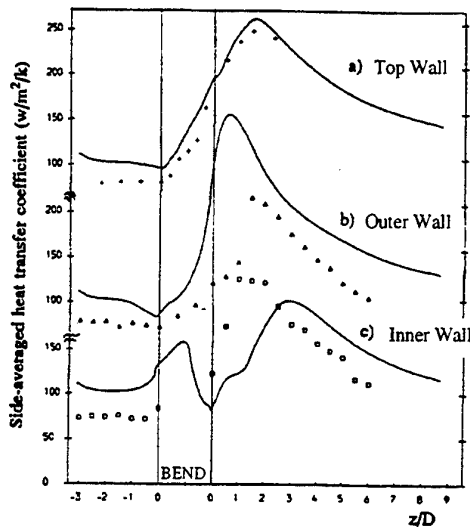


Figure 8. Development of the side-averaged coefficient of wall heat flux around a U-bend of strong curvature.  $k-\epsilon/1$ -eqn computations

equation for  $\epsilon$  all the way to the wall is essential to mimic the flow behaviour correctly.

Following emergence of a more detailed LDA mapping of the flow field for this case [1], Iacovides et al [23], produced further flow computations. The EVM in the core was first replaced by the high-Re ASM and then a zonal ASM was extended across the viscous sub-layer.

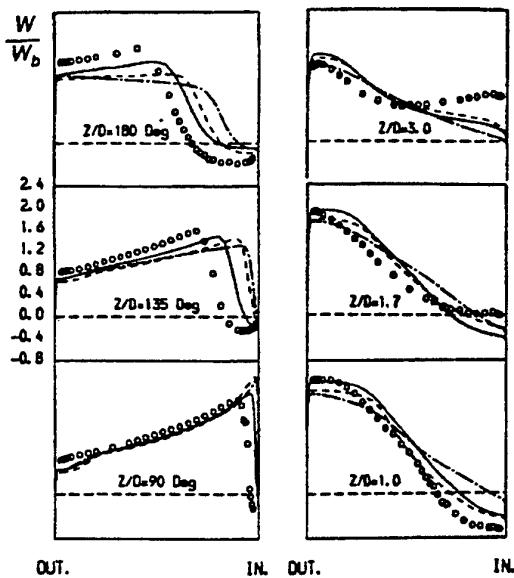


Figure 9. Comparison of streamwise velocity profiles along the symmetry plane of a U-bend of strong curvature. --- :  $k-\epsilon/1$ -eqn, ---- : ASM/1-eqn, — : Low-Re ASM

Figure 9 shows that these refinements, especially the introduction of a near-wall second-moment closure, produce clear improvements in the predicted behaviour, though even

with the best scheme, only half the difference between the measured velocity distributions and those of the  $k-\epsilon/1$ -eqn model is removed.

As far as the effects of rotation are concerned, our group's efforts were mainly concentrated on developing flow through heated rotating ducts where rotational buoyancy effects are also present. The experimental study of Wagner et al [24], on developing flow through heated rotating ducts provided side-averaged Nusselt number data

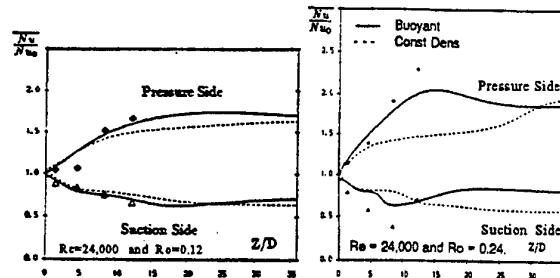


Figure 10. Comparisons of the side-averaged Nusselt number, for developing flow in a rotating square duct. Zonal EVM computations.

for comparisons. Constant-density computations were also performed, in order to separate the Coriolis effects from those of rotational buoyancy. As shown in Figure 10, when rotational buoyancy is not influential the zonal EVM model returns satisfactory Nusselt number predictions, producing the correct enhancement of heat transfer along the pressure side and the corresponding attenuation along the suction side. At higher rotation numbers, however, at which rotational buoyancy becomes significant, as can also be seen in Figure 10, the thermal predictions of the zonal EVM begun to deviate significantly from the corresponding measurements, especially along the suction side. The zonal ASM also failed to return the measured behaviour, while the

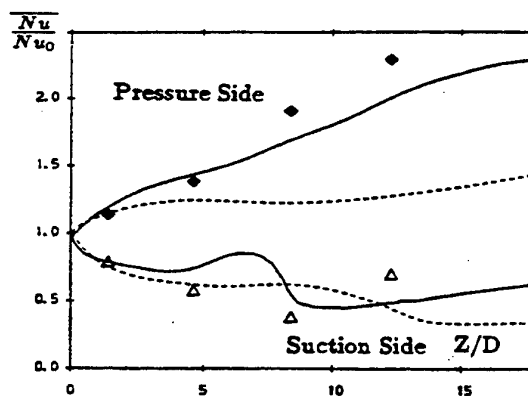


Figure 11. Comparisons of the side-averaged Nusselt number, for developing flow in a rotating square duct. Low-Re-ASM computations.

low-Re EVM return entirely wrong predictions along the suction side. As shown in Figure 11, the low-Re ASM

closure returns a thermal development closer to that measured.

The earlier work on smooth passages has thus revealed that in either curved or orthogonally rotating passages, the presence of the secondary motion necessitates the resolution of the near-wall regions, using either a zonal modelling approach or low-Re models. Because of the presence of streamline curvature, additional predictive improvements are achieved through the introduction of second-moment closures. Differential stress models are found to be preferable to algebraic closures, especially for thermal predictions with the new, realisable closures, shown to be especially promising. In U-bends of strong curvature, the modelling of near-wall turbulence through the use of low-Re second-moment closures appears to be necessary. The same requirement is also necessary for the computation of heat transfer through rotating heated ducts when rotational buoyancy becomes important.

## 5 RECENT WORK

Our more recent effort have been directed to the computation of flow and heat transfer through ribbed passages. Most of the zonal and low-Re models of turbulence developed for flows through smooth passages,

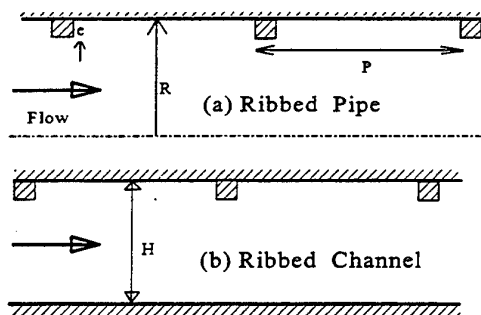


Figure 12. Two-dimensional ribbed passages examined.

with the algebraic stress closures replaced by differential stress transport closures, were first applied to the computation of flow and heat transfer through two-dimensional ribbed passages as shown in Figure 12. Attention was then turned to the computation of flow and heat transfer through three-dimensional ribbed ducts, with either in-line or staggered ribs shown in Figure 13. For the latter arrangement, computations have also been obtained

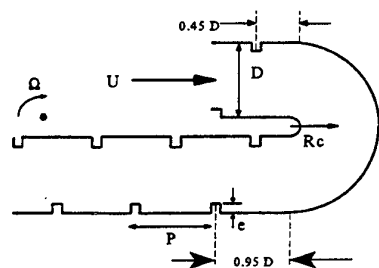


Figure 13. Ribbed, rotating U-bend with staggered ribs.

for rotating conditions.

### 5.1 Heat Transfer in two-dimensional ribbed passages.

Several flows through two-dimensional ribbed passages have been computed, for which local wall heat transfer data are available. These are tabulated below.

Passage	P/e	e/D or e/H	Re	Pr
Pipe	10	0.0675	$24 \times 10^3$	0.71
Pipe	10	0.0675	$64 \times 10^3$	0.71
Channel	10	0.1	$122 \times 10^3$	0.71
Channel	10	0.1	$40 \times 10^3$	5.45

All the cases examined, involved passages long enough for repeating flow conditions to prevail over each rib interval. Consequently, the numerical flow domain covers only one rib interval and repeating flow and thermal boundary conditions are applied. A Cartesian mesh is employed, with the grid nodes falling within the ribs blocked off. In all cases two grids were used, a  $51 \times 60$  and a  $91 \times 110$ . For the

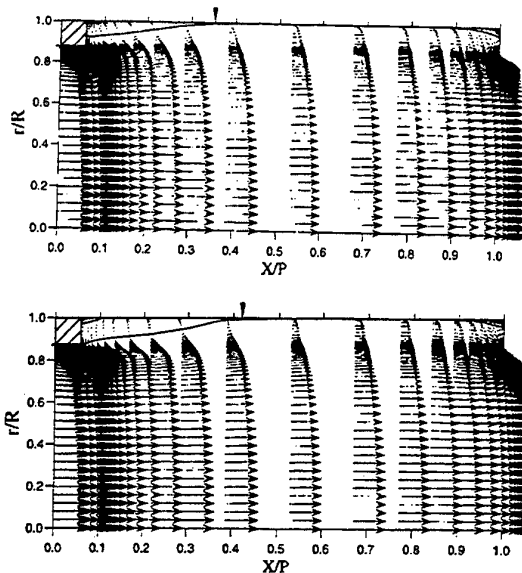


Figure 14 Predicted mean flow field in a ribbed pipe.

first three cases, constant wall heat flux thermal boundary conditions were employed. For the last case constant wall heat flux conditions were applied over the ribbed channel wall. The heat conduction equation was solved within the ribs, assuming that the heat flux, per unit area, into each rib was the same as that for the rest of the duct wall. These thermal boundary conditions were consistent with the heating arrangements in the experimental study [7].

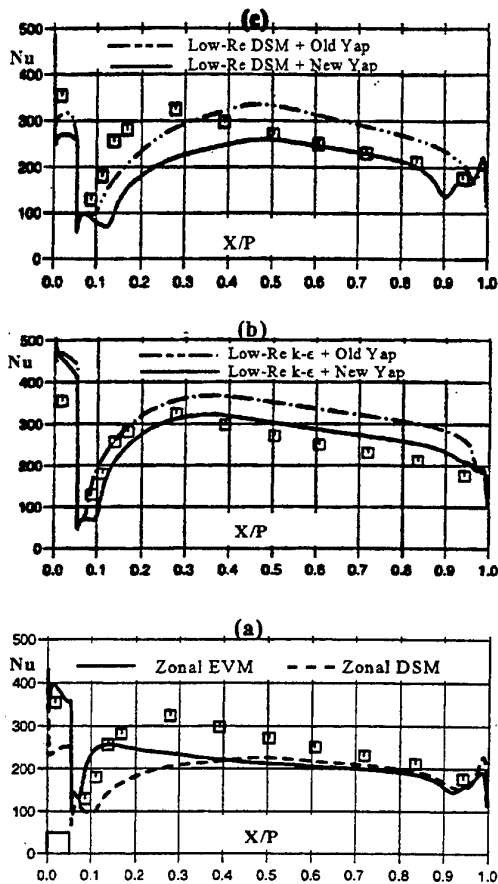


Figure 15. Nusselt number comparisons for ribbed piped, at  $Re=64 \times 10^3$ .

The mean flow fields returned by the zonal EVM and DSM models for the ribbed pipe interval are shown in Figure 14. Downstream of the rib, because of its sensitivity to streamline curvature, the DSM model predicts a longer and wider separation bubble. The corresponding low-Re models produced similar flow fields.

Comparisons for the local Nusselt number for the ribbed pipe, at  $Re=64 \times 10^3$ , presented in Figure 15, reveal that the two zonal models under-predict, by as much as 30%, Nusselt numbers over the first half of the rib interval, while over the second half of the interval, both models are in close agreement with the data. This is not unexpected, since in both zonal model, the scale of the near-wall eddies is assumed to depend on the wall distance, an assumption which is inappropriate for flow separation regions, where transport effects on the turbulent length scale cannot be ignored. In fact when the simplicity of the near-wall model is taken into account, the thermal predictions of the zonal approaches can be said to be surprisingly close to the data. The zonal EVM predicts that the downstream of the rib the Nusselt number rises too quickly to its local maximum, while the Zonal DSM shows the opposite predictive deficiency. The low-Re  $k-\epsilon$ , while with the old Yap term over-predicts levels of wall heat transfer, by about 20%,

while with the new Yap term proposal, agreement with the measured Nusselt number data is very close. The low-Re DSM with the new Yap term returns too low Nusselt number values downstream if the interval, while with the old Yap term the predicted Nusselt number variation is in closer overall agreement with the data.

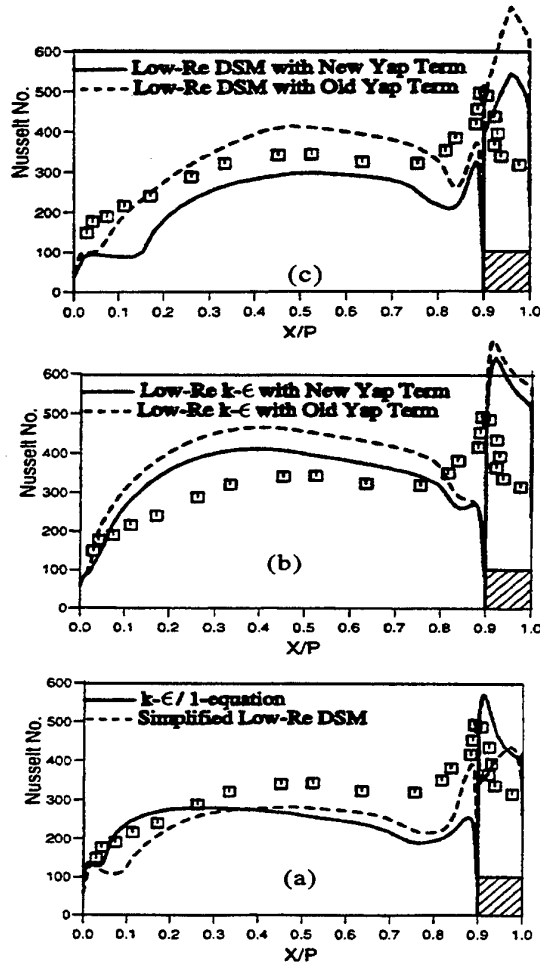


Figure 16. Nusselt number comparisons for ribbed channel, at  $Re=122 \times 10^3$ , and  $Pr=0.71$ .

Comparisons for the ribbed channel, with air as the working fluid,  $Pr=0.71$ , shown in Figure 16, also lead to similar conclusions. It should be noted, that for the ribbed channel, Nusselt number levels rise more gradually downstream of the rib, possibly because only one wall of the plane channel is ribbed and consequently each rib causes a stronger deflection of the flow away from the ribbed surface. The DSM models reproduce this gradual rise more faithfully than the EVM and are therefore in closer agreement with the thermal data. For water,  $Pr=5.45$ , as seen in Figure 17, the relative performance of the models tested does not change.

The two-dimensional comparisons therefore, for axisymmetric and plane geometries, indicate that the zonal models under-predict wall heat transfer but are in some



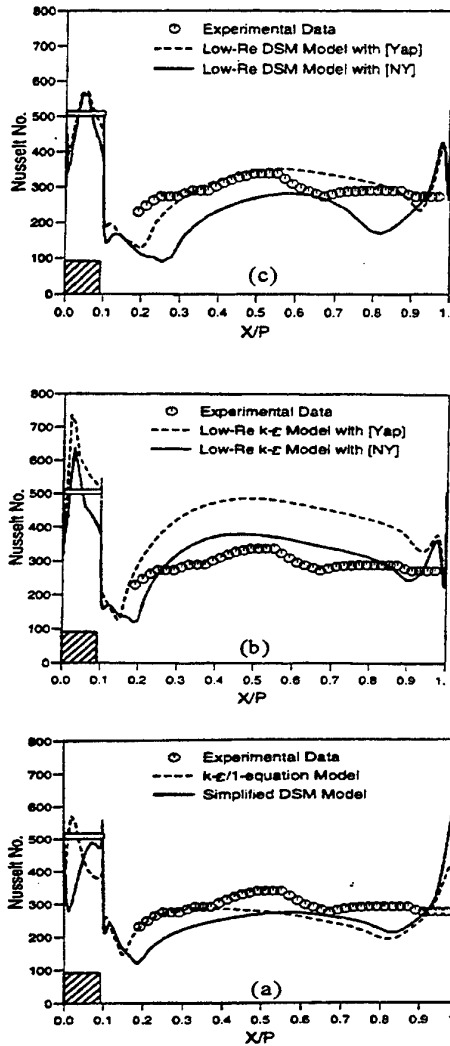


Figure 17. Nusselt number comparisons for ribbed channel, at  $Re=40 \times 10^3$ , and  $Pr=5.45$

regions but are in reasonable overall accord with measured heat transfer data. The new Yap term improves the thermal predictions of the low-Re EVM, resulting in good agreement with the data, while for the low-Re DSM the effect of the new Yap term appears to be too strong leading to unrealistically low levels of wall heat transfer. A re-optimisation of this term appears to be necessary when used with the low-Re DSM tested in this study.

Further tests, involving non-linear k-ε models, as can be seen in Figure 18, showed that both the versions, but especially the 3-equation version, over-predict wall heat transfer over most of the inter-rib region, returning Nusselt numbers up to 20% higher than those of the linear k-ε. Recent work by Cooper [25], in flows over abrupt pipe

$$c_{\mu} = \frac{0.3[1 - \exp(-0.36 \exp[0.75 \eta])]}{1 + 0.35 \eta^{1.5}} \quad (28)$$

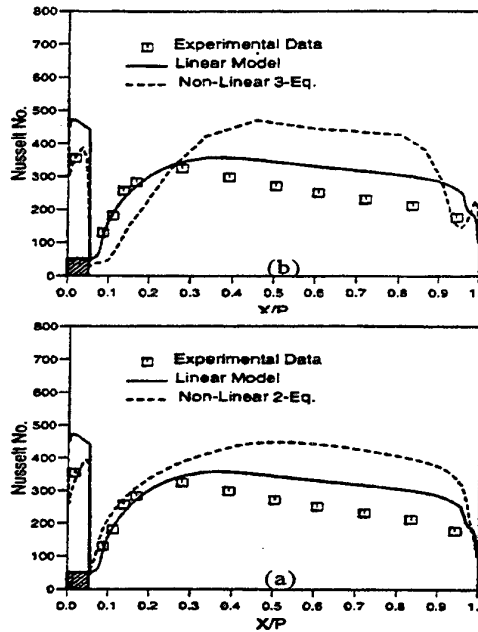


Figure 18. Nusselt number comparisons for ribbed piped, at  $Re=64 \times 10^3$ , using non-linear k-ε models.

$$\text{Where } \eta = \max(S, \Omega)$$

expansions suggested that one possible reason is that use of equation (28) results high levels of  $c_{\mu}$  in regions of flow recirculation. As the comparisons of Figure 19 reveal, a possible remedy may be to limit the maximum value of  $c_{\mu}$  returned by equation (28) to 0.09.

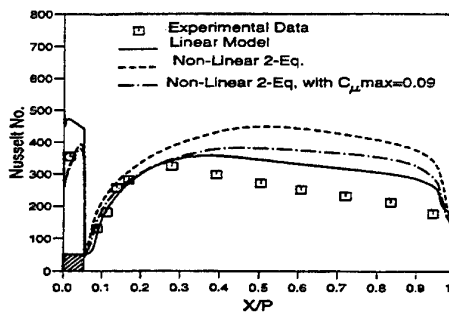


Figure 19. Nusselt number comparisons for ribbed piped, at  $Re=64 \times 10^3$ , using the two-equation non-linear k-ε model. Effect of modification on  $c_{\mu}$ .

## 5.2 Flow and Heat Transfer in three-dimensional ribbed passages.

### 5.2.1 Flow Computations.

One of the first issues to be addressed was that of achieving adequate grid resolution for three-dimensional flows through passages of complex geometries. In an effort

to minimise the number of grid nodes required, the use of body-fitted co-ordinates as those shown in Figure 20, for a square-section duct, with staggered ribs on two opposite walls was first explored. Body-fitted grids allow the flow region around ribs to be resolved with fewer grid nodes than Cartesian grids with blocked regions and also avoids the formation large aspect ratio cells within the flow domain. The zonal EVM computations of Figure 21 show that even body-fitted grids of relatively modest size, can produce grid-independent solutions in ribbed passages.

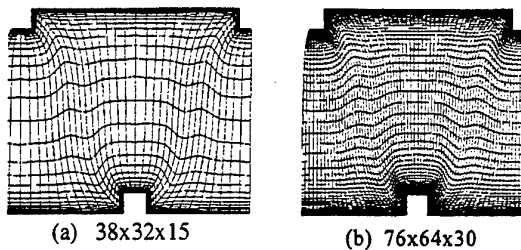


Figure 20. Body-fitted grids employed over a rib-interval.

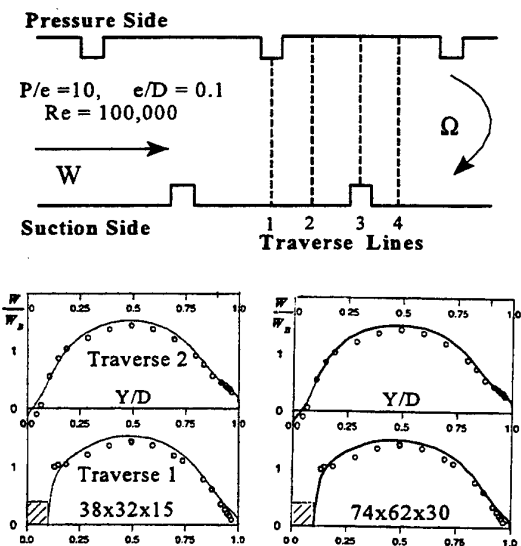


Figure 21. Grid sensitivity comparisons for repeating flow in a duct with staggered ribs, using the zonal EVM.

The resulting comparisons, in Figure 22, reveal that for repeating flow in a straight duct with staggered ribs the zonal EVM reproduces the mean motion correctly and also returns turbulence levels similarly high as those measured [6]. The zonal DSM model returns a somewhat faster flow along the symmetry plane than that measured. The streamwise turbulence intensity is well predicted and also the high shear stress measured over the rib, which the EVM model fails to reproduce is also better predicted by the zonal DSM. The differences in the prediction of the mean flow development appear to arise from the fact that the DSM model, as seen in Figure 23, also returns a strong

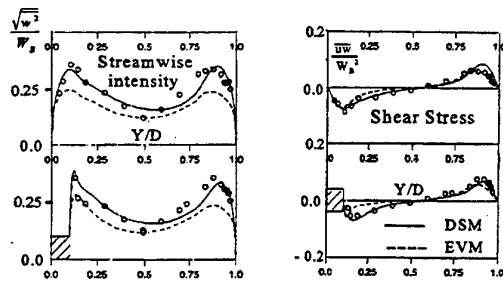
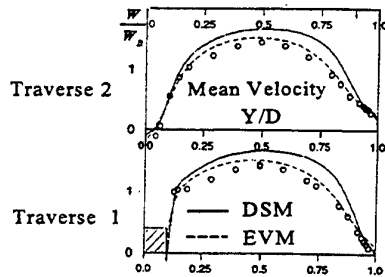


Figure 22. Comparisons for mean and fluctuating velocities for repeating flow in a duct with staggered ribs

turbulence-driven secondary motion, which appears to be stronger than that in the real flow. For a rotating ribbed bend, because of the Coriolis-driven secondary motion, the turbulence-driven motion becomes insignificant. The DSM and EVM models consequently return the same mean flow field which, as shown in Figure 24, is in good agreement with that measured [6]. Figure 24 also shows that the effects of rotation on turbulence, which raises the turbulence levels along the pressure side of the rotating duct, are also better reproduced by the DSM model. While the comparisons presented in Figures 22 to 24 are all for computations using zonal (EVM and DSM) models, low-Re DSM and EVM models returned flow predictions practically identical to those of the corresponding zonal models.

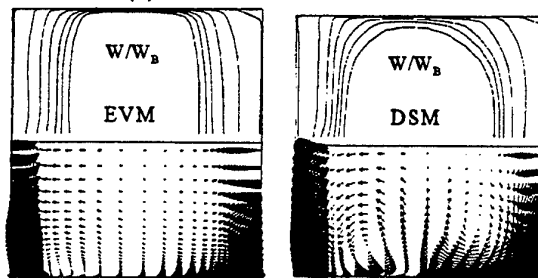


Figure 23. Predicted mean flow fields across the duct at traverse location 2, for repeating flow in a duct with staggered ribs.

Initial attempts to compute the combined effects of rib-roughness and strong curvature have also been made, using body-fitted grids to resolve one of the symmetric halves of

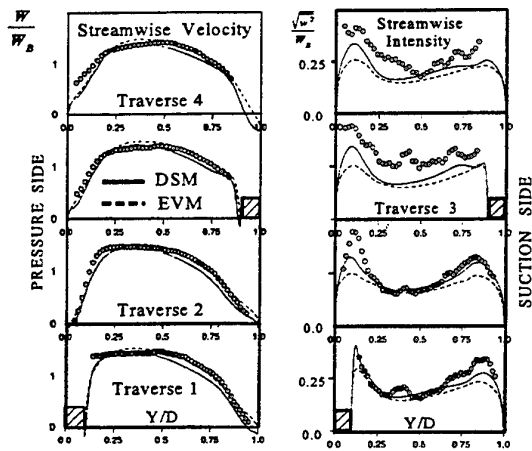


Figure 24. Comparisons for mean and fluctuating velocities for repeating flow in a rotating duct with staggered ribs, at  $Ro=0.2$ .

the flow domain shown in Figure 13. Grids of  $15 \times 32 \times 147$  shown in Figure 25 and also of  $21 \times 44 \times 297$  have been used, both resulting in the same solutions. The measured [6] flow development along the symmetry plane, presented in the velocity profiles of Figure 27, is for the most part well predicted, especially when the zonal EVM is replaced by the zonal DSM closure. As also found in flows through smooth U-bends, Figure 10, the separation bubbles along both the inner and the outer walls are more faithfully reproduced by the zonal DSM, though, evidently, agreement with the experimental data is not complete. As can be seen in Iacovides [16] the more complex flow that results from rotating the ribbed U-bend about an axis parallel to that of curvature, with the Coriolis force opposing that of curvature, is not as closely predicted, even by the DSM closure.

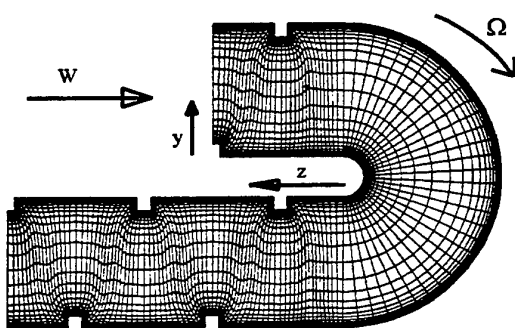


Figure 25. Grid employed for computations through a ribbed U-bend.

The flow comparisons thus reveal that the use of body-fitted grids can considerably reduce the grid requirements in the computation of three-dimensional flows through ribbed passages. Zonal and low-Re modes DSM models are found able to reproduce internal flows affected by rib-roughness and orthogonal rotation or rib-roughness and strong

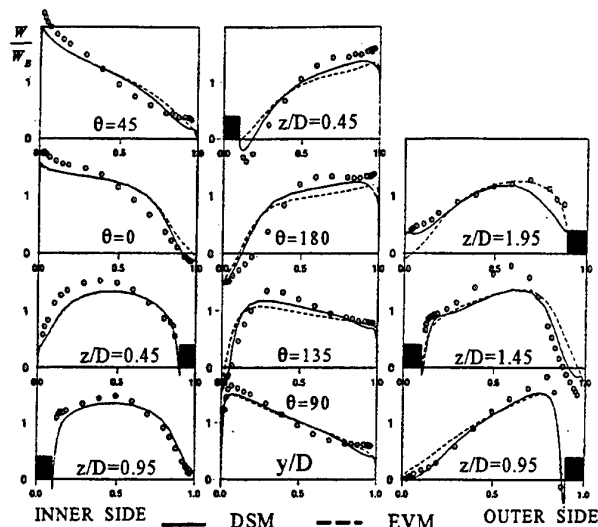


Figure 26. Mean flow comparisons for flow along the symmetry plane of a ribbed U-bend.

curvature. The zonal and low-Re EVM models also reproduce the main flow features present but, as also found in smooth ducts, in regions of flow separation are not as successful as the DSM models. Moreover, the complex turbulence fields present are not as well reproduced by the EVM models, which is insensitive to the effects of streamline curvature and also those of the Coriolis force. However, there is also evidence that, as the flow field becomes progressively more complex, the low-Re extensions to the basic DSM model show more predictive deficiencies.

### 5.2.2 Heat Transfer Computations.

Heat transfer computations have so far covered straight ribbed ducts of square cross-section in which repeating flow conditions are established. Two such geometries have been examined: a straight duct with in-line ribs on opposite walls, and a duct with staggered ribs on opposite walls. In the case of the duct with in-line ribs, the rib-height-to-diameter ratio,  $e/D$  is 0.0675, the rib spacing,  $P/e$  is 10 and data for comparison have been obtained from Baughn et al [26]. For the duct with staggered ribs,  $e/D=0.1$  and  $P/e=10$ , and the case was experimentally examined at UMIST [7].

Comparisons of the Nusselt number distribution along the symmetry line of the ribbed wall, for the duct with in-line ribs, Figure 27, show that the zonal models, as in the two-dimensional cases, under-predict the coefficient of wall heat transfer. The zonal DSM does however reproduce the experimental behaviour more closely than the zonal EVM, returning a more gradual rise in Nusselt number in the recirculation region downstream of each rib and higher levels after re-attachment. The low-Re EVM returns higher Nusselt numbers which, especially with the new Yap term, are very close to the measured values. In common with the zonal EVM and also as noted in two-dimensional channels, the low-Re EVM predicts that in the recirculation region

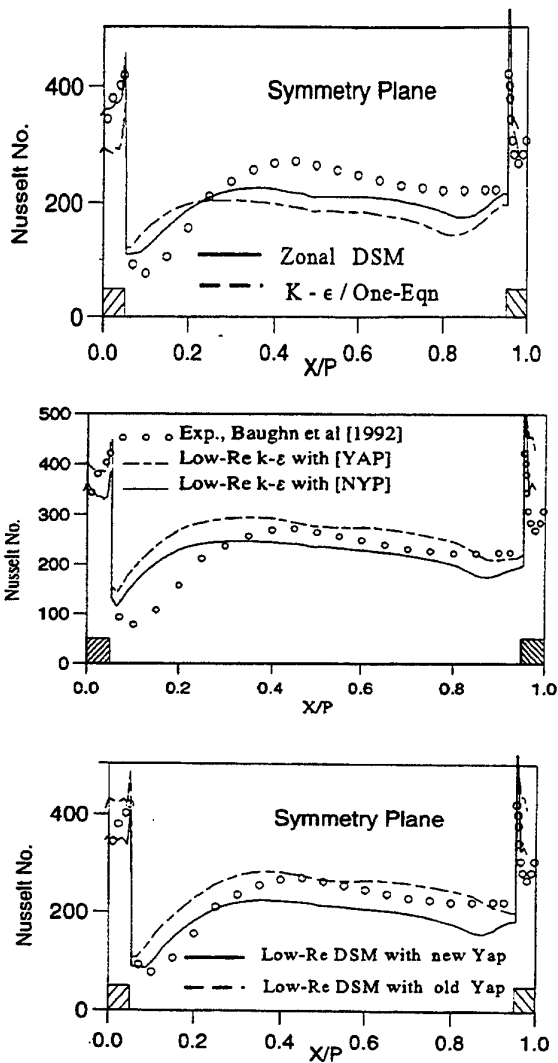


Figure 27. Comparisons of the local Nusselt Number along the centerline of the ribbed wall of a heated duct with in-line ribs.

downstream of each rib, the Nusselt number rises too quickly. As also noted in the two-dimensional cases, the original Yap term causes the low-Re  $k-\epsilon$  to over-predict wall heat transfer. The low-Re DSM comparisons for this case, also lead to conclusions similar to those reached in the two-dimensional case. With the original Yap term, the low-Re DSM produces a Nusselt number distribution that for the most part is close to the measurements and also, in contrast to the EVM, returns a more gradual rise downstream of each rib.

For the passage with staggered ribs, comparisons are presented, for the distribution of local Nusselt number along the symmetry line of the ribbed wall and also for the distribution of the side-averaged Nusselt number along the ribbed wall, Figure 28. The zonal model predictions, show that the Nusselt number is now more severely under-predicted than for the duct with in-line ribs. One possible

cause may be the fact that the rib size in this case is greater. As expected, the introduction of low-Re models leads to the prediction of higher Nusselt numbers. The low-Re EVM, with the original Yap term, while, as in the previous cases, over-predicting the symmetry-line Nusselt number, nevertheless returns the correct distribution of the side-averaged Nusselt number. With the new version of the Yap term, the low-Re  $k-\epsilon$  returns reasonable Nusselt number values along the symmetry line, but under-predicts the side-averaged Nusselt number. The low-Re DSM, with the original Yap term returns the correct distribution of wall heat transfer along the symmetry plane and also the correct distribution of the side-averaged Nusselt number.

The three-dimensional heat transfer computations therefore result in conclusions that are on the whole consistent with those reached in the computations of two-dimensional flow and heat transfer through ribbed passages. Zonal models, because they ignore the effects of transport on the near-wall turbulence scale, under-predict wall heat transfer rates. The low-Re closures are found able to reproduce the correct Nusselt numbers, provided that correction terms are added to the dissipation rate equation. The alternative version to the Yap term proposed, appears to offer some predictive advantages when used with the Low-Re EVM model, but in its current form is found to be too strong when used with the low-Re DSM closure. The second-moment closure, even low-Re extension of the basic DSM model, is found to produce heat transfer predictions that are superior to those of the EVM model and in close accord with the available data.

## 6. CONCLUDING REMARKS

The computation of convective heat transfer in passages affected by strong curvature, orthogonal rotation and rib-roughness has been considered. A series of test cases have been computed, in order to identify the turbulence modelling practices necessary to produce reliable predictions in flows subjected to these influences. Curvature and orthogonal rotation generate secondary motion that requires the integration of the momentum equations across the viscous sub-layer, using either zonal or low-Reynolds numbers models of turbulence. The introduction of second-moment closures can further improve flow and thermal predictions because of the sensitivity of these closures to the effects of streamline curvature and rotation. Some evidence has also emerged that more elaborate, realisable second-moment closures can produce further predictive improvements. For flow and thermal computations through U-bend of strong curvature, it has been found necessary to use high order discretization schemes for the convective transport of all flow variables, including  $k$  and  $\epsilon$ . The presence of the three-dimensional separation bubbles necessitates the extension of second-moment closures across the sub-layer regions, through the use of either zonal or low-Re DSM closures. Low-Re DSM closures are also found to be necessary for the prediction of flows through heated rotating ducts, in which rotational buoyancy

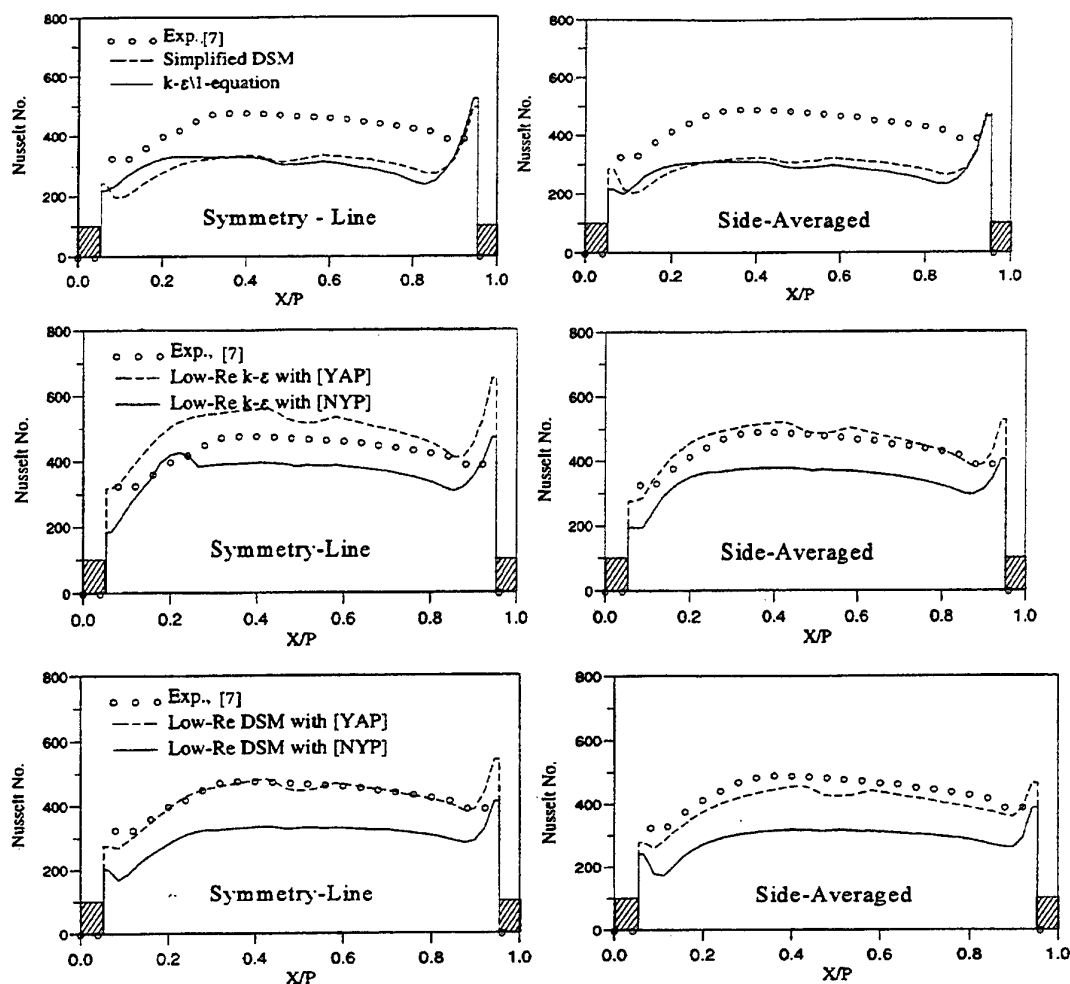


Figure 28. Nusselt-number comparisons for repeating flow through a heated duct with staggered ribs.  $Re=100,000$  and  $Pr=0.71$

becomes influential. For the computation of three-dimensional flows through ribbed passages of complex geometries, the use of body-fitted grids has been found to substantially reduce grid requirements. For the computation of flows affected by strong curvature and rib-roughness it is found necessary to extend the second-moment closure across the viscous sub-layer. As far as the computation of heat transfer through ribbed passages is concerned, the use of low-Re closure appears to be essential. For the low-Re closures tested the inclusion of length scale correction term appears to be necessary. For the low-Re  $k-\epsilon$  an alternative to the Yap term, independent of the wall distance, is found to be more promising than the original version. The low-Re DSM model, because of its sensitivity to the effects of streamline curvature reproduces the turbulence field more faithfully than the EVM model, which in turn leads to thermal predictions superior to those of the low-Re  $k-\epsilon$ . The non-linear  $k-\epsilon$  models examined have been found to fail to reproduce the measured thermal behaviour in the presence of rib-induced separation. Some remedies are proposed but further development of the non-linear models examined is necessary. While agreement with measurements has not

been complete in all the cases examined and further work on more complex flows is still in progress, low-Re differential stress models appear to offer the best route for the reliable computation of convective heat transfer in blade cooling passages.

#### Acknowledgements

Funding for the work presented has been provided by Rolls-Royce plc. The authors gratefully acknowledge both the financial and technical support received and the many useful interactions with Mr J Couplant from Rolls-Royce Derby. The authors also wish to acknowledge the support and encouragement received from Prof. B E Launder and the contributions of Drs T Bo and H-Y Li. The help of Dr Y-M Yuan and Mr G Kelemenis who made their experimental data available in a suitable form, is also acknowledged.

#### References

1. Cheah S C, Iacovides H, Jackson D C, Ji H and Launder B E, 1996 "LDA investigation of the flow

- development through rotating U-ducts.", ASME J of Turbomachinery, **118**, 590-596.
2. Bradshaw P, 1973, "Effects of streamline curvature on turbulent flow.", AGARDograph 169.
  3. Iacovides H and Li H-Y, 1993, "Near-wall turbulence modelling of developing flow through curved ducts and channels.", Proc. IAHR, 5th Int. Symp. on Refined flow modelling and Turbulence Measurements, Paris,
  4. Ellis L B and Joubert P N, 1974, "Turbulent shear flow in a curved channel.", J Fluid Mechanics, **62**, 65-84.
  5. Cotton M A and Jackson J D, 1987, "Calculation of turbulent mixed convection in a vertical tube using a low-Reynolds-number k- $\epsilon$  turbulence model.", 6th Turb. Shear Flows Symp., Toulouse, France.
  6. Iacovides H, Jackson D C, Ji H, Kelemenis G, Launder B E and Nikas K, 1998, "LDA study of flow development through an orthogonally rotating U-Bend of strong curvature and rib-roughened walls.", ASME Journal of Turbomachinery, **108**, 386-391.
  7. Iacovides H, Jackson D C, Kelemenis K, Launder B E and Yuan Y-M, 1998, "Recent progress in the experimental investigation of flow and local wall heat transfer in internal cooling passages of gas-turbine blades.", 2nd EF Conf. Turb. Heat Trns., Manchester, UK.
  8. Wolfshtein M, 1969, "The velocity and temperature distribution in one-dimensional flow with turbulence augmentation and pressure gradient.", Int. J. Heat and Mass Transfer, **12**, 301.
  9. Launder B E and Sharma B I, 1974, "Application of the energy-dissipation model of turbulence to the calculation of flow near a spinning disc.", Letrs in Ht Mass Trans., **1**, 131-138.
  10. Craft T J, Launder B E and Suga K, 1996, "Development and application of a cubic eddy-viscosity model of turbulence", Int. J. Heat and Fluid Flow, **17**, 108-115.
  11. Yap C R, 1987, "Turbulent heat and momentum transfer in recirculating and impinging flows.", PhD Thesis, Dept. of Mech. Engrng, Faculty of Technology, Univ. of Manchester.
  12. Hanjalic K, 1996, "Some resolved and unresolved issues in modelling non-equilibrium and unsteady turbulent flows.", Proc of 3rd Int Symp on Engineering Turbulence Modelling and Measurements. Crete, Greece.
  13. Rodi W, 1976, "A new algebraic stress relation for calculating the Reynolds stresses.", Z Ang Math und Mech, **56**, 219.
  14. Leonard B P, 1979, "A stable and accurate convective modelling procedure, based on quadratic interpolation.", Comp Methods in Applied Mechs and Engrng, **19**, 59-68.
  15. Zhou H and Leschziner M A, 1988, "A local oscillation-damping algorithm for higher order convection schemes, Comp Meth Appl Mech Engrg.
  16. Iacovides H, 1997, "The computation of turbulent flow through stationary and rotating U-bends of with rib-roughened surfaces." 11th Int Conf on Lam and Turb. Flows, Swansea.
  17. Chang, S M, Humphrey, J A C H and Modavi A, 1983, Turbulent flow in a strongly curved U-bend and downstream tangent of square cross-section." Physico-Chemical Hydrodynamics, **4**, 243.
  18. Johnson R W and Launder B E, 1985, Local heat transfer behaviour in turbulent flow around a 180 bend of square cross-section, Int. J. Heat Fluid Flow, **6**, 177.
  19. Choi Y-D, Iacovides H and Launder B E, 1989, "Numerical computation of turbulent flow in a square-sectioned 180° bend.", ASME J. Fluids Engrg., **111**.
  20. Besserman D L and Tanrikut S, 1991, "Comparison of heat transfer measurements with computations for turbulent flow around a 180° bend." ASME Paper 91-GT-2, Int. Gas-Turbine and Aero Congress, Orlando FL.
  21. Iacovides H, Launder B E and Li H-Y, 1996, "Application of a Reflection-Free DSM to Turbulent Flow and Heat Transfer in a Square-Sectioned U-Bend.", Int. Journal of Exp. Thermal and Fluid Science, **13**, 419-429.
  22. Bo T, Iacovides H and Launder B E, 1995, "Convective discretization schemes for the turbulence transport equations in flow predictions through sharp U-bends.", Int. J. Num. Meths in Heat and Fl. Flow, **5**, 33-48.
  23. Iacovides H, Launder B E and Li H-Y, 1995, "The computation of flow development through stationary and rotating U-bends of strong curvature.", Int Journal of Heat and Fluid Flow, **17**, 22-23.
  24. Wagner J H, Johnson B V and Hajek T J, 1989, "Heat transfer in rotating passages with smooth walls.", ASME, Paper 89-GT-272, Int Gas-Turb and Aer Congress.
  25. Cooper D, 1997, "Computation of momentum and heat transfer in a separated flow, using low-Reynolds-number linear and non-linear k- $\epsilon$  models.", M.Res Dissertation, Dept. Of Mech. Engrg., UMIST.
  26. Baughn J W and Yan X, 1992, "Local heat transfer measurements in square ducts with transverse ribs.", ASME, National Heat Transfer Conference.

# VORTEX STRUCTURE AND HEAT TRANSFER IN TURBULENT FLOW OVER A WALL-MOUNTED MATRIX OF CUBES

E.R. Meinders and K. Hanjalić

Faculty of Applied Physics, Delft University of Technology,  
P.O. BOX 5046, 2600 GA, Delft, The Netherlands

## ABSTRACT

The flow structure and the distributions of the local convective heat transfer of a spatially periodic in-line matrix of wall-mounted cubes in a turbulent channel flow is analysed. Infrared thermography was applied to measure the surface temperature field of the cubes, from which distributions of the local heat transfer coefficient were determined. The flow field structure was evaluated from Laser Doppler Anemometry measurements and flow visualisations. The spatial periodicity was confirmed from flow field and heat transfer measurements across the entire matrix. The results showed that the flow has a marked vortex structure only in the immediate proximity of the cube, while the flow above the cube and in the streamwise corridors was hardly distorted, except for a high level of turbulence intensity. Flow separation at the sharp leading top and side edges led to flow recirculations with subsequent flow reattachment at these faces. Flow reattachment of the top shear layer at the channel floor downstream caused a two cell-structure to exist in the inter-obstacle space: an arch-type vortex in the wake of the upstream cube and a horseshoe-type vortex in front of the downstream cube. Further, flow instabilities caused vortex shedding at the side faces which led to periodic motion in its wake. A dimensionless frequency, expressed as the Strouhal number, of  $St = 0.109$  was found. The observed local differences in the flow structure caused marked variation in the distributions of the local heat transfer coefficient. In particular, the top and the side faces of the cube had large spatial gradients due to the flow separation and subsequent reattachment.

## 1. Introduction

Turbulent flow and heat transfer over a wall-mounted matrix of cubes have been widely adopted as an idealised representant of various practical situations encountered in engineering. A typical example is electronics cooling, where the cube matrix has been adopted as a paradigm of densely packed printed circuit boards. The matrix flow involves complex vortical structures and several generic flow phenomena, such as impingement, separation, recirculation, reattachment, where the surface heat transfer from the cubes displays notable dissimilarity from the momentum transport. The involved spatially periodic flow boundary conditions make this configuration well suited for benchmarking purposes to validate turbulence models and numerical methods.

Flows over isolated, wall-mounted cubes have been subject of investigation for several researchers. Castro and Robins [4] performed hot-wire measurements for a single cube on a flat plate for different boundary layer flow conditions. It was shown

that the extent of the wake recirculation and the size of the vortex on top of the obstacle were strongly dependent on the boundary layer thickness of the oncoming flow. The flow around a single wall-mounted cube in a fully developed turbulent channel flow was investigated experimentally by Martinuzzi et al. [10,9,8,11]. The Reynolds number was  $Re_H = 40.000$ , based on the cube height ( $H = 2.5$  cm) and the bulk velocity. The channel height-to-cube ratio was 2. The major flow features were well documented: the horseshoe vortex, induced at the windward face, the arc-shaped vortex in the wake of the cube and the flow recirculations at the top and the side faces of the cube. Further, the studies included a detailed description of the Reynolds stresses and higher order moments. It was found that the horseshoe vortex region was unstable but non-periodic which caused bimodal velocity distributions to exist. Vortex shedding was detected in the wake of the cubical obstacle.

The flow structure around multiple-obstacle configurations in a channel flow received little attention in the literature. Okamoto et al. [18] studied the flow

field in a matrix of surface-mounted square blocks of width  $D = 23$  mm and height  $H = 5$  mm placed in a boundary layer flow. The face-to-face distance  $S$  (in both the streamwise and the spanwise direction) was varied as  $S/H = 2, 3, 5, 7, 10$  and  $13$  to investigate the different flow regimes as imposed by the different distances between the elements. The Reynolds number was constant for all configurations studied,  $Re_H = U_\infty H/\nu = 990$ , where  $U_\infty$  denotes the freestream velocity. They used a two-colour Laser Doppler Anemometer to measure the time-mean velocities and turbulence intensities around the protruding obstacles. The study showed that for  $S/H < 5$  the flow did not reattach at the channel floor and that the inter-obstacle space was fully covered by a large flow recirculation. Reattachment at the channel floor of the separated shear layer was detected at  $S/H > 7$ . They found that the configuration of blocks with spacing  $S/H = 7$  had maximum turbulence intensities around the blocks.

In another paper [14] we report on the convective heat transfer characteristics for a single wall-mounted cube in a developing turbulent channel flow for a Reynolds number range between  $2750 < Re_H < 4970$ , based on the cube size  $H = 15$  mm and the bulk velocity. It was shown that the distributions of the local heat transfer coefficient exhibit large gradients, in particular at the top and the side faces of the cube. This strong variation was caused by the flow structure around the cube. For example, flow separation and reattachment at the top and the side faces of the cube caused significant differences in the local heat transfer. Besides large variations in the heat transfer coefficient at the individual faces, substantial differences were shown to exist between the face-averaged heat transfer coefficients for the different faces of the cube.

Several studies in the literature reported on the convective heat transfer from isothermal three-dimensional protrusions in a matrix arrangement. Moffat and Anderson [2,3,16] dealt with a matrix of aluminium cubes and flat packs mounted on a insulating channel wall. The concept of the adiabatic heat transfer coefficient was successfully applied aimed at eliminating the influence of the upstream thermal boundary conditions. Different parameters were varied: the channel height with respect to the obstacle height, the obstacle sizes (cubes and flat packs), the spanwise and streamwise separation between the components and the Reynolds number. One of the differences as compared to the present study is the lack of spatially periodic kine-

matic boundary condition, because they examined a matrix with a limited number of protrusions. The studies provided much insight in the convective heat transfer for this kind of multiple element configurations. It was shown that a fully developed heat transfer regime was obtained after four or five rows of cubes. Garimella et al. [17,6,7] also focussed on the average convective heat transfer from isothermal copper rectangular prismatic cuboids on a flat plate in a water channel. Their studies included variation of different geometrical parameters (e.g. the channel height, streamwise and spanwise distance between the obstacles, in-line and staggered arrangements) and the flow Reynolds number. The range of Reynolds numbers considered covered laminar, transitional and turbulent channel flows. They observed that the convective heat transfer is significantly dependent on the streamwise separation, channel height and Reynolds number.

In the previous heat transfer studies of multiple three-dimensional protrusions in a matrix arrangement, the focus was primarily on the cube-averaged convective heat transfer from the isothermal protrusions. Further, the cited papers concentrated mainly on isolated wall-mounted cubes in a channel flow. In contrast, this paper deals with the flow structure and the local convective heat transfer characteristics of a cube located in a spatially periodic region of an in-line matrix of cubes. In addition to providing details of the velocity and Reynolds stress fields and distributions of the local heat transfer coefficient, we analysed the interaction between the momentum transfer in the flow and the surface heat transfer.

## 2. Experimental details.

The experiments were performed in a wind tunnel with a  $600 \times 51$  mm rectangular test section. A matrix of cubes of size 15 mm, spaced equidistantly at 45 mm (face-to-face) in both the streamwise and spanwise direction ( $S_x/H = S_z/H = 4$ ), was mounted on one of the channel walls. A schematic of the configuration is given in Fig. 1. The matrix consisted of a total of  $25 \times 10$  cubes in the streamwise and the spanwise direction, respectively. The oncoming flow was straightened with honeycombs and grids. The inflow conditions were controlled by tripping the boundary layer approximately 1 m upstream of the first column of cubes.

The flow and heat transfer measurements were carried out around the 18th row counted from the inlet, at mid-position of the channel. This location en-



sured a fully developed flow in both the streamwise and the spanwise direction independent of the inflow conditions, as was confirmed by velocity measurements at several locations across the entire matrix. The local origin of the cube system is defined in Fig. 1. The  $x$ ,  $y$  and  $z$  direction are in the streamwise, normal and spanwise direction, respectively. The mounting base was machined from formaldehyde which had a low thermal conductivity of 0.33 W/mK. This low value minimised the conductive heat losses through the base plate. The flow field was measured with a Laser Doppler Anemometer (LDA) at a Reynolds number of  $Re_H = 3854$  based on the cube height and the bulk velocity. Smoke and oil-film visualisations were performed in a broader range of Reynolds numbers (1000-8000) to complement the LDA measurements.

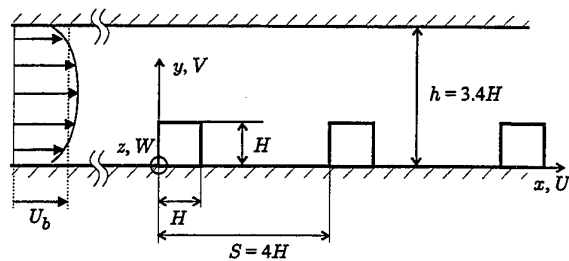
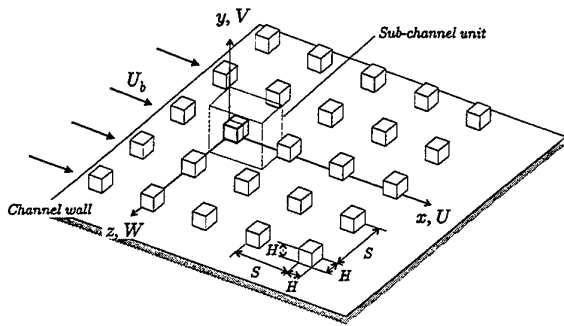


Figure 1: Three-dimensional sketch of the matrix configuration of cubes on the channel wall (upper figure) and the side view of the configuration (lower figure).

Mean velocity and Reynolds stress data were acquired with a two-component back-scatter Laser Doppler Anemometer (TSI 9230/9201) mounted on a three-axis traversing system. The geometrical situation allowed us to use an optical focal length of 120.5 mm which involved a good signal-to-noise ratio and a relatively large beam intersection angle ( $0.380 \pm 0.001$  rad, determined from theodolite measurements and laser beam mapping [15]). The

resulting measurement volume had dimensions of 0.20 mm in length and 0.04 mm in diameter. This small measurement volume minimised velocity gradient bias (less than 2%). In case of larger measurement volumes, this bias can be significant due to relatively large velocity gradients encountered in the vicinity of the cubes.

The measurement of flow reversal was enabled by selecting a preshift frequency of 5 MHz. A mixture of atomised glycerol/water seeded the flow (the particle sizes were between 0.1 and 1  $\mu\text{m}$ ). A TSI IFA-750 was used for data acquisition. Typical data rates ranged between 400-800 Hz. Arithmetic averaging of the Poisson-distributed realisations for obtaining the time-averaged quantities introduces velocity bias. Two different weighting methods were assessed, an interarrival time weighting and inverse velocity weighting, to obtain more appropriate estimates of the time-averaged quantities. The interarrival time only gives reliable results for relatively large data rates [1]. Although data rates in this study were pretty large (the aforementioned range of 400-800 Hz) the inverse velocity is preferred since it provides results without severe constraints [15].

The regular laser probe orientation, perpendicular to the channel floor, allowed the direct measurement of the streamwise  $u$  and the spanwise  $w$  velocity components. The normal velocity component  $v$  was measured with a special designed prism-cube. It consisted of two prisms, one made of glass and the other of a copper alloy, with a mirror at the diagonal plane (hypotenuse). A simplified schematic of this prism cube is given in Fig. 2 (the refraction of the laser beams is omitted to simplify the drawing). The mirror at the hypotenuse plane reflects the laser beams at an angle of exactly 90 degrees and creates a measurement volume in the inter-obstacle spacing (in the wake of the prism cube). For the shown orientation in Fig. 2, a traverse movement of the laser probe in the normal direction results in a translation of the measurement volume in the streamwise ( $x$ ) direction. Vertical and horizontal movement of the laser probe equally cause a translation of the measurement volume in the vertical and normal direction, respectively. The reflected measurement volume enables the measurement of the spanwise  $w$  and normal  $v$  velocity components in coincidence mode. A 90 degrees rotation of the prism cube enables the measurement of the streamwise  $u$  and normal  $v$  velocity components in the region adjacent to the sides of the cube. Measurement of  $w$  and  $v$  in the front region was possible with another 90 degrees of ro-

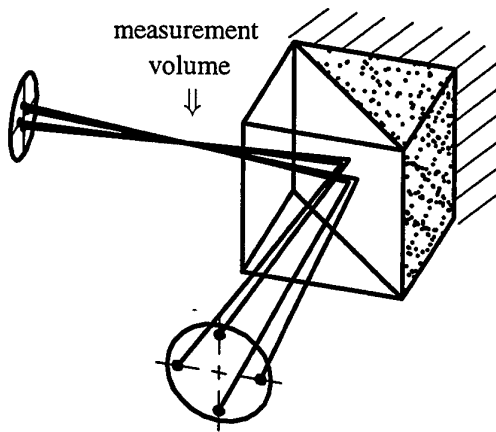


Figure 2: Schematic of the prism-cube for the measurement of the normal velocity component ( $v$ ).

tation. The technique is geometrically constrained by the size of the cube and the intersection angle. Measurements are only possible in a triangular region, bound by the side faces of the cube. Small discrepancies of the  $45^\circ$  angle cause different refractions of the individual laser beams which consequently cause a shift of the waist (the minimum cross-section of the laser beam). The resulting misalignment of the measurement volume may cause fringe gradients which attributes to artificial turbulence intensities [1]. However, the machine specifications were better than  $0.01^\circ$  which excluded this error. The position error of the measurement volume as caused by small deviations of the  $90^\circ$  reflections is estimated to be with 1%. In order to obtain a quantifiable validation of this estimation, some velocity and Reynolds stresses data measured with the prism cube were duplicated with the LDA system in the standard orientation. These results confirmed that the accuracy of the prism-cube results is similar to that of the regular LDA-results [15]. In addition to this method, normal velocities were obtained from a reconstruction technique which is primarily based on different LDA measurements with an inclined probe at different inclination angles. These inclined measurements required a special arrangement of the optics to ensure accurate results. From uncertainty analysis it was derived that the reconstructed normal velocities were less accurate than the prism-cube results, namely 10%. A detailed description of both techniques is given in [15].

Coincidence windows between  $50\text{-}100\ \mu\text{s}$  were used to resolve the Reynolds shear stresses  $\overline{u'v'}$ ,

$\overline{u'w'}$  and  $\overline{v'w'}$ . The first and higher order statistical quantities are determined from 10000 samples which gave a statistical uncertainty of less than 0.02 m/s. The maximum experimental uncertainty is estimated to be at maximum 5% for the mean velocities and 10% for the Reynolds normal and shear stresses based on methods reviewed in the literature [1,5].

Oil-film visualisations were performed to complement the LDA measurements. A visualisation mixture was made from jet fuel, toner and low-viscosity transmission oil. During the course of the experiment, the mixture accumulates at locations on the surface where the shear stresses are low (for example flow reattachment and separation areas) and is removed at locations subjected to high shear stresses. Evaporation of the jet-fuel (after several minutes) causes a significant viscosity increase of the mixture which causes a fixation of the visualisation pigment (and thus the streakline pattern) to the surface. This enables the identification of critical points and lines in the surface plot.

Heat transfer was measured using heat transfer assemblies which consisted of cubes made from an internally heated copper cubical core covered by a layer of epoxy of thickness 1.5 mm. The local convective heat fluxes through the outer surface of the cube are determined from a three-dimensional analysis of the temperature distribution in the epoxy layer with temperature boundary conditions for both the internal and external surface. The internal surface is kept at a constant temperature because of the high thermal conductivity of the copper core. The external boundary conditions are measured with infrared thermography. The experimental method and the measurement techniques are already thoroughly discussed in previous work [12,13,15] to which reference is made for more background information of the heat transfer technique. The technique involved an experimental uncertainty of 5-10% in the heat transfer coefficients.

#### 4. Flow characteristics

A consistency validation was performed from mass conservation at four different sub-planes at periodic up- and downstream locations of the cube. These planes ( $x/H = -1.5$  and  $2.5$ ,  $z/H \geq 0$  and  $x/H = -1.5$  and  $2.5$ ,  $z/H \leq 0$ ) are centred around the local symmetry plane at  $z/H = 0$  at the middle of the cube in question. The spatially periodic and symmetric situation requires a necessarily equal mass flow rate through the four sub-planes. For each sub-

section, seven velocity profiles in normal direction were measured at equidistant locations. The four sections were determined at the following locations:  $x/H = -1.5$  and  $2.5$ ,  $z/H = 0, \pm 0.33, \pm 0.66, \pm 1, \pm 1.33, \pm 1.66$  and  $\pm 2$ . The distance between the individual stations (5 mm) was sufficiently small to ensure a reasonable accurate estimate of the velocity gradients in the spanwise direction. The integrations of the velocity profiles yielded an average mass flow rate of  $6.85 \cdot 10^{-3}$  with deviations less than 1%. These small discrepancies showed the good quality of the spatial periodicity and the symmetry of the matrix flow. The average velocity, derived from the ratio of the mass flow rate and the integration area, yielded a value of  $u_B = 3.86$  m/s. The Reynolds number based on the bulk velocity and the cube size was  $Re_H = 3854$ . The spatial periodicity was further confirmed with LDA measurements across the entire matrix of cubes in both the spanwise and the streamwise direction. The observed deviations were also within 1%. Duplications of the velocity and Reynolds stress data for several stations demonstrated the reproducibility of the measurements (the discrepancies between the measurements were less than 1%).

### General flow structure

In order to get an insight into the effects of the flow structure on the distribution of the heat transfer coefficient, an impression of the flow field around the cube was derived from the LDA-measurements and flow visualisations (see Fig. 3). Distinct vor-

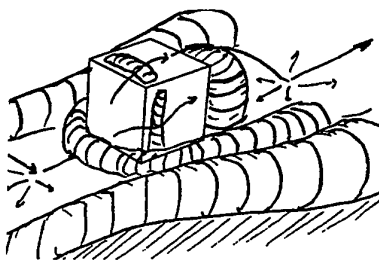


Figure 3: Sketch of the three-dimensional flow pattern around the cube for one spatial period in the matrix.

tex structures were only observed in the immediate proximity of the obstacle, while the core flow in the region above the cubes and the streamwise corridors between them remained almost undistorted. The flow in the inter-obstacle space is characterised by a two-cell structure arising from the reattachment

of the shear layer separated at the leading top edge of the upstream cube. The long-term averaged flow reattachment occurs at a distance of approximately 1.5 cube heights ( $x/H = 2.5$ ) from the leeward face. This shear layer bounds the vortex in the wake of the upstream cube. A horseshoe type of vortex is formed at the windward face of the cube and is deflected downstream along both sides of the cube, weakening further downstream through the interaction with the counter-rotating vortex along the neighbouring cubes.

A vector plot of the velocity field in the symmetry plane  $z/H = 0$  is given in Fig. 4. The plot is a collection of the results obtained from two different measurement techniques. The light vectors, located in the two triangular areas upstream and downstream of the cube are composed from the normal velocities measured with the prism cube and the streamwise velocities, obtained from the direct measurement with the laser probe in the standard orientation. The figure shows that due to the geometrical constraints imposed by the prism-cube, the normal velocities could only be measured in the limited triangular regions. The dark vectors are obtained with the reconstruction technique from two separate velocity measurements acquired at different inclination angles of the laser probe. The results in the overlapping region show good agreement between the two different techniques. It was already argued that the results obtained with the reconstruction technique were less accurate than those acquired with the prism-cube. But the small differences between both results provide sufficient evidence of the reliability of the reconstruction technique. The vortex

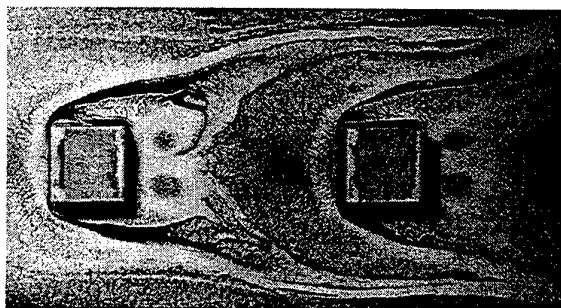


Figure 5: Oil-film visualisation of the surface streaklines of the flow in a spatially periodic matrix flow.

structures can be readily identified from the vector plot in Fig. 4. A downwash of the flow, originating from the horseshoe vortex, is characterised by negative velocities in the proximity of the windward cube

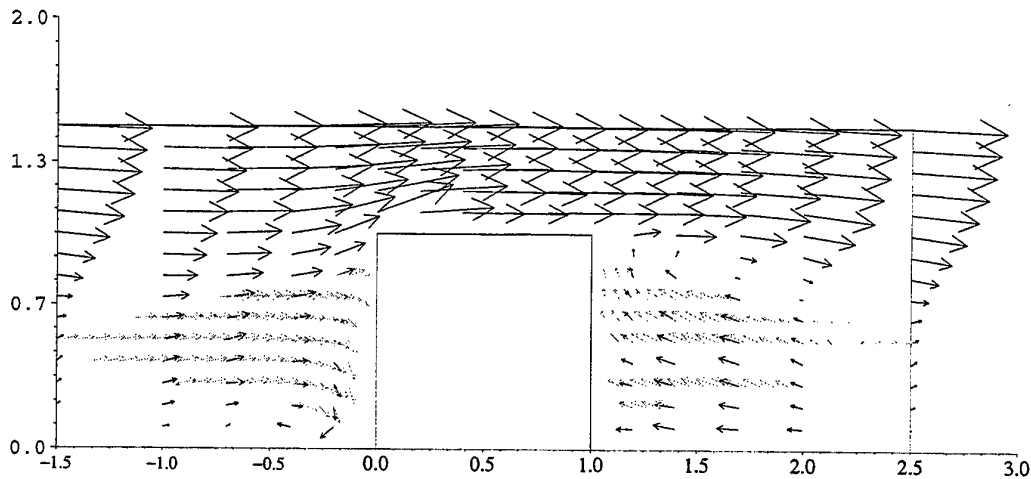


Figure 4: Long-term average vector plot in the  $xy$ -plane for one half of a spatial period in the matrix at  $z/H = 0$ .

wall. The wake flow is dominated by the arc-shaped vortex, causing a strong upwash close to the leeward face. The velocity vectors close to the top leading edge, Fig. 4, indicate that the flow separates and causes a recirculation bubble to exist in the vicinity of the leading top edge. Although it was not possible to measure this with the used LDA set-up, the flow reversal was apparent from the surface streak lines of the oil-film visualisations given in Fig. 5. The top face shows pigment removal close to the leading edge which originates from the recirculation flow. Flow reattachment is found at approximately 4 mm downstream of the leading edge, as appears from the more or less smeared pigment pattern.

A further analysis of the visualisation in Fig. 5 reveals the imprint of the horseshoe-type vortex in front of the obstacle as the white line, bending around the cube along the separation line. This vortex joins the horseshoe vortex generated upstream in the corridor region, see Fig. 5. The influence of the extensions of other horseshoe vortices, induced in front of the cubes more upstream, diminishes. At  $x/H = 0.5$ , both co-rotating horseshoe vortices interact with each other but do not fully merge. If they are of comparable strength, the interaction at this location leads to negative normal velocities close to the obstacle side face, positive values at the symmetry line  $z/H = 2$  and zero values at the interface. This hypothesis is supported by the  $v$ -measurements given in Fig. 6 in the  $yz$ -plane at  $x/H = 0.5$ . Note that the traverses shown are measured with the prism cube. Also for this orientation, the measurement is geometrically constrained. Negative velocities are

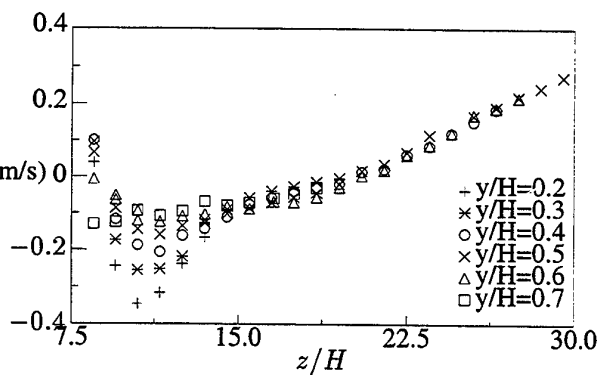


Figure 6: Profiles of the normal velocity  $\bar{v}$  at  $x/H = 0.5$  at different heights  $y/H$ .

found around  $z/H = 0.5$  to  $1.0$  due to the first horseshoe vortex, which decrease gradually with an increase in height  $y/H$ . Positive velocities are observed around  $z/H = 2$  due to the extension of the upstream horseshoe vortex with zero velocities around  $z/H = 1.4$  due to the superposition of the two co-rotating vortices. Because of the flow symmetry, the effects of the two extensions of the upstream horseshoe vortex are superimposed, resulting in an intensification of the effect.

Vector plots of the streamwise and spanwise velocities  $u$  and  $w$  with superimposed trajectories are given in Fig. 7 for one half of a spatial period in the matrix for  $y/H = 0.25, 0.50$  and  $0.75$ . The flow symmetry was verified with velocity measurements across the entire  $xz$ -plane at different stations showing negligible differences. This symmetry allowed

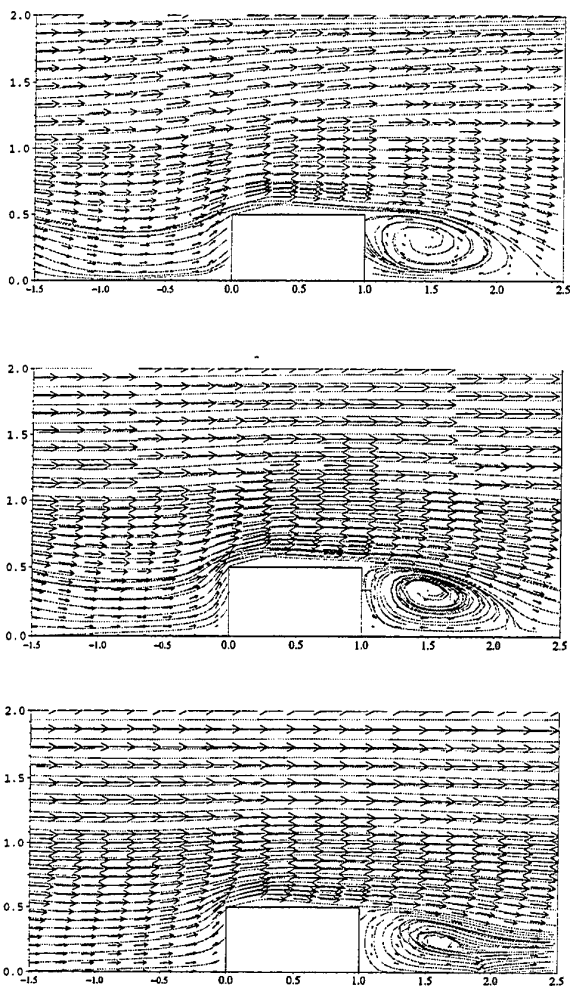


Figure 7: Vector plots with streamlines in the  $xz$ -plane for one half of a spatial period in the matrix for  $y/H = 0.25$  (first),  $y/H = 0.50$  (second) and  $y/H = 0.75$  (third).

us to concentrate on only one symmetric half of the spatially periodic domain. An almost undistorted corridor region between the cube arrays is obvious from the plots. The oncoming flow is bended towards the cube sides to separate at the leading side face, creating a small recirculation bubble close to the leading side edge. As a consequence, the separated shear layer reattaches at approximately 5 mm downstream from the side edge. This was demonstrated from measurements of the streamwise component at 0.5 mm distance from the wall ( $z/H = 8/7.5$ ). These measurements show a negative velocity up to 5 mm distance ( $x/H = 1/3$ ) from the leading edge, Fig. 8. The vortex tubes are aligned along the leading side edges with their origin at the channel floor. Their imprints can be seen from the

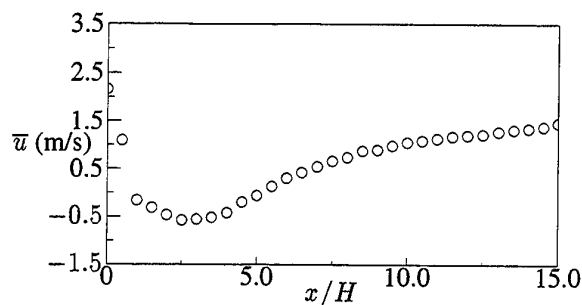


Figure 8: Profile of the mean velocity  $\bar{u}$  at  $y/H = 0.5$  and  $z/H = 8/7.5$ .

oil-film picture as the nodal pigment accumulation close to the leading side edge. The oil-film pattern at the side faces (not shown in the paper) showed a white feather-type imprint of the side recirculation close to the leading edge. This structure is qualitatively similar to that found for a single cube in a developing turbulent channel flow [15].

The wake flow shows the recirculation of the arc-type vortex. The results at the three different levels  $y/H$  show a gradual growth of the recirculation area towards the channel wall. An extrapolation of the separation line, where the velocity changes sign, gives a reattachment point at  $x/H = 2.5$ . The oil-film visualisation in the wake of the cube indicates two pigment concentrations which refer to two counter-rotating foci. These vorticity concentrations are the imprints of the wake vortex and its location agrees reasonably well with the LDA measurements at  $y/H = 0.25$ , extrapolated towards the channel wall. The shear layer reattached in the inter-obstacle spacing at  $x/H = 2.5$  as observed from the pigment accumulation. This location is in good agreement with the LDA observations. The three vector plots show that the centres of the two recirculations are at about the same location. If the wake vortex was closed, the centres of the recirculations would shift towards the symmetry line for cross-sections at increasing height  $y/H$ . This shift is not observed which suggests that the wake vortex is not closed at its top. The results indicate that the wake vortex consists of two separate spirally wound vortices with origins at the channel floor and that their endings are diffused in the downstream shear layer.

The vector plots show further that the streamlines in the inter-obstacle space upstream of the cube are more or less parallel and undistorted for  $y/H = 0.75$ , with exception of the wake vortex region and close to the windward face, whilst the streamlines are sig-

nificantly curved at the plane  $y/H = 0.25$ . This curvature indicates that much air is advected away along the side whilst at higher locations, much more air flows over the obstacle top.

The co-rotating horseshoe vortices can not clearly be seen from the  $u$ -component at  $y/H = 0.25$  since no local acceleration in the streamwise direction is generated by this vortex structure. This means that the vortex is advected away with the velocity of the bypassing flow.

### Dynamic behaviour: vortex shedding

Flow instabilities which are initiated at the side faces cause the flow to fluctuate in a periodic manner. These coherent structures in the wake flow were detected from power density spectra of the time series of the spanwise velocity component. Since the flow was highly turbulent, vortex shedding occurs at a broader range of frequencies. The dominant characteristic frequency was derived from the location in the spectrum which corresponded to the maximum energy. Long-time averaged spectra were obtained from time durations of 500,000 data points which corresponded to 20,000-40,000 vortex shedding cycles. This number of realizations was required to ensure a sufficiently large signal-to-noise ratio. A slotting, sample-and-hold and re-sampling method were compared to justify the accuracy of the calculated power density spectra, and thus the accuracy of the wake frequencies [1]. The three methods reproduced the wake frequencies within 0.5 Hz. This value also pertains to the uncertainty of estimating the frequencies from the spectra and the experimental uncertainty involved. A typical example of a power density spectrum is given in Fig. 9. The coherent structure in the flow (vortex shedding) is apparent from the increased activity around  $f = 27$  Hz. The dashed line indicates the contributions from the incoherent structures in the flow which is the turbulent power density spectrum.

Wake frequencies were measured for a range of mass flow rates. These frequencies were made dimensionless with the bulk velocity and the cube size to yield the Strouhal number,  $St = Hf/u_B$ . These Strouhal numbers are plotted versus the Reynolds number in Fig. 10. All shown results were determined from 500,000 data points. When an experimental uncertainty of 5% is taken into account, a constant Strouhal number of  $St = 0.109$  is found for the Reynolds number range of  $2000 < Re_H < 6000$ . The deviations for  $Re_H < 2000$  are ex-

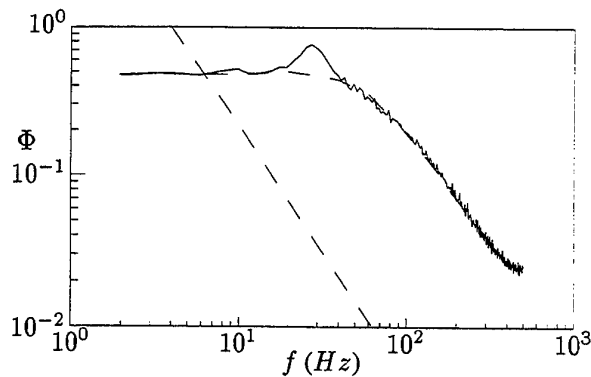


Figure 9: Power density spectrum of the  $v$ -component at the station  $x/H = 2, y/H = 0.5, z/H = 0.5$  for  $u_B = 3.9$  m/s.

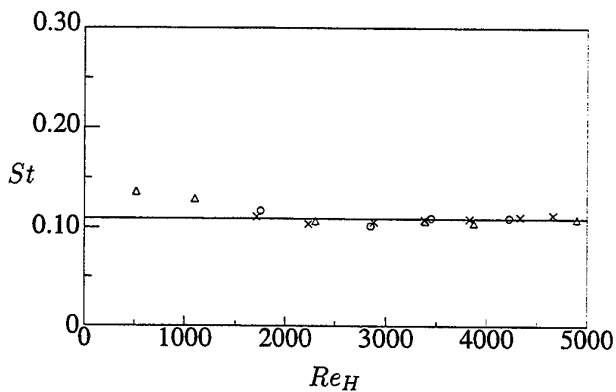


Figure 10: Strouhal numbers ( $St = Hf/u_B$ ) versus the Reynolds number  $Re_H$ .

plained by larger experimental uncertainty or possible Reynolds number effects.

It is noted that the power density spectrum in Fig. 9 decays with a power of  $-5/3$  for the inertial subrange which is usually found in turbulence spectra for high Reynolds numbers away from the wall. Also note that the noise level becomes important around the truncation of the spectrum,  $\Phi \approx 0.03$ .

### Second order moments

Grey-value representations of the Reynolds normal stresses  $\overline{u'^2}$  and  $\overline{w'^2}$  in the plane of symmetry, given in Fig. 11, directly show the anisotropy of the turbulent stress field. Note that both plots are presented at the same scale to allow a quantitative comparison. While the streamwise fluctuations  $\overline{u'^2}$  become largest in the shear layer and horseshoe vortex region, the fluctuations in the spanwise velocity  $\overline{w'^2}$  exhibit maxima where the side shear layers interfere, which is approximately around the reattachment point  $x/H = 2.5$ . The vortex shedding from

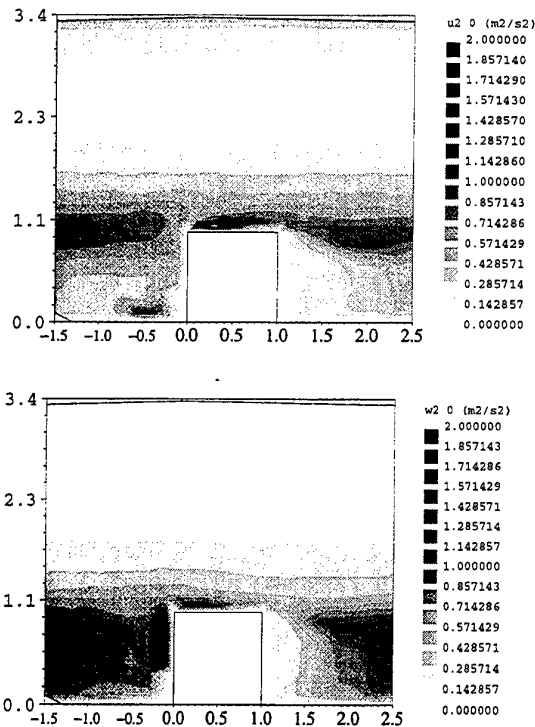


Figure 11: Grey-values plots of the Reynolds normal stresses  $\overline{u'^2}$  and  $\overline{w'^2}$  for one spatial period at the symmetry plane  $z/H = 0$ .

the lateral faces causes significant fluctuations in the  $z$ -direction. However, the fluctuations  $\overline{w'^2}$  in the wake vortex region are rather small. Apparently, the unstable shedding behaviour is only prevalent in the shear layer enveloping the arc vortex and is almost diminished at the centreline  $z/H = 0$ . A qualitatively similar maximum in the spanwise velocity fluctuations around the reattachment point was also observed for a single wall-mounted cube in a fully developed turbulent channel flow [10]. For this single cube configuration, the mechanism of vortex shedding contributed also to the production of turbulence. The maxima in  $\overline{u'^2}$  in the vicinity of the top face, where the shear layer separates and subsequently reattaches, are accompanied by a strong streamwise velocity gradient  $\frac{\partial \overline{u}}{\partial x}$ , see Fig. 4, leading to large values of the streamwise normal stress production term  $\overline{u'^2} \frac{\partial \overline{u}}{\partial x}$ . Although the velocity gradient diminish further downstream in the shear layer,  $\overline{u'^2}$  contributes still significantly to the streamwise normal stress production.

Measurement of the Reynolds normal stresses  $\overline{v'^2}$  with the prism-cube provides the third component for the turbulent kinetic energy  $k = 0.5 (\overline{u'^2} + \overline{v'^2} + \overline{w'^2})$  in the triangular region. It is noted that the Reynolds stresses  $\overline{v'^2}$  obtained with the reconstruct-

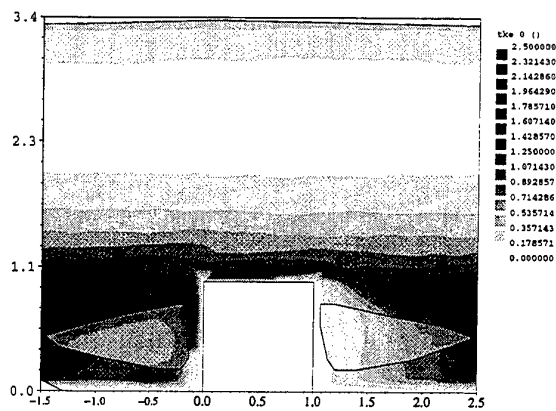


Figure 12: Turbulent kinetic energy  $k$  for one spatial period at the symmetry plane  $z/H = 0$ .

tion technique were not accurate enough and are therefore, not considered in this paper. Values of  $k$  are given in Fig. 12 in the two triangles in front and in the wake of the obstacle. In the remaining part of the spatial period,  $\overline{v'^2}$  is assumed as  $\overline{v'^2} = 0.5 (\overline{u'^2} + \overline{w'^2})$  leading to  $k_{2D} = 0.75 (\overline{u'^2} + \overline{w'^2})$  where  $\overline{u'^2}$  and  $\overline{w'^2}$  were obtained from the LDA measurements with the probe in the standard orientation. These values of  $k_{2D}$  are also given in Fig. 12. Although the above assumption is not fully accurate, particularly in the wake and reattachment region (see Fig. 11) the agreement between  $k$  and  $k_{2D}$  is sufficiently good (differences are at maximum 10 %) to allow at least a qualitative interpretation of the turbulent kinetic energy field with  $k_{2D}$ .

The turbulent kinetic energy above the cubes (the core region of the channel) is rather small and increases gradually towards the opposing channel wall. The large Reynolds normal stresses found in the shear layer region and around the reattachment point lead to local maxima in the turbulent kinetic energy. A maximum in  $k$  is found downstream in the shear layer at approximately one cube distance behind the leeward face where the shear layer is broadening and the turbulence level is decaying due to turbulent advection. The large values of  $k$  in the horseshoe vortex region at the windward face of the obstacle indicates that this vortex structure is unstable and highly turbulent. Unstable behaviour of the horseshoe vortex was also observed for a single cube in a fully developed channel flow [10,9]. For this single cube, bimodal non-periodic behaviour of the velocity components was observed which was attributed to the flipping between two flow modes. In the case of a spatially periodic matrix flow, no bimodal be-

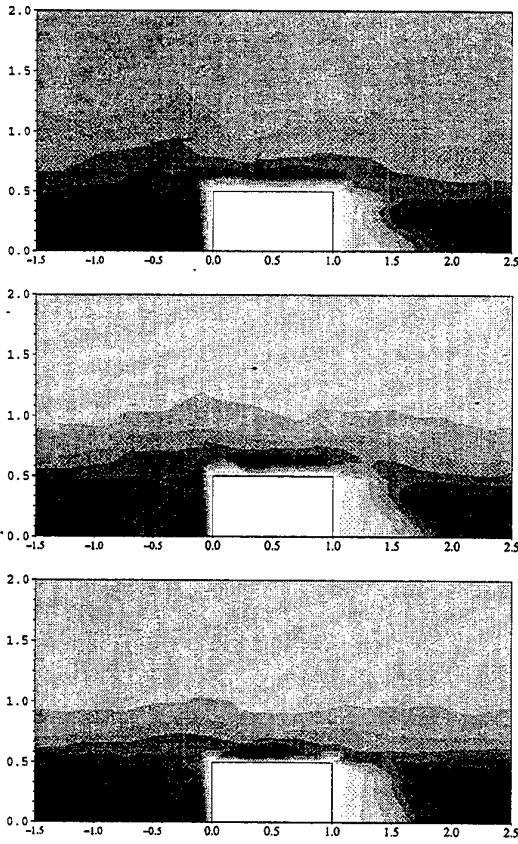


Figure 13: Grey-values plot of the turbulent kinetic energy  $k_{2D} = 0.75 (\overline{u'^2} + \overline{w'^2})$  in the  $xz$ -plane for one half of a spatial period in the matrix for (a)  $y/H = 0.25$ , (b)  $y/H = 0.50$  and (c)  $y/H = 0.75$ .

haviour was detected from the measured probability density functions in the horseshoe region.

The turbulent kinetic energy,  $k_{2D} = 0.75 (\overline{u'^2} + \overline{w'^2})$  in the  $xz$ -plane is given in Fig. 13 for one half of a spatial period in the matrix flow for  $y/H = 0.25$ ,  $0.50$  and  $0.75$ . The flow impingement at the windward obstacle face cause local maxima in  $k$ , in particular at  $y/H = 0.50$ . The increased turbulent kinetic energy at  $y/H = 0.25$  close to the front face of the cube is attributed to the horseshoe vortex. Similarly to the top face, the local maxima close to the sides are caused by the intermittent reattachment of the shear layers which were separated at the sharp leading side edges. Flow instabilities at these faces are amplified and initiate the vortex shedding behind the trailing side edges. The high turbulence levels directly behind these faces are, therefore, explained by the periodic fluctuating velocities. Again the turbulent kinetic energy is rather low in the centre of the wake vortex indicating that the perturbations induced by the vortex shedding are damped. High  $k$ -

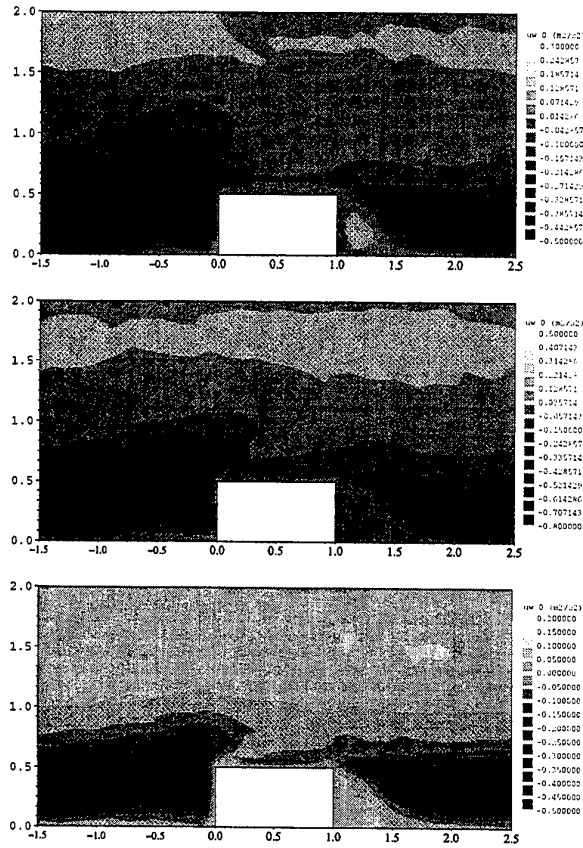


Figure 14: Grey-value representation of the Reynolds shear stresses  $\overline{u'w'}$  in the  $xz$ -plane for one half of a spatial period in the matrix for (a)  $y/H = 0.25$ , (b)  $y/H = 0.50$  and (c)  $y/H = 0.75$ .

concentrations are found at the symmetry-line at approximately  $x/H = 2$  which is mainly due to the turbulent interaction between both side shear layers.

The Reynolds shear stress  $\overline{u'w'}$  exhibits maxima at locations of large curvature of the mean streamlines. For example, at the obstacle windward face, the flow is directed around the cube causing large values in  $\overline{u'w'}$ , see Fig. 14 (the figures show iso-value plots of the Reynolds shear stress  $\overline{u'w'}$  at  $y/H = 0.25$ ,  $0.5$  and  $0.75$ ). The strong interaction between the wake vortex and the shear layer causes the maxima in the obstacle wake. The maxima shift towards the plane  $y/H = 0$  where the flow reattaches and gradually move outwards for locations closer to the cube-front. Reynolds shear stresses  $\overline{v'w'}$  are given in Fig. 15 for  $x/H = 0.5$ . These principle values were measured with the prism-cube when the measurement volume was reflected into the second quadrant, the side area of the cube (see Fig. 2 for the orientation in question). It has been men-



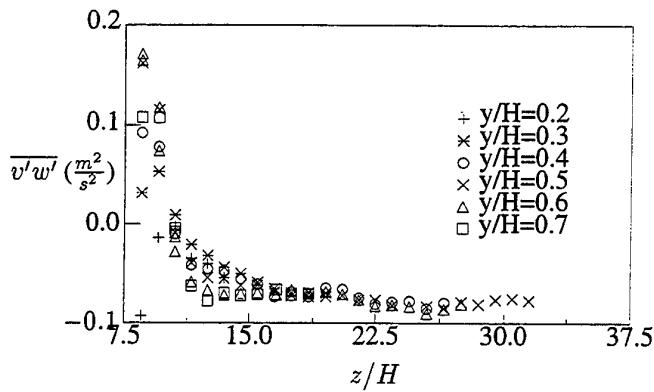


Figure 15: Profiles of the Reynolds shear stresses  $\overline{v'w'}$  at  $x/H=0.5$ .

tioned that these cross-terms can not be measured with conventional Laser Doppler Anemometry since the measurement equipment will then block the flow. The values again are obtained only in the triangle shaped region due to the geometrical restrictions of the method. The shear stresses become maximum in the vicinity of the first horseshoe vortex.

### Vorticity fields

The grey-values representation of the normal component of the vorticity vector  $\overline{\omega}$ ,  $\omega_y = (\frac{\partial w}{\partial x} - \frac{\partial u}{\partial z})$ , given in Fig. 16 show large vorticity concentrations in the near obstacle wake directly behind the lateral faces at locations where the velocity field exhibit strong spatial gradients. These maxima coincide with maxima in the turbulent quantities, represented as  $k$ . The vorticity concentrations at the side faces close to the leading edges are due to the rotating side vortices. The vorticity concentrations further downstream at the lateral faces are artifacts and are caused by the discontinuity in the velocity field: velocity measurements were performed up to 1 mm from the side edges.

### 5. Convective heat transfer

Heat transfer was measured at one powered element in the spatially periodic matrix flow, while all other cubes remained unpowered. The inlet temperature is used as a reference which, in this case, equals the adiabatic surface temperature [16]. The heat transfer measurements were reproduced at different cubes in separate experiments and the results were well within the 10% uncertainty limit. Heat transfer experiments were performed in the Reynolds number range of  $2380 < Re_H < 5280$ . The temperature of

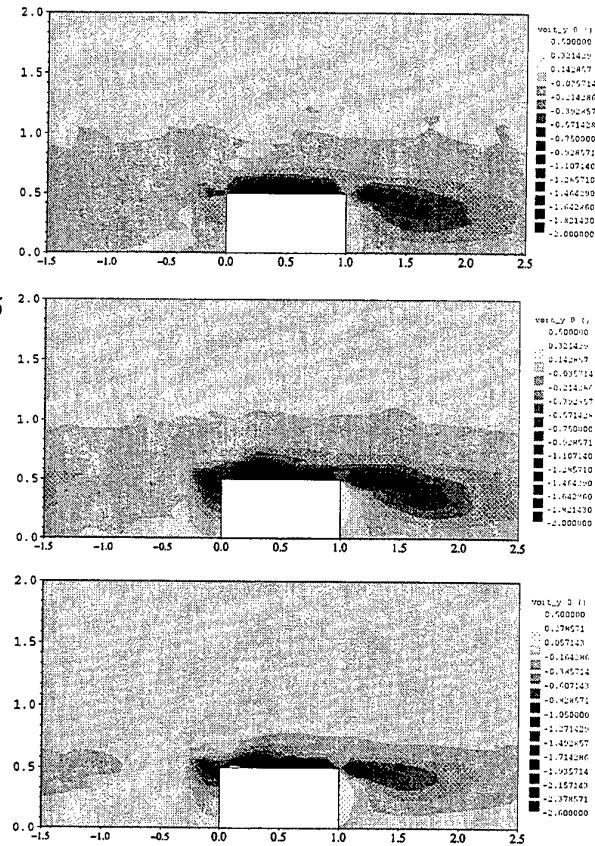


Figure 16: Vorticity  $\omega_y = (\frac{\partial w}{\partial x} - \frac{\partial u}{\partial z})$  in the  $xz$ -plane for one half of a spatial period in the matrix for (a)  $y/H = 0.25$ , (b)  $y/H = 0.50$  and (c)  $y/H = 0.75$ .

the copper core was kept at  $75^\circ C$  for all the heat transfer measurements. The inlet temperature was between  $19-21^\circ C$ . The surface temperature distributions were validated with liquid crystal measurements, as described in [12].

The surface-average heat transfer coefficients  $\overline{h}$  were derived from the surface integrated convective heat flux and surface temperature. The cube-average heat transfer coefficients,  $\overline{h}_c$  were derived in a similar way, but the convective heat flux and surface temperature are then an average over all the five faces of the cube exposed to the air flow. The results are shown in Fig. 17 as a function of the Reynolds number  $Re_H$ . Despite a small experimental uncertainty, the data follow an almost linear regression. A large heat transfer coefficient found at the front face is indicative for the impinging flow at this face. The side and top faces typically have the lowest averaged convective heat transfer coefficient which is due to the flow reversal, as shown later. The face-averaged heat transfer at the rear face is the lowest of all faces. The small deviations in the face-averaged heat trans-

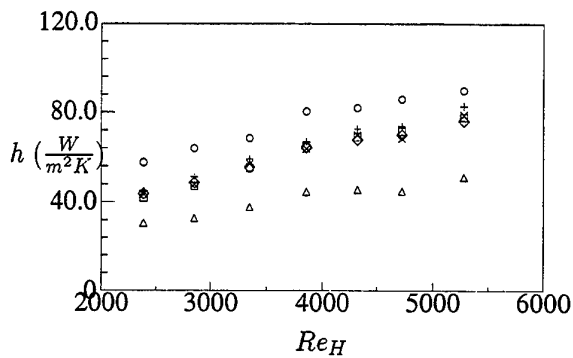


Figure 17: Surface and cube averaged  $h$  as a function of the Reynolds number  $Re_H$ : (+) side (north), (o) front, (x) side (south), ( $\Delta$ ) rear, ( $\square$ ) top and ( $\diamond$ ) cube average.

fer coefficients can be traced back to deviations in the power supply. The sum of the total convective and radiative heat transfer from the five faces exposed to the air flow are denoted as (+) in Fig. 18 as a function of the Reynolds number  $Re_H$ . The total supplied power to the heat source in the matrix cube which is product of the voltage drop and the current is given in the same figure, indicated by (o). The difference between both values is the heat leakage through the sixth face mounted to the channel wall, and consists of the conduction losses through the base plate and the lead wires. For all considered Reynolds numbers, this heat loss is approximately in the range 10-15 %, where the smaller values pertain to the higher Reynolds numbers and vice versa.

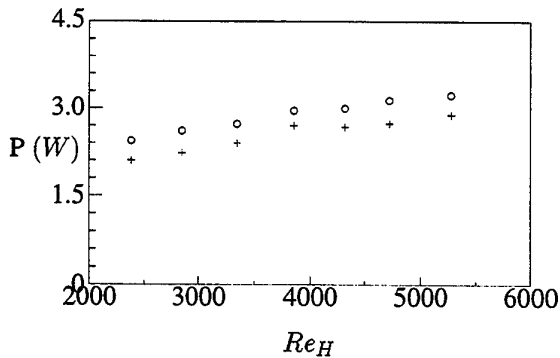


Figure 18: Total supplied power and the total heat through the five faces of the cube exposed to air flow as a function of the Reynolds number  $Re_H$ : (+) heat flow and (o) power supply.

Distributions of the heat transfer coefficient are shown along the paths ABCDA and ABCD in Fig 19 for different Reynolds numbers. The profiles are

normalised with the cube-averaged heat transfer coefficient for the corresponding Reynolds number, as given in Fig. 17, and collapse within the experimental uncertainty. This suggests that the local heat transfer characteristics are similar throughout the range of Reynolds numbers considered ( $2380 < Re_H < 5280$ ). Because of this similarity, the discussion can be focussed on one characteristic distribution of the local heat transfer coefficient, related to the characteristic flow field. Fig. 19 reveals that the heat transfer coefficient distributions show large spatial gradients at a relatively small surface. This reflects a complexity of the flow structure around the matrix, with flow recirculations and reattachment, and a strong variation in the heat transfer coefficients. Despite this variation, the heat transfer displays a full symmetry indicating that local buoyancy effects are negligible. The flow is, therefore, classified as forced convection for all Reynolds numbers considered.

As mentioned earlier, the heat transfer at the windward face (FRONT) benefits from the turbulent flow impingement and is maximum compared to the other faces. The peaks towards the side edges, see Fig. 19(a), are due to a local acceleration of the fluid, and thus causing an local increase in the heat transfer coefficient. Close to the mounting wall edge, the heat transfer coefficient shows a local minimum (the front face in the lower figure of Fig. 19) which is traced back to the presence of the horseshoe vortex. Heat convected away from the hot cube surface recirculates in the vortex causing the local vortex temperature to rise. This increased temperature level prevents a beneficial removal of heat at this location. A similar observation was made for the side faces (SIDES) of the cube. The side recirculations acted as insulation layers and, therefore, caused local minima close to the leading edge. On the contrary, the fresh air from the intermittent reattaching shear layer at approximately 5 mm downstream towards the trailing edge cause the local maxima in the heat transfer coefficient. Similar features are found at the top face, shown in the lower plot in Fig. 19 (TOP). The bound vortex, located in the vicinity of the top leading edge, causes the heat transfer to become minimum at about the centre of the vortex core. The subsequent maximum is due to the reattachment of the separated shear layer. The convective heat transfer from the leeward face is worst compared to the other faces which is mainly attributed to the wake vortex. The recirculating heat prevented also a beneficial cooling for this face.

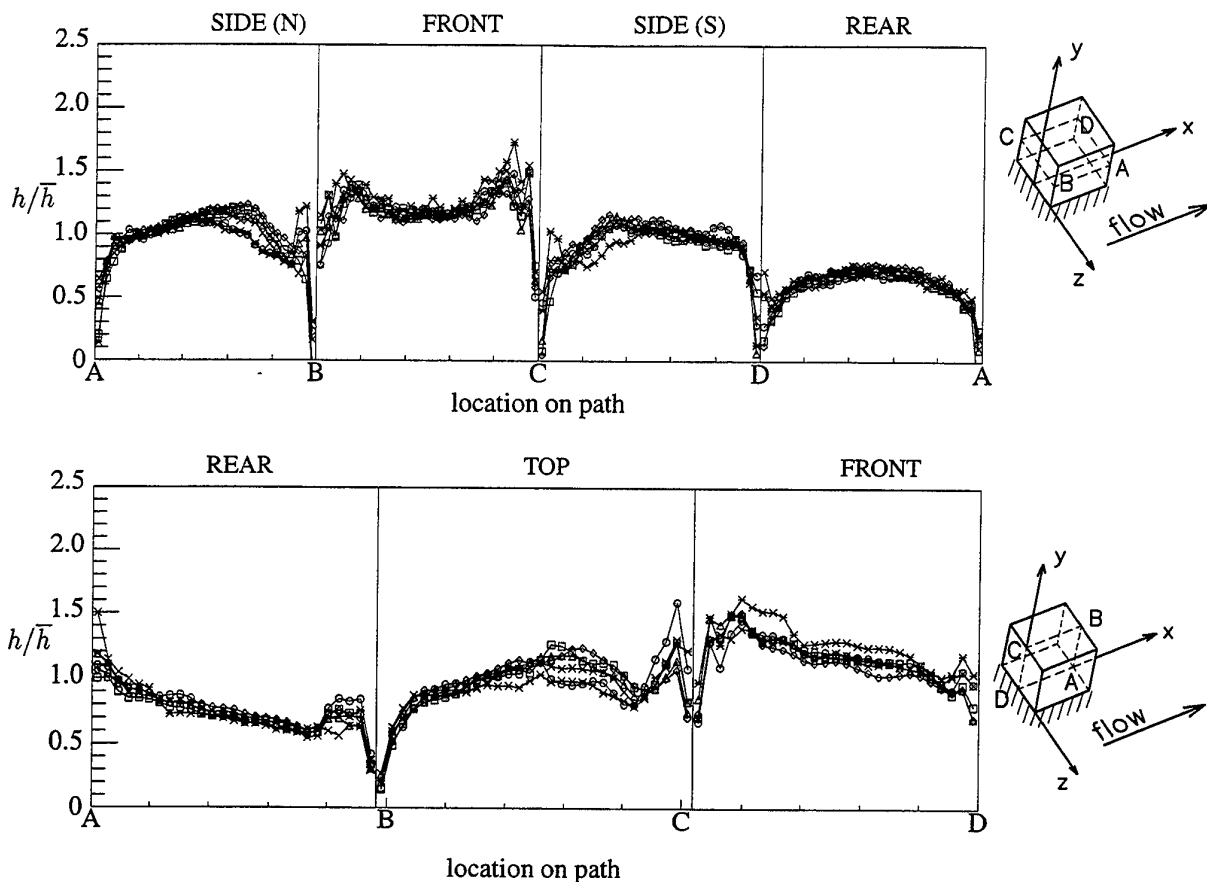


Figure 19: Heat transfer coefficient distributions along paths **ABCDA** and **ABCD** as a function of the Reynolds number  $Re_H$ : (\*) 2851, (o) 3348, (x) 3854, ( $\Delta$ ) 4321, ( $\square$ ) 4722 and ( $\diamond$ ) 5279.

## 6. Conclusions

The flow field structure and distributions of the heat transfer coefficient of a wall-mounted cube in a spatially periodic matrix flow were studied experimentally. It was shown that the flow in the immediate proximity of the obstacle is characterised by a two-cell structure which was caused by the shear layer reattachment in the inter-obstacle space. A horse-shoe type of vortex originates at the front face; an arc-shaped vortex exists in the wake. Flow separation at the sharp leading top and side edges caused flow recirculations to exist close to the edges and subsequent reattachment at the faces more downstream. The flow in the periodic matrix flow exhibited vortex shedding in the wake of the cube. A typical dimensionless shedding frequency of  $St = 0.109$  was found. The periodic fluctuations caused by the vortex shedding and the high velocity gradients were both responsible for large values of the turbulent kinetic energy in the free shear layers in the wake of the cube. The pronounced differences in the flow structure around the cube caused large gra-

dients in the distributions of the local heat transfer coefficient. Similarity of these distributions, scaled with the cube-averaged heat transfer coefficient, indicated that no Reynolds number effects existed in the range of Reynolds numbers investigated ( $2380 < Re_H < 5280$ ). Regions of intense flow recirculations with subsequent flow separation showed relatively small values of the local heat transfer coefficient. In contrast, areas where the flow reattached were generally characterised by large values of the heat transfer coefficient.

## Acknowledgements

This work was financially support by Philips Research, the Netherlands. Bart Hoek and Jaap Beekman are gratefully acknowledged for their technical contributions to the work. Further, Shinnosuke Obi and Theo van der Meer are acknowledged for the useful discussions.

## Nomenclature

$D$	channel height ( $m$ )
$f$	frequency ( $Hz$ )
$h$	heat transfer coefficient ( $W/m^2K$ )
$\bar{h}$	average $h$ ( $W/m^2K$ )
$H$	cube size ( $mm$ )
$k, k_{2D}$	turbulent kinetic energy ( $m^2/s^2$ )
$Re_H$	Reynolds number ( $=u_B H/\nu$ )
$St$	Strouhal number ( $=fH/u_B$ )
$u_B$	bulk velocity ( $m/s$ )
$\bar{u}, \bar{v}, \bar{w}$	mean velocity ( $m/s$ )
$\overline{u'^2}, \overline{v'^2}, \overline{w'^2}$	Reynolds normal stress ( $m^2/s^2$ )
$\overline{u'v'}, \overline{u'w'}$	Reynolds shear stress ( $m^2/s^2$ )
$x$	coordinate in streamwise direction ( $m$ )
$y$	coordinate in spanwise direction ( $m$ )
$z$	coordinate in normal direction ( $m$ )

## Greek Symbols

$\nu$	kinematic viscosity ( $m^2/s^2$ )
$\Phi$	power spectral density

## References

- [1] Absil, L.H.J., 1996, Analysis of the laser Doppler measurement technique for application in turbulent flows, *Ph.D. thesis*, Faculty of Aerospace, Delft University of Technology.
- [2] Anderson, A.M. and Moffat, R.J., 1990, Convective heat transfer from arrays of modules with non-uniform heating: experiments and models, *PhD thesis, Report No HMT-43*
- [3] Anderson, A.M. and Moffat, R.J., 1992, The adiabatic heat transfer coefficient and the superposition kernel function: part I - Data for arrays of flatpacs for different flow conditions, *Journal of Electronic Packaging*, Vol. 114, pp. 14-21.
- [4] Castro, I.P. and Robins, A.G., 1977, The flow around a surface-mounted cube in uniform and turbulent streams, *J. Fluid Mech.*, Vol. 79, part 2, pp. 307-335.
- [5] Durst, F., Melling, A. and Whitelaw, J.H., 1976, Principles and practise of Laser Doppler anemometry, Academic Press, New York.
- [6] Garimella, S.V. and Eibeck, P.A., 1990, Heat transfer characteristics of an array of protruding elements in single phase forced convection, *Int. J. Heat and Mass Transfer*, Vol. 33, No 12, pp. 2659-2669.
- [7] Garimella, S.V. and Eibeck, P.A., 1990, Effect of spanwise spacing on the heat transfer from an array of protruding elements in forced convection, *Int. J. Heat and Mass Transfer*, Vol. 34, No 9, pp. 2427-2430.
- [8] Hussein, H.J., and Martinuzzi, R.J., 1996, Energy balance for turbulent flow around a surface mounted cube placed in a channel, *Physics of Fluids*, Vol 8 No 3 pp. 764-780.
- [9] Larousse, A., Martinuzzi, R. & Tropea, C., 1991, Flow around surface-mounted, three-dimensional obstacles, *8th Symp. on Turbulent Shear Flows*, TU-Munich/Germany, 1, pp. 14-4-1/14-4-6
- [10] Martinuzzi, R.J., 1992, Experimentelle Untersuchung der Umströmung wandgebundener, rechteckiger, prismatischer Hindernisse, *Ph.D. thesis*, Erlangen, Germany.
- [11] Martinuzzi, R.J and Tropea, C., 1993, The flow around surface mounted, prismatic obstacles placed in a fully developed channel flow, *J. Fluids Engineering*, Vol. 115, pp. 85-92.
- [12] Meinders, E.R., Meer, T.H. van der, Hanjalić, K. and Lasance, C.J.M., 1997, Application of infrared thermography to the evaluation of local convective heat transfer on arrays of cubical protrusions, *Int. J. Heat and Fluid Flow*, Vol 18, No 1, pp. 152-159.
- [13] Meinders, E.R., Meer, T.H. van der & Hanjalić, K., 1998a, Local convective heat transfer from an array of wall-mounted cubes, *Int. J. of Heat and Mass Transfer*, Vol 41 No 2, pp. 335-346.
- [14] Meinders, E.R., Martinuzzi, R. and Hanjalić, K., 1998b, The local convective heat transfer of a single wall-mounted cube in a turbulent channel flow, submitted for publication consideration.
- [15] Meinders, E.R., 1998c, Experimental study of heat transfer in turbulent flows over wall-mounted cubes, *Ph.D. thesis*, Faculty of Applied Sciences, Delft University of Technology, Delft, Netherlands.
- [16] Moffat, R.J. and Anderson, A.M., 1990, Applying heat transfer coefficient data to electronics cooling, *Journal of Heat Transfer*, Vol. 112, pp. 882-890
- [17] Morris, G.K. and Garimella, S.V., 1997, Composite correlations for convective heat transfer from arrays of three-dimensional obstacle, *Int. Journal of Heat and Mass Transfer*, Vol. 40 No 2, pp. 493-498
- [18] Okamoto, S., Tsunoda, K., Katsumata, T., Abe, N. & Kijima, M., 1996, Turbulent near-wakes of periodic array of square blocks on a plate, *Int. J. of Heat and Fluid Flow*, Vol. 17, pp. 211-218.

# CONVECTIVE HEAT TRANSFER TO A ROTATING DISK WITH ROUGHENED SURFACES

B.P. Axcell, C. Thianpong and J.E. Byrne

The Manchester School of Engineering  
University of Manchester, U.K.

## ABSTRACT

An investigation has been made of local heat transfer to a rotating disk in the presence of an imposed axial flow using thermochromic liquid crystals and the transient heating technique. Preliminary measurements were made for a smooth disk, for which the experimental data encompassed the laminar boundary layer, the transitional zone and the beginning of the turbulent region. Measurements were then made for arrangements in which trip wires were used to disturb the boundary layer, the intention being to gain information on the height of roughness protrusions needed to modify convective heat transfer. The work then proceeded to the main topic of the investigation, the influence of surface roughness on convective heat transfer to the disk. Two types of roughness have been studied: concentric circular ribs of a rectangular cross-section and small, isolated square studs arranged in a square pitch on the disk surface. In each case three roughness configurations have been investigated and the results have been compared with data for a smooth disk. The augmentation of heat transfer by the circular ribs was modest but the isolated studs increased heat transfer rates in turbulent boundary layers by more than a factor of two and reduced the transitional Reynolds number by an order of magnitude.

## 1 INTRODUCTION

The complex flow field associated with a disk rotating in a stationary fluid, Fig 1, was first considered by Von Karman (1). There are three velocity components:  $w$  in the axial direction towards the disk,  $v$  tangentially in the direction of disk rotation and  $u$  radially outwards over the surface. Von Karman calculated velocities in the radial and tangential directions for both laminar flow and turbulent flow and subsequent measurements of radial and tangential velocities (2) were in good agreement with his predictions for laminar flow. Under turbulent conditions, however, only the tangential component was modelled satisfactorily by Von Karman's analysis.

The boundary layer thickness  $\delta$ , defined by the distance from the rotating disk where the tangential component of the fluid velocity  $v$  is equal to  $0.005\omega r$ , is given by

$$\delta (\omega/v)^{1/2} = 5 \quad (1)$$

for laminar flow, independent of radial position, and by

$$\delta = 0.526 r^{3/5} (v/\omega)^{1/5} \quad (2)$$

for turbulent boundary layers (1). Transition between the two regions occurs over a transitional range defined approximately by  $2 \times 10^4 < Re_\omega < 3 \times 10^5$  where  $Re_\omega$  is the rotational Reynolds number (3).

The laminar solution for the velocity field was extended to the case of heat transfer from a rotating plate to still air (4), leading to a solution for local Nusselt numbers given by the following expression:

$$Nu = 0.33 Re_\omega^{0.5} \quad (3)$$

Numerous studies of laminar forced convection from rotating disks to various fluids have been performed and local Nusselt numbers, in both experimental and theoretical investigations, seem to have been correlated by expressions such as equation 3 with a square root dependence on Reynolds number.

Investigations have also been made for heat transfer to rotating disks with turbulent boundary layers. Experimental data (5) have been correlated by

$$Nu_{\text{mean}} = 0.015 Re_\omega^{0.8} \quad (4)$$

The corresponding equation for local heat transfer coefficients is

$$Nu = 0.019 Re_\omega^{0.8} \quad (5)$$

and this equation may also be derived using Reynolds analogy between heat and momentum transfer starting with data for the frictional torque on a disk rotating in air (6). The results of most investigations on turbulent convection from rotating disks have been broadly in agreement with equations (4) and (5), see, for example, (7-13).

Very few investigations appear to have been made on heat transfer from rotating disks with rough surfaces. An investigation of the frictional drag of a disk coated with coarse sand (6) (typical particle diameters would have been about 250  $\mu\text{m}$ ) showed that, although the frictional drag in the turbulent region was

increased quite appreciably, the roughness reduced the transitional Reynolds number only marginally, from  $3 \times 10^5$  to  $2 \times 10^5$ . The authors argued that the minimum transitional Reynolds number would be fixed by the intersection of Von Karman's equations for frictional torque in laminar flow and in turbulent flow; this gives a Reynolds number of about  $6 \times 10^4$ . A small high speed jet on the axis was found to produce the greatest reduction in the transitional Reynolds number, to about  $10^5$ , an effect of the introduction of turbulence into the flow. The same investigation also demonstrated that, however highly the disk surface was polished, it was unexpectedly difficult to increase the transitional Reynolds number beyond  $3 \times 10^5$ .

The topic of heat transfer in rotating disk systems has been studied extensively because of the application to gas turbines (14). However, the rather basic problem of heat transfer to a rotating disk in the presence of an imposed axial flow has not received much attention and no investigations appear to have been made for turbulent boundary layers on rotating rough disks in axial flows. Data for laminar boundary layers over a rotating disk in an axial flow have been successfully correlated by Jackson et al. (15) using a combination of the rotational Reynolds number and an axial Reynolds number related to the approaching flow:

$$Nu = 0.32 \left[ Re_{\omega}^2 + 88 \left( Re_a \frac{r}{R_p} \right)^2 \right]^{1/4} \quad (6)$$

where  $Re_a = W \rho r / \mu$ ,  $W$  was the velocity of the imposed axial flow and  $R_p$  was the radius of the pipe used to direct the axial flow towards the disk. Predicted heat transfer coefficients obtained using a numerical method were slightly smaller than the experimental values, the discrepancy increasing as the axial flow rate increased. The difference was explained by the presence of turbulence in the approaching flow, which would influence the laminar boundary layer over the rotating surface. The combination of rotational and axial Reynolds numbers shown in equation 6 did not successfully correlate data for the turbulent part of the boundary layer, which appeared to be influenced far less significantly by the axial flow.

The present investigation used the same experimental apparatus as in the study by Jackson et al. (15) and it covered a similar range of rotational speeds and axial flows. Initially some of the earlier experiments were repeated, in which most of a smooth disk surface was covered by a laminar boundary layer. Then the disturbance caused by a single circular trip wire was investigated. This was followed by the main phase of the work in which turbulent boundary layers were induced on the rotating disk by surface roughness protrusions.

## 2 EXPERIMENTAL APPARATUS

The test facility is shown in Fig 2 and it was designed to permit measurements of heat transfer to a rotating disk in the presence of an axial flow using the transient heating technique and liquid crystal thermometry. Air was drawn into the rig via a filter (to prevent contamination of the liquid crystals) and a bell mouth entry section. The mass flow rate was controlled by a valve situated between the entry section and a fan and it was monitored using a pitot tube and a static pressure tapping located at the throat of the converging section. The fan outlet discharged into a 480 mm diameter vertical pipe, the bottom of which contained air heaters rated at 47 kW. The air flow, which was heated to temperatures of up to  $60^\circ\text{C}$ , then passed through various flow conditioning devices to give a uniform velocity profile at the top of the pipe immediately prior to impingement on the rotating disk, see Fig 3. Air velocities of between 1.5 and 6 m/s were investigated, corresponding to pipe Reynolds numbers of between  $5 \times 10^4$  and  $2 \times 10^5$ . The disk diameter was 560 mm, giving a maximum rotational Reynolds number of  $6 \times 10^5$  at the maximum rotational speed of 1275 rev/min. The gap between the top of the pipe and the disk was set at 120 mm to give an average exit velocity in the radial direction equal to the approaching axial velocity. The presence of the air heaters and the flow conditioning devices produced rather high turbulence intensities of 8% to 10% in the axial velocity at the top of the pipe; these also were fairly uniform across the pipe diameter, Fig 4.

In order to provide a controlled transient the heated air flow was initially discharged to ambient through a bypass line which had the same hydraulic resistance as the experimental flow system. At the same time the pipe work above the bypass was trace heated to a temperature equal to that of the air so that the air temperature would not decrease when the air was directed upwards towards the disk. The disk itself remained at ambient temperature and it was isolated thermally from the heated pipe below by a shutter. The temperature of the disk was monitored by two Type K thermocouples embedded in the disk with their junctions near the surface; these had to be disconnected before the disk was set in motion. Once air and pipe temperatures were steady and equalized the flow was directed towards the rotating disk by operating two mechanically-linked valves, which were also linked pneumatically to the sliding shutter at the top of the pipe.

The disk was constructed from 15 mm thick perspex, which was sufficient to give transient behaviour which was effectively that of conduction into a semi-infinite solid. Preliminary measurements were made with a smooth disk surface so that results could be compared with earlier data. The convective heat transfer over most of the disk for these tests was in the laminar region with only the outermost radial positions in the

transitional or turbulent regions. Then a trip wire in the form of a ring was attached to the disk surface to disturb the boundary layer. Different thicknesses of wire and various ring diameters were investigated to give a range of wire sizes and radial locations. The information from these tests was used to specify the size of roughness protrusion required to make a substantial difference to convective heat transfer. In general the roughness height to disturb a laminar boundary layer needs to be comparable with the boundary layer thickness while for additional turbulence promotion in turbulent boundary layers the roughness height should be considerably in excess of the thickness of the viscous sub-layer (which could be of the order of 1% or less of the boundary layer thickness). Calculations using equations 1 and 2 suggested boundary layer thicknesses of the order of 2 mm for laminar flow and of the order of 10 mm for turbulent flow. Tests with trip wires confirmed that protrusions of a millimetre would influence convection significantly and the first measurements with a rough surface were made with this roughness height.

It was not possible to generate rough surfaces by sticking particles onto the disk surface because this would have created a surface layer of unknown thermal conductivity. Instead the rough surfaces were prepared by machining the disks, see Fig 5. Two types of roughness were investigated: concentric circular ribs 1.5 mm wide and isolated square studs having a cross-section of 1.5 mm by 1.5 mm. Three combinations of roughness height  $e$  and pitch  $p$  were studied, as shown in Table 1. The first tests were made with a roughness height of a millimetre and a pitch of 12 mm, which represents a pitch to height ratio close to the optimum of 9:1 found for augmenting the turbulence intensity in two-dimensional boundary layer flows over rectangular ribs (16). The disk with circular ribs was then further machined to leave protrusions of 2.5 mm with the same pitch and the height of the studs on the other disk was increased by gluing pieces of 1.5 mm thick perspex sheet onto the top of the studs. Finally 50% of the protrusions were removed from both disks to return the pitch to height ratios to a value closer to the optimum spacing for conventional boundary layers.

Surface temperatures were recorded using encapsulated thermochromic liquid crystals, commercially available as Licritherm Ink. These were painted along a radial strip of the disk with a radial scale mounted adjacent to their trailing edge, see Fig 6. The crystals are transparent below 31.4°C when a red display is initiated and then at 31.8°C they become green, before turning blue and transparent again at higher temperatures. The green colour change was chosen for this investigation because it has the narrowest bandwidth. The status of the thermochromic liquid crystals was recorded using a computer-controlled motor-driven camera in conjunction with a powerful electronic flash, which would recharge in as little as a second. The system gave information on temperatures

at regular intervals during the transient on up to 36 colour slides. The computer responded to signals from an optical sensor which was fixed near the rotating shaft and which was activated by a black strip attached to the shaft. This ensured that the camera and flash operated when the strip of liquid crystals was in the field of vision of the camera and that there would be a fixed number of revolutions and hence a fixed time interval between pictures.

The heat transfer coefficient at a given radius was calculated from the time at which the liquid crystal at that position changed colour using an analytical solution for transient conduction into a semi-infinite solid. The solution assumes one-dimensional conduction, a constant air temperature and a constant heat transfer coefficient. The surface temperature  $T_s$  is related to the initial disk temperature  $T_0$  and the air temperature  $T_a$  by

$$\frac{T_s - T_0}{T_a - T_0} = 1 - \exp(\beta^2) \operatorname{erfc}(\beta) \quad (7)$$

$$\text{where } \beta = \frac{h \sqrt{t}}{\sqrt{(\rho_d c_d k_d)}} \quad (8)$$

and  $\operatorname{erfc}(\beta)$  is the complementary error function  $1 - \operatorname{erf}(\beta)$ . For  $\beta < 1$  the error function may be evaluated from

$$\operatorname{erf}(\beta) = \frac{2}{\sqrt{\pi}} \sum_{n=0}^{\infty} \frac{(-1)^n \beta^{2n+1}}{(2n+1) n!} \quad (9)$$

The value of  $\beta$  was calculated iteratively using equations 7 and 9 from the air temperature, the initial disk temperature and the temperature at which the liquid crystal changes colour and then the heat transfer coefficient at a particular radius was evaluated from the time at which the liquid crystal changed colour at that location using the properties of perspex and equation 8.

Heat transfer coefficients for a disk rotating in still air could not be measured directly using this experimental approach but this information was obtained for laminar boundary layers by extrapolating the results for various axial velocities to zero approach velocity.

### 3 EXPERIMENTAL RESULTS

Results for the smooth disk (see Fig 7, for example) were in good agreement with the earlier work by Jackson et al.(15). Most of the disk was covered by a laminar boundary layer with a transitional region and the beginning of a turbulent boundary layer at the edge of the disk. The data derived for a laminar boundary layer on a disk rotating in still air were consistent with established correlations, which gives confidence in the experimental technique. Transition to a turbulent boundary layer began at a Reynolds number of  $10^5$  to  $2 \times 10^5$ , depending on the axial velocity and it can be seen

that the influence of the axial flow velocity diminished sharply following transition. Nusselt numbers in the very short turbulent region were consistent with established correlations for smooth disks such as equation 5, again giving confidence in the measurement technique.

The presence of a trip wire disturbed the laminar boundary layer locally but in most cases smooth disk behaviour was re-established downstream of the wire. This was to be expected for a wire of 1 mm diameter located where the rotational Reynolds number was  $3 \times 10^4$ , Fig 8, in view of the comments of Theodorsen and Regier (6). The line plotted on the graph shows the values for a boundary layer on a smooth disk. Smooth disk behaviour, again shown by a solid line, was also re-established downstream of larger wires at a greater radius corresponding to a rotational Reynolds number of  $10^5$ , Fig 9, but the downstream behaviour was now turbulent. These results confirmed that roughness protrusions of the order of 1 mm in height would modify the convection locally and so the first measurements using rough surfaces were made with this roughness height.

Local Nusselt numbers for a disk with 1 mm circular ribs and an axial velocity of 1.5 m/s, Fig 10, were only slightly enhanced relative to the smooth disk data, at most 20 to 30 %, except in the intermediate Reynolds number range  $6 \times 10^4 < Re_\omega < 2 \times 10^5$  when a greater enhancement was due to an earlier transition to turbulent flow. The lines plotted on this graph and in the following figures represent Nusselt numbers for boundary layers on smooth disks calculated from equations 5 and 6. A similar modest enhancement was observed with the highest axial velocity for this first roughness configuration, Fig 11. The greater rib heights of the second roughness configuration, Figs 12 and 13, produced a further slight enhancement in Nusselt numbers, due chiefly to a further reduction in the transitional Reynolds number. The data for the third roughness configuration, in which the spacing between ribs was doubled, were almost indistinguishable from those for the same roughness height but closer pitch shown in Figs 12 and 13.

The experimental data for a disk with studs of the first roughness configuration are shown in Fig 14 for an axial flow velocity of 1.5 m/s. The laminar boundary layer extended to a rotational Reynolds number of about  $10^4$  with a turbulent region evident for higher Reynolds numbers; this displayed a 0.8 power law dependency. Correlations for boundary layers on a smooth disk are shown for comparison. Raising the axial flow velocity to 6.3 m/s increased heat transfer in the laminar zone but not significantly in the turbulent region, Fig 15. It is noticeable that at a given axial flow velocity the data for the turbulent boundary layer for a range of rotational speeds appear to depend very largely on the rotational Reynolds number.

Further increases in rates of heat transfer for the

taller studs of the second and third roughness configuration were rather modest, Figs 16 and 17. The principal effect of increased roughness height appears to have been a reduction in the transitional Reynolds number. The data also seem rather insensitive to roughness pitch for a given roughness height.

#### 4 DISCUSSION

The influences of both trip wires and circular ribs on the rates of heat transfer to the rotating disk were relatively small. This is, perhaps, not surprising as the dominant velocity component close to the moving surface will tend to be the tangential velocity  $v$  of Fig 1 except at high imposed axial flow rates and low rotational speeds. Hence the velocity across the circular ribs will often be only of a second order when compared with the velocity component along the ribs and indeed the protrusions could even tend to constrain the flow to some extent to a motion in the radial direction. Heat transfer rates in the turbulent boundary layer at the edge of the disk with circular ribs for low axial flow velocities were only a little higher than those observed with smooth disks which were similar to the values suggested by the correlation for turbulent boundary layers on smooth disks rotating in still air (equation 5).

In contrast the influence of isolated studs on the disk increased heat transfer rates very considerably and the difference in effectiveness of the two types of roughness can be seen in Fig 18. Although turbulent Nusselt numbers on the studded disks displayed an approximately 0.8 power law relationship with rotational Reynolds number, as in the correlation for smooth disks, the magnitudes of the Nusselt numbers were more than twice the values suggested by equation 5. Hence a uniformly distributed roughness on the surface of a rotating disk can produce a very significant enhancement to the rate of heat transfer. It can be seen from Figs 16 to 18 that the magnitudes of the enhancement in the admittedly rather limited range of roughnesses investigated seemed relatively insensitive to the height of the roughness protrusions, except that the point of transition from a laminar boundary layer to a turbulent boundary layer occurred at a lower Reynolds number with the greater roughness height. There appeared to be almost no effect on the rates of heat transfer for both types of roughness from doubling the roughness spacing; the data for the second and third roughness configurations were almost identical.

The separate influences of the disk rotation and the imposed axial velocity can be most clearly seen in the data for the lowest roughness height and the lowest rotational speed (483 rev/min), Fig 19. The effects of disk rotation and axial flow have been combined by using a modified rotational Reynolds number  $Re'$  defined as follows:



$$Re^* = \sqrt{Re_\omega^2 + Re_a^2} \quad (10)$$

The local Nusselt numbers of Fig 19 are plotted against this parameter in Fig 20; this gives a rather better correlation of data in the turbulent region. Figs 20 and 21 respectively show all the data for studded disks with the first two roughness configurations plotted against this modified Reynolds number. The reduced importance of the imposed axial flow velocity in turbulent boundary layers as compared to laminar boundary layers can be seen by comparing equation 6 (in which the axial Reynolds number has a large weighting) with equation 10 (in which it does not). The relative insensitivity of local turbulent Nusselt numbers to the axial flow velocity make it difficult to extrapolate the results to zero approach velocity. Now, the form of equation 10 can be justified by considering the velocity over an individual stud which will govern the additional turbulence injected into the boundary layer. The velocity vector is formed from the combination of the tangential velocity (which is of the order of  $\omega r$ ) and the radial velocity (which to a first approximation is of the order of the imposed axial velocity  $W$ ) and its direction will, in general, be at an angle to the radius. During the tests it was noticed that at times the colour change in the liquid crystals downstream of a stud propagated along a line at an angle to the radial direction, presumably in the direction of this resultant velocity vector. The direction of this velocity vector also explains why the pitch-to-height ratio for two-dimensional ribs, which has been optimised for conventional two-dimensional flows across them, does not apply to the three-dimensional boundary layers on rotating disks. With the latter the separated flow behind one roughness element will not usually be in the direction of the shortest distance to the next roughness protrusion. The present investigation therefore leaves the question of optimum spacing for artificial roughness on rotating disks unresolved.

## 5 CONCLUSIONS

Convective heat transfer to a rotating disk from an imposed axial flow has been measured using liquid crystal thermometry and the transient heating technique. The presence of circular ribs on the disk surface caused an early transition to turbulent flow but did not otherwise cause a very substantial augmentation of heat transfer. In contrast, isolated studs on the disk surface increased rates of turbulent heat transfer by more than a factor of two when the data are compared with those for smooth disks and the transitional Reynolds number was reduced by an order of magnitude. The influences of disk rotation and axial flow may be represented by combining the rotational Reynolds number and an axial Reynolds number. The optimum spacing of roughness elements on rotating disks has not been established.

## REFERENCES

- (1) Von Karman, T. Über laminare und turbulente Reibung, *Zeitschrift für Angewandte Mathematik und Mechanik*, Vol. 1, 1921, 233-252.
- (2) Gregory, N., Stuart, J.T. and Walker, W.S. On the stability of three-dimensional boundary layers with application to the flow due to a rotating disk, *Phil. Trans. A.*, Vol. 248, 1955, 155-199.
- (3) Cham, T.S. and Head, M.R. Turbulent boundary-layer flow on a rotating disk, *J. Fluid Mech.*, Vol. 37, 1969, 129-147.
- (4) Wagner, C. Heat transfer from a rotating disk to ambient air, *J. Applied Physics*, Vol.19, 1948, 838-839.
- (5) Cobb, E.C. and Saunders, O.A. Heat transfer from a rotating disk, *Proc. Roy. Soc.*, Vol. 236, 1953, 343-351.
- (6) Theodorsen, T. and Regier, A. Experiments on drag of revolving disks, cylinders, and streamline rods at high speeds. NACA Tech. Report 793, 1944.
- (7) Dorfman, L.A. Thermal boundary layer on a rotating disk, *Soviet Physics, "Doklady"*, Vol. 3, 1958, 248-251.
- (8) Davies, D.R. On the calculation of eddy viscosity and heat transfer in a turbulent boundary layer near a rapidly rotating disk. *Quarterly J. Mechanics and Applied Mathematics*, Vol. 12, 1959, 211-221.
- (9) Hartnett, J.P., Shing-Hwa Tsai, and Jontscher H.N. Heat transfer to a non-isothermal rotating disk with a turbulent boundary layer, *ASME J. Heat Transfer*, Vol. 87, 1965, 362-368.
- (10) McComas, S.T. and Hartnett, J.P. Temperature profiles and heat transfer associated with a single disk rotating in still air, 4th Int. Heat Transfer Conference, Versailles, France, 1970, Paper FC7.7.
- (11) Popiel, C.O. and Bogusławski, L., Local heat transfer coefficients on the rotating disc in still air, *Int. J. Heat Mass Transfer*, Vol. 18, 1975, 170-174.
- (12) Newman, B.G. Flow and heat transfer on a disk rotating beneath a forced vortex, *AIAA*, Vol. 21, 1982, 1066-1070.
- (13) Ong, C.L. and Owen, J.M. Computation of the flow and heat transfer due to a rotating disk, *Int. J. Heat Fluid Flow*, Vol. 12, 1991, 106-115.
- (14) Owen, J.M. Flow and heat transfer in rotating disk systems, ICHMT International Symposium in Heat Transfer in Turbomachinery, Athens, August 1992.
- (15) Jackson, J.D., Al-Khatani, S.A. and He, S. Investigation of heat transfer from an imposed axial flow of air to a rotating disk, Eurotherm Seminar 46, Heat Transfer in Single Phase Flows 4, University of Pisa, Italy, 3-4 May 1995, 123-130.
- (16) Okamoto, S., Nakaso, K. and Kawai, I. Effect of rows of two-dimensional square ribs on flow property along plane wall, *JSME International Journal, Series B*, Vol. 36, 1993, 121-129.

## NOMENCLATURE

c	specific heat capacity
e	roughness height
h	heat transfer coefficient
k	thermal conductivity
Nu	Nusselt number $hr/k$
p	roughness pitch
r	radial position on disk
R	radius of disk
$R_p$	pipe radius
$Re_\omega$	Rotational Reynolds number $\rho\omega r^2/\mu$
$Re_a$	Reynolds number of axial flow $\rho Ur/\mu$
$Re^*$	Modified rotational Reynolds number (eqn. 10)
t	time
T	temperature
u	radial velocity component
v	tangential velocity component
w	axial velocity component
W	axial approach velocity

### Greek symbols

$\beta$	parameter defined by eqn 8
$\delta$	boundary layer thickness
$\mu$	dynamic viscosity
$\nu$	kinematic viscosity
$\rho$	density
$\omega$	angular velocity

### Subscripts

a	air
d	disk
mean	mean
s	surface
0	at time $t = 0$

Roughness configuration	Roughness height (mm)	Roughness pitch (mm)	Pitch to height ratio
1	1	12	12
2	2.5	12	4.8
3	2.5	24	9.6

Table 1: Roughness parameters investigated

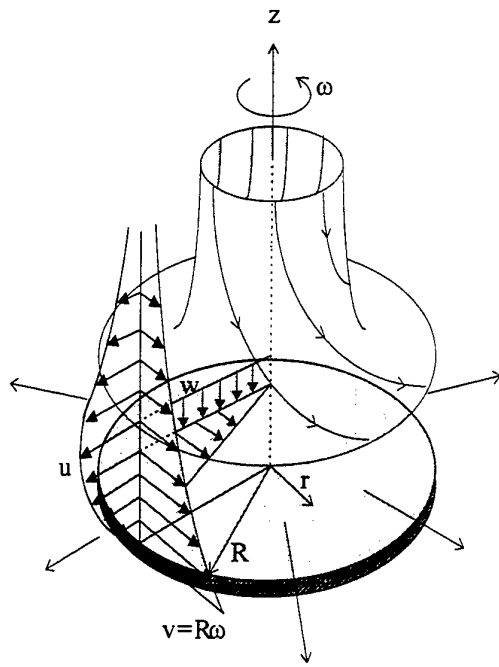


**Figure 1** Flow in the neighbourhood of a disk rotating in a fluid at rest

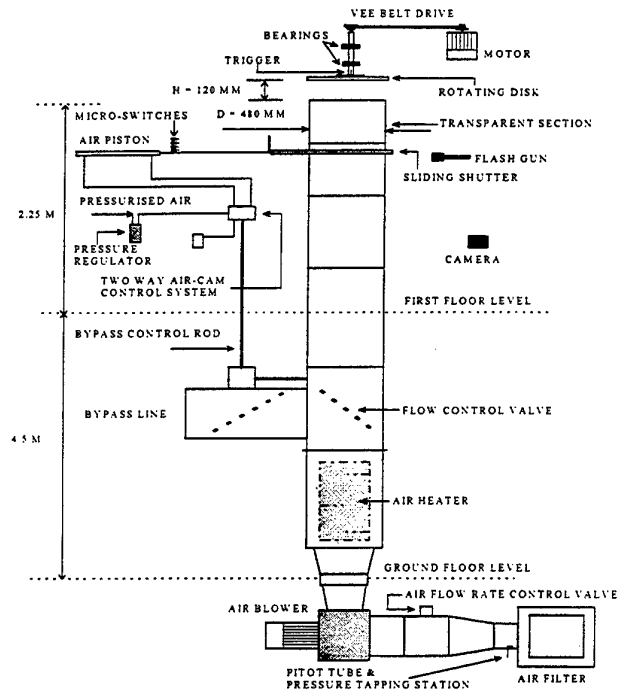


**Figure 2** Apparatus

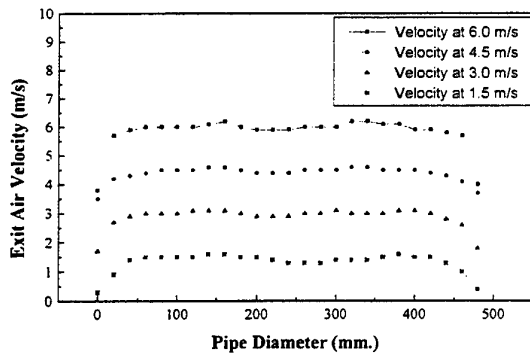


**Figure 3** Axial velocity profiles

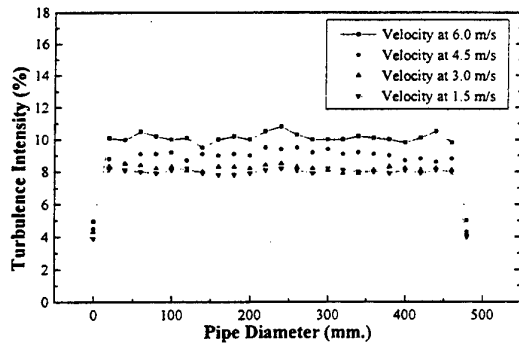


**Figure 4** Turbulence intensities in axial flow

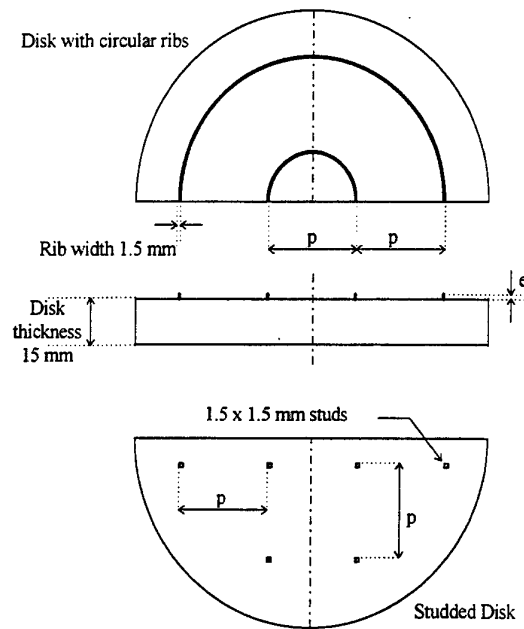


**Figure 5** Geometry of roughened surface

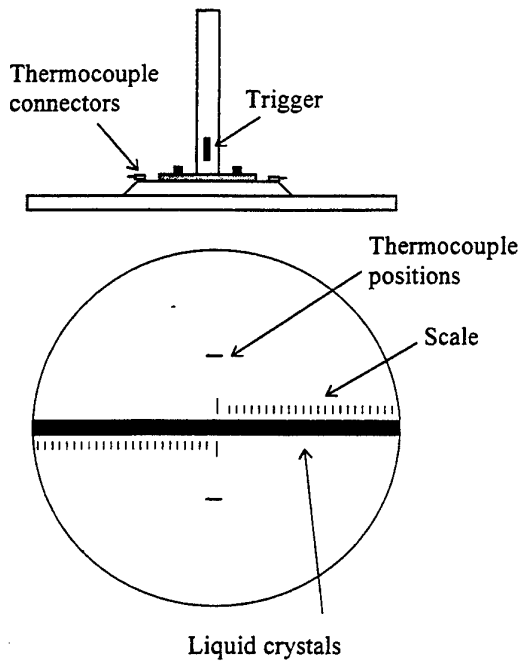


Figure 6 Position of liquid crystals on disk

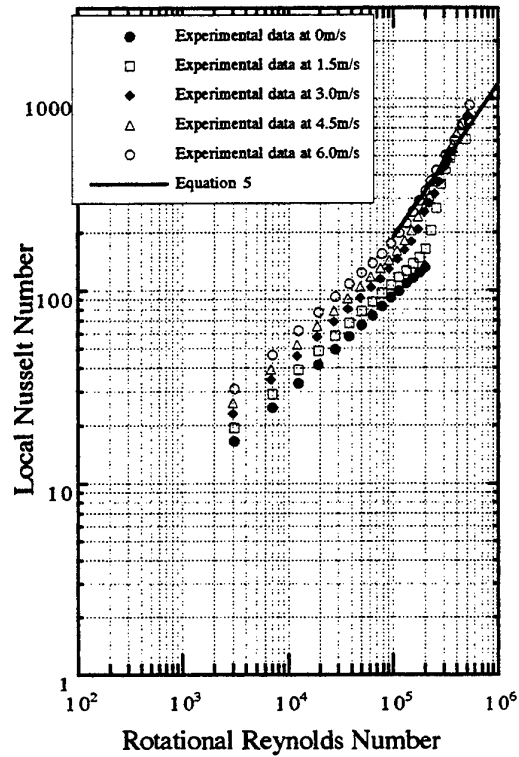


Figure 7 Nu for a smooth disk at 1275 rev/min

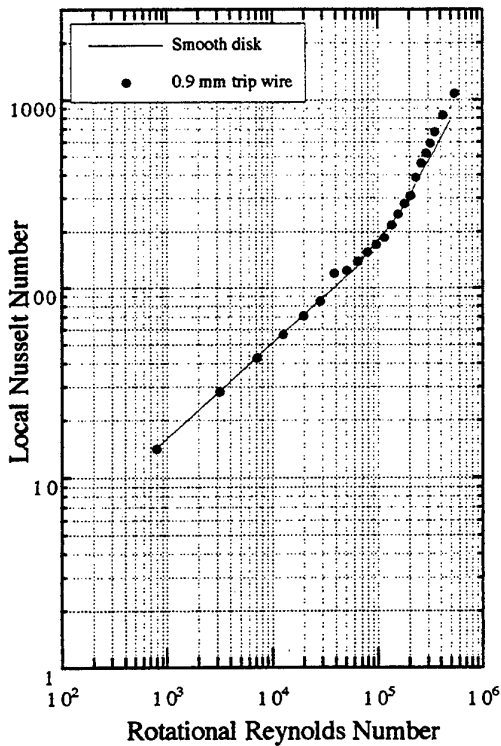


Figure 8 Nu with a 0.9mm trip wire attached at  $r=60\text{mm}$  at 1275 rev/min and 6.0m/s

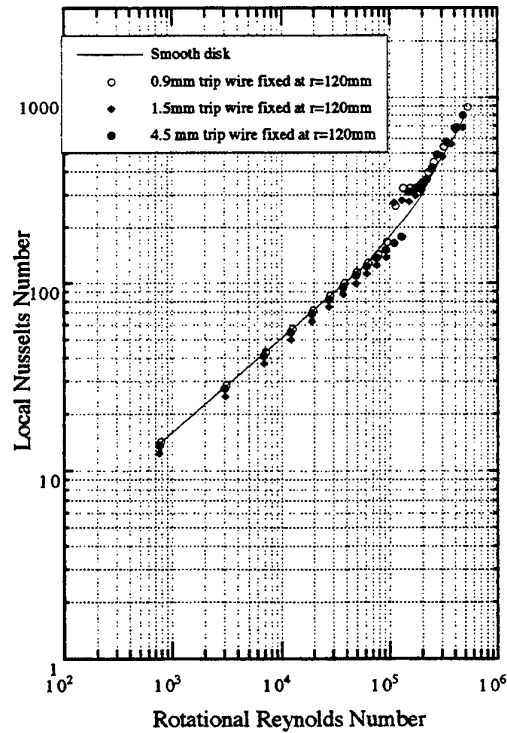


Figure 9 Nu with various trip wires attached at  $r=120\text{mm}$  at 1275 rev/min and 6.0m/s

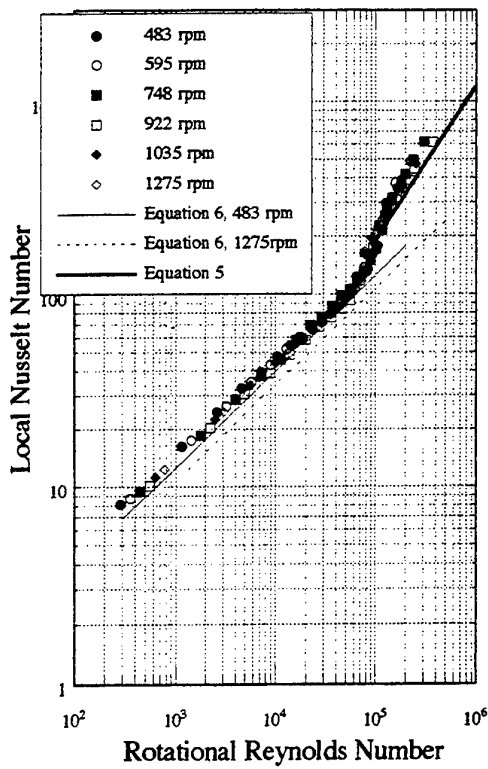


Figure 10 Nu for a disk with 1mm circular ribs at 1.5 m/s axial air speed

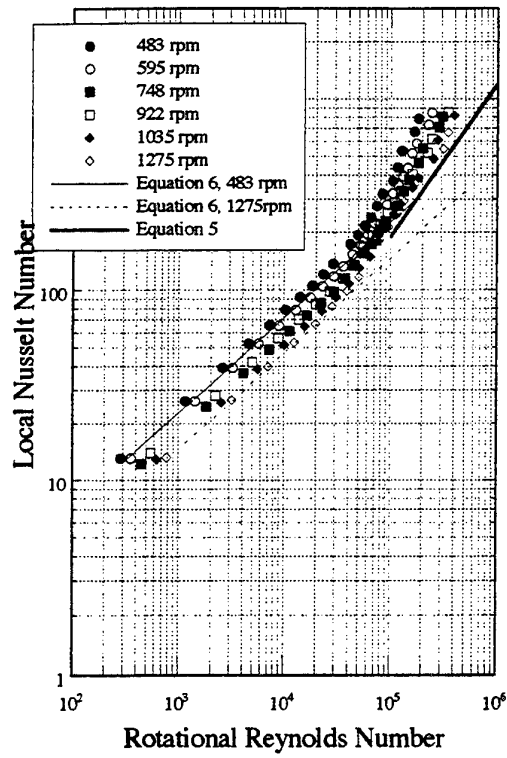


Figure 11 Nu for a disk with 1mm circular ribs at 6.0 m/s axial air speed

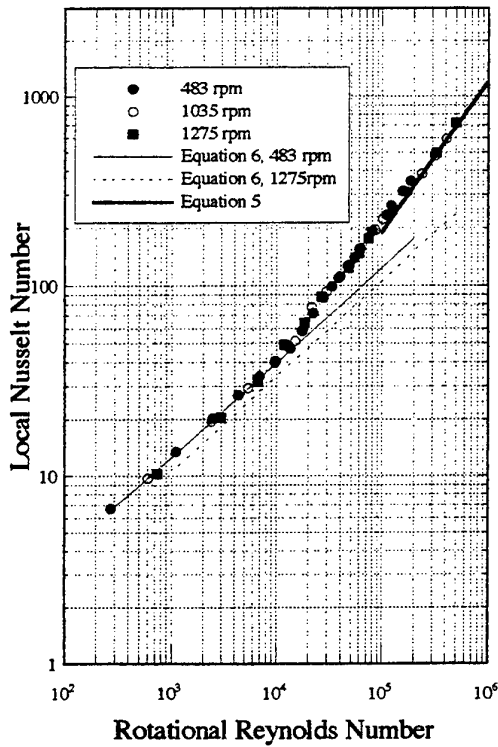


Figure 12 Nu for a disk with 2.5mm circular ribs with 12 mm pitch at 1.5m/s axial air speed

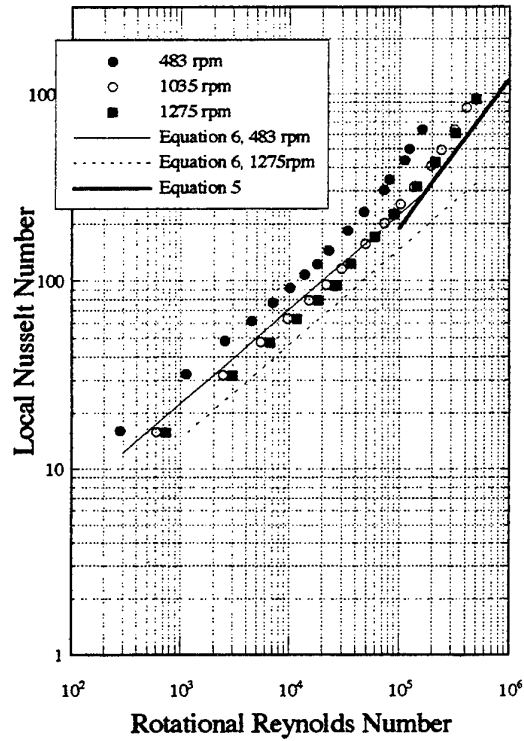


Figure 13 Nu for a disk with 2.5mm circular ribs with 12 mm pitch at 6.0 m/s axial air speed

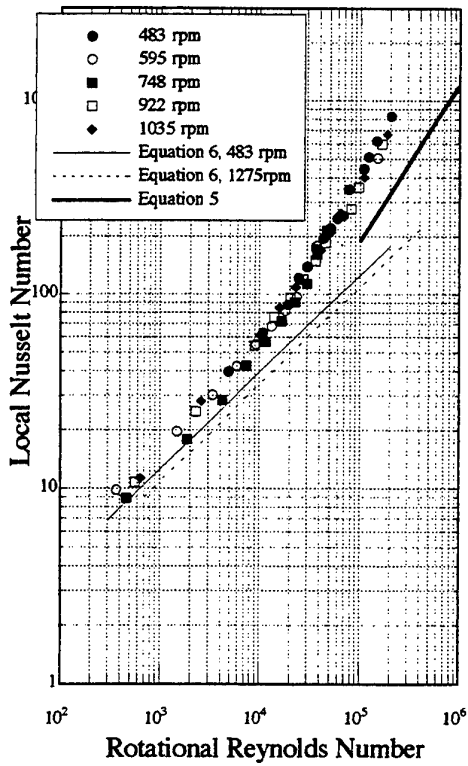


Figure 14 Nu for a disk with 1mm studs at 1.5 m/s axial air speed

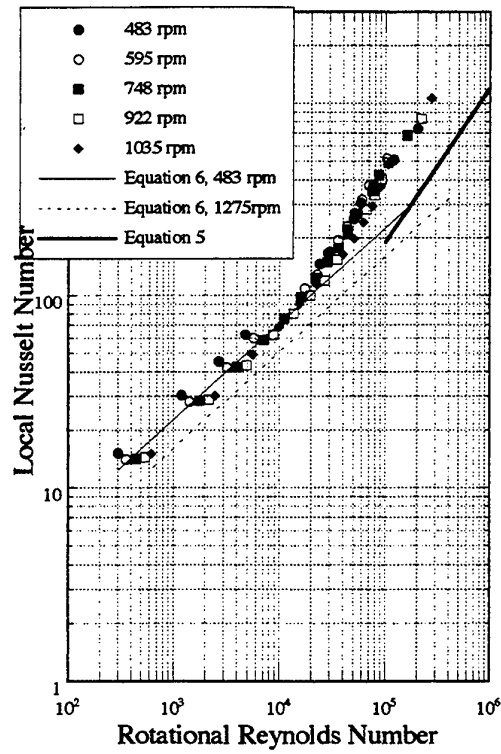


Figure 15 Nu for a disk with 1mm studs at 6.0 m/s axial air speed

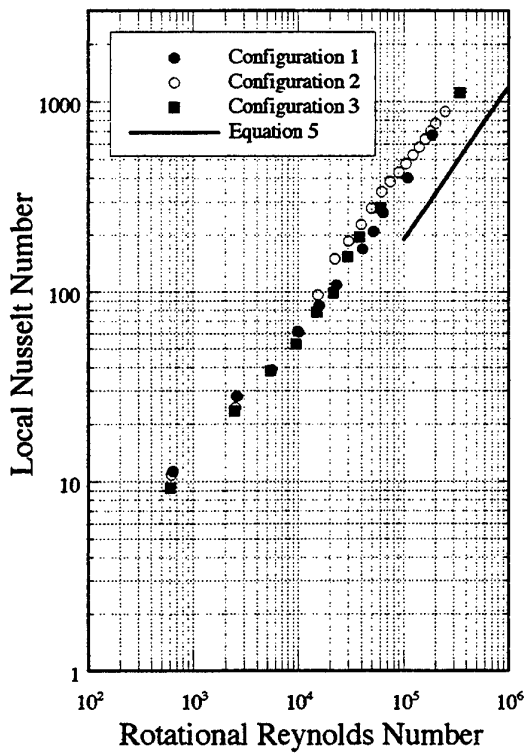


Figure 16 Nu for disks with studs at 1035 rev/min and 1.5 m/s axial air speed

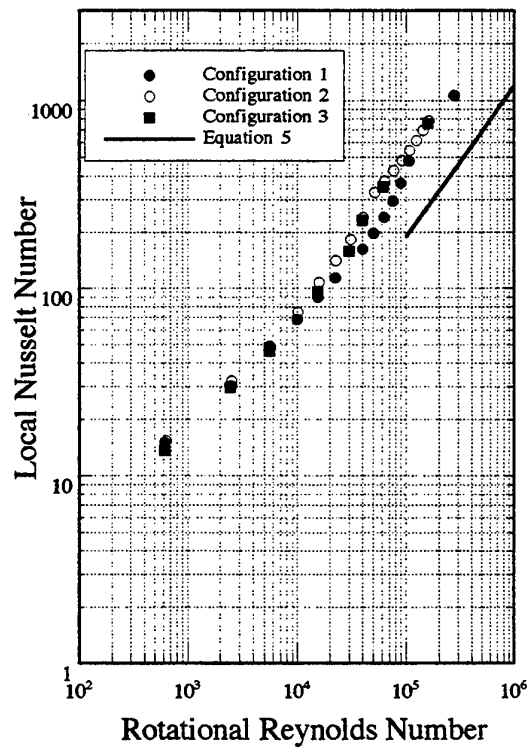


Figure 17 Nu for disks with studs at 1035 rev/min and 1.5 m/s axial air speed

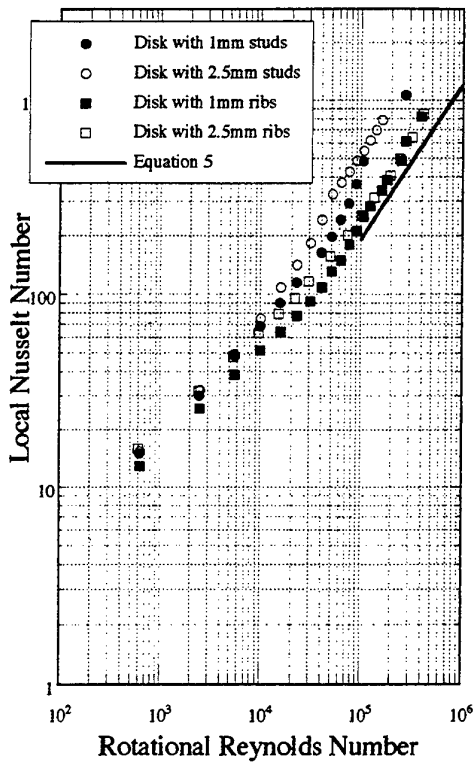


Figure 18 Comparison of effectiveness of the two types of roughness

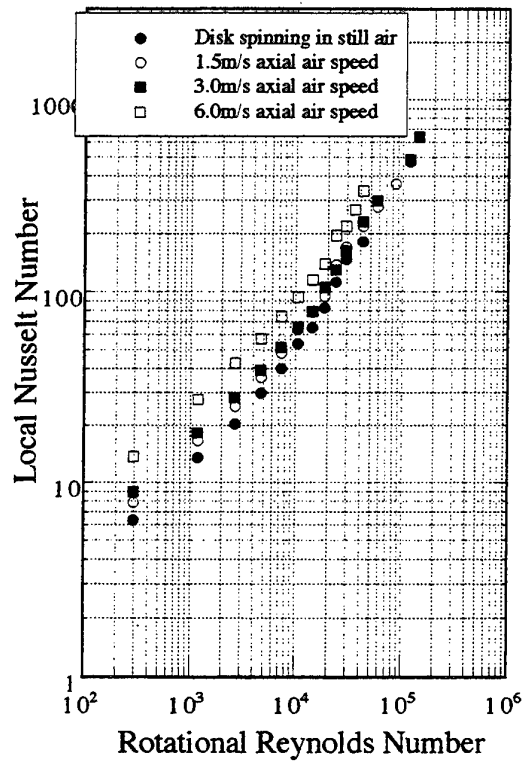


Figure 19 Nu for a disk with 2.5mm studs at 483 rev/min

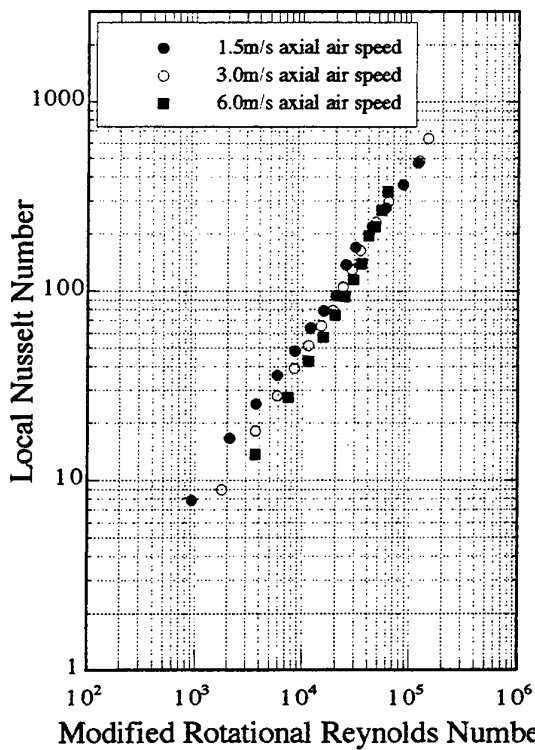


Figure 20 Nu and modified rotational Re for a disk with 2.5mm studs at 483rev/min

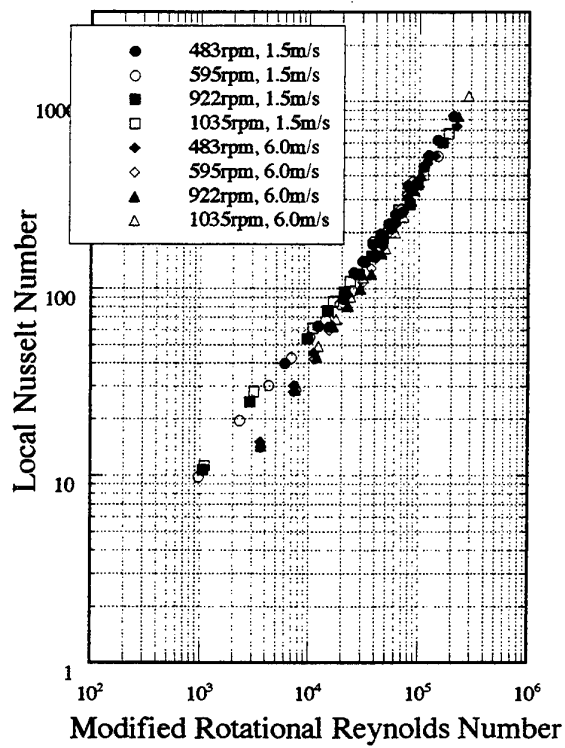
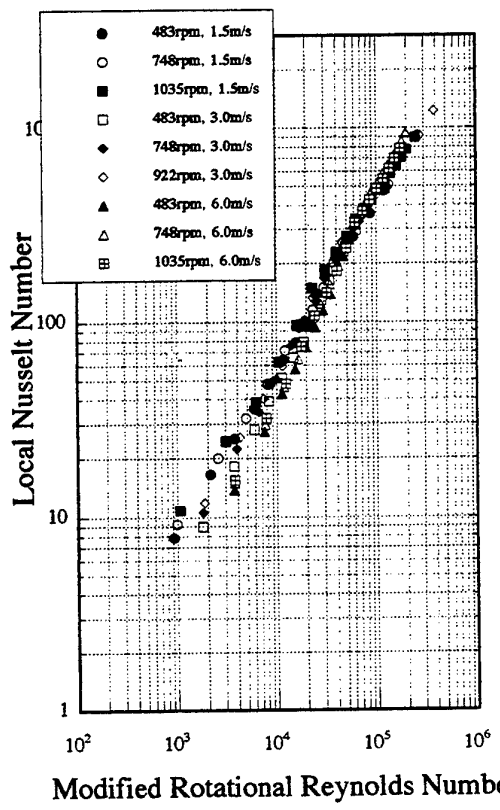


Figure 21 Nu and modified rotation Re for a disk with 1mm studs, all data



**Figure 22 Nu and modified rotational Re for a disk with 2.5mm studs, all data**



## **Session 8**

# **Large-Eddy Simulation for Industrial Flows**



# LARGE-EDDY SIMULATION OF AERONAUTICAL FLOWS

Peter R. Voke

SMME, University of Surrey, U.K.

## ABSTRACT

Progress is reviewed in the large-eddy simulation of flows for aeronautical applications such as turbomachinery blading and aerofoils. Structured and unstructured meshes are compared and the current status of methods using structured meshes and general coordinate transforms is reviewed in some detail. For incompressible flows or compressible flows computed by implicit methods, elliptic equations must be solved and appropriate and efficient methods for this are outlined. An introductory account of dynamic procedures for sub-grid scale modelling is given, together with some results illustrating the current capabilities of LES for aeronautical flows.

## 1 INTRODUCTION

Large-eddy simulation (and the more fundamental related technique of direct numerical simulation, DNS) have established themselves as important tools for the study of turbulent and transitional flows over the past twenty years. It is natural to ask when and how LES will be applied to aeronautical flows, as it has been applied successfully in other areas.

Large-eddy simulation (LES) is a method of studying and predicting turbulent flows. In LES the turbulence is simulated numerically on a computer down to a chosen scale determined by (or related to) the mesh size used for the simulation. LES is three-dimensional and time-dependent, with the turbulent motions and instabilities that are reproduced numerically on the computer often being strikingly similar to those seen in the real turbulent flow quantitatively and qualitatively.

LES is limited by the fact that real turbulence at high Reynolds numbers contains an immense range of scales and hence far too many degrees of freedom for even the most powerful of current computers to mimic precisely. For this reason the scales simulated are cut off at the mesh scale or by a spatial filter whose scale is of the same order of magnitude as the mesh used for the simulation. Turbulent motions of a smaller scale (subgrid-scale motions) are not computed directly since they are unresolved, but because they play an important dynamic role in exchanging energy and momentum with the resolved motions, their effects must be represented by a subgrid-scale model. At solid surfaces, other important processes may not be resolved and a further wall model is then required, distinct from the subgrid-scale model.

LES should be clearly distinguished from other related but different methods of studying and predicting turbulent flows. On the one hand closure models of turbulence represent all the scales of unsteady three-dimensional motion in the form of a statistical model, so that a unique solution may be found for mean flow quantities such as mean velocities, turbulence intensities and dissipation. An LES never produces a unique solution since the numerical turbulence in the LES may continue to evolve chaotically, in 3D, indefinitely – though of course this evolving turbulent solution can be sampled statistically to estimate average quantities, spectra and various other correlations.

On the other hand a still more fundamental approach for low-Reynolds-number turbulent flows exists called direct numerical simulation, in which a mesh fine enough to resolve all the turbulent motions is used and so a sub-grid scale model is not required. There is ample evidence that the best direct numerical simulations that have been performed are impressively realistic representations of real turbulence. However DNS can only be applied to very low-Reynolds-number turbulence which contains the limited range of scales of motion that can be captured by current computers.

LES therefore sits between these two methods and has some advantages and some disadvantages compared to each. On the one hand, compared to closure models, the large-scale turbulent motions which contain most of the turbulent kinetic energy and which carry out most of the turbulent transport processes in the flow are being simulated with some realism; but an LES will often be considerably more expensive than a closure calculation. On the other hand, LES is not limited to low-

Reynolds-number turbulence like DNS and can in fact simulate flows of indefinitely high  $Re$ ; but unlike a DNS an LES can never claim to be exact because of its dependence on the subgrid-scale model and also often on a wall model.

In aeronautical flows there is frequently a wide range of time-scales of motion as well as a range of spatial scales. Trailing vortices can be huge, with correspondingly long time-scales well separated from the length and time-scales of the turbulence in the boundary layers that feed into the vortices. In circumstances like this, LES is not the first technique to turn to since the range of time-scales involved will make a proper simulation that both resolves the small time-scale motions and extends over several periods of the large time-scale motions prohibitively expensive. Clean separation of the time-scales suggests that time-dependent Reynolds-averaged Navier Stokes solution is a more natural – and very much cheaper – alternative. On the other hand, where there is overlap of the time scales, and particularly if dynamically significant interaction is taking place between turbulence and larger structures such as vortices, LES is the right route to understanding and prediction.

LES was invented by meteorologists (1) in the 1960s, but its engineering potential was recognised by engineers quite rapidly (2). Given the fact that an LES is capable of providing an extraordinarily complete picture of a turbulent flow, often more detailed than any practical experiment or closure calculation, we might expect it to become a key tool for engineers. In the next section we consider why it is taking so long for LES to reach the point of contributing directly to the engineering design process, outside of a few very specialist areas.

## 2 THE COST OF LES

In large-eddy simulation of incompressible flow we approximate numerically the Navier-Stokes and continuity equations:

$$\frac{du_i}{dt} = -dp/dx_i - d(u_i u_j)/dx_j + d(2\nu s_{ij})/dx_j$$

$$du_i/dx_i = 0$$

There is of course an equivalent set of equations, including the energy equation, for compressible flow, but we shall concentrate

here on incompressible LES apart from mentioning a few ways in which compressible LES differs practically in computation.

A three-dimensional time-dependent simulation of these equations requires spatial and temporal discretisation. Typically for DNS a spectral discretisation in space will be used for a DNS in a simple geometry, or for more complex geometries spectral elements (similar to high-order finite elements) or perhaps high-order compact finite-difference formulae.

Large-eddy simulations using spectral methods have been performed but it is more common to utilise finite-differences for engineering flows. In the early years, the well-known second-order central finite-volume technique using a staggered mesh arrangement was commonplace, and is still useful for many LES studies. More commonly now higher-order schemes are employed, sometimes upwind-biased and often using compact formulae (3). For the time discretisation, low-order Runge-Kutta is tending to replace the more traditional second-order leapfrog and Adam-Bashforth time-stepping.

To see why one cannot run an LES on a design office PC or even a Unix workstation, we need to look more closely at what is required of the simulation numerically and physically. The turbulence is driven by the non-linear term of the Navier-Stokes equation and implicit treatment of this term is not advantageous since significantly larger time-steps are fatal to the veracity of LES or DNS (unless wave-like solutions are being simulated in an early transitional flow, perhaps). The accuracy requirement for this term therefore determines that the time step of the simulation must obey a CFL limit. The viscous term can be treated implicitly, though this is not absolutely necessary when the mesh is designed so that the viscous stability limit is no tighter than the CFL limit.

In an incompressible LES, the pressure must be solved for implicitly of course, by deriving the discrete form of the Poisson equation for the pressure and solving this by methods similar to the familiar pressure-correction algorithm. To ensure mass conservation, the pressure equation must be solved to good accuracy at each time step: this is potentially the most expensive part of an LES, since the explicit or partly implicit computation of the remaining terms is very fast. In fact, using traditional methods for solving Poisson equations such as

Stone's strongly implicit method, a multigrid relaxation technique, or the preconditioned conjugate gradient method, it is all too easy to find the pressure solution takes up to 100 times longer than the rest of the LES, making a simulation on an adequate mesh that is run for long enough to gather proper statistics quite uneconomic.

This is why throughout the 1980s incompressible LES was performed mostly in very simple geometric configurations. Fast direct Poisson solvers were employed which could produce highly accurate pressure solutions in very short times using Fourier techniques, even when the rest of the LES was based on finite differences. Compressible simulations (mostly DNS) can be completely explicit and avoid these restrictions, but at the expense of requiring a time step dictated by the acoustic CFL limit; in practice they are not any faster than incompressible simulations. When solid surfaces are present as boundaries, it is necessary to use partly or fully implicit time-stepping, or local time steps.

Let us, very approximately, estimate the computational cost of performing a simple LES of a fully turbulent incompressible flow. For the simulation to capture adequately the dynamics of the large eddies in the flow, we might guess that at least 100 grid points would be needed in each of the three directions, so there will be  $10^6$  mesh cells in all. If  $D$  is the large scale of the turbulence, the mesh scale  $\Delta x$  will be about  $D/100$  in size. The time step, subject to a CFL limit such as

$$\Delta t < \Delta x / U$$

will then be 2000 times smaller than the typical time-scales of the eddies,

$$T = D / u_t$$

if the velocity scale governing turbulence production  $u_t$  is 20 times smaller than the bulk flow velocity  $U$ .

To condition the simulation, study the dynamics and obtain adequate turbulence statistics one must simulate for much longer than the typical time-scale of the large eddies; a good simulation of an engineering flow will typically need to be run for about  $50T$  in total. We now can estimate that the simulation requires about  $10^5 (= 50T/\Delta t)$  time steps. This is not unrealistic, though many real simulations require even more time.

How much CPU time will be needed per time step to run an LES? This depends so much on the algorithm involved that is hard to be exact. Typically the advancement of the flow variables for a single cell of the mesh might require 1000 floating point operations, though this depends on the order of accuracy of the numerical schemes used for spatial and temporal discretisation, the type of pressure solution required and the complexity of the subgrid-scale model in use as well as the geometry. However, taking this figure, we find that the whole simulation requires  $10^9$  floating point operations per step, and  $10^{14}$  operations for the entire simulation.

It is immediately clear that a desktop machine with a maximum sustained speed of 10 Mflop/s cannot perform the simulation; it would take  $10^7$  seconds, or about four months. This is why LES is not currently being seen as a design tool in the 1990s or even, for most industrial groups, as a research tool. However, a single processor on a vector supercomputer attaining 100 Mflop/s sustained speed can complete the entire simulation in 11 days, and a current multiprocessor or MPP supercomputer achieving 2 Gflop/s sustained speed will finish it in 14 hours. Planned machines running at 100 Gflop/s sustained or above would perform such an LES rather rapidly.

This is why this type of simulation is classed as a grand challenge problem, motivating the drive towards Teraflop/s machines and beyond. More ambitious simulations of flow over wings, through compressors and turbines or complex ducts, or past and over complex objects, buildings or terrain would require more operations than the estimate above indicate and correspondingly faster computers. When the leading edge computing machines of today become the workstations of tomorrow we should expect to see LES enter the mainstream of industrial aeronautical research and design.

In the following sections we look at a number of innovations and advances that are already allowing LES to be applied to aeronautical and other engineering flows. The numerical capabilities that will be needed in the aeronautical and other production industries in the future are currently being developed and tested.

### 3 PREVIOUS AND CURRENT WORK

To perform a simulation of turbulent flow around a wing section, turbine or compressor blade, engine fairing or aircraft wing-body junction, either finite-element techniques or body-fitted coordinates for a structured finite-difference approach are vital. LES using finite elements is the subject of intense interest by a small number of specialist groups in Japan and the USA. Unstructured grids have considerable advantages in terms of concentrating resolution where it is needed and not elsewhere. The costs, however, can be considerable in terms of the efficiency of pressure solution, in particular.

Using body-fitted coordinates, an LES of flow over a NACA 4412 aerofoil has been performed (4) by Kaltenbach and Choi at an angle of attack of 12 degrees and a chord Reynolds number of 1.64 million. They used second-order finite differences with the contravariant velocities discretised on a staggered mesh – a method which is very similar to that used by us for somewhat less ambitious flows. Their mesh of 638 x 79 x 48 cells was barely adequate for an LES of the 4412 foil, with both streamwise and spanwise cell sizes being rather large in terms of wall units, and a number of less satisfactory results were noted. A smoothing filter was required to suppress grid-scale oscillations in the laminar flow upstream, and transition to turbulence was found to occur immediately following the region in which the filter was applied. Values of the shape factor  $H$  dropped more rapidly in the simulated boundary layer in the mid-chord region of the aerofoil than is found experimentally (5), and near the trailing edge there were substantial differences in the turbulence intensities between simulation and experiment.

Interest in large-eddy simulation of aerofoil flows is continuing, with the formation of a European consortium of universities funded by the CEC and European aerospace industries which aims to perform LES of flow over the Aerospatiale A Aerofoil. This profile has been the subject of separate CEC-funded research on closure models (6). The consortium (LESfoil) is led by The Department of Thermo- and Fluid-Dynamics of Chalmers University of Technology, Sweden and is comprised of Alenia of Torino, Italy, CERFACS of Toulouse, France, Dassault Aviation of France, Fluent Europe of Sheffield, U.K. together with The University of Karlsruhe, Germany and the University of Surrey and UMIST, both of the

U.K. The recently formed grouping plans to simulate the A Aerofoil flow close to maximum lift with meshes similar to those used by Kaltenbach and Choi (4) and also with coarser surface resolution using wall-function boundary conditions. The group will also be performing simulations using unstructured meshes, following some pioneering work by Jansen (7).

Neither of these studies is a truly 3D geometry of course, and significant gains in efficiency result from studying flows in geometries that are complex in 2D but with the third dimension of the LES homogeneous. Subsequent sections of this paper outline some of these methods using Fourier techniques applied for the pressure solution even when the underlying numerical algorithm is based on finite-differences or a finite-volume approach.

LES of flows in truly 3D geometries are not so amenable to numerical tricks. Some fully 3D LES have been done using simple iterative pressure solvers (8, 9) but allowing the accuracy of the pressure solution to be much more slack than is usual. There appear to be no obvious deleterious effects from the looser enforcement of mass conservation that results. This is likely to be the way ahead for LES in really complex 3D geometries too: iterative solvers with modern acceleration techniques (10), applied with a realistic and practical threshold of accuracy for pressure and mass conservation. The fact that in an LES the time step is small means that the pressure changes little from one step to the next (particularly the larger scales of the pressure field) and so an iterative method is solving at each step for a small-scale pressure correction.

Many aeronautical flows are compressible, and the incompressible techniques outlined here are superseded in these cases by explicit coding of a density advancement equation. To avoid the huge expense that would result from tiny time-steps dictated by the acoustic CFL limit in fine mesh regions near solid boundaries, these codes should use some implicit computation in regions where fine meshing is required and accurate representation of the propagation of acoustic waves across these fine meshes is not meaningful physically or required of the simulation. This also results in Poisson-like elliptic equations whose solutions can be obtained in ways related to those described below.

#### 4 GENERAL COORDINATES

For aeronautical applications we are primarily interested in geometries that are quite complex in two dimensions such as a 2D aerofoil or turbine blade row. These situations naturally involve curved surfaces over which the development of boundary layers, including transition, separation, reattachment and sometimes relaminarisation is to be followed. Here the natural approach is to use general curvilinear coordinates, and this section describes one approach to this aspect of the simulation. Note, however, that the Fourier techniques described below for pressure solution also work very well for 2D geometries with sharp corners such as the flow over a square cylinder (11).

There are two main approaches to Navier-Stokes simulation in general curvilinear coordinates: one using scalar generalised equations for the conservation of Cartesian components of momentum; and a second method, used here, based on the fully general covariant Navier-Stokes equations representing the conservation of contravariant vector velocity components.

The familiar Navier-Stokes equations become

$$d(Ju^i)/dt = -J g^{ij} dp/dx^i - J(u^i u^j)_{,j} + 2J(\nu u^j)_{,j} \quad (1)$$

where  $J$  is the Jacobian of the coordinate transformation and  $g^{ij}$  is the metric tensor. These geometric quantities are computed in advance of the simulation to high accuracy. The equations are multiplied by the Jacobian of the transformation  $J$  in order to cast the equations and the discretisation in conservative form.  $p$  is the pressure over density,  $d/dx^i$  is the partial derivative with respect to  $x^i$  and the  $_{,j}$  notation indicates the covariant derivative, involving the connection coefficients, which are computed in advance, like the metric.

The mass conservation law in general coordinates reads

$$d(Ju^i)/dx^i = 0 \quad (2)$$

from which one can derive a generalised Poisson equation for the pressure simply by taking the divergence of equation (1).

In our simulations we use  $Ju^i$ , the contravariant mass flux vector, as a variable except for computing  $s^{ij}$ , and the momentum advancement

is explicit except for the pressure term which is solved by a standard projection method. The spatial discretisation is performed by one of the standard approaches used in LES, with the geometric quantities computed to higher order in space in advance of the simulation and stored, if necessary at several distinct points of a staggered mesh arrangement.

#### 5 FOURIER METHODS

We simulate turbomachinery blades and related flows using an approach similar broadly to that of Kaltenbach and Choi (4) which allows a partial use of the direct Fourier technique for pressure solution. Let us briefly consider how this works.

Taking the divergence of equation, (1), one obtains the general version of the familiar pressure Poisson equation:

$$d(J g^{ij} dp/dx^i)/dx^j = R \quad (3)$$

where  $R$  is the divergence of the provisional velocity (or strictly mass flux) field  $Ju^i$ .

The equation can be discrete Fourier transformed in  $z$  (a very rapid computational task) to obtain a set of decoupled equations, which in the Cartesian case is

$$d^2p/dx^2 + d^2p/dy^2 - k_z^2 p = R \quad (4)$$

and in the general case is not a great deal more complicated, but involves cross-derivatives  $d^2p/dx dy$  as well.

This process can be performed even when the  $z$  derivatives are computed by finite-difference formulae, provided  $z$  in the simulation is periodic and has an even mesh.

The 2D equations (4), one for each value of  $k_z$ , can be solved very fast even when the geometry is complex. Non-zero values of  $k_z$  increase the diagonal dominance of the system of equations, resulting in very rapid convergence of any iterative scheme employed regardless of the type of discretisation used for the  $x$  and  $y$  derivatives. The small number of low- $k_z$  equations which converge too slowly are speeded up using acceleration techniques such as multigrid (10). By this means, it is possible to obtain pressure solution times for LES in 2D complex geometries that are almost as fast (though not as accurate) as the direct solvers available in very simple geometries.

In a complex 2D geometry, equation (4) contains cross-derivative terms which generally affect the diagonal dominance of the matrices and slow the convergence of iterative solutions. These terms increase in magnitude with the skewness of the mesh (they are absent altogether for orthogonal coordinates), indicating that highly skewed meshes should be avoided for the sake of efficiency.

Typically we expect the use of such a Fourier technique to yield performance enhancements in the pressure solution compared to a fully 3D solver of a least a factor of 5 and frequently up to 20. Ratios of 60 are encountered in extreme cases.

## 6 SUBGRID-SCALE MODELS

A dynamic subgrid-scale model is a method of accounting for the unresolved motions and their effect on a large-eddy simulation that uses the information available in the simulation itself maximally.

A large-eddy simulation numerically represents large-scale velocity fields: we can think of it as accurately representing filtered velocity fields after a large-scale filter function has been applied to the true velocity fields. When applied to the Navier-Stokes equations, the filter, represented by brackets  $\langle \rangle$ , results in equations that look superficially very like the time-averaged (Cartesian) Navier-Stokes equations, but involving a filtered nonlinear term  $\langle u_i u_j \rangle$  that cannot be computed. The difference between it and the part that can be computed,  $\langle u_i \rangle \langle u_j \rangle$ , is the subgrid Reynolds stress  $\tau_{ij}$  which is analogous to the familiar Reynolds stress occurring in the time-average Navier-Stokes equations.

The subgrid Reynolds stress represents the effects of the subgrid motions on the resolved fields of the LES. In contrast to the standard Reynolds stress whose length and velocity scales are those of the entire turbulent flow field, the length scale and velocity scale associated with the subgrid Reynolds stress can be deduced simply and on a local basis from the mesh and the resolved velocity field of the simulation. The length scale is derived from the local mesh ( $\Delta$ ) and the velocity scale is dictated by the small-scale motions on the mesh, roughly equivalent to the largest sub-grid velocities.

The earliest estimate for the velocity scale, based on the local strain rate scalar  $s$ , proposed by Smagorinsky (1), was  $s\Delta$ . He went on to combine these scales into the simple gradient diffusion model that bears his name:

$$\begin{aligned} \tau_{ij} - \delta_{ij} \tau_{kk}/3 &= \nu_s s_{ij} \\ \nu_s &= C \Delta^2 s \\ s^2 &= 2 s_{ij} s_{ij} \end{aligned} \quad (5)$$

$C$  can be predicted theoretically from the  $^{-5/3}$  Kolmogorov spectrum for the inertial range in homogeneous isotropic turbulence.

This very simple model proved surprisingly successful, though it is possible that its longevity is partly due to the failure to find any better model for several decades. The model in fact has clear shortcomings. Tests of its predictions against directly simulated flow fields show that the correlation between the tensors in eq. (5) can be low. In shear flows, particularly wall-bounded flows, the model is far too strong and the value of  $C$  has to be decreased in a pragmatic way. The reasons for this are now quite well understood, but this understanding has not led to a breakthrough to a special model for shear flows. Rather, it gave rise to a new approach in which the value of  $C$ , instead of being adjusted artificially based on the experience of the simulator, is deduced from the LES itself. This is called a dynamic procedure (12). It allows the value of  $C$  to respond to local flow conditions, varying in time and space.

A base subgrid-scale model such as Smagorinsky is needed first. We then consider what would happen if the same LES flow field were simulated on a coarser mesh, effectively filtering the velocity field with a filter larger than that actually used for the LES. This coarser filter, called the test filter, is usually chosen to be twice the size of the mesh filter.

The result of applying the test filter, indicated by a square brackets  $[\ ]$ , to the simulated flow fields is the twice-filtered Navier-Stokes equations. Once more the filtered non-linear term is modelled, but in this case the difference

$$T_{ij} = [\langle u_i \rangle \langle u_j \rangle] - [\langle u_i \rangle] [\langle u_j \rangle] \quad (6)$$

is called the subtest-scale stress.

The dynamic model is based on the assumption that the subgrid stress and subtest stress can be modelled in a formally similar manner, by



applying the basis model at both filter scales,  $\Delta$  and  $2\Delta$ .

Germano pointed out an exact identity between the traceless part of the test-to-grid transfer stress, called  $L_{ij}$ , which is computable in the simulation, to the difference between the two modelled stresses, the subtest-scale and the subgrid-scale stress, called  $C M_{ij}$ . (To factor out  $C$  in this way, of course, the models must assume the same value of  $C$  at both test and grid levels.) -

The models for  $T_{ij}$  and  $\tau_{ij}$  are used to compute the tensor  $M_{ij}$  and we can deduce that  $C$  must be

$$C = L_{ij} / M_{ij} \quad (7)$$

This gives five separate equations for  $C$  since five components of each tensor on the right hand side are independent (the tensors being symmetric and traceless).

Lilly (13) showed that a least-squares estimate of the optimal solution for  $C$  is obtained by contracting top and bottom of equation (7) with  $M_{ij}$  and averaging over any homogeneous directions in the flow in which we do not wish the dynamic procedure to generate local variation of  $C$ . The resulting  $C$  will be a function of time and the inhomogeneous coordinates.

The dynamic procedure has been presented above in Cartesian coordinates for the sake of simplicity, but its derivation can be carried out in general curvilinear coordinates by exact analogy and without difficulty. A question does arise regarding the variation of the filter scale on a transformed mesh, but at present we treat the uniform mesh in the transformed plane as defining the filter at both grid and test levels.

The practical computation of  $C$  in general coordinates is considerably more complex than in the Cartesian case owing to the presence of the metric tensor coupling the various components. A simple alternative that we utilise for the simulation whose results are given below is to return to equation (7), or rather its covariant equivalent

$$C = L^{ij} / M^{ij} \quad (8)$$

and select one of the five equations to define  $C$ . This seems justified in the case considered in the next section where there is a clear principal

strain rate and component of the subgrid Reynolds stress, such as the 12 component in a shear flow. The final justification however is the considerable saving in the cost of using the dynamic procedure in this form, and the quality of the results.

Dynamic subgrid procedures have enjoyed dramatic success in the past few years applied to a variety of flows. Their popularity with simulators derives from the way they produce naturally the variation of  $C$  as solid walls are approached (making *ad hoc* damping functions of the Van Driest type unnecessary), the variation of  $C$  with Reynolds numbers (making LES of partially transitional flows a viable option) and the variation of  $C$  with flow type (for instance for stratified and other special flows).

In the simulation of the transitional flow described below, the value of  $C$  increases from zero as the flow becomes unstable and reaches normal LES levels when the flow becomes fully turbulent. In fact both  $M^{ij}$  and  $L^{ij}$  tend to zero in laminar regions, making equations (7) or (8) poorly conditioned or singular. This is not an academic point: the algorithm for computing  $C$  actually behaves unpredictably in laminar or nearly laminar regions and must be modified to ensure that  $C$  approaches zero in a sensible and well defined manner. We do this by changing equation (8) for the 12 component to

$$C = L^{12} / (M^{12} + \epsilon)$$

$\epsilon$  is a selected small quantity, typically of the order of  $10^{-6}$  of the mean values of  $M^{12}$  occurring in turbulent regions.

## 7 FLOW OVER A LEADING EDGE

As an example of the use of these techniques, we show some results from a simulation of the flow over a flat plate with a semi-circular leading edge. The fully general coordinate system around this geometry is needed since an orthogonal coordinate system will have an inconvenient junction between a cylindrical and a Cartesian mesh region just at the critical point where the curved leading edge joins the flat surface, the so-called blend point. This is the point at which the laminar flow separates and starts to become unstable. Any disturbances in this region, including those with a numerical origin, will affect the flow radically and may led to erroneous conclusions.

A previous simulation by us (14) used an orthogonal coordinate system and suffered from the problems indicated, including very rapid and excessive growth of instabilities in the separated shear layer whose origin could be traced to numerical effects. This does not occur in the simulation with fully general curvilinear coordinates.

The overall computational domain involves a curved outer boundary that is  $8d$  (where  $d$  is the plate thickness) from the solid surface. Figure 1 shows a close-up of the leading edge and resulting separation bubble and transition. The point at which the curvature of the surface changes (from cylindrical to planar) is called the blend point.

The simulation uses 408 (streamwise, wrapped round the leading edge) by 72 (wall-normal) by 64 (spanwise) meshes and is performed using the techniques outlined in previous sections, including a generalised dynamic subgrid-scale model. Statistics are gathered by averaging in time once the simulation is in its fully developed state and also over the span direction and on both sides of the plate. The Reynolds number based on plate thickness is 3450.

No small-scale instability is found around the leading edge, but the stagnation point does move from side to side since the total mass flux on both sides of the plate is constrained but the division of the mass flux is not.

Figures 2 and 3 show the mean and RMS fluctuating parts of the streamwise velocity compared with experiment (15) at seven streamwise stations. Both experiment and data have the same very low level of free-stream turbulence ( $<0.1\%$ ) though in the simulation this weak disturbance is imposed artificially through pseudo-random forcing just upstream of the separation point. The data are compared at corresponding values of  $x/l$  where  $l$  is the mean reattachment length, since the experimental bubble is slightly longer ( $2.75d$ , where  $d$  is the leading edge diameter) than the simulated bubble (about  $2d$ ). This is consistent with the higher level of blockage in the simulation ( $1/16$ ). For the same reason the profiles are plotted as functions of  $y/l$ .

The simulation does show higher peaks of  $u'$  occurring closer to the wall, but lack of experimental data (taken with a single hot-wire probe) in the shear layer and the bubble makes detailed comparisons difficult. Apart from this

the agreement is excellent. Figure 4 shows the fluctuating vertical ( $v'$ ) component; experimental data are not available. The levels of this fluctuation and of the principal off-diagonal stress  $u'v'$ , Figure 5, also seem reasonable.

The boundary layers develop in the densely meshed regions on either side of the plate, and are fully turbulent well before they reach the two outflow boundaries. The layers on either side of the plate are statistically independent, just as they would be in the more complex case of a turbine blade. The flow separates and transition takes place as the separated flow becomes unstable, first in a two-dimensional mode but quickly passing into a three-dimensional breakdown which results in reattachment. It should be noted however that the instantaneous reattachment point is highly variable with time and span position.

The large-scale instabilities originating in the bubble subsequently disturb the reattaching boundary layer. As the mean shear at the wall is re-established, large-scale disturbances in the outer region of the boundary layer coming downstream from the separation bubble, rather like a wake, stimulate a secondary transition near the wall. There is some evidence that the mechanisms at work here are similar to those that operate during bypass transition in the presence of free-stream turbulence (14, 16).

## THE FUTURE

LES is evidently a technique that is alive and developing, and in spite of some difficult problems as yet unsolved it already has a wide range of practical applications including some of potential importance in aeronautics.

Full-scale LES has been applied to a wing section and is now being attempted of flow around a high-lift turbine blade row. Various bluff-body flows have been simulated successfully. Of great importance to aeronautics as well as other industrial applications is the use of simulation (normally DNS) to study transition, together with its causes, and ways of controlling and delaying it. DNS is the tool of choice for understanding transitional flows and we may expect to see it emerge as a design tool for transition control in the same time frame as LES for other industrial applications. In the same way, LES may be used as a tool for turbulence control studies in

fully-developed post-transition turbulent boundary layers.

There is no doubt that flows around wing sections, parts of wings and aircraft, external engine flows and turbomachinery blade flows are all amenable to LES and DNS. The techniques required to carry out such simulations are available and are likely to be seen in action increasingly as the necessary computer power is created.

Methods for performing large-eddy and direct numerical simulations using general curvilinear coordinates have been described here together with the use of Fourier techniques for efficient pressure solution in this context. I have shown how it is possible to combine iterative methods with discrete Fourier transforms to obtain very acceptable pressure solution times, comparable with those obtained by direct methods in simpler geometries. Results for a transitional flow using general coordinates in two dimensions demonstrate the efficacy of the approach. These methods are currently in use for the simulation of turbine blade flows and will also be used in the LES of aerofoils in future.

#### ACKNOWLEDGEMENTS

The author gratefully acknowledges the support of EPSRC, DERA and Rolls Royce plc who funded this research. The computations discussed were carried out by Dr Zhiyin Yang of Loughborough University, UK, by in collaboration with the author. I am most grateful for his cooperation and his permission for the use of our results.

#### REFERENCES

- (1) Smagorinsky, J. General circulation experiments with the primitive equations. I. The basic experiment. *Monthly Weather Review*, **91**, 99-164 (1963)
- (2) Schumann, U. Subgrid scale model for finite difference simulations of turbulent flows in plane channels and annuli. *J. Comput. Phys.* **18**, 376-401 (1975)
- (3) Lele, S.K. Compact finite difference schemes with spectral-like resolution. *J. Comput. Phys.* **103**, 16-42 (1992)
- (4) Kaltenbach H.J. and Choi H. (1995) Large-eddy simulation of flow around an airfoil on a structured mesh. *Annual Research Briefs 1995*, Center for Turbulence Research, Stanford University and NASA Ames. 51-60 (1995)
- (5) Hastings R.C. and Williams B.R. Studies of the flow field near an NACA 4412 aerofoil at nearly maximum lift. *Aeronautical Journal* **91**, 29-44 (1987)
- (6) ECARP – European Computational Aerodynamics Research Project: Validation of CFD Codes and Assessment of Turbulence Models. *Notes on Numerical Fluid Mechanics*, **58** (ed. W. Haase *et al.*). Vieweg / CEC DG XII.
- (7) Jansen K. Large-eddy simulation of flow around a NACA 4412 airfoil using unstructured grids. *Annual Research Briefs 1996*, Center for Turbulence Research, Stanford University and NASA Ames. 225-232 (1996).
- (8) Werner H. and Wengle H. Large-eddy simulation of flow over and around a cube in a plate channel. *Turbulent Shear Flows 8*, Springer-Verlag, Berlin. 155-168 (1993)
- (9) Manhart M. and Wengle H. LES and eigenmode decomposition of turbulent boundary layer flow over a hemisphere. *Flow Simulation with High-Performance Computers II: Notes on Numerical Fluid Mechanics*, **52**, Vieweg-Verlag Braunschweig, 275-289 (1996)
- (10) Zeng S. and Wesseling P. Multigrid solution of the incompressible Navier-Stokes equations in general coordinates. *SIAM J. Num. Analysis* **31**, (6) 1764-1784 (1994)
- (11) Voke P.R. Flow past a square cylinder: test case LES2. *Direct and Large-Eddy Simulation II* (ed. Chollet, Voke & Kleiser). 355-373 (1997). (Also following papers in the same volume.)
- (12) Germano M., Piomelli, U., Moin P. and Cabot W.H. A dynamic subgrid-scale eddy viscosity model. *Phys. Fluids A* **3**, 1760-1765 and 3128. (1991).
- (13) Lilly D.K. A proposed modification of the Germano subgrid scale closure method. *Phys. Fluids A* **4**, 633-635 (1992)
- (14) Voke P.R., Yang Z. and Savill A.M. Large-eddy simulation of transition following a leading-edge separation bubble. *Eng. Turb. Model. & Exp. 3* (ed. W. Rodi & G. Bergeles) Elsevier, Amsterdam. 601-610. (1996)

(15) Coupland J., Private Communication (1994).

(16) Voke P.R. and Yang Z.Y. Numerical Study of Bypass Transition, *Phys. Fluids*, 7, 2256-2264 (1995).

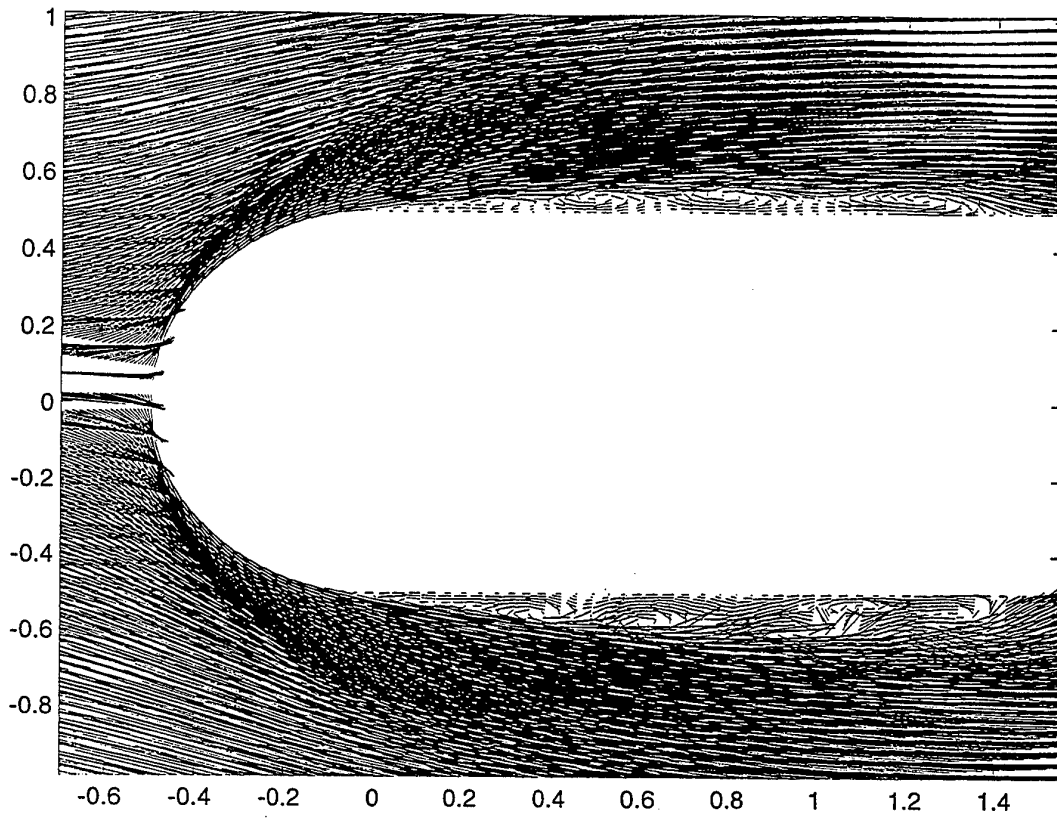


Figure 1. Instantaneous flow field about a plate with curved leading edge: part of the domain.

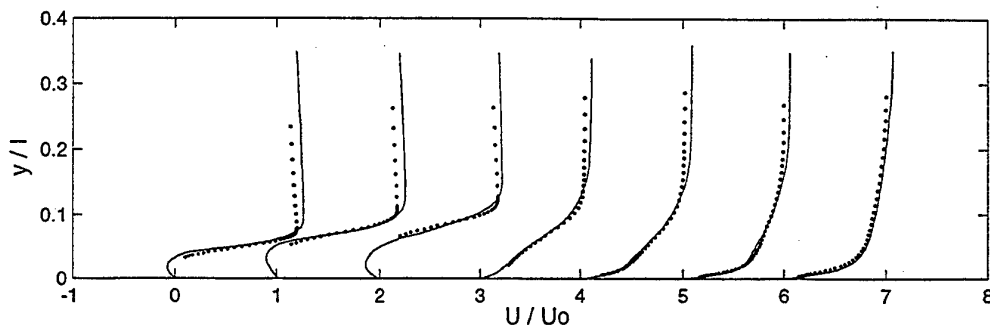


Figure 2. Mean flow velocity  $U$  at seven positions measured from the blend point.  
Left to right,  $x/l = 0.22, 0.44, 0.66, 1.09, 1.27, 1.64$  and  $2.55$ .

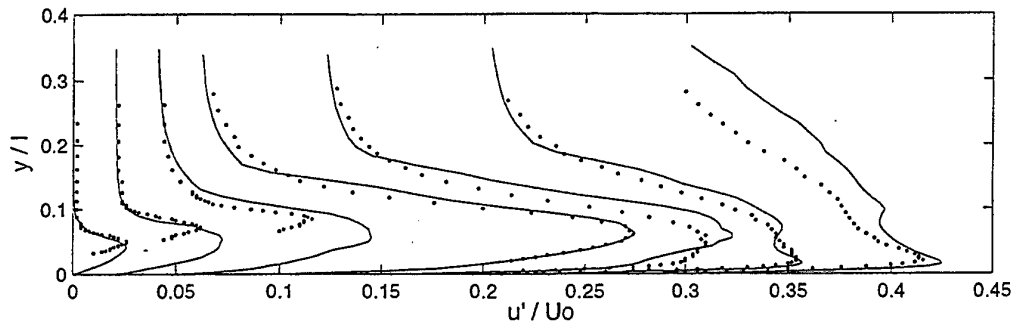


Figure 3. RMS streamwise velocity fluctuation  $u'$ ; as Fig. 2

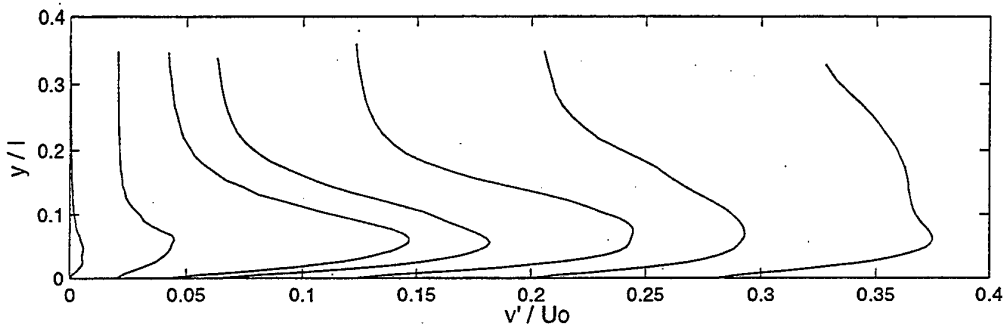


Figure 4. RMS wall-normal velocity fluctuation  $v'$ ; as Fig. 2

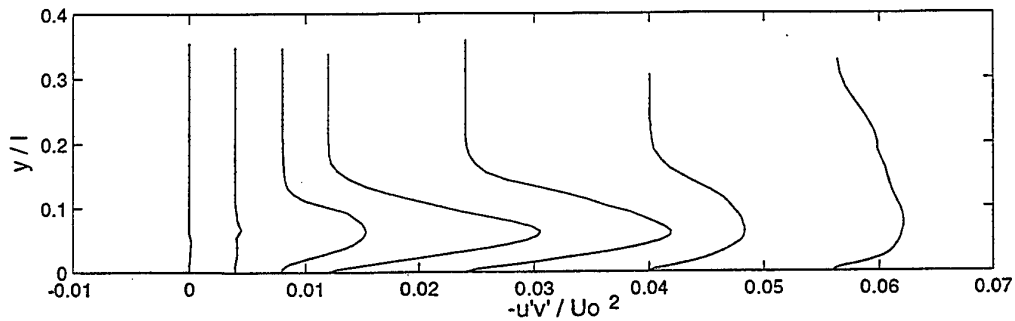


Figure 5. Principal Reynolds stress  $u'v'$ ; as Fig. 2

# LARGE EDDY SIMULATION OF PASSIVE SCALAR FIELDS UNDER SEVERAL STRAIN CONDITIONS

K. Abe and K. Suga

Toyota Central R&D Labs., Inc.  
Nagakute, Aichi 480-1192, Japan

## ABSTRACT

In order to reveal unknown characteristics of turbulent passive scalar fields, large eddy simulations in forced convection regimes were performed under various strain conditions and several fluid Prandtl numbers. By using the simulation results, relations between the dynamic and scalar fields were carefully examined. It was then confirmed that the scalar was transported by a large vortex structure near the examined regions wherever the mean shear vanished, though in the high shear regions, the scalar transport was governed by a coherent structure due to the high shear strain. In addition, *a priori* explorations were attempted by processing the data, focusing currently on the derivation of a possible direction for modeling the passive scalar transport algebraically. The *a priori* tests suggested that an expanded form of the GGDH model introducing quadratic products of the Reynolds stresses was promising for general flow cases.

## 1 INTRODUCTION

In practical fluid machinery, most flows are turbulent and their characteristics play important roles in the heat (scalar) transfer performance of the devices. In fact, turbulent recirculating and impinging flows are often used for augmentation strategies of scalar transfer from walls because it is well known that the heat (scalar) transfer becomes locally maximum near the reattaching and the impinging regions, where the mean shear vanishes. However, the other engineering important shear-free boundaries, such as the gas-liquid interface of an open channel flow and the shear-free (moving) wall of a Couette-Poiseuille flow, do not always contain particularly high heat (scalar) transfer regions. On the other hand, higher order turbulent scalar transfer modeling, particularly in forced convection regimes, usually introduces the mean strain dependency. Thus, a detailed investigation for the relation between the turbulent fluid flow and heat (scalar) transfer under different strain conditions including the shear-free regions is indispensable in modeling the heat (scalar) transfer.

In order to investigate the mechanism of turbulent scalar transfer, it is inevitably required to simultaneously measure dynamic and scalar quantities in the turbulent flows. Although such an experimental measurement is still very difficult especially within the boundary layers, several groups have challenged this problem[1]-[4]. For example, Sakakibara et al.[4] recently measured the velocity and scalar fields in the stagnation region of a plane impinging jet using the digital particle-image velocimetry and the laser-induced fluorescence. Even with these recent sophisticated experimental techniques, it is nearly impossible to measure the turbulent structure in very high or low fluid Prandtl number flows.

On the other hand, due to the recent remarkable development of high performance computers, computational fluid dynamics (CFD) has become a powerful tool for researching turbulent fluid flow and scalar transfer. Among the CFD schemes, direct numerical simulation (DNS) can provide ideal information of the scalar-transport mechanism, including the influence of fluid Prandtl numbers. Thus, several DNS results of scalar transfer have recently been reported (for example, [5]-[9]). Although the results of DNS are reliable, it is not so easy to perform it even in moderately complex geometry, including the aforementioned flow fields with separation and/or impingement, due to the requirement of extremely high grid resolution. Alternatively, large eddy simulation (LES) can be applied to simulate such complex fields. From LES results, turbulence statistics such as the Reynolds stress tensor and the scalar-flux vector can be obtained, though the simulation accuracy is not comparable to that of DNS.

Tsubokura et al.[10] performed LES of a plane impinging jet and provided useful information on the budget of turbulent energy in the stagnation region. Yang & Ferziger[11] conducted both LES and DNS of a separated flow around an obstacle settled in a channel (called an obstacle flow hereafter). Le et al.[12] carried out DNS of a separated flow downstream of a backward-facing step and presented the budget of turbulent energy in the recirculating region. As for flow simulations including shear-free boundaries, Kuroda et al.[13] performed DNS of a turbulent Couette-Poiseuille flow with a moving (almost shear-free) wall. Lombardi et al.[14] simulated a two-phase flow with a gas-liquid interface (hereinafter referred to as an open channel flow). Although the above simulations gave useful knowledge of turbulence in the dynamic fields, detailed data on

the scalar transport in such complex flow fields has not yet been reported.

Therefore, the purpose of the present research is to investigate unknown characteristics of turbulent passive scalar fields by performing LES for a plane impinging jet, an obstacle flow and shear-free flows as well as plane channel flows with several fluid Prandtl numbers. By processing the simulation results, the present study carefully examines relations between the dynamic and scalar fields, focusing on the derivation of a possible direction for modeling the passive scalar transport algebraically.

## 2 SGS MODEL AND COMPUTATIONAL CONDITIONS

### 2.1 SGS model

In this study, a one-equation subgrid-scale (SGS) model developed by the authors was adopted. The filtered governing equations of dynamic and scalar fields may be written as

$$\langle U_i \rangle_{,i} = 0 \quad (1)$$

$$\langle U_i \rangle_{,i} + (\langle U_i \rangle \langle U_j \rangle)_{,j} = - \langle P \rangle_{,i} / \rho + \left\{ \nu (\langle U_i \rangle_{,j} + \langle U_j \rangle_{,i}) - \langle u'_i u'_j \rangle \right\}_{,j} \quad (2)$$

$$\langle \Theta \rangle_{,i} + (\langle U_j \rangle \langle \Theta \rangle)_{,j} = \{ (\nu / Pr + \nu_{SGS} / Pr_{SGS}) \langle \Theta \rangle_{,j} \}_{,j} + Q_{in} \quad (3)$$

where a quantity such as  $\langle U_i \rangle$  is a volume-averaged value with the filter-width  $\Delta$ , and  $u'_i$  is the derivative from it (i.e.,  $u'_i = U_i - \langle U_i \rangle$ ). In Eq. (2), the effects of the Leonard stress and the cross terms are assumed to be negligible compared to that of the SGS Reynolds stress  $\langle u'_i u'_j \rangle$  and thus they are dismissed. In Eq. (3),  $Q_{in}$  and  $Pr_{SGS}$  are the internal scalar source and the SGS Prandtl number, respectively. Equations (2) and (3) can be closed with the following SGS constitutive equation:

$$\langle u'_i u'_j \rangle = \frac{2}{3} K_G \delta_{ij} - \nu_{SGS} (\langle U_i \rangle_{,j} + \langle U_j \rangle_{,i}) \quad (4)$$

where  $K_G (= \langle u'_i u'_i \rangle / 2)$  denotes the SGS turbulent energy. Although the Smagorinsky SGS model was adopted in the present study, the form of SGS eddy viscosity  $\nu_{SGS}$  was modified, taking advantage of the recent proposal by Abe et al. [15] in the two-equation Reynolds-averaged turbulence modeling. The model expression used may be written as

$$\nu_{SGS} = \frac{K_G \tau_{SGS}}{1 + (C_D \tau_{SGS})^2 (\Omega_{mn} \Omega_{mn} + \frac{5}{6} S_{mn} S_{mn})} \quad (5)$$

where  $S_{ij} (= \langle U_i \rangle_{,j} + \langle U_j \rangle_{,i})$  and  $\Omega_{ij} (= \langle U_i \rangle_{,j} - \langle U_j \rangle_{,i})$  are, respectively, the strain-rate and the vorticity tensors. In Eq. (5),  $\tau_{SGS}$  denotes the characteristic SGS time scale, which is modeled in this study as

$$\tau_{SGS} = C_\mu f_\mu \Delta / \sqrt{K_G}, \quad f_\mu = 1 - \exp \{ - (n^* / 26)^2 \} \\ n^* = u_\varepsilon n / \nu, \quad u_\varepsilon = (\nu \varepsilon_G)^{\frac{1}{4}} \quad (6)$$

where  $n$  and  $\varepsilon_G$  are, respectively, the minimum distance from boundaries and the dissipation rate of  $K_G$ .

The presently used one-equation SGS model adopts the following transport equation for  $K_G$ :

$$K_{G,t} + (\langle U_j \rangle K_G)_{,j} = \{ (\nu + C_k \tau_{SGS} K_G) K_{G,j} \}_{,j} - \langle u'_i u'_j \rangle \langle U_i \rangle_{,j} - \varepsilon_G \quad (7)$$

The dissipation rate  $\varepsilon_G$  was algebraically modeled after Okamoto [16]:

$$\varepsilon_G = C_\varepsilon \frac{K_G^{\frac{3}{2}}}{\Delta} + 2\nu (\sqrt{K_G})_{,j} (\sqrt{K_G})_{,j} \quad (8)$$

The model constants used in this study are

$$C_\mu = 0.12, \quad C_D = 0.8, \quad C_k = 0.833 \\ C_\varepsilon = 0.835, \quad Pr_{SGS} = 0.9 \quad (9)$$

All calculations have been performed using the finite difference method with the collocated grid system. For the all spatial discretizations, the second-order central difference was used. As for the time integration of Eqs. (2), (3) and (7), the Crank-Nicholson implicit scheme was employed with the convection terms linearized, in order to guarantee a long time step even around the corners of the obstacle. Note that the computational results obtained from the present scheme are in good agreement with those of the corresponding DNS and experiments as will be shown in §3. Hence, at least in this study, the influence of the linearization of convective terms on the computational results was insignificant.

### 2.2 Computational conditions

The simulations have been performed for fully-developed channel flows with various boundary conditions, a plane impinging jet (PIJ) and a separated flow around an obstacle in a plane channel (OBF).

Computational conditions for the channel-flow cases are listed in Table 1, including boundaries of a moving (almost shear-free) wall and a free surface. In these channel-flow calculations, the flow fields were assumed to be fully developed, and the periodic boundary condition was imposed in both the streamwise ( $x$ ) and spanwise ( $z$ ) directions. It was also assumed that there existed the mean scalar gradient only in the wall-normal ( $y$ ) direction.

In Table 1, the codes, "W - W", "W - M" and "W - F", denote the boundary conditions for the velocity fields. For example, "W - F" means that there exists a fixed wall on one side, and a free surface exists on the other side. As for the scalar field, " $Q_{in} = 1$ " means that there exists an internal scalar source and the two boundaries facing each other hold a constant uniform scalar value [5]. The other scalar condition, " $\Delta \Theta = 1$ ", indicates that there is a difference in the constant scalar values of the two boundaries facing each other and there is no



Table 1 Computational conditions of channel flows.

	Domain	Grid	$Re_\tau$	$Pr$	B. C.
Case 1, 2, 3, 4 [5]	$6.4\delta \times 2\delta \times 1.6\delta$	$64 \times 62 \times 64$	180	0.1, 0.71, 2, 7	W - W, $Q_{in} = 1$
Case 5, 6, 7, 8, 9	$6.4\delta \times 2\delta \times 1.6\delta$	$64 \times 62 \times 64$	180	0.025, 0.1, 0.71, 2, 7	W - W, $\Delta\Theta = 1$
Case 10 [13]	$2.4\delta \times \delta \times 1.6\delta$	$64 \times 62 \times 64$	307	0.71	W - M, $\Delta\Theta = 1$
Case 11 [14]	$4.8\delta \times \delta \times 3.2\delta$	$64 \times 62 \times 64$	180	0.71	W - F, $\Delta\Theta = 1$
Case 12	$4.8\delta \times \delta \times 3.2\delta$	$92 \times 92 \times 80$	180	7	W - F, $\Delta\Theta = 1$

	Resolution	Time step ( $\delta/u_\tau$ )	Sampling time ( $\delta/u_\tau$ )
Case 1, 2, 3, 4 [5]	$\Delta x^+ = 18, \Delta y^+ = 0.5 - 14, \Delta z^+ = 4.5$	$1 \times 10^{-3}$	30 - 48
Case 5, 6, 7, 8, 9	$\Delta x^+ = 18, \Delta y^+ = 0.5 - 14, \Delta z^+ = 4.5$	$1 \times 10^{-3}$	27 - 49
Case 10 [13]	$\Delta x^+ = 11.5, \Delta y^+ = 0.5 - 8, \Delta z^+ = 7.7$	$2 \times 10^{-3}$	102
Case 11 [14]	$\Delta x^+ = 13.5, \Delta y^+ = 0.4 - 5, \Delta z^+ = 9$	$2 \times 10^{-4}$	26
Case 12	$\Delta x^+ = 9.4, \Delta y^+ = 0.1 - 4, \Delta z^+ = 7.2$	$1 \times 10^{-4}$	12

(B.C.: Boundary condition, W: Fixed wall, M: Moving wall, F: Free surface)

scalar source. This condition was called the “wall-transfer” by Rogers et al.[17]. At the free surfaces of cases 11 and 12, an instantaneous constant scalar-flux condition was adopted as a scalar-boundary condition to generate scalar fluctuations there.

The schematic views of the PIJ and the OBF cases are illustrated in Figs. 1 and 2, respectively. Computational conditions used for the velocity field of these cases are summarized in Table 2. They are consistent with the experiments of Tsubokura et al.[10] and the DNS of Yang & Ferziger[11], respectively. Concerning the PIJ case, the flow field was assumed to be statistically two dimensional, and the spanwise periodic condition was used. The boundary condition used at the nozzle exit followed Tsubokura et al.[10], although no velocity perturbation was assumed in this study. For the outlet-boundary condition, a conventional outflow condition was used, with some adjustments for the convective velocities at the outlet surfaces. This condition is practically the same as the “convective boundary condition” employed in the LES of Tsubokura et al.[10]. In the OBF case, the inlet and the outlet flow fields were assumed to be fully developed, and the periodic boundary conditions were applied in both the streamwise and spanwise directions.

As for the scalar field, the fluid Prandtl number of 0.71 was adopted for both the PIJ and the OBF cases. In the PIJ case, the uniform flow with passive scalar of a constant value ( $\Theta_0 = 0$ ) was assumed to be discharged from the nozzle exit to the wall surface keeping a different constant scalar value ( $\Theta_w = 1$ ). In the OBF case, the inlet and the outlet scalar fields were assumed to be fully developed, and the aforementioned “wall-transfer” condition was employed as the boundary condition. Note

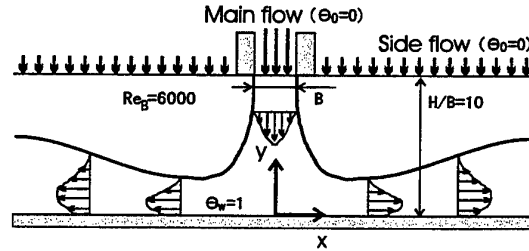


Figure 1 Plane impinging jet.

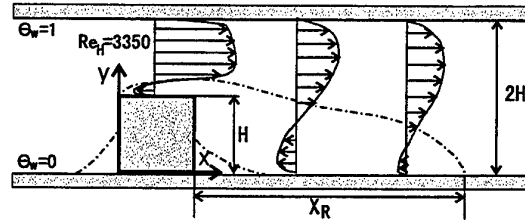


Figure 2 Obstacle flow.

that the grid resolutions in the stagnation region of the PIJ case were  $\Delta x/B \simeq 0.04$  and  $\Delta y/B \simeq 0.003$ , and those in the reattachment region of the OBF case were  $\Delta x/H \simeq 0.23$  and  $\Delta y/H \simeq 0.006$ .

### 3 VALIDITY OF SIMULATION RESULTS

#### 3.1 Fundamental parallel flows

Representative results of the velocity field for the channel-flow cases are compared to those of the corresponding DNS[5][13][14] in Figs. 3 - 5. Note that all the turbulence statistics are evaluated by only the grid-scale (GS) quantities. As seen in Figs. 3 - 5, the present results of the mean velocity and Reynolds

Table 2 Computational conditions of the plane impinging jet and the obstacle flow.

	Domain	Grid	$Re$	$Pr$	B. C.
PIJ[10]	$\pm 20B \times 10B \times 3B$	$246 \times 96 \times 32$	$Re_B = 6000$	0.71	$\Theta_0 = 0, \Theta_w = 1$
OBF[11]	$31H \times 2H \times 2H$	$195 \times 78 \times 62$	$Re_H = 3350$	0.71	W - W, $\Delta\Theta = 1$

	Resolution	Time step	Sampling time
PIJ[10]	$\Delta x/B = 0.03 - 0.86, \Delta y/B = 0.003 - 0.18, \Delta z/B = 0.094$	$2.5 \times 10^{-3} B/U_0$	$250 B/U_0$
OBF[11]	$\Delta x/H = 0.005 - 0.41, \Delta y/H = 0.005 - 0.07, \Delta z/H = 0.032$	$4 \times 10^{-3} H/U_0$	$590 H/U_0$

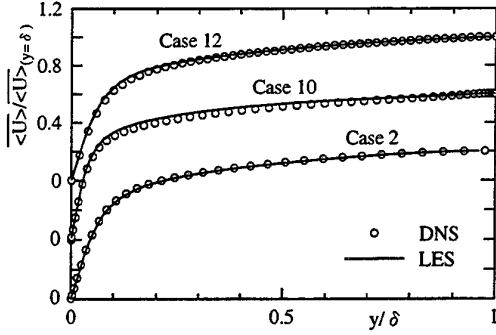


Figure 3 Mean velocity profiles.

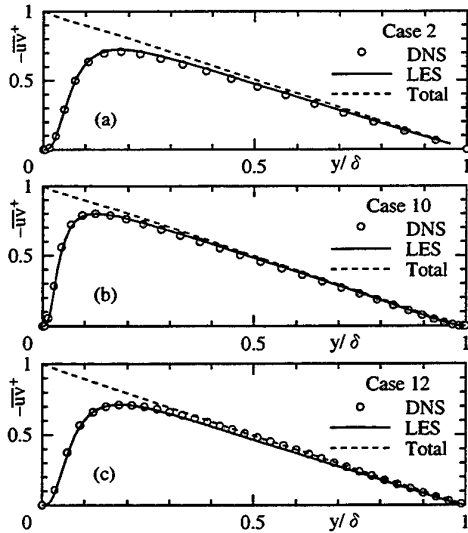


Figure 4 Profiles of Reynolds shear stress.

stresses agree well with the DNS data[5][13][14]. Although there exist slight discrepancies between the present LES and the DNS[5][13][14] in the turbulence intensities in the buffer region near the fixed wall, the prediction accuracy of the present LES is sufficiently enough in evaluating turbulence characteristics.

Computational results of the mean scalar and scalar fluxes are shown in Figs. 6 – 8, where the DNS results of Kim & Moin[5] are included for cases 1 – 3.

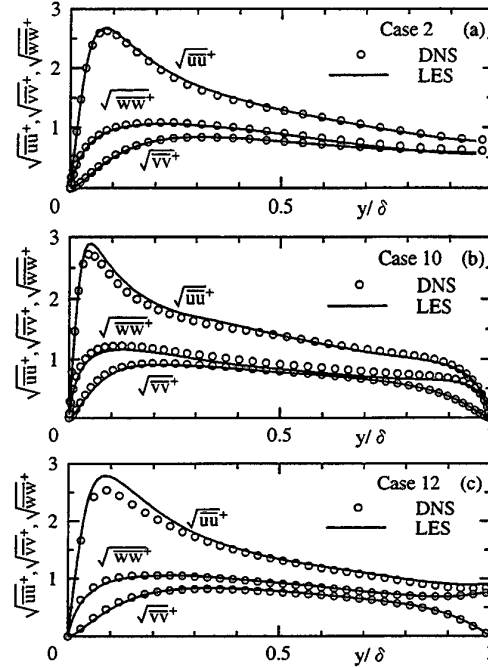


Figure 5 Profiles of turbulence intensities.

As can be understood from Fig. 6, the mean scalar profiles of the present LES show excellent agreement with those of the corresponding DNS[5]. As for the case of  $Pr = 7$ , the predictions are also in good agreement with the experimental correlations of Kader[18]. Furthermore, as can be found in Figs. 7 and 8, the prediction accuracy of the scalar fluxes for cases 1 – 3 is also sufficient (the lines of the DNS results of cases 1 and 2 just overlap the LES results). These validations imply that the present results are expected to be globally appropriate, though there exist neither experimental nor DNS data of the scalar fluxes for cases 4, 10, 11 and 12.

Finally, it can be confirmed from Figs. 4 and 8 that good numerical balances of the mean momentum and scalar transports are obtained only by the GS quantities, because the total shear-stress and scalar-flux profiles are almost straight. This fact indicates that the grid resolutions presently used for

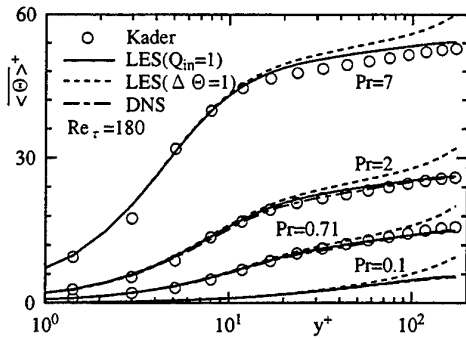


Figure 6 Mean scalar profiles.

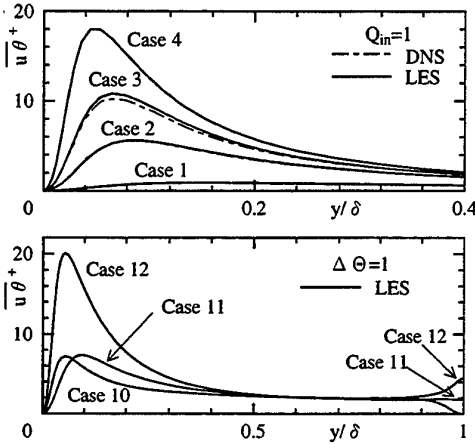


Figure 7 Profiles of streamwise scalar flux.

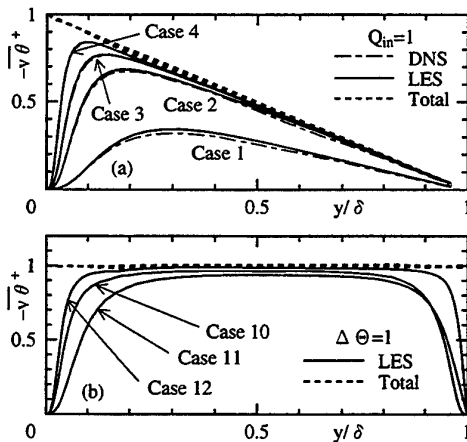


Figure 8 Profiles of cross-streamwise scalar flux.

the channel-flow cases were fine enough to appropriately reproduce fundamental features of turbulent scalar-transport phenomena.

### 3.2 Plane impinging jet and Obstacle flow

Representative results of the PIJ case are shown in Figs. 9 – 11. Figure 9 compares the present simula-

tion results in the stagnation region to those of the experiments of Tsubokura et al.[10]. As seen in the figure, the wall-normal velocity distribution is in excellent agreement with the experiments. Concerning the turbulence intensities, the present LES results show fundamentally the same tendencies as those of the experiments, while the LES underpredicted the profiles. These underpredictions might result mainly from the nozzle-exit flow condition without velocity perturbation used in the present LES. The representative results at the selected sections in the wall-jet region are compared with the experiments in Fig. 10. The reasonable agreement suggests that the prediction accuracy of the present LES is acceptable in that region.

The experimental correlation of the stagnation Nusselt number ( $Nu_S$ ) for air flows proposed by Gardon & Akfirat[19] is

$$Nu_S / \{ Re_B^{0.58} (H/B)^{-0.62} \} = 1.2. \quad (10)$$

The value of the left hand side (L.H.S.) of Eq. (10) evaluated from the present results is 1.13, which reasonably agrees with the correlation. This suggests that the presently simulated distribution of  $Nu$  shown in Fig. 11 is reasonable enough.

Figures 12 – 14 show the representative results of the OBF case. The presently predicted profiles of the separating streamline and the wall friction  $\tau_w$  are shown in Fig. 12. The flow-reattachment length obtained from the present LES is  $X_R/H = 6.65$ , in good agreement with that of the DNS ( $X_R/H = 6.42$ ) by Yang & Ferziger[11]. As seen in Fig. 12 (b), the distribution of  $\tau_w$  is predicted with generally sufficient accuracy, except for the region over the obstacle ( $0 \leq x/H \leq 1$ ). Figure 13 compares the present simulation results of flow quantities to those of the DNS[11]. The LES results are generally in good agreement with those of the DNS, although there are some slight differences between them.

The Nusselt-number distribution in the recirculating region at the lower wall is shown in Fig. 14. As for the maximum scalar-transfer coefficient in the reattachment region of separated flows, after examining a wide range of flow configurations, Reynolds numbers and fluid Prandtl numbers, Ota & Nishiyama[20] proposed the following experimental correlation:

$$\left( \frac{h_R l}{\lambda} \right) / \left\{ \left( \frac{U_0 l}{\nu} \right)^{0.665} Pr^{1/3} \right\} = 0.192 \quad (11)$$

where  $\lambda$ ,  $h_R$  and  $l$  denote the thermal (scalar-field) conductivity, the maximum heat (scalar) transfer coefficient in the reattachment region and the length from the separation to reattachment points, respectively. Taking  $(X_R + 1)$  as  $l$ , the present LES produces the value of 0.209 for the L.H.S. of Eq. (11), while adopting the length from the separation point to the point of  $h_R$  (i.e.,  $l = 4.75$ ), instead of  $(X_R + 1)$ , it gives a value of 0.179. Since both estimated values

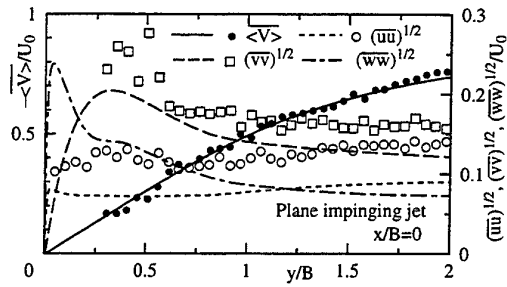


Figure 9 Comparison with the experiments in the stagnation region (lines; predictions, symbols; experiments[10]).

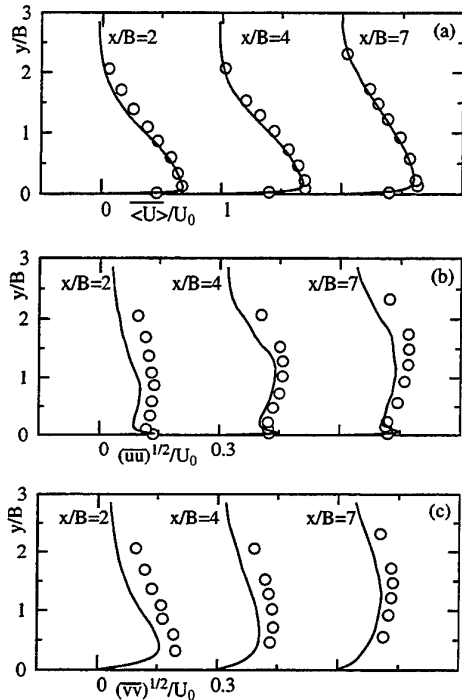


Figure 10 Comparisons with the experiments in the wall-jet region (lines; predictions, symbols; experiments[10]).

reasonably accord with the correlation, the present LES results of the OBF case are thought to be fairly reliable.

From the above discussions, it can be said that the present LES results of both the PIJ and the OBF cases are also sufficiently useful in investigating turbulent scalar-transport phenomena in detail.

## 4 DISCUSSIONS

### 4.1 Turbulence structures and scalar-transport phenomena

Contour maps of the instantaneous distributions of fluctuating variables in the regions near the fixed and moving (shear-free) walls of case 10 are shown in

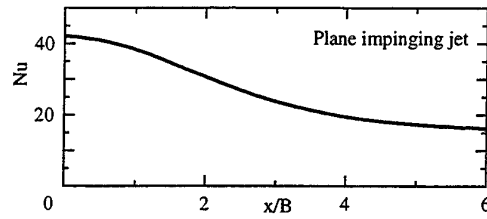


Figure 11 Nusselt number distribution in the plane impinging jet.

Figs. 15 and 16, respectively. As seen in Fig. 15, the scalar fluctuation ( $\theta$ ) in the wall-shear region correlates more strongly with the streamwise velocity fluctuation ( $u$ ) than that normal to the wall ( $v$ ). This observation supports the previous knowledge pointed out by Kim & Moin[5]. Near the shear-free wall, however, no such an apparent correlation can be seen between  $\theta$  and  $u$ , while the correlation between  $\theta$  and  $v$  looks rather stronger as shown in Fig. 16. Distributions of the passive scalar and the velocity vector in the selected  $y$ - $z$  plane from the wall-shear and shear-free regions are shown in Figs. 17 and 18, respectively. In both the figures, streamwise vortex structures can be seen, where the passive scalar is transported from the near-wall regions to the outer regions away from the wall. As previously reported by the other workers (for example, [21][22]), in the near-wall region of turbulent wall-shear flows, there exist coherent structures such as the low and high speed streaks and the streamwise vortices, and they play the most important role in the turbulent scalar transfer. From Figs. 15 and 17, such coherent structures can be recognized in the vicinity of the wall under high shear strain. However, the scales of vortices observed in the shear-free region of Fig. 18 are much larger than those in the wall-shear region, and the edge of a vortex extends to the center of the channel, Fig. 18.

Figure 19 shows the distributions of the passive scalar and the velocity vector in a  $y$ - $z$  plane near the stagnation point of the PIJ case. This kind of flow fields can be divided into two regions, i.e., the stagnation and wall-jet regions. As seen in Fig. 19, the present LES produces large vortex structures in the stagnation region, whose interval is globally equal to the nozzle-exit width  $B$ . This fact is fairly consistent with the findings pointed out by the previous research works[4][23]. It is also found that the passive scalar in the vicinity of the wall is transported to the outer region away from the wall by the upward flow generated by the vortex structures. Distributions of the instantaneous fluctuations of the transport variables in the near-wall region of the PIJ case are shown in Fig. 20. Figure 20 (c) indicates that the regions of positive and negative  $v$  values appear by turns near the stagnation line and this corresponds

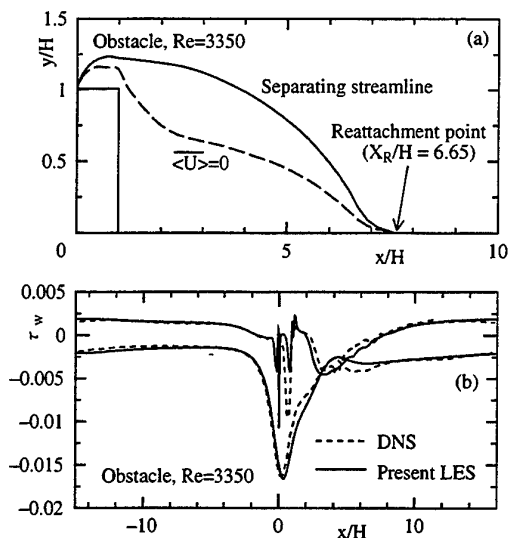


Figure 12 Computational results of the obstacle flow: (a) separating streamline and line of zero streamwise velocity; (b) comparison of wall-friction distributions.

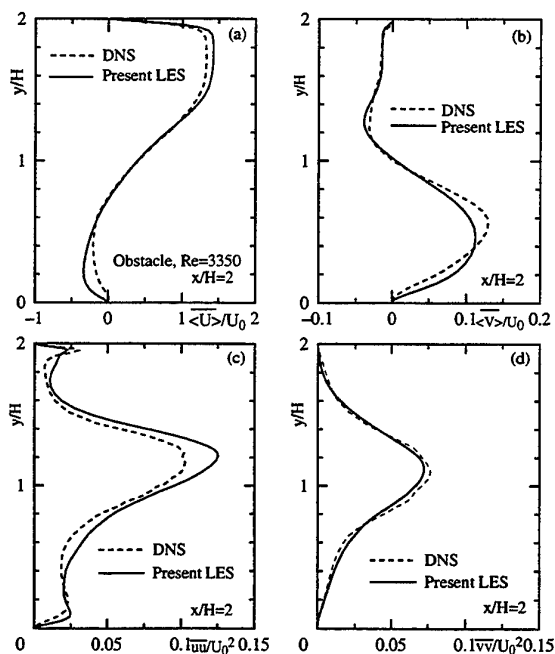


Figure 13 Comparisons with the DNS by Yang & Ferziger[11].

to the vortex structure detected in Fig. 19. From the comparison of Figs. 20 (a) and (c), the strong relation between  $\theta$  and  $v$  in the stagnation region is recognized and this also supports that the large scale vortex structure plays the most dominant role in the scalar-transport phenomena. On the contrary, the correlation between  $\theta$  and  $v$  dies out rapidly in the region where the wall jet starts to develop,  $x/B > 2$ ,

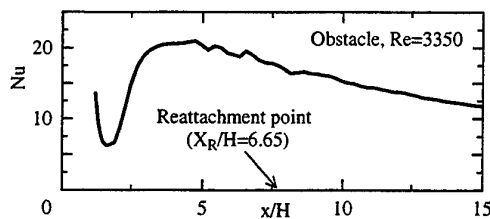


Figure 14 Nusselt number distribution in the obstacle flow.

and the higher correlation between  $\theta$  and  $u$ , which is similar to that found in the wall-shear region of case 10 (see Fig. 15), is recognized. This indicates that the same scalar-transport mechanism as in the channel-flow cases functions in the wall-jet region of the PIJ case.

As for the OBF case, contours of  $\theta$ ,  $u$  and  $v$  in the region near the lower wall downstream of the obstacle are compared in Fig. 21. In the redeveloping region far downstream of the reattachment point,  $x/H > 12$ , it is easily understood that  $\theta$  correlates strongly with  $u$ , as in the channel flows. In the reattachment region, however, the correlation between  $\theta$  and  $v$  looks rather stronger than that between  $\theta$  and  $u$ , although the relation is not so clear as that in the stagnation region of the PIJ case. Distributions of the passive scalar and the velocity vector in a  $y$ - $z$  plane near the reattachment point are shown in Fig. 22. It is clearly seen that the passive scalar near the wall is lifted up by the upward flow of large scale vortices. These aspects observed around the reattachment region, i.e., the moderate correlation between  $\theta$  and  $v$  and the large vortex structure transporting the passive scalar, are essentially similar to those in the region near the shear-free wall of case 10 (see Figs. 16 and 18).

Figures 23 and 24 compare the distributions of the averaged turbulent length ( $k^{3/2}/\epsilon$ ) and velocity ( $\sqrt{k}$ ) scales, respectively. From these figures, the features of the turbulence structures can be statistically recognized. Note that, in the present study, the dissipation rate ( $\epsilon$ ) was evaluated by the residual of the turbulent energy ( $k$ ) budget. As seen in Fig. 23 (a), the turbulent length scales near the shear-free region of case 10 ( $y/\delta \geq 0.8$ ) are larger than those in the wall-shear region ( $y/\delta \leq 0.2$ ) except for the regions very close to the wall surfaces. This tendency corresponds to the aspects observed in Figs. 17 and 18. In contrast to this, the turbulent velocity scales near the shear-free region of case 10 are smaller than those in the wall-shear region, Fig. 24 (a). Hence, the scalar transferring fluid motion near the shear-free wall is not so effective in this case. In fact, the Nusselt number on the shear-free wall ( $Nu \approx 13$ ) is comparable to that of the shear wall ( $Nu \approx 12$ ). On the other hand, in the stagnation region of the PIJ case

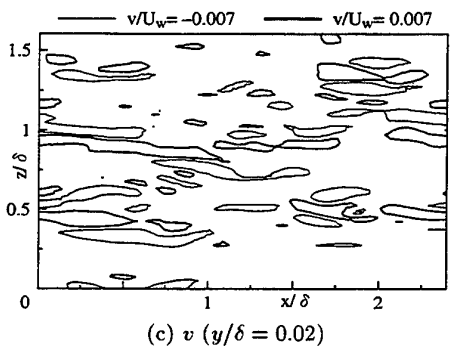
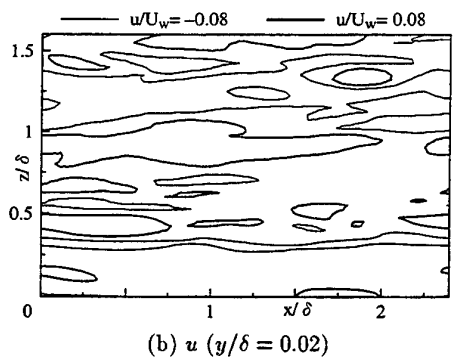
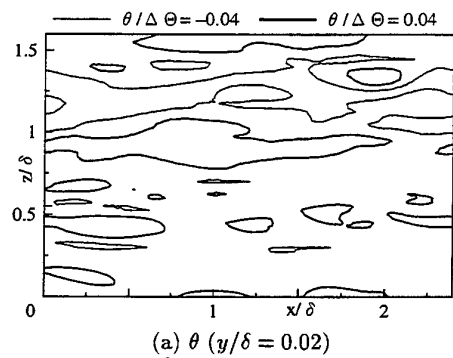


Figure 15 Instantaneous distributions of fluctuating variables in the wall-shear region (case 10).

( $x/B \approx 0$ ) and the recirculating region of the OBF case ( $x/H \approx 5$ ), both the turbulent length and velocity scales are respectively much larger than those in the wall-jet ( $x/B \approx 8$ ) and redeveloping ( $x/H \approx 22$ ) regions. Consequently, the turbulent mixing motions are very active in these regions, leading to the higher level of the scalar-transfer coefficients as shown in Figs. 11 and 14. In the wall-jet region of the PIJ case and the redeveloping region of the OBF case, both the length and velocity scales show the levels similar to the wall-shear region of case 10. This also indicates that the dominant scalar-transport mechanism in these regions is essentially the same as that in the wall-shear regions of the channel flows.

As can be confirmed from the aforementioned discussions, coherent structures generated by high shear strain play the most important role in transporting the passive scalar[5], in wall-shear regions

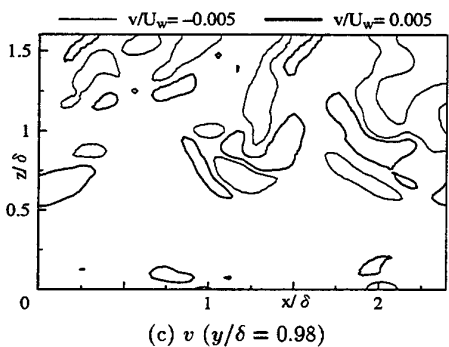
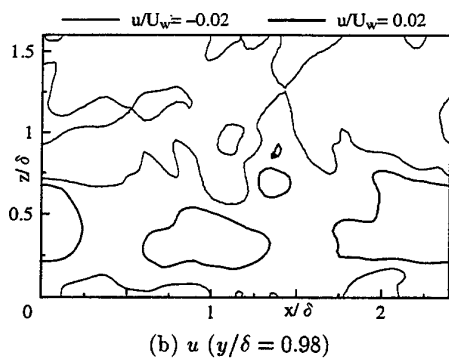
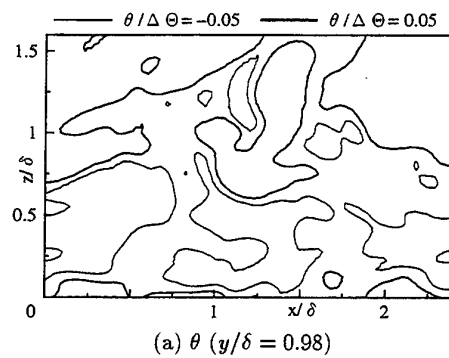


Figure 16 Instantaneous distributions of fluctuating variables in the shear-free region (case 10).

including the wall-jet region of the PIJ case and the redeveloping region of the OBF case. On the other hand, in the regions where the mean shear strain vanishes, such as the regions near shear-free boundaries, stagnation and reattachment points, the passive scalar-transport mechanism is obviously different. In these regions, the turbulence structures which contains large scale longitudinal vortices have a dominant task for the scalar-transport phenomena, while the velocity scale of the vortex motions largely varies corresponding to the flow fields.

#### 4.2 A priori estimation of algebraic scalar-flux models

Algebraic expressions for turbulent scalar flux have been widely used in engineering applications since they provide mean scalar distributions with mod-

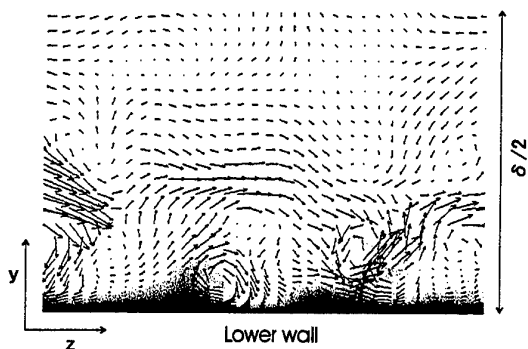


Figure 17 Distributions of passive scalar and velocity vectors in the wall-shear region of case 10 (a darker color corresponds to a lower scalar value).

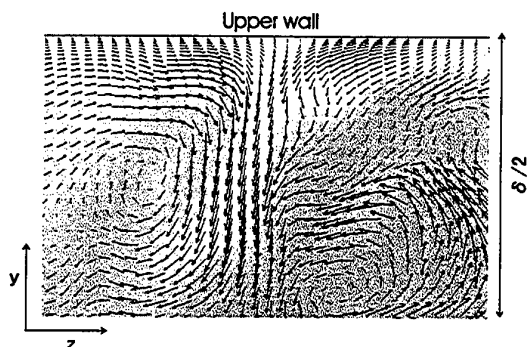


Figure 18 Distributions of passive scalar and velocity vectors in the shear-free region of case 10 (a brighter color corresponds to a higher scalar value).

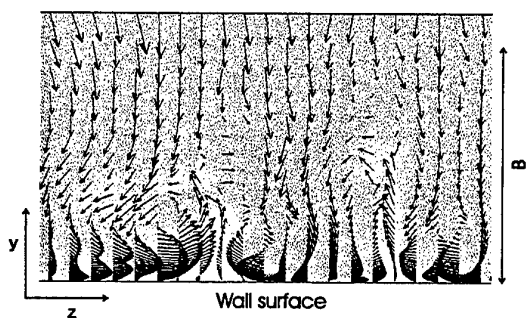


Figure 19 Distributions of passive scalar and velocity vectors in the stagnation region of the plane impinging jet (a brighter color corresponds to a higher scalar value).

erate satisfaction despite their simplicity. Moreover, to improve the model performance, many research groups have recently proposed more advanced algebraic model expressions for the scalar-flux vector[17][24]–[27]. Although these models gave encouraging results, their performance still has a wide margin to be further improved, especially in predicting the correct directions of the scalar-flux

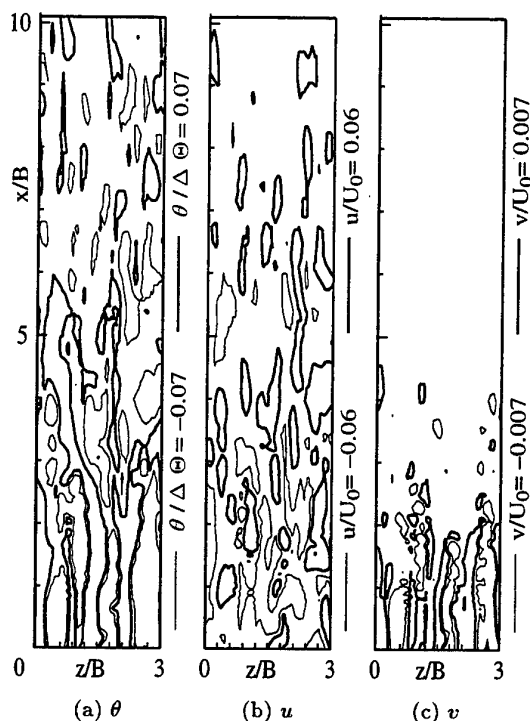


Figure 20 Distributions of instantaneous fluctuations of the transport variables in the plane impinging jet ( $y/B = 0.01$ ).

vectors[28][29]. Thus, in order to derive a possible direction for more appropriately modeling passive scalar fields with an algebraic scalar-flux model, *a priori* explorations are attempted by processing the present LES data.

First, we consider the following GGDH[30] model expression, which is one of the simplest and has been often adopted in many engineering applications:

$$\overline{u_i \theta} = -C_\theta \tau_\theta \overline{u_i u_j} \overline{\Theta}_{,j} \quad (12)$$

where  $C_\theta$  and  $\tau_\theta$  are the model coefficient and the characteristic time scale, respectively.

As pointed out by Kim & Moin[5] and also confirmed by the present study,  $\theta$  in the wall-shear region correlates more strongly with  $u$  than with  $v$ . Kim & Moin[5] thus suggested that it might be an interesting attempt to model the scalar fluxes,  $\overline{u\theta}$  and  $\overline{v\theta}$ , using the Reynolds stresses,  $\overline{uu}$  and  $\overline{vv}$ , since the following relation is expected to hold:

$$\overline{u\theta} \propto \overline{uu}, \quad \overline{v\theta} \propto \overline{vv} \quad (\propto \overline{uv}). \quad (13)$$

As an estimation of the model performance, distributions of the model coefficient  $C_\theta$  in case 2 are shown in Fig. 25, where  $k/\varepsilon$  is adopted as a characteristic time scale  $\tau_\theta$  and the coefficients are calculated by Eq. (12) in the  $x$ - and  $y$ -directions, respectively. As seen in the figure,  $C_\theta$  estimated for  $\overline{v\theta}$  (i.e., in the  $y$ -direction) globally shows a constant value of about 0.3, except for the near-wall region of  $x/\delta < 0.1$ . However,  $C_\theta$  for  $\overline{u\theta}$  (i.e., in the  $x$ -direction) is more

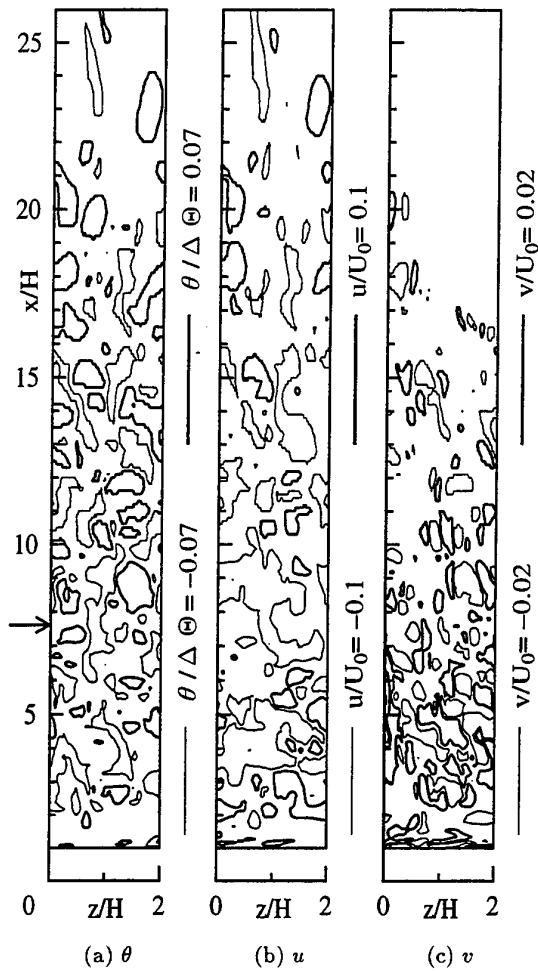


Figure 21 Distributions of instantaneous fluctuations of the transport variables in the obstacle flow ( $y/H = 0.02$ ).

than three times as large as that for  $\overline{v\theta}$ . This indicates that it is impossible to satisfactorily predict both components of the scalar-flux vector by using Eq. (12) with a single scalar coefficient of  $C_\theta$ . In case that the mean scalar gradient exists only in the  $y$ -direction, the following relation between the scalar fluxes can be obtained from Eq. (12):

$$\frac{\overline{v\theta}}{\overline{u\theta}} = \frac{\overline{vv}}{\overline{uv}} \quad (14)$$

Although the GGDH form of Eq. (12) is considered to be a form representing the relation expressed by Eq. (13), Eq. (14) suggests that the ratio of the scalar fluxes in the form is not consistent with that implied by Eq. (12),  $\overline{v\theta}/\overline{u\theta} = \overline{uv}/\overline{uu}$ . This is thought to be the main reason why the GGDH form cannot successfully predict the streamwise scalar flux as pointed out previously[28][29], since the flux ratio directly connects with the direction of the flux vector.

With this in mind, in order to more precisely reflect the relation of Eq. (13), the present study has

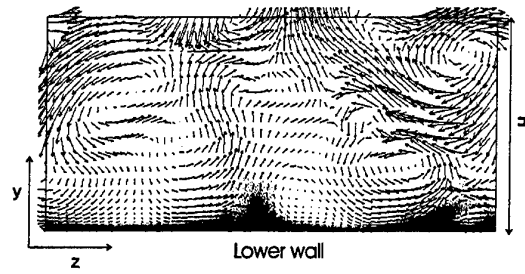


Figure 22 Distributions of passive scalar and velocity vectors in the reattachment region of the obstacle flow (a darker color corresponds to a lower scalar value).

investigated the following tensor expression as an extended gradient-diffusion model:

$$\overline{u_i\theta} = -C_\theta\tau_\theta \overline{u_i u_k} A_{kj} \overline{\Theta}_{,j} \quad (15)$$

where  $A_{ij}$  is a nondimensional tensor. As for the modeling of  $A_{ij}$ , it is reasonable that  $A_{ij}$  is composed of physically appropriate quantities of turbulence. Considering this, the present study simply adopts the normalized Reynolds-stress tensor,  $\overline{u_i u_j}/k$ , as a model for  $A_{ij}$ . Consequently, the model expression investigated here can be written as

$$\overline{u_i\theta} = -C_\theta\tau_\theta \left( \frac{\overline{u_i u_k} \overline{u_k u_j}}{k} \right) \overline{\Theta}_{,j} \quad (16)$$

This form is regarded as a higher-order extension of the GGDH form by using the quadratic products of the Reynolds stress tensor (hereinafter referred to as the quadratic form). In case that only  $\overline{\Theta}_{,y}$  exists, the following relation between the scalar fluxes can be estimated from Eq. (16):

$$\frac{\overline{v\theta}}{\overline{u\theta}} = \frac{\overline{uv^2} + \overline{v^2v}}{(\overline{uu} + \overline{vv})\overline{uv}} \rightarrow \frac{\overline{uv}}{\overline{uu}} \quad (\text{near a wall}). \quad (17)$$

With this form, the ratio of  $\overline{v\theta}/\overline{u\theta}$  becomes nearly  $\overline{uv}/\overline{uu}$  in the near-wall region with high shear strain and thus the quadratic form may be an answer for the discussion by Kim & Moin[5].

Figure 26 compares distributions of the model coefficient  $C_\theta$  for case 2 estimated by the quadratic form. In contrast to Fig. 25, distributions of  $C_\theta$  in both the  $x$ - and  $y$ -directions show nearly the same tendency, where well correlated values around 0.6 are calculated except for the near-wall region. In the vicinity of the wall, although profiles of the estimated  $C_\theta$  change in space, they show almost the same value at the same location. This is a notable feature of the quadratic form and it indicates that the direction of the scalar-flux vector can be predicted by the quadratic form much more precisely, at least for this case.

In what follows, the predictive performance of the GGDH [Eq. (12)] and the quadratic [Eq. (16)] forms has been estimated by *a priori* tests using the



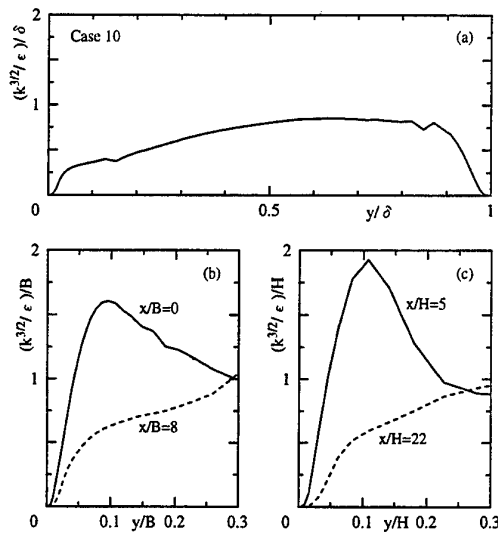


Figure 23 Comparison of turbulent length scales: (a) the Couette-Poiseuille flow (case 10); (b) the plane impinging jet; (c) the obstacle flow.

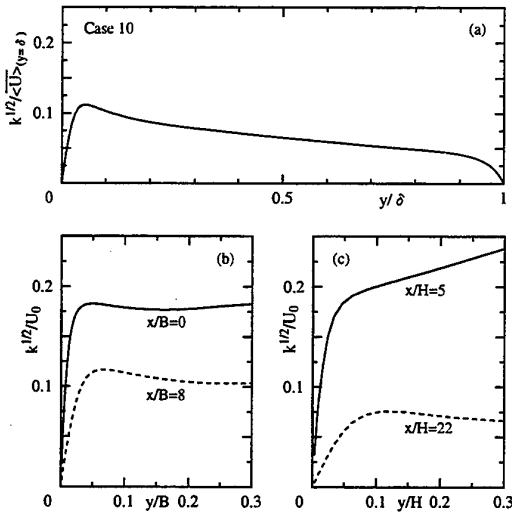


Figure 24 Comparison of turbulent velocity scales: (a) the Couette-Poiseuille flow (case 10); (b) the plane impinging jet; (c) the obstacle flow.

present LES data, focusing especially on the directions of the scalar-flux vector. In Fig. 27 (a), the distributions of the scalar-flux vector angles predicted by the GGDH and the quadratic forms for cases 5 – 9 are compared to those by the simulation results. The correlation coefficients obtained from the simulation results are also shown in Figs. 27 (b) and (c). The distribution of the angle of the principal axis of the Reynolds stress tensor is plotted in the figure as well. As seen in Fig. 27 (a), the vector angle by the quadratic form is much closer to the LES's compared to that of the GGDH form at  $Pr \geq 0.71$ . It is also found that the distributions of scalar-flux

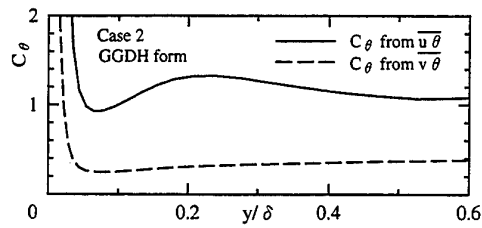


Figure 25 Estimation of  $C_{\theta}$  by using Eq. (12).

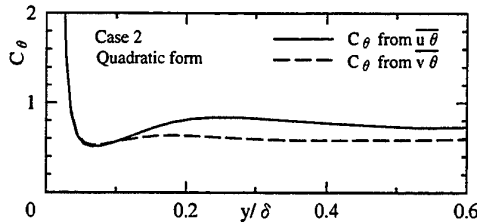


Figure 26 Estimation of  $C_{\theta}$  by using Eq. (16).

vector angle by the LES do not change greatly with the increase of  $Pr$  in the range of  $Pr \geq 0.71$  (hereinafter referred to as the higher  $Pr$  cases for convenience). On the other hand, in the lower  $Pr$  cases, the profiles of scalar-flux vector angle become closer to that by the GGDH form. These indicate that, for successfully predicting the scalar-flux vector angle, some Prandtl-number dependence should be considered especially in lower  $Pr$  cases, whereas it is not always the primary issue in wall-shear flows of high  $Pr$  fluids. These features can be confirmed by the distributions of the correlation coefficients as shown in Figs. 27 (b) and (c). In the higher  $Pr$  cases,  $\theta$  correlates strongly with  $u$ , as pointed out previously. However, the correlation between  $\theta$  and  $v$  relatively increases with the decrease of  $Pr$ , and then it becomes almost the same level as that between  $\theta$  and  $u$  in case of  $Pr = 0.025$ .

The results of the Couette-Poiseuille (case 10) and the open channel (cases 11 and 12) flows estimated in the same manner as the wall-shear flows (cases 5 – 9) are shown in Figs. 28 and 29, respectively. In the shear-free regions near the location of  $x/\delta = 1$ , the GGDH form tends to become a reasonably better approximation irrespective of the Prandtl number, in contrast to the wall-shear regions. As seen in Figs. 28 (b) and 29 (b), near the shear-free regions, the level of the correlation coefficient between  $\theta$  and  $v$  is globally equal to that between  $\theta$  and  $u$ , while on the moving wall of case 10, the correlation between  $\theta$  and  $u$  almost vanishes. These findings suggest that it is difficult to predict the scalar-flux vector angle accurately for various kinds of scalar-transfer fields by using a single expression by the GGDH or the quadratic form.

The following are the representative results for more complex scalar-transfer fields of the PIJ and

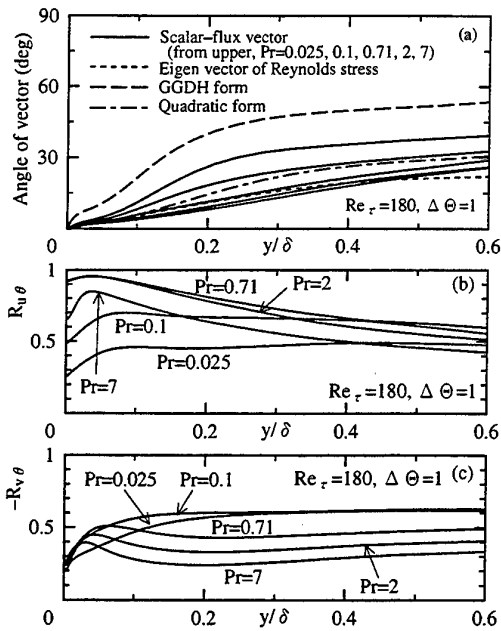


Figure 27 Estimation of angle of vectors and correlation coefficients (cases 5 - 9).

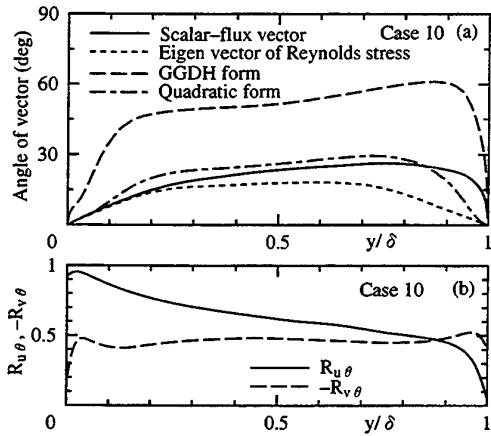


Figure 28 Estimation of angle of vectors and correlation coefficients (case 10).

the OBF cases. Figure 30 compares the distributions of the scalar-flux vector angles and the correlation coefficients in the near-wall region of the PIJ case. As seen in Fig. 30 (a), in the stagnation region, the angles of the LES scalar-flux vector become closer to those of the GGDH form. This tendency is similar to that in the shear-free regions of cases 10 - 12. In the wall-jet region, however, the quadratic form shows good agreement with the LES data, similarly in the wall-shear regions of cases 5 - 9. Distributions of the scalar-flux vector angles and the correlation coefficients in the lower-wall region of the OBF case are shown in Fig. 31. In the redeveloping region, the angles of the LES scalar-flux vector show very good cor-

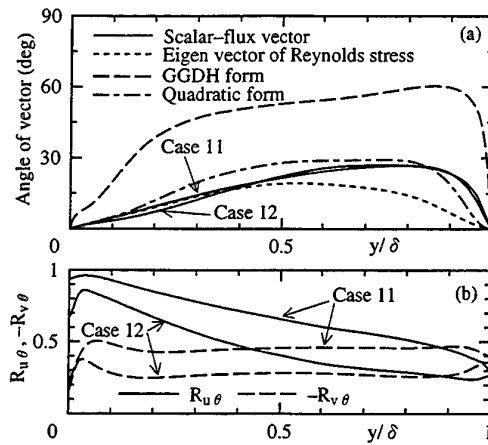


Figure 29 Estimation of angle of vectors and correlation coefficients (cases 11 and 12).

relation with those of the quadratic form, similarly in the wall-shear regions of the channel flows. On the other hand, in the recirculating region, the simulation results are generally situated between those by the GGDH and the quadratic forms. As described before, in the reattachment region of the OBF case, a large scale structure plays a dominant role in transporting the passive scalar, similarly in the shear-free regions. Considering these similarities in the OBF and the shear-free flow cases, it may be suggested that a modeling way for the scalar-flux vector in the shear-free regions may be also effective in the recirculating region.

Spatial distributions of the vector angles of the PIJ and the OBF cases are compared in Figs. 32 and 33, respectively. As seen in the figures, the above discussions on the relation between the simulation results and the model predictions are also effective in the range of flow regions dominant in transporting the passive scalar from the walls.

To investigate further applicability of the present proposal, the GGDH and the quadratic forms are applied to some other fundamental flow fields of engineering interest. They are the channel flow with wall injection and suction whose DNS data were obtained by Sumitani & Kasagi[31], and the Tavoularis & Corrsin's[32] homogeneous shear flow. Figure 34 compares the distributions of the angles of the scalar-flux vectors obtained from the DNS[31] and the experimental[32] data. It is readily seen that the vector angle of the quadratic form correlates very well with the DNS even in the flow regions with wall injection and suction. Furthermore, as seen in Fig. 34 (c), the vector angle of the quadratic form is very close to the experimental one in the homogeneous shear flow. This indicates that the quadratic form is effective in predicting the scalar-transport phenomena in a wide range of flow fields under high shear-strain conditions, regardless of the existence of

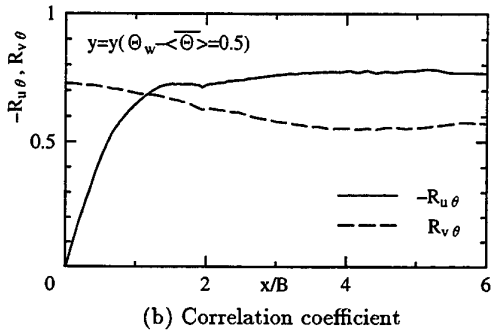
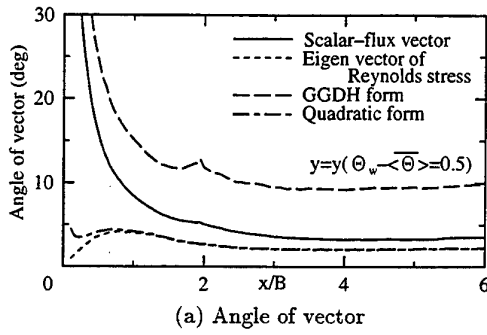


Figure 30 Estimation of angle of vectors and correlation coefficients in the plane impinging jet.

a wall.

Therefore, taking account of the above discussions, in order to construct a new algebraic scalar-flux model applicable to various kinds of scalar-transfer fields, a combined expression of the GGDH and the quadratic forms is expected to be effective. It may be written as

$$\overline{u_i \theta} = -k \tau_\theta \left( C_{\theta 1} \frac{\overline{u_i u_j}}{k} + C_{\theta 2} \frac{\overline{u_i u_k} \overline{u_k u_j}}{k^2} \right) \overline{\theta}_{,j} \quad (18)$$

where  $C_{\theta 1}$  and  $C_{\theta 2}$  are the model coefficients including parameters bridging between the GGDH and the quadratic forms. The model coefficients  $C_{\theta 1}$  and  $C_{\theta 2}$  are to be modeled so that the second term in the right hand side of Eq. (18) may play the most dominant role under conditions with high shear strain, while the first term may mainly work in situations with weak or no shear strain as well as in lower  $Pr$  flow cases.

#### 4.3 Possible extension to modeling the turbulent diffusion vector

The modeling of the turbulent diffusion is another important matter from the engineering viewpoint[33][34]. Therefore, to assess the capability of the present proposal, Fig. 35 compares vector angles of the turbulent diffusion in the  $k$ -equation [i.e.,  $\overline{u_i (u_k u_k / 2)}$ ], the scalar-flux ( $\overline{u_i \theta}$ ) and the aforementioned model expressions. As seen in the figure, vector angles of the turbulent diffusion correlate well with those of the scalar flux and thus those of

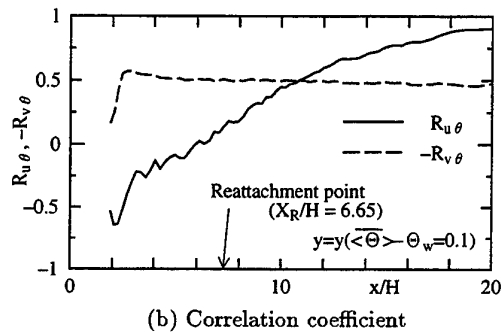
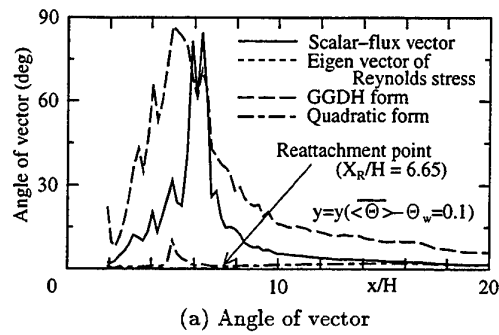


Figure 31 Estimation of angle of vectors and correlation coefficients in the obstacle flow.

the quadratic form in the wall-shear regions. (Some kinks of the turbulent diffusion vector-angle profiles are seen in the proximity of the wall due to the change of sign of the wall-normal turbulent diffusion.) From this estimation, the fluctuating part of turbulent energy ( $u_k u_k / 2$ ) is thought to be transported by a mechanism similar to that of the passive scalar ( $\theta$ ) in wall-shear regions. Interestingly, the vector angles of the turbulent diffusion are rather similar to those of the quadratic form even in the shear-free regions, in contrast to those of the scalar flux. This may be one of the key factors to model the turbulent diffusion phenomena successfully. However, considering the fact that the turbulent diffusion vector is originally derived from the triple moment tensor of the velocity fluctuations, more careful and detailed discussions may be needed to propose an appropriate model.

## 5 CONCLUDING REMARKS

In order to reveal unknown characteristics of turbulent passive scalar fields, LES simulations in forced convection regimes have been performed under various strain conditions and several fluid Prandtl numbers. The following are the main contributions obtained from the present study:

- The present LES simulations have successfully reproduced fundamental features of turbulent scalar-transport phenomena in a wide range of flow fields,

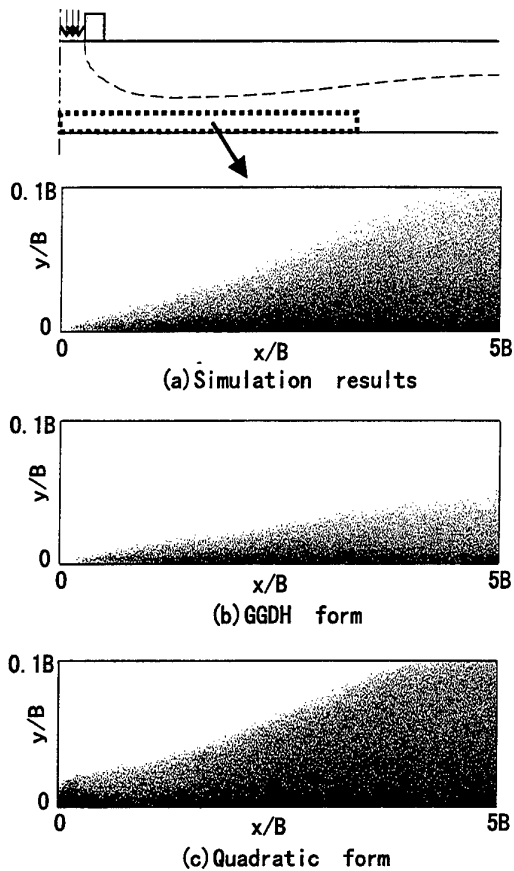


Figure 32 Distributions of vector angles in the plane impinging jet (color ranges from 0 (black) to 30 (white) degrees linearly).

including shear-free boundaries, a flow impingement and a flow separation.

- From the simulation results of the channel-flow cases, it has been confirmed that coherent structures generated by high shear strain play a dominant role in transporting the passive scalar in wall-shear regions. On the other hand, it has been found that there exist large vortex structures in shear-free regions, which mainly transport the passive scalar from boundary surfaces to the outer regions. Especially in the Couette-Poiseuille flow case, the scale of the vortex structure in the shear-free region becomes generally equal to the channel-half width, which is much larger than that in the wall-shear region.
- In more complex fields investigated in this study, i.e., a plane impinging jet (PIJ) and a separated flow around an obstacle (OBF), the dominant scalar-transport mechanism can be also generally classified into two patterns by whether high shear strain exists or not in the near-wall region. This corresponds to the knowledge obtained from the channel-flow cases. In the wall-jet region of the PIJ case and the redeveloping region of the OBF

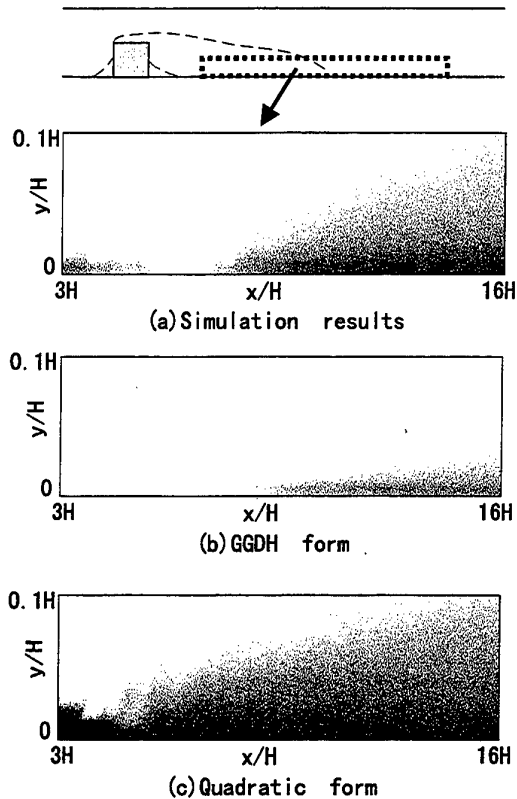


Figure 33 Distributions of vector angles in the obstacle flow (color ranges from 0 (black) to 30 (white) degrees linearly).

case, the fundamental scalar-transport mechanism is the same as that in the wall-shear regions of the channel-flow cases. This is mainly due to the existence of high shear strain and the consequent coherent structures. On the contrary, in the stagnation region of the PIJ case and the recirculating region of the OBF case, there can be seen large vortex structures, similarly in the shear-free regions of the channel-flow cases.

- *A priori* tests of the channel-flow cases have elucidated that the turbulent scalar-flux vectors predicted by the GGDH form hardly align with the simulation results in wall-shear flow regions at  $Pr \geq 0.71$ . In such situations, the use of the quadratic products of the Reynolds stress tensor in the gradient diffusion model showed its possibility to improve the prediction accuracy. On the other hand, the GGDH form returns a quite reasonable approximation for scalar-flux vectors in shear-free flow regions and/or lower  $Pr$  fluid cases.
- In the stagnation region of the PIJ case and the recirculating region of the OBF case, the angles of scalar-flux vectors show better correlations with those of the GGDH form, where large vortex structures play the most important role in scalar-transport phenomena. Both in the wall-jet region

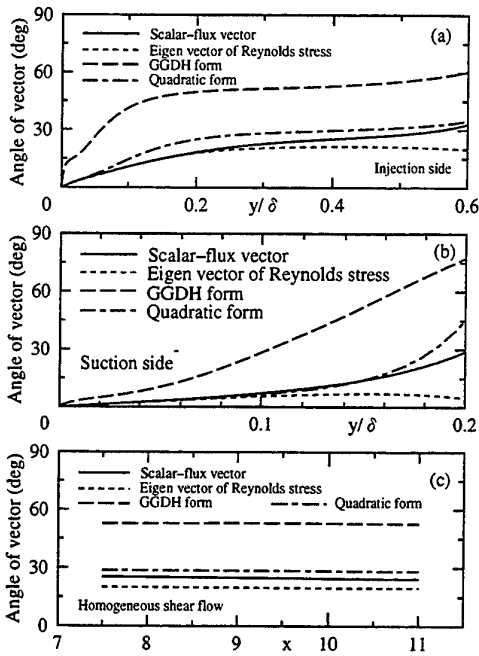


Figure 34 Estimation of angle of vectors: (a) DNS[31] injection side; (b) DNS[31] suction side; (c) homogeneous shear flow[32].

of the PIJ case and the redeveloping region of the OBF case, however, the simulation results return to be closer to the predictions with the quadratic form.

- In order to construct a new algebraic scalar-flux model applicable to various kinds of scalar-transfer fields, a combined model expression is highly recommended, including both the GGDH and the quadratic forms with suitable bridging functions, although further discussions on devising such functions are needed.

## ACKNOWLEDGMENT

The authors wish to express their appreciation to Mr. M. Inagaki of TCRDL for his help and suggestion in developing the computer program used in the present study.

## NOMENCLATURE

- $B$  : nozzle-exit width of plane impinging jet  
 $H$  : height of obstacle or distance from wall to nozzle exit  
 $h$  : heat (scalar) transfer coefficient  
 $K_G$  : SGS turbulent energy,  $\langle u'_i u'_i \rangle / 2$   
 $k$  : Reynolds (ensemble) averaged turbulent energy,  $\overline{u_i u_i} / 2$   
 $Nu$  : Nusselt number,  $hB/\lambda, hH/\lambda, h(2\delta)/\lambda$   
 $\langle P \rangle$  : instantaneous filtered GS pressure

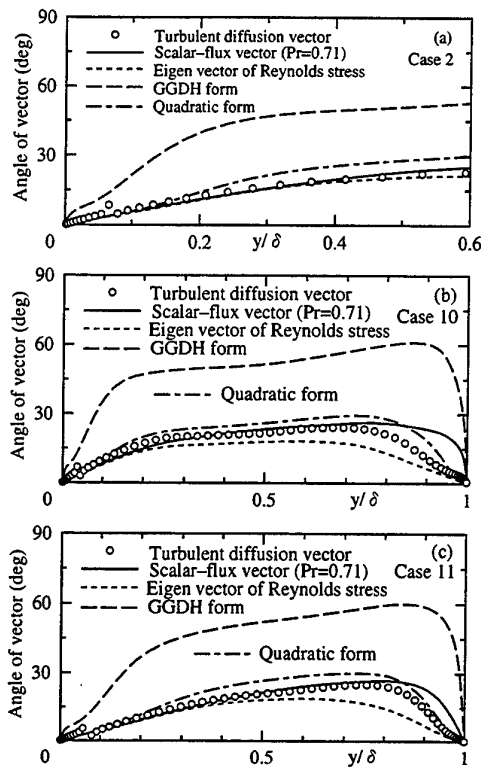


Figure 35 Estimation of angle of vectors for turbulent diffusion.

$Pr, Pr_{SGS}$  : molecular and SGS turbulent Prandtl numbers

$R_{u_i\theta}$  : correlation coefficient of GS velocity fluctuation in  $i$ -direction and scalar fluctuation,  
 $\frac{\overline{u_i \theta}}{\sqrt{\overline{u_i^2}} \sqrt{\overline{\theta^2}}}$

$Re_B, Re_H$  : Reynolds number,  $U_0 B/\nu, U_0 H/\nu$

$Re_r$  : Reynolds number,  $u_r \delta/\nu$

$S_{ij}$  : strain-rate tensor,  $\langle U_i \rangle_{,j} + \langle U_j \rangle_{,i}$

$t$  : time

$U_0$  : reference velocity (PIJ: nozzle-exit velocity, OBF: mean velocity over obstacle)

$U_i$  : velocity in  $i$ -direction

$\langle U_i \rangle, u'_i$  : instantaneous filtered GS velocity and SGS velocity fluctuation,  $u'_i = U_i - \langle U_i \rangle$

$\overline{\langle U_i \rangle}, u_i$  : ensemble-averaged GS velocity and its fluctuation,  $u_i = \langle U_i \rangle - \overline{\langle U_i \rangle}$

$u_r$  : mean friction coefficient on fixed wall

$\langle u'_i u'_j \rangle$  : SGS Reynolds stress tensor

$x, y, z$  : streamwise, wall-normal and spanwise directions

## Greek symbols

$\Delta$  : filter-width,  $(\Delta_x \Delta_y \Delta_z)^{1/3}$

$\delta$  : representative length of channel flows

$\varepsilon$  : dissipation rate of  $k$

$\varepsilon_G$  : dissipation rate of  $K_G$

$\Theta$  : passive scalar

$\langle \Theta \rangle$  : instantaneous filtered GS scalar

$\overline{\langle \theta \rangle}$ : ensemble-averaged GS scalar and its fluctuation  
 $\lambda$ : thermal (scalar-field) conductivity  
 $\nu, \nu_{SGS}$ : kinematic and SGS eddy viscosities  
 $\rho$ : fluid density  
 $\tau_{SGS}$ : SGS characteristic time scale  
 $\Omega_{ij}$ : vorticity tensor,  $\langle U_i \rangle_{,j} - \langle U_j \rangle_{,i}$

### Special symbols

$f_{,i}$ : partial derivative of variable,  $f$ , with respect to coordinate,  $x_i$  (e.g.,  $f_{,i} = \partial f / \partial x_i$ )  
 $\overline{(\ )}$ : ensemble-averaged value  
 $\langle (\ ) \rangle$ : volume-averaged value with filter-width  $\Delta$

### REFERENCES

- [1] Antonia, R. A., Danh, H. Q. and Prabhu, A., Response of a turbulent boundary layer to a step change in surface heat flux, *J. Fluid Mech.*, 1977, **80**, 153-177.
- [2] Hishida, M., Nagano, Y. and Tagawa, M., Transport processes of heat and momentum in the wall region of turbulent pipe flow, *Proc. The Eighth International Heat Transfer Conference* (Edited by Tien, C. L. et al.), San Francisco, 1986, **3**, 925-930.
- [3] Vogel, J. C. and Eaton, J. K., Combined heat transfer and fluid dynamic measurements downstream of a backward-facing step, *Trans. ASME: J. Heat Transfer*, 1985, **107**, 922-929.
- [4] Sakakibara, J., Hishida, K. and Maeda, M., Vortex structure and heat transfer in the stagnation region of an impinging plane jet (simultaneous measurements of velocity and temperature fields by digital particle image velocimetry and laser-induced fluorescence), *Int. J. Heat Mass Transfer*, 1997, **40**, 3163-3176.
- [5] Kim, J. and Moin, P., Transport of passive scalars in a turbulent channel flows, *Turbulent Shear Flows 6*, 1989, 85-96 (Springer).
- [6] Kasagi, N., Tomita, Y. and Kuroda, A., Direct numerical simulation of the passive scalar field in a two-dimensional turbulent channel flow *ASME/JSME Thermal Eng. Proc.*, 1991, **3**, 175-182.
- [7] Lyons, S. L., Hanratty, T. J. and McLaughlin, J. B., Direct numerical simulation of passive heat transfer in a turbulent channel flow, *Int. J. Heat Mass Transfer*, 1991, **34**, 1149-1161.
- [8] Kasagi, N. and Ohtsubo, Y., Direct numerical simulation of low Prandtl number thermal field in a turbulent channel flow, *Turbulent Shear Flows 8*, 1993, 97-119 (Springer).
- [9] Kawamura, H. and Ohsaka, K., DNS of turbulent heat transfer in channel flow with low to medium-high Prandtl number fluid, *Proc. 11th Symposium on Turbulent Shear Flows*, Grenoble, 1997, 8.7-8.12.
- [10] Tsubokura, M., Kobayashi, T. and Taniguchi N., Large eddy simulation of plane impinging jets, *Proc. 11th Symposium on Turbulent Shear Flows*, Grenoble, 1997, 22.24-22.29.
- [11] Yang, K. S. and Ferziger, J. H., Large-eddy simulation of turbulent obstacle flow using a dynamic subgrid-scale model, *AIAA J.*, 1993, **31**, 1406-1413.
- [12] Le, H., Moin, P. and Kim, J., Direct numerical simulation of turbulent flow over a backward-facing step, *J. Fluid Mech.*, 1997, **330**, 349-374.
- [13] Kuroda, A., Kasagi, N. and Hirata, M., Direct numerical simulation of turbulent plane Couette-Poiseuille flows: effect of mean shear on the near wall turbulence structures, *Proc. 9th Symposium on Turbulent Shear Flows*, Kyoto, 1993, 8.4.1-8.4.6.
- [14] Lombardi, P., Angelis, V. D. and Banerjee, S., Direct numerical simulation of near-interface turbulence in coupled gas-liquid flow, *Phys. Fluids*, 1996, **8**, 1643-1665.
- [15] Abe, K., Kondoh, T. and Nagano, Y., On Reynolds stress expressions and near-wall scaling parameters for predicting wall and homogeneous turbulent shear flows, *Int. J. Heat Fluid Flow*, 1997, **18**, 266-282.
- [16] Okamoto, M., Investigation of one-equation subgrid model, *Journal of Institute of Industrial Science, University of Tokyo*, 1997, **49-1**, 3-10 (in Japanese).
- [17] Rogers, M. M., Mansour, N. and Reynolds, W. C., An algebraic model for the turbulent flux of a passive scalar, *J. Fluid Mech.*, 1989, **203**, 77-101.
- [18] Kader, B. A., Temperature and concentration profiles in fully turbulent boundary layers, *Int. J. Heat Mass Transfer*, 1981, **24**, 1541-1544.
- [19] Gardon, R. and Akfirat, J. C., *Heat transfer characteristics of impinging two-dimensional air jet*, *Trans. ASME: J. Heat Transfer*, 1966, **88**, 101-108.
- [20] Ota, T. and Nishiyama, H., A correlation of maximum turbulent heat transfer coefficient in reattachment flow region, *Int. J. Heat Mass Transfer*, 1987, **30**, 1193-1200.
- [21] Iritani, Y., Kasagi, N. and Hirata, M., Heat transfer mechanism and associated turbulence structure in the near-wall region of a turbulent boundary layer, *Turbulent Shear Flows 4*, 1984, 223-234 (Springer).
- [22] Nagano, Y. and Hishida, M., Turbulent heat transfer associated with coherent structures near the wall, *Near-Wall Turbulence*, 1990, 568-581 (Hemisphere).
- [23] Yokobori, S., Kasagi, N. and Hirata, M., *Trans. Japan Soc. Mech. Engrs: Ser. B*, 1983, **49**, 1029-1039 (in Japanese).
- [24] Nagano, Y. and Kim, C., A two-equation model for heat transport in wall turbulent shear flows, *Trans. ASME: J. Heat Transfer*, 1988, **110**, 583-589.
- [25] So, R. M. C. and Sommer, T. P., An explicit algebraic heat-flux model for the temperature field, *Int. J. Heat Mass Transfer*, 1995, **39**, 455-465.
- [26] Abe, K., Kondoh, T. and Nagano, Y., A two-equation heat transfer model reflecting second-moment closures for wall and free turbulent flows, *Int. J. Heat Fluid Flow*, 1996, **17**, 228-237.
- [27] Rhee, G. H. and Sung, H. J., A low-Reynolds-number, four-equation heat transfer model for turbulent separated and reattaching flows, *Int. J. Heat Fluid Flow*, 1997, **18**, 38-44.
- [28] Launder, B. E., *Turbulence* (Edited by Bradshaw, P.), 1976, 231-287 (Springer).
- [29] Suga, K., Development and application of a non-linear eddy viscosity model sensitized to stress and strain invariants, Ph.D Thesis, 1995 (UMIST).
- [30] Daly, B. J. and Harlow, F. H., Transport equations in turbulence, *Phys. Fluids*, 1970, **13**, 2634-2649.
- [31] Sumitani, Y. and Kasagi, N., Direct numerical simulation of turbulent transport with uniform wall injection and suction, *AIAA J.*, 1995, **33**, 1220-1228.
- [32] Tavoularis, S. and Corrsin, S., Experiments in nearly homogeneous turbulent shear flow with a uniform mean temperature gradient. Part I, *J. Fluid Mech.*, 1981, **104**, 311-347.
- [33] Hanjalic, K., Advanced turbulence closure models: a view of current status and future prospects, *Int. J. Heat Fluid Flow*, 1994, **15**, 178-203.
- [34] Kawamura, H., Sasaki J. and Kobayashi, K., Budget and modelling of triple-moment velocity correlations in a turbulent channel flow based on DNS, *Proc. 10th Symposium on Turbulent Shear Flows*, Penn State, 1995, 26.13-26.18.

# DIRECT NUMERICAL AND LARGE EDDY SIMULATIONS IN NUCLEAR APPLICATIONS

G. Grötzbach, M. Wörner

Forschungszentrum Karlsruhe  
Institut für Reaktorsicherheit  
Postfach 3640, D-76021 Karlsruhe, Germany,  
Tel. 0049-7247/824477

## ABSTRACT

Direct numerical and large eddy simulations are powerful tools for analyses of turbulent flows at low, respectively large Reynolds or Rayleigh numbers in fundamental research. The current status of both methods and recent extensions are compiled. The progress achieved with subgrid scale models and numerics makes the method attractive for applications to nuclear research and engineering. Examples of realistic technical flows are discussed. Open problems are mainly related to more general subgrid scale models for large complex containers, to the wall and inlet conditions for high Reynolds number and buoyant flows, and to discretisation schemes for local refinement of spatial resolution. As a classical example for the use of direct simulations, results are presented for a turbulent internally heated horizontal fluid layer. The analysis of the closure terms in the transport equation of the kinetic energy demonstrates major difficulties of the conventional statistical modelling for partially stably stratified convection.

## 1. INTRODUCTION

In developing better safety features for new reactor concepts, most activity is on thermal fluid dynamics. By introducing passive auxiliary systems, i.e. which can be operated without additional power, one tries to ensure by design measures that the after heat can be removed by natural convection even in severe failure situations. The features of such new concepts are analysed by model experiments of different scales, sometimes up to 1:1, and increasingly by thermal hydraulic codes.

In this paper we begin with a description of some typical problems in nuclear thermal hydraulics which are dominated by turbulent momentum, heat, and mass transfer. The trends become obvious to apply more sophisticated turbulence models in the corresponding numerical analyses. The geometrical and physical complexity of the phenomena to be investigated necessitates more detailed prediction capabilities of the numerical models. Consequently, one finds in literature growing interest in using and improving the large eddy simulation method (LES) to nuclear problems. Next we give a description of the basics of the methods of direct numerical simulation (DNS) and large eddy simulation of turbulent flows focusing on recent developments of subgrid scale models, boundary conditions, and numerics which come mainly from basic research. More detailed discussions are given in review papers e.g. by Ciofalo (20), Ferziger (36),(37), Grötzbach (52), Lesieur & Metais (76), Mason (82), Moin & Mahesh (89), Nieuwstadt (95), and Schumann (109). Then, we will discuss some new applications of LES to nuclear problems and point out difficulties of such applications. Subsequently we will concentrate on analyses related to

cooling of core melts inside the pressure vessel and in the core catcher. Finally, we will conclude on further developments which are required to get the methods of direct numerical and large eddy simulation more suited for nuclear or other technical applications.

## 2. METHODS AND TRENDS IN NUCLEAR THERMAL HYDRAULICS

Some characteristics of nuclear thermal hydraulics indicate the requirements for engineering codes which should be fulfilled for detailed quantitative analyses. The geometries to be considered range from simple channels of different dimensions over open or closed containers to large ones with complex geometrical boundaries. In large containers one has to model forced, mixed, and natural convection at large Reynolds ( $Re$ ) and Rayleigh ( $Ra$ ) numbers, including flows like jets or mixing layers. The complex internal structures like fuel pin bundles, guiding tubes for internal instrumentation systems, and heat exchanger bundles form small gaps which are sometimes treated by porous body models. The channel flows may extend to small  $Re$  and  $Ra$ . Thus, one finds a wide spectrum of channel dimensions, of characteristic non-dimensional numbers, and flow types in the same application.

Examples of analyses of passive decay heat removal within a complete model of the European Fast Reactor by means of the FLUTAN code by Weinberg et al. (124), investigations of thermal mixing in the upper plenum of the PHENIX reactor with the TRIO-VF code by Roubin & Astegiano (103), or investigations of local problems, like the thermal barrier in a pump housing

with the N3S code by Archambeau et al. (2). Most investigations are combined turbulent momentum and heat transfer tasks in three-dimensional geometry.

Typical for nuclear safety investigations is also that one is often faced with exotic or prototypical situations: Prototypical with respect to geometry, type of fluid, and flow conditions. Therefore, there exist no validated physical models for such conditions. An important example is the cooling of a molten core inside the vessel of the reactor or in a special core catcher device. It is very hard to perform model experiments with real materials like molten  $\text{UO}_2$  or steel, or with multi-phase multi-component mixtures of these fluids. In any case one would avoid using real nuclear heating to get internal heat sources in larger amounts of these fluids. Therefore, simple model fluids are used widely applying Joule heating or transient cooling down of the test fluids to mimic the internal heat sources; for an overview of recent experiments see Nourgaliev et al. (99). As such modelling of internally heated fluid layers hinders detailed local heat transfer and turbulence analyses, we have nearly no turbulence data available to develop and validate modern turbulence models locally. So, rather integral experimental information has to be used for validation of the models and codes.

The numerical models used in the nuclear field to analyse in detail turbulent heat transfer are basing on Reynolds averaged Navier Stokes equations (RANS). Most applications are run with first order turbulence models, like with variants of the  $k-\varepsilon$  model and a turbulent Prandtl number concept (2),(103),(124). Recently a combination of the  $k-\varepsilon$  model and a second order heat flux model was developed for forced and buoyant flows by Carteciano et al. (16). The model behaved very well in a benchmark in which blind predictions for an experiment were required (4). The problem with the first order models is that one has to classify the practical application into this or that flow type. This is mostly not possible in large containers with internal structures. Therefore, in trying to achieve more universal models with better prediction capabilities one also considers the application of full second order closure models basing on RANS. Current experience with these models is that second order models require very fine grids for practical applications (2); as a consequence wider applications can only be expected on future parallel high performance computer systems.

For these and other reasons, there is a growing interest in the nuclear field in Large Eddy Simulation (LES). This method is not based on the time-averaged equations, but on the local and instantaneous Navier Stokes equations filtered spatially, typically over the grid widths. With this method one simulates the spatially resolved scales of turbulence and uses models only for the non-resolved, hopefully more universal small scales, so-called subgrid scale models (SGS). As turbulence is time-dependent and three-dimensional, LES have to be performed always in three dimensions and time-

dependent. The engineering flow problems in nuclear heat transfer or safety are also mainly three-dimensional; and according to the experience in (2), many flows become time-dependent even when stationary inlet conditions are used. Therefore, one has anyway to use three-dimensional time-dependent representations of the task, and performing an LES instead of applying a RANS-based first order turbulence model should not result in too excessive extra computing efforts. Breuer et al. (15) found the LES being a factor of eight slower than a two-layer  $k-\varepsilon$  model for flows around surface mounted obstacles, but giving much more reliable results and more information; and Ciofalo found only a factor of two compared to a standard  $k-\varepsilon$  model for an element of a crossed-corrugated heat exchanger (21). The results of the LES were again superior to the ones of the RANS model.

### 3. DIRECT SIMULATION METHOD

The basic equations describing laminar and turbulent flow with heat transfer are the conservation equations for mass, momentum, and energy. For a Newtonian fluid with constant material properties they can be written in terms of the primitive variables, i.e. in terms of  $u_i$  for the components of the velocity vector ( $i=1,2,3$ ),  $p$  for pressure, and  $T$  for temperature:

$$\partial_i u_i = 0 \quad (1)$$

$$\partial_i u_i + \partial_j (u_i u_j) = \partial_j (1/\sqrt{Gr} \partial_j u_i) - \partial_i p - (T_{ref} - T) g_i / |g| \quad (2)$$

$$\partial_i T + \partial_j (T u_j) = \partial_j (1/(\text{Pr} \sqrt{Gr}) \partial_j T) + Q \quad (3)$$

The symbols are  $t$  for time,  $g_i$  for components of the gravity vector,  $Q$  for dimensionless specific internal heat source,  $Gr$  for Grashof number  $|g| \beta \Delta T_w D^3 / \nu^2$ ,  $\beta$  for volumetric expansion coefficient,  $\Delta T_w$  for difference between wall temperatures,  $D$  for channel height,  $Pr$  for Prandtl number  $\nu/\alpha$ ,  $\nu$  and  $\alpha$  for the diffusivities of momentum respectively heat, and  $T_{ref}$  for reference temperature. The validity of the Boussinesq approximation is assumed in the buoyancy term. Eq. (1 to 3) are normalized by the channel height  $D$ , velocity  $u_w = (|g| \beta \Delta T_w D)^{1/2}$ , time  $D/u_w$ , and temperature difference  $\Delta T_w$ .

The method of direct numerical simulation of turbulence is directly based on eq. (1 to 3). Since the turbulent fluctuations carrying the kinetic energy are mainly produced at large scales, but this energy is dissipated at small scales, the method has to be based on the full conservation equations for mass, momentum, and energy. All scales have to be resolved by the grid, from the largest macroscopic structures of the flow down to the smallest scales of turbulence. The features of turbu-



lence require to solve these equations always in three dimensions and in time.

If these requirements are met in the simulations, no subgrid scale models and no wall models are needed. Such simulations do not depend on any model coefficient. The first direct simulations were those by Orszag & Patterson (100) for decaying isothermal isotropic turbulence, those by Lipps (78) for weakly turbulent and those by Grötzbach (46) for fully turbulent Rayleigh-Bénard convection of air, and those by Kim (69) for forced convection in channels with heat transfer. Overviews on more recent direct simulations are given by Kasagi (64) and Moin & Mahesh (89). Examples for direct simulations of compressible flows are those e.g. by Friedrich & Bertolotti (38) and of purely buoyant flows by Wörner & Grötzbach (132).

## 4. LARGE EDDY SIMULATION METHOD

### 4.1. Separation of resolved and subgrid scales

To derive equations for large eddy simulations, one has to separate the flow variables in a resolved and an unresolved part. This can be done by applying a low-pass filtering procedure as introduced by Leonard (75) and non-linear or linear filter functions, or by using the formal volume integration method as applied by Schumann (108). The more general method is the filtering approach, because the actual grid width  $\Delta x$ , and the width of the filter can be chosen separately (82). The filtered field  $\bar{f}$  for a quantity  $f = u, p, T$  is defined by the spatial filtering procedure:

$$\bar{f}(\underline{x}, t) = \int f(\underline{y}, t) G(\underline{x} - \underline{y}) d\underline{y} \quad (4)$$

Here we split the quantity  $f$  in its filtered large scale part  $\bar{f}$  and in its subgrid scale fluctuation part  $f'$  by  $f = \bar{f} + f'$ . Using non-linear filter functions  $G(\underline{y})$ , like the widely applied Gaussian filter, the filtered non-linear terms in the Navier Stokes or thermal energy equations take the following form:

$$\overline{u_i u_j} = \overline{u_i} \overline{u_j} + \overline{u_i' u_j'} + \overline{u_i' u_j} + \overline{u_i u_j'} \quad (5)$$

$$\overline{u_j T} = \overline{u_j} \overline{T} + \overline{u_j' T'} + \overline{u_j' T} + \overline{u_j T'} \quad (6)$$

The first term on the right hand side represents the resolvable part of the instantaneous local turbulent shear stresses and heat fluxes, the last term represents the subgrid scale contributions which have to be modelled. The filtered non-linear terms look formally like the Reynolds terms which are deduced by time-averaging. The main difference is that time-averaging is replaced by filtering over typically mesh cell volumes  $V$ . Therefore, the meaning of the unknown terms is different from those in RANS models: they do not contain the complete momentum and heat exchange due to the turbulent fluctuations, but only that part corresponding to the unresolved

small scales. This means, for decreasing grid width and hence for better spatial resolution, the models for the subgrid scale terms have to converge to zero, i.e. to a direct simulation.

The second and third terms on the right hand side in eq. 5 and 6 result from using non-linear filters and contain filtered cross-products between filtered resolved and unresolved quantities. They vanish when linear filters like the box filter are used. Germano (40) shows that details of the filters are not important compared to the importance of the subgrid scale models. Indeed it was shown on the basis of simulation results for complex channels by Neto et al. (94) that the cross-products can be neglected. Recently Härtel & Kleiser (57) found theoretically that in inhomogeneous flows near walls the energy transfer between grid scales (GS) and subgrid scales (SGS) is independent on the type of filter applied. Nevertheless, Ghosal & Moin (42) developed a filter method with variable filter width to improve accuracy for inhomogeneous flows in complex geometries.

### 4.2. Subgrid scale models

In LES the dissipation of turbulent kinetic energy is partly in the unresolved scales, whereas the production is in the resolved scales. The SGS models become more important with increasing Reynolds number or increasing grid width, and have to model more of the total dissipation. In the coarse grid limit the subgrid scale models should account for about the complete turbulence like the models used for the Reynolds terms. Accordingly, most existing subgrid scale models are formally deduced from statistical models. The main difference is that the length scale is not the mixing length as used in Reynolds models, but it is a representative for the local grid width, because this is a measure for the unresolved turbulent exchange of momentum and heat.

#### 4.2.1. Algebraic SGS models

Most subgrid scale models are first order models because they are based on an eddy diffusivity concept, introducing an effective eddy diffusivity and conductivity for the subgrid scales:

$$\overline{u_i' u_j'} = 2 \nu_t S_{ij} \quad (7)$$

$$\overline{u_j' T'} = a_t \partial \bar{T} / \partial x_j \quad (8)$$

where  $S_{ij} = 0.5 (\partial \bar{u}_i / \partial x_j + \partial \bar{u}_j / \partial x_i)$  is the local and instantaneous deformation rate of the resolved flow field.

The first subgrid scale model introduced for the momentum fluxes is the still widely used Smagorinsky model (115). It incorporates the mean grid width  $h = V^{1/3}$  as a length scale for the subgrid scale diffusivity and a coefficient  $C_s$ ,

$$\nu_t = (C_s h)^2 S \quad (9)$$

where  $S = \sqrt{S_{ij} S_{ij}}$ . The model was first used by Deardorff (26) for channel flows. Following the ideas of Schumann (108) it was later extended by Moin & Kim (87) to include the van Driest damping function to reduce SGS contributions near walls. Examples for newer applications to slightly complex flows are those for a crossed corrugated heat exchanger element (21), for the flow around a cylinder to determine the forces on an offshore platform by Lu et al. (80), and for a turbulent plane jet by Weinberger et al. (125).

The Smagorinsky model became more attractive again when Germano et al. (41) developed a method to calculate dynamically the local coefficient  $C_s$  from the actually simulated resolved scales by applying a test filter which is typically two times coarser than the one used to separate the SGS from the GS. This dynamic model gets the subgrid scale contributions down to zero in those areas in which the resolution allows for direct simulations. In principal, this dynamic calculation of the instantaneous model coefficients can be combined with any SGS model. An analysis of the dynamic Smagorinsky model on anisotropic grids was performed by Scotti et al. (111). An anisotropic dynamic model in tensor form was developed by Abbà et al. (1) to improve the accuracy in channel flows near walls.

Further improvements can be achieved by introducing backscatter of kinetic energy from the small scales to the large scales, which was found to occur within the buffer layer in plane channel flows, e.g. by Piomelli et al. (101), or in stably stratified fluid layers, e.g. by Kaltenbach et al. (63). It is argued that in such cases a stochastic backscatter is necessary (82). There exist proposals for backscatter models in (56),(74), (83),(109). Successful applications of dynamic SGS models are numerous, e.g. those by Breuer & Rodi (14) and by Jones & Wille (62). There seem to occur some problems with coarse grids and large Reynolds numbers, see Sullivan & Moeng (117), and with transitional flow in flat plate boundary layers, see Voke et al. (123). Combinations of dynamic models with backscatter also exist, e.g. the model by Mason included in the code comparison of Nieuwstadt et al. (96). Such comparisons as well as the one in (62) and especially the experience by Breuer (11) with applications to the flow past a cylinder indicate that for practical high Reynolds number LES the influence of changing the type of a model is considerably less than of changing the spatial discretisation scheme.

#### 4.2.2. Transport equation based SGS models

More sophisticated first order models aim to provide some decoupling of the subgrid scales from the local grid scales in time or in space. Examples for one-equation models based on a transport equation for the kinetic energy in the subgrid scales are the one for channel flows at high Reynolds numbers (108), or that

for moderate Reynolds numbers including rough walls (53). Those authors use the theory of isotropic turbulence to calculate all local coefficients of their models. The calculation accounts for the local grid details including the actual finite difference approximation, the resolution capability, and the grid anisotropy. Such one-equation models allow to treat backscatter in a natural manner. Corresponding methods and tests are given in Ghosal et al. (43) and Davidson (25).

Full second order models do not apply eq. (7,8), but solve modelled transport equations for the cross-correlation terms. Such a model was developed and used by Deardorff (28). From the knowledge and computing capabilities available at that time he concluded that full second order SGS models do not give any advantage over simpler models. Just recently Fureby et al. (39) reconsidered a simplified version of Deardorff's model. Contrary to Deardorff they found major advantages of their second order model regarding the treatment of turbulence anisotropy in channel flows near walls. Their promising model does not need any information on the distance to the next wall.

A good compromise between first and second order modelling was found e.g. by Schemm & Lipps (104), Sommeria (116), and Schmidt & Schumann (105). They use algebraic simplifications of the second order equations together with a one- or two-equation model. These models, which reproduce meteorological flows quite well, are the counterparts to the so-called algebraic stress models, ASM, in Reynolds modelling.

#### 4.2.3. Subgrid scale heat flux models

The turbulent subgrid scale heat flux, eq. (8), is often calculated by using a turbulent Prandtl number  $Pr_{sgs}$  for the subgrid scales:

$$a_i = \nu_i / Pr_{sgs} \quad (10)$$

The values to be used for  $Pr_{sgs}$  are about 0.4, see e.g. (20),(28),(53). The values have to be modified slightly when e.g. backscatter models are included (109). The small value means that at small scales the transfer of heat is much more intensive than that of momentum. It is found for fluids with molecular Prandtl numbers of about one that modifications of the value of  $Pr_{sgs}$  do not change simulation results too much for forced flows at large Reynolds numbers (53). This approach is often used in meteorology, e.g. by Deardorff (27), Moeng (86), and also in applications of LES to technical flow problems, e.g. by Ciofalo & Collins (22), Neto et al. (94), Murakami et al. (91), by Voke & Gao (122), by Braun & Neumann (12), and by Grand et al. (44).

More complicated subgrid scale heat flux models also exist, similar to the first order and second order SGS shear stress models discussed above. The conclusions on the necessity and relevance of these models are the same, because all these investigations, except (39), (108), were performed for flows with heat transfer.

Careful comparisons of four codes using different sub-grid scale models and different numerics show that their results agree quite well for simple meteorological conditions (96); this points to the robustness and universality achieved currently with the method of LES at least for simple meteorological conditions.

The influence of the type of fluid, i.e. the molecular Prandtl number  $Pr$ , needs special discussion. The form of the spectra of temperature fluctuations at small scales strongly depends on the Prandtl number. For highly viscous fluids, this is for large values of  $Pr$ , the temperature spectra extend to much smaller scales than the velocity spectra, whereas fluids with small values of  $Pr$ , e.g. liquid metals, effectively filter off small scale fluctuations so that the smallest scales in the temperature field are much larger than in the velocity field. This behaviour could be treated by applying the dynamic filtering of Germano to the heat flux model, see e.g. (20) and with the self-adaptive subgrid scale heat flux model of (45). The latter uses a one-equation model in combination with the extended theory of (108) to calculate the model coefficients by using the theory of isotropic turbulence and the local value of the time averaged dissipation  $\langle \varepsilon \rangle$ . This model and the calculation of the coefficients were successfully used to perform simulations for forced convection in plane channels and annuli at Reynolds numbers from some  $10^4$  to some  $10^5$  and for fluids with Prandtl numbers from 0.007 to 7 (45),(49). This theory, applied to the SGS shear stress and heat flux models, is also used to judge in advance on the suitability of grids for adequate direct simulations (48),(49). This SGS model was extended for stably stratified flows by applying modified length scales, Seiter (112).

#### 4.2.4. Other subgrid scale treatment

The SGS models discussed above are applied in physical space. Models were also developed for spectral methods; they model the subgrid scale contributions in wave number space. Such models, like that by Chollet & Lesieur (19), are based on the Eddy Damped Quasi Normal Markovian (EDQNM) theory by Kraichnan (71). Because of their complexity from the point of view of an engineer these models are not widely used. Such models were e.g. applied to study the diffusion in isotropic turbulence (77) or by Naitoh & Kuwahara (93) to study the flow in a cylinder of a piston engine. A version for applications in physical space is the structure function model by Normand & Lesieur (97). The selective structure function model is applicable to highly intermittent, transitional, and separated flows, and the filtered structure function model to spatially developing flows. These models, which were also extended for irregular grids, are now more often used; applications are given in the overviews (44),(76).

All subgrid scale models, which were discussed above, explicitly introduce physical assumptions to model the momentum and heat fluxes by the unresolved

scales. To minimise numerical diffusion one usually uses numerical discretisation methods in space which are of second or fourth order. There are also methods which do not involve subgrid scale models, instead the numerical scheme has sufficient numerical diffusion or damping to mimic the effective diffusion due to the sub-grid scales. In using third order upwind schemes, like the one introduced by (66), one can successfully simulate many turbulent flows without using SGS models, like the impinging wall jet by Muramatsu (92) and the flow around and through cars by Hashiguchi (58). Similarly Boris et al. (11) found that the Piecewise Parabolic Method (PPM) also has intrinsic SGS features. Of course, the numerical diffusion does not always sufficiently meet the requirements of the subgrid scales; therefore, all results gained from such pseudo-direct simulations have to be checked carefully.

## 5. BOUNDARY CONDITIONS

Formulating boundary conditions for DNS or LES is a more serious problem than with Reynolds models, because one needs time-dependent wall conditions and inlet or outlet conditions which account for realistic local turbulent fluctuations.

No-slip wall conditions and prescribed wall heat fluxes or surface temperatures can be discretised without further approximations when the viscous and conductive wall layers are resolved by the grid. Corresponding spatial resolution criteria were specified and tested from an engineering point of view (48),(49). To analyse terms of statistical models near walls from the results of direct simulations, much finer grids are required than the specified two to three mesh cells to be used in the viscous and conductive wall layers. At large turbulence levels and with coarse grids near walls, suitable time-dependent formulations of wall laws have to be applied. Methods for high Reynolds number flows are the one in (108) for shear stresses and in (53) for heat fluxes at different Prandtl numbers and wall roughness. Universal extensions for pure buoyant convection can hardly be determined (112). These approximations relate the instantaneous local shear stresses and heat fluxes to the velocity and temperature fluctuations in the next fluid mesh cell by using time-averaged wall laws. Therefore, this approach is only applicable to fully developed statistically stationary flow. The same restriction holds also for the two-layer model by Manhart & Wengle (81) which uses a power law velocity distribution. Other approximations were developed, but it turned out to give no significant improvement in practical applications (20).

Channels with an inlet and an outlet require specifications for all physical variables for every mesh cell on such a boundary at each time. Currently no sufficient theoretical tools are available to formulate such boundary conditions for realistic turbulent flows. Therefore,

periodic boundary conditions are applied in the mean flow direction when ever possible. When real inlet and outlet conditions have to be considered, approximations have to be chosen.

For the inlet, several procedures of different complexity were realised, depending on the physical problem to be considered. Surle et al. (118) used constant values at the inlet. Constant radial profiles from separate calculations with a Reynolds model were taken in (92). To get time-dependent inlet values Dai et al. (24) used constant values superposed by sinusoidal fluctuations, and Neto et al. (94) superposed fluctuations with white noise features. Some methods to access the tremendous problems with such conditions are discussed in a recent overview (89). When real turbulent inlet signals are required, the only available solution is to perform a separate DNS or LES for a periodic channel with roughly the required flow parameters and store the results for one plane perpendicular to the mean flow direction at each time step. These data are used as time-dependent inlet conditions. Realisations of this method are reported e.g. in (14),(91),(122). By analysing a turbulent plane jet the latter method was found superior to using artificial inlet conditions (125).

Approximations for the outlet are either to assume that all gradients normal to the outflow surface are zero. This works roughly with incompressible flows, see Schmitt & Friedrich (107). However, it might become problematic due to reflections in case of compressible flows. The more accepted method is to apply a convective outflow condition, like in (11), but serious problems were reported from applications to backward facing steps by Bärwolff et al. (3) and to mixing chambers by Moin & Kravchenko (88). Both apply additional buffer regions to decouple the upstream area from the distortions at the outlet. Non-reflecting new outlet conditions were developed (1).

## 6. NUMERICS

So far it looks like the progress of LES towards engineering applications would strongly depend on the availability of adequate subgrid scale models and boundary conditions. In fact, real retardation comes mainly from the numerics because one needs the combination of accurate discretisation and integration schemes in combination with large numerical efficiency, especially as regards to the solvers for the system of equations. The solvers are the dominant part which in complex geometries determine the computational costs. They are not discussed here, because they would require a separate careful evaluation.

Accurate discretisation and solution algorithms are required to solve the basic equations or the filtered equations including the respective SGS models in space and time. Of course, spectral schemes are very accurate, and are therefore used for simulations of the transition

from laminar to turbulent flow in channels, see e.g. Kleiser & Zang (70) and the comparison in (110). However, they cannot be applied to an arbitrary, complex geometry. For simple channels they are often used in combination with finite difference schemes, like in the models or applications in (69),(77),(86). Thus, for engineering applications one has to rely on finite volume or finite element based discretisations.

For spatial discretisation, mainly finite difference and finite volume schemes are used. They are efficient and flexible, especially for structured non-orthogonal grids (23),(14). Higher order schemes have been shown to need less nodes than lower order schemes to gain the same spatial resolution of the smallest scales (89). The order of the schemes must be even to have small numerical diffusion. The numerical diffusion must be much smaller than the diffusion introduced by the SGS model. This obviously holds only for fourth and higher order schemes, but the accuracy of the lower order schemes can be improved by using pre-filtering with a filter width of  $2\Delta x$  (88). Third order schemes are widely used in Japan; their inherent numerical diffusion mimics SGS features implicitly and without any control, see remarks above. They were recently extended to a multi-directional finite difference scheme for skewed flow (58). Among the upwind schemes the second order QUICK scheme has unacceptable strong diffusive features (14). Higher order upwind-biased schemes, which are designed to have reduced aliasing, are even worse than second order central schemes, Kravchenko & Moin (72). In comparing central and upwind schemes of several orders for the flow past a cylinder, strong influences of the scheme were found e.g. on the separation length and on the turbulence level (11). It is concluded that for an LES the numerical dissipation produced by a scheme is more crucial than its formal order of accuracy, and these influences are much stronger than those from using different subgrid scale models.

More efficient spatial discretisation in critical areas, e.g. in the layer near solid surfaces, is recently achieved with finite volume schemes by introducing local grid refinement methods. Deck (30) used it to resolve the details of the flow around a square cylinder and Fureby et al. (39) in the sublayer of a channel flow. Multi-block grids are realised in the pseudo-DNS which are extensively used in the Japanese automotive industry for the flow around cars, through the interior, or through the engine compartment (58). Moving multi-block grids are applied on curvilinear coordinates for pseudo-DNS of the vortex formation in a 4-valve piston engine by Meinke et al. (85). The step to use hybrid unstructured grids is also gone by Ducros et al. (33) in an LES of a pipe flow. Zonal grid embedding by using B-splines looks promising because it is of high accuracy order and it conserves energy even for incompressible flows, but it seems currently to require too much computational effort (88).

The finite element method is the most flexible, but less computationally efficient method to discretise spatially a complex flow domain. The large flexibility to concentrate the elements where they are needed lets one expect to get practically efficient and accurate simulations. The method was used with a Smagorinsky model for an unsteady wake behind a cylinder by Kato & Ikegawa (65). Special test filters were developed to make the method applicable with the dynamical model on parallel computers, and LES-suited mesh generators, see Jansen (61). An application of the finite element based multi-purpose code N3S to the square cylinder benchmark is evaluated in Rodi et al. (102).

For integration in time, schemes are required for the convective terms which are at least of second order. A DNS as well as a LES has to capture all resolved fluctuations in time, because one does not want to filter off the highest spatially resolved frequencies. Therefore, usually all convective terms are treated by explicit methods, like by the Euler-leapfrog method or the Adams-Bashforth scheme. The Courant stability criterion ensures a sufficient resolution in time.

Nevertheless, there are reasons to use implicit schemes for some terms. With DNS one uses fine grids near walls, but there the viscous terms become dominant over the convective terms. When the diffusion terms are treated explicitly, their stability limit strongly reduces the time step width. This is avoided by using implicit time integration of the diffusion terms like the Crank-Nicholson scheme (69). The same arguments hold for the energy equation, especially with liquid metals; there, it is only the implicit treatment of the thermal diffusion which enables such simulations on current computer systems (126). Another example is the implicit treatment of terms with azimuthal transport in pipe flows because the azimuthal grid width goes to zero near the axis, whereas the others remain finite and determine the resolved scales, Eggels et al. (34). Sometimes even the convective terms are treated implicitly in LES when one accepts to lose the highest resolvable frequencies only locally in those areas in which the grid is locally refined (21),(89).

## 7. SOME REACTOR RELATED SIMULATIONS

As in other research and application fields, there were large expectations on the possibilities of DNS and LES growing up in nuclear thermal hydraulics. From a methodological point of view and from the rapidly increasing computational power, one could expect around '90 that it should be possible and reasonable to modify newer multi-purpose codes to analyse prototypical three-dimensional time-dependent engineering problems by means of LES (51). And after first promising results in several groups, in '95 even expectations were formulated that this could also be a method to access two-phase problems, Hassan et al. (60).

### 7.1. Applications of increasing complexity

#### 7.1.1. Channel and bundle flows

Going back to the roots of large eddy simulation in Europe, one should remember that Schumann started his developments in 1970 in the Institute for Reactor Development at the Nuclear Research Centre Karlsruhe, now Institute for Reactor Safety. After having set up a model and code basis, we were rather early using our first LES, and later also our DNS, to investigate problems motivated by actual nuclear applications. Of course, for a long time these investigations were bound to simple geometries. E.g., LES were used to study pressure fluctuation induced forces on the inner rod in axial forced flow through an annulus, to study anisotropic eddy diffusivities in channels with secondary currents or spanwise thermal inhomogeneity, and to clarify the principal mixing capabilities in a strongly buoyancy influenced vertical flow in the downcomer of the HDR-reactor. Combined LES of the momentum field and DNS of the thermal field helped to improve eddy conductivity concepts for liquid metal forced convection in channels. Compilations and discussions of this work are given in (49),(110).

Recent LES in literature are for increasing geometrical complexity. By using an LES for two parallel rectangular channels coupled by a narrow gap Biemüller et al. could show experimentally and by LES, coherent periodic vortices travel along the gap causing these systematic fluctuations (10). Investigations for heat exchanger tube bundles in cross-flow are performed by Hassan & Lee (59). For single pins they determined the spectra of the drag and lift forces from 2d and 3d simulations by using the GUST code. Recent simulations for bundle flows and comparisons between RANS models and LES are presented at this conference, Laurence (73).

#### 7.1.2. Convection in pools

The direct numerical simulations in the nuclear field concentrated, as in other fields, on providing data for statistical turbulence models, here especially for buoyant convection. The first applications were motivated by core catcher investigations for Fast Breeder Reactors (47). Results of recent simulations for internally heated fluid layers will be discussed later. The simulations for Rayleigh-Bénard convection first focused on learning to perform adequate DNS (48), because this convection type is experimentally well investigated, in contrast to the internally heated fluid layer. Later simulations aimed at investigating and improving statistical turbulence models for pure buoyant convection. The temperature variance equation was analysed for air (54) and for sodium (129), the transport equation for the destruction of temperature variances for both fluids (130), and the heat flux budget (127). The terms in the kinetic energy equa-

tion were analysed (128) and the differences of the pressure transport in Rayleigh-Bénard and internally heated convection layers (132). Some of the analyses resulted in proposals for model improvements, like for the dissipation by Ye et al. (134), some were realised in the multipurpose code FLUTAN (16). Turbulence data for calibration of second order turbulence models are also provided by pseudo-direct simulations with FLOW-3d for a cubical box (98).

### 7.1.3. Thermal striping

Meanwhile, multi-purpose codes are available which are extended for LES. Thus, the geometrical complexity of the investigated problems increases. A series of separate effect analyses for isolated problems from complex nuclear flows are performed with the TRIO-VF code and variants of the structure function model (44),(76). These investigations mainly concentrate on the thermal interaction of temperature fluctuations with solid structures (thermal striping). This is a serious problem in large reactor systems because it may limit the lifetime of components by thermal fatigue. Coherent vortices are simulated in the mixing layer behind a backward facing step in (94). Fallon et al. (35) investigate the influence of thermal stratification on the formation or suppression of these vortices. A jet impinging on a wall is investigated with the Smagorinsky model (122) and with the aid of the third order upwind scheme with the AQUA code (92). The mixing in round jets as a model to mimic the exit from single subassemblies at the core outlet is investigated with the filtered and selective structure function model with the TRIO-VF code and a special purpose code, Urbin et al. (120). Good agreement between the results of both codes was found except for steeper spectra from TRIO, because with this code coarser grids have to be used. The transfer conditions of special model experiments with model fluids to sodium conditions was also analysed with TRIO, Tenchine & Moro (119), and good agreement between measured and simulated temperature fluctuations was found.

For a more quantitative analysis of thermal striping it is necessary to treat the turbulent convective heat transfer coupled with the thermal conduction in the solid structures. This is achieved in the applications by Ushijima & Tanaka (121) to the upper plenum flow including the instrumentation plug, in the applications of the finite element code N3S using a dynamic Smagorinsky model to the flow in the thermal barrier in a pump shaft (2), and in the applications of the STAR-CD code using unstructured grids and no SGS model to the flow through a T-junction, Simoneau et al. (114). Of course, with this task LES is superior to any RANS based calculation because the dynamics of interest are a result of the large scale structures and are without additional modelling a direct outcome of a simulation.

Thermal striping investigations for the upper plenum with its complex internal structures are currently at the limit of the computational possibilities. The simpler

model experiment CORMORAN was investigated with TRIO with the  $k-\epsilon$  model and with the structure function model (118). This holds also for the upper plenum simulation for the PHENIX reactor, in which every sub-assembly exit was resolved with a grid of 233,000 cells, except that the selective structure function model is applied (103). The time mean results of the statistical and LES modelling types agree well, but the LES offers additional data on the temperature fluctuations as they are necessary for the designer.

### 7.1.4. Two-phase flows

Two-phase or multi-phase flows are those with the highest geometrical and physical complexity. In nuclear engineering and safety they occur frequently, in particle or gas transport in fluids, in phase change phenomena by freezing or boiling, in stratified liquid pools with free surfaces or swimming crusts, up to the challenging problem of jet fragmentation and droplet formation combined with the rapid heat transfer and phase change which may lead to vapour explosions. There is work going on to improve current methods or to develop new ones treating the interfacial phenomena explicitly.

Some applications, in which turbulence has to be included, belong to the area of flows with homogeneously distributed separated phases. The common tools for such flows are multi-field multi-fluid models assuming interpenetrating fields. Turbulence modelling is widely done by zero-dimensional physical models; this means, the interfacial momentum, heat, and mass transfer is modelled by friction factors, Nusselt numbers, and Sherwood numbers respectively. This modelling becomes inadequate at higher void fractions when the topology of the phases develops towards heterogeneous distributions. Similarly, the treatment of turbulence at large scale interfaces is up to now included only in form of such simple models. The use of standard RANS based turbulence models is hindered by the poor knowledge basis we have on turbulence in two-phase flows. Thus, progress is mandatory and there is a good chance for the DNS and LES community to fill this tremendous gap and to provide methods for detailed local analyses in multi-phase flows. However, as the problem is challenging, we are still at the begin of a long development, and the following literature does not always belong to the nuclear field.

Simulations for dispersed phases started early in history of LES with studies of the transport of passive particles in channels, Deardorff & Peskin (29). Recent work on particle dispersion in channel flows is e.g. by Dehning (31) using a one transport equation subgrid scale model. Now, somewhat more complex flows are possible and Chen & Pereira (17) study with the structure function model the particle dispersion in a plane mixing layer. Such numerical investigations require DNS or LES because of the flow instabilities. Similarly, Maxey & Chang (84) treat micro-bubbles passively, this

means the bubbles have no consequences on the velocity field. The authors study by DNS and an Eulerian treatment of the bubbles how small scale vortices of isotropic turbulence interact with the bubbles and modify their mean rise velocity.

Simulations of turbulence at free interfaces is a growing subject. The interfaces in the first simulations for sheared and unsheared flow are kept plane, see Banerjee (5) and Lombardi et al. (79). The investigations concentrate on the turbulence statistics in the boundary layers near interfaces and on the mechanisms causing these statistics. For the sheared cases situations are found similar to the ones near solid walls with ejection and sweep cycles, whereas for unsheared cases long living roughly two-dimensional upwellings are observed. Work on wave formation is discussed at this conference, Banerjee (6).

Developments of methods for direct and large eddy simulations of turbulent bubbly flows are ongoing in the authors team. The basic ideas of LES are applied to the turbulence in the liquid phase and also to the phase topology in dispersed two-phase flows. Thus, in a separated phase treatment the large scale interfaces will be resolved and calculated by adequate numerical schemes, whereas the small scale part will be treated by an interfacial area concentration equation. Accordingly, the interfacial exchange terms consist of resolved parts and subgrid scale parts. In a first step we consider DNS and LES of bubbly flows in simple geometries. Finally, the method will be implemented in a code for technical applications. This work is basing on supporting experiments on statistical and local turbulence in bubbly flows, Cherdron et al. (18).

So far we saw that DNS and especially LES is increasingly supplementing research engineers in the nuclear field in those areas in which statistical models have serious problems with accuracy, reliability, prediction capabilities, or even fail from a methodological point of view. This holds mainly for three-dimensional time-dependent flows in complex geometries and with local instabilities. All applicators state that the larger computational expense for LES is compensated by the gain of more information from the simulations.

## 7.2. Experiences and open problems

The subgrid scale models for nuclear flows, especially in large components, should be as universal as possible. Existing models reach a high degree of perfection at low Reynolds numbers, but at Reynolds numbers and flow types of interest it is found necessary to choose certain models. E.g. Voke et al. (123) prefer the Smagorinsky model with manually adapted local coefficients for a transitional stratified flat plate boundary layer, and Fallon et al. (35) prefer the selective structure function model for a backward facing step. Barsamian and Hassan (7) decided to develop a new modelling of the filtered cross-products for cross-flow through heat ex-

changer bundles. Thus, models which have no wall distances as length scales, as the one in (39) are not yet common and need further assessment.

The wall condition formulation should not depend on the type of flow. For high Reynolds numbers we still have to use modelled wall conditions in which the wall shear is approximated instead of using the no-slip condition. All wall laws hold only for fully developed statistically stationary forced flows. Therefore, wall approximations cannot be applied to separated flows (35). On the other hand, there is a small sensitivity against the type of wall condition applied even in geometrically determined flows (21). If the tendency towards transport equation subgrid scale models holds on, the problem with the wall conditions will grow because wall conditions for higher order models can hardly be formulated. Thus, a solution can only come from the numerical side, i.e. to use efficient discretisation methods, e.g. with local grid refinement or with unstructured grids, which allow to resolve the viscous and thermal wall layers.

Finite channels with a turbulent inlet flow need meaningful time-dependent turbulence data at the inlet plane. This is found in many investigations to be a sensitive requirement, e.g. in (113),(114),(125). Existing approximate methods do not seem to get rid of the problem (89). Thus, the only possible, but expensive solution is still to use simulation data from a separate simulation with periodic boundary conditions for a similar flow. The outlet conditions are less serious, but need some more improvements.

The spatial discretisation schemes should show very small numerical diffusion and should allow for an accurate and efficient discretisation of the geometry. Regarding numerical diffusion and accuracy, many of the single-purpose simulation codes reach a very high academic standard, but this cannot be expected from the robust multi-purpose codes. The quite common QUICK scheme turns out to be inappropriate to LES; it damps out all turbulence (11). And second order central schemes do not always guarantee sufficiently small numerical diffusion, as it is shown by the pseudo-direct simulations with the STAR-CD code (114). So, one has to expect that the coefficients of subgrid scale models depend on the discretisation and integration schemes actually used in the codes. On the other hand, the large flexibility and accuracy to correctly reproduce complex geometries is an advantage of the new code generation with unstructured grids. Convincing examples are those by Simoneau et al. (114) who use STAR-CD for a T-junction, those first demonstrations of the capabilities of TRIO\_U, but obviously in the structured mode, by Barsamian et al. (9), or those with the finite element code N3S (2). Proceeding to unstructured grids needs special care with the widely used dynamic model because extended test filters have to be applied (61).

Time integration schemes should be applied so that the Courant number is below one in most areas, because otherwise spatially resolvable high-frequency fluctuations



are filtered out. Courant numbers slightly above one may only be acceptable locally, where grids are strongly refined (21). As implicit time integration schemes are found in most multi-purpose codes, it is left to the user to choose the adequate Courant number range; the large damping found with the STAR-CD code may come from allowing Courant numbers up to ten (114).

The solution algorithms and solvers used in such codes are optimised for large robustness, often at the expense of efficiency. On the other hand, an LES needs about the same spatial discretisation as a good RANS calculation, but it needs more time steps (103). With the current computer generation we are at the limits of what can be realised with RANS models. Thus, many users try to simplify the problem when it shall be investigated also by LES.

Using coarser grids is a dangerous simplification, because multi-purpose codes have non-negligible numerical diffusion. This may lead on coarse grids to time-independent results, as observed with the first T-junction calculations (113). A reduction of the problem to two dimensions is also found; e.g. the cross-flow simulations for heat exchanger bundles with the GUST code are performed in 2d (8). Such simulations should be interpreted with special care because 2d and 3d turbulence behave different; e.g., 3d treatment is necessary even when the mean flow stays rather 2d in the transitional flow behind a circular cylinder (11).

Symmetry is also sometimes assumed as a measure to save CPU-time. All upper plenum simulations were performed with azimuthal symmetry, e.g. with 60° symmetry (121), 90° symmetry (103), and 180° symmetry (119). From these simulations, as well as from the results for the flat plate boundary layer (123) it is concluded that the symmetry assumption leads to insufficient results. The only rule which can be given here is, the macroscopic length scale of the flow must be much smaller than the periodicity or symmetry length chosen (48),(49).

## 8. CONTRIBUTIONS BY DNS TO COOLING OF CORE MELTS

In giving some example results we come back to the classical field for DNS applications in simple geometries, i.e. the analysis of turbulence data for flows or for parameter ranges for which no other sources of data are available to improve statistical turbulence models.

### 8.1. Problem

Single-phase convective cooling of an internally heated fluid was intensively investigated by model experiments in the seventies for fast breeder reactors; now, for new water cooled reactors, the parameter range has to be extended to larger Rayleigh numbers  $Ra = g\beta QD^5 / (\nu\alpha\lambda)$  and other geometry. In addition,

detailed turbulence data are needed to provide adequate computational tools. An overview of experiments is given in (99). The experiments mainly aim on determining the heat fluxes across the boundaries, dependent on Rayleigh number and surface position. Temperature data are provided seldom; turbulence data were only determined by Kikuchi et al. (67),(68) for the untypical case with an adiabatic lower boundary.

The first consistent set of turbulence data for this flow were provided by direct simulations for a periodic channel with small horizontal extensions (47),(49). They show that the lower 80% of the layer is stably stratified and about half the height therein is dominated by a counter gradient heat flux. Thus, statistical turbulence models using gradient assumptions are not adequate for this type of flow; this was also confirmed by practical applications of such models by Dinh & Nourgaliev (32). Turbulence data for calibration of second order turbulence models are also provided by those simulations, as well as by pseudo-direct simulations with FLOW-3d for a cubical box (98). The earlier simulations are verified by a simulation in a channel with large horizontal extension (50). These results, and those by the LES in (112) confirm that this flow shows the seldom feature of a decreasing macroscopic wavelength with increasing Rayleigh number. This allows for a reduction in the size of the computational domain and consequently for finer grids at large  $Ra$ .

Recent DNS reach Rayleigh numbers as high as  $Ra=10^9$ , and are therefore suited to analyse higher order turbulence models. The mechanisms in the flow are investigated in (106) and their interaction with the pressure diffusion in (132). The following analysis of the k-equation is taken from the detailed statistical analyses in (133). Most of the statistical results of this simulation series will be included in the WWW databank (131).

### 8.2. Case specifications

The convection in an internally heated fluid layer is characterised by the Rayleigh number  $Ra = Gr \cdot Pr$ , the Prandtl number, and the Damköhler number  $Da = QD^2 / (\lambda \Delta T_{max})$ , where  $Q$  is the specific internal heat source and  $\Delta T_{max}$  is the maximum temperature difference between fluid and wall. For normalisation we use the channel height  $D$ , the velocity scale  $u_0 = (g\beta \Delta T_{max} D)^{1/2}$ , and the temperature scale  $\Delta T_{max,0}$ . As a result we get the non-dimensional equations (1) to (3) in which the dimensionless heat source is equal to  $Da_0 / (Pr Gr^{1/2})$ . To get the non-dimensional temperature maximum close to one,  $Da_0$  is determined from the energy balance  $Da_0 = Nu_b + Nu_t$ , by initial guesses for the Nusselt numbers at top and bottom. Here we consider the model fluid water,  $Pr=7$ , in the fully turbulent regime at  $Ra=10^8$ . Following experimental correlations for  $Nu$  we choose  $Da_0=35$  for this Rayleigh number. The bottom and top wall are kept at Temperature  $T_w=0$ .



Sufficient experience and some experimental information is available to specify adequate grids and to validate the results (49),(50). Nevertheless, an extensive discretisation study was performed investigating all spatial parameters including theoretical expressions for smooth vertical grid width distributions (106). We use  $X_{1,2} = 4$  for the horizontal extensions of the control volume to which periodic boundary conditions are applied. The numbers of mesh cells are  $N_{1,2} = 160$  and  $N_3 = 55$ . The vertical grid widths are  $\Delta x_{3,w} = 0.0057$  and  $\Delta x_{3,cb} = 0.012$ .

The simulation with the computer code TURBIT was started on a coarser grid from artificial initial values with zero velocities, with a roughly trapezoidal vertical mean temperature profile, and with random temperature fluctuations superimposed to it. When the simulation reached a steady state in a statistical sense, the results were interpolated to a finer grid. After repeating this procedure, the simulation was continued on the finest grid to obtain results for a certain time interval in which the flow is statistically stationary and which can be used for statistical analysis.

### 8.3. Flow structures

The temperature profile has the minima at both walls and a maximum near the upper wall. This indicates the following mechanisms: The fluid is stably stratified throughout the channel height except for the thin upper layer with cold, heavier fluid. From this layer plumes or thermals develop due to Rayleigh-Taylor instability which move cold fluid into the heated core.

The isosurface for a temperature value of  $T = 0.88$  is given in Fig. 1 for an arbitrary time. It shows in only  $\frac{1}{4}$  of the computational domain the principal phenomena and intermittent character of this flow.  $T = 0.88$  is found very near the upper cold wall, because the boundary layer is very thin there, and in a larger distance to the lower cold wall, because the boundary layer is thick there. From the temperature profile it is known that hotter fluid is between both isosurfaces. The upper and lower isosurfaces are connected by some plume-like structures in which cold fluid is very fast plunging downward. Plumes with downward movement concentrate in knot-like structures. The plumes are horizontally connected by thin spoke patterns with slower fluid. The spoke patterns exist only in a thin near-wall layer. The colour code marks the values of the dynamic pressure. The pressure values are on average larger near the upper wall; there, negative deviations are found in the spoke areas where e.g. larger negative vertical velocities occur. They are smaller on average near the lower wall; there positive pressure deviations occur where the larger negative vertical velocities exist, i.e., where the plumes plunge down. From such figures one can deduce conclusions on the mechanisms forming the cross-correlations in the transport equation models (132).

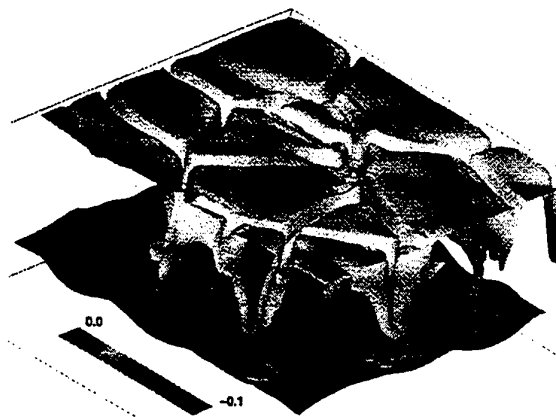


**Fig. 1:** Isosurface for instantaneous temperature  $T = 0.88$ , colour code for dynamic pressure,  $Ra = 10^8$ . One quarter of horizontal cross-section.

The structures found in this simulation have also been found in our earlier simulations and are verified for smaller  $Ra$  by comparisons to experiments e.g. in (49),(50). The macroscopic length scale is determined by the typical horizontal extension of the cell-like structures or by the distances between the knots. Figure 1 makes obvious that the cell size is much smaller than the computational domain and that the flow will not be limited by the horizontal size of the periodic domain.

The dynamics of this flow is analysed for several  $Ra$  by means of movies. The spoke pattern like structures are attracted by the few dominant plume areas. By withdrawing spokes, small cells contract to knots and remaining cells are enlarged. Within these calm areas new spokes develop due to local Rayleigh-Taylor instabilities. They grow to slice like spokes, match with other spokes, and divide existing larger cells. The plumes don't appear regularly, but some plume areas move slowly in the horizontal direction. Some plumes merge and may form new knot-like plume centres. The dynamics of the flow found here is comparable to that found at a smaller Rayleigh number (50), except that at larger  $Ra$  more and more plumes detach from the wall, degenerate to thermals, and do not penetrate deeply into the lower boundary layer (133).

### 8.4. Balance equation of turbulent kinetic energy

The standard turbulence model in most engineering codes is any variant of a  $k-\epsilon$  model. It is a first-order model because it is based on eddy diffusivity assumptions for turbulent shear stresses and heat fluxes. As we already saw, the eddy conductivity concept is not adequate for the thermal energy equation, we want to study here the diffusion assumptions in the kinetic energy equation. For fully developed convection in an infinite horizontal fluid layer, the transport equation for  $k = 1/2 \langle u'u' \rangle$  reduces to:

$$0 = \frac{\partial}{\partial x_3} \left[ - \left\langle u_3' \frac{u_3' u_3'}{2} \right\rangle - \langle u_3' p' \rangle + \frac{1}{\sqrt{Gr}} \frac{\partial k}{\partial x_3} \right] + \langle u_3' T' \rangle - \frac{1}{\sqrt{Gr}} \left\langle \frac{\partial u_3'}{\partial x_3} \frac{\partial u_3'}{\partial x_3} \right\rangle$$

$$D_k \qquad G_k \qquad \varepsilon$$

Here  $D_k$  denotes the diffusion of  $k$ , consisting of a turbulent part  $D_{k,t}$  and a molecular part  $D_{k,m}$ . Responsible for the production  $G_k$  is the buoyancy force represented by the turbulent heat flux. The dissipation is  $\varepsilon$ . The prime  $Y'$  for any variable  $Y$  denotes in this chapter deviations from the time mean value  $\langle Y \rangle$ , i.e. the fluctuation in the Reynolds sense.

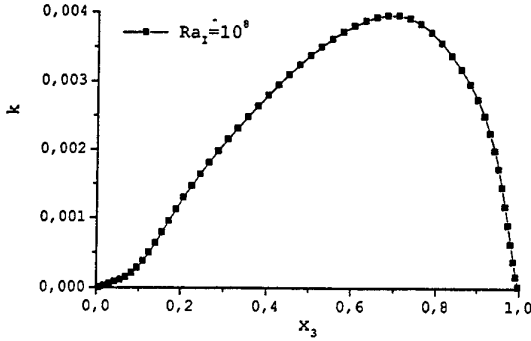


Fig. 2: Vertical profile of the kinetic turbulence energy,  $Ra=10^8$ .

The vertical kinetic energy profile analysed from the simulation results shows an increase from the lower wall at  $x_3 = 0$  to a wide maximum value at about 70% channel height, followed by a rapid decrease to the upper wall at  $x_3 = 1$ , Fig. 2. The position of the maximum is below the one of the heat flux maximum, which is contained as the production term in the analysed energy budget, Fig. 3.

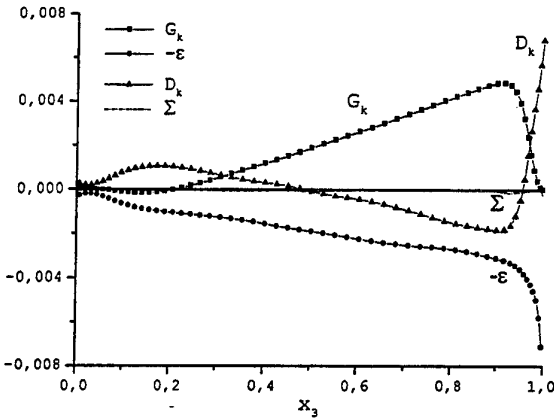


Fig. 3: Terms in the  $k$ -equation,  $Ra=10^8$ .

The production is zero at both walls, is positive and increasing in the upper part of the channel, and is negative in the lower part of the channel. The dissipation is increasing throughout the channel, forming a sharp peak next to the upper wall. There are only two vertical positions where local equilibrium exists; elsewhere, the diffusion term redistributes the energy. Next to the upper

wall it has completely to balance the dissipation. As all terms are analysed independently, the small value of the out-of-balance term  $\Sigma = G_k + D_k - \varepsilon$  is a measure for the accuracy of the analysis and indicates that the flow is sufficiently developed.

Terms that have to be modelled in the  $k$  equation are the cross-correlations in the diffusion term and the dissipation. Here we consider closure assumptions for the diffusive transport. The velocity triple-correlation is the dominant one, Fig. 4; it is large and has large gradients. The pressure velocity cross-correlation is comparably small and has a large gradient only next to the upper wall. The areas in which the pressure correlation is positive or negative are consistent with the discussion of Fig. 1. In contrast to this result, the turbulent diffusion in Rayleigh-Bénard convection is dominated by the pressure diffusion; the reasoning is discussed in (132). Both terms change sign at different positions and can therefore not be modelled together as it is usually done.

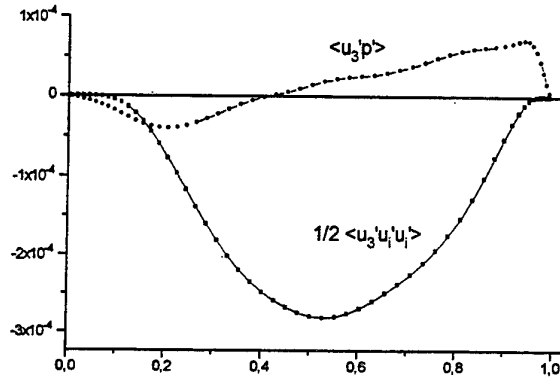


Fig. 4: Terms from turbulent diffusion  $D_{k,t}$  for  $Ra=10^8$ .

The model commonly used for closure of turbulent diffusion in the  $k$ -equation is:

$$- \left\langle u_3' \frac{u_3' u_3'}{2} \right\rangle - \langle u_3' p' \rangle = \frac{\nu_t}{\sigma_k} \frac{\partial k}{\partial x_3} \quad (11)$$

where  $\nu_t$  is the turbulent diffusivity for momentum calculated from the standard  $k$ - $\varepsilon$  model,

$$\nu_t = C_\mu k^2 / \varepsilon \quad (12)$$

and  $\sigma_k$  is a turbulent Prandtl number for kinetic energy. In analysing the right hand side of equation (11) from the simulation results we use the common coefficients  $C_\mu=0.09$  and  $\sigma_k=1$ . In considering the sign, the left hand side of eq. 11 shows downward directed energy fluxes for the lower 85% of the channel height and upward directed fluxes for the upper 15%, Fig. 5. As the energy maximum is found in Fig. 2 to be at 70% height, a counter-gradient flux occurs between 70% and 85%. Indeed, the modelled term deviates qualitatively in this area from the correct right hand side values. Quantitatively, both curves deviate drastically: the cross-correlations reach values beyond  $10^{-4}$ , the model reaches values somewhat above  $10^{-6}$ . Drastically corrected values of the turbulent Prandtl number would be required to

correct for this quantitative difference, but such a measure is of course not meaningful.

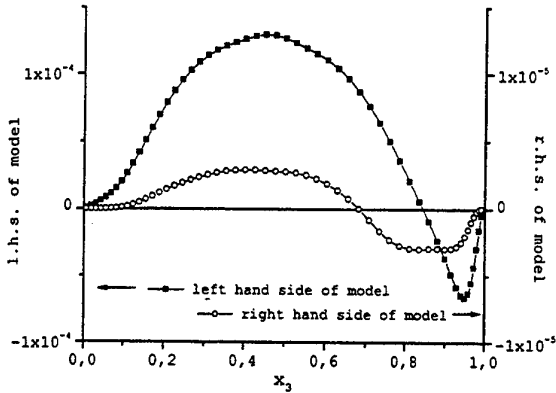


Fig. 5: Left and right hand side of the diffusion model eq. 11,  $Ra=10^8$ .

From the temperature profile it is known that using eddy conductivities is not practicable with this partially stratified convection; from the  $k$ -budget it follows that also simple gradient diffusion concepts fail to model the turbulent diffusion of  $k$ . As a consequence one tends towards second order closures, but there gradient diffusion is used again for closure. At least for the turbulent heat flux equation we already showed that those closure terms are also problematic (133). The relevance of these conclusions has to be checked by careful practical applications of such models.

## 9. CONCLUSIONS

The methods of direct numerical and large eddy simulation are powerful tools to analyse turbulent flows in detail. With increasing progress in numerical methods and with the rapid growth of the computational power, the methods become more attractive and applicable to a wider community. In nuclear reactor research and engineering the methods are nowadays used for similar tasks as in other disciplines, but they may be of different importance.

The DNS method is used in fundamental research to study mechanisms in certain flows. Here, in the nuclear field, we have sometimes to rely on numerical methods because the fluids, like liquid metals, are scarcely accessible for local measurements. DNS is also used for the determination of turbulence statistics to develop special features of statistical turbulence models. The core melt investigations are an example for a fluid of comparable limitations; so DNS is the only method which up to now could contribute reliable and detailed data to the necessary improvements of turbulence models. Results of such simulations were also discussed in this paper. DNS is also a data source to improve existing and to develop new subgrid scale models for low-Reynolds number flows.

The large eddy simulation is the method to access high Reynolds or Rayleigh number flows. Usually, in switching over from Reynolds models to LES, one aims at increased accuracy, at better predictability, and sometimes also at using the time-dependent features to study flows with instabilities. In the nuclear field full advantage of LES is taken by applying it intensively to the thermal fluid-structure interaction problem. Conventional theoretical methods rely heavily on input from special purpose experiments, whereas LES produces the temperature fluctuation data required for thermal fatigue analyses without any additional modelling. In this context we find realisations of the method in multi-purpose codes and recent impressive applications to complex geometries like to the upper plenum of a large reactor with internal structures.

Two-phase or multi-phase multi-component flows are a challenge to any numerical model. Again, natural features of LES could simplify the physical modelling of the geometrically and physically complex flow. Ongoing developments are related to fundamental aspects of the flow at interfaces and to the interface-turbulence interaction. Work on this topic is of tremendous interest, but we are far from having the methods and tools available to access technical problems right now.

The increasing importance of LES in nuclear applications does not mean that the existing modelling is ideal. There are a number of accurate subgrid scale models for low-Reynolds number flows, like variants of the dynamic model or the structure function model, but when changing from one flow type to another, other models have still to be selected. Existing models need to be improved and assessed for high Reynolds number flows, e.g. to be independent on the wall distance and to remove the turbulent Prandtl number problem. There is obviously a new tendency towards transport equation models. Existing wall conditions allow only for rough approximations; they fail e.g. for separated and purely buoyant flows. A solution may come from the numerical side with the ability to resolve the sublayers by local grid refinement or by unstructured grids. Turbulent inlet conditions still remain expensive, because they can only be provided by separate periodic simulations. Here the community should form an adequate data base. Second order spatial schemes are academically not accepted, but they are standard in many codes for complex geometries. The robust upwind-schemes turn out to be inadequate for LES. The progress in numerics, especially in the efficiency of the solvers, made it possible to widely apply LES methods in multi-purpose codes and to investigate geometrically complex flows. The number of nodes which can be used is still below what is needed. The trend towards finite element and unstructured grid discretisations may help to save computing effort and will accelerate the trend towards practical applications of LES in engineering.

## REFERENCES

- (1) Abbà, A., Bucci, R., Cercignani, C., Valdetaro, L., 1995. New Variants to the Dynamic Subgrid Scale Model. *Small-Scale Structures in Three-dimensional Hydrodynamic and Magnetohydrodynamic Turbulence*, Ed. M. Meneguzzi et al., Springer, 231-237.
- (2) Archambeau, F.D., Laurence, D., Martin, A., Maupu, V., Pot, G., 1997. Refined Turbulence Modelling for Power Generation Industry. *J. Hydraulics Research* **35**, 749-771.
- (3) Bärwolff, G., Wengle, H., Jeggle, H., 1996. Direct Numerical Simulation of Transitional Backward-Facing Step Flow Manipulated by Oscillating Blowing/Suction. *Engng. Turbulence Modelling and Experiments* **3**, Ed. W. Rodi, G. Bergeles, Elsevier, 219-228.
- (4) Baumann, W., Carteciano, L., Weinberg, D., 1997. Thermal Propagation Effects in a Vertical Turbulent Flow Behind a Jet Block - A Benchmark Exercise. *J. Hydraulics Research*, **35**, 843-864
- (5) Banerjee, S., 1994. Upwellings, Downdrafts, and Whirlpools: Dominant Structures in Free Surface Turbulence. *Appl. Mech. Rev.* **47**, S166-S172.
- (6) Banerjee, S., 1998. Turbulent transport processes across fluid-fluid interfaces. *This conference*
- (7) Barsamian, H.R., Hassan, Y.A., 1994. Modified Subgrid Scale Model for Large Eddy Simulation of Tube Bundle Cross Flows. *Flow-Induced Vibration*, ASME, PVP 273, 283-288.
- (8) Barsamian, H.R., Hassan, Y.A., 1997. Large Eddy Simulation of Turbulent Crossflow in Tube Bundles. *Nucl. Engng. and Design*, **172**, 103-122.
- (9) Barsamian, H.R., Hassan, Y.A., Cueto, O., Emonot, Ph., 1998. Application of the Dynamic Subgrid Scale Model to TRIO-U. *6th Int. Conf. on Nucl. Engng.*, ICONE-6074
- (10) Biemüller, M., Meyer, L., Rehme, K., 1996. Large Eddy Simulation and Measurement of the Structure of Turbulence in Two Rectangular Channels Connected by a Gap. *Engng. Turbulence Modelling and Experiments* **3**, Ed. W. Rodi, G. Bergeles, Elsevier, 249-258.
- (11) Boris, J.P., Grinstein, F.F., Oran, E.S., Kolbe, R.L., 1992. New Insights into Large Eddy Simulation. *Fluid Dynamics Research* **10**, 199-228.
- (12) Braun, H., Neumann, H., 1996. Experimental and Numerical Investigation of Turbulent Heat Transfer in a Channel with Periodically Arranged Rib Roughness Elements. *Engng. Turbulence Modelling and Experiments* **3**, Ed. W. Rodi, G. Bergeles, Elsevier, 643- 654.
- (13) Breuer, M., 1997. Numerical and Modeling Influences on Large Eddy Simulations for the Flow Past a Circular Cylinder. *Turbulent Shear Flows* **11**, Grenoble, 3.
- (14) Breuer, M., Rodi, W., 1994. Large-Eddy Simulation of Turbulent Flow through a Straight Square Duct and a 180° Bend. *Direct and Large Eddy Simulation I*, Ed. P. Voke et al., Kluwer Acad. Press, 273-285.
- (15) Breuer, M., Lakehal, D., Rodi, W., 1995. Flow Around a Surface Mounted Cubical Obstacle: Comparison of LES and RANS-Results. *Notes on Num. Fluid Mech.*, **53**, Vieweg, 22-30.
- (16) Carteciano, L.N., Weinberg, D., Müller U., 1997. Development and Analysis of a turbulence Model for Buoyant Flows. *4th World Conf. on Experimental Heat Transfer, Fluid Mechanics and Thermodynamics*, Brussels, Pisa Edition ETS, **3**, 1339-1346.
- (17) Chen, X.-Q., Pereira, J.C.F., 1996. Large-Eddy Simulation of Particle Dispersion in Plane Mixing Layers. *Engng. Turbulence Modelling and Experiments* **3**, Ed. W. Rodi, G. Bergeles, Elsevier, 259-271.
- (18) Cherdron, W., Grötzbach G., Samstag, M., Sengpiel, W., Simon, M., Tiseanu, I., 1998. Experimental Investigations of Air/Water Bubbly Flow in Vertical Pipes. *Third Int. Conference on Multiphase Flow*, Lyon.
- (19) Chollet, J.P., Lesieur, M., 1981. Parameterisation of Small Scales of Three-Dimensional Isotropic Turbulence Utilising Spectral Closures. *J. Atmos. Sci.* **38**, 2747-2757.
- (20) Ciofalo, M., 1994. Large-Eddy Simulation: A Critical Survey of Models and Applications. *Advances in Heat Transfer*, **25**, Academic Press, 321-419.
- (21) Ciofalo, M., 1996. Large-Eddy Simulations of Turbulent Flow with Heat Transfer in Simple and Complex Geometries Using Harwell-FLOW3D. *Appl. Math. Modelling*, **20**, Elsevier, 262-271.
- (22) Ciofalo, M., Collins, M.W., 1992. Large-Eddy Simulation of Turbulent Flow and Heat Transfer in Plane and Rib-roughened Channels. *Int. J. Num. Methods in Fluids* **15**, 453-489.
- (23) Ciofalo, M., Stasiek, J., Collins, M.W., 1993. Flow and Heat Transfer in Corrugated Passages: Direct and Large Eddy Simulation and Comparison with Experimental Results. *Engng. Turbulence Modelling and Experiments* **2**, Ed. W. Rodi, F. Martelli, Elsevier, 283-292.
- (24) Dai, Y., Kobayashi, T., Taniguchi, N., 1994. Large Eddy Simulation of Plane Turbulent Jet Flow Using a New Outflow Velocity Boundary Condition. *Int. J. of JSME*.
- (25) Davidson, L., 1997. Large Eddy Simulation: A Dynamic One-Equation Subgrid Model for Three-Dimensional Recirculation Flow. *Turbulent Shear Flows* **11**, Grenoble, 26-1 - 26-6.
- (26) Deardorff, J.W., 1970. A Numerical Study of Three-Dimensional Turbulent Channel Flow at Large Reynolds Numbers. *J. Fluid Mech.* **41**, 453-480.
- (27) Deardorff, J.W., 1972. Numerical Investigation of Neutral and Unstable Planetary Boundary Layers. *J. Atmos. Sci.* **29**, 91-115.
- (28) Deardorff, J.W., 1973. The Use of Subgrid Transport Equations in a Three-Dimensional Model of Atmospheric Turbulence. *J. Fluids Eng.* **95**, 429-438.
- (29) Deardorff, J.W., Peskin, R.L., 1970. Lagrangian Statistics from Numerically Integrated Turbulent Shear Flow. *The Physics of Fluids*, **13**, 584-595.

- (30) Deck, T., 1995. Numerische Simulation einer Kanalströmung um einen quaderförmigen Körper mit Hilfe lokaler Gitterverfeinerung. *Dissertation* Univ. Karlsruhe.
- (31) Dehning, C., 1993. Numerische Untersuchung des Bewegungsverhaltens von Partikeln in turbulenter Kanalströmung bei hohen Reynolds-Zahlen. *Dissertation*, Univ. Kaiserslautern.
- (32) Dinh, T.N., Nourgaliev, R.R., 1997. Turbulence Modelling for Large Volumetrically Heated Liquid Pools. *Nucl. Engng. and Design*, **169**, 131-150.
- (33) Ducros, F., Nicoud, F., Schönfeld, T., 1997. Large Eddy Simulations of Compressible Flows on Hybrid Meshes. *Turbulent Shear Flows 11*, **3**, Grenoble, 28-1 - 28-6.
- (34) Eggels, J.G.M., Unger, F., Weiss, M.H., Westerweel, J., Adrian, R.J., Friedrich, R., Nieuwstadt, F.T.M., 1994. Fully Developed Turbulent Pipe Flow: A Comparison between Direct Numerical Simulation and Experiment. *J. Fluid Mech.*
- (35) Fallon, B., Lesieur, M., Delcayre, F., Grand, D., 1997. Large Eddy Simulations of Stable-Stratification Effects Upon a Backstep Flow. *Eur. J. of Mech., B/Fluids*, **16**, 625-644.
- (36) Ferziger, J.H., 1983. Higher-level Simulations of Turbulent Flow. *Computational methods for turbulent, transonic, and viscous flows*, Ed. J.A. Essers, Hemisphere Publ. Co., Washington, 93-182.
- (37) Ferziger, J.H., 1996. Recent Advances in Large Eddy Simulation. *Engng. Turbulence Modelling and Experiments 3*, Ed. W. Rodi, G. Bergeles, Elsevier, 163-175.
- (38) Friedrich, R., Bertolotti, F.P., 1997. Compressibility Effects Due to Turbulent Fluctuations. *Appl. Scientific Research*, **57**, 165-194.
- (39) Fureby, C., Gosman, A.D., Tabor, G., Weller, H.G., 1997. Large Eddy Simulation of Turbulent Channel Flows. *Turbulent Shear Flows 11*, Grenoble, 28-13 - 28-18.
- (40) Germano, M., 1991. Turbulence: The Filtering Approach. *J. Fluid Mech.* **238**, 326-336.
- (41) Germano, M., Piomelli, U., Moin, P., Cabot, W.H., 1991. A Dynamic Subgrid-Scale Eddy Viscosity Model. *Phys. Fluids A*, **3**, 1760-1765.
- (42) Ghosal, S., Moin, P., 1995. The Basic Equations for the Large Eddy Simulation of Turbulent Flows in Complex Geometry. *J. Comp. Phys.* **118**, 24-37.
- (43) Ghosal, S., Lund, T.S., Moin, P., Akselvoll, K., 1995. A Dynamic Localization Model for Large-Eddy Simulation of Turbulent Flows. *J. Fluid Mech.*, **286**, 229-255.
- (44) Grand, D., Urbin, G., Menant, B., Villand, M., 1997. Large Eddy Simulations in Nuclear Reactors Thermalhydraulics. *J. Hydraulics Research*, **35**, 831-842.
- (45) Grötzbach, G., 1981. Numerical Simulation of Turbulent Temperature Fluctuations in Liquid Metals. *Int. J. Heat Mass Transfer* **24**, 475-490.
- (46) Grötzbach, G., 1982. Direct Numerical Simulation of Laminar and Turbulent Bénard Convection. *J. Fluid Mech.* **119**, 27-53.
- (47) Grötzbach, G., 1982. Direct Numerical Simulation of the Turbulent Momentum and Heat Transfer in an Internally Heated Fluid layer. *Heat Transfer 1982*, Eds. U. Grigull et al. **2**, Hemisphere, 141-146.
- (48) Grötzbach, G., 1983. Spatial Resolution Requirements for Direct Numerical Simulation of the Rayleigh-Bénard Convection, *J. Comp. Phys.* **49**, 241-264.
- (49) Grötzbach, G., 1987. Direct Numerical and Large Eddy Simulation of Turbulent Channel Flows. *Encyclopedia of Fluid Mech.*, Ed. N.P. Chermisinoff, Gulf Publ. Houston, **6**, 1337-1391.
- (50) Grötzbach, G., 1989. Turbulent Heat Transfer in an Internally Heated Fluid Layer. *Refined Flow Modelling and Turbulence Measurements*. Eds. Y. Iwasa et al., Un. Ac. Press, 267-275.
- (51) Grötzbach, G., 1990. Simulation of Turbulent Flow and Heat Transfer for Selected Problems of Nuclear Thermal-Hydraulics. *The First Int. Conf. on Supercomputing in Nucl. Applications*; Ed. Japan Atomic Energy Research Institute, Tokyo, Publ. Nuclear Energy Data Center, Tokai-mura, Japan, 29-35.
- (52) Grötzbach, G., 1995. Direct numerical and large eddy simulation of turbulent heat transfer. *Turbulence, Heat Mass Transfer 1*, Ed. K. Hanjalic, J.C.F. Pereira, Begell House, 25 - 39
- (53) Grötzbach, G., Schumann, U., 1977. Direct Numerical Simulation of Turbulent Velocity-, Pressure- and Temperature-Fields in Channel Flows. *Turbulent Shear Flows I*, Ed. Durst, F. et al., Springer, 370-385.
- (54) Grötzbach, G., Wörner, M., 1992. Analysis of Second Order Transport Equations by Numerical Simulations of Turbulent Convection in Liquid Metals. *5<sup>th</sup> Nuclear Reactor Thermal-Hydraulics*, **2**, ANS, 358-365.
- (55) Grötzbach, G., Wörner, M., 1993. Analysis of Flow Mechanisms in Rayleigh-Bénard Convection at Small Prandtl Numbers. *Joint Int. Conf. on Mathematical Methods and Supercomputing in Nucl. Applications*, Ed. H. Küsters et al., Kernforschungszentrum Karlsruhe **1**, 236-247.
- (56) Härtel, C., Kleiser, L., 1994. Subgrid-Scale Modelling in the Near-Wall Region of Turbulent Wall-Bounded Flows. *Direct and Large Eddy Simulation I*, Ed. P. Voke et al., Kluwer Acad. Press, 97-107.
- (57) Härtel, C., Kleiser, L., 1997. Gallilean Invariance and Filtering Dependence of Near-Wall Grid-Scale/Subgrid Scale Interactions in Large-Eddy Simulation. *Phys. Fluids*, **9**, 473-475.
- (58) Hashiguchi, M., 1996. Turbulence Simulation in the Japanese Automotive Industry. *Engng. Turbulence Modelling and Experiments 3*, Ed. W. Rodi, G. Bergeles, Elsevier, 291-308.
- (59) Hassan, Y.A., Lee, S., 1993. Application of Large Eddy Simulation to Three-Dimensional Tube Bundle Flows., *6th Int. Top. Meeting on Nucl. Reactor Thermal*

- Hydraulics*, Eds.: M. Courtaud, J.M. Delhay, 2, 1415-1419
- (60) Hassan, Y.A., Pruitt, J.M., Steininger, D.A., 1995. A Perspective on Large Eddy Simulation of Problems in the nuclear-industry, *Nucl. Technology*, 112 324-330.
- (61) Jansen, K., 1996. Large Eddy Simulation of Flow Around a NACA 4412 Airfoil Using Unstructured Grids. *Center for Turbulence Research, Annual Research Briefs*, 225-232.
- (62) Jones, W.P., Wille, M., 1996. Large Eddy Simulation of a Round Jet in a Cross Flow. *Engng. Turbulence Modelling and Experiments 3*, Ed. W. Rodi, G. Bergeles, Elsevier, 199-208.
- (63) Kaltenbach, H.-J., Gerz, T., Schumann, U., 1991. Transport of Passive Scalars in Neutrally and Stably Stratified Homogeneous Turbulent Shear Flows. *Advances in Turbulence 3*, Ed. A.V. Johansson, P.H. Alfredsson, Springer.
- (64) Kasagi, N., 1997. Progress in Direct Numerical Simulation of Turbulent Transport and its Control. *Turb. Heat Mass Transfer*, 19-34.
- (65) Kato, C., Ikegawa, M., 1991. Large Eddy Simulation of Unsteady Turbulent Wake of a Circular Cylinder Using the Finite Element Method. *Advances in Num. Simulation of Turbulent Flows*, Ed. I. Celik et al., 117, ASME, 49-56.
- (66) Kawamura, T., 1985. Direct Numerical Simulation of a Turbulent Inner Flow by Finite-Difference Methods, AIAA paper, 1985, 1-10.
- (67) Kikuchi, Y., Kawasaki, T., Shioyama, T., 1982. Thermal Convection in a Horizontal Fluid Layer Heated Internally and from Below, *Int. J. Heat Mass Transfer*, 25, 363-370.
- (68) Kikuchi, Y., Shioyama, T., Kawara, Z., 1986. Turbulent Heat Transport in a Horizontal Fluid Layer Heated Internally and from below. *Int. J. Heat Mass Transfer* 29, 451-461.
- (69) Kim, J., 1988. Investigation of Heat and Momentum Transport in Turbulent Flows Via Numerical Simulations. *Transport Phenomena in Turbulent Flows*. Ed. M. Hirata, N. Kasagi, Hemisphere, New York, 715-730.
- (70) Kleiser, L., Zang, T.A., 1991. Numerical Simulation of Transitional Wall-Bounded Shear Flows, *Ann. Rev. Fluid Mech.* 23, 495 - 537
- (71) Kraichnan, R.H., 1976. Eddy Viscosity in Two and Three-Dimensions. *J. Atmos. Sci.* 33, 1521-1536.
- (72) Kravchenko, A.G., Moin, P., 1997. On the Effect of Numerical Errors in Large Eddy Simulations of Turbulent Flows. *J. Comp. Phys.*, 131, 310-322
- (73) Laurence, D., 1998. LES and RANSE of turbulent flow in tube bundles. *This conference*
- (74) Leith, C.E., 1990. Stochastic Backscatter in a Sub-grid-Scale Model: Plane Shear Mixing Layer. *Phys. Fluids A2*, 297-299.
- (75) Leonard, A., 1974. Energy Cascade in Large-Eddy Simulations of Turbulent Fluid Flows. *Adv. Geophys.* 18A, 237-248.
- (76) Lesieur, M., Metais, O. 1996. New Trends in Large Eddy Simulations of Turbulence. *Ann. Rev. Fluid Mech.*, 28, 45-82.
- (77) Lesieur, R., Rogallo, R., 1989. Large-Eddy Simulation of Passive Scalar Diffusion in Isotropic Turbulence. *Phys. Fluids A 1*, 4, 718-722.
- (78) Lipps, F.B., 1976. Numerical Simulation of Three-Dimensional Bénard Convection in Air. *J. Fluid Mech.* 75, 113-148.
- (79) Lombardi, P., De Angelis, V., Banerjee S., 1995. Direct Numerical Simulation of Near-Interface Turbulence in Coupled Gas-Liquid Flow, *Phys. Fluids 8*, 1643-1665.
- (80) Lu, X., Dalton, Ch., Zhang, J., 1996. Application of Large Eddy Simulation to an Oscillating Flow Past a Circular Cylinder. *Engng. Turbulence Modelling and Experiments 3*, Ed. W. Rodi, G. Bergeles, Elsevier, 187-197.
- (81) Manhart, M., Wengle, H., 1993. A Spatiotemporal Decomposition of a Fully Inhomogeneous Turbulent Flow Field. *Theoret. Comput. Fluid Dynamics.* 5, 223-242.
- (82) Mason, P.J., 1994. Large-Eddy Simulation: A Critical Review of the Technique. *Q.J.R. Meteorol. Soc.* 120, 1-26.
- (83) Mason, P.J., Thomson, D.J., 1992. Stochastic Backscatter in Large-Eddy Simulations of Boundary Layers. *J. Fluid Mech.* 242, 51-78.
- (84) Maxey, M.R., Chang, E.J., 1996. Direct Simulations of Microbubble Dynamics and Turbulent Flow. *Engng. Turbulence Modelling and Experiments 3*, Ed. W. Rodi, G. Bergeles, Elsevier, 273-278.
- (85) Meinke, M., Hofhaus, J., Abdelfattah, A., 1998. Simulation of Vortex Ring Interaction. *IUTAM Symposium on Dynamics of Slender Vortices*. Ed. E. Krause, Kluwer.
- (86) Moeng, C.H., 1984. A Large-Eddy-Simulation Model for the Study of Planetary Boundary-Layer Turbulence. *J. Atmos. Sci.* 41, 2052-2062.
- (87) Moin, P., Kim, J., 1982. Numerical Investigation of Turbulent Channel Flow. *J. Fluid. Mech.* 118, 341-377.
- (88) Moin, P., Kravchenko, A.G., 1998. Numerical Issues in Large Eddy Simulations of Turbulent Flows. *Conf. On Num. Methods for Fluid Dynamics*, Oxford.
- (89) Moin, P., Mahesh, K., 1998. Direct Numerical Simulation: A Tool in Turbulence Research. *Ann. Rev. Fluid Mech.*, 30, 539-78.
- (90) Murakami, S., 1992. Comparison of Various Turbulence Models Applied to a Bluff Body. *J. Wind Engng.* 52, 164-179.
- (91) Murakami, S., Mochida, A., Tominaga, Y., 1994. Numerical Simulation of Turbulent Diffusion in Cities. *The Effect of Urbanisation on Windfields, Air Pollution Spreading and Wind Forces*, Ed. E.J. Plate, Kluwer Academic Publishers.
- (92) Muramatsu, T., 1993. Intensity and Frequency Evaluations of Sodium Temperature Fluctuations Related to Thermal Stripping Phenomena Based on Numerical

- cal Methods. *Fifth Int. Symposium on Refined Flow Modelling and Turbulence Measurements*, Presses Ponts et Chaussées, Paris, 351-358.
- (93) Naitoh, K., Kuwahara, K., 1992. Large Eddy Simulation and Direct Simulation of Compressible Turbulence and Combusting Flows in Engines Based on the BI-SCALES method. *Fluid Dynamics Research* 10, 299-325.
- (94) Neto, A.S., Grand, D., Métais, O., Lesieur, M., 1993. A Numerical Investigation of the Coherent Vortices in Turbulence Behind a Backward-Facing Step. *J. Fluid. Mech.* 256, 1-25.
- (95) Nieuwstadt, F.T.M., 1990. Direct and Large-Eddy Simulation of Free Convection. *9th Intern. Heat Transfer Conference*, Amer. Soc. Mech. Engng., I, 37-47.
- (96) Nieuwstadt, F.T.M., Mason, P.J., Moeng, C.-H., Schumann, U., 1993. Large Eddy Simulation of the Convective Boundary Layer: A Comparison of four Computer Codes. *Turbulent Shear Flow 8*, Ed. F. Durst et al., Springer-V., 343-367.
- (97) Normand, X., Lesieur, M., 1992. Direct and Large-Eddy Simulations of Transition in the Compressible Boundary Layer. *Theoret. Comput. Fluid Dynamics* 3, 231-252.
- (98) Nourgaliev, R.R., Dinh, T.N., 1996. An Investigation of Turbulence Characteristics in an Internally Heated Unstably Stratified Fluid Layer. *Nat. Heat Transfer Conference. Houston, Texas*
- (99) Nourgaliev, R.R., Dinh, T.N., Sehgal, B.R., 1997. Effect of Fluid Prandtl Number on Heat Transfer Characteristics in Internally Heated Liquid Pools with Rayleigh Numbers up to  $10^{12}$ . *Nucl. Engng. and Design*, 168, 165-184.
- (100) Orszag, S.A., Patterson jr., G.S., 1972. Numerical Simulation of Turbulence. *Statistical Models and Turbulence*, Lecture Notes in Physics, Ed. M. Rosenblatt, C. van Atta. Springer-V., Berlin, 127-147.
- (101) Piomelli, U., Zang, T. A., Speziale, C. G., Hussaini, Y., 1990. On the Large-Eddy Simulation of Transitional Wall-Bounded Flows. *Phys. Fluids A* 2 (2), 257-265.
- (102) Rodi, W., Ferziger, J.H., Breuer, M., Pourquie, M., 1997. Status of Large Eddy Simulation: Results of a Workshop. *J. Fluids Engng.*, 119, 248-262.
- (103) Roubin, P.H.L., Astegiano, J.C., 1997. Computation of the Flow Structure and Temperature Mixing in the Core Outlet Region of the Phenix Reactor. *8th Int. Top. Meeting on Nucl. Reactor Thermal-Hydraulics*, 1388-1394.
- (104) Schemm, C.E., Lipps, F.B., 1976. Some Results from a Simplified Three-Dimensional Numerical Model of Atmospheric Turbulence. *J. Atmos. Sci.* 33, 1021-1041.
- (105) Schmidt, H., Schumann, U., 1989. Coherent Structure of the Convective Boundary Layer Derived from Large-Eddy Simulations. *J. Fluid Mech.* 200, 511-562.
- (106) Schmidt, M., Wörner, M., Grötzbach, G., 1997. Direkte numerische Simulation der Konvektion in einer Fluidschicht mit interner Wärmequelle. FZKA 5916, Forschungszentrum Karlsruhe.
- (107) Schmitt, L., Friedrich, R., 1987. Large-Eddy Simulation of Turbulent Backward Facing Step Flow. *Notes on Num. Fluid Mech.* Ed. M. Deville, 20, Vieweg, 355-362.
- (108) Schumann, U., 1975. Subgrid Scale Model for Finite Difference Simulations of Turbulent Flows in Plane Channels and Annuli. *J. Comput. Phys.* 18, 376-404.
- (109) Schumann, U., 1993. Direct and Large Eddy Simulation of Turbulence - Summary of the State of the Art 1993, *Introduction of the Modeling of Turbulence*, von Karman Lecture Series 1993-02, Ed. D. Olivari.
- (110) Schumann, U., Grötzbach, G., Kleiser, L., 1980. Direct Numerical Simulation of Turbulence. *Prediction Methods for Turbulent Flows*. Ed. W. Kollmann, Hemisphere Publ. Co., Washington, 123-258.
- (111) Scotti, A., Meneveau, C., Fatica, M., 1997. Dynamic Smagorinsky Model on Anisotropic Grids. *Phys. Fluids*, 9, 1856-1858.
- (112) Seiter, C., 1995. Numerische Simulation turbulenter Auftriebsströmungen in horizontalen Kanälen. FZKA 5505, Forschungszentrum Karlsruhe.
- (113) Simoneau, J.P., Noe, H. Menant, B., 1995. Large Eddy Simulation of Mixing Between Hot and Cold Sodium Flows - Comparison with Experiments. *7th Int. Meeting on Nucl. Reactor Thermal-Hydraulics*, 2, NUREG/CP-0142, 1324-1332.
- (114) Simoneau, J.P., Noe, H. Menant, B., 1997. Large Eddy Simulation of Sodium Flow in a Tee Junction - Comparison of Temperature Fluctuations with Experiments. *8th Int. Top. Meeting on Nucl. Reactor Thermal-Hydraulics*, 3, 1404, 1411.
- (115) Smagorinsky, J.S., 1963. General Circulation Experiments with the Primitive Equations: 1. The Basic Experiment. *Mon. Weather Rev.*, 91, 99-164.
- (116) Sommeria, G., 1976. Three-Dimensional Simulation of Turbulent Processes in an Undistributed Trade Wind Boundary Layer. *J. Atmos. Sci.* 33, 216-241.
- (117) Sullivan, P.P., Moeng, C.H., 1992. An Evaluation of the Dynamic Subgrid Scale Model in Buoyancy Driven Flows, *Tenth Symposium on Turbulence and Diffusion*, American Meteorological Society, Boston, MA, 82-85.
- (118) Surle, F., Berger, R., Menant, B. Grand, D., 1993. Comparison Between Sodium Stratification Tests on the Cormoran Model and Trio-VF Computations. *6th Intern. Top. Meeting on Nucl. Reactor Thermal Hydraulics*, I, Ed. M. Courtaud, J.M. Delhaye, 533-540.
- (119) Tenchine, D., Moro, J.P., 1997. Experimental and Numerical Study of Coaxial Jets. *8th Int. Top. Meeting on Nucl. Reactor Thermal-Hydraulics*, 3, 1381-1387.
- (120) Urbin, G., Brun, C., Métais, O., 1997. Large Eddy Simulations of Three-Dimensional spatially Evolving Round Jets. *Turb. Shear Flows 11*, Grenoble.

- (121)Ushijima, S., Tanaka, N., 1993. Direct Numerical Simulation of Fluid-Structure Thermal Interaction Occurring in the Presence of Internal Waves. *6th Int. Top. Meeting on Nucl. Reactor Thermal-Hydraulics*, 2, 1397-1404.
- (122)Voke, P.R., Gao, S., 1994. Large-Eddy Simulation of Heat Transfer from an Impinging Plane Jet. *Int. J. Num. Methods Engng.*
- (123)Voke, P.R., Yang, Z., Savill, A.M., 1996. Large Eddy Simulation and Modelling of Transition Following a Leading-Edge Separation Bubble. *Engng. Turbulence Modelling and Experiments* 3, Ed. W. Rodi, G. Bergeles, Elsevier, 601-610.
- (124)Weinberg, D., Rust, K., Hoffmann, H., 1996. Overviewreport on Passive Decay Heat Removal. FZKA-5667, Forschungszentrum Karlsruhe.
- (125)Weinberger, C., Rewerts, J., Janicka, J., 1997. The Influence of Inlet Conditions on a Large Eddy Simulation of a Turbulent Plane Jet. *Turb. Shear Flows* 11. Grenoble, 25-17 – 15-22.
- (126)Wörner, M., Grötzbach, G., 1992. Analysis of Semi-Implicit Time Integration Schemes for Direct Numerical Simulation of Turbulent Convection in Liquid Metals. *Notes on Num. Fluid Mech.*, 35, Ed. J.B. Vos et al., Vieweg, 542-551.
- (127)Wörner, M., Grötzbach, G., 1993. Turbulent Heat Flux Balance for Natural Convection in Air and Sodium Analysed by Direct Numerical Simulations. *Fifth Int. Symposium on Refined Flow Modelling and Turbulence Measurements*, Presses Ponts et Chaussees, Paris, 335-342.
- (128)Wörner, M., Grötzbach, G., 1993. Analysis of Diffusion of Turbulent Kinetic Energy by Numerical Simulations of Natural Convection in Liquid Metals. *6th Int. Top. Meeting on Nucl. Reactor Thermal Hydraulics*, Eds.: M. Courtaud, J.M. Delhaye, I, 186 – 193.
- (129)Wörner, M., Grötzbach, G., 1994. Analysis of Thermal Variance Equation for Natural Convection of Air and Sodium. *Heat Mass Transfer* 1, Ed. K. Hanjalic, J.C.F. Pereira, Begell House, 332-337.
- (130)Wörner, M., Grötzbach, G., 1996. Analysis of the Transport Equation of Temperature Variance Dissipation Rate by Direct Numerical Simulation Data of Natural Convection. *Engng. Turbulence Modelling and Experiments* 3, Eds.: W. Rodi, G. Bergeles, Elsevier Science B. V., 229-238
- (131)Wörner, M., Grötzbach, G., 1997. DNS Data Base of Turbulent Natural Convection in Horizontal Fluid Layers. World Wide Web-page //www.fzk.de/IRS/eng
- (132)Wörner, M., Grötzbach, G., 1998. Pressure Transport in Direct Numerical Simulations of Turbulent Natural Convection in Horizontal Fluid Layers. *Int. J. Heat and Fluid Flow*, in press.
- (133)Wörner, M., Schmidt, M., Grötzbach, G., 1997. DNS of Turbulence in an Internally Heated Convective Fluid Layer and Implications for Statistical Modelling. *J. Hydraulics Research*, 35, 773-797
- (134)Ye, Q.-Y., Wörner, M., Grötzbach, G., Jovanovic, J., 1997. Modelling Turbulent Dissipation Rate for Rayleigh-Bénard Convection. *Turbulence, Heat Mass Transfer* 2, Eds.: K. Hanjalic, T.W.J. Peeters, Delft University Press, 331-340.



## Poster papers



# LARGE EDDY SIMULATION OF NATURAL CONVECTION IN A VERTICAL SLOT

D. J. Bergstrom<sup>1</sup> and X. Huang<sup>2</sup>

<sup>1</sup>Department of Mechanical Engineering  
University of Saskatchewan, Canada

<sup>2</sup>CERCA, Montreal, Quebec, Canada

## ABSTRACT

Although natural convection in a vertical slot has been widely studied using both experimental and numerical techniques, significant questions remain to be answered regarding the flow structure in the turbulent regime. From a modelling point of view, the vertical slot represents one of the simplest configurations in which the structure of turbulent buoyancy-driven convection can be studied. The present paper reports the results of a Large Eddy Simulation in which only the largest turbulent motions are resolved, while the smaller motions are approximated by subgrid scale models for the Reynolds stress and turbulent heat flux. For a Rayleigh number of  $Ra = 8 \times 10^5$ , the instantaneous flow field exhibits a cellular structure similar to that observed in the transitional regimes. One implication of the spatial nonhomogeneity of the velocity and temperature fields in the vertical direction is that the local turbulence structure is influenced by the coherent motion. Only upon spatially averaging in the vertical direction are the characteristic profiles for the average vertical velocity and temperature recovered.

## 1. INTRODUCTION

Buoyancy remains an important facet of many industrial and environmental flows. Turbulent heat transfer can be significantly affected by buoyancy in ways which depends on the local flow configuration. A practical application in which there is a strong and influential coupling between the temperature and velocity fields is air flows in rooms. Although extensive research has been conducted to determine the supply air flow rates and properties needed to obtain acceptable ventilation and conditioning, much less research effort has been directed at developing ways to effectively distribute the supply air throughout the room. Since this problem requires specific knowledge of the velocity, temperature and humidity throughout the room, computational modelling and simulation represent an attractive tool for developing improved designs for room air flow distribution.

The thesis research of Huang (1) considered the application of Large Eddy Simulation (LES) methods to the prediction of buoyant air flows in rooms. The choice of LES was motivated in part by the fact that many air flows in rooms are unsteady and three-dimensional, with regions of turbulent and almost laminar flow. Furthermore, any large scale unsteady motion in a room will have significant impact on the comfort level of the occupants. Given the flow characteristics and application described above, LES seemed to represent an attractive method for computational modelling.

Most air flows are buoyant, due to the need for heating in cold climates and cooling in warm climates. Often buoyancy has a significant contribution to the forces driving the flow. Therefore, any LES model must incorporate subgrid scale (SGS) models for both the Reynolds stress and turbulent heat flux which perform well in buoyant flows. As one means of assessing their SGS model performance, Huang and Bergstrom (2) considered simulation of buoyancy driven flow in a nearly cubical cavity with differentially heated side walls, which in some ways resembles air flow in a room with isothermal walls at different temperatures. The predictions for the mean velocity and temperature profiles on the isothermal walls demonstrated reasonable agreement with the data available from experiments and two-dimensional direct numerical simulations (DNS). At Rayleigh numbers for which the flow is turbulent, the boundary layers on the isothermal walls become extremely thin, and the core of the cavity – apart from the top and bottom surfaces – is characterised by relatively little motion. This flow structure makes the application of LES problematic, since the near-wall resolution becomes comparable to that in a direct numerical simulation. Recall that in engineering applications the desired advantage of LES is that only large scale structure needs to be resolved, which can hopefully be accomplished on grids not radically different than those used for Reynolds Average Navier-Stokes (RANS) methods.

A more likely flow for application of LES methods is the case of natural convection in a vertical cavity. Curiously, one of the earliest investigations of this flow was also motivated by engineering concerns in the building industry, in this case the performance of double paned window units in reducing heat losses (3). In the limit of very high aspect ratios, the buoyancy driven cavity problem resembles the case of an infinite vertical slot. The flow pattern is one of warmer fluid ascending the hot wall and cooler fluid descending the cold wall. One important feature of this flow is the strong turbulence production associated with the Couette-like flow structure in the interior of the cavity. The boundary layers for the turbulent flow case are not nearly as thin as for the cubical cavity. This feature, together with the expectation of strong large scale turbulent motions in the interior of the slot, makes this flow a likely candidate for the application of LES.

To summarise, the paper presented below describes the preliminary results of a LES prediction for turbulent natural convection in a vertical slot. Although the application motivating the study is air flows in rooms, the paper focuses on using this simple flow configuration to assess the performance of LES using a functional scale similarity SGS model. One important feature of turbulent natural convection in a vertical slot is the presence of coherent structures in the form of recirculation cells. These cells introduce spatial inhomogeneity in the vertical direction, and also imply a contribution to the heat transfer from coherent motions. In the remainder of the paper, we first review the results of other studies reported in the literature, including some recent DNS investigations. Next, we describe the numerical method and SGS models. Finally, we present some specific results for the instantaneous and time average velocity and temperature fields.

## 2. LITERATURE REVIEW

At least three direct numerical simulations of natural convection in a vertical slot have been reported in the literature. In all cases, the flow was unstratified, i.e. the vertical temperature gradient in the center region of the cavity was negligible. Generally periodic boundary conditions were used in the vertical and spanwise directions, with no-slip and isothermal conditions implemented on the slot walls. Phillips (4) considered flows at Rayleigh numbers of  $Ra = 4.6 \times 10^4$  and  $1.28 \times 10^5$ , and obtained predictions for the time average vertical velocity and temperature fields, as well as the second moments. He noted the existence of relatively thick laminar shear layers next to the slot walls for the relatively low Rayleigh numbers he considered.

Boudjemadi *et al* (5) obtained DNS predictions of flows with Rayleigh numbers of  $Ra = 10^5$  and  $5.4 \times 10^5$ . They emphasised the importance of strong quasi-constant turbulent shear in the center of the slot, with strongly viscous flow at the walls. They used their DNS data to evaluate the budgets for the Reynolds stress and turbulent heat flux components. The most extensive calculations to date appear to be those of Versteegh and Nieuwstadt (6), who considered Rayleigh numbers up to  $Ra = 5 \times 10^6$ . They also used the largest solution domain, 12 slot widths high and 6 slots widths wide. One of the major focuses of their post-processing was an attempt to resolve the coherent structure observed in the turbulent flow field. They found this structure to be similar to the two-dimensional velocity and temperature patterns associated with the first linear stability. Such structure was previously studied in laminar transitional flow by Lee and Korpela (7) and Chait and Korpela (8) using numerical simulations. Neither of the other two DNS studies mentioned the existence of the residual instability flow patterns, although they would not necessarily be evident from time-averaged results alone.

The latter two DNS studies presented comparisons to the recent experimental data of Betts and Bokhari (9), who performed their measurements in a tall enclosure which approximated an infinite channel for a Rayleigh number of  $Ra = 8.3 \times 10^5$ . One of the problems encountered by such experiments is ensuring that the cavity is tall enough to eliminate any effect of the end walls, such as stratification. Often it is also difficult to produce a flow which evidences the strong symmetry implied by the boundary conditions.

Dol *et al* (10) used the DNS results of (5) and (6) to assess the performance of differential and algebraic second-moment closures. They noted that some of the serious problems associated with application of second-moment closures to thermal convection include: 1) the possible presence of large-scale coherent structures; and 2) the large-scale three-dimensional, unsteady motions encountered even in ostensibly two-dimensional flows. Although these concerns argue in favour of LES, one should temper this conclusion with the realisation that natural convection in a vertical slot can -- in some regards -- be adequately predicted with a rather simple closure, e.g. a low Reynolds number  $k-\epsilon$  model (11).

## 3. LES MODEL

### 3.1 Volume Average Transport Equations

The mathematical model consists of the conservation equations of mass, momentum and thermal energy for

incompressible flow of a Newtonian fluid using the Boussinesq approximation:

$$U_{i,i} = 0 \quad (1)$$

$$\dot{U}_i + (U_j U_i)_{,j} = -\frac{1}{\rho} P_{,i} - \beta g_i \Theta + \nu U_{i,jj} \quad (2)$$

$$\dot{\Theta} + (U_j \Theta)_{,j} = \alpha \Theta_{,jj} \quad (3)$$

*Coarse-graining* of the field variables in the LES is performed by volume averaging. The volume average operator is defined as follows:

$$\bar{\phi} = \frac{1}{\Delta V} \iiint \phi dV \quad (4)$$

where  $\Delta V$  is the volume of the control volume under consideration. The control volumes are defined by the numerical grid used to discretise the solution domain. In volume averaging the transport equations, terms involving derivatives result in surface average quantities, defined as follows:

$${}^j(\phi) = \frac{1}{\Delta S_j} \iint \phi dS_j \quad (5)$$

where  $\Delta S_j$  is the control surface perpendicular to the  $x_j$  direction. The presence of the surface averages is problematic in so far as the transport equations will be solved following the finite volume method, which determines the field variables at a finite number of discrete points. The surface averages are not known. To complete the coarse-graining procedure they will be modelled in terms of the volume average and the subgrid scale (SGS) fluctuation fields. The SGS fluctuation of a field variable is obtained by subtracting the volume average of the variable from its instantaneous values, i.e.

$$u_i = U_i - \bar{U}_i \quad ; \quad \theta = \Theta - \bar{\Theta}$$

Since the volume average quantity of a variable is only defined at the node points of the control volumes, the SGS fluctuation also represents a discrete field. Introducing the decomposition above into the transport equations, and expressing the surface averages in terms of combinations of volume average and SGS fluctuations, we obtain the following form of the

transport equations, upon which the numerical solution will be based:

$$\bar{U}_{i,i} = 0 \quad (6)$$

$$\begin{aligned} \dot{\bar{U}}_i + (\bar{U}_j \bar{U}_i)_{,j} = & -\frac{1}{\rho} \bar{P}_{,i} - \beta g_i \bar{\Theta} \\ & + \nu \bar{U}_{i,jj} + (\tau_{ij} + \xi_j)_{,j} \end{aligned} \quad (7)$$

$$\dot{\bar{\Theta}} + (\bar{U}_j \bar{\Theta})_{,j} = \alpha \bar{\Theta}_{,jj} + (\sigma_j + \psi_j)_{,j} \quad (8)$$

Two additional terms appear in the transport equations for momentum and energy as a result of linearising the convective transport terms. The subgrid scale Reynolds stress,  $\tau_{ij}$ , and turbulent heat flux,  $\sigma_j$ , are defined as follows based on the SGS fluctuations:

$$\tau_{ij} = -\overline{u_i u_j} \quad (9)$$

$$\sigma_j = -\overline{u_j \theta} \quad (10)$$

The other two terms are the cross-correlation terms associated with the interactions between the large scale and subgrid scale motions. The cross correlation terms  $\xi_j$  and  $\psi_j$  represent momentum and thermal fluxes, defined respectively as:

$$\xi_j = -{}^j(\bar{U}_i u_j) - {}^j(u_i \bar{U}_j) \quad (11)$$

$$\psi_j = -{}^j(\bar{\Theta} u_j) - {}^j(\theta \bar{U}_j) \quad (12)$$

### 3.2 Subgrid Scale Models

The purpose of the SGS modelling is to relate the SGS Reynolds stress, turbulent heat flux and cross-correlation terms solely to the solvable large scale fields. In this case, we choose to use a *dynamic model* following the approach of Germano *at al* (12), although our model does not adopt an eddy viscosity model formulation. We introduce a second grid, called the test grid, which has a characteristic length  $\Delta'_i$  which is larger than that of the original grid,  $\Delta_i$ ; in our case,  $\Delta'_i = 2 \Delta_i$ . The essential idea is to sample the large scale turbulent motion resolved by the grid-scale (i.e. finite volume)

fields, and use it to infer the SGS fluxes. We proceed by introducing a second decomposition of the instantaneous field in terms of the test-grid average and its fluctuation, i.e.

$$U_i = \overline{U}_i + u_i = \overline{\overline{U}}_i + u'_i \quad (13)$$

where the double bar, e.g.  $\overline{\overline{U}}_i$ , indicates volume averaging on the test grid, and the prime, e.g.  $\tau'_{ij}$  denotes a fluctuation with respect to the test-grid volume average. Using the supersedity principle, we can express the SGS Reynolds stresses on the two grid levels as follows:

$$\tau_{ij} = -\overline{u_i u_j} = -\overline{\overline{U}_i \overline{U}_j} + \overline{U_i U_j} \quad (14)$$

$$\tau'_{ij} = -\overline{\overline{u'_i u'_j}} = -\overline{\overline{U}_i \overline{U}_j} - \overline{\overline{U}_i \overline{U}_j} \quad (15)$$

The difference between the SGS Reynolds stress on the grid-scale and test-grid levels, denoted  $T_{ij}$ , is given by

$$T_{ij} = \tau'_{ij} - \overline{\tau_{ij}} = \overline{\overline{U}_i \overline{U}_j} - \overline{\overline{U}_i \overline{U}_j} \quad (16)$$

The quantity  $T_{ij}$  represents the inter-grid Reynolds stress, and most importantly is calculable numerically by test-grid averaging the grid-scale volume average velocity fields.

The specific dynamic model used in this simulation is the functional scale similarity (FSS) model developed by Huang (1). It postulates a relationship between the grid-scale and inter-grid Reynolds stress of the following form:

$$\tau_{ij} = \sqrt{C_{ij} C_{jj}} T_{ij} \quad (17)$$

where no summation is implied. Each coefficient in equation (17) represents the ratio of  $\tau_{ii}$  over  $T_{ii}$  in a specific coordinate direction,  $j$ . These ratios are calculated based on the assumption of a simple functional form for the distribution function  $f(x)$  of the SGS velocity fluctuation with length scale. This enables the following contributions to the total turbulent momentum flux to be evaluated:

$$\text{subgrid portion: } -\tau_{ii} = \int_0^{\Delta_i} f(x) dx$$

$$\text{inter-grid portion: } -T_{ii} = \int_{\Delta_i}^{2\Delta_i} f(x) dx$$

$$\text{solvable portion: } -t_{ii} = \int_{\Delta_i}^{\infty} f(x) dx$$

In the integration's above,  $\Delta_i$ , is the characteristic length scale of the surface on which the Reynolds stress is acting, e.g.

$$\Delta_i = \sqrt{\Delta x_2 \Delta x_3}$$

Using the relations above enables the coefficients  $C_{ij}$  in equation (17) to be evaluated based on the instantaneous solution field, which in turn determines  $\tau_{ij}$ . In a similar fashion, the SGS heat flux is determined from the following relation,

$$\sigma_j = \sqrt{C_{\theta j} C_{jj}} \Omega_j \quad (18)$$

based on the inter-grid heat flux given by

$$\Omega_j = \sigma'_j - \overline{\sigma_j} = \overline{\overline{\Theta U}_j} - \overline{\overline{\Theta U}_j} \quad (19)$$

The other part of the SGS model is the cross-correlation, which in this case is represented by the following eddy viscosity model relations:

$$\xi_j = \alpha_j \frac{\overline{U}_i^{j+1/2} - \overline{U}_i^{j-1/2}}{\Delta x_j} \quad (20)$$

$$\psi_j = \alpha_j \frac{\overline{\Theta}^{j+1/2} - \overline{\Theta}^{j-1/2}}{\Delta x_j} \quad (21)$$

The eddy diffusivity  $\alpha_j$  in the  $j$  direction is calculated based on the local velocity scale fluctuation,  $\check{u}_j$ , and mean length scale,  $\overline{\Delta}_j$ , for the control volume surface under consideration, i.e.

$$\alpha_j = \frac{1}{2} \overline{\tilde{u}_j \Delta_j} \quad (22)$$

The eddy viscosity can also be viewed as dynamic, in so far as it depends on the level of the SGS fluctuations predicted by the model, and goes to zero in laminar flow. An important contribution of the cross-correlation term is that it provides the dissipation of energy that typically is not adequately handled by a scale similarity model alone.

In the implementation of this model, the contribution of spatial inhomogeneity of the grid-scale fields to the inter-grid fluxes was eliminated by first subtracting the time-average fields. Another important facet of the model is the use of length scale information derived from the control volume surface on which a specific flux is acting. More details of the FSS model can be found in the thesis of Huang (1).

#### 4. NUMERICAL METHOD

The LES model was implemented in a finite volume code designed to solve unsteady, three-dimensional, incompressible flow using a non-uniform grid and a Cartesian coordinate system. Since volume averaging was used for both the theoretical coarse-graining and the numerical discretisation, the two processes became in some sense coupled.

The Navier-Stokes solver used a fractional step method on a collocated grid. Within a single time step, the momentum equation is first solved explicitly without the pressure gradient term. Next cell surface fluxes are obtained using a consistent physical interpolation which includes the pressure gradient across the face. In a procedure resembling the that of the SIMPLE scheme on a staggered grid, a Poisson equation derived from continuity is next solved to obtain a pressure correction field. In the final calculation of the time step, the pressure correction field is used to update the pressure, node velocity and surface flux fields. Having solved the velocity field, the energy equation is then solved implicitly for the temperature field. A one dimensional QUICK scheme is used to estimate transported quantities at the control volume face in the transport equations.

The numerical algorithm has been extensively tested on two-dimensional and three-dimensional benchmark problems, including high Reynolds number lid-driven and buoyancy-driven cavity flows which are still in the laminar regime. The results compare very favourably with the best predictions of other researchers using

different numerical techniques, see reference (13) for details.

#### 5. NUMERICAL RESULTS

The numerical model was used to perform a LES of natural convection in a vertical slot for a Rayleigh number based on the slot width of  $Ra = 8 \times 10^5$ . The slot was  $h = 0.5$  m wide. It extended 1 m in the spanwise direction and 2 m in the vertical direction, giving spanwise and vertical aspect ratio's of 2 and 4, respectively. For the purpose of presentation, the coordinate direction perpendicular to the slot walls will be denoted  $x$ , the spanwise direction denoted  $y$  and the vertical direction denoted  $z$ . The hot wall was located at  $x = 0$ , and the cold wall at  $x = h$ . The numerical grid used 41, 41 and 61 control volumes in the  $x$ ,  $y$  and  $z$  directions, respectively. The grid was non-uniform in the  $x$  direction with local refinement in the near-wall region.

Typically the solution was started from initial fields corresponding to a uniform temperature equal to the average of the two isothermal walls, and zero velocity. The boundary conditions corresponded to no-slip and constant temperature at the slot walls. The flow was assumed to be homogeneous in the lateral ( $y$ ) and vertical ( $z$ ) directions. Accordingly, zero gradient and periodic boundary conditions were used in the lateral and vertical directions, respectively. As will be seen from the results presented below, the use of periodic boundary conditions has implications for any cell structure which may develop in the slot. The simulation used a numerical time step of  $\delta t = 0.001$  s, and an averaging period of 2 s.

The results to be discussed below correspond to the solution fields in the lateral mid-plane of the slot. Unless otherwise specified, the velocity and temperature scales used to nondimensionalise the results are the diffusion velocity scale,  $\alpha/h$ , and the temperature difference between the two isothermal walls,  $\Delta T_w$ . The flow pattern is first visualised in terms of instantaneous velocity vectors as shown in Fig. 1. The velocity field clearly illustrates an irregular pattern of cells of recirculating fluid, which appear to alternate in direction. Although generally the flow is upward along the hot wall and downward along the cool wall as would be expected, in the center region a strong circulation cell is observed to be rotating in the counterclockwise direction. It sweeps fluid downward along the hot wall and upward along the cold wall. Contour lines based on the magnitude of the velocity vector are shown in Fig. 2. Again, we observe four relatively strong recirculation cells, with weaker and smaller cells sandwiched between them. Vectors corresponding to the fluctuation of the instantaneous velocity field (relative to the time-average

or mean velocity field) are shown in Fig. 3. The fluctuation also reveals the signature of a cellular pattern, although less so. Extremely strong fluctuations develop in the region of the counterclockwise recirculation cell, as it opposes the natural direction of the flow. Versteegh and Nieuwstadt (6) reported velocity fluctuations which were large enough to cause momentary flow reversal, even in the region of maximum mean velocity.

The isotherms for the instantaneous temperature field are presented in Fig. 4. The effect of the cellular pattern is to concentrate the region of steep temperature gradients next to the isothermal walls. Tongues of warmer and cooler fluid are also swept into the center of the slot by the action of the recirculation cells. In between these intrusions of warmer and cooler fluid, the temperature in the center of the slot appears to be relatively uniform.

One obvious consequence of the cellular structure of the flow is that the mean velocity and temperature fields will be strongly influenced by their relative location within the recirculation cell pattern. This is illustrated for the vertical velocity component in Fig. 5, and the temperature in Fig. 6. In both cases, the mean values have been plotted at different vertical sections in the flow. The variation in local mean transport at different sections is striking.

When the mean vertical velocity and temperature profiles at different sections are spatially averaged over the vertical extent of the slot, we obtain the *average* velocity and temperature profiles shown in Fig.'s 7 and 8, respectively, for the half of the slot next to the hot wall. In each case, we have also shown the experimental measurements of Betts and Bokhari (9) for a flow with a slightly higher Rayleigh number,  $Ra = 8.3 \times 10^5$ . With respect to the vertical velocity component, the LES prediction has a peak value which is somewhat higher and closer to the wall than in the experiment. For comparison, the DNS results of Versteegh and Nieuwstadt (6) predicted peak values which were 30 percent lower than in the experiment. Perhaps a more significant discrepancy is the slight curvature of the average velocity profile in the interior region of slot. Recall that the previous DNS studies and experiments emphasised a strong Couette-like flow in the interior of the slot, characterised by a uniform velocity gradient. A perhaps related discrepancy is observed in the LES prediction for the spatially averaged mean temperature profile shown in Fig. 8. The LES profile is almost 'flat' in the interior of the slot, whereas the DNS and experimental data suggest a finite gradient. Both of these deficiencies might be attributed to the under-development of the mean fields due to the relatively short averaging period.

The final plots presented are for the subgrid scale Reynolds stress component,  $\tau_{33}$ , and turbulent heat flux component,  $\sigma_3$ , shown in Fig.'s 9 and 10, respectively. The instantaneous contour plots reveal a non-uniform spatial distribution with steep gradients in the vicinity of the strong counterclockwise recirculation cell in Fig. 1. This was also the region in which the velocity fluctuations were greatest, see Fig. 3. The peak normalised value for the normal Reynolds stress in the vertical direction was  $\tau_{33} = 0.0045V_b^2$ , and for the vertical turbulent heat flux was  $\sigma_3 = 0.53V_b \Delta T_w$ .

## 6. CONCLUSIONS

The present paper reports preliminary results for a LES prediction of natural convection in a vertical slot at a Rayleigh number of  $Ra = 8 \times 10^5$ . The LES uses a dynamic functional scale similarity model to predict the SGS fluxes based on the inter-grid SGS fluxes calculated from the resolved fields. The velocity and temperature fields in the lateral mid-plane of the slot give evidence of irregular circulation cells, which introduce a strong spatial inhomogeneity to the flow in the vertical direction. Similar recirculation patterns were identified by Versteegh and Nieuwstadt (6) in their DNS results. They suggested that the coherent motions were related to the first instability mode. The cellular structure leads to distinctly different mean velocity and temperature profiles at different vertical sections in the slot, although the spatially-averaged profiles are similar to the experimental and DNS results. Some aspects of the average mean velocity and temperature profiles suggests that the solution field may be under-developed, or the averaging time too short. Further simulations should also consider the effect of the vertical aspect ratio of the solution domain on the specific cellular patterns, since the use of periodic boundary conditions in this direction obviously affects the size and number of cells.

## Acknowledgments

DJB gratefully acknowledges the support of the Natural Sciences and Engineering Research Council of Canada; computer time for the simulations was provided to XH by CERCA.



## Nomenclature

$f$	distribution function
$g_i$	gravity vector
$P$	pressure
$S$	surface area
$T_{ij}$	inter-grid Reynolds stress
$u_i$	velocity fluctuation
$U_i$	velocity vector
$V$	volume
$x_i$	coordinate
$\alpha$	thermal diffusivity
$\alpha_j$	turbulent diffusivity
$\beta$	thermal expansion coefficient
$\Delta_i$	grid length scale
$\theta$	temperature fluctuation
$\Theta$	temperature difference
$\nu$	kinematic viscosity
$\rho$	density
$\sigma_j$	SGS turbulent heat flux
$\tau_{ij}$	SGS Reynolds stress
$\Omega_j$	inter-grid heat flux
$\xi_{ij}$	cross-correlation for velocity
$\psi_j$	cross-correlation for temperature

## References

- Huang, X., Volume Average Technique for Turbulent Flow Simulation, Ph.D. Thesis, Department of Mechanical Engineering, University of Saskatchewan, 1997.
- Huang, X. and D.J. Bergstrom, LES of buoyant cavity: subgrid scale models for inhomogeneous flows, 11<sup>th</sup> Symp. on Turbulent Shear Flows, Grenoble, 1997, 23:24-29.
- Batchelor, G.K., Heat transfer by free convection across a closed cavity between vertical boundaries at different temperatures, *Quart. Appl. Math.*, 1954, Vol. 12, pp. 209-233.
- Phillips, J.R., Direct simulations of turbulent unstratified natural convection in a vertical slot for  $Pr = 0.71$ , *Int. J. Heat Mass Transfer*, 1996, Vol. 39, pp. 2485-2494.
- Boudjemadi, R., V. Maupu, D. Laurence and P. Le Quere, Budgets of turbulent stresses and fluxes in a vertical slot natural convection flow at Rayleigh  $Ra = 10^5$  and  $5.4 \cdot 10^5$ , *Int. J. Heat and Fluid Flow*, 1997, Vol. 18, pp. 70-79.
- Versteegh, T.A.M. and F.T.M. Nieuwstadt, Coherent structures in natural convection between two vertical, differentially heated walls, 2<sup>nd</sup> Int. Symp. on Turbulence, Heat and Mass Transfer, Delft, 1997, pp. 471-480.
- Lee, Y. and S.A. Korpela, Multicellular natural convection in a vertical slot, *J. Fluid Mech.*, 1983, Vol. 126, pp. 91-121.
- Chait, A. and S.A. Korpela, The secondary flow and its stability for natural convection in a tall vertical enclosure, *J. Fluid Mech.*, 1989, Vol. 200, pp. 189-216.
- Betts, P.L. and I.H. Bokhari, New experiments on turbulent natural convection of air in a tall cavity, *UMIST Mech. Eng. Rept.*, CS10/091/95, Manchester, UK.
- Dol, H.S., K. Hanjalic and S. Kenjeres, A comparative assessment of the second-moment differential and algebraic models in turbulent natural convection, *Int. J. Heat and Fluid Flow*, 1997, Vol. 18, pp. 4-14.
- Ince, N.Z. and B.E. Launder, On the computation of buoyancy-driven turbulent flows in rectangular enclosures, *Int. J. Heat and Fluid Flow*, 1989, Vol. 10, pp. 110-117.
- Germano, M., U. Piomelli, P. Moin and W.H. Cabot, A dynamic subgrid-scale eddy viscosity model, *Phys. Fluids, A*, 1991, Vol. 3, pp. 1760-1765.
- Huang, X. and D.J. Bergstrom, A collocated method for three-dimensional viscous incompressible flow, submitted to *Computers and Fluids*.

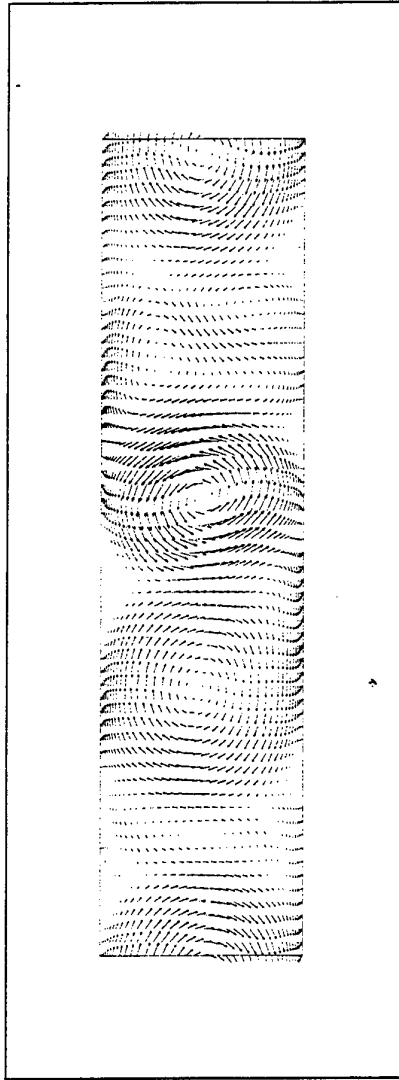


Figure 1: Instantaneous velocity vector.

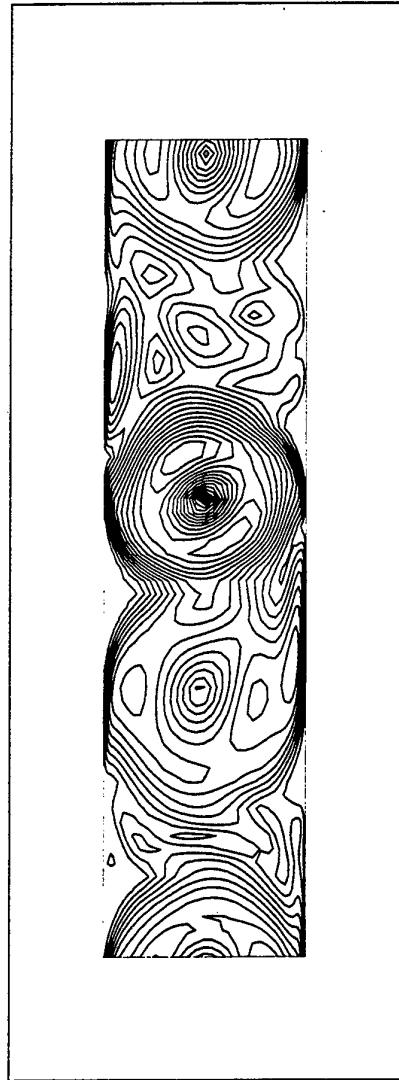


Figure 2: Contour of velocity magnitude.

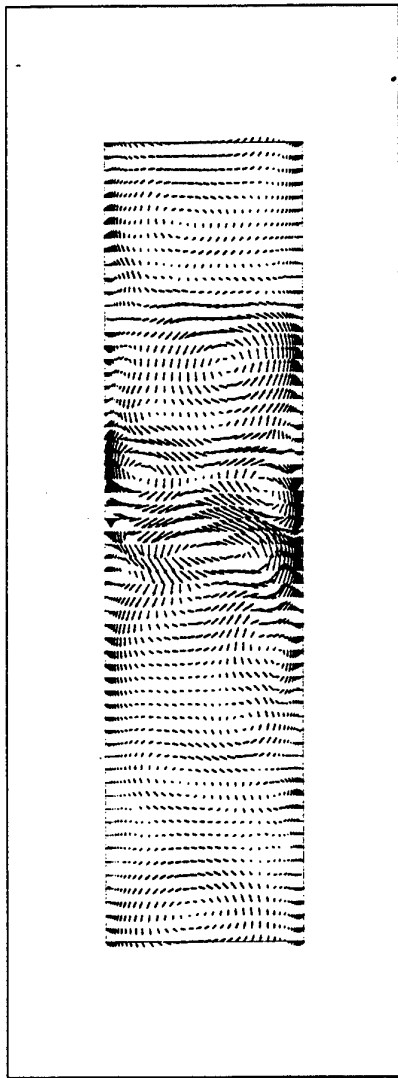


Figure 3: Fluctuation velocity vector.

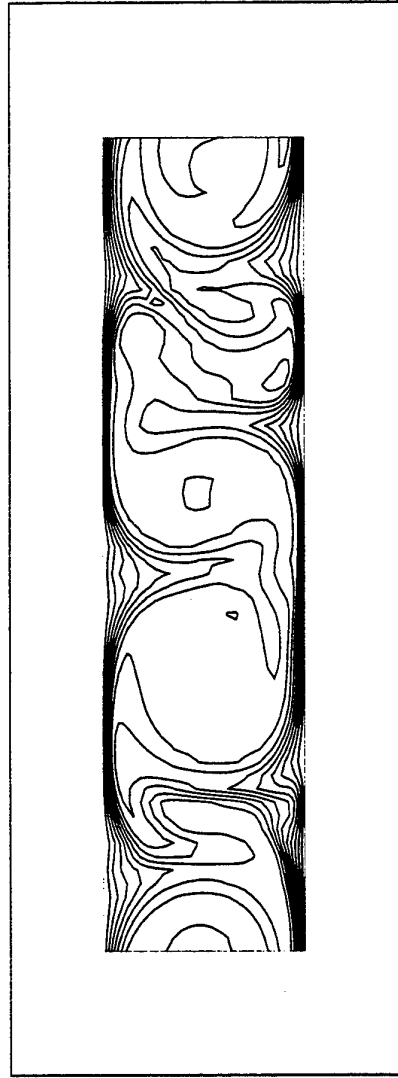


Figure 4: Instantaneous isotherms.

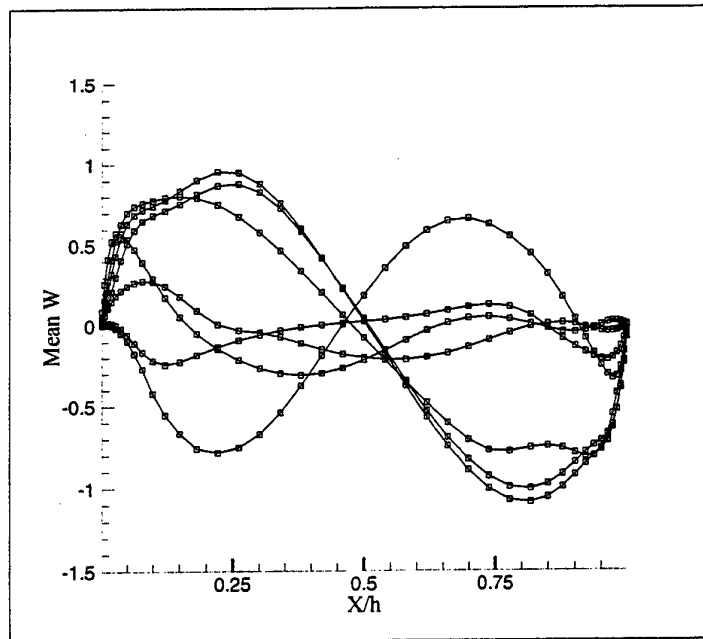


Figure 5: Mean vertical velocity profiles.

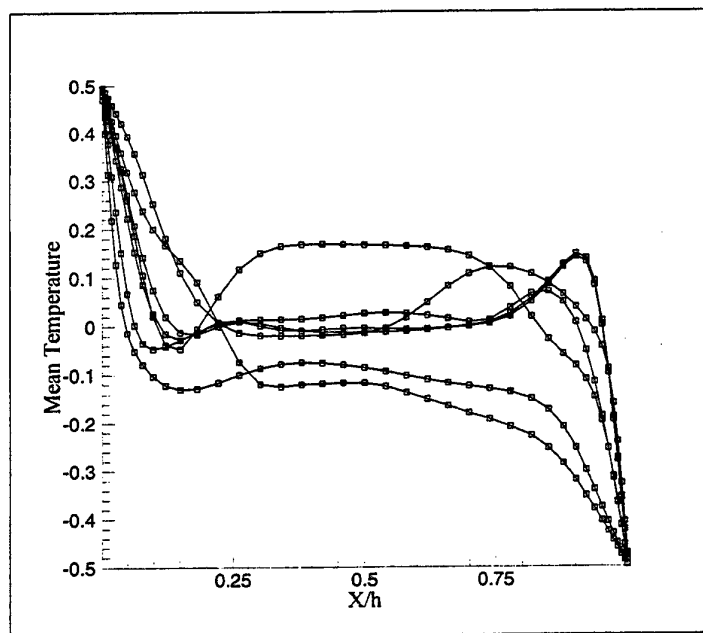


Figure 6: Mean temperature profiles.

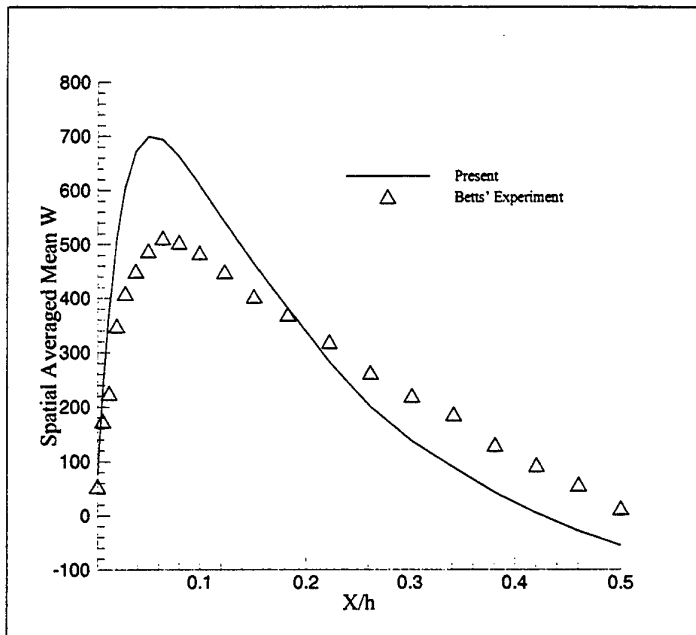


Figure 7: Average vertical velocity profile.

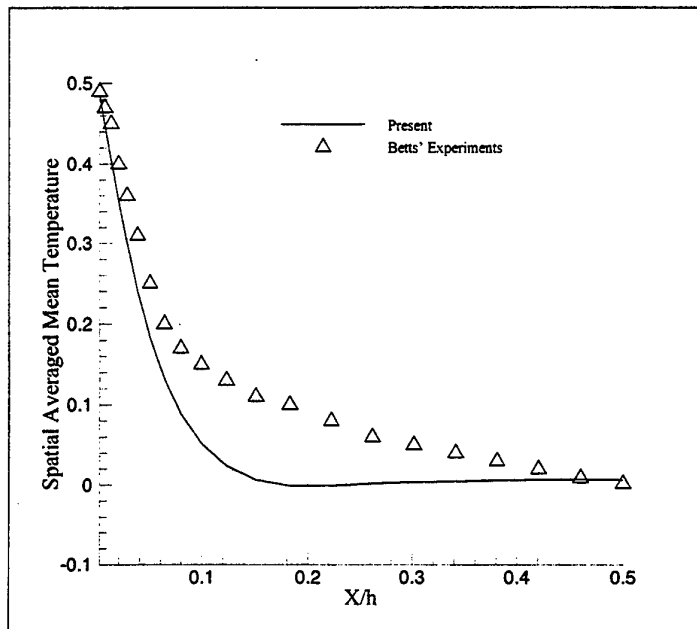


Figure 8: Average temperature profile.

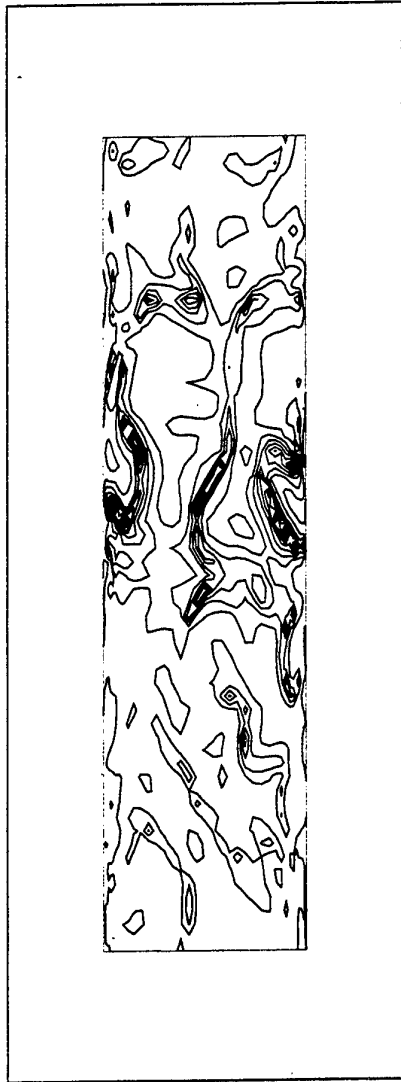


Figure 9: SGS Reynolds stress,  $\tau_{33}$ .

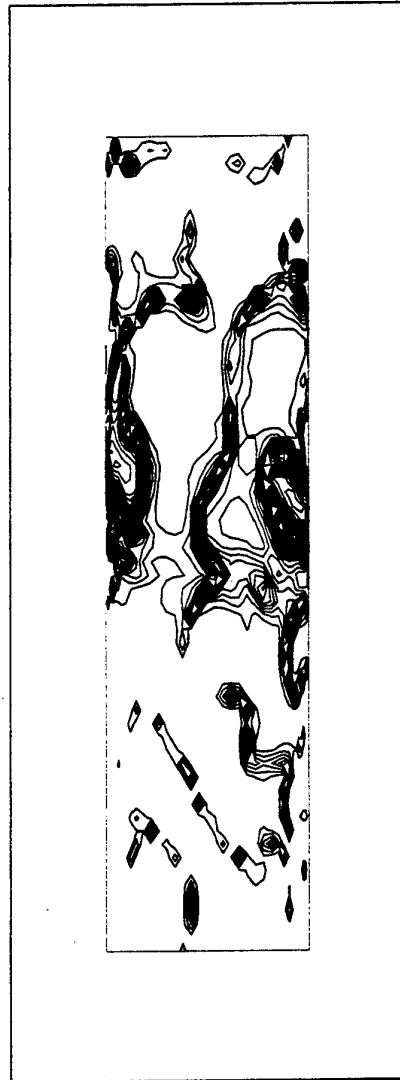


Figure 10: SGS turbulent heat flux,  $\sigma_3$ .

# INFLUENCE OF THE ROUND JET FLOW STRUCTURE ON THE DISTRIBUTION OF LOCAL HEAT TRANSFER AND ITS FLUCTUATIONS ON IMPINGED SURFACE

L. Bogusławski

Chair of Thermal Engineering  
Poznań University of Technology, Poland

## ABSTRACT

The results of experimental investigations of influence of the flow structure on heat transfer on the impinged flat surface have been presented. The wire sensor of constant temperature anemometer was used for velocity measurements. The surface sensor of constant temperature anemometer was used for heat transfer and its fluctuations measurements. The distributions of velocity and turbulent fluctuations of velocity at stagnation and wall region were compared with distribution of the local heat transfer coefficient and its fluctuations on the surface impinged by round jet. The comparison of the power density spectrum of velocity and heat transfer fluctuations shape was used as a indicator of turbulence influence on momentum and heat transport phenomena. This kind of analysis suggest that external turbulence influence mainly along streamline rather than crosswise main flow direction.

## 1 INTRODUCTION

Intensity of the heat transfer on the surface is strongly dependent on the turbulence and its structure in the flow above surface. The free jet impinged surface give possibility to study influence of turbulence on heat transfer in wide range of turbulence level from  $\sim 0.5\%$  to over  $\sim 20\%$ . The turbulent structure of free jet changes downstream of flow. Moreover one can recognise existence of many very characteristic, ordered structures in certain regions of jet flow. This give possibility to investigate change in flow structure and its influence on local heat transfer coefficient and fluctuations of heat transfer coefficient.

For heat transfer fluctuations measurements fast response sensor was used (1).

Radial distributions of the relative heat transfer coefficient as a results of flow structure above surface have been presented. This give possibility to compare structure of flow and heat transfer fluctuations. Many previous investigations indicate non uniform distributions of local heat transfer at stagnation point region e.g. (2), (3), (4), (5). The question is, what kind of phenomena is responsible for such kind of the radial distributions of heat transfer coefficient.

## 2 MEASUREMENT TECHNIQUE AND APPARATUS

Measurements were done in open wind tunnel that generate free, round jet. The constant temperature anemometer (CTA) with hot wire sensor was used for flow structure measurements. The 16-bit digital acquisition system with computer analysis of

experimental data was used. The jet impinged flat, adiabatic surface which was located in different nozzle to surface distances. In the surface there was mounted CTA surface sensor connected with CTA bridge. This kind of sensor can measure the local heat transfer fluctuations on the surface till about 5kHz.

Under certain assumption average CTA bridge signal can be interpreted as the heat transfer coefficient at stagnation point (1). Outside of stagnation point CTA bridge signal is a function of shear stresses and additionally by analogy a function of heat transfer. In both regions the structure of fluctuating component of the signal and shape of its energy spectrum is weak dependent an assumption concern interpretation of the raw CTA signal.

## 3 RESULTS OF MEASUREMENTS

Measurements of radial distribution of the heat transfer and its fluctuations were done for short nozzle to surface distances from 2 till 12 where violent change of flow structure in impinging free jet occurs. In this region changes of flow structures of jet, that influence on the heat transfer process on the surface, were very fast. Very interesting, from point of view future analysis is the characteristic shape of power spectrum of turbulent fluctuations at distances of  $X/D=3$  presented in figure 1. It is visible clear maximum of plot at frequency of order 0.8 kHz. This shape of power spectrum ought to be easily detected in other flow regions if influence of turbulence exist. It is possible to looking for such shapes of spectrum of other fluctuating values.

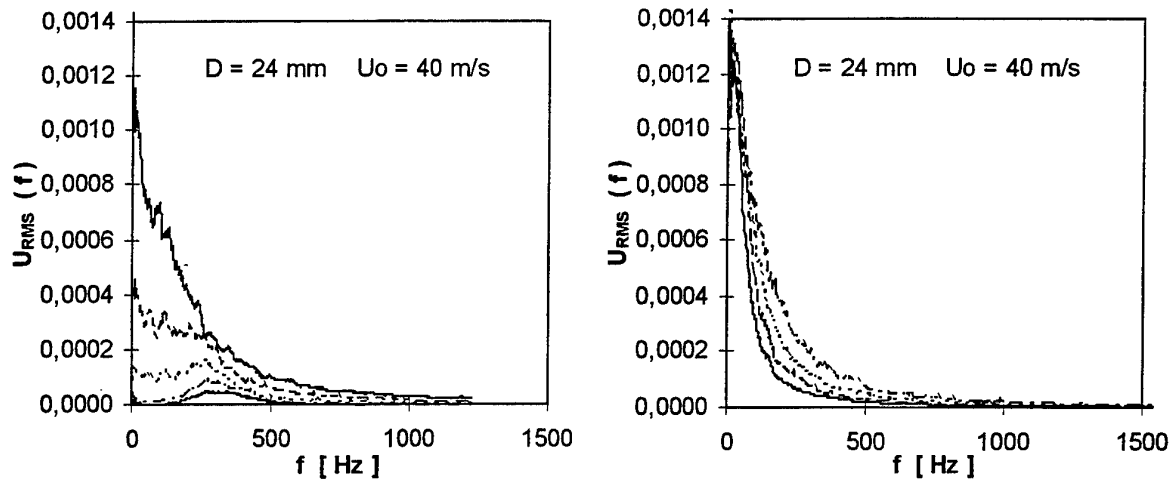


Figure 1 Velocity fluctuations spectrum along free jet axis at distances  $X/D$   
 a) 3, 4, 5, 6, 8 and b) 10, 12, 14, 16

Character of impinging flow fluctuations influence on fluctuations of heat transfer on the surface. It is possible that character of fluctuations can influence on value of average heat transfer. For example at distance nozzle outlet to surface of  $X/D=3$  a very characteristic shape of heat transfer fluctuations spectrum is similar to shape of velocity fluctuations spectrum what is

shown in figure 2. The amplitude of the heat transfer fluctuations on the surface are dumped nevertheless structure looks similar. This similarity of power spectrum of fluctuations give possibility to identify range of influence of external flow on the heat transfer process on the surface impinged by turbulent jet.

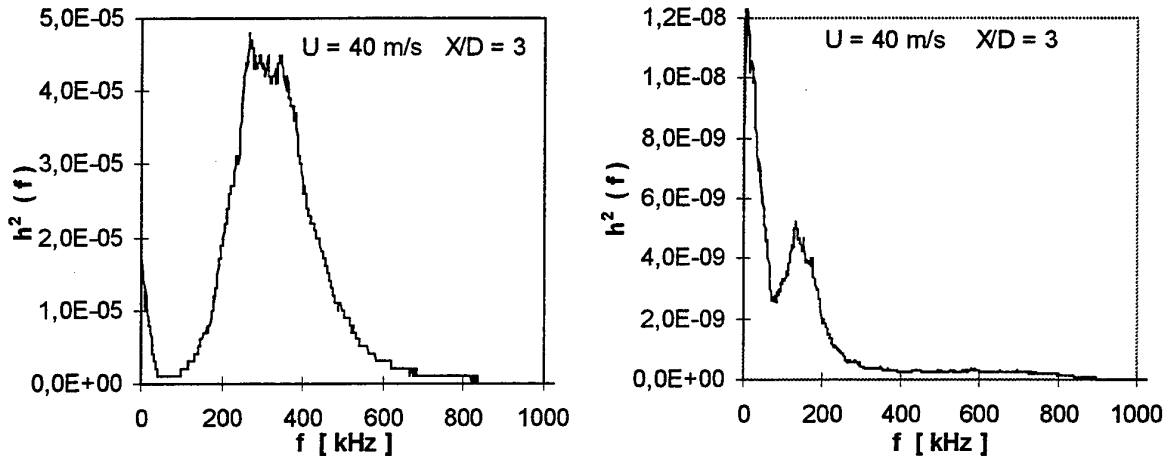


Figure 2 Power spectrum of jet velocity fluctuations and fluctuations of heat transfer coefficient at stagnation point for  $Re=5 \cdot 10^4$  and  $X/D=3$

Using fast response sensor there was possible to measure average value and its fluctuations as well. As an example the radial distribution of the signal from the CTA surface sensor is presented in figure 3 for three nozzle to surface distances. As mentioned, the signal can not be interpreted as shear stress distribution (or by analogy heat transfer distribution) in region  $r/D$

from 0 to  $\sim 0.5$ . Nevertheless for larger distances, distribution of surface sensor signal good correspond to distributions of heat transfer established make use other methods. The main advantages of used method of measurements is possibility to measure average value and turbulent fluctuations of heat transfer coefficient on the wall as well.



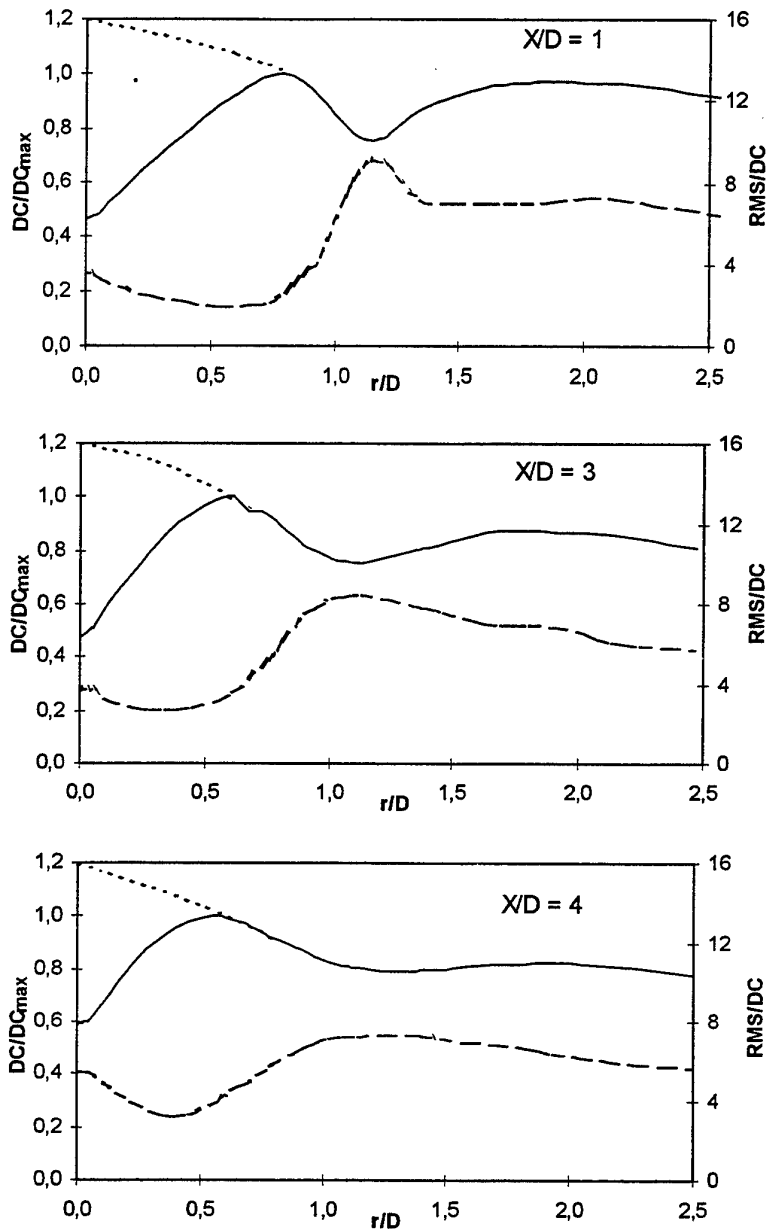


Figure 3 Radial distributions of the local heat transfer coefficient and its fluctuations

The radial distribution of turbulent fluctuations on the wall shows very characteristic relation between distribution of average value and its turbulent fluctuations. At distances of  $r/D > \sim 0.5$  average value of signal go down and reach local minimum. At the some region the rms of fluctuations increase and reach maximum value exactly at the some place where average value of signal has minimum. Next average value of signal grows slowly but rms of fluctuations decreases. There is no direct relation between heat transfer and turbulence in this region. Time average

local heat transfer decrease when fluctuations increase. At this region the gradient of velocity changes is, perhaps, of great weight in heat transfer process. So there is no relation between both distributions in this region.

The power spectrum of turbulent velocity fluctuations in free jet for different radiuses at constant  $r/D$  distances is presented in figure 4. This plots give information concern structure of external flow which can influence on the near wall flow.

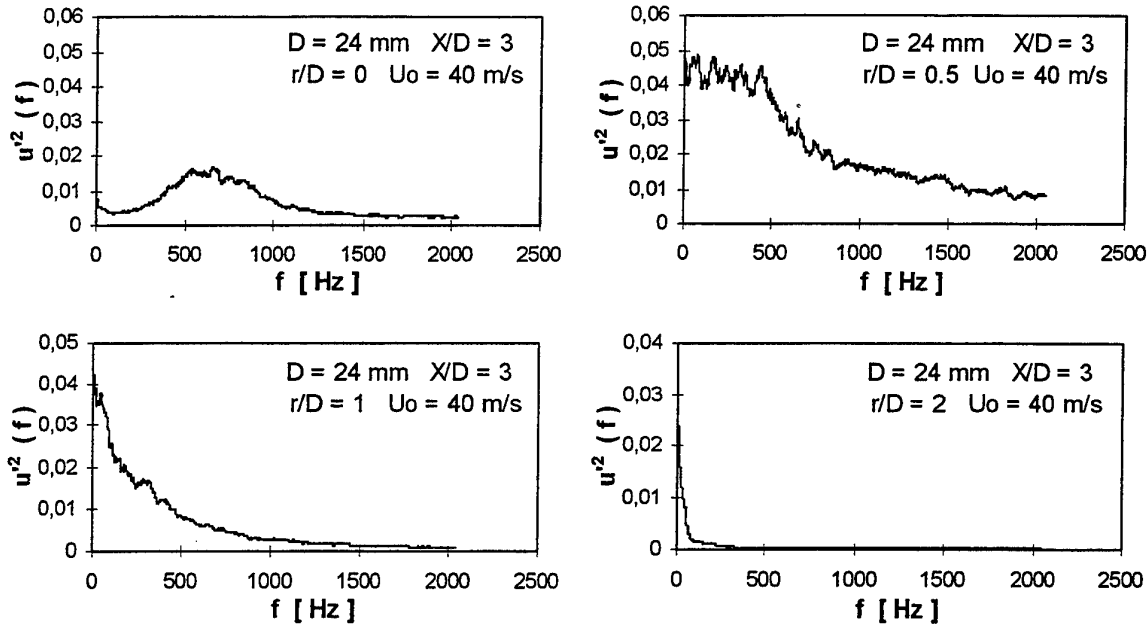


Figure 4 Power density spectrum of free jet velocity fluctuations at distance 3D from nozzle outlet

The jet impinging flat surface change main direction of motion what cases conversion of flow kinetic energy and turbulence as well. The heat transfer process on the surface is dependent on wall jet flow. The question is ,

how strong the influence of external flow turbulence on near wall region which decided on heat transfer is?

The power density spectrum of heat transfer signal measured on surface downstream of wall jet for distance  $x/D=3$  is presented in figure 5.

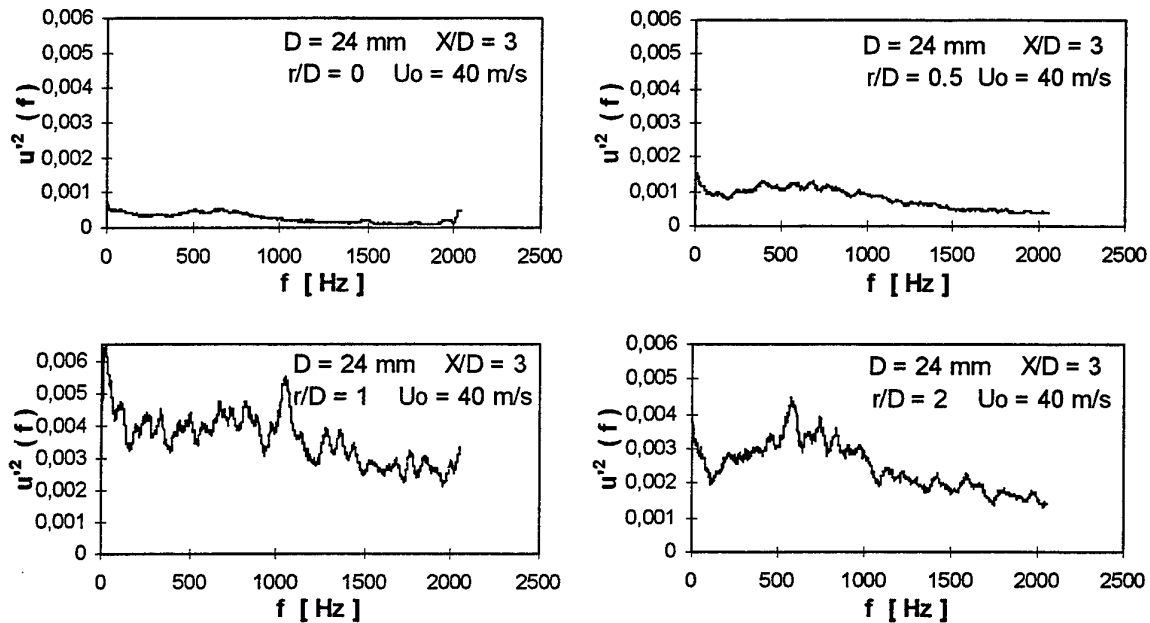


Figure 5 Distributions of the power density spectrum of the CTA surface sensor signal which corresponds to heat transfer fluctuations

Shape of power spectrum of heat transfer fluctuations at stagnation point is very similar to free turbulent jet velocity fluctuations power spectrum at jet axis. Distribution of power spectrum shows the some characteristics , flat maximum at frequency  $\sim 0.8$  kHz. This similarity of shapes of power spectrums suggests that the structure of velocity fluctuations at stagnation point influence on heat transfer fluctuations along the radius.

For larger radius the heat transfer fluctuations power spectrum loss similarity to spectrum of free jet

velocity fluctuations at the some radiuses. For most  $r/D$  distances the spectrum of heat transfer fluctuations on the surface keep shape similarity to very characteristic stagnation point spectrum. This suggests that turbulence influence downstream of wall jet rather then across wall layer.

This observation was confirm by measurements of power spectrum of velocity fluctuations 3mm above the surface what is presented in figure 6.

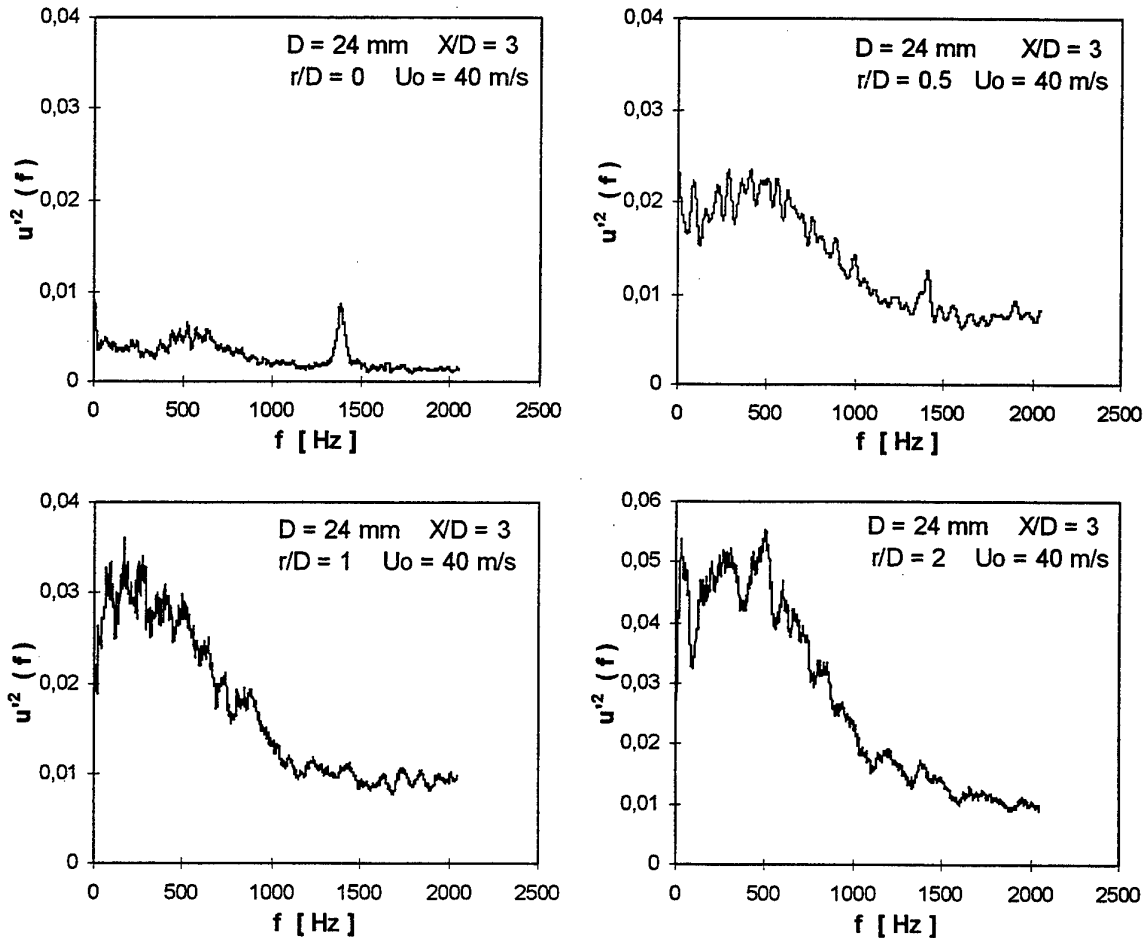


Figure 6 Distribution of the power density spectrum of velocity fluctuations in distance 3mm above the surface for different  $r/D$  distances

Shapes of this plots are similar to shapes of heat transfer fluctuations power spectrum. So this confirm that fluctuations on the surface control fluctuations of flow close above surface. Structure of near wall flow look to be dependent on flow structure near stagnation region.

This comparison indicate that structure of velocity and heat transfer fluctuations are strongly dependent on flow structure at stagnation point region.

The distribution of time average velocity and its fluctuations measured above surface in radial direction indicated that intensity of velocity fluctuations not coincide with radial distributions of average velocity. For example the radial distribution of both values for distance  $x/D$  are shown in figure 7.

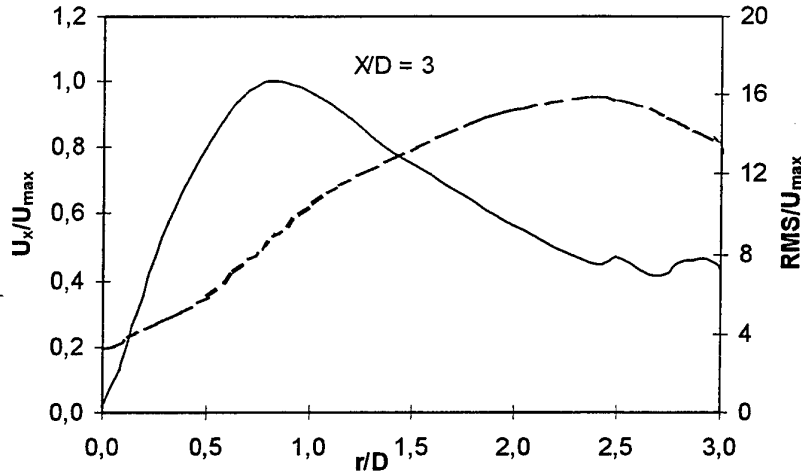


Figure 7 The radial distributions of the flow velocity and its fluctuations in distance 3mm above the surface

The velocity increase monotonously from small value at stagnation point, reach maximum at distance  $r/D \sim 0.8$  and next slowly decrease. The turbulence level increase also but reach maximum at  $r/D \sim 2$  and next decrease. There is no direct relation between both plots.

This distributions not so good coincide with distributions of local heat transfer coefficient. The very characteristic local minimum of heat transfer plot do not corresponds to any velocity characteristics.

#### 4 CONCLUSIONS

At beginning the decreasing trend of the heat transfer is associated with inverse trend of change of velocity measure above surface. In certain distance heat transfer grow and next keep the some level. In this region trend of heat transfer change looks like variation of turbulent fluctuations in flow close above surface. Nevertheless the local minimum of heat transfer corresponds with maximum of heat transfer fluctuations what suggests existence of different kinds of influences and turbulence is important when reach high enough level.

Measurements indicated that near stagnation point region there were region of very low turbulence level. In this region heat transfer drop down. Next turbulence fast increase. This is perhaps the reason that heat transfer change trend and slowly increases follows the turbulence level plot. Analysis of presented plots

indicted that distribution of heat transfer is not direct dependent on turbulence of flow above surface for small nozzle to surface distance.

#### 5 REFERENCES

- (1) Boguslawski, L. Measurement technique of stagnation point heat transfer and its fluctuations by means of a constant temperature sensor, Proceedings of Turbulent Heat Transfer Conference, 1-6, San Diego, May 1996
- (2) Popiel Cz. O., Boguslawski L., Mass or heat transfer in impinging single, round jets emitted by a bell shaped nozzle and sharp ended orifice, 8-th Int. Heat and Mass Transfer Conference, Vol. 4, 46-49, San Francisco 1986
- (3) Gardon R., Akfirat J.C., The role of turbulence in determining the heat transfer characteristics of impinging jets, int. heat transfer conference, 1965, pp. 1261-1272
- (4) Martin H., Heat and mass transfer between impinging gas jet and solid surfaces, Advances in Heat Transfer, 13, 1977, 1-60
- (5) Hansen L.G., Webb B.W., Air impingement heat transfer from modified surfaces, Int. Heat Mass Transfer 36, 1993, 989-997
- (6) Lee D.H. et. all, Heat transfer from a flat plate to a fully developed axisymmetric impinging jet, ASME J. of Heat Transfer 117, 1995, 772

# EXPERIMENTAL INVESTIGATION OF HEAT TRANSFER ENHANCEMENT FOR TURBULENCE DRAG-REDUCING FLOW IN A TWO-DIMENSIONAL CHANNEL

P.W. Li<sup>1</sup>, H. Daisaka<sup>2</sup>, Y. Kawaguchi<sup>3</sup>, A. Yabe<sup>3</sup>, K. Hishida<sup>2</sup>, M. Maeda<sup>2</sup>

<sup>1</sup> Mechanical Engineering Laboratory, AIST, MITI, 1-2 Namiki, Tsukuba 305, Japan

The Energy Conservation Center; New Energy and Industrial Technology Development Organization, Tokyo, Japan

<sup>2</sup> Keio University, 3-14-1 Hiyoshi, Yokohama 223, Japan

<sup>3</sup> Mechanical Engineering Laboratory, AIST, MITI, 1-2 Namiki, Tsukuba 305, Japan

## ABSTRACT

The heat transfer of turbulence flow for drag-reducing surfactant aqueous solution in a two-dimensional channel was investigated experimentally. Wire mesh plug was inserted into the channel to take the role of destroying micelle structure temporarily so as to enhance heat transfer for surfactant solution. The thermal entrance region for surfactant solution was found longer than that of water case. For the solution with surfactant concentration ranges from 30ppm to 90ppm there were no significant differences found in heat transfer performance in the channel without plug. The critical Reynolds number increases with the increasing of surfactant solution. A dependency of the variation trend of Nusselt number versus Reynolds number to the channel's height was proposed to be utilized in the designing of heat exchangers using surfactant solution. It was found that when there was wire mesh plug inserted in the channel, the surfactant concentration influenced the heat transfer significantly. If the flow Reynolds number is close to the critical Reynolds number, the heat transfer of turbulence surfactant solution can be enhanced more efficiently using wire mesh plug. A LDV measurement of turbulence structure for the flow after mesh was conducted. The mesh plug was found play a role to destroy micelle super structures and thus to re-introduce strong turbulence in the flow in case of enhancing heat transfer after mesh plug.

**Key words:** Active techniques for heat transfer augmentation, Drag-reducing, Turbulent heat transfer, Forced convection heat transfer.

## 1. INTRODUCTION

The phenomena, in which adding a small quantity of certain drag reduction additives to water will significantly reduce the turbulence flow skin friction, was firstly reported by Mysels<sup>(1)</sup> and Tom<sup>(2)</sup>. They identified that low concentration of certain soap or polymer additives resulted in a reduction of up to 80% in turbulence energy losses in pipe flow. From then on, there have being investigations about drag-reducing additives and related turbulence flow characteristics. Some surfactants have also shown to be very effective drag-reducers<sup>(3)</sup>. As it performs better than polymer in resistance from mechanical degradation, much interest has been averted recently to drag-reducing surfactant in turbulence drag reduction study.

For practical application, drag-reducing additives are indeed in great potential in reducing power supply of pump in long distance fluid transportation in industry like petrochemical or even to prevent flooding in sewers by increasing the flow rate during times of overloading by heavy rain<sup>(4)</sup>. Recently, surfactant solutions are also recommended to be used in district heating and cooling systems<sup>(5)</sup>. It is preferred in such case that the utilization of drag-reducing fluid do not result any decrement in heat transfer performance while retaining its drag-reducing ability. However we can not achieve this two benefits at the same time. There has serious heat transfer reduction even in a larger percentage than that of drag-reduction been found for

drag-reducing turbulent flow<sup>(6)</sup>. As the adding of drag-reducing material will made the solution to be Non-Newtonian fluid. This flow and heat transfer thus shows quite different characteristic from that of Newtonian fluid.

Of the information available for turbulence heat transfer of drag-reducing fluid, most of them were about polymer solutions. It is believed generally for polymers that the hydraulic and thermal entry lengths are significantly longer than that for Newtonian fluid. The polymer concentration, polymer type, flow rate of the solution were proved to affect the thermal entrance length and heat transfer reduction significantly<sup>(7)</sup>. Although surfactant solutions share common with polymer solutions in some rheology properties, their performance in drag reducing has already been proved in quite difference. Therefore the present work will focus on surfactant solution to investigate its heat transfer characteristics and to develop enhancement methods.

It should be mentioned to the critical Reynolds number and critical temperature for the surfactant solution, above either of them the drag reducing effect will disappear with the flow and heat transfer characteristics being Newtonian fluid dominated. And on the other hand, if the Reynolds number and temperature decrease to lower than critical Reynolds number and critical temperature, the surfactant solution will regain its drag-reducing ability and at the same time its heat transfer ability will

decrease to be characterized by Non-Newtonian fluid<sup>(6)</sup>. So for the purpose of reducing drag force, the working condition of the surfactant solution should be kept both under critical Reynolds number and critical temperature. On the other hand, a same heat transfer performance like that of Newtonian fluid can be attained by either keeping at higher temperature above critical temperature or running at higher Reynolds number larger than critical Reynolds number. It was already proved that the critical Reynolds number for drag reduction degradation is different for different pipes. To investigate the relationship of heat transfer performance to the critical Reynolds number is thus one issue of the present paper.

Gasljevic et al.<sup>(8)</sup> reported an experimental investigation to the heat transfer of aqueous solution of Ethoquad T13 and NaSal with a mass concentration of 2300 ppm in a pipe. They found that the hydraulic and thermal entrance lengths were around 117 and 130 times of diameter of the pipe for their case and that the entrance regions were in same order of magnitude for friction and heat transfer, unlike in the case of polymer solutions. Entry flow with wire mesh plugs was induced in their study to enhance heat transfer however, an increment of heat transfer coefficient was at a great expense of pressure drop over the plug and therefore the method was not recommended by them. It should be noted that at high concentration of surfactant the critical Reynolds number is very high for the solution. So it may be better to consider the rheology properties of surfactant solution because the surfactant concentration and thereby characterized micelle structure in surfactant solution affect the turbulence distribution significantly. The destruction of micelles super structure under high shear stress is the key for the flow to change from drag-reducing flow to turbulence flow. And the critical shear stress corresponding to critical Reynolds number is very sensitive to surfactant concentration<sup>(9)</sup>. It is also clear that the critical shear stress of lower concentration solution is smaller than that of high concentration solution. Thus for less cost of pressure drop our experiment was conducted for flow with low surfactant concentration.

It was recommended by Steiff et al.<sup>(10)</sup> that heat exchanger which can generate high shear flow such as plate heat exchangers may have high efficiency of heat transfer. Kawaguchi et. al<sup>(11)</sup> also found in a two-dimensional channel that corresponding to a high shear gradient near the heating wall a high diffusivity layer exist in the flow of surfactant solution. Comparatively there is little data on heat transfer of surfactant solutions in flat plat channels. The present study, therefore, intend to develop a phenomenological understanding of the heat transfer and enhancement methods of drag-reducing solutions in two-dimensional channel through experiments.

## 2. EXPERIMENTAL SETUP AND PROCEDURE

The experimental tests were done using a setup

consisted of a 2m<sup>3</sup> tank, a centrifugal pump with variable-speed control, water channel, connection pipes and measuring instruments as is shown in Fig. 1.

The 2m<sup>3</sup> tank serves as reservoir for surfactant aqueous solution with its temperature be conditioned at a set value through electric heating and tap water cooling. A motored disturber was installed to ensure the solution temperature to be of uniform in the tank. The temperature fluctuation in the tank was thus controlled to be within  $\pm 0.2^{\circ}\text{C}$  around the set value during testing circulation through these above instrumentation.

The water channel, made of perspex, is 6 meters in length, 500mm in spanwise and 40mm or 30mm in height depend on testing case. At its entrance a honeycomb rectifier in length of 150mm with 10mm  $\times$  10mm rectangular openings was used to remove large eddies. In order to bump any pressure disturbance a specially designated settling chamber equipped with a distributor and a smooth contraction nozzle was used in front of the honeycomb and a collection chamber was installed at the end of the channel. To make it possible for the entry conditions to be of hydraulic fully developed, the channel was made of three segments. The heating test section, 1.6 meters in length and starting from two meters downstream the entrance of the channel, has a stainless steel film heater glued to the inner side of one spanwise wall. The current and voltage through the film heater was measured to estimate the uniform wall heat flux. The channel was also designed possible to insert a mesh in front of heating section to enhance heat transfer. After the two-dimensional channel the flow was collected to pass an electrical-magnetic flow meter and then return back to reservoir through a pipe. The calibrated resolution of the flow meter is 0.01 m<sup>3</sup>/min.

The flow rate was modulated through speed variation of the pump. And the centrifugal pump did not cause any noticeable degradation to the surfactant solution.

There were 25 thermocouples for wall temperature measurements attached flush to the heating wall on the plane of spanwise and covered by the film heater properly. At the thermal entrance region thermocouples were arranged more closely between one and other.

The pressure drop was measured with a high precision pressure transducer in resolution of 0.1 Pa. The uncertainty for our measurement of friction coefficient is estimated to be about 1 to 2 percent.

The temperature measurements by thermocouples were acquired by IM DA 100-01E data acquisition unit which has 40 channels and easy to communicate with computer. In order to make sure of the experimental system being steady state, all the temperature readings were monitored to be almost constant before any data acquisition. And the heat transfer data in this work are averages obtained over several minuets. The transport properties for data reduction were based on the inlet fluid temperatures

because we set same heat flux for all the tests and the fluid bulk temperature had no much increment for all the cases. The uncertainty of heat transfer coefficients was estimated not larger than 8 percent in the tests.

As the concentration of surfactant is very small, the thermal-physical properties of solvent were used in the data reduction. This also make it convenient to compare the results of surfactant solution with that of water. The height of the channel was taken as the characteristic length for Reynolds number and Nusselt number.

The surfactant tested in our experiment was Cetyltrimethyl ammonium chloride (CTAC) named Catinar CTC-70ET as a product by Toho Kagaku Co. Japan. Its effective temperature in drag reducing ability ranges from 10 °C to 40 °C. The chemical

formula of CTAC is  $C_{16}H_{33}N(CH_3)_3Cl$  with molecular weight of 320.00 g/mole. The surfactant solution was prepared by adding a certain weight concentration of CTAC to tap water. A same weight concentration of Sodium Salicylate was added to the solution as counter-ion material.

Wire mesh was expected in this study to play such a role to destroy the micelles super structure through creating high shear stress in the solution temporarily. A special fitting made the sandwiched wire mesh possible to be inserted in front of the heating section. Two types of stainless steel mesh, namely type-A and type-B, were used in the test. They have the same wire diameter in 0.19 mm and a different opening rate. There are 7.6 wires average in 1.0 cm mesh for type-A and 19.2 for type-B.

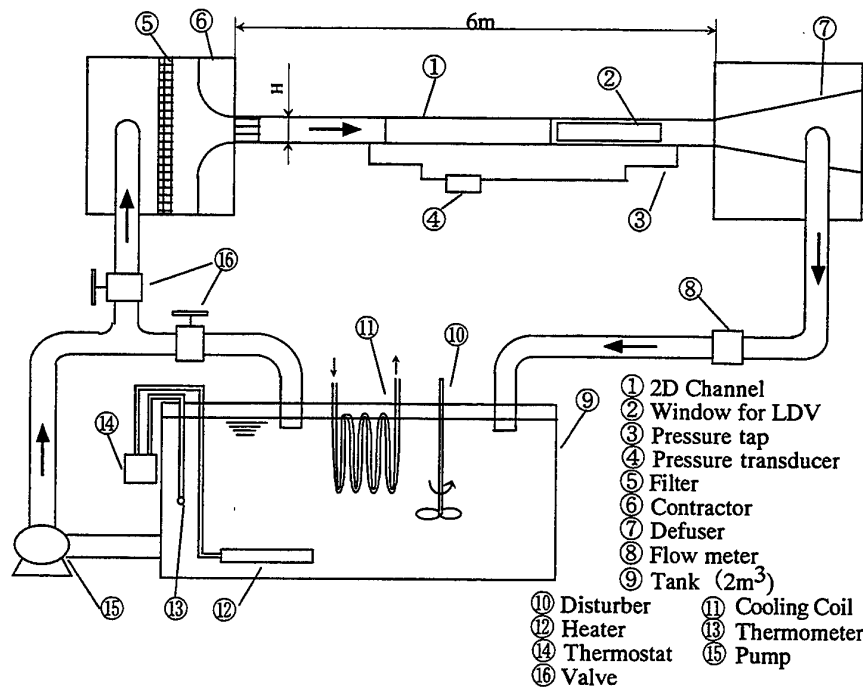


Figure 1 Diagram of the experimental setup

### 3. RESULTS AND DISCUSSIONS

#### 3.1 Drag reducing test

The friction factors under six concentrations were measured with the flow bulk temperature equaled to 30°C. The channel for this test is 40mm in height. Fig.2 was plotted in terms of friction factor and Reynolds number, where the solid line represents the friction factor of water given by Dean's equation<sup>(12)</sup> for two-dimensional channel and the dashed line the Virk's friction factor asymptote<sup>(13)</sup> for drag reducing flow. The critical Reynolds number for 25 and 30 ppm solution are found smaller than  $3 \times 10^4$ . And their drag-reducing effect can reach the asymptote as same as

that of other cases. With the increasing of surfactant concentration the critical Reynolds numbers increase and for 60ppm and 90ppm solution the critical Reynolds number are even larger outside the maximum Reynolds number of our test facility. The existing of different critical Reynolds numbers for different concentration was because of the different length of rod-like micelles. The rod-like micelles and their aggregations, which is called super structured micelles, are generally believed to affect the drag reducing ability for surfactant solution. The length of rod-like micelles was proved increases with the increasing of surfactant concentration<sup>(9)</sup>. Because the losing of drag-reducing ability is caused by the destruction of super structured micelles at high shear stress, the longer of the rod-like micelles the more

difficult to destroy the super structured micelles. This can also be found that the transition region from drag-reducing flow to complete turbulence flow in Fig.2 in respect of Reynolds number is larger for the higher concentration solution.

There is a minor increment of the friction factor before critical Reynolds number if the surfactant concentration increase larger than 30 ppm. This reflects a minor increment of the viscosity of surfactant solution when the concentration increases although the main friction properties were controlled by micelle structure in solution. A bump in the two curves for 60 ppm and 90 ppm was found. Bewersdorff et al. <sup>(14)</sup> also reported in their work for CTAB solutions about the bump however the reason is still not clear.

The degradation of drag-reducing effect is generally accompanied by the regaining of heat transfer ability to same order as that of solvent flow. For the destruction of micelle structure by high shear stress the high concentration surfactant solution will be with more difficulties because of its high critical Reynolds number and related critical shear stress. It is no doubt that this characteristic will has a reflection also in heat transfer.

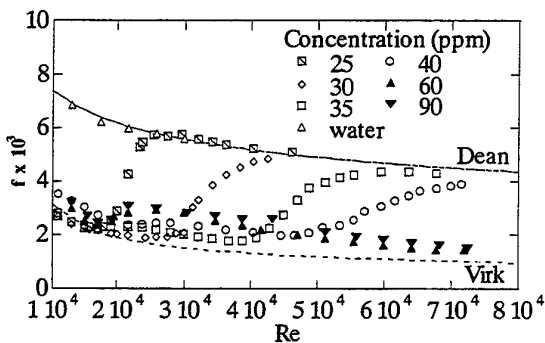


Figure 2 The friction factor at different concentration

### 3.2 Heat transfer characteristics

#### 3.2.1 Two-dimensional local heat transfer

The Reynolds numbers here for the heat transfer test were subjected to not larger than critical Reynolds number in order to keep its drag-reducing ability in heat exchanging. The channel used here was 40mm in height. With bulk temperatures equaling to 30 °C three solutions with surfactant concentration equaling to 30ppm, 60ppm, and 90ppm were tested for two Reynolds numbers respectively. The variation trend of local heat transfer Nusselt number versus streamwise normalized position of heating plate is shown in Fig. 3.

The heat transfer coefficients of surfactant solution are smaller than that of water case even the surfactant concentration is in such a small order. Actually the thermal properties of surfactant solution were not changed significantly from that of solvent since the concentration of surfactant is very small.

However, the micelle structures in surfactant solution depress the turbulence fluctuation to make the flow as "pseudo-laminar" flow. Therefore the turbulence diffusion is very weak for surfactant solution flow and thus results lower heat transfer intensity. This phenomenon reflects a special property characterized by surfactant solution in which the micelle structure and related rheology properties must be considered.

Like that for drag-reducing intensity, heat transfer coefficients also have no significant differences for the three solutions in different concentration. This means that at one certain Reynolds number, which is smaller than any of the critical Reynolds number of the three cases the prohibiting of turbulence fluctuation by micelle structures is almost in same intensity even the surfactant concentration of the solution is different.

Compared to water case the thermal entrance region is longer for surfactant solutions and increases with the increasing Reynolds number. A correlation relating the entrance region and fully developed region in the formula given by Hufschmidt <sup>(15)</sup> for Newtonian fluid can be adopted here to fit our data.

$$Nu(x) = Nu_{\infty} [1 + C/(x/H)] \quad (1)$$

The C in Eq. (1) depends on Reynolds number and Prandtl number. For the present experimental data C for water is about 0.2 and around 1.0 for surfactant solutions. The larger value of C reflects a longer thermal entrance length.

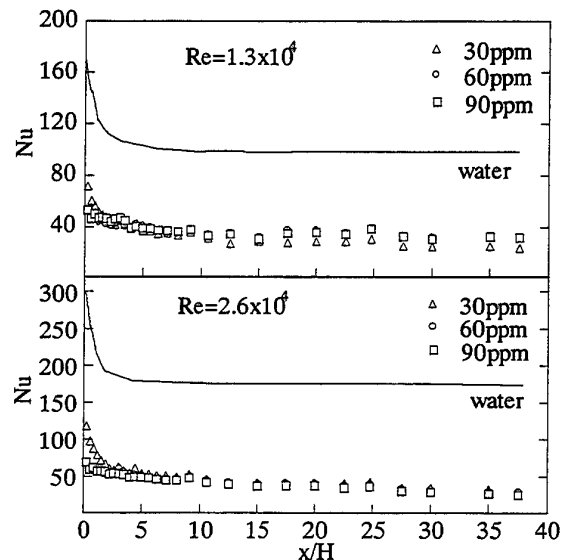


Figure 3 Local heat transfer coefficients distribution

#### 3.2.2 The heat transfer recovery

With the reverse of friction factor from drag-reducing flow to turbulence flow the heat transfer coefficient will also recover to the same as solvent does coincidentally. Shown in Fig. 4 is the heat transfer Nusselt number at



fully developed section versus Reynolds number with channel height of 30mm and 40mm respectively. The surfactant concentration of the solution tested here is 30ppm with inlet temperature of 30°C. We see that the recovery starting point of heat transfer is almost as same as that of friction factor both for the two different channels. This coupled variation of friction factor and heat transfer coefficient reflects a strong dependency of heat transfer to the turbulence structure characterized by drag-reducing flow.

Unlike Newtonian fluid, here the variation trends of dimensionless heat transfer data versus Reynolds number was found affected by the characteristic length of the flow ducts. The critical Reynolds number for the channel with height of 30mm is smaller than that for the channel with a height of 40mm. From the rheology properties of the solution, it is already known that the critical shear stress is unique for surfactant solution and above it the deformation of micelle structure occur. Under same Reynolds number the flow shear stress in small duct is higher than that in larger duct, therefore the drag-reducing ability in small duct degrade earlier than that in larger duct in respect to Reynolds number. The measurement of friction factor for pipes with surfactant solution also show that the critical Reynolds number is not unique where the degradation of drag-reducing ability occurs<sup>(9)</sup>. This should be considered in case of connection for ducts with different dimensions where the flow should be controlled with Reynolds number for the smaller duct not larger than its critical Reynolds number, otherwise friction force may go up suddenly in the whole system. However in order to solve the problem of heat transfer reduction this character may be utilized where we can run the flow in heat transfer duct with a high shear stress to get same order of heat transfer as solvent does at least. As the critical Reynolds number is different in different channel, we can arrange the duct with a contracted section where the shear stress may be higher than critical shear stress and thus a same heat transfer intensity as that of solvent can be achieved.

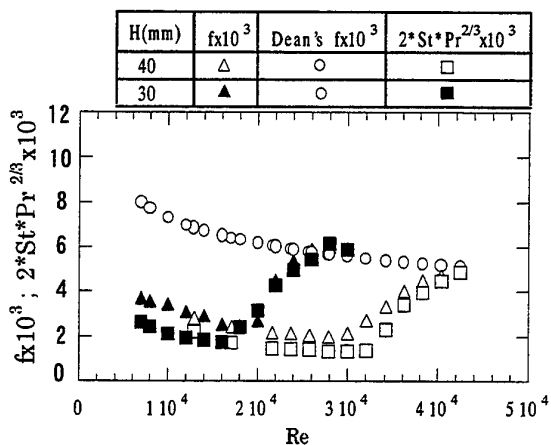


Figure 4 The effect of channel height to flow and heat transfer

### 3. 2. 3 Heat transfer enhancement

From Fig.4 it is already clear that the heat transfer coefficient of surfactant solution is lower than that of solvent if the solution pertain to drag-reducing flow at same time. According to the rheology properties of surfactant solution the quite possible way to enhance heat transfer is to recover the flow from drag-reducing flow to turbulence flow thus the heat transfer coefficient will be as same as that of solvent. To do this a high shear stress is the necessary condition for the destruction of micelle structure. One way to induce high shear stress is just to run the flow higher than critical Reynolds number where the fluid is totally subjected to high shear stress. Such a case was already depicted by the above discussions in section 3.2.2. Another way is to induce temporary higher shear stress so as to destroy micelle structure temporarily in the flow. The following discussion will be on the later.

In order to destroy the micelle structure in surfactant solution stainless wire mesh was used in this study. An insertion of five juxtaposed sheets of A-type wire mesh was put in front of the heating section. The wire mesh was tested showing negligible effect to the heat transfer of water in the present channel.

The heat transfer tests for two different concentrations at four different Reynolds numbers were done on the channel with height of 40mm and the inlet temperature of the flow equaling to 30°C. It is interesting to note from Fig.5 that with the increasing of Reynolds number mesh can enhance heat transfer more and more effectively. With the increasing of surfactant concentration the effect of mesh to heat transfer enhancement becomes smaller. Generally speaking, the cases of high surfactant concentration or low Reynolds number shown a low sensitivity to heat transfer enhancing activation.

To go over the drag reduction test results we can find that Reynolds number of  $2.4 \times 10^4$  is close to critical Reynolds number in 30ppm case. Thus the additional shear stress needed for the breaking up of micelles structure is not so large. But at a smaller Reynolds number the kinetic energy of the fluid is not enough and thus the breaking up of micelles structure is more difficult. For the surfactant concentration at 40ppm, critical Reynolds number is larger, and therefore at a same Reynolds number the present additional shear stress is not enough to break up the micelle structure.

The heat transfer enhancement effect by mesh is sensitive to the surfactant concentration. This is because that the micelle structure of the solution is affected sensitively by surfactant concentration. In the work of Gasljevic et al.<sup>(8)</sup>, they used sixteen sheets of wire mesh to enhance heat transfer for a drag reducing surfactant solution flow at 2300 ppm in a pipe. As a result, they did not see an expected effect of heat transfer enhancement but saw an unacceptable pressure drop. In our case the surfactant concentration is not so high that we can run the flow at a Reynolds number closer to critical Reynolds number and thus we saw an

improvement of heat transfer coefficient at lower cost of pressure drop over the wire mesh.

From the above discussion it can lead to a conclusion that the mesh produce additional shear stresses which increase with the increasing of Reynolds number. And only when the total shear stress is larger than critical shear stress the heat transfer enhancing effect can appear. As the surfactant concentration

affects the critical shear stress very much the heat transfer enhancement effect of mesh is also affected remarkably by the concentration of surfactant. The surfactant concentration of the solution and its corresponding critical Reynolds number in the duct must be considered as a whole if a mesh is expected to enhance the heat transfer of surfactant solution.

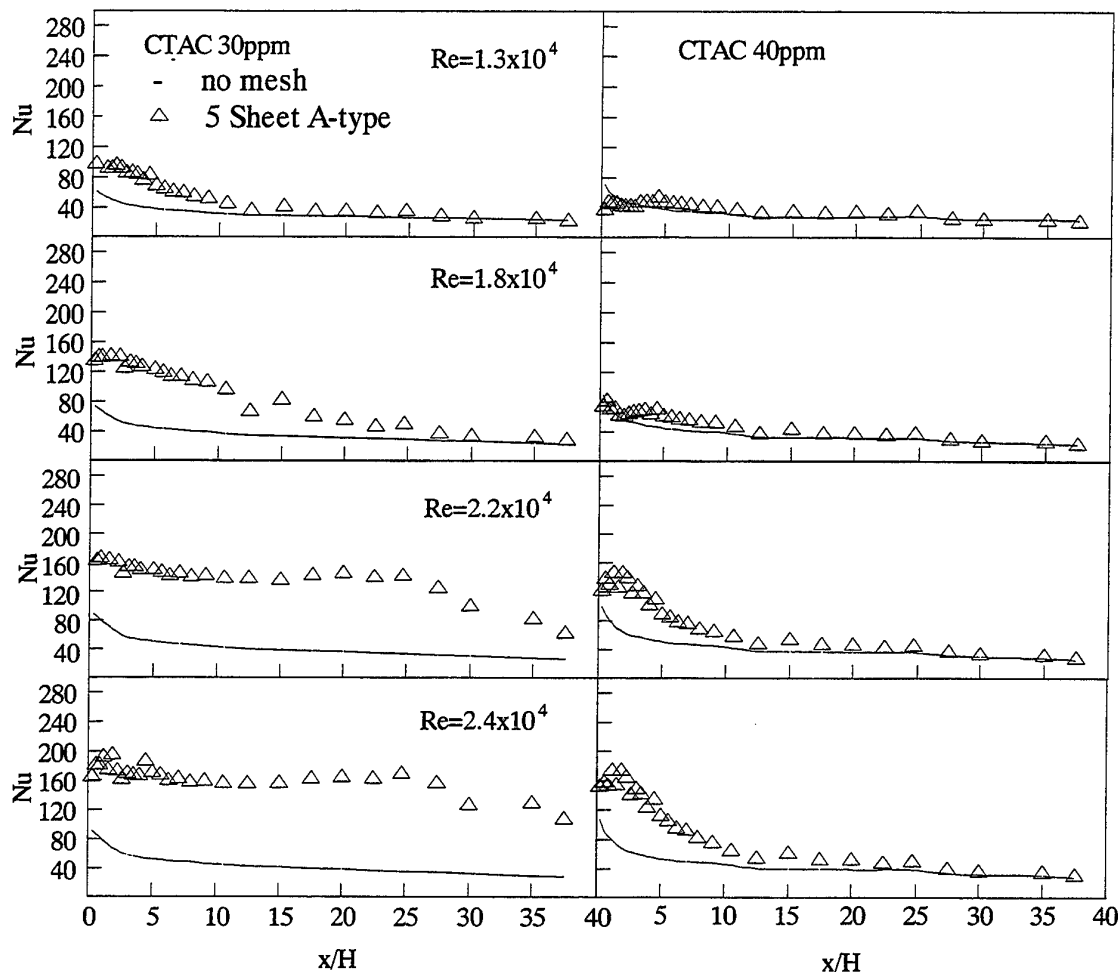


Figure.5 The effect of heat transfer enhancement by mesh

As the rod-like micelles in surfactant solution always tend to aggregate to be super-ordered structures. Here we can see another interesting phenomena from the heat transfer results that the local heat transfer coefficients decrease after the mesh and recover to the same as plug-less case within a certain distance. This implies that after destruction by mesh the rod-like micelles aggregate to be large order structures again. This also reflects a temporary and localized characteristic. However it is appreciable for drag-reduction purpose because the solution can regain its drag-reducing ability after mechanical destruction. Corresponding to the recovery distance is a recovery

time. This time is actually related to the formation of large order micelle structure and increases with the increasing of flow velocity because under high velocity the formation becomes more difficult. When the flow velocity is large enough to produce a shear stress larger than critical shear stress the recovery time will be infinitely large and the flow is in turbulent. The surfactant concentration influences the recovery time negatively where higher concentration of surfactant results a shorter recovery time. Under the present tested conditions the recovery time for 5 sheets A-type mesh plug was around two to three seconds based on the velocity of the flow.

### 3. 2. 4 The turbulence structure after mesh

For the case where there is heat transfer enhancement effect by mesh the turbulence structure after mesh were measured using LDV. Typically the turbulence structures at the position with  $x/H$  equaling to 1, 6, 25, and 30 for 30ppm solution with inlet temperature of 30°C are shown in Fig. 6. Here the Reynolds number is  $2.2 \times 10^4$  with channel height of 40mm. As the solution of 60ppm did not show any significant heat transfer improvement by mesh plug at such a Reynolds number, the measurement for 60ppm case can be taken for reference as drag-reducing flow even just after mesh. The test for water case however gives a reference as turbulence flow.

Corresponding to the local heat transfer coefficient distribution at positions of  $x/H$  equaling to 1, 6, the heat transfer is enhanced well and at positions of  $x/H$  equaling to 25, 30, the heat transfer coefficient decrease to be as same as that of drag-reducing solution.

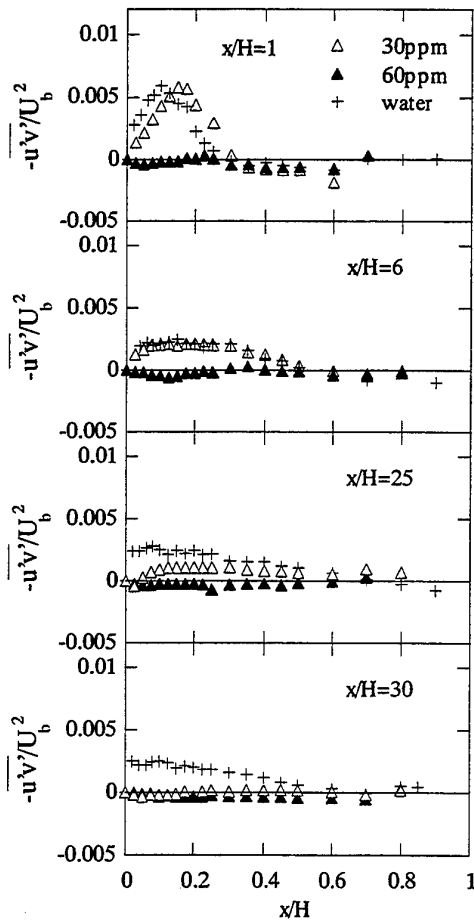


Figure 6 Turbulent structure after mesh

It is shown in Fig.6 that the turbulence stress in high heat transfer coefficient region is almost as same as that of water which reflect a real turbulence state. This indicates that mesh play a role to destroy the

micelles super structure and thus resulting a temporary turbulence flow after the mesh. When it goes done stream the flow recovered to be drag-reducing flow thus we see that the turbulence structure at position of  $x/H$  equaling to 25 and 30 experiencing a changing from turbulence to drag-reducing state.

### 3. 2. 5 The effect of mesh structure to heat transfer

As the pressure drop resulted by wire mesh plug is related to energy losing, the plug should be properly arranged to minimize pressure drop while to enhance heat transfer at most. The later discussion will turn to the relationship of the pressure drop over plug to the heat transfer enhancement effect.

To evaluate the heat transfer enhancing effect and the related expense of pressure drop, Nusselt number, which was averaged over the heating section, and pressure drop over the testing section including mesh plug at several Reynolds numbers were plotted in Fig.7. The pressure drop including mesh plug is represented by  $dp$  and that for the flow without mesh plug is noted by  $dp_0$ . The average Nusselt number of the heating plate with mesh plug is  $\bar{Nu}$  while  $\bar{Nu}_0$  represent that for the case with no mesh.

The two types of mesh were tested with different number of sheets included in the plug. The numbers attached to the symbols in Fig.7 represent the total number of sheet in the mesh plug. It is obvious that because of the different dimensions of mesh the heat transfer improvement and its related cost of pressure drop are not same for the two types of mesh.

For A-type mesh the drag force increment and heat transfer coefficient increment were shown for three plugs different in sheet number by empty symbols marked 1, 3 and 5 in Fig. 7. The value of  $\bar{Nu}/\bar{Nu}_0$  for the plug with five sheets of A-type mesh seems even higher than the plug with one sheet of B-type mesh at the tested four Reynolds numbers although their pressure drop values are almost same.

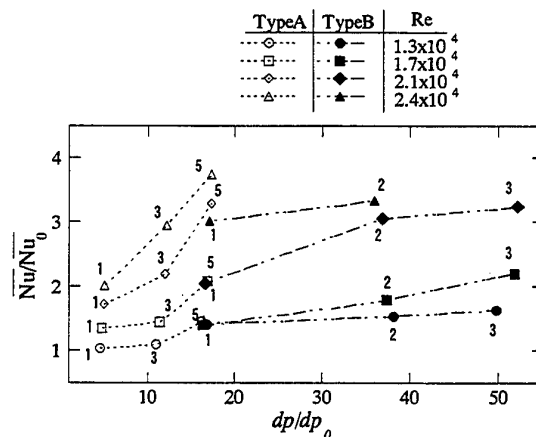


Figure 7 Average Nusselt number vs. pressure drop

For B-type mesh the test results for 1 sheet, 2 sheets, and 3 sheets were shown in Fig.7 by blackened

symbols marked 1, 2 and 3 correspond to the mesh's sheet number of the plug. The heat transfer increment is not linearly proportional to the pressure drop increment. When the Reynolds number is large enough a small heat transfer increment will be at an expense of large pressure drop.

Nevertheless the comparison of benefit in heat transfer improvement and cost of pressure drop between A-type and B-type mesh implies that there is optimum dimension for the mesh to create an effect of heat transfer enhancement with less expense of pressure drop. The A-type mesh in this study may be recommended at the present conditions to enhance heat transfer for surfactant solution.

#### 4. CONCLUSIONS

Heat transfer and enhancement for turbulence flow of drag-reducing surfactant solution was experimentally investigated in a two-dimensional channel. In order to enhance heat transfer of surfactant solution wire mesh was used as a plug in front of heating section. Several points should be mentioned as the conclusions of this work.

For the solution with lower concentration of surfactant the critical Reynolds numbers is lower. When the flow Reynolds number larger than critical Reynolds number the heat transfer of the solution will recover to as same as that of solvent coincidentally with the degradation of drag-reducing ability. For high concentration surfactant solutions the friction factors at Reynolds number smaller than critical Reynolds number are little bit larger than that for solution with lower surfactant concentration.

The critical Reynolds number is an important factor to the heat transfer enhancement. The variation trend of heat transfer Nusselt number versus Reynolds number was found having dependency on the channel's height in case of surfactant solution. Based on this characteristic a proper arrangement of flow duct with different dimensions for the surfactant solution at a proper concentration is possible to keep drag-reducing ability in one flow section and recover heat transfer ability as solvent does in other flow sections.

The thermal entrance region of surfactant solution is longer than that of water even at lower concentration and increase with increasing Reynolds numbers like that of Newtonian fluid. The heat transfer coefficient in two-dimensional channel for surfactant solution with concentration ranges from 30ppm to 90ppm shown no significant difference. However, the heat transfer enhancement effect by means of wire mesh inserting was influenced by the surfactant concentration seriously. With the increasing of Reynolds number the wire mesh plug takes more effectiveness to enhance heat transfer. To speak as a whole, the enhancement of heat transfer by mesh for high concentration surfactant solution or at low Reynolds number is more difficult.

The LDV measurement of velocity and turbulence intensities shown that with the heat transfer enhancement and decrement the flow after mesh experiences a changing from turbulence to drag-reducing flow. The role of mesh in enhancing heat transfer is to destroy the micelle structure and therefore to activate turbulence in the flow.

The coupled investigation of heat transfer enhancement and thereby resulted pressure drop shown that the pressure drop is not linearly in proportion to heat transfer improvement. It is possible to optimize the parameters of wire mesh for better heat transfer enhancement and less cost of thereby induced pressure drop. The A-type wire mesh studied in this work is preferable for its heat transfer enhancement ability at a relatively lower cost of pressure drop.

#### NOMENCLATURE

$dp$	Pressure drop (Pa)
$f$	Friction factor $\tau_w/(0.5\rho U_b^2)$
$h$	Heat transfer coefficient (W/m <sup>2</sup> K)
$H$	Channel height (m)
$Nu$	Nusselt number $hH/\lambda$
$Re$	Reynolds number $U_b H/\nu$
$u'$	Turbulence velocity fluctuation in streamwise direction (m/s)
$-\overline{u'v'}$	Term that times $\rho$ (density of solvent (Kg/m <sup>3</sup> )) representing Reynolds stress (m <sup>2</sup> /s <sup>2</sup> )
$U_b$	Streamwise bulk velocity (m/s)
$v'$	Turbulence velocity fluctuation directed in channel's height (m/s)
$x$	Downstream distance from starting point of heating plate
$\rho$	Density of solvent (Kg/m <sup>3</sup> )
$\tau_w$	Wall shear stress (Pa)
$\lambda$	Thermal conductivity (W/m·K)
$\nu$	Kinematic viscosity (m <sup>2</sup> /s)

#### ACKNOWLEDGEMENT

Li Peiwen, one of the author, wishes to express sincerely thanks for the support of NEDO (New Energy and Industrial Technology Development Organization, Tokyo, Japan) industrial technology research program.

#### REFERENCES

- (1) Mysels, K.J., US Patent 2492173, December 27, 1949.
- (2) Toms, B.A., in Proc. 1st Int. Rheol. Cong., North Holland Publishing Co., 1949, P.135.
- (3) Lu, B., Li, X., Zakin, J.L., Talmon, Y., A Non-Viscoelastic Drag Reducing Cationic Surfactant System,

Journal of Non-Newtonian Fluid Mech., Vol.71,1997, pp59-72.

(4) Sellin RHJ (1984), Third International Conference on Drag Reduction, Bristol, UK, Paper I3.

(5) Pollert, J., Zakin, J.L., Myska, J., and Kratochvil, P., 1994, Czech Republic, Proc. Int. District heating and Cooling 1994 conference, pp.141-156.

(6) Kawaguchi, Y., Daisaka, H., Yabe, A., Hishida, K., and Maeda, M., Existence of Double Diffusivity Fluid Layers and Heat Transfer Characteristics in Drag Reducing Channel Flow, Proc. 2th International Symposium on turbulence Heat and Mass Transfer, June,1997, Delft.

(7) Ken H. Toh and Afshin J. Ghajar, Heat Transfer in the Thermal Entrance Region for Viscoelastic Fluids in Turbulent Pipe Flows, Int. J. Heat Mass Transfer. Vol. 31, No.6, pp1261-1267, 1988.

(8) Gasljevic, K., Matthys, E.F., Experimental Investigation of Thermal and Hydrodynamic Development Regions for Drag-Reducing Surfactant Solutions, ASME Journal of Heat Transfer, Vol.119, Feb. 1997, pp80-88.

(9) D. Ohlendorf, W. Interthal, and H. Hoffmann, Surfactant system for drag reduction: Physico-chemical properties and rheological behaviour, Rheol

Acta Vol.25, pp468-486 (1986).

(10) Steiff, W. A, Groth, S., Helmig, J., Kleuker, H. -H., Wocadlo, T., Weinspach, P. -W., Progress in the Application of Drag Reducing Additives in District Heating Systems, In Proc. Int. Symp. on Fluids for District Heating, B.Bohm ed., Technical University of Denmark, Copenhagen, Denmark, pp35, 1991.

(11) Kawaguchi, Study on a thermal boundary layer of drag-reducing surfactant solution- Measurement of temperature fluctuation. ASMA IMECE, forum on Measurement Techniques in Multiphase flows, Dallas) Nov. 97.

(12) Dean, R.B., Reynolds Number Dependence of Skin Friction and Other Bulk Flow Variables in Two-Dimensional Rectangular Duct Flow, Journal of Fluid Engineering, Vol. 100, June. 1978, pp215-223.

(13) Virk, P. S., Drag Reduction Fundamentals, AIChE Journal Vol.21, No.4, July 1975, pp625-656.

(14) Bewersdorff, H. W., and Ohlendorf, D., The behavior of Drag-reducing cationic surfactant solutions, Journal of Colloid and Polymer Science, Vol. 266, No. 10 (1988), pp941-953.

(15) Hufschmidt, W., Int. J. Heat Mass Transfer , 9-6 (1966), pp.539.

# AN EXPERIMENTAL ESTIMATION OF TURBULENCE KINETIC ENERGY IN LOW TURBULENCE BUOYANT FLOW

T. G. Karayiannis and Y. S. Tian

School of Engineering System and Design, South Bank University,  
103 Borough Road, London SE1 0AA, UK

## ABSTRACT

Low turbulence natural convection was experimentally studied in an air filled square cavity at  $Ra=1.58 \times 10^9$ . This buoyancy induced turbulent flow is basically anisotropic and inhomogeneous. A 2-D Laser Doppler Anemometer with a Burst Spectrum Analyser was used for the velocity measurements. The turbulence kinetic energy was estimated based on the two-dimensional measurements with an accuracy of 4%. The ratio of the Reynolds shear stress to the turbulence kinetic energy varies in the boundary layer of this low turbulence buoyant flow. The non-dimensional dissipation of the turbulence kinetic energy is also presented.

## 1 INTRODUCTION

Fluid flow phenomena can be complicated by three factors, namely geometry, physical nature and mathematical formulation. In the past ten years, developments in computers and mesh generating methodology (1) largely overcame the difficulties in dealing with complicated geometries. However, progress in understanding the physical behaviour and producing mathematical descriptions of complicated fluid flow problems is limited. Some problems, such as low turbulence natural convection in cavities, can be very simple in geometry but very complicated in physical nature and mathematical formulation. The complexity is due to the nature of the turbulent flow and the coupling of the momentum and thermal fields in the buoyancy induced convection. In addition, as pointed out by Ostrach (2), natural convection in confined spaces is more complex than external convection. Classical boundary-layer theory allows simplifications to be made for the external convection problem, i.e. the region outside the boundary layer is not affected by the boundary layer. Further, the velocity and temperature profiles in the fully developed turbulent boundary layer can be theoretically determined (3). For confined natural convection, on the other hand, boundary layers form near the walls enclosing the region exterior to them which forms the core region. The core flow can not be really determined from the boundary conditions because it is partially or fully encircled by the boundary layers hence depending on them. The boundary layers in turn are influenced by the core. Hence the solution of this problem is still a challenge

in spite of the developments in measurement techniques and instrumentation as well as in numerical methods and computer power.

In numerical studies, direct simulation is still too costly due to the fine grid size, small time steps and large number of iterations needed. And even with such conditions sometimes unreasonable results were predicted, for example, the double peak profile of turbulent kinetic energy (4). Most researchers are now using turbulence models such as the  $k-\epsilon$  model. In such models, the wall function is very helpful in describing forced convection flows. However, there is no suitable wall function for natural convection. The theoretical velocity profile in the fully developed turbulent boundary layer in natural convection (3) is not so useful because the flow in cavities hardly reaches such conditions. The low-Reynolds number  $k-\epsilon$  models were developed to include the near wall region. The numerical results from various  $k-\epsilon$  models are non-unique, and none can correctly predict whole velocity and temperature fields. The standard  $k-\epsilon$  model predicts higher rate of change near the wall than experimentally reported and the low-Reynolds number  $k-\epsilon$  model often gives laminar flow results. Generally, the  $k-\epsilon$  models have difficulty accounting correctly for the anisotropic flow features. The discrepancy between the experimental and numerical results is obvious, specially for turbulent quantities. A good model should be able to correctly and accurately predict flows over a range of control parameters.

Patel et al (5) reviewed past work on low turbulence flow near wall regions and pointed out that some

models fail to reproduce even the simplest case; and even those that perform considerably better need further refinement if they are to be used with confidence to calculate near-wall and low Reynolds number flows. Mansour et al (6), Spezial et al (7) and recently Sarkar and So (8) evaluated the two-equation models for near wall turbulence. The difficulty in correct simulation increases when buoyancy is involved in the flow as very limited experimental data are available. Experimental data of turbulent quantities are highly desired for turbulent model modification and CFD code validation. In this paper, the turbulence kinetic energy is estimated based on two-dimensional measurements in an air filled square cavity. The ratio of the Reynolds stress to the turbulence kinetic energy is presented at the mid-height of the cavity. The dissipation of turbulence kinetic energy at the wall was calculated based on the Jones-Launder model (9, 10).

## 2 EXPERIMENT FACILITY AND PROCEDURE

The experimental work was conducted at a Rayleigh number of  $1.58 \times 10^9$  in an air filled square cavity shown in figure 1. The quantities near the wall were intensively measured, and included  $\bar{T}$ ,  $T'$ ,  $\bar{u}$ ,  $u'$ ,  $\bar{v}$ ,  $v'$  and  $\overline{u'v'}$ . The cavity, the experimental rig and the instrumentation used were described in (11-13) and

will not be repeated here. A summary is given instead emphasising the accuracy of the instruments used and their ability to record turbulent quantities. A 2-D Laser Doppler Anemometer (LDA) equipped with a Burst Spectrum Analyser (BSA) was used in the velocity measurement. The two channels of the LDA were set to burst simultaneously so that the Reynolds stress could be measured. Incense smoke was used as seeding which lasted for more than 24 hours. The velocity profile was measured on a non-uniform fine mesh. For every measuring point, either 20K readings or four minutes of data were taken. The highest data rate was more than 300 readings/second near the velocity peak and the lowest was only 2 readings/second in the core area. The 3-D traverse mechanism which carried the LDA probe was calibrated using a dial indicator (with 0.01 mm accuracy). The accuracy for the laser location was better than 0.1 mm. The technical problems with velocity measurements and our approach for their solutions were discussed in (14). A detailed account of the experimental facility, procedure and error analysis was given in (11). The vertical and horizontal velocity fluctuation and the distribution of the turbulence kinetic energy and its dissipation are presented in this paper. The thermal field variation and the mean velocity distribution were presented in (12) and (15) respectively.

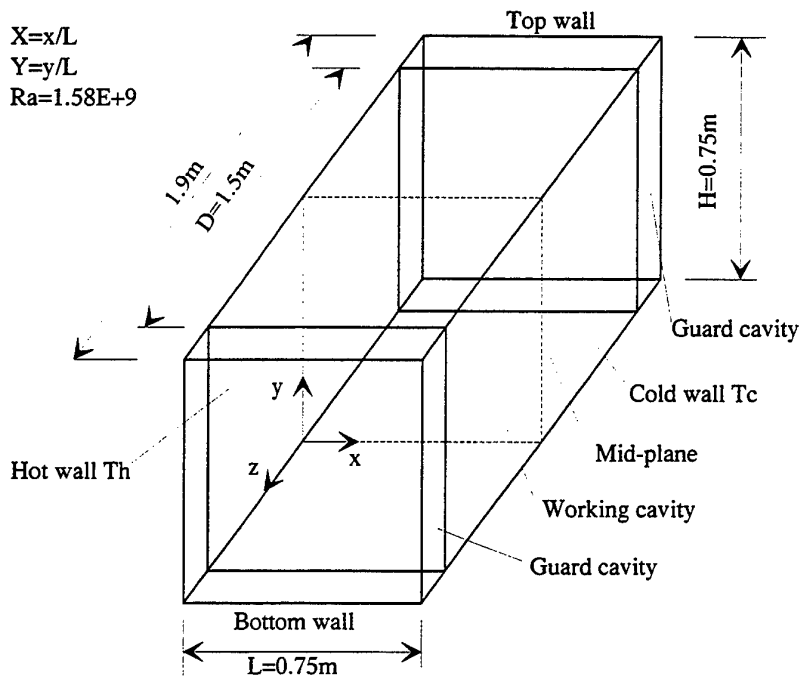


Figure 1. Schematic view of the air filled cavity.

### 3 RESULTS

#### 3.1 Experimental results

The experimental results of  $v'_{rms}$  and  $u'_{rms}$  at different heights are shown in figure 2. A constant was added to the data to clarify the presentation. The velocity fluctuations are concentrated in the boundary layer and decrease to almost nothing outside the boundary layer. The small recorded value in the core area is caused by the electronic noise (11). The distribution of fluctuation quantities is basically anti-symmetric. The fluid flow in the cavity is caused by the temperature difference between the two vertical isothermal walls and the main flow stream is along these two walls. Some flow is also formed along the horizontal walls since these are highly conductive. One feature shown in figure 2 is the difference between the peak values of  $v'_{rms}$  and  $u'_{rms}$ , i.e.  $v'_{rms}$  is more than two times  $u'_{rms}$  in the boundary layer at the mid-height of the cavity. At the corners, there is a change in the flow direction as the fluid flow meets the horizontal walls. This causes some low turbulence in the corner regions. The

velocity fluctuations were detected everywhere along the walls with the vertical fluctuations dominating. The horizontal velocity fluctuations are significant near the top hot corner and the bottom cold corner.

In turbulence modelling, one important hypothesis is the Kolmogorov hypothesis of local isotropy (16). But the dissipation in confined flows is in reality anisotropic, particularly close to solid boundaries. For natural convection in cavities, the flow is limited near the solid walls so that the flow must be anisotropic. On the wall, the velocity and its fluctuation equal to zero. The flow reaches the strongest anisotropic point at the outer edge of the viscous sub-layer ( $\Delta X=0.002$ ,  $v'_{rms}/u'_{rms}=5$ ), i.e. the turbulence kinetic energy in the vertical direction can be up to 25 times as high as in the horizontal direction. Outside the viscous sub-layer, the level of the anisotropy decreases across the boundary layer. In the core area, the fluid is stationary with negligible velocities and no fluctuations. In this area, the flow can always be treated as an isotropic flow.

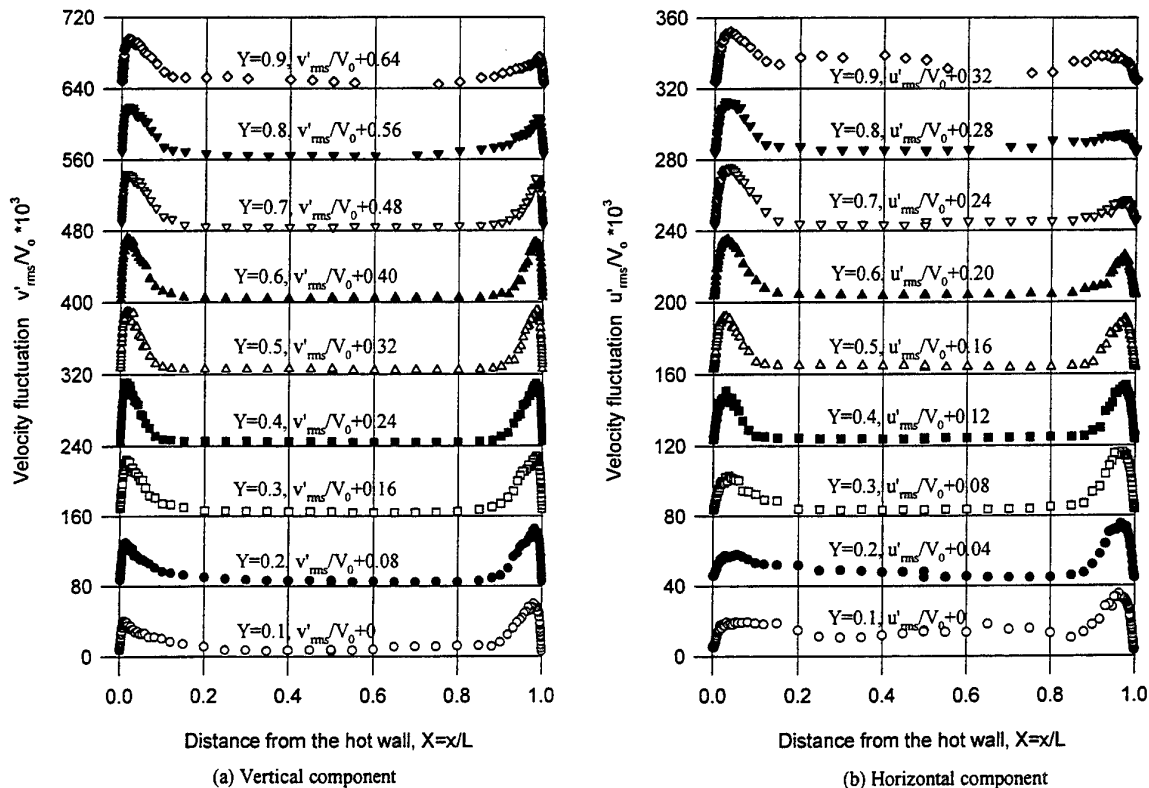


Figure 2. The velocity fluctuation at different heights.



### 3.2 The turbulence kinetic energy

In this deep cavity ( $Ar_z=2$ ), the flow is two dimensional at the mid-section. This means that  $\bar{w}=0$ . In isotropic turbulent flow,  $w'$  is of the same order as  $u'$  and  $v'$  even if  $\bar{w}=0$  (17). In this anisotropic turbulent natural convection, it is very hard to estimate  $w'$  without direct measurements. Following Launder (18), the variation of the instantaneous velocity components with distance from the wall take the form

$$u' = \bar{b}_2 x^2 + \dots \quad (1)$$

$$v' = a_1 x + b_1 x^2 + \dots \quad (2)$$

$$w' = a_3 x + b_3 x^2 + \dots \quad (3)$$

where the coefficients  $a_i$  and  $b_i$  are functions of time but their time average is zero. Very close to the wall, equations (1-3) suggest that

$$k = \frac{\overline{u'^2} + \overline{v'^2} + \overline{w'^2}}{2} \propto x^2 \quad (4)$$

$$-\overline{u'v'} \propto x^3 \quad (5)$$

Experimental evidence of Kreplin and Eckelmann (19) and numerical evidence of Spalart (20) suggest that

$$\overline{u'^2} \leq \overline{w'^2} \leq \overline{v'^2} \quad (6)$$

Although these reports were not for natural convection flows, it is reasonable to extend this finding for our case, as the presence of the wall dominates the turbulent characteristics of the flow. The fluid flow in the cavity is a low turbulence boundary wall shear flow. The turbulent fluctuations are limited in the boundary layers. As a first estimation, we can use

$$\overline{w'^2} = \frac{\overline{u'^2} + \overline{v'^2}}{2}, \quad (7)$$

i.e. the turbulent fluctuation in the  $z$  direction contributes one third of the turbulent kinetic energy and hence

$$k = \frac{1.5(\overline{u'^2} + \overline{v'^2})}{2} \quad (8)$$

The mean velocity both in the  $x$  and  $y$  directions was measured using the LDA with BSA with an accuracy of 0.07% (11). As stated in section 2, either 20K readings (in the boundary layer) were taken or the measurement took 4 minutes (in the core region) at each measuring point. The flow parameters near the

walls were of particularly interest in this part of the research. The experimental results were a statistical average of 20,000 readings at each point so that its error was negligible. If the estimated  $\overline{w'^2}$  has an accuracy of 20%, the estimated turbulent kinetic energy will be true with an accuracy better than 4%. (The contribution of  $w'$  to the turbulence kinetic energy is only one third.)

The experimental results at different heights based on equation (8) are shown in figure 3. A contour plot of the results based on all measured values is depicted in figure 4. They not only indicate that the turbulence flow is limited in the boundary layer but also that its intensity increases along the flow direction until the horizontal walls are encountered by the flow.

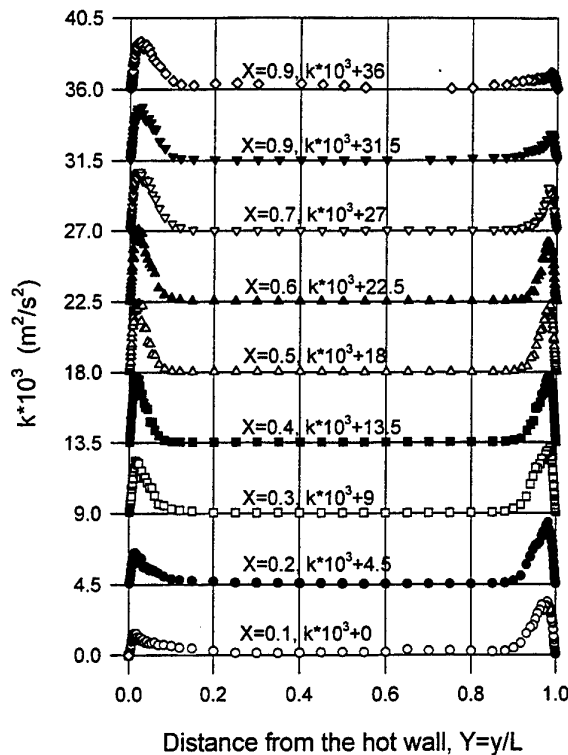


Figure 3. Distribution of estimated turbulent kinetic energy at different heights.

### 3.3 The ratio of the Reynolds stress to turbulence kinetic energy

Bradshaw et al (21) formulated a one-equation model and suggested that for a wide range of flows, the ratio of the Reynolds shear stress to the turbulence kinetic energy is constant. The measurements of Townsend

(22) indicated that for boundary layers, wakes and mixing layers the ratio is very nearly the same, 0.3. In a thin, free shear flow the ratio is also expected to have a value of 0.3 (23). The ratio of Reynolds stress and turbulent kinetic energy is depicted in figure 5. The present results only reach this value at their highest point. This should be considered in low turbulence modelling, for instance, in the equation describing the relation between  $\nu_t$  and time average turbulence parameters

$$\nu_t = C_\mu f_\mu \frac{k^2}{\varepsilon} \quad (9)$$

where  $C_\mu$  is related to the above ratio and assumed constant at 0.09. Numerical studies should include this variation and hence attempts should be made to elucidate the variation of the damping function ( $f_\mu$ ) used in the equation above to allow for such variation.

#### 4 DISCUSSION

The ratio of the Reynolds shear stress to turbulence kinetic energy at the cavity mid-height, figure 5, indicates that the one-equation model is not complete and for completion a turbulence length scale or its equivalent is needed, i.e. a two-equation model is required (24). By far, the most popular two-equation model is the  $k-\varepsilon$  model. The viscous dissipation of turbulence kinetic energy,  $\varepsilon$ , is defined as (24, 25)

$$\varepsilon = \nu \frac{\partial u'_i}{\partial x_k} \frac{\partial u'_i}{\partial x_k} \quad (10)$$

Hinze (25) pointed out that equation (10) is only suitable for a homogeneous turbulence flow. Although most real turbulence flows are inhomogeneous, when the concept of homogeneous turbulence flow is applied the standard  $k-\varepsilon$  turbulence models can predict very reasonable results for most cases. This is possible through the use of the wall functions, i.e. universal distribution. However, when the turbulence model must be extended to include the important influence of molecular viscosity very close to the wall, the model must be modified to account for the diffusive transport of  $k$  and  $\varepsilon$  by molecular viscosity and the anisotropic nature of the dissipation processes. Jones and Launder (9) suggested an alternative version of the viscous dissipation of turbulent kinetic energy, i.e. very close to the wall

$$\varepsilon = 2\nu \left( \frac{\partial k^{1/2}}{\partial x} \right)^2 \quad (11)$$

and in dimensionless form

$$\varepsilon^+ = \frac{\nu \varepsilon}{u_\tau^4} \quad (12)$$

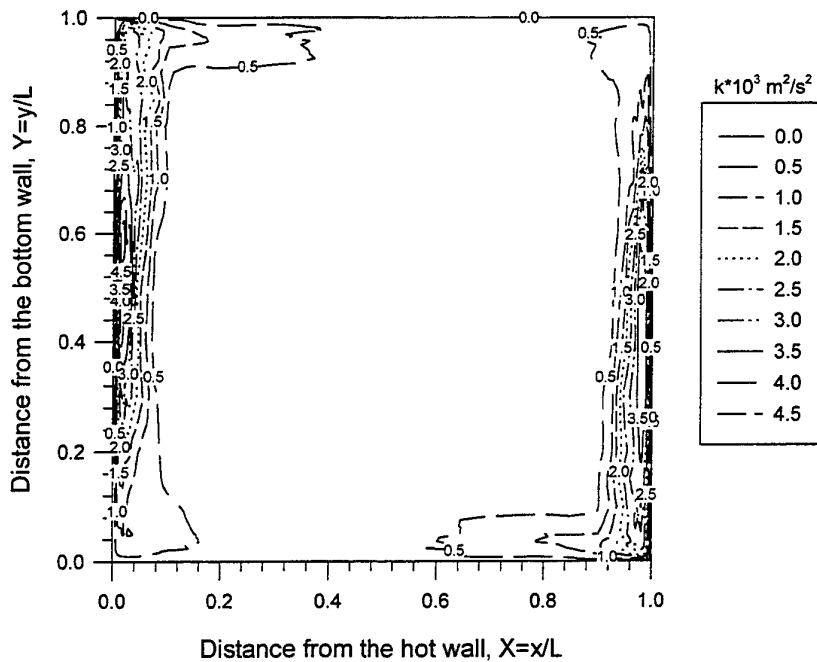


Figure 4. Distribution of the estimated turbulent kinetic energy,  $k \cdot 10^3 \text{ m}^2/\text{s}^2$ .

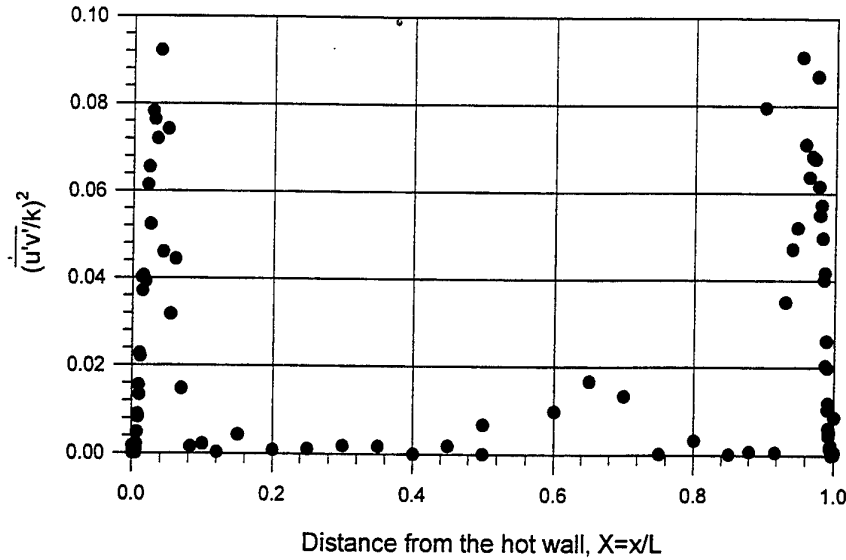


Figure 5. Squared ratio of Reynolds stress and turbulent kinetic energy.

where  $u_\tau$  is the friction velocity, i.e.

$$\begin{aligned}
 u_\tau &= \sqrt{\tau_w / \rho} \\
 &= \sqrt{\left( \mu \frac{d\bar{v}}{dx} \right)_w} / \rho \\
 &= \sqrt{\left( \nu \frac{d\bar{v}}{dx} \right)_w}
 \end{aligned} \quad (13)$$

Substitution of equations (11) and (13) into (12), gives

$$\varepsilon^+ = 2 \frac{\left( \frac{\partial \sqrt{k}}{\partial x} \right)^2}{\left( \frac{d\bar{v}}{dx} \right)_w^2} \quad (14)$$

Many two-equation low-Reynolds number turbulence models were developed based on the Jones-Launder model (9, 11) which is very useful for many cases. However, for natural convection in cavities, if  $k$  and  $\varepsilon$  are set to zero at all surfaces,  $k$  and  $\varepsilon$  values either converge to zero at all grid points or diverge (27-29). It is not easy to set the boundary conditions for  $\varepsilon$ . Changes have been suggested and were reviewed in (11). Ince and Launder (30) proposed:

$$\tilde{\varepsilon} = \varepsilon - 2\nu \left( \frac{\partial k^{1/2}}{\partial x_j} \right)^2 \quad (15)$$

and at the wall

$$\tilde{\varepsilon}_w = 0 \quad (16)$$

This equation avoids the difficulties in setting the boundary conditions for  $\varepsilon$  although it does not contribute to the understanding of the viscous dissipation of turbulence kinetic energy. If results of  $\varepsilon$  were obtained by direct measurements or estimated from measured data, they could be useful for modification of the turbulence models. For natural convection in cavities, the changes of the turbulence kinetic energy along the isothermal wall are negligible compared with the changes normal to the wall so that  $\varepsilon_w$  can be estimated based on equation (11). The dimensionless dissipation of turbulence kinetic energy is shown in figure 6. Along the flow direction,  $\varepsilon^+$  increases from  $Y=0.1$  to  $Y=0.5$  and after  $Y=0.6$  it nearly reaches a constant value of 0.04. Patel (5) summarised that  $\varepsilon^+$  equals 0.05-0.10 with the higher values occurring at larger Reynolds numbers. The lower values in this study are due to the lower turbulence level. The difference between the hot wall and cold wall is possibly due to the temperature difference, 40 K in this study. The peak point of the

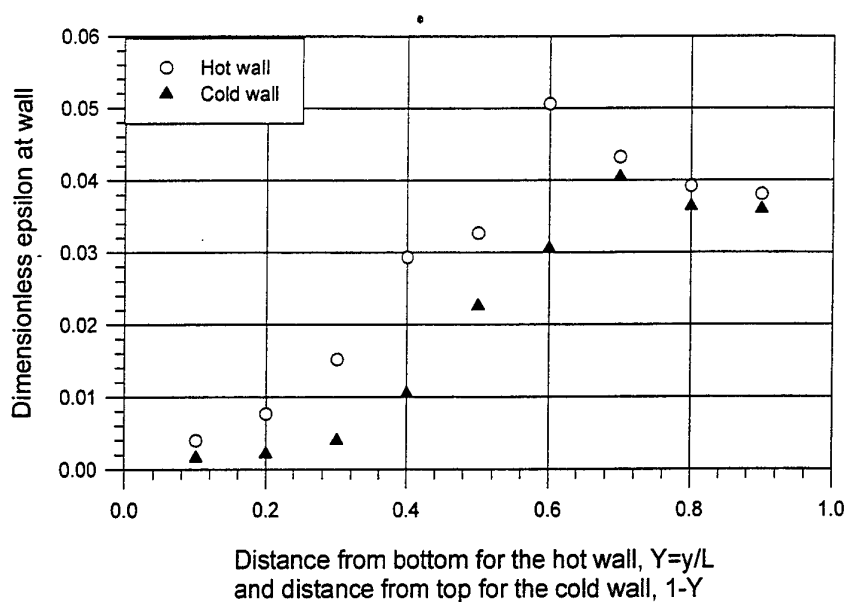


Figure 6. Dimensionless epsilon at the hot and cold walls.

velocity profile is closer to the wall at the cold wall than that at the hot wall. This gives a larger velocity gradient at the cold wall.

## 5 CONCLUSIONS

A buoyancy driven low turbulence natural convection was experimentally studied in an air filled differentially heated square cavity at  $Ra=1.58 \times 10^9$ . The experiments were conducted with high accuracy. Based on the experimental data and the analysis presented above it can be concluded that:

- (i) The turbulent natural convection in the cavity is a wall shear flow hence it is inhomogeneous and anisotropic.
- (ii) The distribution of the turbulence kinetic energy is anti-symmetric and limited in the boundary layer along the isothermal walls. It was estimated from two-dimensional measurements with an accuracy of 4%.
- (iii) The ratio of the Reynolds shear stress to the turbulence kinetic energy is not constant in the boundary layer. The ratio is equal to one third only at the peak point across the boundary layer.
- (iv) The estimated viscous dissipation of turbulence kinetic energy at the wall shows that  $\epsilon_w$  is not constant along the isothermal walls in the cavity. Its value is indicative of the low turbulence level in the cavity and its value is in good agreement with other reports.

It is hoped that the above described work will contribute in CFD validations and further numerical modelling attempts in low level turbulence convection and the evaluation of near wall turbulent models.

## ACKNOWLEDGEMENTS

The authors acknowledge the useful discussions on turbulence and LDA measurements with Prof. R. D. Matthews and Dr. M. Tabarra of the School Engineering Systems and Design of South Bank University.

## Nomenclature

$a_i$ :	coefficient in equations (1-3)	
$Ar_z$ :	aspect ratio for z-direction,	$Ar_z=D/L$
$b_i$ :	coefficient in equations (1-3)	
$C_\mu$ :	constant in equation (9)	
$D$ :	depth of the cavity,	m
$f_\mu$ :	the damping function	
$g$ :	gravitational acceleration	$m/s^2$
$H$ :	height of the cavity	m
$k$ :	turbulence kinetic energy	$m^2/s^2$
$L$ :	width of the cavity	m
$Ra$ :	Rayleigh number	
	$Ra = \frac{g\beta(T_h - T_c)L^3}{\alpha\nu}$	
$T$ :	temperature,	K

$u_\tau$ : friction velocity

$$u_\tau = \sqrt{\frac{\tau_w}{\rho}} \quad \text{m/s}$$

$u, v, w$ : velocity component in  $x, y,$  and  $z$  direction  
m/s

$x$ : variable

$x, y, z$ : coordinate

$X, Y, Z$ : dimensionless coordinate

### Greek letters

$\alpha$ :	thermal diffusivity	$\text{m}^2/\text{s}$
$\beta$ :	thermal expansion coefficient	$1/\text{K}$
$\epsilon$ :	viscous dissipation of turbulence kinetic energy	$\text{m}^2/\text{s}^3$
$\tilde{\epsilon}$ :	defined in equation (15)	$\text{m}^2/\text{s}^3$
$\mu$ :	dynamic viscosity	$\text{kg}/\text{m}\cdot\text{s}$
$\nu$ :	kinematic viscosity	$\text{m}^2/\text{s}$
$\rho$ :	fluid density	$\text{kg}/\text{m}^3$

### Superscripts

—:	time or integral average
' :	fluctuation component
+	dimensionless parameter

### Subscripts

rms:	root mean square
t:	turbulence
w:	the wall
z:	component along the depth of the cavity

### REFERENCES

- (1) Gosman, A. D., Developments in industrial computational fluid dynamics. ICHME Symposium Series No. 140, 1997.
- (2) Ostrach, S., Natural convection in enclosures. Trans. of ASME, J. Heat Transfer, 1988, Vol. 110, pp. 1175-1190.
- (3) George, W. K., and Capp, S. P., A theory for natural convection turbulent boundary layer next to heated vertical surfaces. Int. J. Heat Mass Transfer. 1979, Vol. 22, pp. 813-826.
- (4) Paolucci, S., Direct numerical simulation of two-dimensional turbulent natural convection in an enclosed cavity. J. Fluid Mech. 1990, Vol. 215, pp. 229-262.
- (5) Patel, V. C., Rodi, W., and Scheuerter, G., Turbulence models for near-wall and low Reynolds number flows: a review. AIAA, 1984, Vol. 23, No. 9, pp. 1308-1319.
- (6) Mansour, N. N., Kim, J. and Moun, P., Near-wall  $k-\epsilon$  turbulence modeling. AIAA Journal, 1989, Vol. 27, No. 8, pp. 1068-1073.
- (7) Spezial, C. G., Abid, R., and Anderson, E. C., A critical evaluation of two-equation models for near wall turbulence. AIAA report, 1990, 90-1481.
- (8) Sarkar, A. and So, R. M., A critical evaluation of near-wall two-equation models against direct numerical simulation data. Int. J. Heat and Fluid Flow. 1997, Vol. 18, No. 2, pp. 197-208.
- (9) Jones, W. P. and Launder, B. E., The prediction of laminarisation with a two-equation model of turbulence. Int. J. Heat Mass Transfer, 1972, Vol. 15, pp. 301-314.
- (10) Launder, B. E. and Spalding, D. E., Lectures in Mathematical Models of Turbulence. 1972, Academic Press.
- (11) Tian, Y. S., Low turbulence natural convection in an air filled square cavity. PhD Thesis, South Bank University, 1997.
- (12) Tian, Y. S., Karayiannis, T. G., Wen, J. X. and Matthews, R. D., Temperature distribution in low turbulence natural convection in a square cavity. 4th world conference on experimental heat transfer, fluid dynamics and thermodynamics. 1997, Vol. 4, pp. 2267-2274, Brussels.
- (13) Tian, Y. S., Karayiannis, T. G., Matthews, R. D. and Wen, J. X., Reynolds stress in low turbulence natural convection in a square cavity. 11th Int. Heat Transfer Conf. Korea, 1998.
- (14) Tian, Y. S., Karayiannis, T. G. and Matthews, R. D., Velocity measurement in low turbulence natural convection using two-dimensional LDA with BSA. 4th Int. Conf. on Optical Methods and Data Processing in Heat and Fluid Flow. 1998, pp. 65-73, London.
- (15) Karayiannis, T. G., Tian, Y. S., Matthews, R. D. and Wen, J. X., Velocity distribution in low turbulence natural convection in a square cavity. 5th UK National Heat Transfer Conf., 1997, Vol. 1, Session C, London.
- (16) Stanisic, M. M., The Mathematical Theory of Turbulence, 2nd Ed., 1988, Springer-Verlag.
- (17) Cebeci, T. and Bradshaw, P., Physical and computational aspects of convective heat transfer. 1988, Springer-Verlag Inc.
- (18) Launder, B. E., Second moment closure: methodology and practice. Proc. of the Ecole d' Eté d' Analyse Numerique-Modelisation Numerique de la Turbulence, Clamart, France, 1982.
- (19) Kreplin, H. P., and Eckelmann, H., Behaviour of the three fluctuating velocity components in the wall region of a turbulent channel flow. Phys. Fluids, 1979, Vol. 22, No. 7, pp. 1233-1239.
- (20) Spalart, P. R., Direct simulation of a turbulent boundary layer up to  $Re_\theta=1410$ . J. of Fluid Mech. 1988, Vol. 187, pp. 61-98.

- (21) Bradshaw, P., Ferriss, D. H. and Atwell, N. P., Calculation of boundary layer development using the turbulent energy equation. *J. of Fluid Mechanics*, 1967, Vol. 28, Pt. 3, pp. 593-616.
- (22) Townsend, A. A., *The Structure of Turbulent Shear Flow*. 2nd ed., 1976, Cambridge University Press.
- (23) Libby, P. A., *Introduction to Turbulence*. 1990, Taylor & Francis, Chapter 10.
- (24) Wilcox, D. C., *Turbulent Modeling for CFD*. 1993, DCW Industries, Inc., Chapter 4.
- (25) Hinze, J. O., *Turbulence*. 2nd ed., 1975, McGraw-Hill.
- (26) Chou, P. Y., On the velocity correlations and the solution of the equations of turbulent fluctuation. *Quart. Appl. Math*, 1945, Vol. 3, pp. 38.
- (27) Ozoe, H., Mouri, A., Ohmuro, M., Churchill, S. W., and Lior, N., Numerical calculation of laminar and turbulent natural convection in water in rectangular channels heated and cooled isothermally on the opposing vertical walls. *Int. J. Heat Mass Transfer*, 1985, Vol. 28, No. 1, pp. 125-138.
- (28) Ozoe, H., Mouri, A., Ohmuro, M., Churchill, S. W., and Lior, N., Numerical calculation of three-dimensional turbulent natural convection in a cubical enclosure using two-equation model for turbulence. *Trans. of ASME, Journal of Heat Transfer*, 1986, Vol. 108, pp. 806-813.
- (29) Nobile, E., Sousa, A. C. M., and Barozzi, G. S., Turbulence modelling in confined natural convection. *Heat and Technology*, 1989, Vol. 7, No. 3-4, pp. 24-35.
- (30) Ince, N. Z. and Launder, B. E., On the computation of buoyancy-driven turbulent flows in rectangular enclosures. *Int. J. Heat and Fluid Flow*, 1989, Vol. 10, No. 2, pp. 110-117.

# AN EXPERIMENTAL STUDY OF MIXED CONVECTION

J-P MORO\*, M. SAEZ\* and E. HOPFINGER\*\*

\* CEA / Grenoble DTP / SETEX / LETS, 17, rue des Martyrs 38054, Grenoble, France

\*\* Laboratoire des Ecoulements Géophysiques et Industriels / IMG, Domaine Universitaire, 38041 Grenoble, France

## ABSTRACT

The aim of the COPPEC experiments, performed at the Atomic Energy Commission of Grenoble (CEA) in collaboration with Electricité de France (E.D.F), is to establish a reliable data base for improving thermal-hydraulic codes, in the field of turbulent flows with buoyancy forces. The flow considered is mixed convection in the Reynolds and Richardson number range :  $Re=10^3$  to  $6.10^4$  and  $Ri=10^{-4}$  to 1. Measurements of mean and turbulent flow quantities are made as close to the wall as 0.01 mm corresponding to  $y^+ \approx 0.1$ . Experiments are carried out in an upward turbulent flow between vertical parallel plates at different wall temperatures.

## 1 EXPERIMENTAL APPARATUS

The experimental apparatus is shown schematically in figure 1.1. It consists of a rectangular duct made of aluminium with a cross section of 1.5 m (plate width) \* 0.12 m (plate spacing). The test section is 7.5 meters in length and is located 7.5 meters from the duct entrance. The hydraulic developing region is thus about 94 times the equivalent diameter. There are two jackets behind the heat transfer surface. Through one jacket, cooled water is circulated to maintain the cold wall at constant temperature. Through the other jacket, heated oil is circulated to maintain the wall at higher temperature. Insulating side walls prevent lateral heat loss.

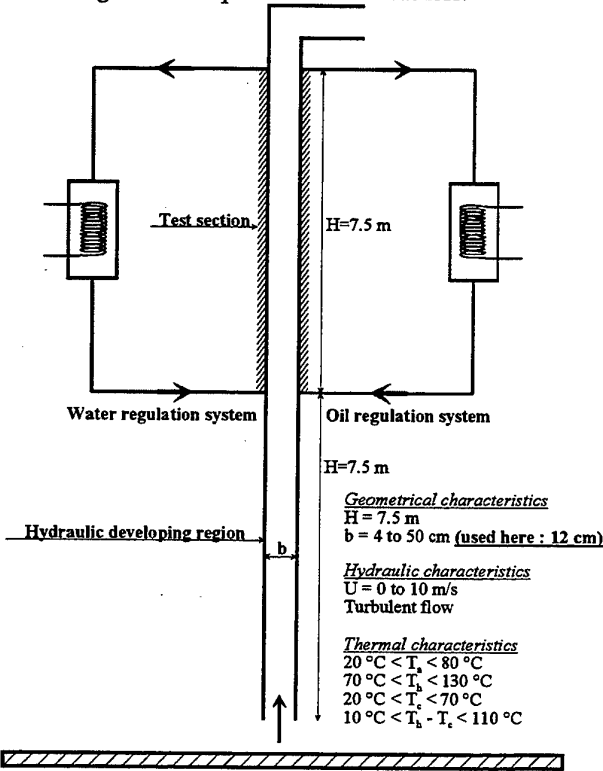


Figure 1.1 : Sketch of the experimental apparatus.

The experiments are made in the range  $Re=10^3$  to  $6.10^4$  and  $Ri=10^{-4}$  to 1.

$$Re = U_d D_h / \nu \text{ and } Ri = g\beta(T_h - T_c) D_h / U_d^2.$$

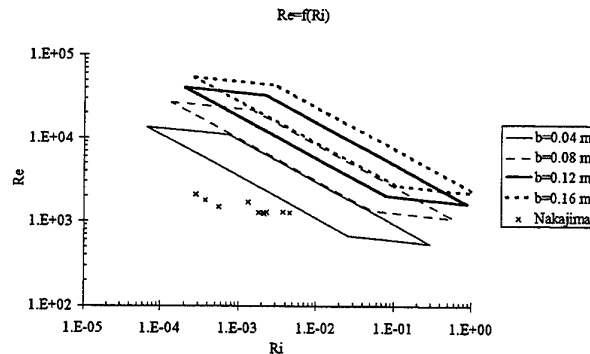


Figure 1.2 : Operating range.

## 2 MEASUREMENT TECHNIQUES

### 2.1 Displacement and coordinate systems

The difference in temperature between the two plates of the channel does not permit the use of a fixed origin. The method for determining the origin in the  $y$  direction consists of inductive displacement measurements. The accuracy in determining the origin is better than two microns. Measurements of velocity and temperature are carried out as close as 0.01 mm from the wall.

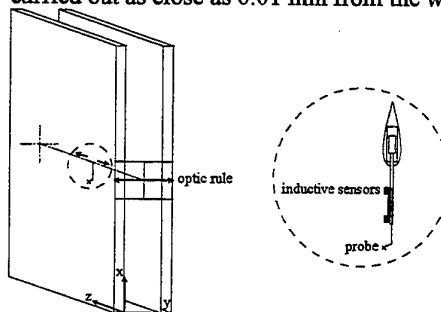


Figure 2.1 : Displacement and coordinate systems.

## 2.2 Measurements of velocity and temperature

### 2.2.1 Modes of hot-wire anemometer operation

Measurements of velocity and temperature are made with hot-wire anemometers operating at two modes :

- the constant-temperature mode, in which the probe resistance (and its temperature) is kept constant by varying the current. The main part of the probe consists of a platinum-plated tungsten wire of diameter 5 microns and 1.25 mm in length (Dantec 55P51) ;
- the constant-current mode, in which the probe temperature varies. The probe used as a resistance wire consists of a thin platinum wire of diameter 1 micron and 0.35 mm in length (Dantec 55P31).

### 2.2.2 Hot-wire probe

The hot-wire calibration consists in performing a velocity calibration at a number of different fluid temperatures. Figure 2.2 presents calibration plots.

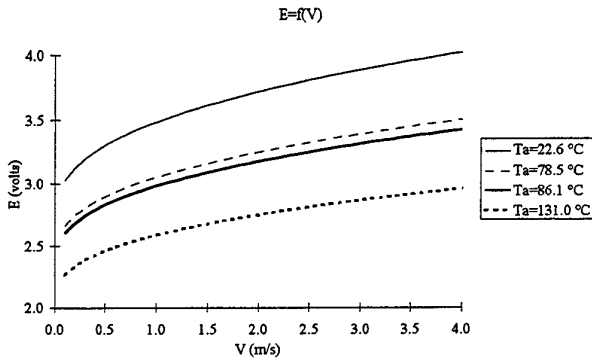


Figure 2.2 : Dependence of hot-wire voltage on air velocity for different ambient fluid temperatures.

We express our calibration relationship in the form  $E^2 = A^* + B^*V^n$  for each value of the temperature and we determine the parameters by a least-squares curve-fitting procedure. The calibration coefficients are found to vary linearly with temperature. Figure 2.3 shows the dependence of the hot-wire voltage on length to diameter ratio. King's law remains valid down to a few  $\text{cm}\cdot\text{s}^{-1}$ .

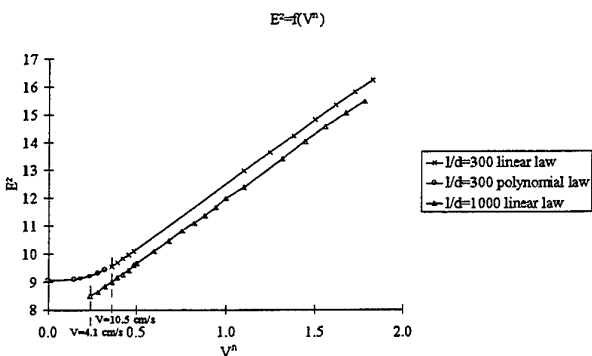


Figure 2.3 : Dependence of hot-wire voltage on length to diameter ratio ( $n=0.45$ ).

### 2.2.3 Cold wire probe

The method for measuring fluctuating fluid temperature is to operate a thin wire at a low overheat ratio in the constant-current mode. Typical temperature calibration data are shown in figure 2.4.

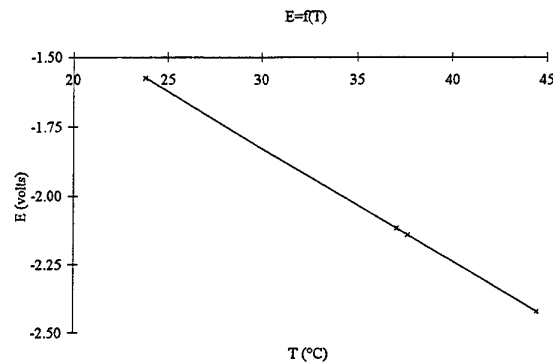


Figure 2.4 : Dependence of cold wire voltage on ambient fluid temperatures.

### 2.2.4 Measurements of velocity and temperature

In order to measure simultaneously velocity and temperature, it is necessary to use a dual sensor probe. This probe consists of two wires, one of which is used as a hot-wire and the other one as a cold wire. The cold wire is located 0.5 mm upstream of the hot-wire. The spatial dimension of the two-element hot-wire make the method inaccurate close to the wall.

Mean and statistical quantities of temperature and velocity can be obtained with a single hot-wire operated at different overheat ratios. We have, therefore, developed this technique.

The response equation for the sensor operating at two different overheat ratios can be expressed as :

$$\left\{ \begin{array}{l} \overline{E_1^2} = A_1^* + B_1^* \overline{U}^n : a_{w1} \\ \overline{E_2^2} = A_2^* + B_2^* \overline{U}^n : a_{w2} \end{array} \right. \quad (1)$$

$$\left\{ \begin{array}{l} \overline{E_1^2} = A_1^* + B_1^* \overline{U}^n : a_{w1} \\ \overline{E_2^2} = A_2^* + B_2^* \overline{U}^n : a_{w2} \end{array} \right. \quad (2)$$

Calibration coefficients vary linearly with temperature :

$$\left\{ \begin{array}{l} A_1^* = A_{1,1} + A_{1,2} \overline{T} \\ B_1^* = B_{1,1} + B_{1,2} \overline{T} \\ A_2^* = A_{2,1} + A_{2,2} \overline{T} \\ B_2^* = B_{2,1} + B_{2,2} \overline{T} \end{array} \right. : a_{w1}$$

$$\left\{ \begin{array}{l} A_1^* = A_{1,1} + A_{1,2} \overline{T} \\ B_1^* = B_{1,1} + B_{1,2} \overline{T} \\ A_2^* = A_{2,1} + A_{2,2} \overline{T} \\ B_2^* = B_{2,1} + B_{2,2} \overline{T} \end{array} \right. : a_{w2}$$

$$A_{1,1}, A_{1,2}, A_{2,1}, A_{2,2}, B_{1,1}, B_{1,2}, B_{2,1}, B_{2,2} : \text{Ctes}$$

Eliminating velocity from (1) and (2), a second-order polynomial equation for temperature (3) is obtained :

$$c_3 \overline{T}^2 + c_2 \overline{T} + c_1 = 0 \quad (3)$$

$$\left\{ \begin{array}{l} c_1 = (\overline{E_2^2} - A_{2,1})B_{1,1} - (\overline{E_1^2} - A_{1,1})B_{2,1} \\ c_2 = (\overline{E_2^2} - A_{2,1})B_{1,2} - (\overline{E_1^2} - A_{1,1})B_{2,2} \\ \quad + A_{1,2}B_{2,1} - A_{2,2}B_{1,1} \\ c_3 = A_{1,2}B_{2,2} - A_{2,2}B_{1,2} \end{array} \right.$$



The value of temperature is expressed by (4) :

$$\bar{T} = \frac{-c_2 + \sqrt{c_2^2 - 4c_1c_3}}{2c_3} \quad (4)$$

Then, knowing the temperature, the corresponding value of velocity can be evaluated from calibration relationship (1) or (2) :

$$\bar{U} = \left( \frac{\bar{E}_1^2 - A_1^*}{B_1^*} \right)^{\frac{1}{n}} = \left( \frac{\bar{E}_2^2 - A_2^*}{B_2^*} \right)^{\frac{1}{n}} \quad (5)$$

A validation of this method, which requires very accurate calibration, was carried out in the experimental calibration apparatus for mean velocity and temperature.

This method can be extended to measure turbulent quantities with longitudinal velocity fluctuation with a probe operating at three overheat ratios :

$$\begin{cases} \bar{e}_1^2 = \alpha_1^2 \bar{u}^2 + \beta_1^2 \bar{\theta}^2 + 2\alpha_1\beta_1 \bar{u}\bar{\theta} & : a_{w1} \\ \bar{e}_2^2 = \alpha_2^2 \bar{u}^2 + \beta_2^2 \bar{\theta}^2 + 2\alpha_2\beta_2 \bar{u}\bar{\theta} & : a_{w2} \\ \bar{e}_3^2 = \alpha_3^2 \bar{u}^2 + \beta_3^2 \bar{\theta}^2 + 2\alpha_3\beta_3 \bar{u}\bar{\theta} & : a_{w3} \end{cases} \Rightarrow \bar{u}^2, \bar{\theta}^2, \bar{u}\bar{\theta}$$

$$a_{w1} < a_{w2} < a_{w3}$$

### 3 EXPERIMENTAL RESULTS FOR FORCED CONVECTION

We present first results obtained in the forced convection regime. These results serve as a verification of the measurement technique close to the wall and give the conditions at the entrance of the test section.

#### 3.1 Two-dimensionality

Measurements of mean velocity, as a function of  $z$ , at different Reynolds numbers, are presented in figure 3.1. These results were obtained at the beginning of the test section. It is seen from figure 3.1 that in the central part the variation in mean velocity is within measurements error of less than 1% in the range :  $1 \leq U_0 \leq 15 \text{ m.s}^{-1}$ .

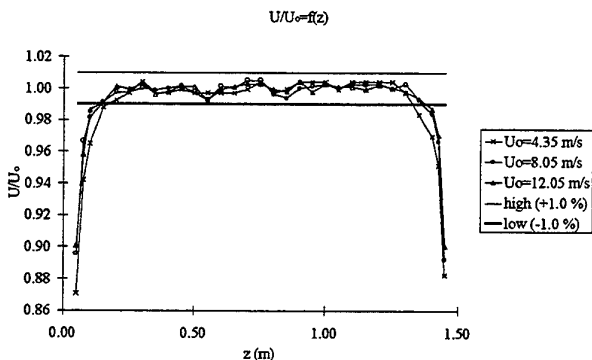


Figure 3.1 : Mean velocity as a function of  $z$  with Reynolds number.

#### 3.2 Near wall corrections

In figure 3.2 is shown the mean velocity near the wall normalised by the respective wall parameters.

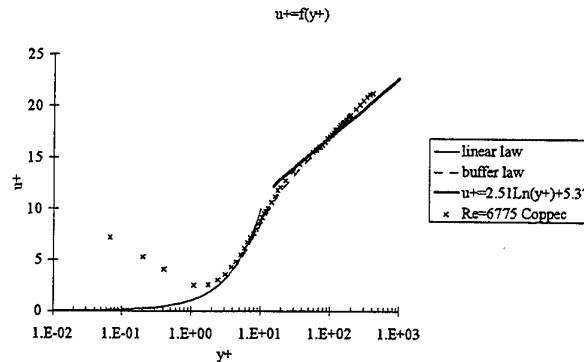


Figure 3.2 : Normalised mean velocity in the viscous sublayer, buffer layer and logarithmic layer for  $Re=6775$ .

Figure 3.2 indicates that a hot-wire placed close to a wall measures an apparent velocity larger than the true value because of the additional heat loss from the wire to the wall. A correction procedure has, therefore, been derived on the basis of a two-dimensional numerical study with the TRIO code developed by the CEA. This study confirms experimental findings that suggest that wall correction of hot-wire measurements is of the form :

$$\frac{\Delta \bar{U}}{\bar{u}^*} = \frac{\bar{U}_m - \bar{U}}{\bar{u}^*} = f(y^+) = \exp \left[ \sum_{i=0}^n a_i y^{+i} \right]$$

where  $\bar{U}_m$  is the measured mean velocity and  $\bar{U}$  the mean velocity give by the universal profile in the viscous sublayer.

Figure 3.3 shows the computed corrections for hot-wire readings close to conducting walls which predict correction for  $y^+ < 6$ , in good agreement with experiments.

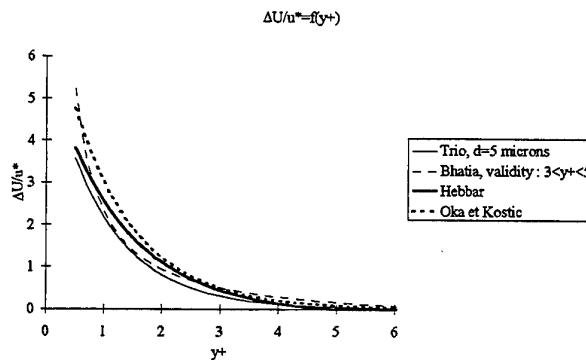


Figure 3.3 : Computed corrections of wall influence on hot-wire measurements.

Figure 3.4 shows the measured and corrected mean velocity profile close to the wall for  $Re=6775$ . The correction is inadequate down to  $y^+ \approx 0.4$ .

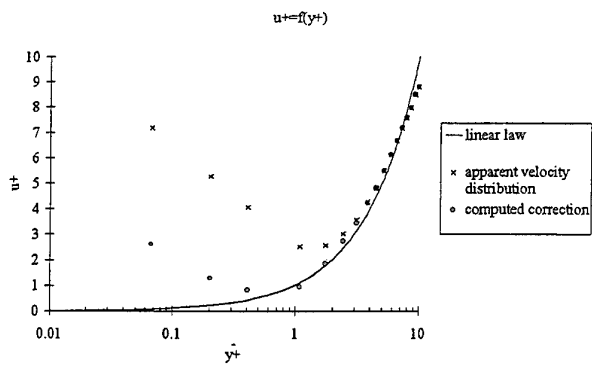


Figure 3.4 : Measured and corrected mean velocity.

### 3.3 Distribution of the r.m.s longitudinal turbulence intensity

Measured r.m.s values of the velocity fluctuations are presented in figure 3.5. These are in good agreement, both in magnitude and variation with distance from the wall, with the results of Antonia (1994) obtained in a fully developed duct flow. There is a systematic increase in turbulence intensity with Reynolds number.

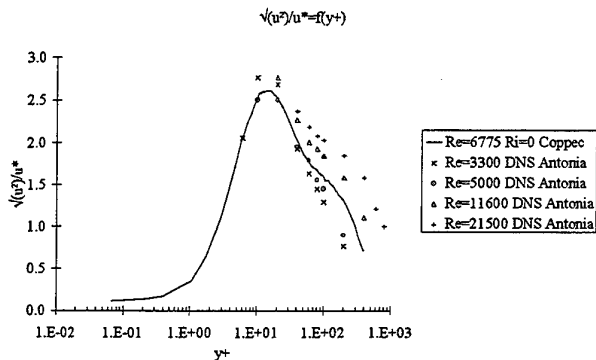


Figure 3.5 : Variation with  $y^+$  of the r.m.s longitudinal turbulence intensity.

### 3.4 Friction factor

The variation of the friction factor with Reynolds number is shown in figure 3.6. The results agree with published values to better than 1 %.

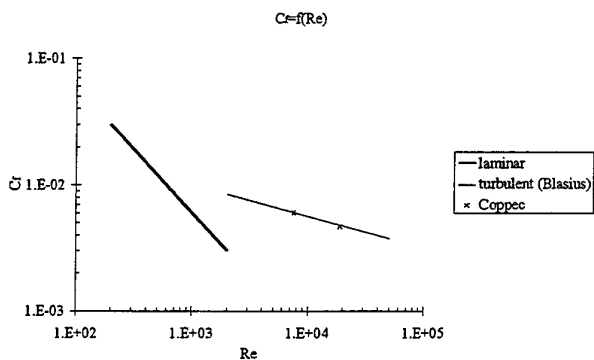


Figure 3.6 : Variation of the friction factor with  $Re$ .

## 4 EXPERIMENTAL RESULTS FOR MIXED CONVECTION

### 4.1 Experimental conditions

In this section, we present experimental results obtained for mixed convection. The measurements were made at a distance from the entrance:  $x=6000$  mm ( $x/D_h = 100$ ), for a Reynolds number  $Re=6775$  and for the following values of Richardson:  $3.7 \cdot 10^{-3}$ ,  $7.4 \cdot 10^{-3}$ ,  $8.8 \cdot 10^{-3}$ ,  $1.5 \cdot 10^{-2}$ ,  $2.1 \cdot 10^{-2}$ ,  $2.2 \cdot 10^{-2}$ ,  $3 \cdot 10^{-2}$  and  $4.6 \cdot 10^{-2}$ .

### 4.2 Mean velocity and temperature profiles

Distributions of mean velocity and temperature are shown in figures 4.1, 4.2, 4.3 and 4.4 (heated wall at  $y=0$ ).

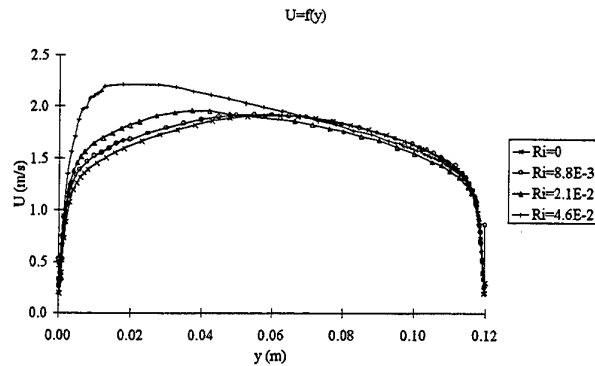
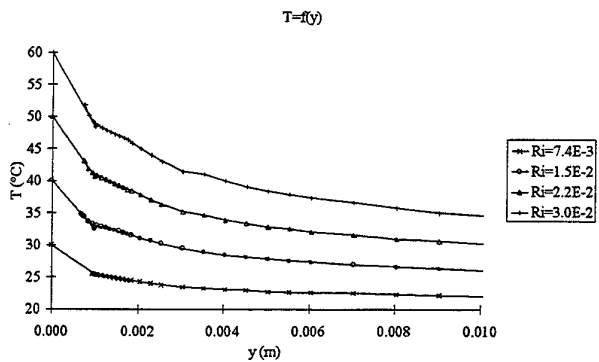
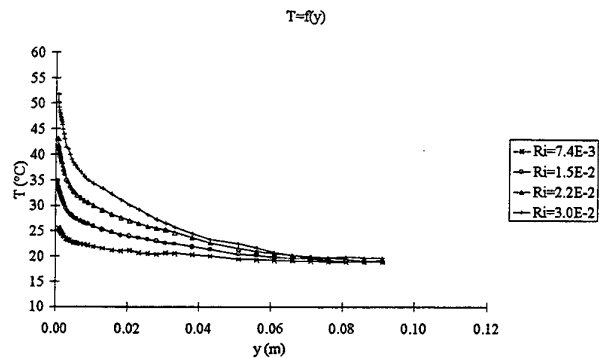


Figure 4.1 : Mean velocity with  $y$  for  $Re=6775$ .



Figures 4.2, 4.3 : Mean temperature variation with distance from the wall obtained with a cold wire for  $Re=6775$ .

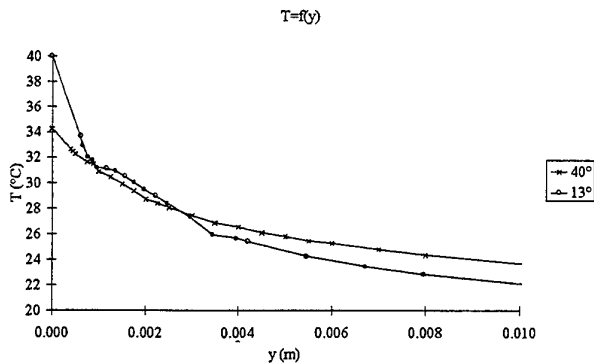


Figure 4.4 : Mean temperature variation with distance from the wall obtained with a cold wire for  $Re=6775$  and  $Ri=2.1.10^{-2}$ .

The effects of the buoyancy force are confirmed. The buoyancy deforms the distribution of mean velocity. The velocity profiles are asymmetric. The estimated uncertainty in mean velocity and temperature is respectively within 2 and 1 %.

A few experiments were made to determine the inclination of the wire prongs with respect to the wall which minimises the conduction prong - wire (figure 4.4). The optimum inclination was found to be  $13^\circ$ . Results shown in figures 4.2 and 4.3 were obtained with a cold wire with an inclination of  $13^\circ$ .

#### 4.3 Distribution of the longitudinal turbulent velocity

Figure 4.5 shows the longitudinal turbulent velocity.

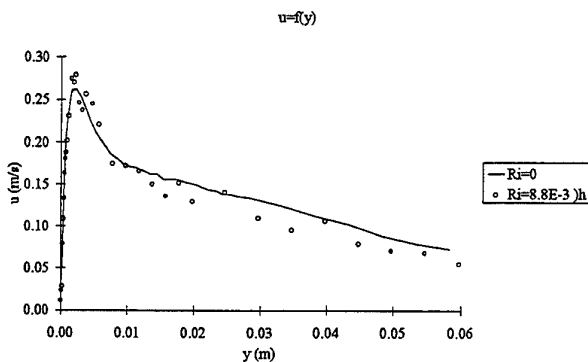


Figure 4.5 : Longitudinal turbulent velocity.

The distribution of the longitudinal turbulent velocity is carried out with a probe operating at three different overhear ratios. Dispersion of longitudinal turbulent velocity with a curve determined by a least-squares curve fitting procedure is lower than 15 %.

Nakajima et al. (1980) shows that the buoyancy force acts to reduce the turbulence intensities in the aiding flow. We observe the same tendency.

#### 4.4 Distribution of temperature fluctuations

Distributions of turbulent temperature fluctuations are shown in figure 4.6. The measurements are made with a cold wire of diameter 1 micron and 0.35 mm in length.

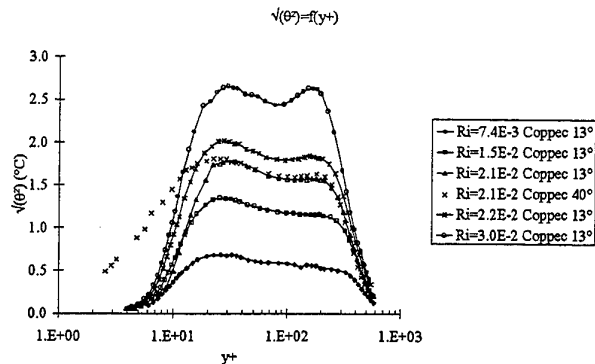


Figure 4.6 : Variation of temperature fluctuations with distance from the hot wall for  $Re=6775$ .

To account for the influence of temperature, it is possible to predict the behaviour of transfer function and time-constant of the probe. The plateau level from Petit et al. (1985) is given by :

$$H_p = 1 - 2l_c/l = 0.75 \quad \text{with: } l_c = d/2 \sqrt{\lambda_{wire}/Nu\lambda}$$

Figure 4.7 shows the dependence of temperature fluctuations with length to diameter ratio.

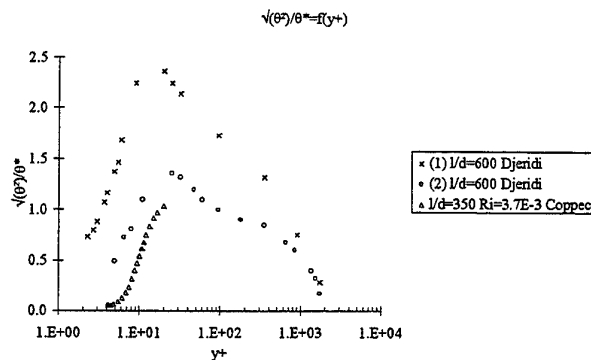
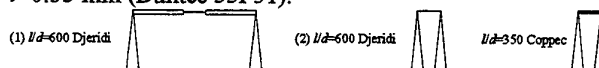


Figure 4.7 : Variation of temperature fluctuations with  $y^+$ . Djeridi (1990) :  $d=0.6 \mu\text{m}$ ,  $l=0.40 \text{ mm}$ , Coppet :  $d=1 \mu\text{m}$ ,  $l=0.35 \text{ mm}$  (Dantec 55P31).



The active length of the wire must be lower than the length between prongs in order to cancel the incidence of prongs boundary layer.

For some probe positions from the wall ( $y=0.5, 5, 33$  and  $60 \text{ mm}$ ), we present, in figure 4.8, temperature fluctuations spectra. The procedure which gives access to the temperature fluctuations spectra is by Fourier transform.

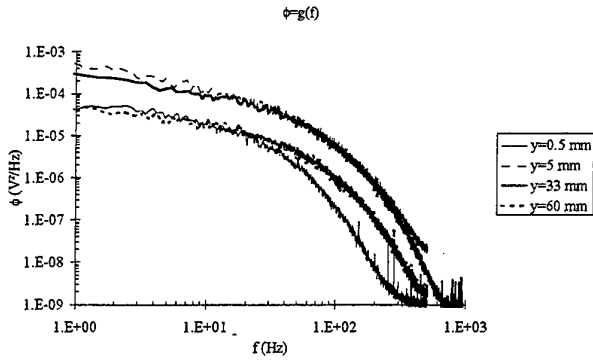


Figure 4.8: Temperature fluctuations spectra with distance from the wall for  $Re=6775$  and  $Ri=2.1.10^{-2}$ .

Spectra normalised by local mean velocity are presented in figure 4.9. Spectra at  $y=5$  and  $33$  mm from the wall are similar with large amplitude at low frequency and also those at  $y=0.5$  and  $60$  mm are close.

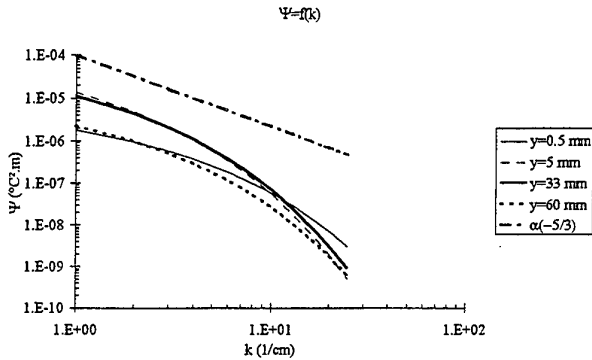


Figure 4.9: Temperature fluctuations spectra with distance from the wall for  $Re=6775$  and  $Ri=2.1.10^{-2}$ .

## 5 FRICTION VELOCITY

The friction velocity for a fully-developed flow can be written as :

$$u^* = \sqrt{-\frac{D_h}{\rho} \frac{\partial P}{\partial x}} \quad \text{where } \frac{\partial P}{\partial x} \text{ is the pressure gradient.}$$

In the case of COPPEC, the measurement of the friction velocity from the pressure gradient, of the order of a few Pascal / meter, is inadequate. The friction velocity has therefore been determined using the distribution of velocity.

Near the wall, thermal energy and momentum equations can be described as follows :

$$\frac{\partial}{\partial y} \left( \alpha \frac{\partial \bar{T}}{\partial y} - \overline{v\theta} \right) = 0 \quad (1)$$

$$\frac{\partial}{\partial y} \left( \nu \frac{\partial \bar{U}}{\partial y} - \overline{uv} \right) + g\beta(\bar{T} - T_0) = 0 \quad (2)$$

By expanding  $\overline{v\theta}$  in series and integrating equation (1), we obtain :

$$\bar{T} = T_w - \frac{q_w}{\lambda} y + \frac{1}{\alpha} \left[ \frac{1}{3!} \left( \frac{\partial^3 \overline{v\theta}}{\partial y^3} \right)_{y=0} y^4 + \dots \right] \quad (3)$$

By expanding  $\overline{uv}$  in series and integrating equation (2), we obtain :

$$\bar{U} = \frac{\tau_w}{\mu} y - \frac{1}{2} \frac{g\beta(T_w - T_0)}{\nu} y^2 + \frac{1}{2} \frac{g\beta q_w}{\lambda \nu} y^3 + \frac{1}{\nu} \left[ \frac{1}{3!} \left( \frac{\partial^3 \overline{uv}}{\partial y^3} \right)_{y=0} y^4 + \dots \right] \quad (4)$$

The influence of  $\overline{uv}$  is very small near the wall. Therefore, neglecting the  $\overline{uv}$  term in equation (4), the relationship for the mean velocity used for the estimation of wall shear stress is :

$$\bar{U} = \frac{\tau_w}{\mu} y - \frac{1}{2} \frac{g\beta(T_w - T_0)}{\nu} y^2 + \frac{1}{2} \frac{g\beta q_w}{\lambda \nu} y^3 \quad (5)$$

The application of this method to the measurements made for  $Ri=2.1.10^{-2}$ , in the region  $9y^+ < y^+ < 11y^+$ , give  $u^* = 0.098 \text{ m.s}^{-1}$ .

In the isothermal case ( $Re=6775$ ), the application of the method give  $u^* = 0.093 \text{ m.s}^{-1}$ .

## 6 CONCLUSIONS

It as been demonstrated that with a single hot-wire, operated at different overheat ratios, it is possible to measure as close to the wall as  $y^+ \approx 0.1$ . The processing method for the measurement of simultaneous velocity and temperature with a probe operating at three overheat ratios requires to be optimised.

To reduce diffusion effect, a new cold wire probe and new measurements will be made.

A method for correcting for heat loss to the wall has been proposed. This method permits to obtain a quantitative correction of the wall influence on hot-wires and takes into account the velocity profile and the effects the wall material has on the heat loss.

Buoyancy effects on the mean velocity and temperature profiles are examined. The buoyancy strongly affects the flow structure when the Richardson number is greater than  $10^{-2}$ .

## NOMENCLATURE

- $a_w$  overheat ratio
- $A^*, B^*$  calibration coefficients
- $A^* = A_1 + A_2 \bar{T}$   $B^* = B_1 + B_2 \bar{T}$
- $b$  spacing of the parallel plates [m]
- $c_p$  specific heat at constant pressure [ $\text{J.Kg}^{-1}.\text{K}^{-1}$ ]

$C_f$	friction factor [-] $C_f = 2\tau/\rho u^2$
$d$	diameter of the wire [m]
$D_h$	equivalent diameter [m] $D_h = b/2$
$E$	anemometer output voltage [volts]
$f$	frequency [Hz]
$g$	gravitational acceleration [m.s <sup>-2</sup> ]
$H$	amplitude transfer function of the wire
$k$	wave number [m <sup>-1</sup> ] $k = 2\pi f/\bar{U}$
$l$	length of the wire [m]
$l_c$	cold length [m]
$Nu$	Nusselt number [-]
$q$	heat flux [J.m <sup>-2</sup> .s <sup>-1</sup> ]
$\bar{U}$	local mean velocity [m.s <sup>-1</sup> ]
$U_d$	bulk velocity [m.s <sup>-1</sup> ]
$U_0$	maximum velocity [m.s <sup>-1</sup> ]
Re	Reynolds number [-] $Re = U_d D_h/\nu$
Ri	Richardson number [-] $Ri = g\beta(T_h - T_c)D_h/U_d^2$
$\bar{T}$	mean temperature [K]
$u^*$	friction velocity [m] $u^* = \sqrt{\tau/\rho}$
$u^+$	dimensionless velocity [-] $u^+ = \bar{U}/u^*$
$u$	longitudinal turbulence velocity [m]
$x$	distance from the entrance [m]
$y$	distance from the heated wall [m]
$y^+$	dimensionless distance from the wall [-] $y^+ = yu^*/\nu$

#### Greek symbols

$\alpha$	velocity sensitivity [volts/(m.s <sup>-1</sup> )] $\alpha = \frac{\partial \bar{E}}{\partial \bar{U}} = \frac{1}{2}n(B_1 + B_2 \bar{T})\bar{U}^{n-1}\bar{E}^{-1}$
$\beta$	temperature sensitivity [volts/K] $\beta = \frac{\partial \bar{E}}{\partial \bar{T}} = \frac{1}{2}(A_2 + B_2 \bar{U}^n)\bar{E}^{-1}$
$\lambda$	thermal conductivity [W.m <sup>-1</sup> .K <sup>-1</sup> ]
$\nu$	cinematic viscosity [m <sup>2</sup> .s <sup>-1</sup> ]
$\rho$	density [Kg.m <sup>-3</sup> ]
$\phi$	energy spectrum [°C <sup>2</sup> .Hz <sup>-1</sup> ]
$\psi$	energy spectrum [°C <sup>2</sup> .m] $\psi = \phi \frac{df}{dk} = \phi \frac{\bar{U}}{2\pi}$
$\theta^*$	friction temperature [K]

$$\theta^* = q_w/\rho c_p u^*$$

$\tau$  shear stress [Pa]

#### Subscripts

$c$  : at the cooled wall,  $h$  : at the heated wall,  $w$  : wall

#### ACKNOWLEDGEMENTS

The authors would like to thank Dr. D. Tenchine of the CEA and D. Laurence of E.D.F for helpful discussions.

#### REFERENCES

- (1) Anselmet, F., Antonia, R. A., Benabid, T. and Fulachier, L. (1990). Effect of wall suction on the transport of the scalar by coherent structures in a boundary layer. *Struct. of Turb. and Drag Red.*, ed. Gyr, A., Springer-Verlag, 349-356.
- (2) Antonia, R. A. and Kim, J. (1994). Low Reynolds number Effects on near wall turbulence. *J. Fluid Mech.*, 276, 61.
- (3) Bhatia, J. C., Durst, F. and Jovanovic, J. (1982). Corrections of hot-wire anemometer measurements near walls. *J. Fluid Mech.*, 122, 411-431.
- (4) Blair, M. F. and Bennet, J. C. (1987). Hot-wire measurements of velocity and temperature fluctuations in a heated turbulent boundary layer. *J. Phys. E. : Sci. Instr.*, 20, 209-215.
- (5) Bruun, H. H. (1995). Hot-wire anemometry. Principles and signal analysis. Oxford Science Publications.
- (6) Champagne, F. H. (1978). The temperature sensitivity of hot-wires. *Proc. Dynamic Flow Conf.*, Marseille, 101-113.
- (7) Djeridi, H. (1992). Etude de la liaison entre un scalaire passif et sa dissipation en écoulements turbulents libre et de paroi. *Ph.D. Thesis*. University Aix-Marseille II.
- (8) Fulachier, L. (1978). Hot-wire measurements in low speed heated flow. *Proc. Dynamic Flow Conf.*, Marseille, 465-487.
- (9) Lienhard, J. H. and Helland, K. N. (1989). An experimental analysis of fluctuating temperature measurements using hot-wires at different overheats. *Exp. in fluids*, 7, 265-270.
- (10) Nakajima, M., Fukui, K., Ueda, H. and Mizushima, T. (1980). Buoyancy effects on turbulent transport in combined free and forced convection between vertical parallel plates. *Int. J. Heat Mass Transf.*, 23, 1325-1336.
- (11) Petit, C., Pranthoen, P., Lecordier, J. C. and Gajan, P. (1985). Dynamic behaviour of cold wires in heated airflows (300 < T < 600 K). *Exp. in fluids*, 3, 169-173.
- (12) Tsuki, T. and Nagano, Y. (1988). Characteristics of a turbulent natural convection boundary layer along a vertical flat plate. *Int. J. Heat Mass Transf.*, vol. 31, n° 8, 1723-1734.

# MODELLING TURBULENT DIFFUSION IN A ROTATING CYLINDRICAL PIPE FLOW

A.F. Kurbatskii and S.V. Poroseva

Institute of Theoretical and Applied Mechanics  
Siberian Division of RAS, Novosibirsk, RUSSIA

## ABSTRACT

Influence of accuracy of the turbulent diffusion model (TDM) included in the Reynolds stress tensor model (RSTM) on describing behaviour of mean velocity components as well as Reynolds stresses has been studied for a case of an isothermal incompressible flow in a rotating cylindrical pipe. RSTMs used usually in the practice, can not reproduce correctly behaviour of statistical characteristics along the rotating pipe axis, in particular. Because of strong inhomogeneity of the flow, one of the reasons of such shortage of RSTMs could be insufficient accuracy of TDMs applied. A new tensor - invariant model for the triple velocity correlations has been developed by the authors. Comparison of results obtained by this model and experimental data for a swirling isothermal flow in a short cylindrical pipe, demonstrates that it is the only TDM, at present, describing satisfactorily behavior of the triple velocity correlations over the whole flow field, from the pipe axis to the wall. Though testing the RSTM with application of different TDMs in a developed stationary pipe flow shows that the use of more accurate TDM does not result in cardinal improvement of reproducing the second - order velocity moment behaviour near a pipe wall, it creates the basis to develop more physically correct models for pressure - strain correlations and dissipation tensor, and, finally, get the RSTM which will be possible to apply to more wide range of flows.

## 1 INTRODUCTION

Turbulent swirling flows are widely used in modern technological processes and occur in the natural environment as large-scale concentrated vortex formations. Rotation in such flows has a strong influence on turbulent momentum, heat, and mass transport.

The influence of rotation on the flow structure is determined, among other factors, by the way vorticity is produced. In the present work, a turbulent incompressible isothermal flow in a rotating cylindrical pipe is considered. Such flows are of interest because they occur in various engineering systems, like, e.g., heat exchangers and rotor cooling systems. Moreover, such type of a turbulent flow possesses by all features of boundary-layer flows of practical interest, whose rotation is caused by a rotating surface, and also the core of a pipe flow at a moderate swirl, models turbulent transport in natural concentrated vortex formations. Thus, the results of the investigation of turbulence structure in a pipe flow can be applied to a wide area of practical situations.

Despite the simple geometry of a pipe flow, there are great experimental difficulties associated with flow measurements even in the case of a non-rotating pipe. Therefore, correct flow modelling is important. Models developed for the velocity field of a turbulent flow can be further used for description of scalar fields. Such assumption, in the case of a pipe flow, is based on works (1-3), where it was shown from the experimental data similarity of turbulent transport of velocity and scalar moments (1), and that heat effects have no influence on the evolution of the velocity moment profiles under swirl (2,3).

As it is known from experiments (4-7, in particular), under the swirl, the structure of turbulence changes essentially in dependence on both pipe length and degree of the flow swirl, i.e., behaviour of the second- and higher-order moments is non-monotonic with increasing both these parameters. In a pipe flow, it is possible to distinguish two regions with the different structure of turbulence: the "short pipe" area ( $x/D \leq 30$ ), and the "long pipe" one ( $x/D = 68 \div 168$ ). In the former region, strong suppression of turbulent intensities in both radial and longitudinal directions is observed (4). In the later one, the profiles of statistical characteristics reach their limit shapes (5-7), therefore this area is called in literature as "saturation region" sometimes. So, profiles of the longitudinal component of the mean flow velocity become similar, but its limit profile at  $N = 1$  is still far from to be parabolic as the one in a laminar flow. Profiles of the circumferential component of the mean flow velocity have the parabolic limit shape ( $W/W_0 = (r/R)^2$ ), whereas it is known that for a forced rotational flow, this function should be linear. Also experiments show that both limit profiles of  $U$  and  $W$  are not affected, in fact, by the Reynolds number, and the profile of  $W$  does not depend on the value of  $N$ . Turbulent friction decreases along a pipe as well as with the swirl parameter increasing down to its limit value. **Important note:** in transition area, from one region to another, kinetic turbulence energy increasing is observed. These and other features of a swirling pipe flow demonstrate how complex is its structure and that a good model of turbulence must reflect them.

The mathematical modelling of turbulence structure of a flow in a rotating pipe with  $k - \epsilon$  models does not give satisfactory results. In particular, a model for a developed pipe flow gives a linear limit profile for

$W$ , as it would be in the case of solid body rotation, that is in contradiction with experimental data.

In our research, we had two aims:

- to consider possibilities of some known Reynolds stress transport models to describe the turbulence structure of both regions as well as the transition area between them in an isothermal rotating pipe flow;
- to clarify the question if the use in the RSTM of more correct model for turbulent diffusion results in better description of turbulence structure in the case of pipe flow, in particular, in the near-wall area and under the swirl.

## 2 VERIFICATION OF RSTMs IN DIFFERENT REGIONS OF A ROTATING PIPE FLOW

### 2.1 Governing equations

The set of exact transport equations for the mean velocity vector and the turbulent stress tensor in the case of stationary incompressible flow is written in the general tensor form as:

$$U^j U_{i,j} = \nu g^{jk} U_{i,jk} - \langle u_i u^j \rangle_{,j} - \tilde{P}_{,i} / \rho \quad /1/$$

$$U_{,i}^i = 0; \quad U^k \langle u_i u_j \rangle_{,k} = D_{ij} + P_{ij} + \Pi_{ij} - \varepsilon_{ij},$$

where

$$\varepsilon_{ij} = 2 \nu g^{km} \langle u_{i,m} u_{j,k} \rangle \text{ is the dissipation tensor;}$$

$$D_{ij} = - \langle u_i u_j u^m \rangle_{,m} -$$

$$\langle \langle pu_i \rangle_{,j} + \langle pu_j \rangle_{,i} \rangle / \rho + \nu (g^{km} \langle u_i u_j \rangle_{,k,m})$$

is the diffusion term;

$$P_{ij} = - \langle u_j u^k \rangle U_{i,k} - \langle u_i u^k \rangle U_{j,k}$$

is the production term;

$$\Pi_{ij} = \langle p (u_{i,j} + u_{j,i}) \rangle / \rho$$

is the pressure - strain correlation. To close set /1/, terms  $D_{ij}$ ,  $\Pi_{ij}$ , and  $\varepsilon_{ij}$  should be modelled.

### 2.2 Reynolds stress transport models

On this stage of our research, we used the simple gradient diffusion model of Daly-Harlow (8) to model  $D_{ij}$  in each tested RSTM.

The dissipation tensor  $\varepsilon_{ij}$  is modelled by the isotropic expression with correction on low Reynolds numbers near a solid wall (9), and the equation for the kinetic turbulence energy dissipation rate is used in the following form (9,10):

$$U^k \varepsilon_{,k} = \left[ g^{km} (\nu \varepsilon_{,k} + C_e \frac{k}{\varepsilon} \langle u_k u^l \rangle_{,l}) \right]_{,m} \quad /2/$$

$$+ (C_{e1} P - C_{e2}^* \varepsilon) \frac{\varepsilon}{k} - \frac{2 \nu \varepsilon}{x_n^2} f_1,$$

$$P = \frac{1}{2} \cdot P_{ii} = - \langle u_i u^k \rangle U_{i,k}; \quad C_e, C_{e1}, C_{e2}, C_{e3} \text{ are}$$

model constants,  $C_{e2}^* = \max(1.4, C_{e2} f_2 (1 - C_{e3} Ri))$  (10),  $f_1$  and  $f_2$  are damping functions (9). The Richardson number characterises influence of streamline curvature on turbulence like there of medium stratification on turbulent transport (11). Equation /2/ at  $Ri = 0$  transforms into "standard" equation for the turbulent dissipation.

There were considered two model expressions (12,13) for the pressure - strain correlation  $\Pi_{ij}$ .

In (12), the correlation  $\Pi_{ij}$  is considered as a sum of three terms:

$$\Pi_{ij} = \Pi_{ij}^{(1)} + \Pi_{ij}^{(2)} + (\Pi'_{ij}^{(1)} + \Pi'_{ij}^{(2)}) f(x_n) \quad /3/$$

$$\text{where } \Pi_{ij}^{(1)} = - C_1 \frac{\varepsilon}{k} (\langle u_i u_j \rangle - \frac{2}{3} \delta_{ij} k), \quad /4/$$

$$\Pi_{ij}^{(2)} = - C_2 (P_{ij} - \frac{2}{3} \delta_{ij} P), \quad /5/$$

$$\Pi'_{ij}^{(1)} = C'_1 \frac{\varepsilon}{k} (\langle u_n^2 \rangle g_{nn} \delta_{ij} - \frac{3}{2} (\langle u_n u_j \rangle g_{in} + \langle u_n u_i \rangle g_{jn})), \quad /6/$$

$$\Pi'_{ij}^{(2)} = C'_2 \frac{\varepsilon}{k} (\Pi_{nn}^{(2)} g_{nn} \delta_{ij} - \frac{3}{2} (\Pi_{nj}^{(2)} g_{in} + \Pi_{ni}^{(2)} g_{jn})), \quad /7/$$

$f = (1/5) k^{3/2} / (\varepsilon x_n)$  is a damping function,  $C_1 = 1.5$ ,  $C_2 = 0.6$ ,  $C'_1 = C'_2 = 0.3$ .

It is shown in (13) that in the case of an axisymmetric swirling flow, the convective transport tensor can be inserted in expression /5/ to get better result:

$$C_{ij} = \frac{\partial}{\partial x_k} (U_k \langle u_i u_j \rangle):$$

$$\Pi_{ij}^{(2)} = - C_2 (P_{ij} - C_{ij} - \frac{1}{3} \delta_{ij} (P_{kk} - C_{kk})), \quad /8/$$

Verification of three RSTMs was carried out. Model 1 (denoted further by M1) which was suggested in (10), includes equation /2/ ( $Ri \neq 0$ ) and model expressions /3/ - /7/ to close set /1/. In the second model (M2), equation /2/ at  $Ri = 0$  is used as well as expressions /3/ - /7/. At present, M2 is considered as the "standard" model and some its properties have been analysed for a turbulent flow in a long cylindrical rotating pipe in (14). Model 3 (M3) is similar to M2, but instead of expression /5/, its modification /8/ is used.

### 2.3 Numerical procedure

In each model, the set of the closed equations for required functions ( $U$ ,  $W$ ,  $k$ ,  $\varepsilon$ ,  $\alpha = \langle w^2 \rangle - \langle v^2 \rangle$ , and the rest turbulent stresses) was written in the axisymmetric cylindrical frame of references in the boundary layer approximation. The calculation conditions were the same as that of the experiments (4), where a swirling

flow was obtained by conveying a fully-developed turbulent flow from the stationary pipe section of the 100-diameter length into a rotating pipe of the same diameter. For solving the differential equations, the control volume technique (15) was used. Boundary conditions:

$$\frac{\partial U}{\partial r} = \frac{\partial k}{\partial r} = \frac{\partial \varepsilon}{\partial r} = \frac{\partial \langle u^2 \rangle}{\partial r} = \frac{\partial \alpha}{\partial r} =$$

$$\langle uv \rangle = \langle vw \rangle = \langle uw \rangle = W = 0 \quad (r=0);$$

$$U = k = \varepsilon = \langle u^2 \rangle = \alpha = \langle uv \rangle = \langle vw \rangle = \langle uw \rangle = 0,$$

$$W = W_0, \quad (r=R).$$

The grid was not uniform along  $r$ , with total number of nodes in this direction being 128. Size of  $\delta x$  was  $0.05 R$ . More details on the numerical procedure can be found in (10).

## 2.4 Results and discussion

Results of calculations were compared with the data of experiments (4-7). In experiments (4), statistical characteristics of a turbulent flow (the first- and second-order moments of the velocity field) were measured in the exit section of a short rotating pipe at  $x/D = 25$ ,  $Re_m = 37000$ ,  $N \leq 0.6$ . In (5-7), behaviour of the mean flow velocity components (longitudinal and circumferential) as well as the longitudinal turbulence intensity was studied in the long rotating section of a cylindrical pipe ( $x/D \leq 168$ ) at  $Re_m = 0.5 \div 3 \cdot 10^4$  and  $N = 0.5 \div 3$ . Because experiments were carried out under different conditions, quantitative comparison of the data is difficult.

M1 reproduces satisfactorily transformation of the  $U$  and  $W$  profiles, as well as there of Reynolds stress profiles under moderate flow swirl ( $N \leq 0.6$ ) in a short rotating pipe ( $x/D = 25$ ) (10). Here, efficiency of this model for the case of a long pipe flow is considered.

The results of calculation of the damping coefficient  $Ku$  of the longitudinal turbulent kinetic energy component at three values of the swirl parameter ( $N = 0.34; 0.62; 1.0$ ) and  $Re_m = 37000$  are shown on Fig.1 in dependence on a distance along the pipe axis. To make qualitative comparison, experimental points from (6) at  $Re_m = 3 \cdot 10^4$  are given also at  $N = 0.5; 1.0$  in sections  $x/D = 11, 36, 68$ , and  $168$ . It is seen, that at  $N = 1$  the model predicts almost total suppression of turbulence intensity in the section  $x/D = 168$ . It is necessary to note that experimental data (4) give more strong suppression of turbulence in the initial section of a rotating pipe ( $x/D = 25$ ) than the data (6) do. Thus, M1 reproduces correctly transformation of the longitudinal component of  $k$  in a short pipe and qualitatively correct behaviour of  $Ku$  with increasing a distance along the axis of a rotating long pipe under moderate swirl ( $N = 0.34$ ). At strong swirl ( $N = 1$ ) the model does not describe turbulence structure adequately. Influence of the Reynolds number on

behaviour of  $Ku$  along a pipe calculated by M1 is shown on Fig. 2.

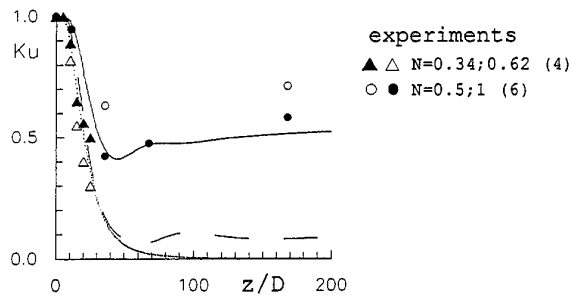


Figure 1 Behaviour of  $Ku$  along a pipe axis ( $r/R = 0$ ) calculated by M1 at different  $N$ : (—) -  $N = 0,34$ , (---) -  $N = 0,62$ , (....) -  $N = 1$ . Experiments: (4) at  $Re_m = 3.7 \cdot 10^4$ , (6) at  $Re_m = 3 \cdot 10^4$ .

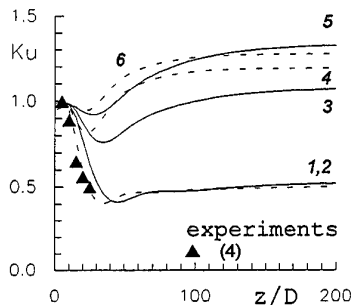


Figure 2 Behaviour of  $Ku$  along a pipe axis at different  $Re$  ( $r/R = 0, N = 0.34$ ): (—) -  $Re_m = 3.7 \cdot 10^4$ , (---) -  $Re_m = 10^4$  (curves 1,2 - M1; 3,4 - M2; 5,6 - M3).

Note also, that the model describes decreasing the friction coefficient in consequence of "laminarization" of the longitudinal velocity profile (more exactly, its parabolization) and anisotropy of kinetic turbulence energy components as well as tendency of the profiles of  $U$  and  $W$  to their limit shapes of stabilization regime. However, these profiles are not in quantitative agreement with the experimental ones. Moreover, their dependence on both the Reynolds number and the swirl parameter is observed, and stabilization regime is reached on distances much larger from the entrance of a rotating pipe than it was obtained in experiments (5-7).

Some results of calculations by M2 are given on Figs. 2-4. The model does not describe behaviour of the damping coefficient  $Ku$ , as it is seen from Fig. 2, and other statistical characteristics (figures for which are not shown in this paper) in a short pipe flow, though increasing the turbulence intensities in the section  $68 \leq x/D \leq 168$  of a rotating pipe, which was observed in (6), is reproduced qualitative correctly. Dependence of  $Ku$  on the Reynolds number is observed at different pipe lengths and swirl parameters in contradiction with experimental data.

The model describes transformation of the components of the mean flow velocity to their limit shapes at  $Re_m = 10^4$ ,  $N = 0.5$  (Figs.3,4; see also Fig.2,



curve 3). However, it is observed much earlier than in experiments and the limit profile of  $W$  (Fig. 4) does not coincide with the experimental one. At high Reynolds numbers (Fig.2), stabilization regime is not reached at all.

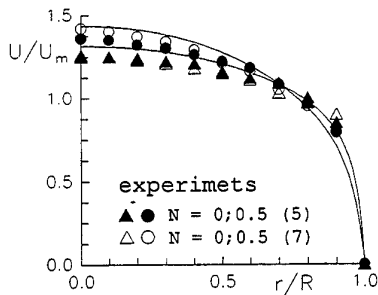


Figure 3 (—) calculations by M2 at  $Re_m = 10^4$ . Experiments: (5) at  $Re_m = 10^4$ ; (7) at  $Re_m = 2 \cdot 10^4$ .

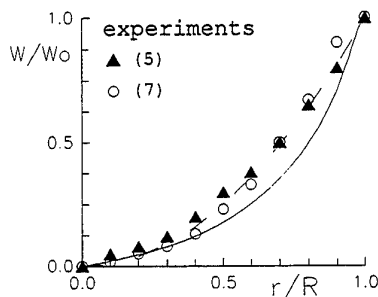


Figure 4 Calculations: by M2 (—); parabolic profile (---). Experimental data (5) at  $Re_m = 10^4, 3 \cdot 10^4$ .

Thus, the most known and simple variant of RSTM does not describe correctly neither "short pipe" region, no "long pipe" one.

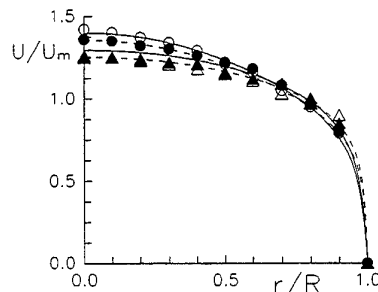


Figure 5 Calculations by M3: (—) -  $Re_m = 10^4$ , (---) -  $Re_m = 3.7 \cdot 10^4$ . Other denotations see on Fig.3.

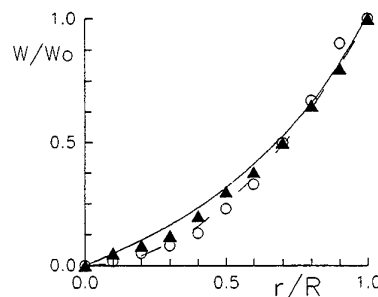


Figure 6 Denotations are on Fig. 4.

The calculation results obtained by M3 are presented on Figs. 2,5,6. The profiles of the longitudinal and circumferential components of the mean flow velocity are shown at sections  $x/D = 160/5$ ,  $120/7$  at different swirl parameters. At moderate swirls, the model reproduces correctly transformation of the profile  $U$  along a pipe and gives its correct limit shape (Fig. 5). It is seen, that dependence of  $U$  on the Reynolds number is weak in stabilization regime in accordance with experimental data (5-7). The profile of the circumferential velocity component (Fig. 6) reaches its limit parabolic dependence on the radial coordinate at  $N \leq 1$ , not depending on  $Re$ . Other statistical characteristics reach their limit profiles either, but their characteristics along a pipe is described only qualitatively as, for instance, behaviour of  $Ku$  (Fig.2). For this characteristic of turbulence structure, there is observed in calculations weak dependence on the Reynolds number, but this dependence remains along the whole pipe length.

## 2.5 Conclusions

The structure of a turbulent flow in a cylindrical pipe is transformed in a complicated way along the whole length of a rotating pipe. Experiments show, in particular, that although the longitudinal component of the mean flow velocity is tending to the profile typical for a laminar flow, kinetic turbulence energy is suppressed strongly only in the initial section of a pipe, but then, its increasing is observed. As data of calculations demonstrate, RSTMs, even those which were developed specially for a swirling flow (10,13), can not describe structure of both regions of a flow, transition area between them, as well as that of a flow under strong swirl.

## 3 TURBULENT DIFFUSION MODELS

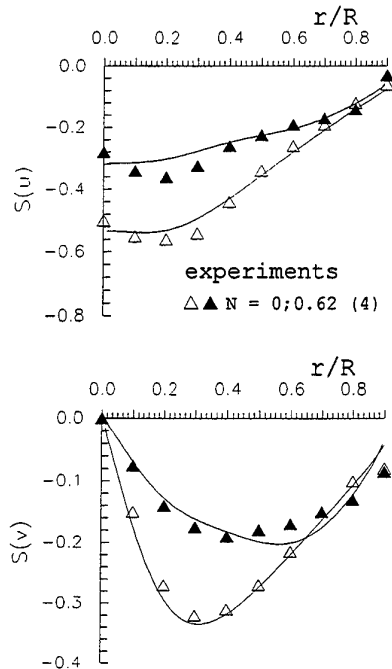
There are different approaches to improve results obtained by RSTMs. Taking into account that turbulent diffusion plays the important role in both cases of stationary and rotating pipe flows (16), here, we consider the question: how accuracy of the turbulent diffusion model used in the RSTM influences on description of turbulent structure in such flow.

Research has been carried out in three stages.

### 3.1 Verification of TDMs in a short pipe flow

During the first stage, we tested models suggested in (8,17-20). Verification of models was carried out in a developed isothermal incompressible pipe flow at  $Re_m = 37000$ . Both cases of stationary and rotating pipe flow were considered. The model differential transport equations for the third-order velocity moments were solved in the output section of a short cylindrical pipe ( $x/D = 25$ ). The first- and second-order velocity

moments necessary for calculation were obtained as a preliminary by the Reynolds stress transport model (10). The results of calculations were compared with experimental data (4,21-22). In details this stage of our researches was discussed in (19,23), therefore here we note only that verification showed that a new model for the triple velocity correlations which we developed in (19), is the only model, at present, describing correctly the behaviour of the triple velocity correlations over the whole pipe flow, from the axis to the wall as well as under swirl. Some results obtained by this model in a swirling flow are presented on Figs. 7,8



Figures 7,8 Skewness factors in a rotating pipe flow. (—) - profiles calculated by model (19)

### 3.2 Calculation of a stationary pipe flow by the RSTM with different TDMs

#### 3.2.1 Models

On the base of data obtained on the previous stage of research, we chose four TDMs (8,17-19) for testing.

1. The simple Daly - Harlow model (8) (with the following notation as 'DH') ( $C_{s1} = 0.22$ ):

$$\langle u_i u_j u_k \rangle = -C_{s1} \cdot \tau (\langle u^m u_k \rangle \langle u_i u_j \rangle_{,m}) \quad /9/$$

2. The Hanjalic - Launder model (17) (with the following notation as 'HL') ( $C_{s1} = 0.18$ ):

$$\langle u_i u_j u_k \rangle = -C_{s2} \cdot \tau (\langle u^m u_j \rangle \langle u_i u_k \rangle_{,m} + \langle u^m u_i \rangle \langle u_j u_k \rangle_{,m} + \langle u^m u_k \rangle \langle u_i u_j \rangle_{,m}) \quad /10/$$

Both models are of gradient type and, as it was shown in (18,19), they do not yield, in particular, satisfactory

results for triple velocity correlations in the near-wall area of a flow where turbulent transport reaches its maximum.

Two other models were derived from the exact equation for the triple velocity correlations  $\langle u_i u_j u_k \rangle$ :

$$\frac{D \langle u_i u_j u_k \rangle}{Dt} = \quad /11/$$

$$P_{ijk1} + P_{ijk2} + D_{ijk} + \Pi_{ijk} - \varepsilon_{ijk},$$

where  $P_{ijk1}$  and  $P_{ijk2}$  are production terms due to Reynolds stresses interacting with their gradients as well as mean strains and do not need modelling,  $D_{ijk}$ ,  $\Pi_{ijk}$ , and  $\varepsilon_{ijk}$  represent the terms of diffusion, pressure-containing correlation, and dissipation, respectively.

3. The third model we included in the RSTM, was suggested in (18) for the triple correlations in the near-wall area and has strong experimental basis. This model (we note further as 'NT') describes correctly behaviour of the triple velocity correlations near a pipe wall in a developed, non-isothermal flow in contrast to other known models. Moreover, it is simple enough and gives satisfactory results in other geometries flow also. However, the model does not describe adequately the core of a flow (18,19).

4. Also we tested the model (19) (hereafter referred as 'KP'). The model is derived from /11/ where the advective term and  $\varepsilon_{ijk}$  are neglected. The dissipation term can be neglected, as it was shown in (24), in the assumption that the length scale of two-point velocity correlations is much less than there of a mean flow.

For the pressure-containing correlation  $\Pi_{ijk}$ , the new tensor-invariant model expressions of "rapid" and "return-to-isotropy" parts are suggested.

From the integral representation of  $\langle u_i u_j p_k \rangle$  obtained by solution of the corresponding Poisson equation for the pressure fluctuations, it is possible to derive the following expression for  $\Pi_{ijk}$ :

$$\Pi_{ijk} = -\frac{1}{\rho} (\langle u_i u_j p_{,k} \rangle + \langle u_j u_k p_{,i} \rangle +$$

$$\langle u_i u_k p_{,j} \rangle) = a^n_{mijk} U^n_{,n} + b_{ijk},$$

on the same assumption as it was done to exclude  $\varepsilon_{ijk}$  from /11/. The general model form for the tensor function  $a^n_{mijk}$  in an incompressible flow reduces (19) to

$$a^n_{mijk} = C_3 (\langle u_i u_j u_m \rangle \delta_k^n + \langle u_j u_k u_m \rangle \delta_i^n + \langle u_i u_k u_m \rangle \delta_j^n) + C_4 (\langle u_i u_j u^n \rangle \delta_{km} + \langle u_j u_k u^n \rangle \delta_{im} + \langle u_i u_k u^n \rangle \delta_{jm})$$

For "return-to-isotropy" part of the correlation  $\Pi_{ijk}$ , the following model expression is suggested:

$$b_{ijk} = -\frac{\langle u_i u_j u_k \rangle}{C_{s3} \cdot \tau} + b_{ijk r} \langle u^t u^r \rangle_{,t}$$

The general form for the tensor function  $b_{ijk}$ , linear relatively Reynolds stresses in a point and symmetric with respect to rearrangement of index  $i, j$ , and  $k$ , can be written as

$$b_{ijk} = C_6 (\langle u_j u_k \rangle \delta_{ir} + \langle u_i u_j \rangle \delta_{kr} + \langle u_i u_k \rangle \delta_{jr}) + C_7 (\langle u_j u_r \rangle \delta_{ik} + \langle u_i u_r \rangle \delta_{jk} + \langle u_k u_r \rangle \delta_{ij}) + C_8 (\delta_{ik} \delta_{jr} + \delta_{ij} \delta_{kr} + \delta_{jk} \delta_{ir}) \cdot E.$$

Here,  $C_{33}$  and  $C_{3-8}$  are model constants obtained by comparing the calculated profiles with the experimental ones (19,20).

Model expression for the diffusion term  $D_{ijk}$  is derived using the quasinormality hypothesis that any fourth-order cumulants are zero and applying the high Reynolds number approximation:

$$D_{ijk} = -(\langle u_i u_j \rangle \langle u_k u^m \rangle + \langle u_j u_k \rangle \langle u_i u^m \rangle + \langle u_k u_i \rangle \langle u_j u^m \rangle), m$$

The resulting model for the triple correlations  $\langle u_i u_j u_k \rangle$  includes ten (or six, in the case of a stationary pipe flow) model transport equations for the triple velocity correlations which can be expressed one through another and solved in sequence.

### 3.2.2 RSTM and numerical procedure

For testing TDMs, we used standard RSTM (M2) described in 2.2, where for  $D_{ij}$ , models *DH*, *HL*, *NT*, and *KP* were sequentially introduced.

To make possible the application of any model for triple velocity correlations in the numerical procedure (see item 2.3), we should leave  $D_{ij}$  in set /1/ in its general form:  $-\langle u_i u_j u^m \rangle, m$ . However, the price for the procedure universality is decreasing of the forward-step size  $\delta x$  to  $0.001 R$  to avoid instability of the scheme, and, as the result, essential increasing of computer time. In this sense, further work is necessary to improve the procedure efficiency. Also, we found that the differential equations for  $\langle v^2 \rangle$  and  $\langle w^2 \rangle$  should be solved rather than for  $k$  and  $\alpha$  to avoid non-physical oscillations of solution near the axis pipe which appear in the later case. The corresponding boundary conditions are changed on

$$\frac{\partial \langle v^2 \rangle}{\partial r} = \frac{\partial \langle w^2 \rangle}{\partial r} = 0 \quad (r=0);$$

$$\langle v^2 \rangle = \langle w^2 \rangle = 0 \quad (r=R).$$

Calculations were carried out at  $Re_0 = 4 \div 5 \cdot 10^4$ .

### 3.2.3 Results and discussion

Calculations made with the *DH*-model use, showed that simple, non-tensor-invariant model can not describe correctly, in particular, behaviour of  $\langle v^2 \rangle$  and  $\langle w^2 \rangle$  near the pipe axis. The condition  $\langle v^2 \rangle = \langle w^2 \rangle$  at  $r=0$  is not obtained in contradiction with experimental data. Such problem did not appear in (10,14) because

the rigid boundary condition for  $\alpha$  was used. Application of tensor-invariant models such as *HL* and *KP* has not such failing. Moreover, Figs. 9,10 show that *DH* model does not describe behaviour of triple velocity correlations at all.

*NT*-model included in the numerical procedure, results in solution oscillations growing with each step along the  $x$ -axis. Changing empirical constants in M2 does not improve results. So, it seems to be sensible to use this model to calculate the near-wall area in given flow sections and consider it as a limit case, possibly, for other TDMs taking into account strong experimental basis of *NT*-model.

Models *HL* and *KP* are both tensor-invariant, but the former is of gradient type, whereas the later not. Calculations showed that in M2 to get the best results, empirical coefficients  $C_1$ ,  $C_2$ , and  $C_2'$  in model expressions /4,5,7/ for the pressure-strain correlation should be taken in both cases equal to 1.7, 0.5, and 0.4 respectively, that is in agreement with conclusions of (23); coefficient  $C_d$  in the damping function  $f_1$  (9) should be chosen 1 instead of 0.5;  $C_{e1} = 1.35$ ;  $C_{e2} = 1.8$ . The rest constants were the following. For *HL*-model:  $C_1' = 0.4$ ,  $C_e = 0.25$ ,  $C_{s2} = 0.18$  (instead of 0.11 usually used). For *KP*-model:  $C_1' = 0.3$ ,  $C_e = 0.3$ ,  $C_{s3} = 0.12$ ,  $C_3 = 0.1$ ,  $C_4 = 0.8$ ,  $C_6 = -1.2$ ,  $C_7 = -0.2$ ,  $C_8 = 0.4$ .

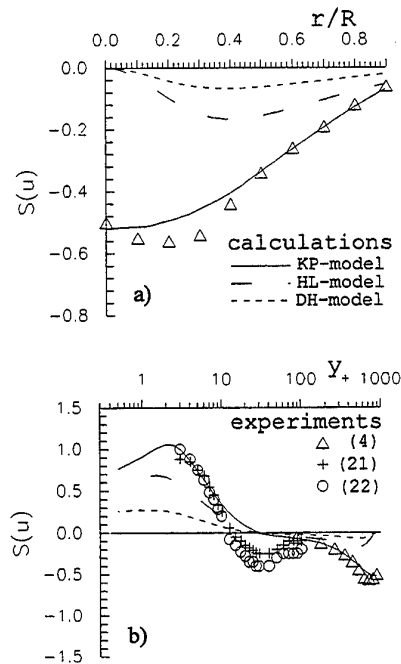


Figure 9a,b Profiles of  $S(u)$  in a stationary pipe flow

Some results are shown in Figs. 9-11. Note, that experimental data shown on Figs 9b,10b, were obtained at different values of the momentum thickness Reynolds number. It can be seen from Fig. 11 that it does not great matter for calculating the first- and second-order velocity moments, how correct models for turbulent diffusion we use. At least, it is so for a case of

a stationary pipe flow, in spite of the fact that a flow is strongly inhomogeneous in the whole area. Figs. 9,10 show shortages of *HL* - model in describing skewness factors. The worst result (in the flow core) has been obtained for  $\langle u^3 \rangle$ , because of its zero value on the pipe axis. For the rest triple velocity correlation, the *HL* - model gives in the flow core results quantitatively comparable with ones obtained with the *KP* - model use. Note also, that in spite of the fact that these models describe behaviour of triple velocity correlations near a pipe wall much better than *DH* - model does, anyway we should keep in the RSTM the damping near-wall functions.

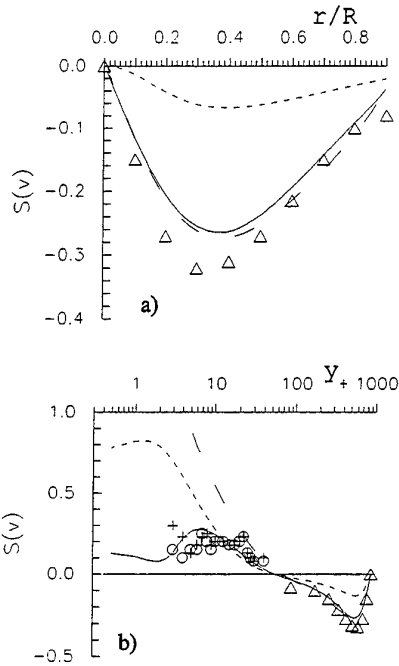


Figure 10a,b Profiles of  $S(v)$  in a stationary pipe flow. Denotations are the same as ones on Fig. 9

### 3.2.4 Conclusion

For the case of a stationary pipe flow, to calculate the first- and second-order velocity moments, the main condition for the TDM used in the RSTM is its tensor-invariance and the *HP* - model is the best choice at present. The reason lies in model expressions used for dissipation and pressure-strain correlation terms to close set /1/. In some sense, they give an predetermined result. The use of more accurate TDMs, such as *KP*, gives us possibility to develop more physically correct models for  $\Pi_{ij}$  and  $\varepsilon_{ij}$ , and, finally, get the RSTM which will be possible to apply to more wide range of flows. Also, such model can be used for researching turbulent transport of components of the turbulent kinetic energy as well as developing models for heat and mass transport.

At present, we research influence of accuracy of TDMs (*HL* and *KP*) on description by the RSTM of a flow in a long rotating pipe. The results are expected to be presented on the conference.

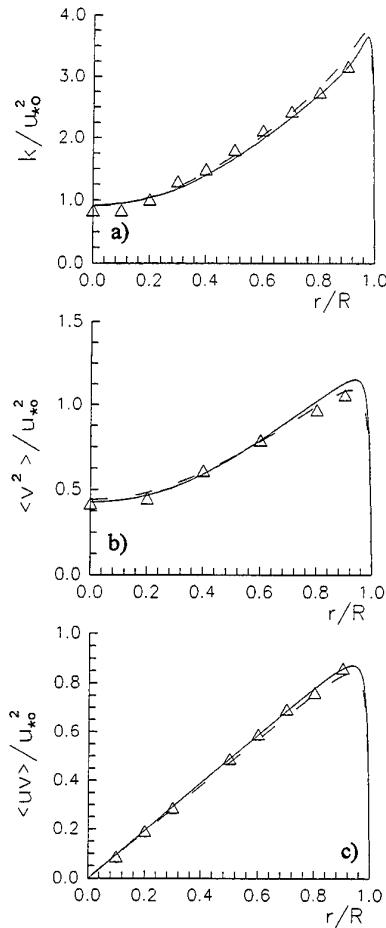


Figure 11 Denotations see on Fig.9

### ACKNOWLEDGEMENT

This work was supported by the Russian Foundation of Basic Research under grant N 96-02-16001. We are also grateful to the Organising Committee of the THT-2 for support owing to which participation of Dr. S.V. Poroseva in work of the conference became possible.

### Notation

$U_i, u_i$	covariant components of mean and fluctuating velocities
$f_{,i}$	differential operator defined by $\partial f / \partial x_i$
$x_i$	coordinates
$x_n$	normal distance to a pipe wall
$g^{ij}$	metric tensor
$\delta_{ij}$	Kronecker symbol
$D/Dt$	mean substantial derivative
$\langle \dots \rangle$	means ensemble averaging

$r, x$	radial and axial coordinates
$R, D$	pipe radius and diameter
$U, W \dots$	longitudinal and circumferential components of mean flow velocity
$u, v, w$	longitudinal, radial, and circumferential components of fluctuating velocity
$W_o$	rotating pipe wall velocity
$U_m$	mean axial flow velocity
$U_o$	mean velocity at pipe center
$N = W_o / U_m$	swirl parameter
$k = 1/2 \langle u_i^2 \rangle$	turbulent kinetic energy
$\varepsilon$	dissipation rate of $k$
$\bar{P}, p$	mean pressure and pressure fluctuation
$\rho$	flow density
$\nu$	kinematic viscosity
$\tau = k / \varepsilon$	time scale of the velocity field
$\delta x$	forward - step in the grid
$Ri$	Richardson number
$Re_m = U_m D / \nu, Re_o = U_o D / \nu$	Reynolds numbers
$S(u_i) = \langle u_i^3 \rangle / \langle u_i^2 \rangle^{3/2}$	skewness factor
$Ku = \langle u^2 \rangle (N > 0) / \langle u^2 \rangle (N = 0)$	

## References

- (1) Nagano, Y., and Tagawa, M., Statistical characteristics of wall turbulence with a passive scalar, *J.Fluid Mech.*, 1988, Vol. 196, pp.157 - 185.
- (2) Sadovskii, M.V., Research on Behaviour of Probability Density Distribution and Velocity and Temperature Fluctuation Spectra in a Turbulent Flow in a Rotating Pipe by Thermoanemometric Technique (in Russian), Ph.D. Thesis, 1991 (Moscow Physics and Technics Institute).
- (3) Cannon, J.N., and Kays, W.M., Heat transfer to a fluid flowing inside a pipe rotating about its longitudinal axis, *ASME J.Heat Transfer*, 1969, Vol. 92, pp.135 - 140.
- (4) Zaets, P.G., Safarov, N.A., and Safarov R.A. Experimental study of turbulence characteristics behaviour under rotating a pipe around its longitudinal axis (in Russian), Modern problems of continuous medium mechanics, 1985, pp.136 - 142 (Moscow Physics and Technics Institute)
- (5) Kikuyama, K. et al. Flow in an axially rotating pipe (a calculation of flow in the saturated region), *Bull. JSME*, 1983, Vol. 26, N 214, pp. 506 - 513
- (6) Nishibori, K., Kikuyama, K., and Murakami M. Laminarization of turbulent flow in the inlet region of an axially rotating pipe, *Bull. JSME*, 1987, Vol. 30, N 260, pp. 255 - 262.
- (7) Imao, S., Itoh, M., and Harada, T. Turbulent characteristics of the flow in an axially rotating pipe, *Int. J. Heat and Fluid Flow*, 1996, Vol.17, N 5, pp. 444 - 451.
- (8) Daly, B.J., and Harlow, F.H. Transport equations in turbulence, *Phys. Fluids*, 1970, Vol.13 (11), pp. 2634 - 2649.
- (9) So, R.M.C., Yoo, G.J. On the modeling of low-Reynolds-number turbulence, NASA Contractor Report 3994, 1986.
- (10) Kurbatskii, A.F., Poroseva, S.V., Yakovenko, S.N., Calculation of statistical characteristics of a turbulent flow in a rotated cylindrical pipe, *High Temperature*, 1995, Vol. 133, N 5, pp. 738 - 748.
- (11) Bradshaw, P. The analogy between streamline curvature and buoyancy in turbulent shear flow, *J.Fluid Mech.*, 1969, Vol. 36, pp.177 - 191.
- (12) Launder, B.E., Reece, G.J., Rodi, W. Progress in the development of a Reynolds stress turbulent model, *J. Fluid.Mech*, 1973, Vol. 68, pp. 537 - 566.
- (13) Launder, B.E. Second-moment closure and its use in modelling turbulent industrial flows, *Int.J. for Numer. Meth. in Fluids*, 1989, Vol. 9, pp. 963 - 985.
- (14) Hirai, S., Takagi, T., Matsumoto, M. Contribution towards a Reynolds - stress closure for low - Reynolds - number turbulence, *Trans. JSME*, 1989, Vol. 52 (476 B), pp. 1608 - 1616.
- (15) Spalding, D.B., GENMIX: a General Computer Program for Two - Dimensional Parabolic Phenomena, 1977 (Pergamon Press).
- (16) Hinze, J.O., Turbulence, 1959 (McGraw-Hill Book Co., New York).
- (17) Hanjalić, K., and Launder, B.E., A Reynolds stress model of turbulence and its application to thin shear flows. *J.Fluid Mech.*, 1972, Vol. 52, pp.609 - 638
- (18) Nagano, Y., and Tagawa, M., Turbulence model for triple velocity and scalar correlations, *Turbulent Shear Flows 7*, 1991, pp. 47- 62 (Springer-Verlag, Berlin, Heidelberg ).
- (19) Poroseva, S.V., Model of higher - order velocity moments transport for a developed turbulent flow in a cylindrical pipe (in Russian), Ph.D. Thesis, 1996, p. 131 (Novosibirsk State University).
- (20) Dekeyser, I., and Launder, B.E., A comparison of triple - moment temperature - velocity correlations in the asymmetric heated jet with alternative closure models, *Turb. Shear Flows 4*, 1983, pp. 102 - 117 (Springer, Berlin).
- (21) Karlsson, R.I., and Johansson, T.G., LVD measurements of higher order moments of velocity fluctuations in a turbulent boundary layer, *Laser anemometry in fluid mechanics*, 1988 (LadoanInstituto Superior Tecnico, Lisbon).
- (22) Fontaine, A.A., and Deutsch, S., Three-component, time-resolved velocity statistics in the wall region of a turbulent pipe flow, *Experiments in Fluids*, 1995, Vol. 18, pp. 168 - 173.
- (23) Kurbatskii, A.F., and Poroseva, S.V., Turbulence model for the triple velocity correlations, *Proceed. of the 7th Inter. Symp. on Computational Fluid Dynamics*, Beijing, China, 1997, pp.435-439.
- (24) Chou, P.Y., On velocity correlations and the solutions of the equations of turbulent fluctuation, *Quart. Appl. Math.*, 1945, Vol. 3, N 1, pp. 38 - 54.
- (25) Morris, P.J., Modelling the pressure redistribution terms, *Phys. Fluids*, 1984, Vol. 27 (7), pp. 1620 - 1623.

# EXPERIMENTAL INVESTIGATION OF HEAT TRANSFER IN PULSATING TURBULENT PIPE FLOW

S.A.M Said<sup>1</sup>, A. Al-Farayedhi, M. Habib, S.A. Gbadebo, A. Asghar, S. Al-Dini

Mechanical Engineering Department  
King Fahd University of Petroleum & Minerals  
Dhahran, 31261 Saudi Arabia.

## ABSTRACT

The effect of pulsation on the heat transfer coefficient in the thermal entrance region of turbulent air-flow in a pipe was experimentally investigated. The pipe wall was kept at uniform heat flux. Reynolds number was varied from 6400 to 42000 while frequency of pulsation ranged from 1 to 13 Hz. The results show an enhancement in the mean Nusselt number of about 9 % at frequency of 2 Hz and Reynolds number of about 15000. The rate of enhancement of the mean Nusselt number decreased as the Reynolds number increased. Also, the frequency range at which enhancement occurred widened slightly and fell between 1.5 Hz and 3.5 Hz for Reynolds number between 15000 and 33000. A reduction of heat transfer coefficient was observed at higher frequencies and the effect of pulsation diminished as the Reynolds number became very high.

Keywords: pulsating flow; heat transfer coefficient; thermal entrance; turbulent pipe flow

## INTRODUCTION

Pulsating flows are characterized by periodic fluctuations of the mass flow rate about a non-zero mean value. These fluctuations are usually caused by periodic pressure gradient. The rapid development in heat, chemical and other branches of industrial engineering has generated particular interest in the study of unsteady turbulent flows which occur in practice, typical of which is a pulsating flow. Pulsation arises at the inlet and exhaust ducts of reciprocating engines; in pipeline flows fed by reciprocating pumps and compressors; and in flows whose operation is based on wave action such as pulse-jet and cardiovascular flow systems (blood circulation).

An important potential application identified for flow pulsation is the enhancement of the convective heat transfer coefficient, especially in internal flows. There have been numerous studies in this regard. However, the heat transfer phenomena in pulsating flows are still not clearly understood and conflicting results are reported in the literature. Martinelli et al.(1943), using semi-sinusoidal velocity pulsation on the tube side of a vertical heat exchanger, found no significant effect on the heat transfer coefficient of water. West and Taylor (1952) reported an increase of 60 - 70 % in the heat transfer coefficient at a pulsation frequency of 1.67 Hz as the amplitude ratio increased. Haveman and Rao (1954) found a change

of up to 30 % in the Nusselt number of air with an increase above a certain critical frequency and decrease below it. Lemlich (1961) reported maximum increase of 80 % in the Nusselt number of water in the transition region, while Lemlich and Hwu (1961) observed a 51 % and 27 % enhancement of the Nusselt number of air in laminar and turbulent regimes, respectively. Baird et al.(1966) found an increase up to 41% in the Nusselt number of water when a high displacement amplitude, leading to flow reversal, was employed. Mamayev et al. (1976) obtained enhancement and reduction in the heat transfer coefficient of air in the laminar regime, while enhancement up to 44 % was observed in the turbulent regime. Karamercan and Gainer (1979) also reported a considerable enhancement of the heat transfer coefficient of water, up to a factor of 5.84, at high displacement amplitudes, leading to flow reversal. A reduction of up to 20 % of the heat transfer coefficient of water was reported by Liao and Wang (1988), with their results showing the dependence of heat transfer on amplitude rather than frequency. Al-Haddad and Al-Binally (1989) observed an increase in the Nusselt number of air above a critical dimensionless number, composed of  $Re$  and frequency parameter and no significant effect below it. Genin et al. (1992) found no significant effect of pulsation on the Nusselt number of water in an electrically heated tube.

<sup>1</sup> Author to whom all correspondence should be addressed

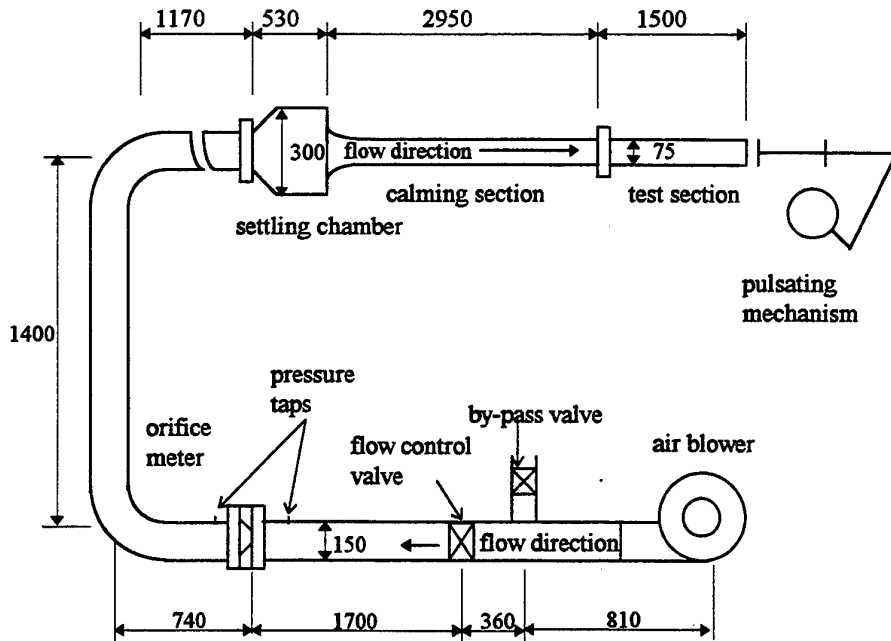
Similarly, Isshiki et al. (1993) introduced pulsations in air flowing turbulently in an electrically heated tube. Their frequency ranged in the ratio of 0.32 to 3.3 of turbulent bursting frequency, measured at 9.73 Hz. In their results, the Nusselt number was found to be unaffected at frequencies greater than the bursting frequencies, while it varied periodically at lower frequencies.

Apart from the work of Park et al. (1982), it appears that previous studies have not been focused on the effect of pulsation in the thermal entrance region of pipe flow. Hence, the objective of the present work is to investigate, experimentally, the effect of pulsation on the heat transfer coefficient in the thermally developing region of turbulent flow in a pipe, using air as the working fluid.

### EXPERIMENTAL SET-UP AND INSTRUMENTATION

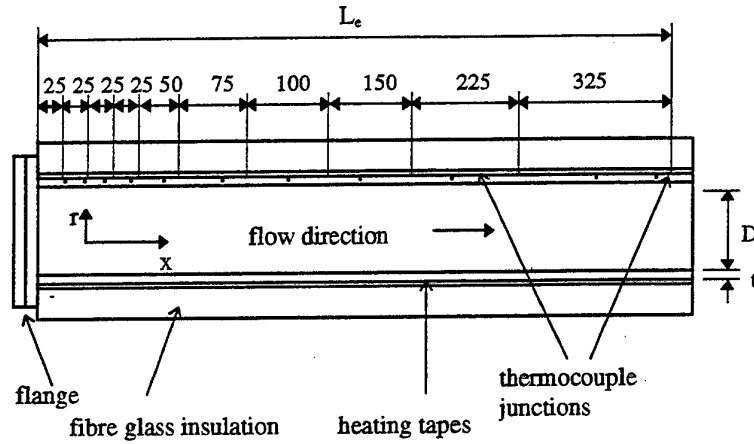
The experimental set-up is shown in Figure 1a and has been described in detail by Gbadebo (1996). It is an open loop system in which air, as the working fluid, is admitted at atmospheric pressure by using a blower. The air is discharged to the atmosphere after

the test section. The set-up consists of the air blower, piping system, orifice meter, settling chamber, calming section, test section and pulsating mechanism. The test section, made of copper, is heated by six Amox fiber insulated heating tapes wrapped helically around it. The pipe and heating tapes together, are insulated by fiber glass insulation material. The air flow and consequently the Reynolds number were controlled by a main control valve and a by-pass valve. A Betz type projection micro-manometer was used to determine the pressure drop across the orifice meter, while a multipoint digital thermometer was used to record surface temperatures at the locations shown in Fig. 1b. As regards to the relative setting of flow and power during the test series, it was felt that coherent data could be collected if the heat flux was adjusted in proportion to the mass flow rate so as to get a fairly uniform rise in the bulk mean temperatures. In order to validate the assumption of constant fluid properties along the test section, and at the same time have a considerable bulk-to-surface temperature difference, an axial temperature rise between 10 °C and 15 °C was maintained. To minimize the effect of natural convection,  $Gr / Re^2$  was kept to a value of less than 10 %.



(Dimensions in mm)

Fig. 1a Test Set-up



(Dimensions are in mm.)

Fig. 1b Test Section

#### DATA REDUCTION PROCEDURE

Data was collected when the pipe surface temperatures showed virtually no variation or a variation of less than  $0.2^\circ\text{C}$  per hour. The measured parameters included: air mass flow rate, power supplied, heat loss, surface temperatures of the pipe along the test section, fluid inlet temperature, and the frequency of pulsation. Further details of these measurements can be obtained from Gbadebo (1996). Using this data, the fluid local and mean heat transfer coefficients were determined as outlined below.

The heat input to the test section through the heating tape segments was controlled by measuring the voltage across each segment. The heat loss by radial conduction to the surroundings through the insulation is given by:

$$q_{loss,x} = -k_{ins} \frac{T_o(x) - T_i(x)}{[r_i \ln(r_o / r_i)]_j} \quad [1]$$

The heat conduction in the axial direction is given by :

$$q_{cond,x} = -k_{pipe} A \left[ \left( \frac{dT}{dx} \right)_{j+1} - \left( \frac{dT}{dx} \right)_{j-1} \right] \quad [2]$$

The mean bulk temperature is calculated from the net heat transfer as:

$$T_{b,x} = \frac{q_x}{m C_p} + T_{in} \quad [3]$$

The heat transfer coefficient is given by:

$$h_x = \frac{q_x / \pi D L}{T_{s,x} - T_{b,x}} \quad [4]$$

where  $q_x$  is the net heat transfer rate into the working fluid. The average heat transfer coefficient is given by:

$$\bar{h} = \frac{1}{L} \int_0^L h_x dx \quad [5]$$

The local and average Nusselt numbers are given by:

$$Nu(x) = \frac{h_x D}{k} \quad [6]$$

$$\bar{Nu} = \frac{\bar{h} D}{k} \quad [7]$$

An uncertainty analysis of various measured parameters was carried out based on the method of Kline and McClintock (1953). The uncertainty levels in the Reynolds number and mean Nusselt number are 2.5 % and 4 %, respectively. During this study, a total of 55 tests was carried out. Each pulsating test was preceded by the corresponding steady flow test at



the same Reynolds number. In order to validate the experimental results, the axial variation of surface temperature and the Nusselt number for the steady flow case were compared with the data reported in Kays and Crawford (1980). The effect of pulsation on heat transfer is assessed by obtaining the ratio of the heat transfer coefficient or Nusselt number under the influence of pulsation to the corresponding steady values for flow without pulsation. This ratio is referred to as the relative Nusselt number.

### EXPERIMENTAL RESULTS AND DISCUSSION

Since the present work is devoted to studying the effect of pulsation in the thermal entrance region of a hydrodynamically fully developed, turbulent air flow in a pipe, it becomes pertinent to examine the behavior of the local Nusselt number along the test section, under the influence of pulsation frequency. The first set of results therefore relates to the effect of pulsation on the local Nusselt number. The relative local Nusselt number variations along the pipe for different flow Reynolds numbers are shown in Figs. 2-5. It can be seen that, to some extent, the relative local Nusselt numbers exhibit a pattern similar to that of steady flow. As can be seen from the figures, local heat transfer enhancement takes place close to the inlet. A pulsating frequency of 1 Hz (Fig. 2) resulted in enhancement at a Reynolds number of less than or equal to 14867, and the trend extended down to a length of about 4 pipe diameters. However, a reduction in the heat transfer coefficient was observed along the test section for Re greater than 14876. Enhancement was observed along the entire test section for Re up to 25377 at a pulsation

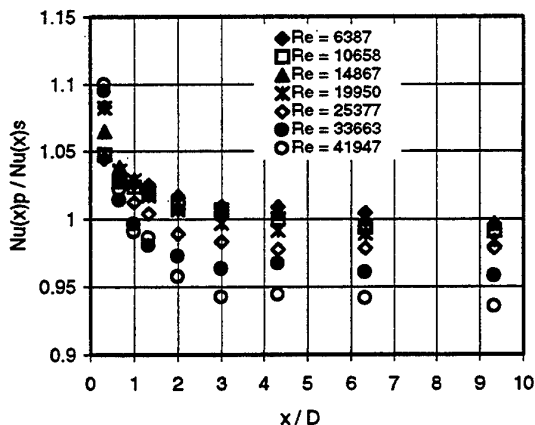


Figure 2 Effect of pulsation on local Nusselt numbers at different flow Reynolds numbers ( $f = 1\text{Hz}$ )

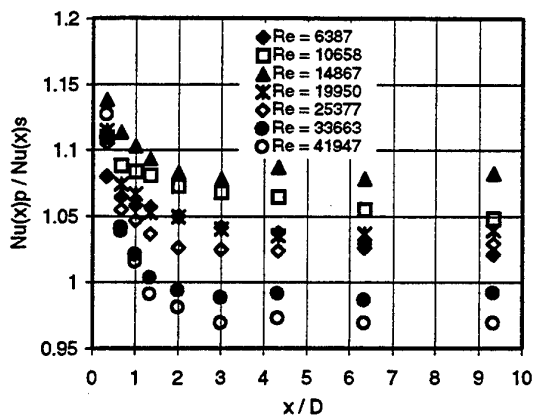


Figure 3 Effect of pulsation on local Nusselt numbers at different flow Reynolds numbers ( $f = 2\text{Hz}$ )

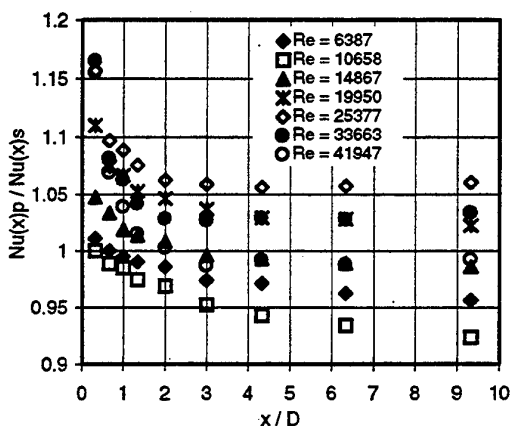


Figure 4 Effect of pulsation on local Nusselt numbers at different flow Reynolds numbers ( $f = 3\text{Hz}$ )

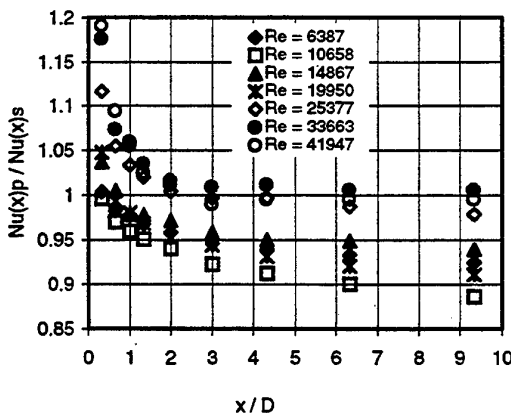


Figure 5 Effect of pulsation on local Nusselt numbers at different flow Reynolds numbers ( $f = 4\text{Hz}$ )

frequency of 2 Hz as shown in Fig. 3. Enhancement is high both at the inlet and down the test section, with a maximum increase of about 14% close to the

inlet and 11 % at the exit for Reynolds number of 14867. A similar pattern was exhibited at a pulsating frequency of 3 Hz and a range of Reynolds number from 14867 to 33663, as shown in Fig. 4. In this case, heat transfer enhancement is observed along the entire test section, increasing up to 16 % near the inlet and 9 % at the exit of the test section for  $Re = 25377$ . Pulsation at frequencies higher than 4 Hz resulted in reduction in the local Nusselt numbers along the test section for all the Reynolds numbers, with relative enhancement confined very close to the inlet, between 1 and 2 pipe diameter lengths. The reason for the considerable local enhancement close to the inlet may be due to the strong agitation of the thermal boundary layer (whose growth has just begun) by the imposed pulsation.

The second set of results is concerned with the effect of pulsation on the mean Nusselt number. The mean Nusselt numbers for steady and corresponding pulsating flows at different pulsating frequencies, considered in the experiment, are summarized in Table 1. Figures 6-8 show the overall relative mean Nusselt number as a function of the pulsation frequency for flow Reynolds numbers ranging from 6387 to 41947. As can be seen, a maximum heat transfer enhancement of about 9 % was obtained at a frequency of 2 Hz and  $Re = 14867$ . The enhancement frequency range is between 1.5 Hz and 2.5 Hz for curves corresponding to Reynolds numbers from 6387 to 14867 with maximum enhancement occurring at a pulsation frequency of 2 Hz as shown in Fig. 6. For the Reynolds numbers 19950 and 25377 (Fig 7), the enhancement frequency band increased slightly to between 1.5 Hz and 3.5 Hz, with a maximum enhancement of about 7 % occurring

at a pulsation frequency of 3 Hz, corresponding to  $Re = 25377$ . There is a relatively small enhancement of about 4 % at a pulsation frequency of 3 Hz for  $Re = 33663$ , while little or negligible enhancement was observed at a frequency of 4 Hz for a Reynolds number of 41947, as shown in Fig. 8. However, as the frequency of pulsation increased, ( $f > 4$  Hz), an overall reduction in the heat transfer coefficient was observed for the whole range of Reynolds numbers considered in this study. A maximum reduction of about 13 % was observed at 9 Hz for  $Re = 41947$  (see Fig. 8).

Figures 9 and 10 show the plots of the relative mean Nusselt number versus the flow Reynolds number for different values of pulsation frequencies. Also shown in Fig. 11 is the plot of maximum enhancement values obtained in the study at different Reynolds numbers. This plot act as a prediction chart whereby for a given flow, one can predict the pulsation frequencies at which enhancement in the heat transfer coefficient (relative to the steady flow value) can be obtained. As can be seen from Fig. 11, enhancement of the mean Nusselt number is achieved at a pulsation frequency of 2 Hz for Reynolds numbers in the 6000 to 20000 range. However, enhancement is achieved at a pulsation frequency of 3 Hz for Reynolds numbers in the 20000 to 35000 range as shown in Fig. 11. Another feature of these figures is that, at high Reynolds number, the effect of pulsation on heat transfer becomes negligible. This can be attributed to the fact that at these Reynolds numbers, the flow is highly turbulent and the turbulent intensity probably has a more dominant effect on the flow compared to the imposed pulsation

Table.1 Summary of Experimental Results

Re	Mean Nusselt number								
	Steady Flow	Pulsating Flow Frequency $f$ (Hz)							
		1	2	3	4	6	9	12	13
6387	35.68	35.83	36.83	34.47	33.47	34.43	33.88	34.40	31.01
10658	45.22	45.11	48.26	42.74	41.25	40.95	43.94	43.91	39.69
14867	54.08	54.09	58.51	53.51	51.23	50.18	52.89	53.42	49.09
19950	66.48	66.61	69.84	69.05	62.07	59.53	61.41	60.36	58.16
25377	77.84	76.77	80.51	82.98	77.27	72.54	73.32	73.19	71.00
33663	92.50	90.46	93.31	97.20	94.89	87.84	84.44	89.27	91.76
41947	107.56	102.33	105.77	108.20	108.60	98.02	93.25	105.64	

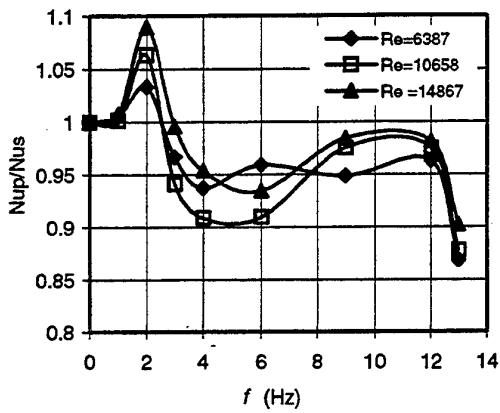


Figure 6 Relative mean Nusselt number as a function of pulsation frequency (Re = 6387, 10658 and 14867)

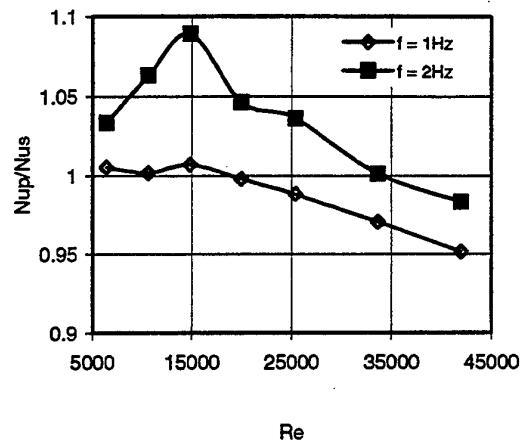


Figure 9 Relative mean Nusselt number as a function of flow Reynolds number (f = 1 and 2 Hz)

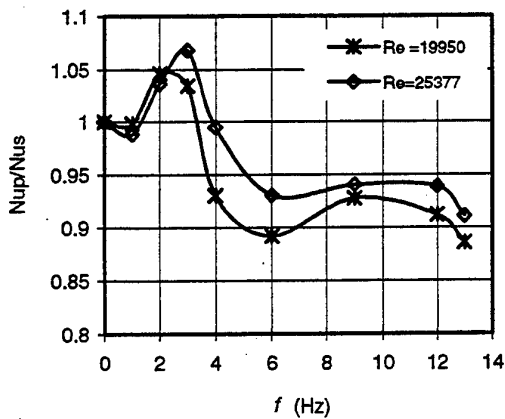


Figure 7 Relative mean Nusselt number as a function of pulsation frequency (Re=19950 and 25377)

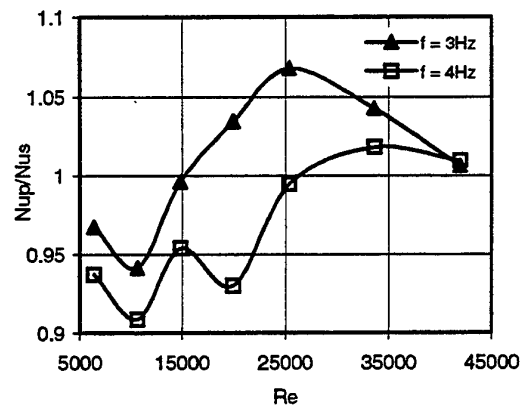


Figure 10 Relative mean Nusselt number as a function of flow Reynolds number (f=3 and 4 Hz)

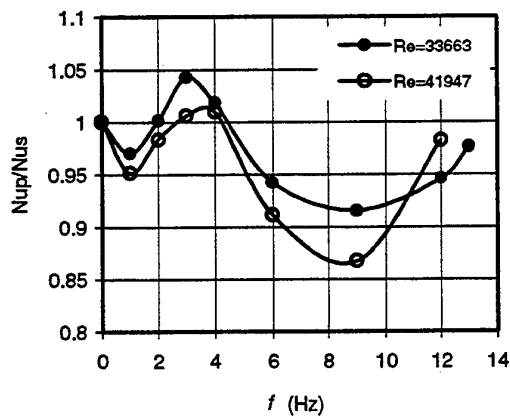


Figure 8 Relative mean Nusselt number as a function of pulsation frequency (Re = 33663 and 41947)

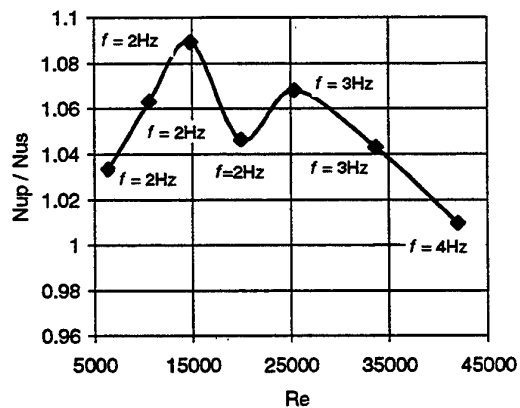


Figure 11 Maximum enhancement values of the relative mean Nusselt number at different pulsation frequencies

## ANALYSIS OF THE PRESENT DATA IN RELATION TO THE BURSTING PHENOMENON.

The effect of pulsation of the mass flow rate has been found to be related to the bursting process of the turbulent boundary layer [Mizushina et al. (1973), Ramaprian and Tu (1983)]. Turbulent bursts are a series of quasi-cyclic or periodic activities that occur near the wall of a turbulent boundary layer, and these have been related to the well known phenomenon of intermittency in the small scale structure of turbulence. This intermittent occurrence of bursts at the edge of the inner layer plays a key role in turbulent energy production [Rao et al. (1971)]. These bursts, according to studies carried out by Mizushina et al. (1973), take place at certain 'preferred' range of frequencies centered around a mean frequency. They obtained the upper and lower limit of this range from a histogram of the frequency of occurrence of bursts. These frequencies were found to be dependent on flow Reynolds number in the range  $10^3 - 10^5$ . From their measurements, Ramaprian and Tu (1983) developed approximate relationships for the mean, upper and lower bounds of this range expressed as:

$$\omega D / U^* \approx 1.58 Re^{0.125} \quad [8]$$

$$\omega_{bU} D / U^* \approx 31 Re^{0.125} [10^{-(3.32-0.667 \log Re)}] \quad [9]$$

$$\omega_{bL} D / U^* \approx 166 Re^{-0.54} \quad [10]$$

where  $D$  = pipe diameter,

$\omega$  = Circular bursting frequency,  $(2\pi f_b)$ ,

$U^* = (\tau_0 / \rho)^{1/2}$  is the friction velocity that can be obtained from the Blasius formula for the coefficient of resistance.

The importance of the bursting process in turbulent energy production makes it essential for turbulent heat transfer. With such an analogy, the data on heat transfer with pulsating flows has been classified and discussed using the turbulent bursting model [Liao et al. (1988), Genin et al. (1992)]. This classification is shown in Fig. 12. Mizushina et al. (1973) found that if the pulsation frequency is close to the turbulent burst frequency, then certain resonance interaction occurs which may show up as stimulation or suppression of corresponding frequencies in the turbulent energy spectrum and as changes in the characteristics of turbulent transfer. Consequently, this has its effect on the increase or reduction of the heat transfer coefficient. However, when the pulsation frequency lies outside the preferred range, such pulsation does not affect turbulent bursts and the mean bursting frequency is equal to that of steady flow at the same Reynolds number [Liao et al. (1988)].

The present data (represented by boundaries of the data) as well as the data of other investigators are presented in Fig. 12. As can be seen, the bulk of the present data falls into the preferred range of the bursting frequencies (regimes B and C). It is also observed that the pulsation frequencies at which overall heat transfer enhancement occurs are very close to the mean bursting frequency line. It is apparent that an increase in the heat transfer coefficient is presumably the result of changes in the mean bursting frequencies which are now controlled by the imposed pulsation frequencies. Therefore, based on this model, the critical frequencies at which resonance interaction between the bursting frequencies and those of imposed pulsation are likely to have occurred are in the neighborhood of 2 Hz and 3 Hz.

The model of the bursting phenomenon has also been able to predict the results of other investigators such as Haveman and Rao (1954) and Liao and Wang (1988). The data reported by Haveman and Rao (1954) lies in the preferred range, which agrees with their findings that the Nusselt number is increased for a pulsation frequency above a certain value and is decreased for a pulsation frequency below it. The data of Liao and Wang (1988) falls in the 'low-frequency regime' (regime A) outside the preferred range where the mean bursting frequency is independent of pulsation frequency and, as reported, their results showed no dependence of frequency as well as a reduction in the heat transfer coefficients.

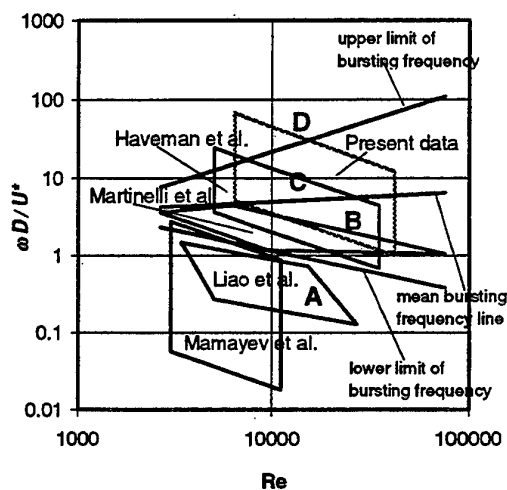


Figure 12 Classification of data on heat transfer with pulsating turbulent pipe flow

It is also worth pointing out that the findings of some investigators such as Martinelli et al. (1943) and Mamayev et al. (1976) do not match with this concept. The data of Martinelli et al. (1943) falls in

the 'intermediate frequency regime' (regime B) of the preferred range of bursting frequencies where heat transfer is expected to be affected by the imposed pulsation frequencies. However, as their results showed, the overall heat transfer coefficient was not affected by the pulsation. This, according to Liao and Wang (1988), may probably be due to the fact that a semi-sinusoidal pulsation was imposed on the flow. In the case of Mamayev et al. (1976), the frequency range lies outside the preferred range in regime A, below the lower limit of the turbulent bursting frequency where  $(\omega D/U^*) \ll 1$  and, as a result, the flow is expected to exhibit quasi-steady behavior [Ramaprian and Tu (1983)]. Here, the process of heat transfer, like that of the turbulent bursting frequency should be independent of pulsation frequency and depend on the amplitude [Liao and Wang (1988)]. However their results showed a considerable dependence on frequency and an increase in heat transfer coefficients.

## CONCLUSIONS

The effect of pulsation on the heat transfer coefficient in the thermal entrance region of a hydrodynamically fully developed turbulent air flow in a pipe heated with a uniform heat flux has been experimentally studied. The flow Reynolds number was varied from 6387 to 41947 while the pulsation frequency ranged from 1 Hz to 13 Hz. Overall enhancement of the heat transfer coefficient was indicated at frequencies of 2 Hz and 3 Hz. Enhancement at 2 Hz was observed for low to medium Reynolds numbers with a maximum of 9 % recorded at Re near 15000. For medium to higher Reynolds numbers, an increase in the Nusselt number was observed at a pulsation frequency of 3 Hz but this time with a maximum of 7 % at Re slightly above 25000. On the other hand, at frequencies of pulsation greater than 4 Hz, a reduction in the average heat transfer coefficient was observed for the full range of Reynolds numbers considered in the experiment.

At those frequencies that yielded overall enhancement, observation of the local Nusselt number behavior under the influence of pulsation revealed that improvement is more pronounced close to the inlet as well as towards the exit of the test section. However, at other frequencies, enhancement still takes place near the inlet while reduction dominates downstream.

Based on the bursting process model, it can be concluded that the critical frequencies, where resonance interaction between bursting and pulsation frequencies occur, are in the neighborhood of 2 and 3 Hz.

## ACKNOWLEDGMENT

The authors would like to acknowledge the support of King Fahd University of Petroleum and Minerals. This work is a part of the University funded project, No. ME/ Heattransfer/161.

## NOMENCLATURE

$A$	: pipe cross sectional area ( $m^2$ )
$D$	: pipe diameter (m)
$f$	: frequency of pulsation (Hz)
$f_b$	: turbulent bursting frequency (Hz)
$\bar{h}$	: average heat transfer coefficient ( $W/m^2 \cdot ^\circ C$ )
$h_x$	: local heat transfer coefficient ( $W/m^2 \cdot ^\circ C$ )
$k$	: thermal conductivity of air ( $W/m \cdot k$ )
$k_{ins}$	: thermal conductivity of the insulation material ( $W/m \cdot k$ )
$k_{pipe}$	: thermal conductivity of the pipe ( $W/m \cdot k$ )
$\dot{m}$	: mass flow rate (kg/s)
$Nu$	: mean Nusselt number
$Nu(x)$	: local Nusselt number
$\frac{Nu_p}{Nu_s}$	: relative mean Nusselt number
$\frac{Nu(x)_p}{Nu(x)_s}$	: relative local Nusselt number
$q_x$	: the rate of heat transfer (W)
$q_{cond,x}$	: axial conduction heat transfer rate (W)
$r_i$	: inner radius of insulation (m)
$r_o$	: outer radius of insulation (m)
Re	: Reynolds number
$T_b$	: bulk temperature ( $^\circ C$ )
$T_o(x)$	: outer axial surface temperature of the insulation material ( $^\circ C$ )
$T_i(x)$	: inner axial surface temperature of the insulation material ( $^\circ C$ )
$T_{in}$	: inlet temperature ( $^\circ C$ )
$T_s$	: surface temperature ( $^\circ C$ )
$x$	: distance along the test section (m)

## SUBSCRIPTS

$j$	: segment
$x$	: axial

## REFERENCES

1. Al-Haddad, A. and Al-Binally, N., 1989. Prediction of Heat Transfer Coefficient in Pulsating Flow. *Int. J. Heat and Fluid Flow*, **10** (2), 131-133.
2. Baird, M.H.I., Duncan, G.J., Smith, J.I. and Taylor, J. 1966. Heat Transfer in Pulsed Turbulent Flow. *Chemical Engineering Science*, **21**, 197-199.
3. Gbadebo, S. A. 1996. An Experimental Investigation of Heat Transfer in The Thermally Developing Region of a Pulsating Pipe Flow., M.S. Thesis, King Fahd University of Petroleum & Minerals Dhahran, 31261, Saudi-Arabia.
4. Genin, L.G., Koval, A.P., Manchka, S.P. and Sviridov, V.G., 1992. Hydrodynamics and Heat Transfer with Pulsating Fluid Flow in Tubes. *Thermal Engineering*, **39** (5) 30-34.
5. Havemann, H.A. and Rao, N.N., 1954. Heat Transfer in Pulsating Flow. *Nature*, **7** (4418), 41.
6. Isshiki, S., Obata, T., Kasagi, N., Hirata, M. 1993. Experimental Study on Heat Transfer in a Pulsating Pipe Flow. *Nippon Kikai Gakkai Ronbunshu, B Hen / Trans. J.S.M.E, Part B*, **59** (563), 145-151.
7. Karamercan, O.E. and Gainer, J.L., 1979. The Effect of Pulsation on Heat Transfer. *Industrial Engineering Chem. Fund.* **18** (1), 11-15.
8. Kays, W. M. and Crawford, M. E., 1980. Convective Heat and Mass Transfer, 2nd. Ed., McGraw-Hill Book Co., New York.
9. Kline, S. J. and McClintock, 1953. Describing Uncertainties in Single-Sample Experiments, *Mechanical Engineering*, **3**, Jan.
10. Lemlich, R., 1961. Vibration and Pulsation Boost Heat Transfer. *Chemical Engineering*, May, 171-176.
11. Lemlich, R. and Hwu, C., 1961. The effect of Acoustic Vibration on Forced Convective Heat Transfer. *A.I.Ch.E. Journal*, **7**(1), 102-106.
12. Liao N.S. and Wang C.C. 1988. On Convective Heat Transfer in Pulsating Turbulent Pipe Flow, *Experimental Heat Transfer, Fluid Mechanics and Thermodynamics*, 536-542.
13. Mamayev, V.V., Nosov, V.S and Syromyatnikov, N.I., 1976. Investigation of Heat Transfer in Pulsed Flow of Air in Pipes. *Heat Transfer - Soviet Research*, **8** (3), 111-116.
14. Martinelli, R.C., Boelter, L.M.K., Weinberg, E.B. and Yakahi, S., 1943. Heat Transfer to a Fluid Flowing Periodically at Low Frequencies in a Vertical Tube. *Transaction of ASME*, Oct. 789-798.
15. Mizushima, T., Maruyama, T. and Shiozaki, Y., 1973. Pulsating Turbulent Flow in a Tube *Journal of Chemical Engineering, Japan*, **8**, 210-216.
16. Park, J. S., Taylor, M. F. and McEligot, D. M., 1982. Heat Transfer to Pulsating Turbulent Gas Flow, *Proc., 7th. Int. Heat Transfer Conference*, **3**, 105-110.
17. Ramaprian, B. R and Tu, S. W., 1983. Fully Developed Periodic Turbulent Pipe Flow, Part 2: The detailed Structure of The Flow, *J. Fluid Mech.*, **137**, 59 - 81.
18. Rao, K. N., Narassihma, R. and Narayanan, M. A. B., 1971. The Bursting Phenomenon in a Turbulent Boundary Layer, *J. Fluid Mech.*, **48**, Part 2, 339-352.
19. West, F.B. and Taylor A.T., 1952. The Effect of Pulsations on Heat Transfer in Turbulent Flow of Water Inside Tubes. *Chemical Engineering Progress*, **48** (1), 39 - 43.

# ON THE ABILITY OF TURBULENCE MODELS TO PREDICT THE COMPLEX TURBULENT FLOWS: THE APPLICATION OF SCALING ANALYSIS.

A.V. Gorin and D.Ph. Sikovsky

Institute of Thermophysics,  
Siberian Division of RAS, Novosibirsk, Russia.

## ABSTRACT

An asymptotic analysis developed for the wall region of flows with strong adverse pressure gradients has shown that there exist the linear stress layer, in which the mean velocity obeys the "half-power-law". It is found that the widely used turbulence models such as the standard  $k$ - $\epsilon$ -model and Gibson & Launder model of Reynolds stress transport have no physical solution in linear stress layer and thus unsuitable for the wall region of complex turbulent flows with the strong near-wall Reynolds stress gradients. It is shown that this deficiency is a consequence of the unjustified omitting of cross-diffusion term in the dissipation transport equation. The inclusion of this term remedies the situation.

## 1 INTRODUCTION

Following Townsend (1) it is commonly supposed that turbulent flows have double structure consisting of the large-scale energy containing eddies and small-scale velocity fluctuations. Today there are no doubts that the large-scale structures play an important role in turbulent momentum, heat and mass transport.

This role becomes significant in so-called complex turbulent flows or flows with complicated geometry. The commonly encountered feature of complex turbulent flow is the occurrence of flow separations near the abrupt changes of surface geometry. Downstream the separation shear layer is developed and reattached at the surface forming the recirculation region with enhanced near-wall heat transfer. Enhancement of transfer processes in the vicinity of reattachment in the recirculating region is caused by large-scale turbulent structures originating from shear layer, which are entrained into the region of fluid retarded by strong adverse pressure gradient and produces high turbulence intensities.

In view of these features of separated flows there should be certain requirements for the turbulence models used to predict the velocity and turbulence intensity fields. Among them one of the most essential is the proper near-wall treatment. It is of utmost importance for the prediction of heat and mass transfer, because it is in the vicinity of the wall where the largest temperature gradients exist as evidenced by experimental and numerical practice (2). Historically, the turbulence modelling did not deal with the direct solving of the momentum and heat transport equations near the wall. First turbulence model  $k$ - $\omega$  of Kolmogorov (3) was designed to predict turbulent velocity field in the fully developed turbulent flows (so-called high-Reynolds-number model) where the effects of molecular viscosity can be neglected. Near the wall, where this effects is important, the equations of model

become singular. Because of this, on the wall the boundary conditions of matching with the "law of the wall"

$$U = v_\tau \left( \frac{1}{\kappa} \ln \frac{y v_\tau}{\nu} + B \right), \quad k = c_1 v_\tau^2, \quad \omega = c_2 \frac{v_\tau}{y} \quad [1]$$

where  $U$  is the mean velocity,  $k$  is the turbulent energy,  $\omega$  is the quasivorticity,  $v_\tau$  is the friction velocity,  $\kappa=0.41$  is von Karman constant,  $B=5.0$ ,  $c_1$ ,  $c_2$  are the universal coefficients needed to be determined from the experiment.

More recently this way of near-wall treatment was developed and is known today as the using of wall functions. Based on the friction velocity as the characteristic scale the wall functions for the velocity and the temperature are widely used in the numerical practice but they failed to predict turbulent flowfield in separated and reattached flows where  $v_\tau$  goes to zero. There are clear experimental evidences that logarithmic law of the wall becomes invalid in the vicinity of separation or reattachment point and within the recirculating region (4,5). Because of this today there are the tendency to abandon the wall function usage and to resolve the near-wall viscous sublayer in a more detailed way by employing the low-Reynolds-number models (2). It inevitably leads to increasing complications of model equations along with the significant increase of computational efforts due to drastic fining of mesh.

An alternative approach is the elaboration of possible universal wall functions for the separated and reattached turbulent flows. If these wall functions were found the numerical modelling of complex turbulent flows would be much simplified in predicting heat and mass transfer in view of its "near-wall character" above mentioned. The search of possible universal wall functions should be based on the similarity theory of

turbulent flows. It is the similarity theory that establish the validity of logarithmic law-of-the-wall [1] (6) in the case of local equilibrium state of the near-wall turbulence.

In the present paper the similarity analysis developed recently in (7,8) is applied to the checking the ability of turbulence models to predict the complex turbulent flows. Scaling laws of near-wall turbulence were derived in (7,8) on the basis of the general similarity considerations, which do not imply any turbulence closure scheme. Hence, the realistic turbulence models must have a solutions being consistent with the scaling laws. For the convenience of reading the brief derivation of the similarity relations for the near-wall turbulent momentum and heat transfer are presented in §§2,3. In §4 the turbulence models such as standard  $k-\varepsilon$ -model and the Reynolds stress transport models are investigated.

## 2 SCALING LAWS OF NEAR-WALL TURBULENCE

Consider the three-dimensional unsteady turbulent flow of incompressible fluid near the plain wall. Averaged momentum equations has the form

$$\frac{\partial \langle v_i \rangle}{\partial t} + \langle v_j \rangle \frac{\partial \langle v_i \rangle}{\partial x_j} + \frac{\partial \langle p \rangle}{\partial x_i} = \nu \Delta \langle v_i \rangle + \frac{\partial \sigma_{ij}}{\partial x_j} \quad [2]$$

$$\frac{\partial \langle v_i \rangle}{\partial x_i} = 0 \quad [3]$$

where  $v_i$  is the fluid velocity,  $p$  is the pressure divided by density,  $\nu$  is the viscosity, angle brackets denotes the averaging,  $\sigma_{ij} = \langle v_i \rangle \langle v_j \rangle - \langle v_i v_j \rangle$  - tensor of turbulent stresses.

Let  $U_0$ ,  $u'$  be the characteristic scales of averaged and fluctuating velocities respectively and  $L$  is the spatial scale of velocity field (for example, the turbulent boundary layer thickness). We also assume that  $u' \ll U_0$ . When Reynolds numbers  $U_0 L / \nu$ ,  $u' L / \nu$  are large enough there should exist thin viscous sublayer near the wall with the characteristic thickness  $\delta_v$  being the monotonically increasing function of the viscosity. It is suggested that the viscous sublayer is the only region in fully developed turbulent flow where the viscosity affects directly the turbulence statistical regime. By the statistical regime is implied the full set of all moments of velocity and pressure fields and the related quantities such as average production and dissipation rate of turbulent energy. Outside of viscous sublayer  $y \gg \delta_v$ , does not affect the statistical regime of turbulent flow, which is in agreement with the principle of Reynolds number similarity (1,6).

The greater is Reynolds number, the thinner is the viscous sublayer thickness and the smaller the ratio

$\delta_v / L$ . It means that in the limit of infinite Re number the turbulent flow in the outer region  $y = O(L)$  becomes inviscid and the slip boundary conditions for the velocity should be imposed

$$\langle \vec{v} \rangle \rightarrow \vec{u}_s, \quad \vec{u}_s \cdot \vec{n} = 0, \quad y/L \rightarrow 0 \quad [4]$$

where  $\vec{n}$  is the normal vector,  $\vec{u}_s$  is the slip velocity vector parallel to the wall. Substituting [4] into [2],[3], one can obtain the boundary conditions for the turbulent stresses

$$\frac{\partial \sigma_{i2}}{\partial y} \rightarrow \alpha_i + \frac{\partial u_{si}}{\partial t} + u_{sj} \frac{\partial u_{si}}{\partial x_j} - \frac{\partial \sigma_{i1}}{\partial x} - \frac{\partial \sigma_{i3}}{\partial z}, \quad i = 1, 3 \quad [5]$$

$$\frac{\partial \langle p \rangle}{\partial y} \rightarrow 0 \quad [6]$$

where we adopted  $x_1 = x$ ,  $x_2 = y$ ,  $x_3 = z$ ,  $\alpha_i = \partial \langle p \rangle / \partial x_i |_{y=0}$  - wall pressure gradient and the viscous terms are omitted.

The following estimates  $\alpha_i = O(U_0^2 / L)$ ,  $\partial \sigma_{ij} / \partial x_j = O(u'^2 / L)$  ( $j=1,3$ ) allow us to neglect normal turbulent stresses in rhs of [5] after which it can be rewritten in the form

$$\frac{\partial \tau_i}{\partial y} \rightarrow \alpha_i + \frac{\partial u_{si}}{\partial t} + u_{sj} \frac{\partial u_{si}}{\partial x_j} = \alpha_{ef,i}, \quad i = 1, 3 \quad [7]$$

where  $\tau_i = \sigma_{i2}$  is the vector of turbulent shear stresses.

From [7] it is follows that

$$\tau_i = \tau_{i0} + \alpha_{ef,i} y + \dots, \quad y/L \rightarrow 0$$

where  $\tau_{i0}$  is some constant. Below it will be shown that  $\tau_{i0}$  is equal to the wall shear stress vector

$$\tau_{w,i} = \nu \frac{\partial \langle v_i \rangle}{\partial y} \Big|_{y=0} \text{ so that}$$

$$\tau_i = \tau_{w,i} + \alpha_{ef,i} y + \dots, \quad y/L \rightarrow 0 \quad [8]$$

In the vicinity of the flow separation or the reattachment the wall shear stress values are lowered and the ratio  $\beta_{ef} = \alpha_{ef} L / \tau_w$  may be very large. Consider this case in which there are exist the wide interval

$$\frac{\tau_w}{\alpha_{ef}} \ll y \ll L, \quad [9]$$

where both the relation [8] is valid and the first term in this relation can be neglected



$$\tau_i = \alpha_{ef,i} y + \dots, \quad \frac{\tau_w}{\alpha_{ef}} \ll y \ll L \quad [10]$$

This interval can be named the linear stress layer. Within this layer the turbulent shear stress gradient  $\bar{\alpha}_{ef}$  is the only relevant parameter of the turbulence statistical regime. The dimensionality considerations leads to the following relation for the mean shear (7,8)

$$\frac{\partial \langle v_i \rangle}{\partial y} = \frac{K}{2} \frac{\alpha_{ef,i}}{\alpha_{ef}} \left( \frac{\alpha_{ef}}{y} \right)^{1/2} \quad [11]$$

where  $K$  is an universal constant. Integration of [11] gives the "half-power law"

$$\langle \bar{v} \rangle = \bar{u}_s + K \frac{\bar{\alpha}_{ef}}{\alpha_{ef}} \left( \alpha_{ef} y \right)^{1/2}, \quad \frac{\tau_w}{\alpha_{ef}} \ll y \ll L \quad [12]$$

where the relation [4] has taken into account determining the constant of integration.

Consider the viscous sublayer and assume that here the following law of the wall is valid

$$\langle \bar{v} \rangle = \frac{\bar{\tau}_w}{\tau_w^{1/2}} f(y_+) \quad [13]$$

where  $y_+ = \tau_w^{1/2} y / \nu$  is the distance to the wall in wall units,  $f$  is an universal function having the following asymptotics

$$f(y_+) = \frac{1}{\kappa} \ln y_+ + B + \dots \quad [14]$$

Relations [13], [14] are the generalization of [1] and can be derived with the aid of the similarity hypothesis that the wall shear stress vector  $\bar{\tau}_w$  is the only relevant parameter of turbulence statistical regime within the viscous sublayer. To check this hypothesis one can substitute [13],[14] into [2],[3] and extract the leading order terms for  $y_+ \rightarrow \infty$ . It gives after simple algebra

$$\begin{aligned} \tau_i &= \tau_{w,i} + \alpha_i y + \frac{1}{\kappa} \frac{\partial \tau_{i,j}}{\partial x_j} \ln y_+ + \dots \\ &+ \frac{1}{\kappa^2} \nu_{\tau,j} \frac{\partial \tau_{i,j}}{\partial x_j} y \ln^2 y_+ + \dots, \quad y_+ \rightarrow \infty \end{aligned} \quad [15]$$

where we have introduced for convenience the friction velocity vector  $\bar{v}_\tau = \bar{\tau}_w / \tau_w^{1/2}$ .

From [15] it is seen that  $\tau_i$  depends only on  $\bar{v}_\tau$  if all terms in rhs of [15] except the first can be neglected. It can be shown that it is possible if

$$1 \ll y_+ \ll \min \left\{ P_+^{-1}, \text{Re}_\tau \ln^{-2} \text{Re}_\tau \right\} \quad [16]$$

where  $P_+ = \frac{\nu \alpha}{v_\tau^3}$  is the pressure gradient

parameter (pressure gradient in wall units),

$\text{Re}_\tau = \frac{v_\tau L}{\nu}$ . In turn the interval [16] may exist only if

$P_+$  is small enough, namely,  $P_+ \leq 10^{-2}$  (7,8). Then in this interval  $\tau_i \approx \tau_{w,i}$  in agreement with the similarity hypothesis suggested. Hence it can be named as the constant stress layer.

Consider now the region  $y = O(\tau_w / \alpha_{ef})$ . On

the one hand since here  $y_+ = O(P_+^{-1})$  the law of the

wall [13],[14] is no longer valid. On the other hand the

condition [10] does not hold, so the "half-power law" does not hold yet. In other words the

region  $y = O(\tau_w / \alpha_{ef})$  is an intermediate between the

regions of logarithmic [14] and half-power [12]

asymptotics of velocity, in which respectively the wall

shear stress and pressure gradient are the only relevant

parameters. Therefore one can suppose that in this

region both  $\bar{\tau}_w$  and  $\bar{\alpha}$  determined uniquely the

turbulence statistical regime. This supposition agrees

with the relation [8], but the expression [15] will also

agree with [8] in the leading order of approximation

only if

$$\bar{\alpha}_{ef} = \bar{\alpha} + \frac{1}{\kappa} \frac{\partial \bar{v}_\tau}{\partial x_j} \ln \frac{v_\tau^3}{\nu \alpha_{ef}} + \frac{1}{\kappa^2} (\bar{v}_\tau \nabla) \bar{v}_\tau \ln^2 \frac{v_\tau^3}{\nu \alpha_{ef}} \quad [17]$$

where we used the fact that in the

region  $y = O(\tau_w / \alpha_{ef})$  or  $y_+ = O(v_\tau^3 / \nu \alpha_{ef})$  the

following relation is true

$$\ln y_+ = \ln \left( \frac{v_\tau^3}{\nu \alpha_{ef}} \right) + \ln \left( \frac{\alpha_{ef} y}{\tau_w} \right) = \ln \left( \frac{v_\tau^3}{\nu \alpha_{ef}} \right) + O(1) \quad [18]$$

From [13],[14],[18] it is follows that in the

region  $y = O(\tau_w / \alpha_{ef})$

$$\langle \bar{v} \rangle = \frac{\bar{v}_\tau}{\kappa} \ln \frac{v_\tau^3}{\nu \alpha_{ef}} + O(v_\tau) \quad [19]$$

On the other hand, velocity in this region

should be equal in the leading order to the slip velocity

according to [4],[12]. Therefore, one can write

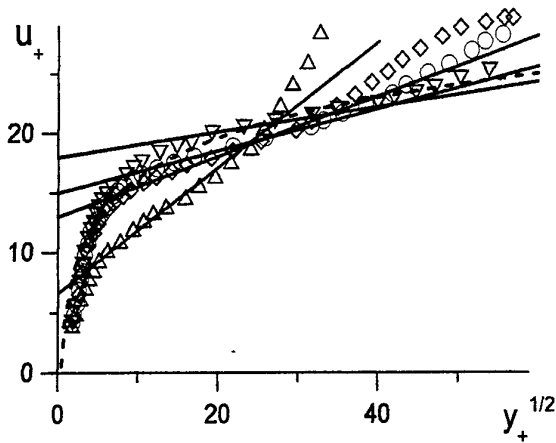


Fig. 1a. Profiles of mean velocity in separated and reattaching flow downstream the reattachment point (9). Downstream distance  $x/x_p$ :  $\Delta$ -1.26,  $\diamond$ -1.69,  $\circ$ -1.99,  $\nabla$ -2.86.  $x_p$ - reattachment position.

$$\bar{u}_s = \frac{\bar{v}_\tau}{\kappa} \ln \frac{v_\tau^3}{v\alpha_{ef}} + O(v_\tau) \quad [20]$$

Asymptotic relation [20] is valid when the value of criteria  $\varepsilon = v\alpha_{ef}/v_\tau^3$  is small enough, namely,  $\varepsilon \leq 10^{-2}$  (7,8). Otherwise dimensionality considerations leads to the following general expression

$$\bar{u}_s = \bar{v}_\tau \Phi \left( \frac{v_\tau^3}{v\alpha_{ef}}, \frac{\bar{v}_\tau \cdot \bar{\alpha}_{ef}}{v_\tau \alpha_{ef}} \right) \quad [21]$$

In this case, however, slip velocity is much lower than  $U_0$  and does not affect seriously the near-wall turbulent shear stress gradient, which becomes equal to wall pressure gradient in line with [7], i.e.  $\bar{\alpha}_{ef} \approx \bar{\alpha}$ .

Summing up the above analysis, one can conclude the following. There exist the turbulent flows with the strong turbulent stress gradient near the wall, in which  $\frac{y}{\tau} \frac{\partial \tau}{\partial y} = O(1)$ . These flows can be called local non-equilibrium flows in contrast to equilibrium flows, where  $\frac{y}{\tau} \frac{\partial \tau}{\partial y} = o(1)$ . The term "equilibrium" means the equality of the production and the dissipation of turbulent energy, in local non-equilibrium flows the turbulent diffusion of energy appears. First of all the local non-equilibrium flows is the flows in which the maximum of turbulent shear stress  $\tau_m$  exists being greater than the wall shear stress  $\tau_w$ . There the value of parameter  $\beta_{ef} = \alpha_{ef} L / \tau_w = O(\tau_m / \tau_w) \gg 1$  and near the wall

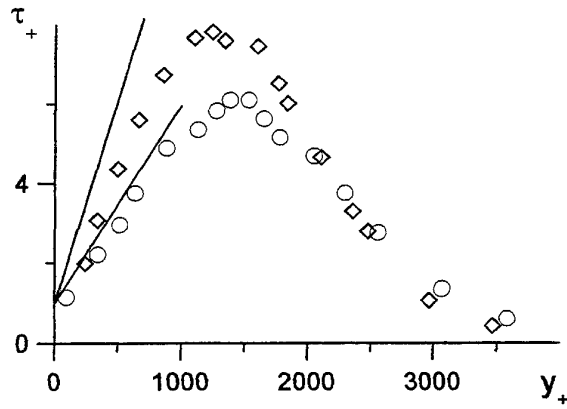


Fig. 1b. Profiles of Reynolds shear stress in separated and reattaching flow downstream the reattachment point (9). The definition of symbols are the same as on Fig. 1a.

the "half-power law" [12] should be observed in the interval [9] of almost linear turbulent shear stress [10]. The logarithmic law of the wall [13],[14] can be valid only if the value of  $\varepsilon = v\alpha_{ef}/v_\tau^3$  is small enough, otherwise it breaks down.

In the majority of cases the complex turbulent flows are the local non-equilibrium flows. Fig.1a,b present the distributions of mean velocity and Reynolds shear stresses respectively in the two dimensional separated turbulent flow over the normal plate with the splitter plate (9) downstream the reattachment point (so-called relaxing or redeveloping boundary layer). The "half-power law" is clearly observed on Fig. 1a but the logarithmic law of the wall (dotted line) does only for those sections where  $\varepsilon < 0.01$ . For each velocity profile the straight line is drawn following the expression [12]

$$u_+ = u_{s+} + K \left( \frac{\alpha_{ef} y}{v_\tau^2} \right)^{1/2} = u_{s+} + K (\varepsilon y_+)^{1/2} \quad [22]$$

with  $K=2.5$ . It is readily seen that "half-power law" is observed in the region of almost linear Reynolds shear stress, where the equation [8] is valid (straight lines on Fig. 1b). The points of intersection of line [22] with the ordinate axis gives the slip velocity in wall units  $u_{s+} = u_s/v_\tau$ . The values of  $u_{s+}$  for the profiles of Fig. 1a is presented in Fig. 2. in comparison with the based on [20] expression

$$u_{s+} = \frac{1}{\kappa} \ln \frac{1}{\varepsilon} + D \quad [23]$$

with  $\kappa=0.4$ ,  $D=1.7$ .

If the value of parameter  $\varepsilon$  is not small, the interval [16] does not exist. It means that the Reynolds shear stress gradient affects the turbulence statistics in the buffer zone and the viscous sublayer. When the value of parameter  $\varepsilon$  is large enough ( $\varepsilon \gg 10^{-2}$ ), the wall shear stress should be irrelevant parameter of the turbulence statistical regime within the viscous sublayer. It means that the latter depends only on  $\nu$  and  $\bar{\alpha}_{ef}$ . Then instead of [13],[14] we have, on dimensional grounds, another law of the wall

$$\bar{u} = \frac{\bar{\alpha}_{ef}}{\alpha_{ef}} (\nu \alpha_{ef})^{1/3} F\left(\frac{\alpha_{ef}^{1/3} y}{\nu^{2/3}}\right) \quad [24]$$

where  $F$  is an universal function. Matching [24] with [12] gives

$$\bar{u}_s = O\left((\nu \alpha_{ef})^{1/3}\right) \ll U_0, F(t) = Kt^{1/2} + \dots, t \rightarrow \infty \quad [25]$$

It follows from [25] that the contribution of pressure gradient term in [7] is dominant, so

$$\bar{\alpha}_{ef} \approx \bar{\alpha} \quad [26]$$

### 3 HEAT TRANSFER

Let the wall be heated or cooled forming the distribution of the averaged heat flux (divided by the density and specific heat) on the wall  $q(\bar{x}, t) = a \partial \langle T \rangle / \partial y|_{y=0}$ . The temperature of the free stream away from the wall will be assumed to equal zero without loss of generality (so that the temperature  $T$  used below is the difference between the local temperature and the free stream temperature). The problem is to predict the wall heat transfer coefficient  $h_w = q/T_w$ . The averaged equations of heat transport can be written in the form

$$\frac{\partial \langle T \rangle}{\partial t} + \langle v_j \rangle \frac{\partial \langle T \rangle}{\partial x_j} = a \Delta \langle T \rangle + \frac{\partial q_{t,j}}{\partial x_j} \quad [27]$$

where  $a$  is the thermal diffusivity,  $q_{t,j} = \langle v_i \rangle \langle T \rangle - \langle v_i T \rangle$  - turbulent heat flux.

If the fluid Prandtl number  $Pr = \nu/a$  is not very low ( $Pr \geq 1$ ), the structure of the temperature field is similar to the structure of the velocity field. In the outer region where the turbulence is fully developed, there should be no influence of molecular viscosity and thermal diffusivity on the statistical regime of temperature fluctuations ("Peclet number similarity

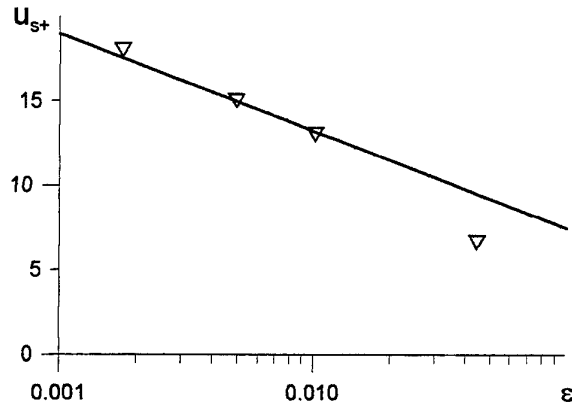


Fig. 2. Slip velocity vs.  $\varepsilon$

principle"). In view of [4] the following boundary conditions for the averaged temperature can be imposed

$$\langle T \rangle \rightarrow T_s, \quad y/L \rightarrow 0 \quad [28]$$

where  $T_s$  is the "slip temperature". It also be called as the temperature on the edge of near-wall zone as it will be seen below.

Analogous to [5] the boundary condition for the normal turbulent heat flux can be written

$$\frac{\partial q_{t,y}}{\partial y} = \frac{\partial T_s}{\partial t} + \bar{u}_s \cdot \nabla T_s - \frac{\partial q_{t,x}}{\partial x} - \frac{\partial q_{t,z}}{\partial z}, \quad y/L \rightarrow 0 \quad [29]$$

If there is no the sudden changes of the heat flux in the streamwise direction and the wall is heated uniformly enough, then the following estimate can be made

$$\frac{\partial q_{t,y}}{\partial y} = O\left(\frac{q}{L}\right) \quad [30]$$

Therefore, near the wall

$$q_{t,y} \approx q, \quad y/L \rightarrow 0 \quad [31]$$

In other words, there should not exist an interval analogous to [9], where the values of turbulent heat flux is essentially differs from wall heat flux. This distinction between the heat and momentum transport arises from the presence of the pressure gradient in the momentum transport equation [2] and the absence of the analogous term in the heat transport equation [27].

On the other hand, within the interval [9] the turbulent shear stress gradient  $\bar{\alpha}_{ef}$  is the only relevant parameter of the turbulence statistical regime.

Consider now the region of thermal sublayer, where the viscosity and thermal diffusivity affect

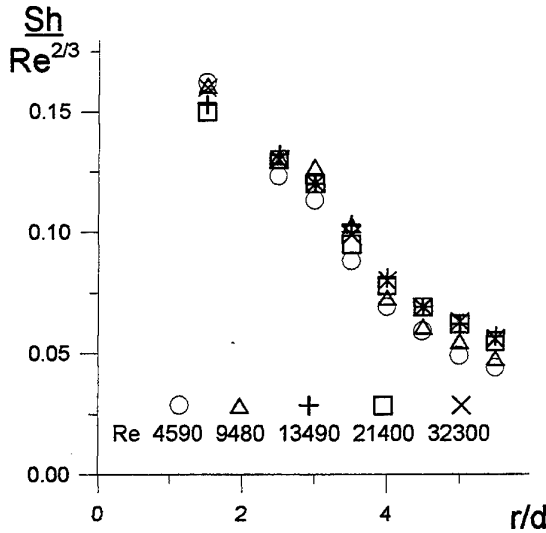


Fig.3. Radial distributions of the complex  $ShRe^{-2/3}$  beneath the round impinging jet at different  $Re$  numbers (14).

directly the statistics of temperature fluctuations. As it was established above if the value of parameter  $\varepsilon$  is small enough, there exists an interval  $y_+ \ll \min\{t_+^{-1}, Re_\tau \ln^{-2} Re_\tau\}$ , in which the wall shear stress vector  $\bar{\tau}_w$  and the molecular viscosity  $\nu$  are the only relevant parameters of turbulence statistical regime. Adding the thermal diffusivity  $\alpha$  to this list and employing the well-known dimensionality considerations (6), the following law of the wall for the averaged temperature can be derived

$$\langle T \rangle = \langle T_w \rangle - \frac{q}{\nu_\tau} f_t(y_+, Pr) \quad [32]$$

$$f_t(y_+, Pr) = \frac{1}{\kappa_t} \ln y_+ + B_t(Pr) + \dots, y_+ \rightarrow \infty \quad [33]$$

where  $\kappa_t$  is the universal constant,  $f_t, B_t$  are the universal functions. Matching of the [32],[33] and [28] gives the expression for the "slip temperature"

$$\langle T_s \rangle = \langle T_w \rangle - \frac{T_\tau}{\kappa_t} \ln \frac{1}{\varepsilon} + O(T_\tau) \quad [34]$$

where  $T_\tau = q/\nu_\tau$  is the friction temperature.

Comparing the [34] and [20] it is easy to derive the "extended Reynolds analogy"

$$\frac{\nu_\tau^2}{u_s} = \frac{\kappa}{\kappa_t} \frac{q}{(\langle T_w \rangle - \langle T_s \rangle)}, \text{ or } \frac{c_f}{2} = Pr_t \frac{u_s}{U_0} St \quad [35]$$

where  $Pr_t = \kappa/\kappa_t$  is the turbulent Prandtl number,  $c_f = 2\tau_w^2/U_0^2$  is the friction coefficient.

When the value of parameter  $\varepsilon$  is large enough ( $\varepsilon \gg 10^{-2}$ ), the temperature law of the wall [32],[33] is no longer valid. Instead of it the analogous to [24] law of the wall can be written with the "inverse half-power law" asymptotics (7)

$$\langle T \rangle = \langle T_w \rangle - \frac{q}{(\nu\alpha)^{1/3}} F_t\left(\frac{\alpha^{1/3} y}{\nu^{2/3}}, Pr\right) \quad [36]$$

$$F_t(t) = K_t t^{-1/2} + B_t(Pr) + \dots, \quad t \rightarrow \infty \quad [37]$$

where  $K_t$  is a universal constant,  $B_t$  is the universal function.

Matching of [36],[37] with the [28] enables us to derive the wall heat transfer coefficient

$$\frac{q}{(\langle T_w \rangle - \langle T_s \rangle)} = \frac{(\nu\alpha)^{1/3}}{B_t(Pr)} \quad [38]$$

Introducing the Nusselt criterion the expression [38] can be rewritten

$$\begin{aligned} Nu &= \frac{qL}{a(\langle T_w \rangle - \langle T_s \rangle)} = \frac{Pr}{B_t(Pr)} \left(\frac{\alpha L^3}{\nu^2}\right)^{1/3} = \\ &= \frac{Pr}{B_t(Pr)} C_\alpha^{1/3} Re^{2/3} \end{aligned} \quad [39]$$

where  $C_\alpha = \alpha L/U_0^2$  is the pressure gradient coefficient. The latter is independent of  $Re$ , because the pressure gradient is created by the outer inviscid flow. Then according to [39] the wall heat transfer obeys the "two-third law"  $Nu \sim Re^{2/3}$  (7) established first in (10).

The "two-third law"  $Nu \sim Re^{2/3}$  for the wall heat transfer coefficient in turbulent separated and reattached flow is well-known (11,12). It is also valid for such flows, which are at first site not related to the class of separated flows. A notable example is the impinging jet on a heated surface (13). Fig. 3 presents experimental data of Popiel & Boguslawski (14) for the mass transfer on the surface beneath the round impinging jet. In a fully developed turbulent regime ( $Re = U_m d/\nu \gg 10^4$ ,  $d, U_m$  are the nozzle diameter and exit mean velocity) it is seen the very good collapse of the radial distributions of the values  $ShRe^{-2/3}$  beginning from the point of first maximum of mass transfer coefficient  $r/d > 1.7$  (near the stagnation point  $r/d > 1.7$  the correlation  $Sh \sim Re^{1/2}$  was observed in (14)).

The explanation of these facts arises from the analysis of the structure of near-wall turbulence within the impinging jet experimentally investigated in

(15,16). The large-scale turbulent vortices developing in the jet are collided with the wall. During this interaction of vortices with the wall the strong instantaneous pressure gradients are induced causing the unsteady flow separations near the wall (15). On the background of the lowered wall shear stress in this region the strong fluctuating pressure gradients prevents the forming of the region of constant shear stress near the wall. When there are the large instantaneous pressure gradient along the wall, the linear stress layer are adjacent to the viscous sublayer, so the heat and mass transfer scaling [39] is valid.

It should be noted that the processes of near-wall momentum and heat transport in turbulent separated and reattached flows are essentially unsteady. Because of this the obtained above relation should be considered as an instantaneous relations for the large-scale flow quantities (7).

#### 4 TURBULENCE MODELING: DISSIPATION TRANSPORT EQUATION REVISITED

In preceding section we have obtained the scaling laws for the near-wall turbulence in the separated and reattached flows and other local non-equilibrium flows. We have shown that the distinctive property of local non-equilibrium flows is the existence of linear turbulent shear stress region in the vicinity of the wall and the region of "half-power law" of the velocity profile [12]. This expression with the empirically verified relation [21] for the slip velocity may become the proper wall functions for the complex turbulent flows.

However, before this wall functions to be elaborated it is necessary to make sure that the turbulence models used are consistent with the scaling laws being the base of wall functions. Any model pretending to predict the complex turbulent flows must possess a solution in the form [10],[11].

Write out the scaling relations for the turbulence quantities of interest in the linear stress layer in the inertial reference frame moving with the slip velocity  $u_s$ , the  $Ox$ -axis of the frame being aligned with the vector  $\alpha_{ef}$

$$\begin{aligned} \tau &= \alpha_\varepsilon y, & U &= K(\alpha_{ef} y)^{1/2} + const, \\ \varepsilon &= a_\varepsilon \alpha_{ef}^{3/2} y^{1/2}, & k &= a_k \alpha_{ef} y, & \langle v^2 \rangle &= a_v \alpha_{ef} y \\ \langle u^p \rangle &\sim (\alpha_{ef} y)^{p/2} \end{aligned} \quad [40]$$

where  $\tau = -\langle u'v' \rangle$  is Reynolds shear stress,  $u$  is the mean velocity in  $x$ -direction,  $k$  is the turbulent kinetic energy,  $\varepsilon$  is the rate of its dissipation,  $\langle u^p \rangle$

denotes any  $p$ -th order moments of velocity fluctuation,  $K, a_k, a_\varepsilon$  - universal constants.

Consider at first the standard  $k$ - $\varepsilon$ -model, which have the following form suitable to the order of approximation of thin shear layer

$$\begin{aligned} \tau &= \nu_t \frac{\partial U}{\partial y}, & \nu_t &= C_\mu \frac{k^2}{\varepsilon} \\ \frac{d}{dy} \left( \frac{\nu_t}{\sigma_k} \frac{dk}{dy} \right) + \tau \frac{dU}{dy} - \varepsilon &= 0, \\ \frac{d}{dy} \left( \frac{\nu_t}{\sigma_\varepsilon} \frac{d\varepsilon}{dy} \right) + C_{\varepsilon 1} \frac{\varepsilon}{k} \tau \frac{dU}{dy} - C_{\varepsilon 2} \frac{\varepsilon^2}{k} &= 0 \end{aligned} \quad [41]$$

where  $\nu_t$  is the eddy viscosity and the commonly used values of constants are

$$C_\mu = 0.09, C_{\varepsilon 1} = 1.44, C_{\varepsilon 2} = 1.92, \sigma_k = 1.0, \sigma_\varepsilon = 1.3 \quad [42]$$

Substitution [40] in [41],[42] gives

$$\begin{aligned} a_k &= -C_\mu^{-1/2} \frac{3C_{\varepsilon 1} \sigma_\varepsilon - \sigma_k}{3C_{\varepsilon 2} \sigma_\varepsilon - \sigma_k} = -2.81 \\ a_\varepsilon &= \frac{2^{-1/2} C_\mu^{-1/4} (3C_{\varepsilon 1} \sigma_\varepsilon - \sigma_k)^{5/4}}{\sigma_k^{1/2} \sigma_\varepsilon^{1/2} (C_{\varepsilon 2} - C_{\varepsilon 1})^{1/2} (3C_{\varepsilon 2} \sigma_\varepsilon - \sigma_k)^{3/4}} = 2.72 \end{aligned} \quad [43]$$

so the turbulent energy is negative.

Relations the same as [43] were obtained earlier by Durbin & Belcher (17). They considered the similar problem [40]-[42] for the adverse pressure gradient boundary layer (instead  $\alpha_{ef}$  they used only the pressure gradient  $\alpha$ ), but they failed to calculate the values of  $a_k, a_\varepsilon$  correctly (in (17) the erroneous values  $a_k = 3.95, a_\varepsilon = 5.37$  were given)!

It follows from [43] that standard  $k$ - $\varepsilon$ -model has no solution in the linear stress layer. This is the explanation of the well-known fact that standard  $k$ - $\varepsilon$ -model is very inaccurate for flows with strong adverse pressure gradients and with separation and reattachment. The conclusion should be made that standard  $k$ - $\varepsilon$ -model is unable to predict adequately the complex turbulent flows, which is commonly local non-equilibrium.

The searching for the reason why standard  $k$ - $\varepsilon$ -model behaves so bad has shown that the source of trouble is in the transport equation for the rate of dissipation  $\varepsilon$ . The analysis performed has shown that the weak point of  $\varepsilon$ -equation is the gradient approximation of diffusion term

$$D_i = -\frac{v_i}{\sigma_\varepsilon} \frac{\partial \varepsilon}{\partial x_i} \quad [44]$$

In the paper of Hanjalic & Launder (18) (earlier the same was done by B. I. Davydov) the transport equation for  $D_i$  was derived on the basis of Navier-Stokes equations. Using some traditional assumptions this equation becomes

$$D_i \sim -\frac{k}{\varepsilon} \left( \langle u_i' u_j' \rangle \frac{\partial \varepsilon}{\partial x_j} + C_{D1} \varepsilon \frac{\partial \langle u_i' u_j' \rangle}{\partial x_j} \right) \quad [45]$$

Omitting the last term leads to the gradient approximation [44]. In defense of such omitting Hanjalic & Launder pointed out that the near-wall gradients of dissipation is usually much greater than the Reynolds stress gradients in agreement with the well-known scaling of constant stress layer that assumed to exist near the wall

$$\varepsilon = \frac{v_\tau^3}{\kappa y}, \quad \langle u_i' u_j' \rangle \sim v_\tau^2 = \text{const} \quad [46]$$

But in the case of linear stress layer with the scaling [40] the ignoring of the last term in rhs of [45] is unjustified. One should use both terms, which in the frame of  $k$ - $\varepsilon$ -model become

$$D_i = -\frac{v_i}{\sigma_\varepsilon} \frac{\partial \varepsilon}{\partial x_i} - 2C_D k \frac{\partial k}{\partial x_i} = -\frac{v_i}{\sigma_\varepsilon} \frac{\partial \varepsilon}{\partial x_i} - C_D \frac{\partial k^2}{\partial x_i} \quad [47]$$

where  $C_D$  is the new constant.

The additional term in [47] may be treated as the effect of cross-diffusion flux of dissipation due to the turbulent energy gradient.

In view of [47], the modified transport equation for  $\varepsilon$  is

$$\frac{\partial}{\partial y} \left( \frac{v_i}{\sigma_\varepsilon} \frac{\partial \varepsilon}{\partial x_i} \right) + C_D \frac{\partial^2 (k^2)}{\partial y^2} + C_{\varepsilon 1} \frac{\varepsilon}{k} \tau \frac{\partial U}{\partial y} - C_{\varepsilon 2} \frac{\varepsilon^2}{k} = 0 \quad [48]$$

The solution of the problem [40],[41] with modified equation for  $\varepsilon$  [48] is of the form

$$K^4 = \frac{4(3C_{\varepsilon 2} \sigma_\varepsilon - \sigma_k - 4C_D \sigma_k \sigma_\varepsilon / C_\mu)(3C_{\varepsilon 1} \sigma_\varepsilon - \sigma_k - 4C_D \sigma_k \sigma_\varepsilon / C_\mu)}{C_\mu \sigma_k^2 \sigma_\varepsilon^2 (C_{\varepsilon 2} - C_{\varepsilon 1})^2} \Phi_{ij,2} = -C_2 \left( P_{ij} - \frac{1}{3} P_{kk} \delta_{ij} \right)$$

$$a_k^2 = \frac{1}{C_\mu} \frac{(3C_{\varepsilon 1} \sigma_\varepsilon - \sigma_k - 4C_D \sigma_k \sigma_\varepsilon / C_\mu)}{(3C_{\varepsilon 2} \sigma_\varepsilon - \sigma_k - 4C_D \sigma_k \sigma_\varepsilon / C_\mu)}$$

$$a_\varepsilon = \frac{KC_\mu a_k^2}{2} \quad [49]$$

To estimate the newly introduced constant  $C_D$  through the known from the experiment coefficient  $K$  in the "half-power law" [22] the following relations has obtained

$$C_D = \frac{C_\mu K}{4a_k} \left( \frac{C_{\varepsilon 2} C_\mu K a_k^2}{2} - \frac{C_{\varepsilon 1} K}{2} - \frac{a_k}{\sigma_\varepsilon K} \right),$$

$$a_k = \frac{3}{C_\mu \sigma_k K^2} + \left( \frac{9}{C_\mu^2 \sigma_k^2 K^4} + \frac{1}{C_\mu} \right)^{1/2} \quad [50]$$

Below we will use the value of  $K = 2.5$  as the appropriate experimental estimate of this coefficient (see Fig. 1). After substituting this value in [50] it gives  $C_D = 0.1152$ , and the following values of coefficients in [40]

$$a_k = 15.18, \quad a_\varepsilon = 11.62 \quad [51]$$

It should be mentioned that essential improvement of the turbulence prediction of non-equilibrium flows by  $k$ - $\varepsilon$ -model due to including of cross-diffusion term was reported recently (19), although the form of cross-diffusion term used in (19) differs from [45]. The present analysis based on scaling considerations gives the clear physical explanation of it.

The results obtained are also important for the second-moment closure schemes where the dissipation transport equation is also used. For example, the model of Gibson and Launder (2) consists of equations, which in the case of thin shear layer approximation are of the form

$$\frac{\partial}{\partial y} \left( C_s \frac{k}{\varepsilon} \langle v^2 \rangle \frac{\partial \langle u_i u_j \rangle}{\partial y} \right) + P_{ij} + \Phi_{ij} - \frac{2}{3} \varepsilon \delta_{ij} = 0$$

$$P_{ij} = - \left\{ \langle u_i u_k \rangle \frac{\partial U_j}{\partial x_k} + \langle u_j u_k \rangle \frac{\partial U_i}{\partial x_k} \right\}$$

$$\Phi_{ij} = \Phi_{ij,1} + \Phi_{ij,2} + \Phi_{ij,w}$$

$$\Phi_{ij,1} = -C_1 \frac{\varepsilon}{k} \left( \langle u_i u_j \rangle - \frac{2}{3} k \delta_{ij} \right)$$

$$\Phi_{ij,2} = -C_2 \left( P_{ij} - \frac{1}{3} P_{kk} \delta_{ij} \right)$$

$$\Phi_{ij,w} = C_{1w} \frac{\varepsilon}{k} \left( \langle v^2 \rangle \delta_{ij} - \frac{3}{2} \langle v u_i \rangle \delta_{j2} - \frac{3}{2} \langle v u_j \rangle \delta_{i2} \right) f_w +$$

$$+ C_{2w} \left( \Phi_{22,2} \delta_{ij} - \frac{3}{2} \Phi_{i2,2} \delta_{j2} - \frac{3}{2} \Phi_{j2,2} \delta_{i2} \right) f_w$$

$$f_w = \frac{C^{3/4} k^{3/2}}{\kappa \varepsilon \nu}$$

$$\frac{\partial}{\partial y} \left( C_\varepsilon \frac{k}{\varepsilon} \left( \nu^2 \right) \frac{\partial \varepsilon}{\partial y} \right) + C_{\varepsilon 1} \frac{\varepsilon}{2k} P_{kk} - C_{\varepsilon 2} \frac{\varepsilon^2}{k} = 0 \quad [52]$$

with the additional to [42] model constants

$$C_1 = 1.8, C_2 = 0.6, C_{1w} = 0.5,$$

$$C_{2w} = 0.3, C_\varepsilon = 0.22, C_\varepsilon = 0.18 \quad [53]$$

Substituting [40] in [52] one can obtain the set of algebraic equations for the values  $a_k, a_\varepsilon, a_\nu, K$ . Numerical evaluation of the roots has shown that there is no physical solution as well as in the case of standard  $k$ - $\varepsilon$ -model.

It was also shown that the inclusion of the additional source term known as "Yap correction" (2,20)

$$S_\varepsilon = \max \left\{ 0.83 \frac{\varepsilon^2}{k} (f_w - 1) f_w^2, 0 \right\} \quad [54]$$

into the dissipation equation does not remedy the situation. To obtain the physical solution and the value  $K=2.5$  one should replace the factor 0.83 in [54] by 3.37. Then the values

$$a_k = 7.40, a_\varepsilon = 6.37, a_\nu = 1.81 \quad [55]$$

are obtained.

Including the above suggested additional cross-diffusion term

$$D^{cross} = \frac{\partial}{\partial x_i} \left( C_D k \frac{\partial (u_i u_j)}{\partial x_j} \right) \quad [56]$$

in the lhs of dissipation transport equation [52] with  $C_D=0.5822$  has enabled us to obtain the following solution

$$K = 2.50, a_k = 7.41, a_\nu = 1.81, a_\varepsilon = 6.38 \quad [57]$$

Note that this values are almost the same as those [55] for "Yap-corrected model".

In the case of large positive near-wall turbulent energy gradients  $\partial k / \partial y$  the additional cross-diffusion term [56] acts like a source in the dissipation equation. It should be noted that it is the usual practice to include the additional source term in the dissipation equation for the improvement of the performance of  $k$ -

$\varepsilon$ -model and the Reynolds stress transport models, especially for the heat transfer predictions. One of the examples is the discussed above correction of Yap (2,20) [54]. These additional terms are artificial contrary to the natural way of using the cross-diffusion term [56].

## 5 CONCLUSIONS

The similarity analysis has shown that in the non-equilibrium turbulent flows with the strong turbulent stress gradient near the wall ( $\frac{y}{\tau} \frac{\partial \tau}{\partial y} = O(1)$ ) the

averaged velocity obeys the "half-power law" in the linear stress region and the "inverse half-power law" is valid for the averaged temperature. Checking for the consistency with the "half-power law" is revealed that the standard  $k$ - $\varepsilon$ -model and the Gibson & Launder model of Reynolds stress transport have no solutions in the linear stress layer.

This fact may be the crucial physical reason why these models predict poorly the turbulent flows with the strong adverse pressure gradients and separated and reattached flows.

It has shown that the major source of error is the dissipation transport equation, where the important term of the cross-diffusion of dissipation under the turbulent stresses gradient was omitted. The inclusion of this term permits to obtain the realistic solution in the linear stress layer in agreement with the experiment.

It is hoped that the inclusion of the cross-diffusion term in the dissipation equation will improve the predictive capabilities of turbulence models, where this equation are employed, for the complex turbulent flows.

The work was supported by the Russian Foundation for Basic Research, Grant No. 98-01-00739

## 6 REFERENCES

- (1) Townsend, A.A. The Structure of Turbulent Shear Flows, 1976, Cambridge University Press, Cambridge.
- (2) Launder, B.E. On the computation of convective heat transfer in complex turbulent flows, ASME J. Heat Transfer, 1988, V. 110, P.1111-1128.
- (3) Kolmogorov, A.N. The equation of turbulent motion in an incompressible viscous fluid, Izv. Akad. Nauk SSSR, Ser. Fiz., 1942, V. 6., No.1-2, P. 56-58.
- (4) Simpson, R. L. Turbulent boundary-layer separation, Ann. Rev. Fluid Mech., 1989, V. 21, P.205-234.
- (5) Jovic, S., Driver, D. Reynolds number effect on the skin friction in separated flows behind a backward-

- facing step, *Experiments in Fluids*, 1995, V. 18, No.6, P.464-467.
- (6) Monin, A.S., Yaglom, A. M. *Statistical Fluid Mechanics*, vol. 1, 1971, ed. by J. Lumley, MIT Press, Cambridge, MA.
- (7) Gorin, A.V., Sikovsky, D. Ph. Scaling of wall turbulence in separated and reattached flows, *Turbulence, Heat and Mass Transfer 2*, Proc. 2th Int. Symp., June 9-12, 1997, ed. by K. Hanjalic & T.W.J.Peeters, Delft, Delft University Press, P.121-128.
- (8) Gorin, A.V., Sikovsky, D. Ph. Asymptotic theory of adverse pressure gradient and redeveloping boundary layer, *Turbulence, Heat and Mass Transfer 2*, Proc. 2nd Int. Symp., June 9-12, 1997, ed. by K. Hanjalic & T.W.J.Peeters, Delft, Delft University Press, P.129-135.
- (9) Ruderich, R., Fernholz, H.H. An experimental investigation of a turbulent shear flow with separation, reverse flow and reattachment, *J. Fluid Mech.*, 1986, V. 163, P.283-322.
- (10) Gorin, A.V., Sikovsky, D.Ph. Similarity laws of the transfer processes in the turbulent separated flows, *Russ. J. Engineering Thermophysics*, 1995, V.5, P. 145-164.
- (11) Chang, P.K. *Separation of flow*, Oxford, Pergamon, 1970.
- (12) Ota, T., Nishiyama, H. A correlation of maximum turbulent heat transfer coefficient in reattachment flow region, *Int. J. Heat Mass Transfer*, 1987, V.30, No.6, P.1193-1200.
- (13) Martin, H. Heat and mass transfer between the impinging gas jets and solid surfaces, *Advances in Heat Transfer*, 1977, V. 13, P. 1-60.
- (14) Popiel, C. O., Boguslawski, L. Mass or heat transfer in impinging, single, round jets emitted by a bell-shaped nozzle and sharp-ended orifice, *Heat Transfer 1986, Proc. of Eight Int. Heat Transfer Conf., San Francisco, CA USA, V.3., P. 1187-1192*
- (15) Didden, N., Ho, C.M. Unsteady separation in a boundary layer produced by impinging jet, *J. Fluid Mech.*, 1985, V.160, P.235-256.
- (16) Kataoka K. et al., Quasi-periodic large-scale structure responsible for the selective enhancement of impinging jet heat transfer, *Heat Transfer 1986, Proc. of Eight Int. Heat Transfer Conf., San Francisco, CA USA, V.3., P. 1193-1198.*
- (17) Durbin, P.A., Belcher, S.E. Scaling of adverse pressure gradient turbulent boundary layers, *J. Fluid Mech.*, 1992, V.238, P.699-722.
- (18) Hanjalic, K., Launder B.E. A Reynolds stress model of turbulence and its application to thin shear flows, *J. Fluid Mech.*, 1972, V.52, Pt.4, P.609-638.
- (19) Yoon, B.K., Chung, M.K. Computation of compression ramp flow with a cross-diffusion modified  $k$ - $\epsilon$ -model, *AIAA J.*, 1995, V.33, No.8, P.1518-1520.
- (20) Launder, B.E. Modelling convective heat transfer in complex turbulent flow, *Engineering Turbulence Modelling and Experiments 2*, ed. W. Rodi & P. Martelli, Elsevier Science Pub., 1993, P. 3-22.



# THE EFFECT OF NATURAL CONVECTION ON LOCAL HEAT TRANSFER FOR A LIQUID METAL FLOW IN A HEATED HORIZONTAL TUBE UNDER A LONGITUDINAL MAGNETIC FIELD.

V.G. Sviridov, N.G. Razuvanov, A.V. Ustinov

Moscow Power Engineering Institute,  
Russia, Moscow

## ABSTRACT

Local heat transfer for a liquid metal flow in a heated horizontal pipe was experimentally investigated. The flow conditions model those in a Tokamak fusion reactor. Three alternatives of heat flux distribution on the outer tube surface were examined. Temperature fields, streamwise distributions of local and average heat transfer coefficients were measured. The profound effect of natural convection on the measured parameters was observed. A longitudinal magnetic field does not diminish the effects of natural convection.

## 1 INTRODUCTION

Experimental investigations of heat transfer for an anisothermic liquid metal flow in a horizontal tube under a longitudinal magnetic field are being made at the Moscow Power Engineering Institute. This case corresponds to a flow in toroidal channels of a blanket in the Tokamak fusion reactor. The MHD pressure losses can be considerably decreased in this flow pattern.

Our previous experiments (1 - 3) were made in one cross-section of a tube with uniform or non-uniform two-side distribution of heat flux along the tube circumference. They suggested strong effect of natural convection on the temperature fields: the profiles of averaged temperature became non-symmetric, the wall temperature increases gradually when moving from the bottom to the top of the tube, and the heat transfer intensities changed significantly along the tube perimeter. With a magnetic field, these effects were further enhanced. The experimental vertical components of the velocity (3) show the existence of one or two secondary vortices having axes parallel to the direction of a main flow.

Streamwise distributions of the local heat transfer coefficients were investigated in (4) for the case when the effect of natural convection is insignificant. A longitudinal magnetic field decreases heat transfer and increases the thermal entrance region. The aim of this work is to obtain the experimental data on temperature fields and streamwise distribution of heat transfer coefficients in the heated tube under influence of natural convection and a longitudinal magnetic field.

## 2 EXPERIMENTAL CONDITIONS

The flow pattern and heat flux distribution are shown in Fig. 1. Three heating alternatives were considered: 1) uniform heat flux distribution along the tube perimeter  $q_1 = q_2 = \text{const}$ ; 2) the heat flux on the left half of the tube is greater than that on the right one  $q_1 > q_2$ ; 3) one-side heating - only one half of the tube is heated  $q_2 = 0$ .

The detailed description of the test facility is presented in (1).

Here, certain of its main characteristics are given:

- the working liquid is mercury,
- the inner diameter is  $d = 19$  mm,
- the length of the heated section is  $l/d = 42$ .

The Reynolds, Hartmann, and Rayleigh numbers were as follows:

$$\text{Re} = 5000 \div 50000;$$

$$\text{Ha} = 0 \dots 500,$$

$$\text{Ra} = (g\beta\rho c_p q d^4 / \lambda \nu) = 0 \dots 3 \cdot 10^6.$$

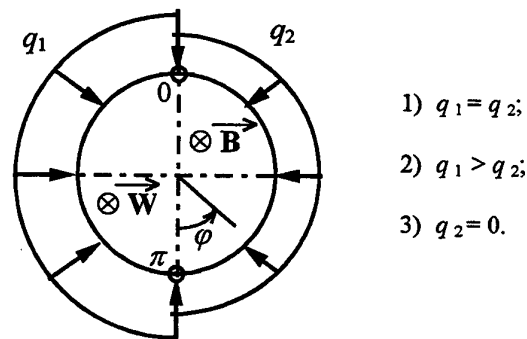


Figure 1 Flow configuration.  
Different cases of applied heat flux.

A longitudinal comb-type probe comprising 6 copper-constantan microthermocouples measures temperature profiles. The experiments are fully automated.

### 3. EXPERIMENTAL RESULTS

The characteristic temperature fields and distributions of the dimensionless wall temperature along the top ( $\pi$  in Fig. 1) and bottom ( $0$  in Fig. 1) generating lines of the tube for the three cases of heating are presented in Fig. 2 - 4. Strong influence of natural convection on the temperature of liquid metal is observed. The results for uniform heating are presented in Fig. 2, where the distribution of temperature along the tube axis is also given.

Beginning at the entrance to the heated section of the tube, the temperatures along the top and bottom generating lines increase, then, at  $x/d = 3 \div 5$ , they diverge. The data for the uniform heat flux are shown in Fig. 2, where the variation of centerline temperature along the tube centerline is also given. Beginning at a coordinate of  $x/d = 13$ , the heat transfer stabilizes, and the temperature data points fall on the line parallel to the distribution of bulk temperature along the tube (dashed line). Solid curves show the data on the wall and center line temperatures [4] without natural convection. The results for non-uniform heating are presented in Fig. 3 - 4. The temperatures increase non-linearly along the top and bottom generating lines. As it was reported in [3], free convection generates one or two secondary vortices having axes parallel to the direction of the main flow: one vortex for one-side heating and two vortices if the heating is non uniform or uniform.

A peculiarity of the temperature data in Fig. 4 is caused by a one-vortex structure of secondary flow in the horizontal tube. The magnetic field does not diminish the effect of natural convection.

The temperatures measured at different Hartman numbers are shown in Fig. 3 - 4.

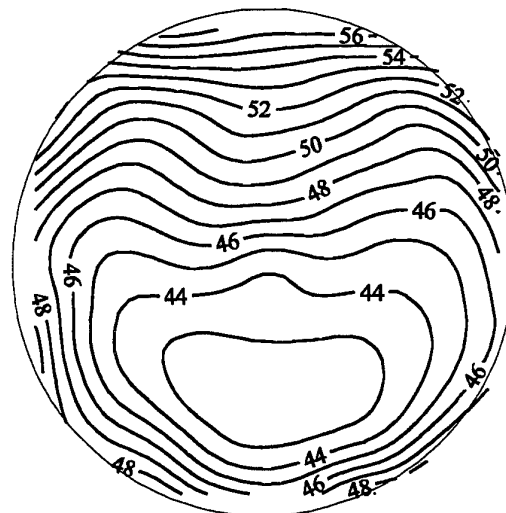
Nusselt numbers for uniform and non-uniform heating are plotted in Fig. 5 - 7.

The Nusselt number is defined as follows:

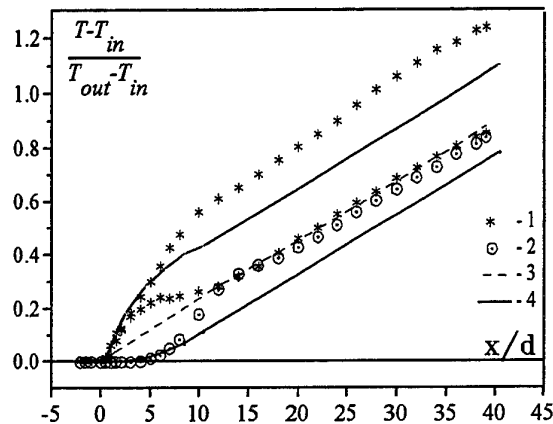
$$\overline{Nu}(x/d) = \frac{q_w d}{\lambda (T_w - T_l)}$$

where:

$T_w$  is the mean wall temperature at cross-section  $x/d$ ;  
 $T_l$  is the bulk liquid temperature at cross-section  $x/d$ ;  
 $q_w = 0.5 (q_1 + q_2)$  is the mean heat flux.



$x/d = 30$



$$q_1 = q_2 = 24 \text{ kWt/m}^2, \text{ Ra} = 1.36 \cdot 10^6, \\ \text{Pe} = 261, \text{ Ha} = 0.$$

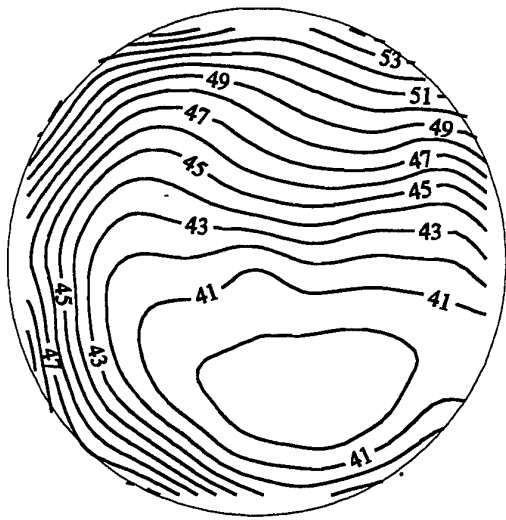
1 - top and bottom point of tube, 2 - bulk temperature, 3 - center of tube, 4 - wall and center point of tube without free convection [4].

Figure 2 Temperature field and non-dimensionless wall temperature on the top ( $\pi$  in Fig. 1) and bottom ( $0$  in Fig. 1.) point of cross-section along the tube (uniform heat flux).

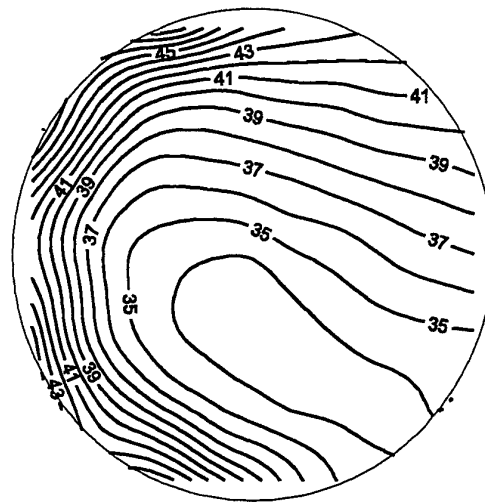
The solid straight line in Fig. 5 - 7 corresponds to turbulent heat transfer without natural convection:

$$Nu = 7 + 0.025 \text{ Pe}^{0.8}.$$

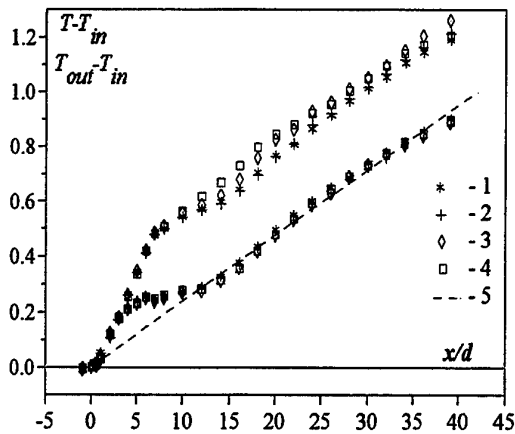
Natural convection enhances heat transfer in a horizontal tube. A magnetic field suppresses turbulence, but does not affect secondary flows



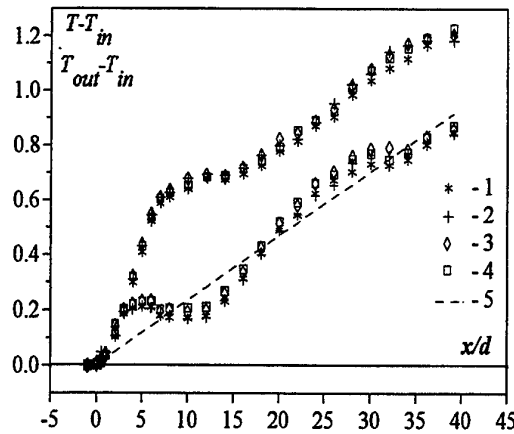
$x/d = 26$



$x/d = 26$



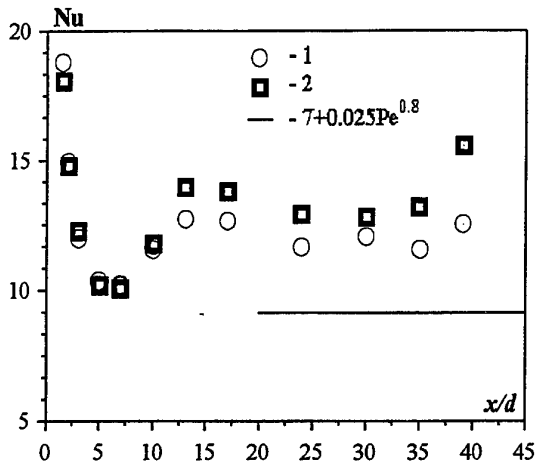
$q_1 = 35 \text{ kWt/m}^2, q_2 = 15 \text{ kWt/m}^2;$   
 $Ra = 1.4 \cdot 10^6, Pe = 261;$   
 1 -  $Ha = 0$ , 2 - 150, 3 - 300, 4 - 450,  
 5 - bulk temperature.



$q_1 = 35 \text{ kWt/m}^2, q_2 = 0 \text{ kWt/m}^2;$   
 $Ra = 0.96 \cdot 10^6, Pe = 261;$   
 1 -  $Ha = 0$ , 2 - 150, 3 - 300, 4 - 450,  
 5 - bulk temperature.

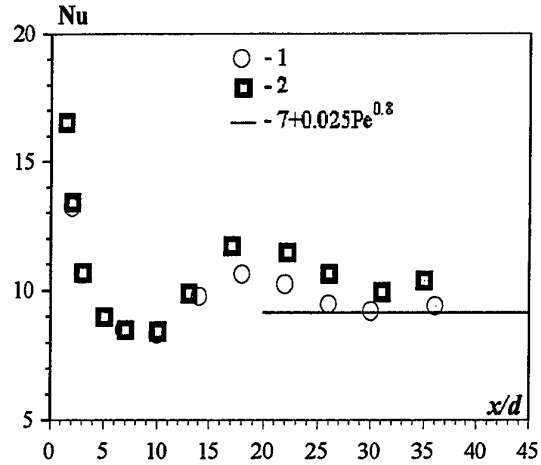
Figure 3 Temperature field and non-dimensionless wall temperature on the top ( $\pi$  in Fig. 1) and bottom (0 in Fig. 1.) point of cross-section along the tube (non-uniform heat flux).

Figure 4 Temperature field and non-dimensionless wall temperature on the top ( $\pi$  in Fig. 1) and bottom (0 in Fig. 1.) point of cross-section along the tube (heat flux from one side only).



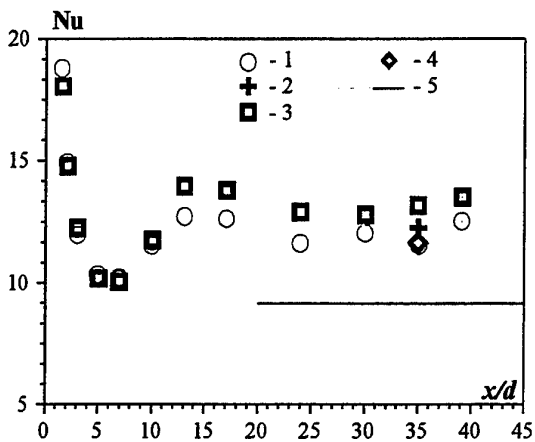
$q_1 = q_2 = 24 \text{ kWt/m}^2$ ,  $Ra = 1.36 \cdot 10^6$ ,  
 $Pe = 261$ ,  $1 - Ha = 0$ ,  $2 - 300$

Figure 5 Mean heat transfer intensity (Nusselt's number) along the tube (uniform heat flux).



$q_1 = 35 \text{ kWt/m}^2$ ,  $q_2 = 0 \text{ kWt/m}^2$ ;  
 $Ra = 0.96 \cdot 10^6$ ,  $Pe = 261$ ;  
 $1 - Ha = 0$ ,  $2 - 300$ .

Figure 7 Mean heat transfer intensity (Nusselt's number) along the tube (heat flux from one side only).



$q_1 = 35 \text{ kWt/m}^2$ ,  $q_2 = 15 \text{ kWt/m}^2$ ;  
 $Ra = 1.4 \cdot 10^6$ ,  $Pe = 261$ ;  
 $1 - Ha = 0$ ,  $2 - 150$ ,  $3 - 300$ ,  $4 - 450$ ;  
 $5 - Nu = 7 + 0.025Pe^{0.8}$  (Lion)

Figure 6 Mean heat transfer intensity (Nusselt's number) along the tube (uniform heat flux).

#### REFERENCES

- (1) Sviridov V.G., Shpansky Yu.S., Razuvanov N.G. Liquid Metal Heat Transfer under the Condition of Fusion Tokamak Reactor. Proc. Of Motion in Liquid Metal Flow in Horizontal Duct under Fusion Relevant Conditions. Proc. Of 19th Turbulence, Heat and Mass Transfer Conference., Lisbon, Portugal, 1994. P.12.4.1-12.4.6.
- (2) Sviridov V.G., Shpansky Yu.S., Razuvanov N.G. Liquid Metal Heat Transfer Investigation. 18th Symposium on Fusion Technology, August 22-26, 1994 Karlsruhe, Germany.
- (3) Sviridov V.G., Shpansky Yu.S., Razuvanov N.G., Ustinov A.V. Heat Transfer and Secondary Symposium on Fusion Technology, September 16-20, Lisbon, Portugal, 1996. P. 1551-1555.
- (4) Genin L.G., Kudryavtseva E.V., Pachotin Y.A., Sviridov V.G. Temperature Field and Local Heat Transfer for a Turbulent Liquid Metal Flow in a Heated Horizontal Tube.// Thermophysics of High Temperatures. 1978. V.16, № 6, P. 1243-1249.

induced by natural convection. Augmentation of the effect of natural convection in a horizontal tube compensates for a decrease in turbulent heat transfer caused by a longitudinal magnetic field.

# OPTIMIZATION OF HEAT TRANSFER CONTROL BASED ON A RECEPTIVITY APPROACH

N.F. Yurchenko

Institute of Hydromechanics,  
National Academy of Sciences,  
Kiev, Ukraine

## ABSTRACT

Basic knowledge of vortex dynamics of flows over heated surfaces, i.e. those affected by buoyancy, was taken as a ground to develop an optimal approach to the boundary layer control directed, in particular, to heat transfer enhancement. This approach is based, on the one hand, on the utilization of a dominant structure, inherent for flows under body forces, in a form of streamwise vortices, and on the other hand, on the analysis of a boundary layer receptivity to such disturbances. Generation of a streamwise vortical structure was shown to represent an effective method to modify heat transfer values and distribution along a surface depending on the basic flow parameters, space scales of the induced vortices and a type of generators used. Combination of a traditional way of heat transfer enhancement using two-dimensional transverse ribs mounted on a surface with the advantage of an inherent vortical structure generated in the flow under given conditions resulted in a design of effective three-dimensional disturbers.

## 1 INTRODUCTION

Fluid transport near a wall is a key point for many industrial processes and design of a wide range of engineering systems. To optimize these processes and design, various flow control methods are known to be used that are based on the regulation of heat/momentum fluxes near the surface by changing space-time characteristics of fluid motion.

Numerous technological applications deal with the fluid motion over curved surfaces having a temperature different from that of the free-stream, i.e. with the flows effected by centrifugal forces and buoyancy. The inherent feature of such flows is the development of secondary flows in a form of a large-scale boundary layer structure, or streamwise vortices. Besides, streamwise counter-rotating vortices were registered in various flows with available body forces, such as

- flows in a gap between concentric cylinders;
- boundary layer flows or jets over concave walls;
- boundary layers over heated surfaces (both in natural and mixed convection cases),
- MHD flows with transverse magnetic fields,
- secondary flows in curved channels and riverbeds,
- Langmuir circulation in ocean upper layers.

These observations display a universal mechanism of vortex dynamics in boundary layers under body forces. It was shown (1) to consist in the interaction of two vorticity sources. For flows over heated surfaces, the first one develops near the surface due to viscosity; the second one arises due to flow temperature stratification and represents body vorticity. Varying differently in a downstream direction, these two vorticity sources

acquire comparable intensities at a certain section where their interaction naturally results in the development of a specific boundary layer structure. Similar situation with a couple of interacting forces, centrifugal and viscous, results in a similar effect in boundary layers over concave surfaces. Analytical estimates of vortical spatio-temporal scales (2) displayed an elongated shape of developing vortices in a flow direction, having shown a good agreement with experimental observations (see, e.g., (3)).

Since the streamwise vortical structure is an inherent feature of flows near heated surfaces, it is natural (i) to use it for a nonintrusive way of the boundary layer control creating favourable flow conditions for its formation with required parameters and (ii) to consider the receptivity of boundary layers under buoyancy to regular longitudinal vortices as a basis for further applications dealt with the control of transport properties near the wall. In addition, it should be mentioned, that in case of the turbulent environment, inflectional velocity profiles typical for flows with embedded longitudinal vortices and connected with the inviscid instability result in a highly unsteady vortex pattern. Artificially organized spanwise nonuniformities in the boundary layer (e.g. due to the arrangement of surface roughness, riblets, temperature gradients over the surface, vortex-generators, etc.) can provide more regular and easily controllable vortical structure.

Encouraging results were published on manipulations with streamwise vortical structure of boundary layers that can be beneficial, for instance, for drag reduction using ribletted surfaces (4, 5, 6).

Thus the present work is aimed to combine traditional methods of heat transfer enhancement with the fundamental knowledge of the vortex dynamics

influenced by buoyancy, as well as a boundary layer response to specially induced vortices.

One of such known methods is based on the application of transverse ribs mounted on a surface (7). Flow separation downstream of the rib yields growing heat transfer from the surface together with growing hydraulic losses. Optimization of the problem means account for the both mentioned effects and the analysis related to a choice of the rib geometry and its most effective downstream location on a surface.

The objective was realized numerically (velocity and temperature fields were calculated in a boundary layer under buoyancy) and experimentally (heat transfer coefficients,  $\alpha$ , were measured under the generation of regular vortices).

## 2 THEORETICAL/NUMERICAL BACKGROUND

Asymptotic analysis of full Navier-Stokes equations using a small parameter  $\epsilon$  explicitly depending on buoyancy,  $\epsilon = \beta(T_s - T_\infty)$ , where  $\beta$  is a coefficient of volumetric thermal expansion,  $T_s$  and  $T_\infty$  are correspondingly surface and free-stream temperature, was made by Nikiforovich (2, 8). The similar analysis was fulfilled for the case of a boundary layer affected by centrifugal forces (contrasting to the traditional Goertler instability analysis, see e.g. (9)), the small parameter having been  $\epsilon = Re_R^{-1}$ ; the emphasis was made to minimum normal space-scales of arising vortices and a downstream section of their formation, both having been expressed in terms of the basic flow parameters, correspondingly,

$$X_o = AR Re_R^{-1/3} \text{ and } L_o = R Re_R^{2/3}$$

where  $R$  is the curvature radius,  $Re_R$  is the Reynolds number based on radius.

The approach validity, as well as physical meanings of the estimated scales, follow from the comparison of the results obtained for the centrifugal case with the known data presented in a form of the Görtler stability diagram (2).

It was shown that the presence of longitudinal vortices by itself does not mean more intense heat transfer near the wall compared to the laminar boundary layer. Heat transfer enhancement occurs only under a condition of a proper downstream distance where longitudinal vortices should be maintained (the necessary condition). A sufficient condition is defined by the correlation between hydro- and thermodynamical parameters what, in particular, is connected with space-time scales of the vortices.

From the viewpoint of a boundary layer control, it means the critical choice of

(i) a downstream location of the disturbers producing the 3D vortical structure and

(ii) values of the space-time scales of generated vortices.

Two-dimensional equations of a stratified boundary layer together with continuity and thermal conductivity equations were solved numerically using a finite-differential method. The calculations showed that buoyancy essentially influences velocity and temperature profiles in a boundary layer and downstream distributions of heat flux,  $Q(x)$ , and shear stress,  $F(x)$ . Moreover, heat flux and shear stress vary differently along the flow resulting in  $Q(x)/F(x) > 1$  and in an evident slope of the curves in Figure 1 both for air, and water, especially when buoyancy was taken into account. The latter fact can be practically used for heat transfer optimization, i.e. creating conditions for greater increment of the heat flux from the surface compared to the growth of shear stress near the wall.

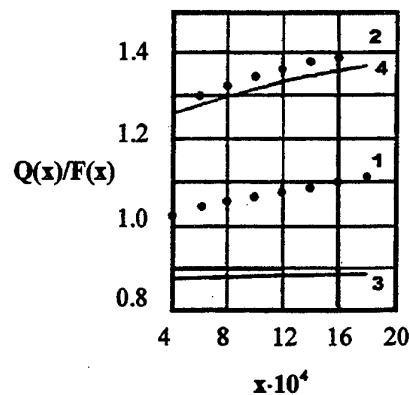


Figure 1 Downstream variation of  $Q(x)$  and  $F(x)$  in flows with buoyancy for  $T_s > T_\infty$ ,  $Pr=0.7$  (1),  $Pr=7.0$  (2) and without buoyancy for  $Pr=0.7$  (3),  $Pr=7.0$  (4).

Following mentioned theoretical results, some practical issues can be deduced for further boundary layer receptivity/control investigations dealt with the experiment optimization and possible applications.

## 3 EXPERIMENT FORMULATION AND TECHNIQUE

Analysis of experimental results on heat transfer enhancement obtained with the 2D ribs mounted over a heated surface normally to the flow direction (7, 10) showed the advantage of the segment-type cross-section compared to the rectangular one.

It was explained by the three-dimensionality of a separation line over the ribs with rounded leading edges contrary to the cases of ribs with sharp leading edges where the separation occurred two-dimensionally along this edge. The three-dimensional character of the separation line can provoke the downstream

formation of large-scale vortices both in the stagnation zone, and in the vicinity of the boundary layer reattachment. However, this vortical structure, as well as a system of streamwise vortices developing in the reattachment zone, can not be very regular in a spanwise direction.

That is why further experimental work was focused on the arrangement of conditions for regular 3D separation, i.e. application of vortex-generators, riblets or roughness elements which caused z-periodic variations of boundary conditions and the subsequent variations of kinematic and thermal parameters of the flow (Figure 2).

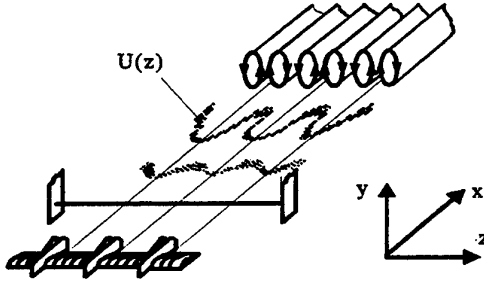


Figure 3 Development of regular streamwise vortices in a boundary layer downstream a vortex-generator array. Typical visualized  $U(z)$  velocity distributions.

The closed type wind tunnel (7) was used with a test section of 2.85m x 0.30m x 0.30m. A test plate (the lower test section wall) was fabricated from a foil mounted on a thermally insulated basement and heated by electric current to  $T_s=40^\circ$  (the temperature difference across the boundary layer was maintained equal to  $T_s-T_\infty=20^\circ$  providing a constant heat flux boundary condition). Free-stream velocities varied in a range of  $U_\infty=10$  m/s - 20 m/s. The experiment sketch is shown in Figure 3.

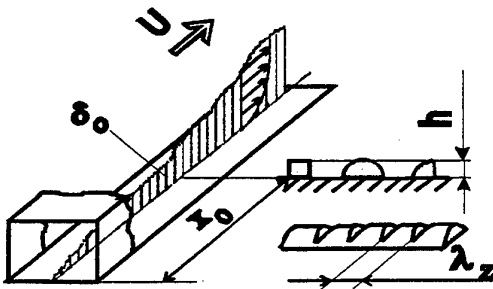


Figure 3 A sketch of a test section and a 3D rib used for heat transfer enhancement

Local surface temperature of a flat horizontal bottom was measured using thermocouples welded to the lower surface of the foil. In addition, oil film flow visualization was used to observe the separation zones

around the transverse ribs. The flow field was investigated downstream of

- (i) two-dimensional, 2D, ribs with various cross-section shapes (see Figure 3),
- (ii) specially designed vortex-generator arrays shown in Figure 2,
- (iii) three-dimensional, 3D, ribs (Figure 3).

All the disturbers were mounted transversely on a test surface (along z-axis) at downstream distances of  $x_0 = 0.4, 0.7$  and 1.8 m that corresponded to the length Reynolds numbers,  $Re = 2.6 \cdot 10^5 - 1.2 \cdot 10^6$ . The height of the 2D disturbers,  $h=5$ mm, and related to the boundary layer thickness, it was within  $h/\delta = 0.31-0.5$ . A set of measurements was made in a turbulent boundary layer tripped at a leading edge.

Vortex-generators were fabricated in a form of double vertical plates smoothly splitted at one end of their upper edges; they were placed in a boundary layer at a zero angle of attack to the mean flow. The arrays of vortex-generators could induce vortices of various scales depending on a distance between adjacent vortex-generators,  $\lambda_z$  (3). Compared to the "separation"-ribs, the vortex generator array is a much "softer" disturber and a more flexible device for  $\lambda_z$  variations possible in the range of  $\lambda_z = 0.4-3.2$  cm with a 0.2 cm step.

3D ribs repeated the size and cross-section geometry of the 2D ones but had regularly spaced valleys along them (3) with a valley depth of about 0.65h and the distance between the adjacent valleys ( $\lambda_z$ ) equal to 12, 18 and 24 mm, the latter having also defined a spanwise space-scale of the generated vortical structure.

#### 4 RESULTS

According to the theoretical conclusions, effects of the downstream location of the disturbers,  $x_0$ , and space-scales,  $\lambda_z$  of generated vortices (boundary layer receptivity) were investigated experimentally at different boundary layer state (from laminar to turbulent).

Figure 4 shows the downstream distribution of heat transfer under various conditions of the vortex structure generation. Rectangles below the horizontal axis denote a position of vortex-generators in the beginning of the laminar-turbulent transition ( $Re=2.3 \cdot 10^5$ ) and at the transition stage which is characterized by the natural development of streamwise vortices ( $Re=4.5 \cdot 10^5$ ). A single vortex-generator showed a negligible effect (curve 3), thus having displayed mild influence of the disturber itself and simultaneously an essential role of a system of generated vortices. Sharp peaks of heat transfer over the vortex-generators are explained by thermal conductivity since the generators made from the foil

were mounted directly on the foil surface of the test plate.

Here a particular point in  $\alpha(\text{Re})$  distribution is the point of a minimum value of heat transfer coefficient. Arising amplified disturbances intensify mixing processes and result in the natural growth of heat transfer. This point appeared to correspond to the most beneficial conditions to control the vortex dynamics in the flow organizing and maintaining longitudinal vortical structure with given parameters until eigen-disturbances developing in a transitional boundary layer have comparatively low amplitudes. In the presence of embedded longitudinal vortices, the effect of intensified general mixing can be supplemented by the effect due to a possibly decreased values of the boundary layer thickness: fixed normal space-scales of vortices can divert the boundary layer thickness from its typical downstream growth, thus creating the effect of less "thermal isolation" of the wall from a free-stream. Curve 6, Figure 4 demonstrates the best obtained result for the generation of regular longitudinal vortices with given parameters at the mentioned point.

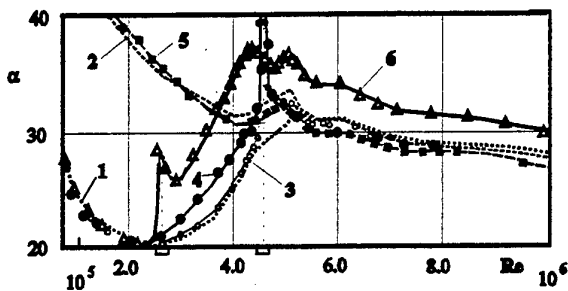


Figure 4 Heat transfer along a heated flat plate depending on a streamwise location  $x_0$  of vortex-generators:  
 1, 2 - reference measurements (without introduced disturbances);  
 3 - a single vortex generator;  
 4, 5, 6 - generation of vortices with  $\lambda_z=1,5$  cm;  
 2, 5 - tripped boundary layer

Generation of vortices further downstream, at Reynolds numbers corresponding to the naturally developed large-scale vortical system during the transition to turbulence (curve 4) including the case of a turbulent boundary layer (curve 5), does not yield the same effect.

The boundary layer receptivity, as a selective response to the scale of generated vortices, is shown in Figure 5 in a form of relative heat transfer distributions  $\alpha/\alpha_0$  along a test plate ( $\alpha_0$  being a heat transfer coefficient in case of natural development of the boundary layer transition to turbulence without the vortex-generators). Some peculiarities of the vortex-

generators design (a shape of their leading edges) were analyzed too.

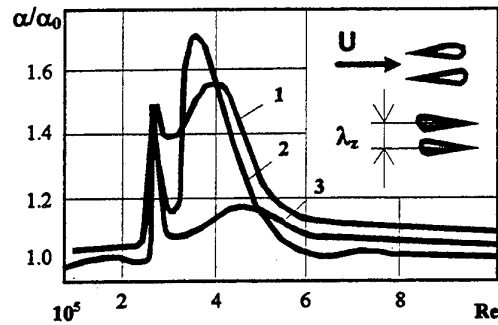


Figure 5 Heat transfer variation  $V_s$   $\text{Re}$  in a boundary layer disturbed by vortex-generators with sharp (1 -  $\lambda_z=1.5$  cm) and rounded leading edges (2 -  $\lambda_z=1.5$  cm; 3 -  $\lambda_z=1.8$  cm).

Compared to the rough influence of the 2D rib, vortex-generators provide wider range of possibilities to manipulate heat transfer. Changing their shape, dimensions and number along a fixed-length holder, one can come to the limiting case when a 3D disturber (vortex-generator array) should be considered as a 2D one. Then the character of  $\alpha/\alpha_0$  distributions obtained with the application of vortex-generators (curve 2) appears to be similar to one typical for a tested 2D rib including the effects in a zone upstream the disturber with decreased heat transfer coefficients due to the local flow stagnation. Scale variation (curves 2, 3) of the introduced regular 3D disturbances intrinsic to flows under body forces proved to be a reliable instrument to control heat transfer.

However, ordinary 2D ribs demonstrated a greater absolute effect. Therefore the two approaches were combined in a form of a 3D rib design. Periodically spaced valleys along the rib resulted in a wavy spanwise distribution of Stanton number values downstream of the rib. Having been similar to the known  $z$ -distribution of velocity in boundary layers with embedded longitudinal vortices shown in Figure 3, this pattern also indicates the development of a regular vortical structure.

Efficiency of the designed 3D ribs is demonstrated in Figure 6.

First of all, the advantage is seen of the ribs with a segment-type profile both for the 2D, and 3D cases. However 3D ribs show 50-70% higher heat transfer factors even in case of the "worse" shape used. The effect is noticeable not only in the range of maximum values of relative heat transfer but also upstream of the rib where the stagnation zone with low heat transfer coefficients was eliminated.



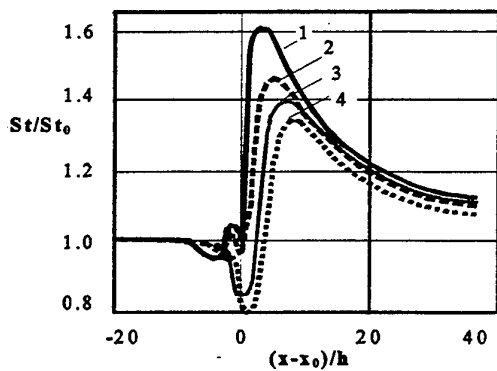


Figure. 6 Heat transfer distribution around 2D (3, 4) and 3D (1,2) transverse ribs of a different shape:  
 1, 3 - segment-type cross section;  
 2, 4 - rectangular cross-section with a rounded leading edge

In addition, it should be mentioned that the available regularly spaced valleys decrease an effective height of a 3D rib compared to the similar 2D one, thus causing less hydraulic losses.

## 5 CONCLUSIONS

The analysis of receptivity, i.e. a boundary layer response to external disturbances, represents an effective method to determine the range of beneficial flow structure modifications depending on the basic flow parameters aimed to obtain heat transfer enhancement with minimum energy losses. The issues of boundary layer receptivity/control and streamwise vortices naturally developing under body forces are directly connected with the solution of various practical problems, for instance, the improvement of turbine-blade design and operation. The insight into the vortex dynamics of flows under consideration yielded the following results.

1. Non-similarity between heat and momentum fluxes in boundary layers effected by buoyancy gives prerequisites for optimization of heat transfer using streamwise vortices as an inherent flow structure.
2. Heat transfer effectiveness depends on the receptivity of a boundary layer to streamwise vortices (its selective response to the space-scale and a downstream location of a vortex-generating device).
3. Practical advantages of the specially designed 3D ribs compared to the traditional 2D ribs consist in
  - increased absolute values of heat transfer coefficients;
  - shorter reattachment zone;
  - vanished stagnation zone upstream of a 3D rib resulted in the growth of heat transfer coefficients there;

- more uniform distribution of local heat transfer in the reattachment zone.

## ACKNOWLEDGEMENTS

The author acknowledges with thanks the possibility to carry out the experiments at the Lithuanian Institute of Physical-Technical Problems of Energetics and further fruitful discussions with Prof. W.S. Saric, Dr. R.B. Rivir and Dr. E.I. Nikiforovich that helped to bring together the insight into the mechanism of vortex dynamics in boundary layers and ideas of its practical application.

## NOMENCLATURE

F	Shear stress
h	Disturber height
$L_0$	Theoretically predicted normal space-scales of vortices
Pr	Prandtl number
Q	Heat flux
R	Radius of surface curvature
Re	Length Reynolds number
$Re_R$	Reynolds number based on radius
St	Stanton number for the controlled case (generated vortices)
$St_0$	Stanton number for natural boundary layer development
$T_s$	Surface temperature
$T_\infty$	Free-stream temperature
$U_\infty$	Free-stream velocity
$X_0$	Theoretically predicted downstream section of longitudinal vortices formation
$x_0$	Downstream location of a vortex-generator
$\alpha$	Heat transfer coefficient
$\beta$	Coefficient of volumetric thermal expansion
$\delta$	Boundary layer thickness
$\varepsilon$	Small parameter in asymptotic analysis, $\varepsilon = (T_s - T_\infty)$ in buoyancy case or $\varepsilon = Re_R^{-1}$ in centrifugal case
$\lambda_\omega$	Spanwise space-scale of longitudinal vortices

## REFERENCES

- (1) Nikiforovich, E.I., Yurchenko, N.F. Vortical flows - properties and analogies, Hydromechanics, 1996, 70, pp. 131-154, Kiev, Ukraine.
- (2) Nikiforovich, E.I., Yurchenko, N.F. Boundary-layer flows with centrifugal forces, ERCOFTAC Bulletin, 1997, 32, pp. 61-65.
- (3) Yurchenko, N.F., Babenko, V.V., Kozlov, L.F. Experimental investigations of longitudinal vortices stability, Eng-Phys.J., 1986, 50, No.2, pp. 201-206.

- (4) Walsh, J., Lindemann, A.M., Optimisation and application of riblets for turbulent drag reduction, AIAA J., 1979, 17, p. 770.
- (5) Launder, B.E, Li, S.P. On the prediction of riblet performance with engineering turbulence models, Applied Scientific Research, 1993, 50, pp. 283-298.
- (6) Djenidi, L., Anselmet, F., Liandrat, J., Fulachier, L. Laminar boundary layer over riblets, Phys. Fluids, 1994, 6 (9), p. 2993.
- (7) Pedishius, A.A., Yanushas, V.I., Zygmantas, G.P., Yapertas, S.S. Heat transfer effected by turbulent separation downstream of wall obstacles, Proc.Lith.Energetics Inst., 1988, No.6943-B, Kaunas, Lithuania.
- (8) Nikiforovich, E.I. A new approach to the study of organized vortical motion effected by body forces, Proc. AGARD Workshop "High speed body motion in water", Kiev, 1-3 Sept. 1997, AGARD-R-827, pp. 12.
- (8) Saric, W. Goertler vortices, Annu. Rev. Fluid Mech., 1994, 26, pp. 379-409.
- (10) Yurchenko, N.F., Zygmantas, G.P. Generation of longitudinal vortices in boundary layers affected by body forces, Eng.-Physical J., 1989, 57, 3, pp. 392-398.

# DIRECT NUMERICAL SIMULATIONS OF TURBULENT FORCED CONVECTION BETWEEN COUNTER-ROTATING DISKS

Roger W. Hill and Kenneth S. Ball

Department of Mechanical Engineering  
The University of Texas at Austin  
Austin, TX 78712 U.S.A.

## ABSTRACT

A Fourier-Chebyshev collocation spectral method is used to simulate the three dimensional unsteady flow inside a cylindrical annular enclosure comprised of two counter-rotating disks and sidewalls. Each disk is taken to be isothermal, with an imposed temperature difference between them, and the sidewalls are adiabatic. Buoyancy forces are neglected. A shallow annulus with aspect ratio,  $h / r_o = 0.06$ , and radius ratio,  $r_i / r_o = 0.13$ , is considered (where  $2h$  is the distance between the disks and  $r_i$  and  $r_o$  are the inner and outer disk radii, respectively). A small gap,  $\delta$ , separates the cylindrical sidewalls, allowing each half of the system to rotate freely from the other. Across the gap, the azimuthal velocity is assumed to vary linearly while the axial and radial velocities are assumed to be zero, thereby creating an enclosed system. The bottom disk is rotated at the maximum speed and the top disk is rotated in the direction opposite that of the lower disk. Results are obtained over a range of  $Re$  including the transition from laminar flow up to approximately three times the critical value of  $Re$ , for cases with both disks rotating at the same speed,  $\Gamma = -1.0$ , with one disk rotating slower than the other,  $\Gamma = -0.4$ , and with one stationary disk,  $\Gamma = 0$  (where  $\Gamma$  is the disk angular velocity ratio, i.e.  $\Gamma = \omega_1/\omega_2$ ). The heat transfer rates between the disks are also obtained, showing the effects of transition to turbulence. The three-dimensional nature of the flows is characterized, and mean and rms turbulence quantities are presented.

## 1 INTRODUCTION

Numerous engineering applications involve rotating disks, either singly or as facing disks or disk stacks. The applications include certain semiconductor manufacturing processes with rotating wafers, magnetic storage devices (disk drives), gas turbine engines, and other rotating machinery. Consequently, the fluid dynamics (and to a lesser extent the heat transfer) have been investigated for various geometries and ranges of conditions.

For the flow above a single spinning disk, von Karman (1) recognized that a similarity solution of the Navier Stokes equations can be obtained provided that the disk is of infinite extent. Batchelor (2) and Stewartson (3) extended the similarity solutions to facing pairs of infinite rotating disks, but they differed on the predicted flow structure. Linear stability theory combined with the von Karman similarity transformation has been employed to assess instabilities and the presence of multiple solutions for both single and pairs of infinite disks (4-6). Numerous single disk experiments have demonstrated the existence of three flow regimes near the disk surface: a laminar flow regime near the disk axis, a region of Ekman spirals at radial locations beyond a critical  $Re$ , and a turbulent flow region at radial locations beyond a higher critical  $Re$  (7-9). Szeri et al. (10-11) and Szeri and Adams (12) assessed the effect of the infinite disk assumption and throughflow on finite open disk flow and stability characteristics, combining experiments with B-spline approximation Galerkin predictions. Several other works considering flow between rotating disks with or without throughflow have been reported (13-16).

The flow between corotating disks has also been extensively studied. A summary of experimental and

numerical observations available at the time is provided in Humphrey et al. (17) and Abramson et al. (18). Chang et al. (19-20) reported two dimensional simulations of flow and heat transfer using a turbulence model, and obtained reasonable agreement with turbulent experimental data. Schuler et al. (21), Humphrey et al. (22), and Iglesias and Humphrey (23) presented results of a combined experimental and numerical program to investigate the onset of instabilities and three dimensional laminar flow between corotating disks in a cylindrical enclosure. Their numerical results include both axisymmetric and three dimensional calculations, and provide insights to the three dimensional effects believed to be related to the appearance of foci of axial vorticity and the source of discrete frequencies found experimentally. However, they noted the disparity between experiment and simulation regarding the onset of instability and assume it to be due to the numerical diffusion in their control volume approach as well as the possibility of inadequate resolution in the three dimensional model. Radel and Szeri (24) used the geometry of Shuler et al. (21) to perform three dimensional steady state analyses using a B-spline numerical scheme and a very coarse grid resolution. They reported finding solutions that are axisymmetric but asymmetric about the axial midplane, in contradiction to the numerical results of Humphrey et al. (22) over the same range of conditions.

Fewer studies have focused on the flow between counter-rotating disks. Gan et al. (25) and Kilic et al. (26) considered the flow between counter-rotating disks in an annular enclosure, for several different values of the disk angular velocity ratio,  $\Gamma$ . They used a finite volume numerical approach combined with a turbulence model in an attempt to match their experimental data. The limiting case where one disk is held stationary,

$\Gamma = 0$ , was also studied by Randriamampianina et al. (27), who used a two dimensional spectral method at low Re (for flows believed to be laminar) and a finite-volume method employing a Reynolds stress transport model for the turbulent regime calculations at higher Re.

The numerical approach employed in the references above either used idealized geometric and/or similarity assumptions, low order spatial approximations, turbulence models, steady state assumptions, or combinations of these. Although at least two very recent studies using an axisymmetric application of spectral methods have considered transitional flow in a rotating disk system (27-28), it is believed that no previous three dimensional studies have been undertaken to examine the flow and heat transfer (particularly the unstable behavior and transition to chaos and turbulence) in a rotating disk geometry using a global spectral method approach. The work reported here was preceded by an axisymmetric study of the same counter-rotating disk problem (28). Additional details of the spectral simulations are also provided by Hill (29).

## 2 NUMERICAL APPROACH

### 2.1 Model Formulation

The coupled equations describing the time-dependent conservation of mass, momentum, and thermal energy are solved subject to the imposed boundary conditions. The system of interest, shown in Fig. 1, is an annular region formed by a bottom(1) and top(2) disk separated by a spacing of  $2h$ , with cylindrical shrouds attached to each disk at the inner and outer disk radii. A small axial clearance,  $\delta$ , separates the shrouds allowing each disk/shroud set to rotate freely from the other. The axial and radial velocities are assumed to be zero across the shroud clearance, thereby creating an enclosed system. This assumption is consistent with Kilic et al. (26), who could control and thus eliminate net mass efflux through the axial clearance in their experimental apparatus. The azimuthal velocity is arbitrarily assumed to vary linearly between the shrouds; due to the relatively small size of the shroud clearance relative to the disk spacing, this assumption is considered to be reasonable. The bottom disk is held at the minimum system temperature and rotated at the maximum speed, and the top disk is held at the maximum system temperature and rotated in the direction opposite that of the lower disk. For simplicity, the inner and outer shrouds and their separating clearance gaps are assumed to represent adiabatic boundaries. It is emphasized that the presence of the axial clearance between the shrouds and the boundary conditions imposed there are not necessitated by the numerical procedure employed in this study, but rather are included to match the geometry considered by Kilic et al. (26).

The time-dependent three-dimensional momentum and thermal energy conservation equations are considered in a polar-cylindrical coordinate system assuming constant properties. The non-linear advective terms in the momentum equation are treated either in non-conservative form or in skew-symmetric form.

Although for a collocation method the non-conservative form does not conserve kinetic energy and is therefore unstable over "long" time integrations, it requires the computation of fewer derivatives and thus less computer time than the skew-symmetric form. Since the two approaches provide equivalent statistical and average results (before the non-conservative computations become numerically unstable), the non-conservative form can be used for cases up to mildly chaotic flow. Above the mildly chaotic regime, the skew-symmetric form is used to ensure numerical stability over the time integration. The skew symmetric form is chosen over the more commonly used (and less computationally intensive) rotational form since the skew symmetric form has been found to converge faster to a grid independent solution (30). The form of the advective terms in the energy equation has been found to have no appreciable effect on the stability of the calculations and is thus left in the non-conservative form.

The following definitions are employed to simplify the non-dimensional form of the conservation equations:

$$C_1 = \left( \frac{r_o + r_i}{r_o - r_i} \right) \quad (1a)$$

$$C_2 = \left( \frac{r_i - r_o}{2} \right) \quad (1b)$$

$$C_3 = -C_2 / h \quad (1c)$$

$$R = C_1 + \frac{r}{C_2} \quad (1d)$$

$$Z = -z / h \quad (1e)$$

$$\tau = \omega_1 t \quad (1f)$$

$$\nabla = \left( \frac{\partial}{\partial R} + \frac{1}{R - C_1} \right) \mathbf{e}_r + \left( C_3 \frac{\partial}{\partial Z} \right) \mathbf{e}_z + \left( \frac{1}{R - C_1} \frac{\partial}{\partial \theta} \right) \mathbf{e}_\theta \quad (1g)$$

$$\nabla^2 = \frac{\partial^2}{\partial R^2} + \frac{1}{R - C_1} \frac{\partial}{\partial R} + C_3^2 \frac{\partial^2}{\partial Z^2} + \frac{1}{(R - C_1)^2} \frac{\partial^2}{\partial \theta^2} \quad (1h)$$

Using these definitions, the non-periodic coordinate directions,  $r$  and  $z$ , are mapped to the interval  $[-1, 1]$  in  $R$  and  $Z$ , for convenience in applying the Chebyshev polynomial expansions to be discussed later. The dependent variables are non-dimensionalized by introducing length, time, and temperature scales based on the outer radius of the disks, the faster disk angular velocity, and the imposed temperature difference between

the two disks. These scales are also used to define the remaining dimensionless parameters:

$$V_r = \frac{v_r}{\omega_1 C_2} \quad (2a)$$

$$V_\theta = \frac{v_\theta}{\omega_1 C_2} \quad (2b)$$

$$V_z = \frac{v_z}{\omega_1 C_2} \quad (2c)$$

$$\Theta = \frac{T - T_C}{T_H - T_C} \quad (2d)$$

$$P = \text{Re} \left( \frac{C_2}{r_o} \right)^2 \frac{p}{\rho(\omega_1 C_2)^2} \quad (2e)$$

$$\text{Re} = \frac{\omega_1 r_o^2}{\nu} \quad (2f)$$

$$\text{Pr} = \frac{\nu}{\alpha} \quad (2g)$$

$$\text{Pe} = \text{Re Pr} \quad (2h)$$

An Adams Bashforth/ second order backward Euler (AB/2BE) time discretization is applied to the conservation equations, giving an implicit treatment of the diffusion terms and an explicit treatment of the advection terms that is second order accurate in time (31). Upon performing the non-dimensionalization and the time discretization, the semi-discrete conservation equations (neglecting buoyancy) become:

continuity:

$$\nabla \cdot \mathbf{v}^{n+1} = 0 \quad (3)$$

R-momentum:

$$\left[ \nabla^2 - \frac{1}{(R - C_1)^2} - \text{Re} \left( \frac{C_2}{r_o} \right)^2 \frac{3}{2\Delta\tau} \right] V_r^{n+1} - \frac{2}{(R - C_1)^2} \frac{\partial V_r^{n+1}}{\partial \theta} = \frac{\partial P^{n+1}}{\partial R} + S_r^{n,n-1} \quad (4)$$

$\theta$ -momentum:

$$\left[ \nabla^2 - \frac{1}{(R - C_1)^2} - \text{Re} \left( \frac{C_2}{r_o} \right)^2 \frac{3}{2\Delta\tau} \right] V_\theta^{n+1}$$

$$+ \frac{2}{(R - C_1)^2} \frac{\partial V_r}{\partial \theta} = \frac{1}{(R - C_1)} \frac{\partial P^{n+1}}{\partial \theta} + S_\theta^{n,n-1} \quad (5)$$

Z-momentum:

$$\left[ \nabla^2 - \text{Re} \left( \frac{C_2}{r_o} \right)^2 \frac{3}{2\Delta\tau} \right] V_z^{n+1} = C_3 \frac{\partial P^{n+1}}{\partial Z} + S_z^{n,n-1} \quad (6)$$

thermal energy:

$$\left[ \nabla^2 - \text{Pe} \left( \frac{C_2}{r_o} \right)^2 \frac{3}{2\Delta\tau} \right] \Theta^{n+1} = S_T^{n,n-1} \quad (7)$$

The source terms,  $S$ , in Eqs. 4-7 include the explicit parts (the previous two time steps) of the non-linear advective terms and the temporal terms (discretized in time) as follows (where  $x$  represents  $r$ ,  $\theta$ , and  $z$  for the radial, azimuthal, and axial directions, respectively):

$$S_x^{n,n-1} = \text{Re} \left( \frac{C_2}{r_o} \right)^2 \left[ (\nabla \cdot \mathbf{v}\mathbf{v} + \mathbf{v} \cdot \nabla \mathbf{v})_x^n - 0.5(\nabla \cdot \mathbf{v}\mathbf{v} + \mathbf{v} \cdot \nabla \mathbf{v})_x^{n-1} \right] - \text{Re} \left( \frac{C_2}{r_o} \right)^2 \left( \frac{4V_x^n - V_x^{n-1}}{2\Delta\tau} \right) \quad (8a)$$

$$S_T^{n,n-1} = \text{Pe} \left( \frac{C_2}{r_o} \right)^2 \left[ 2(\mathbf{v} \cdot \nabla \Theta)^n - (\mathbf{v} \cdot \nabla \Theta)^{n-1} \right] - \text{Pe} \left( \frac{C_2}{r_o} \right)^2 \left( \frac{4\Theta^n - \Theta^{n-1}}{2\Delta\tau} \right) \quad (8b)$$

The pressure Poisson equation is generated by taking the divergence of the momentum equations, and since the divergence of the velocity is zero for incompressible flows, the following equation is obtained:

$$\nabla^2 P^{n+1} = -\nabla \cdot \mathbf{S}^{n,n-1} \quad (9)$$

Equations 4 and 5 cannot be directly solved for the  $V_r$  and  $V_\theta$  velocity components since they appear implicitly in both equations. To decouple the equations, a transformation is introduced for the  $r$  and  $\theta$  velocity components and directional unit vectors, following Patera and Orszag (32). Further details can be found in Hill (29).

The equations are solved subject to the boundary conditions that were discussed above for the system of interest (see Fig. 1). In dimensionless form, they are:

$$\text{at } Z = 1: \quad V_r = V_z = \Theta = 0, \quad V_\theta = R - C_1 \quad (10a)$$

$$\text{at } Z = -1: \quad V_r = V_z = 0, \quad \Theta = 1, \quad V_\theta = \Gamma(R - C_1) \quad (10b)$$

$$\text{at } R = 1 \text{ and } Z > \delta / 2h: \quad V_r = V_z = \partial\Theta/\partial R = 0, \quad V_\theta = 1 - C_1 \quad (10c)$$

$$\text{at } R = 1 \text{ and } Z < -\delta / 2h: \quad V_r = V_z = \partial\Theta/\partial R = 0, \quad V_\theta = \Gamma(1 - C_1) \quad (10d)$$

$$\text{at } R = -1 \text{ and } Z > \delta / 2h: \quad V_r = V_z = \partial\Theta/\partial R = 0, \quad V_\theta = -(1 + C_1) \quad (10e)$$

$$\text{at } R = -1 \text{ and } Z < -\delta / 2h: \quad V_r = V_z = \partial\Theta/\partial R = 0, \quad V_\theta = -\Gamma(1 + C_1) \quad (10f)$$

$$\text{at } R = 1, -1, \text{ and } |Z| < \delta / 2h: \quad V_r = V_z = \partial\Theta/\partial R = 0, \quad V_\theta \text{ varies linearly} \quad (10g)$$

No natural pressure boundary conditions exist to solve Eq. 9. Additionally, a method must be implemented to satisfy the incompressibility constraint of Eq. 3. Both problems are addressed using an influence matrix technique, which is described later. The influence matrix technique provides a direct non-iterative method to determine the pressure field that ensures that the incompressibility constraint is satisfied at every interior point and on the boundary.

To solve the conservation equations at each time step, a Fourier-Chebyshev collocation spectral method is used with no dealiasing (33). Relative to a pseudospectral method, the collocation method provides a simpler approach to specifying the boundary conditions, a slight improvement in convergence characteristics, and the elimination of the need to transfer back and forth between physical and wavenumber space for the non-periodic directions. The physical variables to be determined (velocities, pressure, and temperature) are represented by truncated series expansions of Chebyshev polynomials on a Gauss-Lobatto grid in both the radial and axial directions and by Fourier series on an evenly spaced grid in the periodic azimuthal direction. The form of the expansion for a generic variable,  $\phi$ , is then:

$$\phi(R, Z, \theta, \tau)$$

$$\begin{aligned} &= \sum_{l=0}^{L-1} \sum_{m=0}^{M-1} \sum_{k\theta=-K/2}^{K/2-1} \hat{\phi}_{lmk\theta}(\tau) T_l(R) T_m(Z) \exp(ik\theta) \\ &= \sum_{k\theta=-K/2}^{K/2-1} \hat{\phi}_{k\theta}(R, Z, \tau) \exp(ik\theta) \quad (11) \end{aligned}$$

where  $i$  is the imaginary unit;  $L$ ,  $M$ , and  $K$  are the number of grid points in the radial, axial, and azimuthal

directions, respectively;  $\hat{\phi}_{lmk\theta}$  is the corresponding time-dependent Fourier-Chebyshev coefficient (to be determined); and  $T_l, T_m$  are the Chebyshev polynomials. This discretization approach enables one to generate first and second order spatial derivative operator matrices for the conservation equations in the  $r$ - and  $z$ -directions. Derivatives of the dependent variables in the non-periodic directions are thus evaluated by matrix products (29, 33-34).

Since the quantities of interest are expanded in Fourier series in the azimuthal direction, the simplest approach is to solve for the Fourier expansion coefficients. Upon performing the Fourier transform, the terms involving azimuthal derivatives can be represented by products of the Fourier coefficients and the corresponding Fourier wave numbers, which reduces the three-dimensional equations in physical space to a set of two-dimensional Helmholtz equations for each Fourier wave number.

The general form of the resulting set of discretized Helmholtz equations is as follows (where  $\lambda$  is zero for the pressure Poisson equation):

$$\mathbf{L}_R \hat{\Phi} + \hat{\Phi} \mathbf{L}_Z - \lambda \hat{\Phi} = \hat{S}^* \quad (12)$$

where  $\hat{S}^*$  is the original right hand side source term modified to include the known quantities (boundary conditions) from the left hand side. Thus, a total of  $5 \cdot K$  equations are generated (corresponding to the Fourier transforms of the three velocity components, pressure, and temperature). These equations are solved efficiently using matrix diagonalization techniques (29, 35-36).

To address the issue of the velocity-pressure coupling present in incompressible flows, an influence matrix technique is adopted. This approach is generally credited to Kleiser and Schumann (37), who used it in a pseudospectral simulation of channel flow with one non-periodic direction. The method for one non-periodic direction is well summarized in Canuto et al. (33). In a continuous representation of the Navier-Stokes equations, the influence matrix technique determines the pressures that ensure a divergence free condition throughout the solution domain by forcing the divergence of the velocity on the boundaries to be zero.

For the discretized problem, additional corrections throughout the domain are needed to force the divergence to machine precision zero due to the fact that the momentum equations are not satisfied on the boundary. The technique including the correction for the boundary momentum residuals for two non-periodic directions is described in detail by Tuckerman (38) for Cartesian and cylindrical geometries using a pseudospectral method and by Madabhushi et al. (39) for a Cartesian collocation implementation. Here and in Hill and Ball (28) the correction is extended to a cylindrical collocation implementation.

The influence matrix technique without the boundary momentum correction has been used successfully by others (see for example (40-42)); the motivation for not implementing the correction is primarily a factor of four savings in the memory required to store the influence matrix. However, early on in the

study of flow in the counter-rotating disk system, it was determined that unbounded solutions became a severe problem under chaotic flow conditions unless the correction for the boundary momentum residuals was applied. A detailed summary of the influence matrix technique as used here in the study of transitional flows in cylindrical geometries is provided in Hill (29).

## 2.2 Parallel implementation

Performing three dimensional simulations of fluid flow and heat transfer requires considerable computer resources, both processing time and memory. The large memory requirement is a particular problem when using the influence matrix approach. To enable the numerical exploration of three-dimensional transitional flows, an efficient parallel implementation is desired to increase the wall clock time in which results can be obtained and discoveries made. The Fourier-Chebyshev spectral method described above has been parallelized for both shared memory and distributed memory platforms to perform the three dimensional computations of transitional flow in cylindrical geometries. The approach to parallelizing the computations, as well as scaling and performance benchmarks, are described in detail in Hill (29) and Hill and Ball (43).

Briefly summarized, the approach to parallelizing the computations is based upon the factoring of the three-dimensional problem into a set of two-dimensional problems for each Fourier wavenumber,  $k_\theta$ , described above. The resulting two-dimensional problems are then distributed among the available processing elements (PEs). The Cray proprietary SHMEM (logically shared memory) routines were used to perform the message passing required for the transient simulations. The results presented in this study were obtained using the Cray T3E-600 with 48 PEs at the University of Texas at Austin and the 512 PE Cray T3E at the Pittsburgh Supercomputing Center. Nearly linear scaling was achieved for computations using up to 128 PEs, with a small drop-off in performance beyond 128 PEs.

## 2.3 Solution procedure

At each time step, the solution proceeds by first solving for the temperature field. Assuming boundary pressures of zero, a pressure field and accompanying  $V_r$  and  $V_z$  are calculated. Then employing the pre-determined influence matrix, the corrections to the boundary pressures are determined that will ensure a divergence-free velocity field. Using these boundary pressures, an implicitly determined pressure field, and finally the new  $V_r$ ,  $V_z$ , and  $V_\theta$  values, are calculated at the new time step.

A typical approach to generating three-dimensional results is first to perform a two-dimensional simulation, assuming the flow and temperature field to be axisymmetric. Then this solution is wrapped around to each azimuthal plane as a starting condition for the three-dimensional computations. This solution is then randomly perturbed in the first time step to induce a small three-dimensional disturbance on top of the base flow. The perturbation is typically in the form of a  $\pm 0.1\%$  to  $\pm 1.0\%$  disturbance applied to the velocity

component source terms. Without this disturbance, the solution would remain axisymmetric due to the perfect separation of the Fourier modes.

It should be noted that the Re used to obtain the two-dimensional initial condition may or may not correspond to the Re for the three-dimensional simulation. If at the Re of interest the flow is actually axisymmetric, the disturbance will die out and azimuthal derivatives will tend to zero. However, if the flow is three dimensional, the flow will evolve from the slightly disturbed axisymmetric state to the preferred three-dimensional state corresponding to that Re. Once a solution is available in which three dimensional characteristics are present, that solution may be used as initial conditions for solutions at other Re and/or other grid resolutions (following proper interpolation of the Fourier and Chebyshev expansion coefficients onto the new grid).

To generate the results reported here, different grid resolutions were employed depending upon the specific case. For  $\Gamma = -1.0$ , the grid resolutions ( $r, z, \theta$ ) were  $73 \times 31 \times 128$  for  $Re = 1730$  and  $73 \times 31 \times 512$  for  $Re = 4500$ . For  $\Gamma = -0.4$ , the grid resolutions were  $73 \times 31 \times 64$  for  $Re = 4400$  and  $73 \times 31 \times 384$  for  $Re = 12000$ . For  $\Gamma = 0.0$ , the grid resolutions were  $73 \times 31 \times 128$  for  $Re = 27000$  and  $97 \times 41 \times 256$  for  $Re = 70000$ . For the lower Re cases considered, the grid resolutions were deemed to be adequate when the numerically determined critical values of Re became insensitive to further increases in grid resolution, allowing  $Re_c$  to be determined to within 3-5% as discussed later. For the higher Re cases considered, the grid resolutions were deemed to be adequate when no qualitative changes in the flow behavior were observed, and quantitative changes (in the mean statistics) were small. It is noted that when smaller grids were employed, problems were encountered in solving the energy equation; namely, local temperature values within the computational domain that exceeded the range of the boundary conditions were encountered due to insufficient resolution.

## 3 RESULTS

### 3.1 Isothermal flow for $\Gamma = -0.4$ , $Re = 10^5$

To provide a benchmark for the numerical approach used in this study, results are presented for the isothermal flow for  $\Gamma = -0.4$  and  $Re = 10^5$  and are compared with experimental data taken from the literature (26). In Fig. 2, the time and azimuthally averaged axial variation of  $V_r$  and  $V_\theta$  are shown at  $r/r_0 = 0.85$ . Each profile is normalized by  $(R-C_1)$ , which is the local  $V_\theta$  for disk 1, and the faster bottom disk is on the left. As noted by Hill and Ball (28), the mean velocity profiles between the two disks using two dimensional (axisymmetric) simulations do not agree well with the experimental data from Kilic et al. (26) for this case; thus, it is deemed to be an important benchmark for the three-dimensional simulation.

An important feature of this flow is the presence of a stagnation point along the upper disk, where the

centrifugally driven (radially outward) flow along the bottom disk turns upward at the sidewall, then flows radially inward along the upper disk, and meets the centrifugally driven (radially outward) flow along the more slowly rotating upper disk. The mean location of the stagnation point can be detected by a change in sign in the mean radial velocity component near the upper disk.

In Fig. 2(a), the mean  $V_r$  is negative near the upper disk, indicating that the flow there is radially inward. The mean radial velocity profile at  $r/r_0 = 0.8$  (not shown) is positive near the upper disk, indicating that the flow is radially outward at that location. Thus, the stagnation point occurs (in the mean) between  $0.8 < r/r_0 < 0.85$ , which is consistent with the experimental results of Kilic et al. (26). In addition to properly bracketing the location of the mean stagnation point, the magnitude of  $V_r$  in the Ekman layers on each disk is shown to be very well predicted.

Figure 2(b) shows axial profiles of the mean  $V_\theta$  at  $r/r_0 = 0.85$ , accompanied by the experimental data from Kilic et al. (26). The numerical results match the experimental data much better than in the case of the two dimensional simulations (28). The rotation of the core region is well represented, both in magnitude and trend. In assessing the agreement with the experimental data, it is noted that while Kilic et al. (26) provide some indication of the uncertainties for various system inputs to their experiments (such as probe point positioning), they have not quantified the experimental uncertainties of the flow velocity measurements.

Neither the steady two dimensional finite difference numerical simulations of Kilic et al. (26) using a turbulence model nor the unsteady two dimensional spectral simulations of Hill and Ball (28) could match the experimental data for  $\Gamma = -0.4$  and  $Re = 10^5$ . Thus it is strongly concluded that the problems associated with matching the experimental data when performing an axisymmetric simulation for this counter rotating disk geometry are due to the axisymmetry assumption itself. Though, on average, the azimuthal derivatives are zero, excluding them from the numerical model removes an important player from the physical problem leading to erroneous results.

### 3.2 Transition to unsteady 3D flow

For all of the cases considered in this study, the initial transition in the flow from the steady axisymmetric state with increasing  $Re$  is to an unsteady three-dimensional flow. Critical values of  $Re$  were determined by increasing  $Re$  in small increments following the procedure described previously (Section 2.3). The  $Re_c$  so determined are considered to be accurate to within 3-5%, and are given in Table 1.

Table 1. Critical  $Re$  for onset of unsteady 3D flow.

$\Gamma$	$Re_c$
-1.0	1700
-0.4	4400
0.0	27 000

#### 3.2.1 $\Gamma = -1.0$

Figure 3 shows mean contours (dashed lines indicate negative contour levels) of the three velocity components, temperature, and secondary flow streamfunction in the  $r$ - $z$  plane for  $Re = 1730$ . At this  $Re$ , the flow has just transitioned to unsteady three dimensional flow from a steady two dimensional flow at just below  $Re_c = 1700$ . The mean flow is characterized by radial outflow on both disks that meets to form an inflowing free shear layer in the midplane, with a rotating core of fluid on either side (Figs. 3(a-c)). The mean secondary flow (in the  $r$ - $z$  plane) thus consists of two large counter-rotating circulations, with the centers of rotation occurring near the outer sidewalls (Fig. 3(e)). At this relatively low  $Re$ , the flow is primarily parallel to the disks (except where it turns at the sidewalls) and the temperature distribution is characteristic of diffusion in the axial direction (Fig. 3(d)).

Contours of the root-mean-square (rms) velocity and temperature fluctuations in the  $r$ - $z$  plane for  $Re = 1730$  are shown in Fig. 4. It is apparent that the unsteadiness originates at the outer sidewalls where the two radially outward boundary layers meet and form the free shear layer noted above. The extent of the fluctuations is limited to a small region near the outer sidewalls, beyond approximately  $r/r_0 = 0.80$ . Qualitatively, the distribution of  $V_{\theta,rms}$ ,  $V_{z,rms}$ , and  $T_{rms}$  are similar, with two peaks occurring along the midplane; a strong peak very near the outer sidewalls ( $r/r_0 \approx 0.97$ ) and a second peak near the centers of circulation ( $r/r_0 \approx 0.88$ ). The distribution of  $V_{r,rms}$  has only one peak, occurring just outward of the centers of circulation ( $r/r_0 \approx 0.92$ ).

#### 3.2.2 $\Gamma = -0.4$

Figure 5 shows mean contours of the flow variables in the  $r$ - $z$  plane for  $Re = 4400$ . At this  $Re$ , the flow has just transitioned to unsteady three dimensional flow from a steady two dimensional flow at  $Re = 4300$ . The stronger counter-clockwise secondary circulation induced by the rotation of the bottom disk is evident in Fig. 5(e), resulting in the relatively small temperature gradients near the outer portion of the lower disk and the large temperature gradients near the outer portion of the slower rotating top disk. Where the counter-clockwise circulation and the weaker clockwise circulation meet near the top disk, fluid is forced downward into the core region between the two disks. The center of the counter-clockwise circulation occurs at approximately  $r/r_0 = 0.90$ . The resulting free shear layer is inclined at an angle of approximately  $40^\circ$  to the horizontal midplane.

Contours of the rms velocity and temperature fluctuations in the  $r$ - $z$  plane for  $Re = 4400$  are shown in Fig. 6. The peak rms levels occur for each variable along the path of the free shear layer, which separates from the upper disk near  $r/r_0 = 0.80$  and flows downward along an inclined path as described above. The contours for  $V_{\theta,rms}$ ,  $V_{r,rms}$ , and  $T_{rms}$  all exhibit a two-lobed structure, with the larger peak occurring downstream of the first peak in the direction of the free shear layer. The



distribution of  $V_{z,rms}$  has only one peak, near  $r/r_0 = 0.75$  at the midplane, where the free shear layer has its maximum curvature as it straightens out to flow radially inward along a nearly horizontal path. The spatial extent of the rms fluctuations is considerably larger than the  $\Gamma = -1.0$  case, occupying approximately half of the annular volume.

### 3.2.3 $\Gamma = 0.0$

Figure 7 shows mean contours of the flow variables in the  $r$ - $z$  plane at eight equally spaced azimuthal locations for  $Re = 27000$ . As above, the flow has just transitioned to unsteady three dimensional flow from a steady two dimensional flow at lower  $Re$ . In this case, a single counter-rotating circulation results from the rotation of the bottom disk, and is largely confined to the two boundary layers along each disk (Fig. 7(e)). The radial component of velocity in the core region is negligible (Fig. 7(b)), and the angular momentum in the core region is horizontally stratified (Fig. 7(a)). Sharp gradients in the temperature field develop along the upper disk near the outer sidewall where the relatively cold fluid originating from the bottom impinges on the hot upper disk. In similar fashion, sharp temperature gradients also develop along the bottom disk near the inner sidewall where the relatively hot fluid originating from the top impinges on the cold bottom disk (Fig. 7(d)).

Contours of the rms velocity and temperature fluctuations in the  $r$ - $z$  plane for  $Re = 27000$  are shown in Fig. 8. The only significant rms fluctuation levels occur in a small region along the upper disk adjacent to the outer sidewall, extending radially inward to about  $r/r_0 = 0.8$ .

## 3.3 Turbulent flow at $3 Re_c$

To study the development of turbulence in the counter-rotating disk system, the flow at values of  $Re$  that are approximately three times the respective critical values are considered for each  $\Gamma$ . In all three cases, the flow is chaotic; the flow appears to become increasingly disordered as  $\Gamma$  increases in magnitude at fixed  $Re$ .

### 3.3.1 $\Gamma = -1.0$

In Fig. 9, the secondary flow streamlines and temperature contours in the  $r$ - $z$  plane are presented for  $Re = 4500$ , at eight equally spaced azimuthal locations at a fixed instant in time. This is equivalent to viewing a sequence of instantaneous snapshots separated by small fixed increments in time. The chaotic nature of the flow is evident. The flow is characterized by a large number of pockets of fluid circulation, resulting in significant oscillations in the flow and temperature fields in both space and time. The flow is most chaotic in the region nearest to the outer sidewalls, where the angular velocity of the disks is largest.

Figure 10 shows mean contours of the flow variables in the  $r$ - $z$  plane. When averaged over long enough periods of time or large enough ensembles, the flow with  $\Gamma = -1.0$  exhibits midplane symmetry. The

mean flow field is qualitatively very similar to the lower  $Re$  flow presented in Section 3.2.1 (Fig. 3), only more vigorous. Also, the centers of the two counter-rotating circulations have moved radially inward slightly, to about  $r/r_0 = 0.82$ .

Contours of the rms velocity and temperature fluctuations in the  $r$ - $z$  plane for  $Re = 4500$  are shown in Fig. 11. As with the lower  $Re$  case shown in Fig. 4, the unsteadiness originates at the outer sidewalls where the free shear layer develops. However, in contrast to that case, the spatial extent of the fluctuations is considerably larger, occupying more than half of the annular volume. Remnants of the two-lobed structure in  $V_{z,rms}$  and  $T_{rms}$  remain, although this is no longer a dominant feature.

### 3.3.2 $\Gamma = -0.4$

In Fig. 12, the secondary flow streamfunction and temperature contours in the  $r$ - $z$  plane are presented for  $Re = 12000$ , at eight equally spaced azimuthal locations at a fixed instant in time. Again, the chaotic nature of the flow is evident, and is characterized by numerous pockets of fluid advecting with the flow (Fig. 12(a)). These pockets of fluid result in considerable distortion of the temperature field (Fig. 12(b)). It is also evident upon inspection of Fig. 12(a) that the location of the stagnation point on the upper disk, where the radially opposing boundary layer flows meet to form the downward inclined shear layer, fluctuates wildly. The penetration depth of the shear layer (before it straightens out to flow radially inward along a horizontal path) also varies considerably, resulting in fluctuations in the temperature gradients along the bottom disk in the region below the free shear layer ( $r/r_0 \approx 0.65$  to  $r/r_0 \approx 0.75$ ; Fig. 12(b)).

Figure 13 shows mean contours of the flow variables in the  $r$ - $z$  plane. As with the  $\Gamma = -1.0$  case, the mean flow at  $3 \cdot Re_c$  is qualitatively similar to that near  $Re_c$ , only more vigorous. In Fig. 13, the clockwise circulation along the upper disk at  $r/r_0 < 0.8$  is now well defined, and the center of the counter-clockwise circulation has shifted inward slightly. The temperature gradients on the upper disk near the outer sidewall are also significantly higher (Fig. 13(d)).

In Fig. 14, the rms velocity and temperature fluctuations for  $Re = 12000$  are presented. Significant fluctuation levels occur throughout the entire annular volume, with peaks occurring along the mean path of the free shear layer, penetrating all the way down to the bottom disk.

### 3.3.3 $\Gamma = 0.0$

In Fig. 15, the secondary flow streamfunction and temperature contours in the  $r$ - $z$  plane are presented for  $Re = 70000$  at eight equally spaced azimuthal locations at a fixed instant in time. The flow is observed to be chaotic, with numerous smaller pockets (relative to the previous two cases) of circulating fluid moving radially inward along the upper disk. The corresponding mean flow field is shown in Fig. 16. Once again, it is qualitatively similar to the flow shown in Fig. 7 and

discussed in Section 3.2.3. However, the rms velocity and temperature fluctuations, shown in Fig. 17, are now at significant levels over the entire region along the upper disk. The boundary layer along the bottom disk is still fairly steady at this Re.

### 3.4 Heat transfer results

The values of Nu are obtained by averaging the profiles over all azimuthal planes for several snapshots and then averaging over the snapshots to obtain a single curve for each Re and each disk. For  $\Gamma = -1.0$ , the profiles on each disk may also be combined to generate a single curve corresponding to both disks due to the midplane symmetry.

Figure 18 provides a plot of the radial variation of the average heat transfer rate for Re = 1730 and 4500 and for  $\Gamma = -1.0$ . Near the outer radius, the heat transfer rate is very small due to the turning of the flow and the resultant decrease in temperature gradients as shown in Figs. 3 and 10. Moving radially inward on each disk, the heat transfer rate increases rapidly to a peak around  $r/r_0 = 0.85$ . It then drops to a relatively constant rate that is dependent on Re, followed by another rise near the inner radius caused here by the turning flow. The peak in the heat transfer for Re = 4500 centered around  $r/r_0 = 0.85$  is attributed to chaotic mixing based on an examination of the rms profiles of Fig. 11. Similarly, the relatively constant heat transfer rate midway between the inner and outer radius is attributed to the flow being much less chaotic.

The heat transfer rates for  $\Gamma = -0.4$  and 0.0 are provided in Figs. 19 and 20. For these cases the radial profiles of Nu reflect the behavior of the mean flow and are not dominated by turbulent mixing. In both cases a very strong counter-clockwise rotating secondary flow directly strikes the top disk near the outer radius resulting in the highest heat transfer rates along the top disk. This flow structure similarly results in a very low heat transfer near the outer radius of the bottom disk. At smaller radial locations the heat transfer rate is relatively constant with radial position for  $\Gamma = -0.4$ , whereas it exhibits an asymptotic decrease(increase) for the top(bottom) disk in the case of  $\Gamma = 0.0$ .

## 4 SUMMARY

A Fourier-Chebyshev collocation spectral method is used to simulate the three dimensional unsteady flow and heat transfer inside a cylindrical annular enclosure. Turbulent flows with Reynolds numbers up to  $3 \cdot Re_c$  are simulated, for cases with both disks rotating at the same speed,  $\Gamma = -1.0$ , with one disk rotating slower than the other,  $\Gamma = -0.4$ , and with one stationary disk,  $\Gamma = 0$ . Solutions are obtained over a wide range of Re including the transition from laminar flow, and the benchmark isothermal results agree well with published experimental data. Differences with previously reported numerical results assuming axisymmetry or using turbulence models are also discussed. The heat transfer rates between the disks are also obtained, showing the effects of transition to turbulence. As the rotational

speed of both disks is increased proportionally (thereby maintaining the same speed ratio but increasing the system Re), the flow undergoes a transition from steady to unsteady and chaotic conditions, and the three-dimensional nature of the flow is clearly observable. The fluctuations throughout the flow are associated with a free shear layer that arises from the boundary layers over each disk for the cases  $\Gamma = -1.0$  and  $\Gamma = -0.4$ . For  $\Gamma = 0.0$ , the fluctuations are limited in extent to the boundary layer over the upper disk. Finally, the flow is noticeably more chaotic at the same Re as the magnitude of  $\Gamma$  increases.

## 5 ACKNOWLEDGMENTS

The authors are indebted to SEMATECH, Inc. (Austin, TX) for providing support for this work. Further support provided by the National Science Foundation under Grant Number CTS-9258006, the Pittsburgh Supercomputing Center under Grant Number CTS-960033P, and the Texas Advanced Computing Center at the University of Texas is gratefully acknowledged. Any opinions, findings, and conclusions or recommendations expressed in this publication are those of the authors and do not necessarily reflect the views of the sponsors.

## 6 NOMENCLATURE

2h	disk spacing
Nu	Nusselt number
p	dimensional pressure
P	dimensionless pressure
Pe	Peclet number
Pr	Prandtl number
r, z	dimensional radial and axial coordinates, respectively
R, Z	dimensionless radial and axial coordinates, respectively
Re	Reynolds number
t	time
T	temperature
v	dimensional velocity
V	dimensionless velocity
$\alpha$	thermal diffusivity
$\Gamma$	disk angular velocity ratio, $\omega_2 / \omega_1$
$\delta$	axial clearance between disk shrouds
$\theta$	azimuthal coordinate
$\Theta$	dimensionless temperature
$\nu$	kinematic viscosity
$\rho$	density
$\tau$	dimensionless time
$\psi$	streamfunction
$\omega$	angular velocity

### 6.1 Subscripts

1,2	bottom and top disks, respectively
C,H	cold and hot, respectively
i,o	inner and outer, respectively

$r, \theta, z, T$  radial, azimuthal, axial, and temperature, respectively  
rms root mean square

## 6.2 Superscripts

n time discretization level

## 7 REFERENCES

- (1) von Karman, Th. Über laminare und turbulente reibung, *Z. Angew. Math. Mech.*, 1921, vol. 1, 233-252.
- (2) Batchelor, G. K. Note on a class of solutions of the Navier-Stokes equations representing steady rotationally-symmetric flow, *Quart. J. Mech. Applied Math.*, 1951, vol. 4, 29-41.
- (3) Stewartson, K. On the flow between two rotating coaxial disks, *Proc. Cambridge Philos. Soc.*, 1953, vol. 49, 333-341.
- (4) Holodniok, M., Kubicek, M., and Hlavacek, V. Computation of the flow between two rotating coaxial disks, *J. Fluid Mech.*, 1977, vol. 81, 689-699.
- (5) Holodniok, M., Kubicek, M., and Hlavacek, V. Computation of the flow between two rotating coaxial disks: multiplicity of steady-state solutions, *J. Fluid Mech.*, 1981, vol. 108, 227-240.
- (6) Anaturk, A. R. and Szeri, A. Z. Stability of flow between infinite rotating disks, *J. Math. Phys. Sci.*, 1992, vol. 26, 569-581.
- (7) Chin, D. T. and Litt, M. An electrochemical study of flow instability on a rotating disk, *J. Fluid Mech.*, 1972, vol. 54, 613-625.
- (8) Wahal, S., Oztekin, A., Bornside, D. E., Brown, R. A., Seidel, P. K., Ackmann, P. W., and Geyling, F. T. Visualization of a gas flow instability in spin coating systems, *Applied Phys. Lett.*, 1993, vol. 62, 2584-2586.
- (9) Kobayashi, R. Review: Laminar to turbulent transition of three-dimensional boundary layers on rotating bodies, *J. Fluids Eng.*, 1994, vol. 116, 200-211.
- (10) Szeri, A. Z., Schneider, S. J., Labbe, F., and Kaufman, H. N. Flow between rotating disks. Part 1. Basic flow, *J. Fluid Mech.*, 1983, vol. 134, 103-131.
- (11) Szeri, A. Z., Giron, A., Schneider, S. J., and Kaufman, H. N. Flow between rotating disks. Part 2. Stability, *J. Fluid Mech.*, 1983, vol. 134, 133-154.
- (12) Szeri, A. Z. and Adams, M. L. Laminar throughflow between closely spaced rotating disks, *J. Fluid Mech.*, 1978, vol. 86, 1-14.
- (13) Lai, C. Y., Rajagopal, K. R., and Szeri, A. Z. Asymmetric flow between parallel rotating disks, *J. Fluid Mech.*, 1984, vol. 146, 203-225.
- (14) Elena, L. and Schiestel, R. Turbulence modeling of confined flow in rotating disk systems, *AIAA J.*, 1995, vol. 33, 813-821.
- (15) Nesreddine, H., Nguyen, C. T., and Vo-Ngoc, D. Laminar flow between a stationary and a rotating disk with radial throughflow, *Numer. Heat Transfer A*, 1995, vol. 27, 537-557.
- (16) Iacovides, H. and Chew, J. W. The computation of convective heat transfer in rotating cavities, *Int. J. Heat Fluid Flow*, 1993, vol. 14, 146-154.
- (17) Humphrey, J. A. C., Chang, C. J., and Schuler, C. A. Unobstructed and obstructed rotating disk flows: A summary review relevant to information storage systems, *Advances Information Storage Systems*, 1991, vol. 1, 79-110.
- (18) Abrahamson, S. D., Chiang, C., and Eaton, J. K. Flow structure in head-disk assemblies and implications for design, *Advances Information Storage Systems*, 1991, vol. 1, 111-132.
- (19) Chang, C. J., Schuler, C. A., Humphrey, J. A. C., and Grief, R. Flow and heat transfer between two corotating disks in an axisymmetric enclosure, *J. Heat Transfer*, 1989, vol. 111, 625-632.
- (20) Chang, C. J., Humphrey, J. A. C., and Grief, R. Calculation of turbulent convection between corotating disks in axisymmetric enclosures, *Int. J. Heat Mass Transfer*, 1990, vol. 33, 2701-2720.
- (21) Schuler, C. A., Usry, W., Wever, B., Humphrey, J. A. C., and Grief, R. On the flow in the unobstructed space between shrouded corotating disks, *Phys. Fluids A*, 1990, vol. 2, 1760-1770.
- (22) Humphrey, J. A. C., Schuler, C. A., and Webster, D. R. Unsteady laminar flow between a pair of disks corotating in a fixed cylindrical enclosure, *Phys. Fluids A*, 1995, vol. 7, 1225-1240.
- (23) Iglesias, I. and Humphrey, J. A. C. Two- and three-dimensional laminar flows between disks corotating in a fixed cylindrical enclosure, *Proc. ASME Fluids Eng. Division, FED-Vol. 242*, 1996, pp. 291-304 (ASME, New York).
- (24) Radel, V. S. and Szeri, A. Z. Symmetry breaking bifurcation in finite disk flow, *Phys. Fluids*, 1997, vol. 9, 1650-1656.
- (25) Gan, X., Kilic, M., and Owen, J. M. Superposed flow between two discs contrarotating at differential speeds, *Int. J. Heat Fluid Flow*, 1994, vol. 15, 438-446.
- (26) Kilic, M., Gan, X., and Owen, J. M. Transitional flow between contra-rotating disks, *J. Fluid Mech.*, 1994, vol. 281, 119-135.
- (27) Randriamampianina, A., Elena, L., Fontaine, J. P., and Schiestel, R. Numerical prediction of laminar, transitional and turbulent flows in shrouded rotor-stator systems, *Phys. Fluids*, 1997, vol. 9, 1696-1713.
- (28) Hill, R. W. and Ball, K. S. Chebyshev collocation analysis of axisymmetric flow and heat transfer between counter-rotating disks, *J. Fluids Eng.*, 1997, vol. 119, 940-947.
- (29) Hill, R. W. Parallel Implementation of a Fourier-Chebyshev Spectral Method for the Three Dimensional Navier-Stokes Equations and Application to Transitional Flow in Cylindrical Geometries, Ph.D. Dissertation, The University of Texas at Austin, 1998.
- (30) Zang, T. A. On the rotation and skew-symmetric forms for incompressible flow simulations, *Applied Numer. Math.*, 1991, vol. 7, 27-40.
- (31) Ehrenstein, U. and Peyret, R. A Chebyshev-collocation method for the Navier-Stokes equations with application to double-diffusive convection, *Int. J. Numer. Methods Fluids*, 1989, vol. 9, 427-452.

- (32) Patera, A. T. and Orszag, S. A. Instability of pipe flow, *Nonlinear Problems: Present and Future*, 1982, pp. 367-377 (North-Holland, Amsterdam).
- (33) Canuto, C., Hussaini, M. Y., Quateroni, A., and Zang, T. A. *Spectral Methods in Fluid Dynamics*, 1988 (Springer, New York).
- (34) Ku, H. C., Hirsh, R. S., and Taylor, T. D. A pseudospectral method for solution of the three-dimensional incompressible Navier-Stokes Equations, *J. Comp. Phys.*, 1987, vol. 70, 439-462.
- (35) Haidvogel, D. B. and Zang, T. A. The accurate solution of Poisson's equation by expansion in Chebyshev polynomials, *J. Comp. Phys.*, 1979, vol. 30, 167-180.
- (36) Yang, H. H. and Shizgal, B. Chebyshev pseudospectral multi-domain technique for viscous flow calculation, *Comput. Methods Applied Mech. Eng.*, 1994, vol. 118, 47-61.
- (37) Kleiser, L. and Schumann, U. Treatment of incompressibility and boundary conditions in 3-D numerical spectral simulations of plane channel flows, *Proc. 3rd GAMM Conf. Numer. Methods Fluid Mech.*, 1980, pp. 165-173 (Vieweg, Graunshweig).
- (38) Tuckerman, L. S. Divergence-free velocity fields in nonperiodic geometries, *J. Comp. Phys.*, 1989, vol. 80, 403-441.
- (39) Madabhushi, R. K., Balachandar, S., and Vanka, S. P. A divergence-free Chebyshev collocation procedure for incompressible flows with two non-periodic directions, *J. Comp. Phys.*, 1993, vol. 105, 199-206.
- (40) LeQuéré, P. and Pécheux, J. Numerical simulations of multiple flow transitions in axisymmetric annulus convection, *J. Fluid Mech.*, 1989, vol. 206, 517-544.
- (41) Kuo, D. C. and Ball, K. S. Taylor-Couette flow with buoyancy: onset of spiral flow, *Phys. Fluids*, 1997, vol. 9, 2872-2884.
- (42) Ahmed, I. and Ball, K. S. Spectral simulation of thermocapillary convection with deformable free surface using boundary-fitted coordinates, *Numer. Heat Transfer B*, 1997, vol. 32, 127-149.
- (43) Hill, R. W. and Ball, K. S. Parallel implementation of a Fourier-Chebyshev collocation method for the incompressible Navier-Stokes equations, *SIAM J. Scientific Computing*, 1998, in review.

## 7 FIGURES

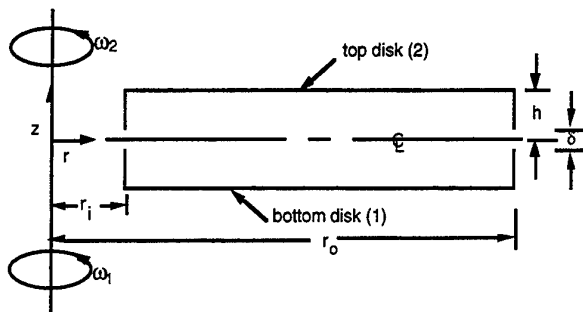
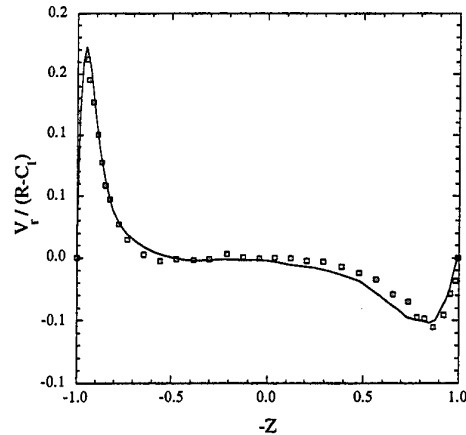
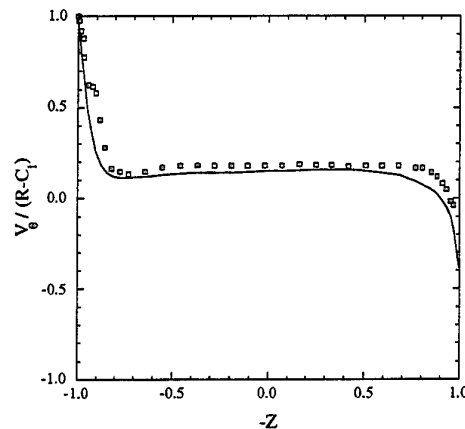


Figure 1 Schematic of coordinate and physical system



(a)  $V_r$  at  $r/r_o = 0.85$



(b)  $V_\theta$  at  $r/r_o = 0.85$

Figure 2 Mean velocity profiles for  $Re = 10^5$  and  $\Gamma = -0.4$ ; symbols denote experimental data of Ref. (26)

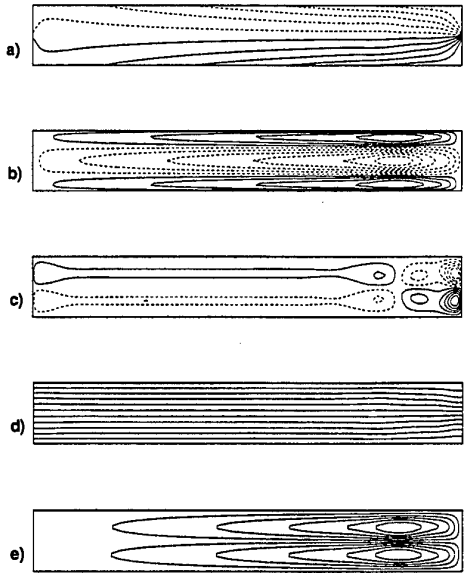


Figure 3 Mean contours of flow variables in the r-z plane for  $\Gamma = -1.0$  and  $Re = 1730$ , with maximum values given in parentheses; (a)  $V_\theta (\pm 2.299)$ , (b)  $V_r (-0.231, 0.174)$ , (c)  $V_z (\pm 0.072)$ , (d) T, (e)  $\psi$

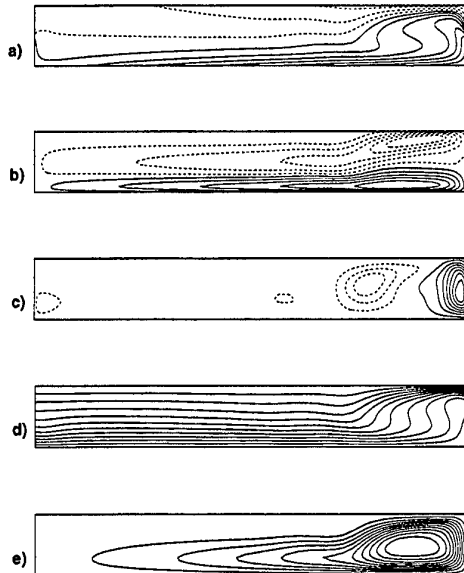


Figure 5 Mean contours of flow variables in the r-z plane for  $\Gamma = -0.4$  and  $Re = 4400$ , with maximum values given in parentheses; (a)  $V_\theta (-0.920, 2.299)$ , (b)  $V_r (-0.278, 0.310)$ , (c)  $V_z (-0.099, 0.198)$ , (d) T, (e)  $\psi$

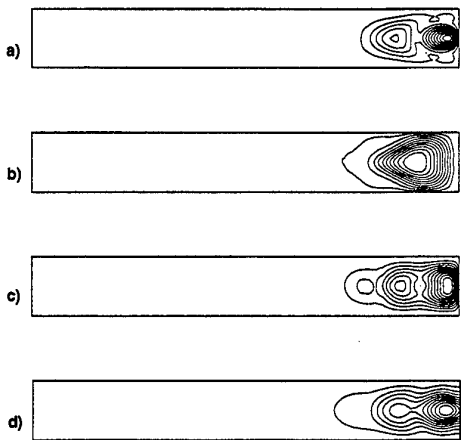


Figure 4 Rms velocity and temperature fluctuations in the r-z plane for  $\Gamma = -1.0$  and  $Re = 1730$ , with maximum values given in parentheses; (a)  $V_{\theta,rms} (0.554)$ , (b)  $V_{r,rms} (0.221)$ , (c)  $V_{z,rms} (0.113)$ , (d)  $T_{rms} (0.101)$

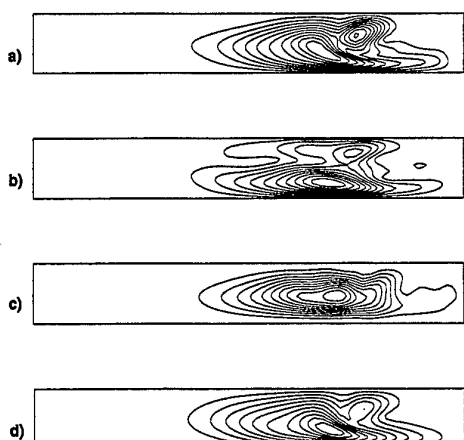


Figure 6 Rms velocity and temperature fluctuations in the r-z plane for  $\Gamma = -0.4$  and  $Re = 4400$ , with maximum values given in parentheses; (a)  $V_{\theta,rms} (0.090)$ , (b)  $V_{r,rms} (0.054)$ , (c)  $V_{z,rms} (0.028)$ , (d)  $T_{rms} (0.055)$

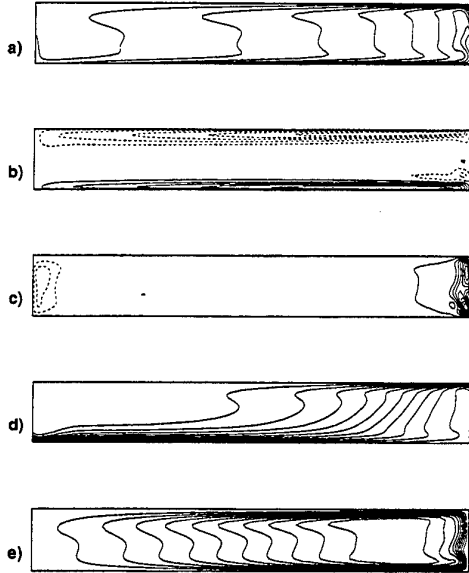


Figure 7 Mean contours of flow variables in the r-z plane for  $\Gamma = 0$  and  $Re = 27000$ ;  
 (a)  $V_\theta$  (2.299), (b)  $V_r$  (-0.246, 0.269),  
 (c)  $V_z$  (-0.049, 0.143), (d) T, (e)  $\psi$

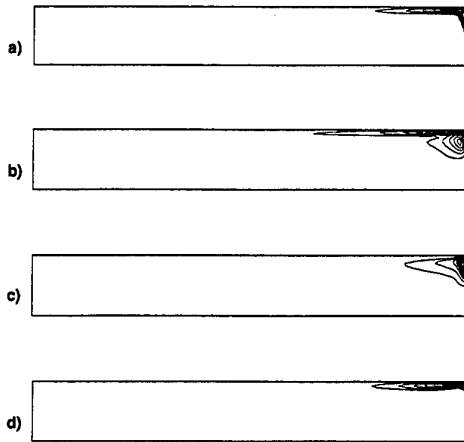


Figure 8 Rms velocity and temperature fluctuations in the r-z plane for  $\Gamma = 0$  and  $Re = 27000$ , with maximum values given in parentheses;  
 (a)  $V_{\theta,rms}$  (0.121), (b)  $V_{r,rms}$  (0.030),  
 (c)  $V_{z,rms}$  (0.035), (d)  $T_{rms}$  (0.066)

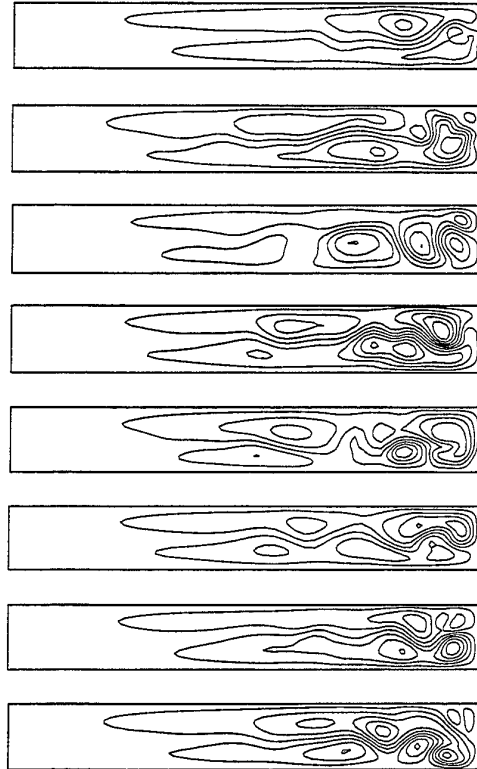


Figure 9(a) Instantaneous secondary flow streamlines in the r-z plane for  $\Gamma = -1.0$  and  $Re = 4500$ , at eight equally spaced azimuthal locations ( $\Delta\theta = \pi/4$ )

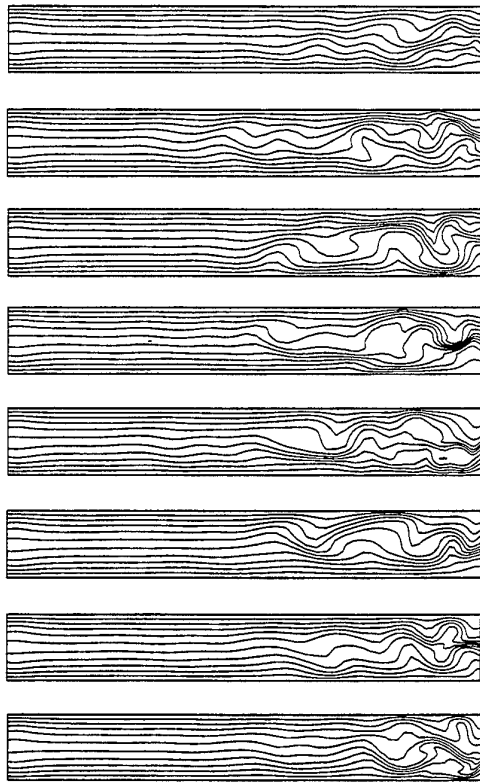


Figure 9(b) Instantaneous temperature contours in the r-z plane for  $\Gamma = -1.0$  and  $Re = 4500$ , at eight equally spaced azimuthal locations ( $\Delta\theta = \pi/4$ )

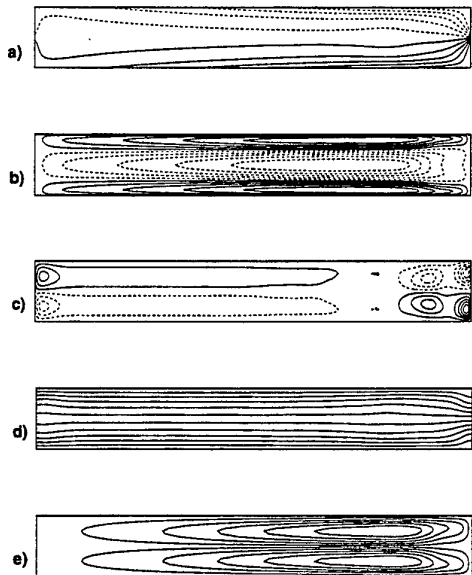


Figure 10 Mean contours of flow variables in the r-z plane for  $\Gamma = -1.0$  and  $Re = 4500$ ;  
 (a)  $V_\theta (\pm 2.299)$ , (b)  $V_r (\pm 0.221)$ ,  
 (c)  $V_z (\pm 0.065)$ , (d)  $T$ , (e)  $\psi$

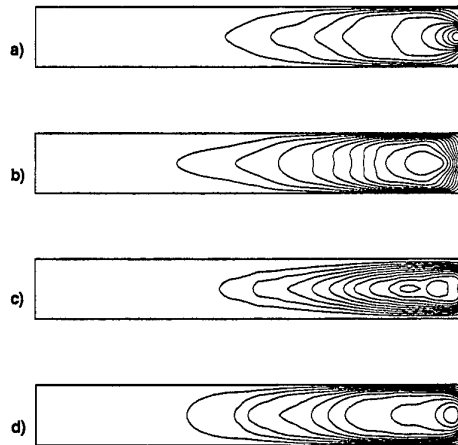


Figure 11 Rms velocity and temperature fluctuations in the r-z plane for  $\Gamma = -1.0$  and  $Re = 4500$ , with maximum values given in parentheses;  
 (a)  $V_{\theta,rms} (0.695)$ , (b)  $V_{r,rms} (0.316)$ ,  
 (c)  $V_{z,rms} (0.217)$ , (d)  $T_{rms} (0.142)$

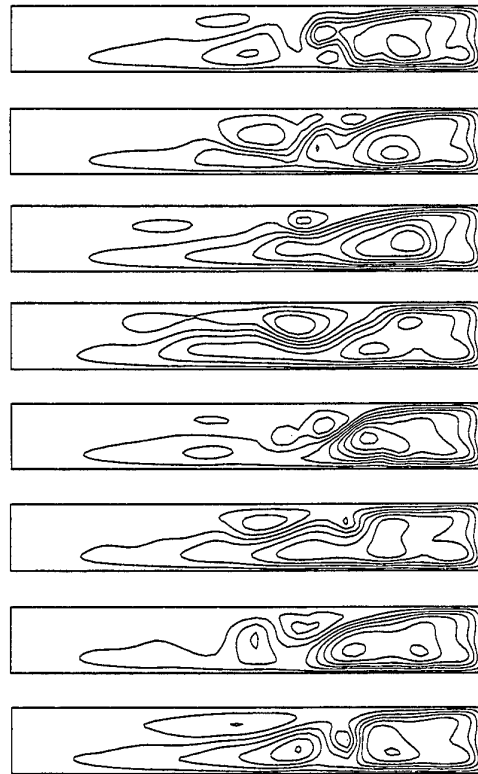


Figure 12(a) Instantaneous secondary flow streamlines in the r-z plane for  $\Gamma = -0.4$  and  $Re = 12000$ , at eight equally spaced azimuthal locations ( $\Delta\theta = \pi/4$ )

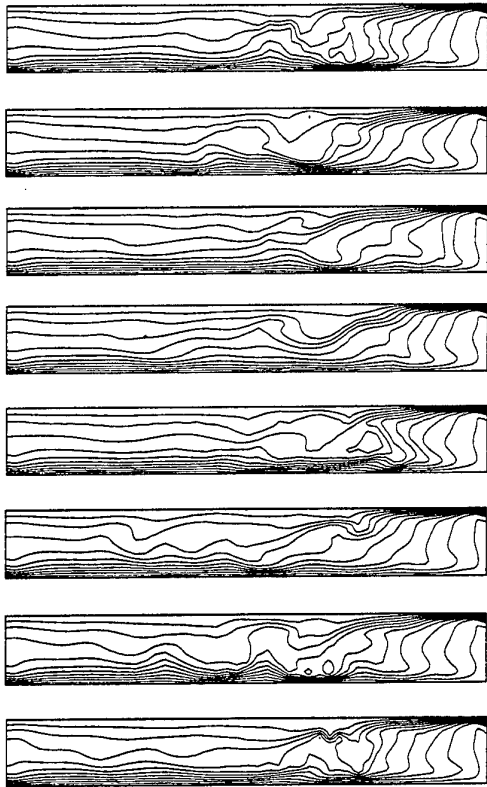


Figure 12(b) Instantaneous temperature contours in the r-z plane for  $\Gamma = -0.4$  and  $Re = 12000$ , at eight equally spaced azimuthal locations ( $\Delta\theta = \pi/4$ )

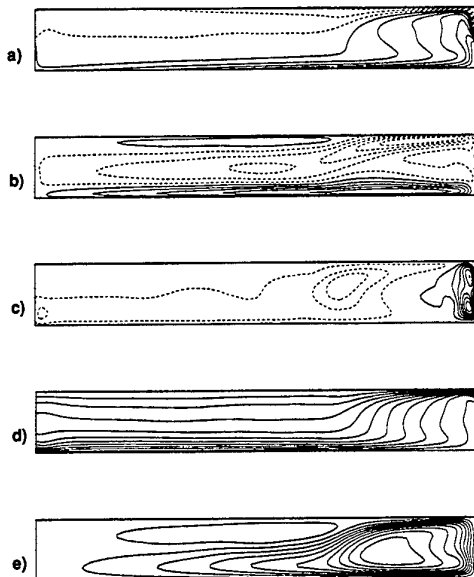


Figure 13 Mean contours of flow variables in the r-z plane for  $\Gamma = -0.4$  and  $Re = 12000$ ;  
 (a)  $V_\theta$  (-0.920, 2.299), (b)  $V_r$  (-0.260, 0.298),  
 (c)  $V_z$  (-0.069, 0.170), (d) T, (e)  $\psi$

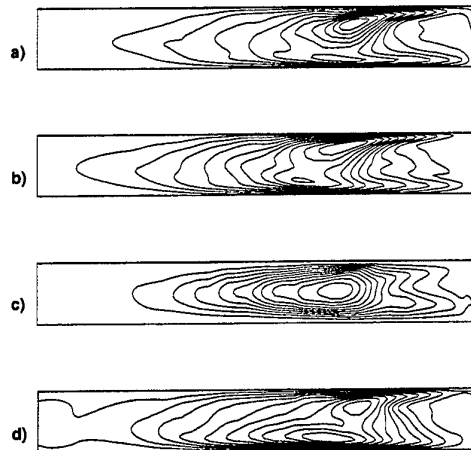


Figure 14 Rms velocity and temperature fluctuations in the r-z plane for  $\Gamma = -0.4$  and  $Re = 12000$ , with maximum values given in parentheses;  
 (a)  $V_{\theta,rms}$  (0.210), (b)  $V_{r,rms}$  (0.129),  
 (c)  $V_{z,rms}$  (0.074), (d)  $T_{rms}$  (0.103)

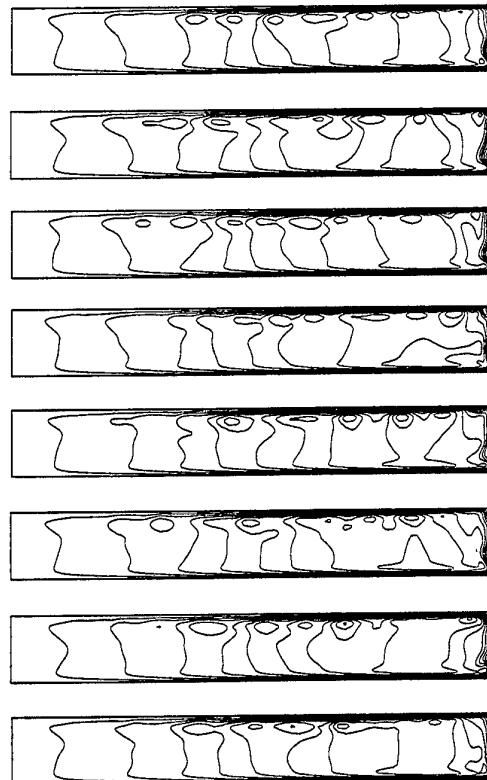


Figure 15(a) Instantaneous secondary flow streamlines in the r-z plane for  $\Gamma = 0$  and  $Re = 70000$ , at eight equally spaced azimuthal locations ( $\Delta\theta = \pi/4$ )



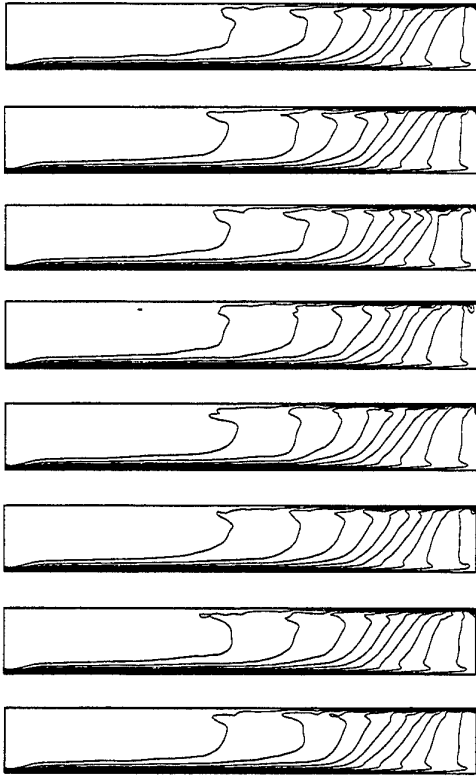


Figure 15(b) Instantaneous temperature contours in the r-z plane for  $\Gamma = 0$  and  $Re = 70000$ , at eight equally spaced azimuthal locations ( $\Delta\theta = \pi/4$ )

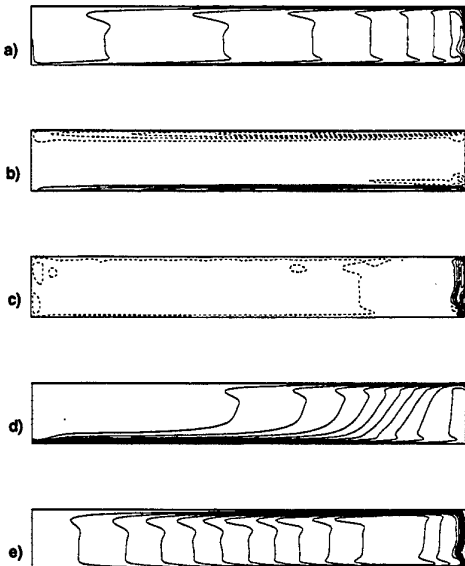


Figure 16 Mean contours of flow variables in the r-z plane for  $\Gamma = 0$  and  $Re = 70000$ ;  
 (a)  $V_\theta$  (2.299), (b)  $V_r$  (-0.238, 0.272),  
 (c)  $V_z$  (-0.039, 0.160), (d) T, (e)  $\psi$

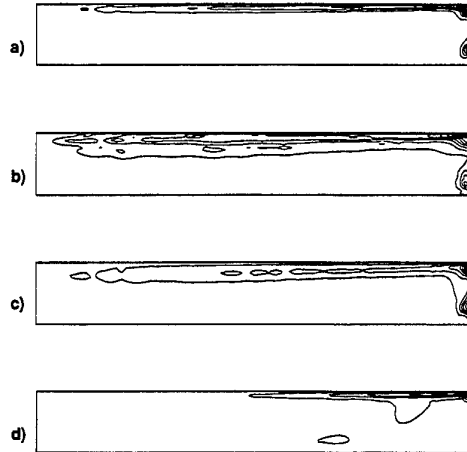


Figure 17 Rms velocity and temperature fluctuations in the r-z plane for  $\Gamma = 0$  and  $Re = 70000$ , with maximum values given in parentheses;  
 (a)  $V_{\theta,rms}$  (0.269), (b)  $V_{r,rms}$  (0.066),  
 (c)  $V_{z,rms}$  (0.077), (d)  $T_{rms}$  (0.136)

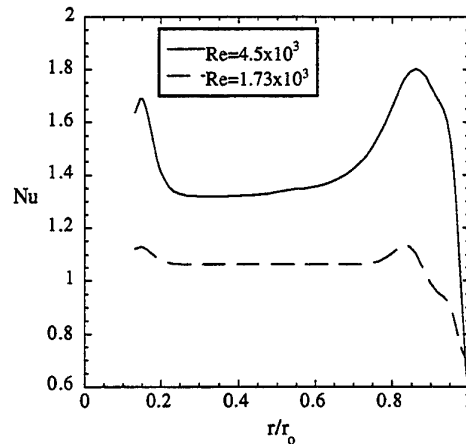


Figure 18 Radial variation of mean Nu for  $\Gamma = -1.0$

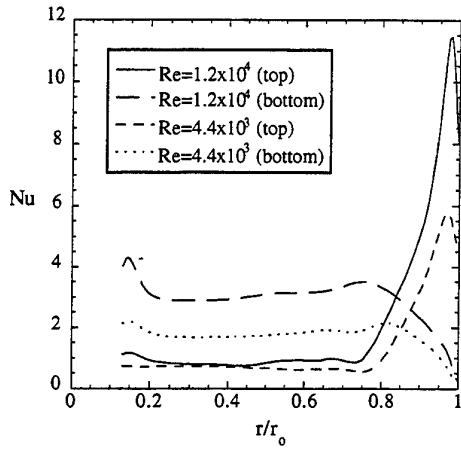


Figure 19 Radial variation of mean Nu for  $\Gamma = -0.4$

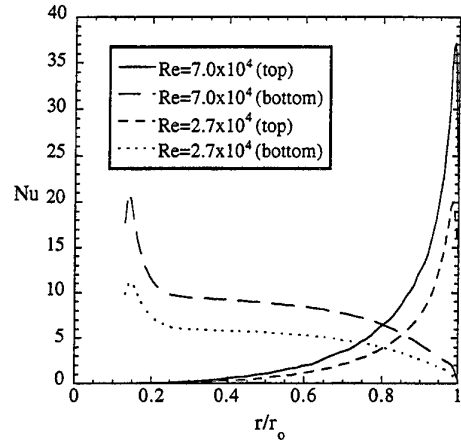


Figure 20 Radial variation of mean Nu for  $\Gamma = 0$

# PREDICTION OF GRID TURBULENCE EVOLUTION WITH A SIMPLE MULTIFRACTAL CASCADE MODEL

P. Diamessis\*, D. Bouris and G. Bergeles\*\*

Laboratory of Aerodynamics, Fluids Section, Department of Mechanical Engineering  
National Technical University of Athens, GREECE

## ABSTRACT

A numerical model is developed, based on the modeling of turbulence by eddies (corresponding to spherical shells in wavenumber space) breaking up into smaller ones as they are convected downstream. The distribution of eddy energy into the daughter eddies follows the laws of multifractal multiplicative processes. The model was applied to grid turbulence. The results for the predicted turbulent kinetic energy  $k$  were from good to very good agreement compared to experimental data and theoretical predictions. The computation of energy spectra  $E(\kappa)$  downstream of the grid are in good agreement with experimental data and Kolmogorov's  $-5/3$  inertial range law; also they allow the computation of other quantities as the dissipation spectra  $D(\kappa)$ , the energy dissipation rate  $\varepsilon$ , one dimensional spectra, length scales etc. Computation of  $\varepsilon$  with very fine resolution, i.e. great number of points along a relatively small interval, makes possible the derivation of the spectrum of fractal dimensions  $f(\alpha)$  of the energy dissipation rate.

\*Current address: Department of Applied Mechanics and Engineering Sciences, University of California San Diego, La Jolla CA. 92093-0413, USA.

\*\* All correspondence should be addressed to this author

## 1 INTRODUCTION

Prediction of a turbulent flow is not feasible because of the great difficulty of the direct numerical solution of the Navier-Stokes equations, a process which requires computer resources by far exceeding the capabilities of today's computers. O.J. Reynolds' approach of decomposing each unknown of the Navier-Stokes equations into the sum of a mean value and a fluctuation comes short for it introduces a new unknown, the Reynolds stress and consequently more unknowns than equations. An attempt, based on fundamental conservation laws, to express the Reynolds stresses in terms of the remaining unknowns introduces new unknown quantities, which if linked among themselves bring forth new unknowns and so on. The challenge therefore consists of cutting short this infinite regression and obtaining a closed mathematical problem.

A rather new theory, the theory of fractals and multifractals has emerged as a hope in the solution of the closure problem. In certain cases, the solutions of the Navier-Stokes equations are expected to exhibit multifractal characteristics while the physical mechanism of turbulence (the mechanism responsible for the generation, diffusion and decay of turbulence) is speculated to be governed by multifractal multiplicative processes (2), (3). However, research on the relation of turbulence and multifractals has not been extended to prediction of turbulent flows, remaining restricted to the computation of fractal dimensions of the contours

of jets, flames, clouds etc. and turbulent cascade theory (2). One exception could be (4), in which the turbulent velocity signal is described by the multifractal Weierstrass - Mandelbrot function generating correct form for the energy and dissipation spectra over inertial and dissipative scales of motion.

The present paper proposes a model for the prediction of turbulence (homogeneous and isotropic at first) based on the physical approach (proposition of a model for the turbulent activity) and the theory of multifractals, especially the application of the latter to turbulent energy cascade.

Turbulence at a specific point in space is visualized as a superposition of eddies, corresponding to the different Fourier components of the turbulent fluctuation. These eddies are superimposed on the mean flow and are assumed to be convected downstream by the local mean velocity (This assumption is no longer valid in flows of high turbulence intensity and variation of the mean velocity along distances of the order of magnitude of the turbulence integral scale). Simultaneously with their movement in space, these eddies realize the cascade of turbulent energy by breaking up into smaller eddies of unequal size in which the energy of the initial eddy is distributed unequally. It is during this process that multifractal laws come into play. Thus, from a take-off point in space we monitor the evolution downstream of a cluster of eddies which constantly break up into smaller ones and are ultimately destroyed into heat due to the effect of viscosity. The concepts used for the

turbulent energy cascade were found in (5), (6), (7) & (8). The concept of eddies corresponding to discrete ranges in the energy spectrum  $E(\kappa)$  of turbulence (spherical shells in wavenumber space) and monitoring their movement in physical space is a novel one. One attempt concerning the prediction of turbulence, through its modeling with shells (cubic) in  $\kappa$ -space, is found in (9). The concept of turbulent eddies and the question of eddy interaction are examined in (10).

The paper is structured as follows: Following the introduction, there is a brief description of the physical system whose turbulence is to be modeled. After that, the numerical model is presented. The model results are presented and discussed, for some experimental cases. In the concluding paragraph, the significance of the model is viewed in relation to other numerical models along with its advantages and disadvantages and its capacity to be extended to more complex turbulent flows. Finally, in appendix A, results concerning the computation of the spectrum of fractal dimensions of the energy dissipation rate  $\varepsilon$  are presented.

## 2 THE PHYSICAL SYSTEM

The physical system to be modeled is the simplest experimental case of homogeneous and isotropic turbulence; grid turbulence. In a rectangular duct, a current of air of constant mean velocity and pressure (downstream and in transverse sections of the flow) goes through a grid of rectangular metallic bars and mesh length  $M$  (Fig. 1). As the wakes of the bars diffuse downstream and eventually unite, at a distance approximately  $x/M=20$  downstream, turbulence reaches a fully developed state. From that point on, turbulent energy cascades gradually from larger to smaller scales simultaneously decaying into heat until at a distance  $x/M=400$  to 500 all initial turbulent energy has been dissipated into heat due to the effect of viscosity. The experimental measurements for model validation were taken from (11), (12) and (13). The heated grid and heated "mandolin" used in (11) and (12), respectively, resulted in temperature fluctuations which did not significantly affect the values of the velocity fluctuations. The initial conditions for each experiment are given in Table 1.

## 3 NUMERICAL MODEL

### 3.1 Definition of an eddy

In turbulence literature, although much used, the term 'eddy' is usually ambiguously defined. Bradshaw (14) defines an eddy as a typical motion in turbulent flow, usually covering a range of wavelengths of less than, say, 10 to 1, so that one can talk of "large" and "small"

eddies in the same volume of fluid. Chorin (15) speaks of an eddy intuitively claiming that one observes motions, or eddies, of various scales as since by looking on a weather map one sees low or high pressure areas that span continents and storms that cover cities while walking down the street one feels gusts of wind on a human scale. Kolmogorov (5) (See also (15)) states that for very large Reynolds numbers turbulent flow can be thought of as a superposition on the average velocity of the "pulsations of the first order" consisting of disordered displacements of separate fluid volumes, one with respect to another. Following Bradshaw's definition and Kolmogorov's 1941 turbulent energy cascade theory, we define an eddy as a spherical shell of very small thickness in  $\kappa$ -space (wavenumber space). For a pictorial representation of  $\kappa$ -space see (14), (16).

More precisely, a shell is a region (a geometric locus) of points  $(\kappa_1, \kappa_2, \kappa_3)$  in wavenumber space satisfying the inequality:

$$\kappa_i^2 < \kappa_1^2 + \kappa_2^2 + \kappa_3^2 < \kappa_{i+1}^2 \quad (1)$$

where wavenumber magnitudes  $\kappa_i$  and  $\kappa_{i+1}$  correspond to the discretization of the region  $[\kappa_{\min}, \kappa_{\max}]$  (The domain of the three dimensional energy spectrum  $E(\kappa)$  in linear segments of length  $\Delta\kappa = \kappa_{i+1} - \kappa_i = (\kappa_{\max} - \kappa_{\min}) / (N-1)$  ( $i=1, \dots, N$  with  $N \rightarrow \infty$ ). The spherical shell has thickness  $\Delta\kappa \rightarrow 0$  and mean radius:

$$\kappa_c = (\kappa_i + \kappa_{i+1}) / 2 \quad (2)$$

Thus the eddy corresponds to the contribution of a certain range of wavenumber magnitudes to the Fourier transform of the spatial correlation tensor.

Every eddy has characteristic length

$$l = 1/\kappa_c$$

energy

$$k_{eddy} = \int_{\kappa_i}^{\kappa_{i+1}} E(\kappa) d\kappa$$

and velocity (17):

$$v_{eddy} = [\kappa_c E(\kappa_c)]^{1/2}$$

The eddy velocity is such that it is independent of the density of the discretization of the active wavenumber domain; in other words of the thickness of the representative energy shell ((7), (17)).

### 3.2 Basic principles

The model is based on the following principles:

a) Turbulence at every point downstream is considered as a superposition of eddies of different characteristic lengths, times and velocities. It is assumed that the eddies do not interact with each other.

b) The cascade of turbulent kinetic energy is considered through the breakup of the eddies into smaller ones and the transfer of their energy to them. The law governing the distribution of the energy of the mother eddy into the daughter ones is derived from the theory of multifractals (Fig. 2).

c) The assumption that in grid turbulence, the pattern of disturbance, i.e. turbulent eddies, is transported by the mean velocity (Taylor's frozen flow hypothesis). This assumption requires that the mean velocity does not change appreciably along distances comparable to the scale of turbulence and that turbulence intensity is low (18). Both of the above prerequisites are satisfied in grid turbulence.

Therefore, at a take off time  $t_{\text{start}}=0$  we assume the simultaneous launching of a package of a large number of eddies from the take off position  $x_{\text{start}}$  and we monitor the movement of every single one -and consequently its offsprings- downstream. After a very short time span  $dt$ , a statistically identical package is launched and so forth. Thus, after every eddy in the initial package (from the largest to smallest one) is launched and eventually dissipated into heat due to the effect of viscosity, the turbulent characteristics of every point downstream will result from the superposition of the corresponding characteristics of all the eddies that are found at that point.

### 3.3 The evolution of an individual eddy

The initial characteristics of the  $i$ -th eddy of a package of  $N$  eddies launched (from take off position  $x_{\text{start}}$ ) are:

a) Characteristic length

$$l_0 \in (\eta_b L_0), \quad l_0 = L_0 - (i-1) \frac{L_0 - \eta}{N-1}$$

where

$$\eta = \left( \nu^3 / \varepsilon \right)^{1/4}$$

and  $L_0$  are, respectively, the length scales of Kolmogorov and the maximum geometric dimension of the flow (mesh length  $M$ ).

b) Wavenumber

$$\kappa_0 = 1/l_0$$

c) Turbulent kinetic energy  $k_i$  per kg of fluid mass computed through the energy spectrum  $E(\kappa)$  at the initial position of fully developed turbulence. It stands that

$$\sum_i k_i = k$$

where  $k$  is given in Table 1.

d) Characteristic velocity  $v_0$  ( $k_i$  and  $v_0$  are computed as indicated in paragraph 2).

e) Eddy turnover time:

$$t_0 = l_0 / v_0 \quad (3)$$

f) Eddy viscous dissipation time:

$$t_0^{\text{diss}} = l_0^2 / \nu \quad (4)$$

The eddy is launched from the take off position, and is transported by the mean velocity  $U$  parallel to the  $x$ -axis. In time  $t_0 = l_0 / v_0$ , the eddy's turbulent energy  $k_i$  is transferred to smaller eddies (through its breakup into eight smaller ones. See next paragraph). The only exception to the above mechanism is when:

$$t_0^{\text{diss}} < t_0 \quad (5)$$

where all the eddy's energy is dissipated into heat due to viscosity, because viscous effects take place much quicker than inertial effects (eddy breakup). The way the size, energy and velocity of the daughter eddies is presented in the coming section while their turnover and viscous dissipation times are computed through relations similar to (3) and (4). We must note that the energy of an eddy, either breaking up into smaller ones or dissipating into heat, remains constant from the beginning of its existence until its breakup or dissipation.

### 3.4 The breakup model of an eddy

The eddy breakup model can be regarded as a cascade model for it is through the breakup of each initial eddy and its subsequent daughter eddies that the cascade of turbulent energy, from larger to smaller scales, is realized. The breakup model is based on a simple multifractal cascade model, the  $p$ -model, of Meneveau and Sreenivasan ((8),(19)) with eddies considered as three dimensional geometrical objects. The  $p$ -model is based on the concept of weighted (non-absolute) curdling introduced by Mandelbrot (16) contrary to the cascade models known as the  $\beta$ -model (7) and the random  $\beta$ -model (20). In the weighted curdling, the conservation of volume applies (the daughter eddies occupy the volume originally occupied by the mother eddy) and although the conservation of energy also applies, the energy of the mother eddy is distributed unequally into the daughter eddies. In the  $\beta$ -model the daughter eddies occupy only  $\beta\%$  of the volume of the mother eddy with the energy however being equally

distributed into each daughter eddy (absolute curdling, where  $\beta$  can be a constant or randomly selected.)

In the present model, we have modified the p-model as follows:

a) The initial turbulent energy is not considered to be isolated on only one eddy of the size of the turbulent integral scale  $l$  but it is distributed among eddies of different sizes encompassing the entire active range of wavenumber magnitudes.

b) The characteristic length of eddies resulting from the breakup of a larger one, is not half that of the original. On the contrary, a random statistical distribution and the conservation of volume are used for its computation. The reason was to render the cascade non-local character rather than local, which means that energy transfer involves not only neighboring wavenumbers but also quite distant ones (21). Otherwise, discontinuities resulted in the computed energy spectra  $E(\kappa)$  downstream, at the first stages of model development.

The proposed model has as follows:

Provided that relation (5) does not hold, each eddy breaks up into two groups of four eddies. The characteristic lengths of the eddies of each group are respectively:

$$l_{daughter}^{(1)} = \gamma \cdot l_{mother} \quad (6a)$$

$$l_{daughter}^{(2)} = \left[ 0.25 \left( l_{mother}^3 - 4 \cdot l_{daughter}^3 \right) \right]^{1/2} \quad (6b)$$

which means that the size of the daughter eddies of the first group is determined (pseudo)randomly through the coefficient  $\gamma$  which is taken from a fully random distribution within the region [0,1]. The size of the daughter eddies of the second group is computed through the conservation of volume, assuming the eddies to be spheres or cubes in their geometry in three dimensional physical space (not to be confused with their description as spherical shells in wavenumber space). The energy and velocity of each daughter eddy are (by 1,2,3,4 we note the daughter eddies of the first group and 5,6,7,8 those of the second one):

$$k_{daughter}^{(1,2,3,4)} = M_0 \cdot k_{mother} \quad (7a)$$

$$k_{daughter}^{(5,6,7,8)} = M_1 \cdot k_{mother} \quad (7b)$$

$$v_{daughter}^{(1,2,3,4)} = M_0^{1/2} \cdot v_{mother} \quad (7c)$$

$$v_{daughter}^{(5,6,7,8)} = M_1^{1/2} \cdot v_{mother} \quad (7d)$$

where  $M_0=0.99/4$  and  $M_1=0.01/4$  are non-random variables so that the conservation of energy applies. Their values were decided after extensive numerical

experimentation. The values of  $M_0$  and  $M_1$  in the original p-model were (0.3/4) and (0.7/4) respectively, but they had to be modified for the case of Yeh and Van Atta. The modifications were made to establish a better energy transfer mechanism between the mother and the daughter eddies. Note that above, the characteristic velocity of an eddy is computed through simple dimensional analysis, because at every position downstream, apart from the take-off position, the energy spectrum of the turbulence is not known a priori. Thus, computation of its velocity through the relation of section (3.1) is not possible.

If relation (5) holds, the eddy's energy is dissipated into heat and the eddy ceases to exist as an entity.

### 3.5 The energy spectrum $E(\kappa)$ at $x_{start}$

The application of our model requires the energy spectrum at a take off position. For the experimental case (11) the energy spectrum  $E(\kappa)$  at a take off position was available at  $x/M=25$ . However, for the case of (12) or (13) the only available measured spectra ( $x/M=59$  and 80) were outside the build-up period of turbulence. Considering a take off position at  $x/M=20$  (the first position where measurements of the turbulent kinetic energy were given) we assumed that under the appropriate normalization, the spectra collapse to a nearly identical form. Thus, given the length scale

$$l = k^{3/2} / \varepsilon$$

and the r.m.s. of the velocity fluctuation  $\overline{u^2}$  a first form of the energy spectrum curve  $E(\kappa)$  was computed. However, such a form of the energy spectrum did not satisfy the integral relation:

$$\int_0^{\infty} E(\kappa) \cdot d\kappa = k \quad (8)$$

As a simple solution, the energy content of the spectrum was reduced by positioning an inertial range, where

$$E(\kappa) \approx \kappa^{-5/3}$$

beginning from a wavenumber  $\kappa=85 \text{ m}^{-1}$  and with a large wavenumber limit such that equation (8) could be satisfied.

## 4 RESULTS AND DISCUSSION

The model was run on a Silicon Graphics workstation R2000A/R3000 at 40 MHz for a package of 20,000 initial eddies. Running time was 40 minutes while a package of  $10^6$  initial eddies required 120 hours of computer time.

The downstream turbulent kinetic energy curve  $k(x/M)$  (Fig. 3) is of the expected parabolic form, on a linear scale. Initially, the smaller eddies are rapidly destroyed so the curve's slope is steep ( $x/M=20$  to  $30$ ). As energy is transferred from the eddies carrying the greater percentage of turbulent energy to smaller and smaller ones the curve's slope is reduced ( $x/M=30$  to  $150$ ) until it tends to become an asymptote of the  $x$ -axis, on the linear scale, where after a certain point the last remains of turbulent energy have been dissipated into heat. The agreement with the experimental data in (11) is quite satisfactory while the predictions rival those of the commonly used  $k$ - $\epsilon$  turbulence model (Calibrated for this experimental case. See (23)). For the initial conditions of (12) the  $k(x/M)$  is overpredicted in the initial period from  $x/M=30$  to  $x/M=100$ . This phenomenon may be attributed to the formulation of the energy spectrum at the take off position according to the assumptions in section (3.5). The eddies located in the small to medium wavenumber range of the take off position energy spectrum have a relatively high energy content. These eddies and their subsequent offsprings tend to dissipate their energy into heat at a longer distance downstream of the grid, contrary to the eddies within the large wavenumber range, which are all dissipated within a few mesh lengths from the take off position.

Energy spectra  $E(\kappa)$  at specific positions downstream were computed by processing the data stored in a file containing the energy and characteristic length (i.e. the wavenumber) of each eddy crossing that position. For the case of (11) the numerical computations (Fig. 4) agree well with experimental measurements with the exception of the large wavenumber range where the spectrum drops with a smaller slope. For the case of (13) (Fig. 5), although the results are in good agreement with the experimental data for the small to medium wavenumber range, they are overpredictive for large wavenumbers. One can speculate that beyond a certain position downstream the turbulence settles down to a steady statistical state close to that of the experimental measurements and independent of small differences that might exist in the initial conditions. For both cases, one can also observe that, for a wavenumber range of a length of a few hundreds, Kolmogorov's  $-5/3$  law is confirmed, indicating the existence of an inertial range:

$$E(\kappa) = \alpha \cdot \epsilon^{2/3} \cdot \kappa^{-5/3} \quad (9)$$

One notices noise in the large wavenumber range, which is attributed to the random nature of the model (From one wavenumber energy is transferred to a larger one of a randomly computed value, thus beyond a certain distance downstream the energy density tends to be "dispersed" in the large wavenumber range resulting in a "noisy" distribution). This noise was limited up to a certain point by ensemble averaging, where the

spectrum at each position was computed as the average of the results of several realizations of the model. In each realization, a different seed was used for the random number generator, simulating initial condition deviations in similar experimental work.

The dissipation spectrum  $D(\kappa)$  is indicative of the density of the dissipation rate at a wavenumber  $\kappa$ . The energy dissipation per wavenumber is strongly dependent on fluctuation velocity gradients and it is computed as (see (21)):

$$D(\kappa) = 2\nu\kappa^2 E(\kappa) \quad (10)$$

In Fig. 6, a comparison between the experimental measurements and numerical results for the dissipation spectrum  $D(\kappa)$ , for (11), is presented for position downstream  $x/M=35$ . The existence of the  $\kappa^2$  factor in relation (10) amplifies any irregularities in the energy spectrum  $E(\kappa)$ . Thus, a dip of greater extent is noticed in the small wavenumber range of the dissipation spectrum  $D(\kappa)$  while the noise in the large wavenumber range of the energy spectrum  $E(\kappa)$  leads to differences between numerical and experimental data. A corresponding diagram for the case of (13) at  $x/M=80$  indicates good agreement with experimental data for the low to medium wavenumber range but differences become significant in the high wavenumber range due to amplification of noise and differences in the corresponding energy spectrum  $E(\kappa)$ .

The dissipation spectrum is a means for the computation of the energy dissipation rate  $\epsilon$  through the equation:

$$\epsilon = \int_0^{\infty} D(\kappa) d\kappa \quad (11)$$

in comparison with the experimental data for both the cases of (11) and (12). In Fig. 7, although the slopes of the two curves are similar in small distances downstream from the grid, the numerical results tend to overpredict  $\epsilon$  because of the inaccuracies resulting from the amplification of noise in the energy spectrum  $E(\kappa)$ . Computation of  $\epsilon$  through the derivative of the turbulent energy  $k$ :

$$\epsilon = -\frac{dk}{dt} = -U \cdot \frac{dk}{dx} \quad (12)$$

(assuming Taylor's frozen flow hypothesis) leads to more accurate results because of the better agreement of numerically computed  $k$  with experimental data. However, both computed  $\epsilon(x/M)$  curves display basically the same behavior: Starting from the take off position, they drop with a constantly decreasing slope. After  $x/M=80$ , they asymptotically go to zero as turbulent energy is destroyed at an a lot slower rate.

Finally, in the same figure the results of the  $k$ - $\varepsilon$  are also displayed for reasons of comparison.

An interesting feature of the turbulent energy dissipation rate  $\varepsilon$  is its multifractal distribution in small spatial intervals (see (2), (8)). Since the generation of such a multifractal distribution would require an enormous amount of samples within a very small distance downstream -of the order of magnitude of the integral scale- it is difficult to derive it from integration of the dissipation spectrum at different points downstream. However, experimental derivations of such distribution are based on the measurement of the surrogate of the turbulent energy dissipation rate  $(du/dt)^2$ . We thus did attempt to derive a similar distribution through our model by computing  $\varepsilon$  at  $10^5$  points within an interval of the length of 10 integral scales  $l$  (See (2) for the case of (11)). The resulting distribution depicted in Fig. 8 is indeed a multifractal one displaying great intermittency as strong peaks are followed by extreme low values. A closer look at the distribution, along a smaller interval on the  $x$ -axis, reveals its scale self-similarity. Manipulation of such a distribution could lead to the computation of its spectrum of fractal dimensions  $f(\alpha)$ . Results are given in appendix A, where the method proposed by Meneveau and Sreenivasan (24) is used.

The turbulence length scale  $l$ , which, though also indicative of the energy carrying eddy sizes, should not be confused with the turbulence integral scale  $L$ , is computed through dimensional analysis:

$$l = c_m \cdot \frac{k^{3/2}}{\varepsilon} \quad (13)$$

where  $c_m=0.09$ . As one can see in Fig. 9, for the case of Yeh and Van Atta, the length scale computed by the  $k$ - $\varepsilon$  model increases according to a  $x^{0.43}$  power law very close to that predicted by theory (See (21)). All length scales increase with approximately the square root of the distance downstream. The curve computed, with calculation of  $\varepsilon$  by (12), follows a similar power law behavior exhibiting many fluctuations due to the "reinforcement" of the corresponding fluctuations in the dissipation rate  $\varepsilon$  ( $\varepsilon$  appears in the denominator of (13)). Computation of the length scale with the values of  $\varepsilon$  resulting from integration of the dissipation spectrum  $D(\kappa)$ , results in a curve exhibiting a satisfactory  $x^{0.62}$  power law, underpredictive, however, in its form due to the overprediction of  $\varepsilon$  through (11) on account of the noise in the large wavenumber range of the energy spectrum  $E(\kappa)$ . A corresponding diagram for the case of Snyder and Lumley is also shown. The results obtained from relation (13) and differentiation of the  $k(x/M)$  curve do not agree with those of the  $k$ - $\varepsilon$  model. This effect is due to the amplification of errors already existing in the corresponding results for  $\varepsilon$ . However, the results obtained through integration of

the dissipation spectrum  $D(\kappa)$  come closer to the  $k$ - $\varepsilon$  data, despite their increase with a  $x^{1.2}$  slope.

While the three dimensional energy spectrum  $E(\kappa)$  is representative of the energy density in all wavenumbers of magnitude  $\kappa$  regardless of direction, the one-dimensional spectrum  $\varphi(\kappa_1)$  is indicative of the energy density in wavenumber vectors  $(\kappa_1, \kappa_2, \kappa_3)$  where  $\kappa_2, \kappa_3$  are constant, i.e. it is indicative of the energy density in the downstream direction, for a certain wavenumber  $\kappa_1$ .  $E(\kappa)$  and  $\varphi(\kappa_1)$  are linked by the following set of equations (see (13)):

$$E(\kappa) = -\frac{1}{2} \cdot \kappa \cdot \frac{d\varphi}{d\kappa} \quad (14)$$

$$\int_0^{\infty} \varphi(\kappa_1) d\kappa_1 = 2k \quad (15)$$

Given the three dimensional energy spectrum  $E(\kappa)$  and the turbulent kinetic energy  $k$  at a certain position downstream, by solving numerically the system of equations (14) and (15) we can compute the one-dimensional energy spectrum  $\varphi(\kappa_1)$  for both the cases of Yeh and Van Atta and Warhaft and Lumley (Fig. 10). This diagram is also indicative of the energy transfer from small wavenumbers to larger ones. The numerically computed spectra tend to overpredict the experimental measurements of Yeh and Van Atta. Especially, at positions near the grid downstream, the slope of the spectra is very low in high wavenumber range. A possible cause for this anomaly can be the vestiges of the aforementioned dips in the 3-D energy spectra  $E(\kappa)$  in the small wavenumber range while the accuracy of the numerical method for the solution of (14) and (15) (Gauss elimination) should be considered. Nevertheless, despite the overprediction the slope of the experimental curve is maintained except for the large wavenumber range where the corresponding "noise" of  $E(\kappa)$  comes into play. The numerical results for the case of Warhaft and Lumley agree better with experimental data presenting however, for the aforementioned reasons, disagreement in the large wavenumber range. In the numerical results for both case, Kolmogorov's  $-5/3$  law is confirmed.

The one dimensional energy spectrum allows the computation of the integral length scale  $L$  of turbulence through the relation (see (12)):

$$L = \frac{\pi}{\frac{4}{3} \cdot k} \cdot \varphi(0) \quad (16)$$

Numerical results for  $L$  are presented in Fig. 11, along with the experimental measurements of Yeh and Van Atta. Although the slopes of both sets of data do not differ extremely the numerical results tend to be



overpredictive. Possible causes are the overprediction of  $\phi(\kappa_1)$  and the noise in  $E(\kappa)$ . The integral length scale was not computed for the data of the experimental case of Snyder and Lumley through (16) because differences in numerical and experimental data for the turbulent kinetic energy lead to an irregular behavior (not strictly increasing according to a power law) of  $L$ .

Another useful piece of information derived from the one dimensional spectrum  $\phi(\kappa_1)$  is its inverse Fourier transform, the longitudinal spatial correlation defined as:

$$R_{11}(r) = \frac{\overline{u(x) \cdot u(x+r)}}{u(x)^2} \quad (17)$$

The Fourier transform pair linking the two above quantities is (14):

$$\phi(\kappa_1) = \frac{1}{2\pi} \cdot \int_{-\infty}^{\infty} \overline{u(x) \cdot u(x+r)} \cdot \exp(-i\kappa_1 r) dr \quad (18)$$

$$\overline{u(x) \cdot u(x+r)} = \int_{-\infty}^{\infty} \phi(\kappa_1) \cdot \exp(i\kappa_1 r) \cdot d\kappa_1 \quad (19)$$

Assuming that the correlation is an even function of  $r$  the one dimensional energy spectrum  $\phi(\kappa_1)$  has a negligible imaginary part and the correlation can be computed from the inverse Fourier cosine transform of the one dimensional power spectrum (See (1)). In Fig. 12, the computed spatial correlation curve (for the experimentally measured and numerically computed spectrum  $\phi(\kappa_1)$  at  $x/M=35$ ) is depicted in comparison to the measurements of Yeh and Van Atta. The inverse Fourier cosine transform was computed for 1000 sample points of the one-dimensional energy spectrum. The inverse Fourier transform of the experimental spectrum differs slightly from the measured correlation in larger  $r$ . The inverse Fourier transform of the numerical spectrum presents differences from the measured correlation curve due to the disagreement between the numerically computed spectrum and the experimentally measured one.

## 5 CONCLUSIONS

When applied to grid turbulence, the model developed provides results (turbulence kinetic energy  $k$ , energy dissipation rate  $\varepsilon$  and turbulence length scale  $l$ ) in generally good agreement with experimental data. However, the presented model's main asset lies in the fact that it computes the energy and dissipation spectra of turbulence downstream and subsequently the turbulence integral length scale and the longitudinal

spatial correlation. As far as direct numerical simulation is concerned, the model offers us equally important information, however within a lot shorter time while providing a deeper insight into the physics of turbulence by not dwelling on the manipulation of mathematical equations. It can also be said that the present model has a simpler structure making it flexible for future application to various engineering problems. Finally, from a viewpoint of mathematical interest, multifractal distributions can be generated allowing the computation of the spectrum of fractal dimensions  $f(\alpha)$  which offers valuable information concerning the set in 3-D space occupied by the turbulent energy dissipation.

The model, however, does have some weaknesses. The velocity of the initial eddy is not a physical quantity expressing its dynamic state and it is computed through simple dimensional analysis. The same can be said for the velocities of the eddies resulting from the breakup of a larger one. Although the statistical character of our model (large number of initial eddies, randomness in size of daughter eddies etc.) counterbalances the above arbitrary assumptions, the conservation laws should be taken more into account.

As specified in a previous section, the randomness in the size of daughter eddies, leads to noise in the large wavenumber range of the energy spectra. Although noise can be expected in any kind of measurements, numerical or experimental, in the present model it leads to appreciable differences between computed quantities and experimental measurements. One option would be to approximate the energy spectra with a best fit function and to use this function to proceed with all required calculations. One possibility would be the use of Chebyshev polynomials which offer very good accuracy in approximation of the measured data.

Finally, the most critical question is whether turbulence can be modeled with non-interacting discrete structures (eddies), resulting from the Fourier transform, without departing significantly from physical reality, particularly the underlying process behind the energy cascade, vortex stretching. The orthogonal decomposition theorem of Lumley (25) and the now blooming wavelet theory (see Farge (26)) offer an alternative approach for isolating the contribution of a certain wavenumber range to the overall turbulent activity.

## APPENDIX-A THE SPECTRUM $f(\alpha)$ OF FRACTAL DIMENSIONS OF THE ENERGY DISSIPATION RATE

### A.1 Summary of the computation procedure

Briefly presented, are the steps followed in the computation of the spectrum of fractal dimensions  $f(\alpha)$

for the multifractal distribution of the energy dissipation rate  $\varepsilon$  illustrated in Fig. 8.

Let  $L$  be the domain of the distribution (in fractal terminology, the support of the measure). The measure is divided into intervals of length  $r_k$ . The procedure outlined below will be repeated for  $n_r$  different box sizes and therefore the box-size is noted by the index  $k$  where  $k=1, \dots, n_r$ .

For a given box size  $r_k$ , one defines the quantity  $X$  as the logarithm of the total measure  $p$  (representing the total dissipation in the box of size  $r_k$ ) in a box of size  $r_k$ :

$$X = \log_{10}(p) \quad (A-1)$$

where:

$$p = \varepsilon_{r_k} = \int_{r_k} \varepsilon(x) dx / \int_L \varepsilon(x) dx \quad (A-2)$$

For a given box size  $r_k$ ,  $X$  assumes values within the interval  $[X_{\min}(r_k), X_{\max}(r_k)]$ . If one plots the diagram of  $X_{\min}(r_k)$  and  $X_{\max}(r_k)$  versus  $\log_{10}(r_k/L)$ , the slope of the graph will correspond to  $\alpha_{\max}$  and  $\alpha_{\min}$  respectively. One must be reminded that for a given box size  $r_k$ :

$$p \approx (r/L)^\alpha \quad (A-3)$$

Intermediate values of  $\alpha$  are obtained as follows: For a given box size  $r_k$ , the interval  $[X_{\min}(r_k), X_{\max}(r_k)]$  is discretized into  $n$  segments of equal length  $\Delta X$ . Every segment is labeled as  $(XX_{i,k})$ , where  $i=1,2,\dots,n$  while the  $k$  index has been defined above. If one plots diagrams of  $(XX_{i,k})$  versus  $\log_{10}(r_k/L)$  these plots will yield slopes  $\alpha_i$ , which are the intermediate values between  $\alpha_{\max}$  and  $\alpha_{\min}$ . (Fig. A-1).

The fractal dimension  $f(\alpha_i)$  corresponding to each value  $\alpha_i$  is computed as follows: One measures the quantity  $N[(XX_{i,k})]$  which represents the number of boxes of size  $r_k$  for which  $X$  assumes values within the interval  $(XX_{i,k})$ . If one plots the diagram of  $\log\{N[(XX_{i,k})] * \Delta X^{1/2}\}$  versus  $\log_{10}(r_k/L)$  the slope of the graph is equal to  $-f(\alpha_i)$  (Fig. A-2). Valuable information is also provided by graphs of  $\log\{N[(XX_{i,k})] * \Delta X^{1/2}\}$  versus  $(XX_{i,k})$  (Fig. A-3).

To eliminate sensitivity of results on the positioning of the boxes during the box counting procedure (division of measure into segments of equal length) one can assume different starting points  $x_0$  arbitrarily chosen within the interval  $[0, 10^{-2} * L]$ , the first box being at  $[x_0, r_k)$ , the second one at  $[x_0 + r_k, x_0 + 2 r_k)$  etc. It is then useful to take an ensemble average of  $N[(XX_{i,k})]$  and  $(XX_{i,k})$  over several realizations of the computation procedure, each one corresponding to a different starting point.

## A.2 Interpretation of the results

One-dimensional cuts of the energy dissipation rate  $\varepsilon$  in 3-D space, i.e. the multifractal measures of  $\varepsilon$ , serve in obtaining information of the fractal characteristics of turbulence in 3-D space, since it is very difficult to make direct three dimensional measurements. The spectrum of fractal dimensions can be interpreted as follows:  $\alpha$  is representative of the order of magnitude of a certain singularity of the dissipation field while  $f(\alpha)$  is equal to the fractal dimension of the subset which is occupied in 3-D space by singularities of corresponding  $\alpha$ .

The spectrum of fractal dimensions  $f(\alpha)$  for a multifractal measure of the energy dissipation rate generated by the cascade model is given in Fig. A-4. Also displayed is  $f(\alpha)$  for both the binomial measure with  $p_1=p_2=0.5$  and  $p_1=1-p_2=0.6$  (see (19),(8)); The spectrum was computed with the aforementioned algorithm) and experimental data (19) for flows such as grid turbulence, wake of a cylinder, laboratory boundary layer and atmospheric turbulence. Unfortunately, the cascade model  $f(\alpha)$  curve has a maximum value of  $f(\alpha=1)=1.17$  while the binomial measure  $f(\alpha)$  curve also exhibits an maximum of  $f(\alpha=1)=1.17$ . This is the dimension of the set where all the singularities of the dissipation are located. Common sense dictates that for a one dimensional cut through the dissipation field, the fractal dimension cannot assume a value greater than 1. Note that, Meneveau and Sreenivasan (8) found  $f(\alpha)=0.96$ . This deviation from experimental measurements and theoretical predictions can be attributed to an inadequate number of data points in the multifractal measure. Only  $10^5$  points were used in cascade model computations whereas Meneveau and Sreenivasan computed their spectra for  $10^6$ - $10^7$ . Under the present capabilities of the computer center at NTUA it was impossible to generate such large distributions. It must be emphasized though, that as the number of data points in the multifractal measure increased so did the smoothness of the curve while its spectral maximum dropped. For  $3 \times 10^4$  points  $f(\alpha)_{\max}=1.49$  while for  $10^5$  points it dropped to  $f(\alpha)_{\max}=1.17$ . Similar observations were made during the computation of  $f(\alpha)$  for the binomial measure (maximum number of points 131072). Thus, better resolution, which entails stronger computational resources, will lead to more accurate results.

One can also note in Fig. A-4 that, large singularities, corresponding to minimum  $\alpha$ , have a very small fractal dimension and this is also the case for the weakest ones, corresponding to maximum  $\alpha$ . Finally, in the cascade model results, the set for which  $\alpha=f(\alpha)=0.87$  is the one on which all of the dissipation is concentrated asymptotically. As noted above, this

result, although agreeing with theoretical predictions, is not the most reliable one as higher resolution is required.

## LIST OF SYMBOLS

$c_m$	Empirical constant for the computation of the turbulence length scale $l$
$D(\kappa)$	Turbulent energy dissipation spectrum at wavenumber $\kappa$
$E(k)$	Turbulent energy spectrum at wavenumber $k$
$k$	Turbulent kinetic energy of entire flow
$l$	Lengthscales of turbulence or individual eddy as denoted by corresponding subscript
$L$	Turbulence integral length scale
$M_i$ ( $i=0,1$ )	Coefficients indicating distribution of energy of mother eddy into daughter eddies
$M$	Mesh size
$R_{11}(r)$	Longitudinal spatial correlation as a function of distance downstream $r$
$t$	Time after eddy launching or characteristic eddy time (as denoted by subscript)
$U$	Mean velocity of the flow
$u$	Downstream component of instantaneous velocity
$x$	Displacement downstream
$\alpha$	Empirical coefficient used in Kolmogorov's $-5/3$ law
$\gamma$	Cascade model coefficient indicating relation of daughter to mother eddy
$\varepsilon$	Turbulent energy dissipation rate
$\eta$	Kolmogorov length scale
$\kappa$	Wavenumber vector of magnitude $\kappa$
$\kappa_i$ ( $i=1,2,3$ )	Components of wavenumber vector $\kappa$
$\nu$	Fluid kinematic viscosity
$\phi(\kappa)$	One dimensional energy spectrum

**NOTE:** The symbols used in the appendix are defined in the corresponding text

## REFERENCES

- (1) Reynolds A.J. *Turbulent Flows in Engineering*, 1974, John Wiley and Sons
- (2) Sreenivasan K.R. *Fractals and Multifractals in Fluid Turbulence*, *Annu. Rev. Fluid Mech.*, 1991, 23, 539-600
- (3) Nelkin M. What do we know about self-similarity in fluid turbulence, *J. Stat. Phys.*, 1989, 54, No. 1/2, 1-15.
- (4) Humphrey J.A.C., Schuler C.A., Rubinsky B. On the use of the Weierstrass-Mandelbrot function to describe the fractal component of turbulent velocity,

*Eighth Symposium on Turbulent Shear Flows*, 1991, 16-21.

(5) Kolmogorov A.N. The local structure of turbulence in incompressible viscous flow at very large Reynolds numbers, *Dokl. Akad. Nauk SSSR*, 1941, 30, 9-13.

(6) Mandelbrot B.B. Intermittent turbulence in self-similar cascades; Divergence of high moments and dimension of the carrier, *J. Fluid Mech.*, 1974, 62(2), 331-358.

(7) Frisch U., Sulem P.L., Nelkin M. A simple dynamical model of intermittent fully developed turbulence, *J. Fluid Mech.*, 1978, 87(4), 719-736.

(8) Meneveau C., Sreenivasan K.R. The multifractal nature of turbulent energy dissipation, *J. Fluid Mech.*, 1991, 224, 429-444.

(9) Blender R. Inertial range spectrum of a fractal model for turbulence, *Z. Phys. B-Condensed Matter*, 1991, 83, 425-427.

(10) Hunt J.C.R., Vassilicos J.C. Kolmogorov's contributions to the physical and geometrical understanding of small-scale turbulence and recent developments, *Proc. Roy. Soc. Lond. A*, 1991, 434, 183-210.

(11) Yeh T.T., Van Atta C.W. Spectral transfer of scalar and velocity fields in heated-grid turbulence, *J. Fluid Mech.*, 1973, 58(2), 233-261.

(12) Snyder W.H., Lumley J.L. Some measurements of particle velocity autocorrelation functions in a turbulent flow, *J. Fluid Mech.*, 1971, 62(2), 305-360.

(13) Warhaft Z., Lumley J.L. An experimental study of the decay of temperature fluctuations in grid-generated turbulence, *J. Fluid Mech.*, 1978, 88(4), 659-684.

(14) Bradshaw P. *An Introduction to Turbulence and Its Measurements*, 1975, Pergamon Press.

(15) Chorin A.J. *Vorticity and Turbulence*, 1994, Springer-Verlag.

(16) Stanisic M.M. *The Mathematical Theory of Turbulence*, 1988, Springer-Verlag (2nd Ed.).

(17) Hinze J.O. *Turbulence*, 1975, McGraw-Hill (2nd Ed.).

(18) Kistler A.L., Vrebalovich T. Grid turbulence at large Reynolds numbers, *J. Fluid Mech.*, 1966, 26(1), 37-47.

(19) Meneveau C., Sreenivasan K.R. Simple multifractal cascade model for fully developed turbulence, *Phys. Rev. Lett.*, 1987, 59(123), 1424-1427.

(20) Benzi R. Paladin G., Parisi G., Vulpiani A. On the multifractal nature of fully developed turbulence and chaotic systems, *J. Phys. A: Math. Gen.*, 1984, 17, 3521-3531.

(21) Tennekes H., Lumley J.L. *A First Course in Turbulence*, 1974, MIT Press.

(22) Van Atta C.W., Chen W.Y. Measurements of spectral energy transfer in grid generated turbulence, *J. Fluid Mech.*, 1969, 38, 743-763.

(23) Launder B.E., Spalding D.B. *Mathematical Models of Turbulence*, 1972, Academic Press.

(24) Meneveau C., Sreenivasan K.R. Measurement of  $f(\alpha)$  from scaling of histograms and applications to dynamical systems and fully developed turbulence, Phys. Lett. A, 1989, 137(3), 103-112.

(25) Lumley J.L. Stochastic Tools in Turbulence, 1970, Academic Press, New York.

(26) Farge M. Wavelet transforms and their applications to turbulence, Annu. Rev. Fluid Mech., 1992, 24, 395-457.

	Initial Position (x/M)	Mean Velocity U(m/sec)	Mesh Size M (m)	Grid Rod Diameter d (mm)	Turbulent Kinetic Energy k ( $m^2/sec^2$ )	Fluid Viscosity $\nu$ ( $10^{-6} m^2/sec$ )
Yeh & Van Atta	25	4.06	0.04	8	0.01922	15.5
Lumley et al.	20	6	0.0254	4.7625 Square Rods	0.258595	15.6

TABLE 1 Initial conditions in experimental cases used for model validation.

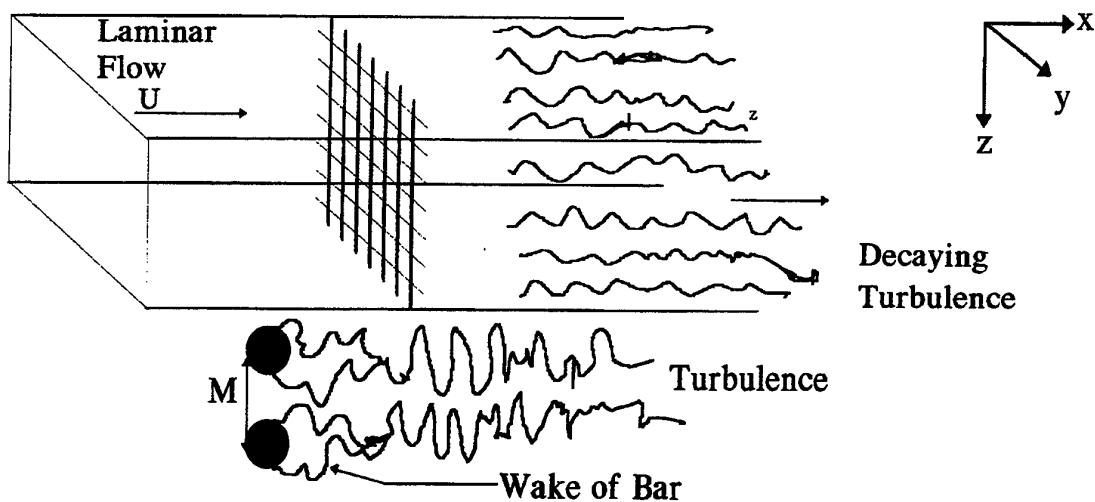


Figure 1 Grid turbulence and close up of adjacent bars.

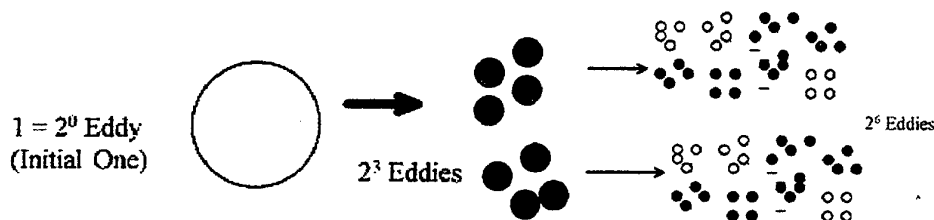


Figure 2 An eddy transported downstream and broken up into smaller ones (Different shadings correspond to different energy contents).

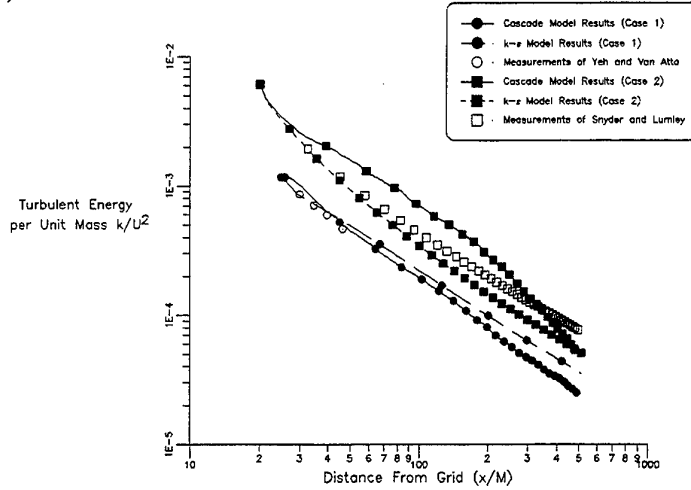


Figure 3 Cascade model results for evolution downstream of the normalized turbulent kinetic energy  $k/U^2$  for initial conditions of two cases (Case 1: (11), Case 2: (12)).

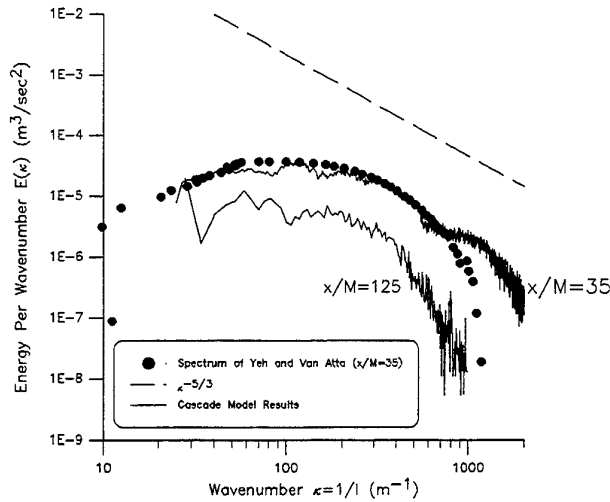


Figure 4 Cascade model results for the three dimensional energy spectrum  $E(\kappa)$  for the initial conditions of (11).

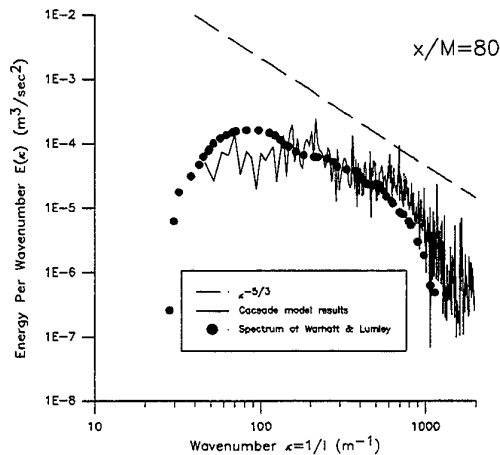


Figure 5 Cascade model results for the three dimensional energy spectrum  $E(\kappa)$  for the initial conditions of (13).

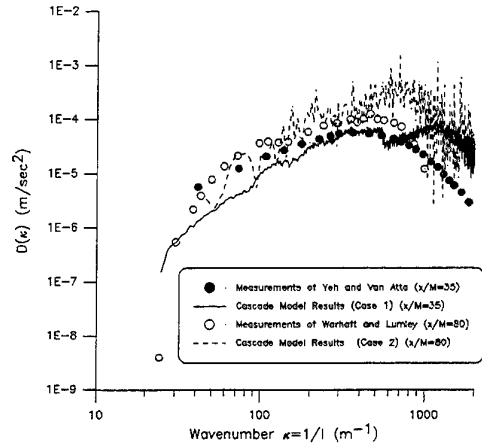


Figure 6 Cascade model results for the dissipation spectrum  $D(\kappa)$  (Case 1: (11), Case 2: (13)).

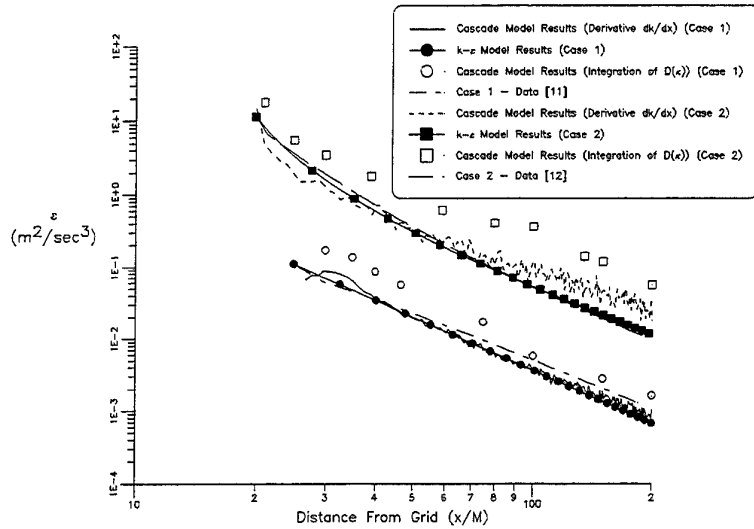


Figure 7 Cascade model results for evolution downstream of the turbulent energy dissipation rate  $\epsilon$  for initial conditions of both cases (Case 1: (11), Case 2: (12)) through two different methods of computation.

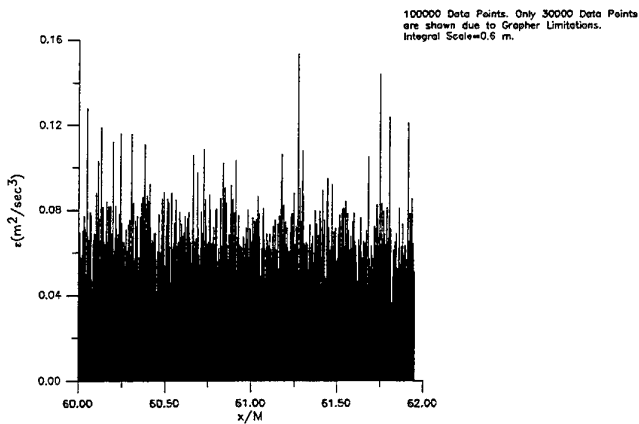


Figure 8 Computation of the energy dissipation rate  $\epsilon$  along very small distances for the initial conditions of (11).

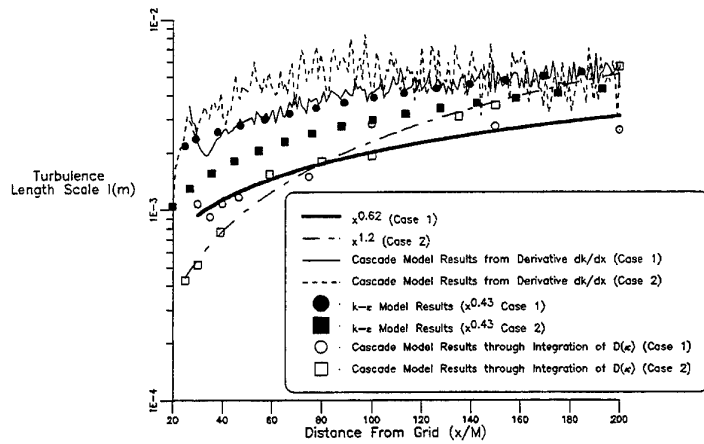


Figure 9 Cascade model results for the evolution of the turbulence length scale  $l$  (Case 1: (11), Case 2: (12)).

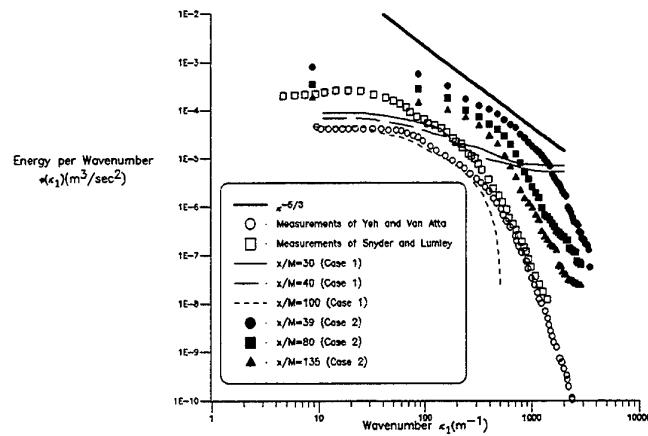


Figure 10 Cascade model results for the one-dimensional energy spectrum  $\phi(\kappa_1)$  (Case 1: (11), Case 2: (13)).

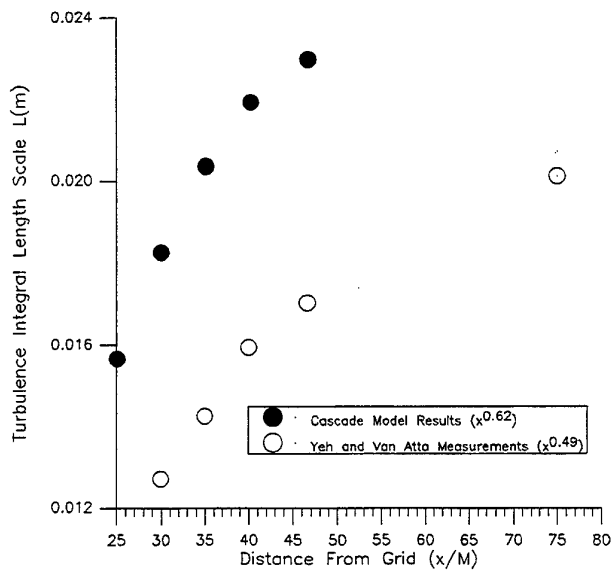


Figure 11 Cascade model results for the integral scale  $L$  of turbulence for the initial conditions of (11).

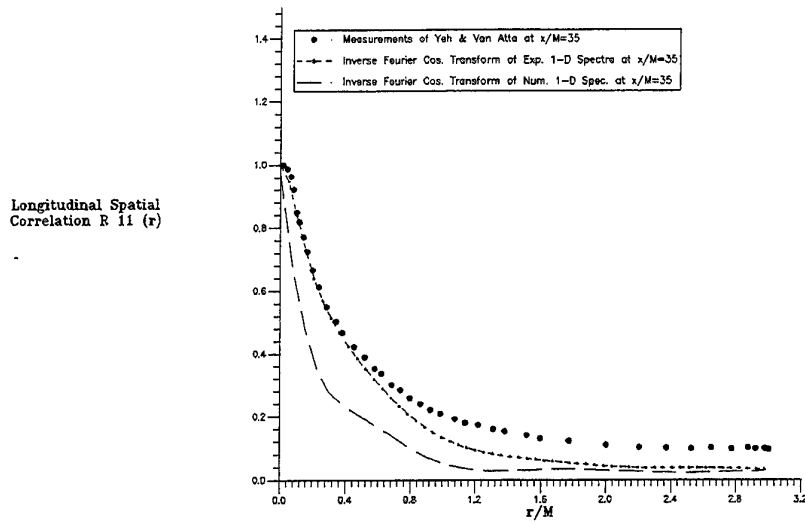


Figure 12 The spatial correlation  $R_{11}(r)$  at  $x/M=35$  as computed through the inverse Fourier cosine transform of  $\phi(\kappa_1)$  for the initial conditions of (11).

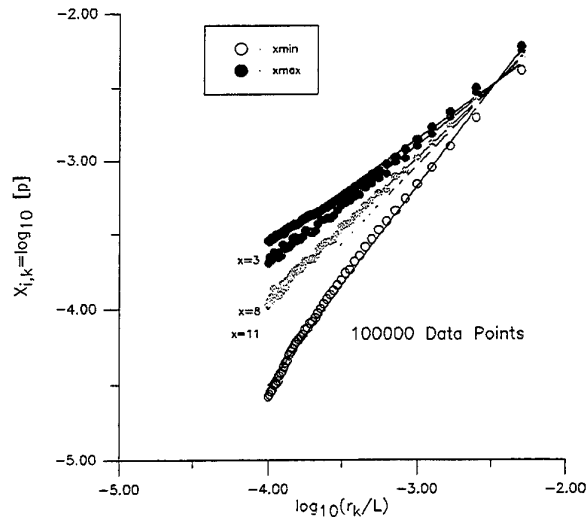


Figure A-1 Graphs of the  $XX_{i,k}$  versus  $\log_{10}(r_k/L)$ .



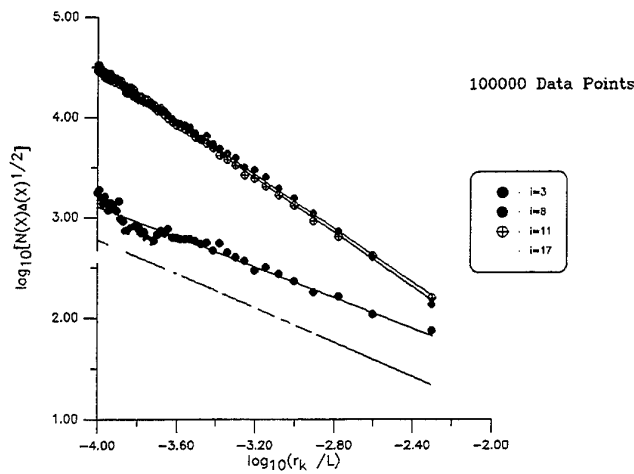


Figure A-2 Graphs of  $\log\{N[(XX_{i,k})] \cdot \Delta X^{1/2}\}$  versus  $\log_{10}(r_k/L)$ . The slope of the different curves correspond to the values of  $f(\alpha)$ .

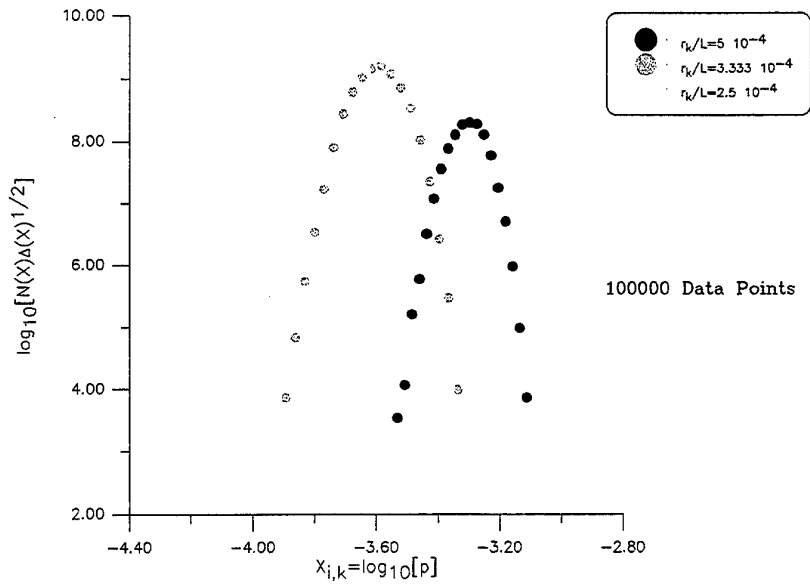


Figure A-3 Histograms of  $X$  for the multifractal measure of  $\varepsilon$  generated by the cascade model. Note that the histograms have been averaged over 50 realizations of the  $f(\alpha)$  computation procedure, with different starting points, while they include the correction factor  $\Delta X^{1/2}$ .

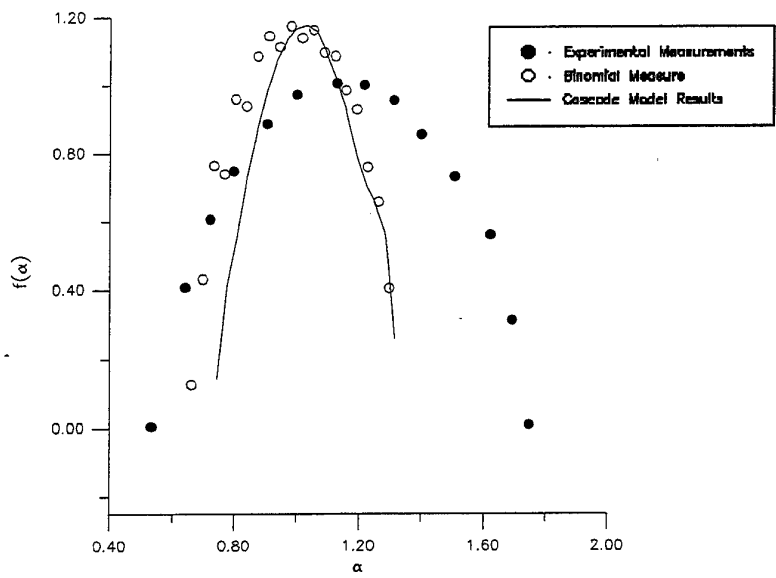


Figure A-4 Cascade model results of the multifractal spectrum of the turbulent energy dissipation rate  $\varepsilon$ . Also displayed are the corresponding spectra for the binomial measure with parameters  $l_1=l_2=0.5$  and  $p_1=1-p_2=0.6$  and that of experimental data found in (8).

# SECOND-MOMENT COMPUTATIONS OF THE THREE-DIMENSIONAL THERMAL WALL JET

T.J. Craft

Department of Mechanical Engineering  
UMIST  
Manchester, UK

## ABSTRACT

The paper reports computational predictions of a fully developed 3-dimensional heated turbulent wall jet, employing a low-Reynolds-number second-moment closure. The method of obtaining similarity equations which allow such a flow to be computed with a two-dimensional solver is outlined, and results are compared to existing experimental data with generally good agreement. The model is found to predict a larger spreading rate of the jet in the lateral direction than normal to the wall, in fact returning a ratio of spreading rates higher than that found experimentally. Initial predictions of the thermal field are reported, which show reasonable agreement with the rather sparse available experimental data.

## 1 INTRODUCTION

Turbulent wall jets can be found in many engineering applications, including boundary layer control devices, film cooling and a variety of ventilation and heating situations. In many cases of interest the jet is 3-dimensional, being discharged from a nozzle close to, and parallel to, a surface and then spreading in both the wall-normal and lateral directions.

Despite their importance in practical applications, there are relatively few experimental or computational studies of 3-dimensional wall jets, and even fewer which consider heat-transfer. A number of experimental studies [1-5], and the review of Launder & Rodi [6], have confirmed that a turbulent wall jet spreads more rapidly in the lateral direction than in the wall-normal direction, with measurements indicating lateral spreading rates of between five and nine times the wall-normal ones.

Kebede [8] reported some early computations of the fully-developed 3-dimensional wall jet. He employed eddy-viscosity models, but was unable to predict the large lateral growth of the jet. On the other hand, some more recent calculations reported at an ERCOFTAC/IAHR workshop on refined turbulence modelling [9], employing Reynolds stress transport models, did show a large lateral spreading rate: in fact *higher* than those reported experimentally. This was attributed by [10] to the ability of the models to predict an anisotropic stress distribution.

When considering the thermal wall jet, different regions of the jet can be studied by varying the relative temperatures of the jet, the ambient air and the wall. For an adiabatic wall, for example, it is the outer, secondary flow induced features of the jet which are most influential, whereas for an incoming jet at the same temperature as the ambient air, but

flowing over a heated wall, the near-wall region is more important.

Some measurements of the thermal field were reported by Koso & Ohashi [7], who studied a heated jet although, unfortunately, the thermal boundary condition at the wall was not well-defined. Their measurements indicated that the thermal spreading rate was also larger in the lateral direction than normal to the wall, although the ratio of lateral to wall-normal spreading rate was less than for the dynamic field. However, their measurements only extended to 50 jet diameters downstream, and a fully-developed state for all quantities was not achieved.

The present study is aimed at extending the computational programme of [10] to include predictions of the thermal field. The work is at a preliminary stage, and this contribution reports the methodology employed and some initial results arising from the study.

## 2 MATHEMATICAL FORMULATION

Although a full 3-dimensional solution would be required to predict the developing jet, for the case of a fully-developed 3-dimensional wall jet, similarity equations can be obtained, allowing the solution to be obtained from a 2-dimensional calculation.

The method employed here is an extension of that described by Kebede [8], who neglected the viscous, near-wall region (since his calculations employed wall-functions) and applied the thin shear layer approximations. In the present work, neither of these approximations is made, and the method is extended to compute the thermal field of the jet.

With the coordinates  $x'_1$ ,  $x'_2$  and  $x'_3$  defined as in Figure 1, where  $x'_3$  is in the streamwise direction,  $x'_2$

the wall-normal and  $x'_1$  the lateral direction, similarity equations can be derived by non-dimensionalising all quantities using a reference length  $\delta_r$  and velocity  $W_r$ :

$$x_1 = x'_1/\delta_r \quad x_2 = x'_2/\delta_r \quad x_3 = x'_3/\delta_r \quad (1)$$

$$U_i = U'_i/W_r \quad \overline{u_i u_j} = \overline{u'_i u'_j}/W_r^2 \quad (2)$$

$$\varepsilon = \varepsilon'/(W_r^3/\delta_r) \quad P = (P' - P'_\infty)/W_r^2 \quad (3)$$

$$\mu = \mu'/(W_r \delta_r) \quad (4)$$

The quantities  $\delta_r$  and  $W_r$  will be defined later, but with suitable definitions they will ensure that the non-dimensional dependent variables are functions of only the cross-jet coordinates  $x_1$  and  $x_2$ . Applying these transformations to the Reynolds averaged Navier-Stokes equations then leads to

$$\begin{aligned} \frac{\partial}{\partial x_1} [\rho U_1^* U_i] + \frac{\partial}{\partial x_2} [\rho U_2^* U_i] &= S u_i \\ + \frac{\partial}{\partial x_1} \left[ \mu (1 + \beta^2 x_1^2) \frac{\partial U_i}{\partial x_1} \right] + \frac{\partial}{\partial x_1} \left[ \mu \beta^2 x_1 x_2 \frac{\partial U_i}{\partial x_2} \right] \\ + \frac{\partial}{\partial x_2} \left[ \mu \beta^2 x_1 x_2 \frac{\partial U_i}{\partial x_1} \right] + \frac{\partial}{\partial x_2} \left[ \mu (1 + \beta^2 x_2^2) \frac{\partial U_i}{\partial x_2} \right] \end{aligned} \quad (5)$$

where the modified convective velocities  $U_1^*$  and  $U_2^*$  are

$$U_1^* = U_1 - \beta U_3 x_1 \quad U_2^* = U_2 - \beta U_3 x_2 \quad (6)$$

and the source terms  $S u_i$  are summarised in Table 1. The continuity equation becomes

$$\frac{\partial U_1^*}{\partial x_1} + \frac{\partial U_2^*}{\partial x_2} + (\alpha + 2\beta) U_3 = 0 \quad (7)$$

and the quantities  $\alpha$  and  $\beta$  are defined as

$$\alpha = \frac{\delta_r}{W_r} \frac{dW_r}{dx'_3} \quad \beta = \frac{d\delta_r}{dx'_3} \quad (8)$$

These two quantities can be related to each other by considering the streamwise momentum balance, which yields:

$$2(A + B)(\alpha + \beta) = -\sigma + 2C(\alpha^2 + 3\alpha\beta + 2\beta^2) \quad (9)$$

where

$$A = \int \int \rho U_3^2 dx_1 dx_2 \quad (10)$$

$$B = \int \int (P + \rho \overline{u_3^2}) dx_1 dx_2 \quad (11)$$

$$C = \int \int \mu U_3 dx_1 dx_2 \quad (12)$$

$$\sigma = \int \mu \left. \frac{\partial U_3}{\partial x_2} \right|_{x_2=0} dx_1 \quad (13)$$

If the usual thin shear layer approximations are made, this approach yields the simpler expression obtained by Kebede in place of equation (9):

$$2(A + B)(\alpha + \beta) = -\sigma \quad (14)$$

Although the more complete forms were employed in the present calculations, negligible differences in the predictions were seen when the thin shear layer approximations were employed.

The value of  $\beta$ , defining the streamwise coordinate stretching, can arbitrarily be taken as unity, as can the total momentum flux  $A$ . The quantity which determines  $W_r$ ,  $\alpha$ , can then be obtained from equation (9) by updating the values for  $B$ ,  $C$ , and  $\sigma$  after each iteration of the solution process.

The transport equations for the Reynolds stresses and dissipation rate  $\varepsilon$  can be similarly transformed, and written in the form

$$\begin{aligned} \frac{\partial}{\partial x_1} [\rho U_1^* \overline{u_i u_j}] + \frac{\partial}{\partial x_2} [\rho U_2^* \overline{u_i u_j}] = \\ - \rho(3\alpha + 2\beta) U_3 \overline{u_i u_j} + P_{ij} + \phi_{ij} - \varepsilon_{ij} + d_{ij} \end{aligned} \quad (15)$$

where  $P_{ij}$ ,  $\phi_{ij}$ ,  $\varepsilon_{ij}$  and  $d_{ij}$  are the production, pressure-strain process, dissipation and diffusion of the Reynolds stresses, and

$$\begin{aligned} \frac{\partial}{\partial x_1} [\rho U_1^* \varepsilon] + \frac{\partial}{\partial x_2} [\rho U_2^* \varepsilon] = \\ - \rho(4\alpha + \beta) U_3 \varepsilon + P_\varepsilon - D_\varepsilon + d_\varepsilon \end{aligned} \quad (16)$$

where  $P_\varepsilon$ ,  $D_\varepsilon$  and  $d_\varepsilon$  represent the generation, destruction and diffusion of  $\varepsilon$ .

The temperature can be treated in a similar fashion, by defining a reference temperature  $T_r$ , non-dimensional temperature  $T = T'/T_r$ , and thermal diffusivity  $\Gamma = \Gamma/(W_r \delta_r)$ . The transformed transport equation for  $T$  can then be written as

$$\begin{aligned} \frac{\partial}{\partial x_1} [\rho U_1^* T] + \frac{\partial}{\partial x_2} [\rho U_2^* T] = \\ - \rho(\alpha + 2\beta + \gamma) U_3 T - \frac{\partial}{\partial x_1} (\rho \overline{u_1 t}) - \frac{\partial}{\partial x_2} (\rho \overline{u_2 t}) \\ + \beta x_1 \frac{\partial}{\partial x_1} (\rho \overline{u_3 t}) + \beta x_2 \frac{\partial}{\partial x_2} (\rho \overline{u_3 t}) - \rho(\alpha + \gamma) \overline{u_3 t} \\ + \frac{\partial}{\partial x_1} \left[ \Gamma (1 + \beta^2 x_1^2) \frac{\partial T}{\partial x_1} \right] + \frac{\partial}{\partial x_1} \left[ \Gamma \beta^2 x_1 x_2 \frac{\partial T}{\partial x_2} \right] \\ + \frac{\partial}{\partial x_2} \left[ \Gamma \beta^2 x_1 x_2 \frac{\partial T}{\partial x_1} \right] + \frac{\partial}{\partial x_2} \left[ \Gamma (1 + \beta^2 x_2^2) \frac{\partial T}{\partial x_2} \right] \\ - (\alpha\beta + 2\beta\gamma + 2\beta^2) \Gamma \left[ x_1 \frac{\partial T}{\partial x_1} + x_2 \frac{\partial T}{\partial x_2} \right] \\ + (\gamma\beta + \gamma^2) \Gamma T \end{aligned} \quad (17)$$

where  $\gamma$  is defined as

$$\gamma = \frac{\delta_r}{T_r} \frac{dT_r}{dx'_3} \quad (18)$$

By considering the total temperature flux balance,  $\gamma$  can be related to  $\alpha$  and  $\beta$  via

$$\begin{aligned} (A_t + B_t)(\alpha + \gamma + 2\beta) = \\ - \sigma_t + C_t(\gamma^2 + 2\alpha\beta + 5\gamma\beta + 4\beta^2) \end{aligned} \quad (19)$$

where

$$A_t = \int \int \rho U_3 T dx_1 dx_2 \quad (20)$$

$$B_t = \int \int \rho \overline{u_3 t} dx_1 dx_2 \quad (21)$$

$$C_t = \int \int \Gamma T dx_1 dx_2 \quad (22)$$

$$\sigma_t = \int \Gamma \left. \frac{\partial T}{\partial x_2} \right|_{x_2=0} dx_1 \quad (23)$$

Again, the total flux  $A_t$  can be prescribed as unity, and equation (19) then employed to update  $\gamma$  after each iteration.

### 3 TURBULENCE MODELLING DETAILS

For the dynamic field the low-Reynolds-number stress model of Craft [11] has been employed. This is based on the high-Reynolds-number realizable model described by Craft et al [12], but extended to account for wall influences *without* employing geometry specific quantities such as wall-distances or normal vectors.

In the present preliminary calculations, a much simpler modelling approach is employed for the turbulent heat fluxes which are approximated using the generalised gradient diffusion hypothesis (GGDH) of Daly & Harlow [13]:

$$\overline{u_i t} = -c_\theta \frac{k}{\varepsilon} \overline{u_i u_j} \frac{\partial T}{\partial x_j} \quad (24)$$

with the coefficient  $c_\theta$  taken as 0.25.

### 4 NUMERICAL DETAILS

The calculations were performed using a modified and extended version of the STREAM computer code, originally developed by Lien & Leschziner [14]. This employs a fully collocated grid arrangement with Rhie & Chow interpolation [15] for the mass fluxes to avoid chequerboarding, Van Leer's MUSCL scheme [16] for convection, and the SIMPLE pressure correction algorithm [17].

In the presently-used version of the code, the modified convection velocities appearing in the transport equations were added, as were the various additional source terms. At the end of each iteration the momentum and temperature flux were corrected and the values of  $\alpha$  and  $\gamma$  updated. Since the temperature was treated as a passive scalar, the dynamic field was first converged without solving the temperature equation. Having obtained a converged velocity field, the thermal field was then solved for.

A simple rectangular Cartesian grid was adopted, covering the domain shown in Figure 2.

with grids of up to 120 (lateral) by 80 (wall-normal), which were clustered near the wall to ensure that near-wall values of  $y^+$  were less than unity. The physical size of the domain was determined by trial and error, and had to be large enough to ensure that the entrainment boundaries were sufficiently far away from the jet that the flow could be considered undisturbed. Because of the large predicted lateral spreading rate, this necessitated a domain with an aspect ratio of around 10.

## 5 RESULTS AND DISCUSSION

Before examining the thermal field, it is instructive to first consider the predictions of the dynamic field. The results presented correspond to a jet at a Reynolds number  $Re = W_m y_{1/2} / \nu$  of 3500, although additional calculations showed that, at Reynolds numbers of this order of magnitude, the results were only very weakly dependent on the Reynolds number.

Figure 3 shows the computed secondary flow vectors in the cross-stream plane, from which it can be seen that the model predicts a strong lateral out-flow and significant entrainment through the upper boundary. The predicted spreading rates are shown in Table 2, together with a number of experimental measurements for comparison. As commented earlier, the wall-normal spreading rate is approximately in agreement with the experimental data, although the lateral rate of spread is overpredicted.

As reported earlier in [10], computations with a linear Reynolds stress closure employing wall-reflection terms returned an even higher spreading rate ratio. When wall-reflection terms were turned off, resulting in almost identical  $\overline{u_1^2}$  and  $\overline{u_2^2}$  predictions, the spreading rate ratio dropped to the level of that predicted by  $k$ - $\varepsilon$  schemes, suggesting that the model's ability to capture the anisotropic stress distribution is crucial to predicting the 3-dimensional wall jet spreading rates.

Figure 4 shows predicted profiles in the vertical plane  $x_1 = 0$ , compared with the data of [5], whilst Figure 5 shows profiles in the horizontal plane through the point of maximum velocity. Generally good agreement with the data is seen, although Figure 4 shows that the streamwise stress component is underpredicted in the near-wall region. As a consequence, the turbulence quantities in Figure 5 are also underpredicted, since these profiles correspond to a distance of  $x_2/y_{1/2} \approx 0.25$ . At the somewhat larger distance of  $x_2/y_{1/2} = 0.47$ , the streamwise stress is still underpredicted, but the other components are in better agreement with the data as shown in Figure 6.

For the initial computations of the thermal field, a constant wall temperature equal to the ambient air temperature was applied. The resultant predicted

spreading rates were

$$\frac{dy_{t1/2}}{dx_3} = 0.07 \quad \frac{dx_{t1/2}}{dx_3} = 0.518 \quad (25)$$

This agrees qualitatively with the findings of [7] that the thermal spreading rate ratio is less than that of the dynamic field, although the experiments did not go sufficiently far downstream for a fully self-preserved state to be attained, and so a quantitative comparison is rather difficult.

Predicted profiles of the mean temperature and turbulent heat fluxes at the symmetry plane  $x_1 = 0$  are shown in Figure 7. Although the experiments of [7] did employ a different wall boundary condition, which explains the difference in the near-wall behaviour of  $\overline{u_2 t}$ , agreement with the data in both this plane and the horizontal plane through the point of maximum temperature (shown in figure 8) is encouraging. The streamwise heat flux,  $u_3 t$  is clearly underpredicted, although this might well be expected with the present rather simple GGDH model for the heat fluxes.

## 6 CONCLUSIONS

The computational method employed has successfully been applied to the 3-dimensional wall jet, and it has been shown that a stress transport model capable of predicting anisotropic normal stresses can predict large lateral spreading rates as are found experimentally. However, some further model refinement is needed to get good quantitative agreement with the experimental spreading rates.

Initial predictions of the thermal field have also shown reasonable agreement with the rather limited available data. Further comparisons should be possible with the emerging data of [19], together with investigations of the effects of varying the jet, ambient and wall temperature, and of employing more elaborate transport models for the turbulent heat fluxes.

## Acknowledgements

The author would like to thank the Royal Society of London for funding the work through a University Research Fellowship.

## Nomenclature

$k$	turbulent kinetic energy.
$P$	mean pressure.
$T'$	dimensional mean temperature.
$T$	non-dimensional mean temperature.
$T_m$	maximum temperature.
$T_r$	reference temperature.
$U'_1, U'_2, U'_3$	dimensional mean velocity components.

$U_1, U_2, U_3$	non-dimensional mean velocity components.
$\overline{u_i u_j}$	Reynolds stress tensor.
$\overline{u_i t}$	turbulent heat flux.
$W_m$	maximum streamwise velocity.
$W_r$	reference velocity.
$x'_1, x'_2, x'_3$	dimensional coordinate directions.
$x_1, x_2, x_3$	non-dimensional coordinate directions.
$y_{1/2}$	jet half-width in wall-normal direction.
$y_{t1/2}$	jet thermal half-width in wall-normal direction.
$x_{1/2}$	jet half-width in lateral direction.
$x_{t1/2}$	jet thermal half-width in lateral direction.
$\alpha, \beta, \gamma$	parameters arising in similarity equations.
$\Gamma$	thermal diffusivity.
$\delta_r$	reference length.
$\varepsilon$	dissipation rate of $k$ .
$\mu$	dynamic viscosity.
$\nu$	kinematic viscosity.
$\rho$	fluid density.

## References

1. Newman, B.G., Patel, R.P., Savage, S.B., Tjio, H.K. "Three-dimensional wall jet originating from a circular orifice", *Aeronautical Quarterly*, 1972, **23**, 188-200.
2. Davis, M.R., Winarto, H. "Jet diffusion from a circular nozzle above a solid surface", *J. Fluid Mech.*, 1980, **101**, 201-221.
3. Fujisawa, N., Shirai, H. "Mean flow and turbulence characteristics of three-dimensional wall jet along plane surface", *Trans. Japan Soc. Aero. Space Sci.*, 1989, **32**, 35-46.
4. Matsuda, H., Iida, S., Hayakawa, M. "Coherent structures in a three-dimensional wall jet", *Trans. ASME J. Fluids Engineering*, 1990, **112**, 462-467.
5. Abrahamsson, H., Johansson, B., Löfdahl, L. "An investigation of the turbulence field in a three-dimensional wall jet", in *Advances in Turbulence VI* (eds. Gavrilakis et al), 1996, Kluwer.
6. Launder, B.E., Rodi, W. "The turbulent wall jet, measurements and modelling", *Ann. Review Fluid Mech.*, 1983, **15**, 429-459.
7. Koso, T., Ohashi, H. "Turbulent diffusion of a three-dimensional wall jet (1st report, mean and turbulent characteristics of velocity and temperature field)", *Bulletin of the JSME*, 1982, **25**, 173-181.
8. Kebede, W. "Numerical study of the three dimensional wall jet", M.Sc. Dissertation, Faculty of Technology, University of Manchester, 1982.
9. Proceeding of 6th ERCOFTAC/IAHR/COST Workshop on Refined Flow Modelling. (eds. Hanjalić & Obi), June 1997, Delft.
10. Craft, T.J. "Computations of plane and 3-dimensional wall jets", 8th Biennial Colloquium on

Computational Fluid Dynamics, April 1998, Dept. of Mech. Eng., UMIST.

11. Craft, T.J. "Developments in a low-Reynolds-number second-moment closure and its application to separating and reattaching flows", To appear in *Int. J. Heat Fluid Flow*.
12. Craft, T.J., Ince, N.Z., Launder, B.E. "Recent developments in second-moment closure for buoyancy-affected flows", *Dynamics of atmospheres and oceans*, 1996, **23**, 99-114.
13. Daly, B.J., Harlow, F.H. "Transport equations in turbulence", *Phys. Fluids*, 1970, **13**, 2634.
14. Lien, F-S., Leschziner, M.A. "A general non-orthogonal finite-volume algorithm for turbulent flow at all speeds incorporating second-moment turbulence-transport closure", *Computer Meth. Appl. Mech. Eng.*, 1994, **114**, 123-167.
15. Rhie, C.M., Chow, W.L. "Numerical study of

the turbulent flow past an airfoil with trailing edge separation", *AIAA J.*, 1983, **21**, 1525-1532.

16. Van Leer, B. "Towards the ultimate conservation difference scheme V, a second-order sequel to Godunov's method", *J. Comput. Phys.*, 1979, **32**, 101.
17. Patankar, S.V. *Numerical Heat Transfer and Fluid Flow*, 1980, McGraw-Hill.
18. Padmanabham, G., Gowda, B.H.L. "Mean and turbulence characteristics of a class of three-dimensional wall jets - Part 1: Mean flow characteristics", *J. of Fluids Engineering*, 1991, **113**, 620-628.
19. Bridon, R., Hammond, G.P., Lock, G.D. "Application of thermal imaging to determine the heat transfer characteristics of three-dimensional, turbulent wall jets", *Proc. of Turbulent heat Transfer - 2*, 1998, Manchester.

$Su_1$	$-\frac{\partial P}{\partial x_1} - \frac{\partial}{\partial x_1}(\overline{\rho u_1^2}) - \frac{\partial}{\partial x_2}(\overline{\rho u_1 u_2}) + \beta x_1 \frac{\partial}{\partial x_1}(\overline{\rho u_1 u_3}) + \beta x_2 \frac{\partial}{\partial x_2}(\overline{\rho u_1 u_3}) - 2\rho\alpha\overline{u_1 u_3}$ $- 2\rho(\alpha + \beta)U_1 U_3 - (3\alpha\beta + 2\beta^2)\mu \left[ x_1 \frac{\partial U_1}{\partial x_1} + x_2 \frac{\partial U_1}{\partial x_2} \right] + 2\alpha^2\mu U_1$
$Su_2$	$-\frac{\partial P}{\partial x_2} - \frac{\partial}{\partial x_1}(\overline{\rho u_1 u_2}) - \frac{\partial}{\partial x_2}(\overline{\rho u_2^2}) + \beta x_1 \frac{\partial}{\partial x_1}(\overline{\rho u_2 u_3}) + \beta x_2 \frac{\partial}{\partial x_2}(\overline{\rho u_2 u_3}) - 2\rho\alpha\overline{u_2 u_3}$ $- 2\rho(\alpha + \beta)U_2 U_3 - (3\alpha\beta + 2\beta^2)\mu \left[ x_1 \frac{\partial U_2}{\partial x_1} + x_2 \frac{\partial U_2}{\partial x_2} \right] + 2\alpha^2\mu U_2$
$Su_3$	$-\frac{\partial}{\partial x_1}(\overline{\rho u_1 u_3}) - \frac{\partial}{\partial x_2}(\overline{\rho u_2 u_3})$ $+ \beta x_1 \frac{\partial}{\partial x_1}(\overline{\rho u_3^2} + P) + \beta x_2 \frac{\partial}{\partial x_2}(\overline{\rho u_3^2} + P) - 2\rho\alpha(\overline{u_3^2} + P)$ $- 2\rho(\alpha + \beta)U_3^2 - (3\alpha\beta + 2\beta^2)\mu \left[ x_1 \frac{\partial U_3}{\partial x_1} + x_2 \frac{\partial U_3}{\partial x_2} \right] + 2\alpha^2\mu U_3$

Table 1: Source terms in the transformed mean momentum equations.

	$dy_{1/2}/dx_3$	$dx_{1/2}/dx_3$	$(dx_{1/2}/dx_3)/(dy_{1/2}/dx_3)$
Present Computations	0.060	0.515	8.56
Abrahamsson et al [5]	0.065	0.32	4.9
Padmanabham & Gowda [18]	0.043	0.22	5.0
Fujisawa & Shirai [3]	0.059	0.32	5.4
Davies & Winarto [2]	0.037	0.32	8.6

Table 2: Dynamic field spreading rates in the 3-dimensional jet.

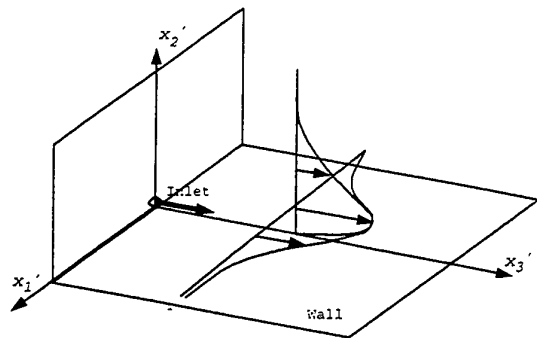


Figure 1: The 3-dimensional jet.

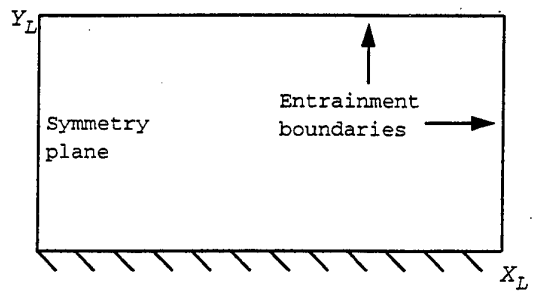


Figure 2: The computational domain.

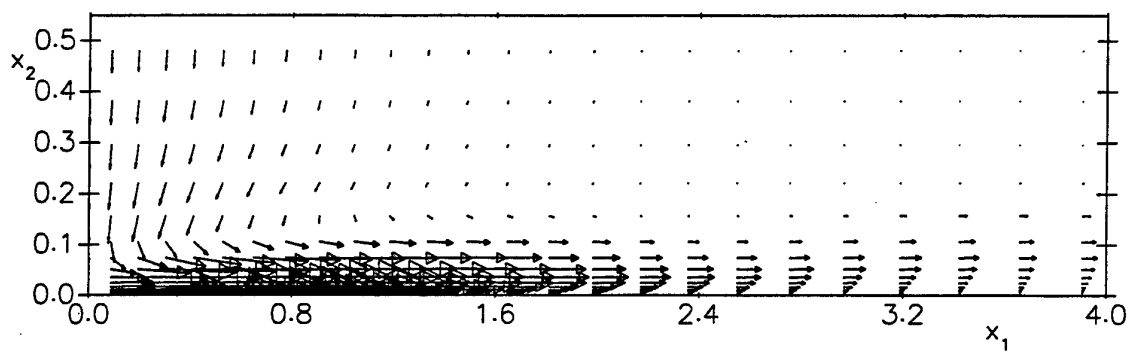


Figure 3: Predicted secondary flow vectors.

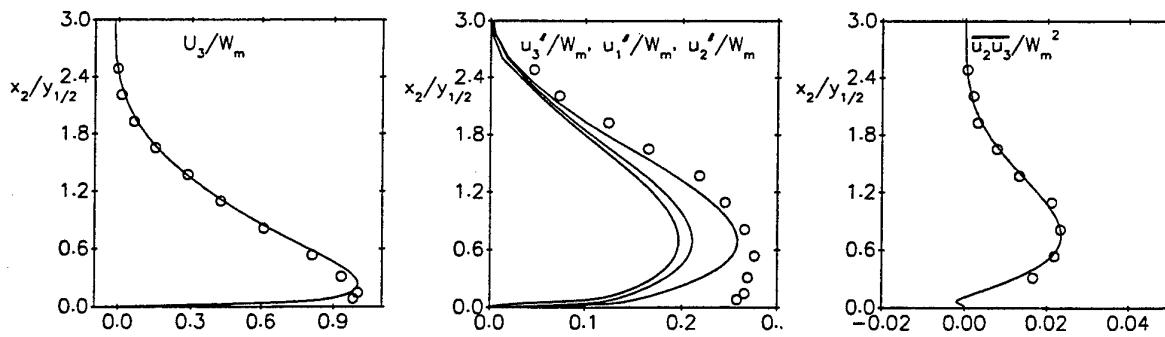


Figure 4: Streamwise velocity, rms velocities and shear stress profiles on the symmetry plane  $x_1 = 0$ .



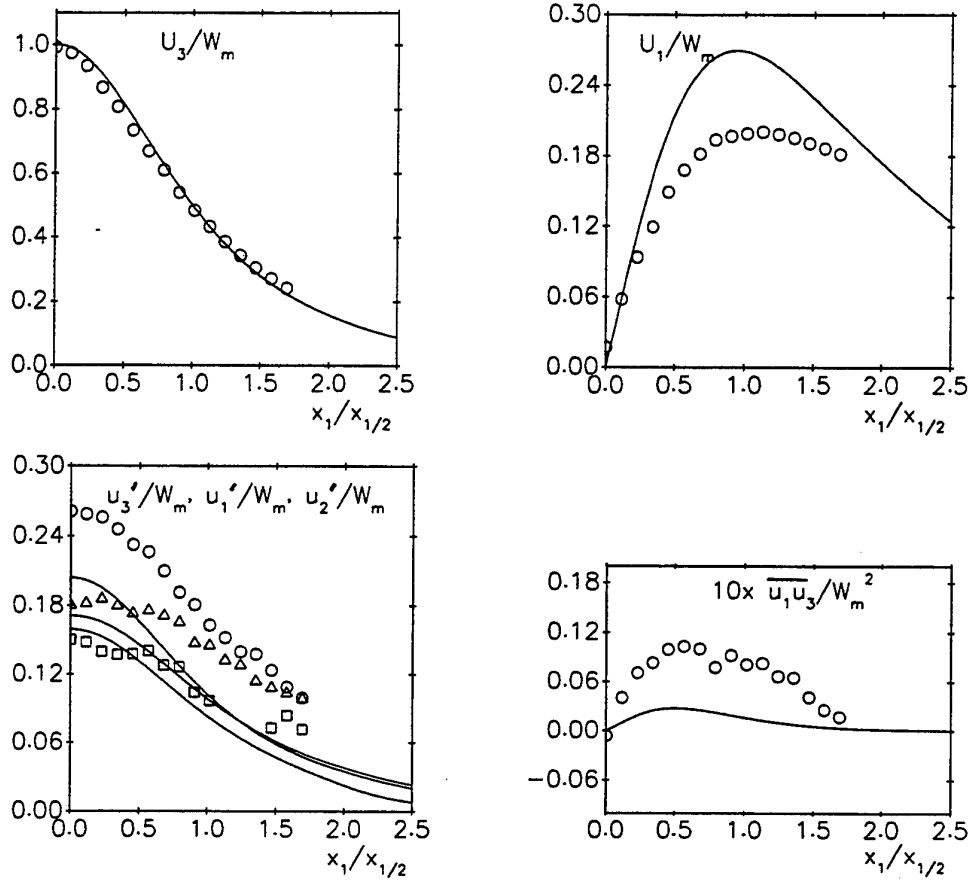


Figure 5: Streamwise velocity, lateral velocity, rms velocities and shear stress profiles on the horizontal plane through the point of maximum velocity.

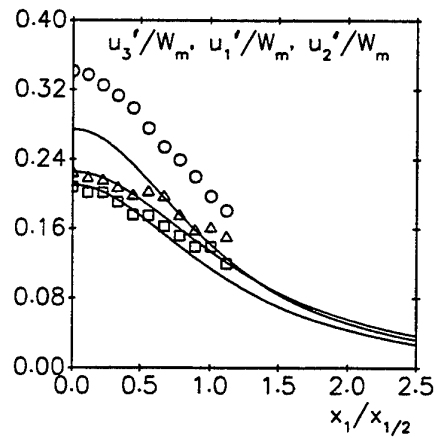


Figure 6: Rms velocity profiles in a horizontal plane through  $x_2 = 0.47y_{1/2}$ .

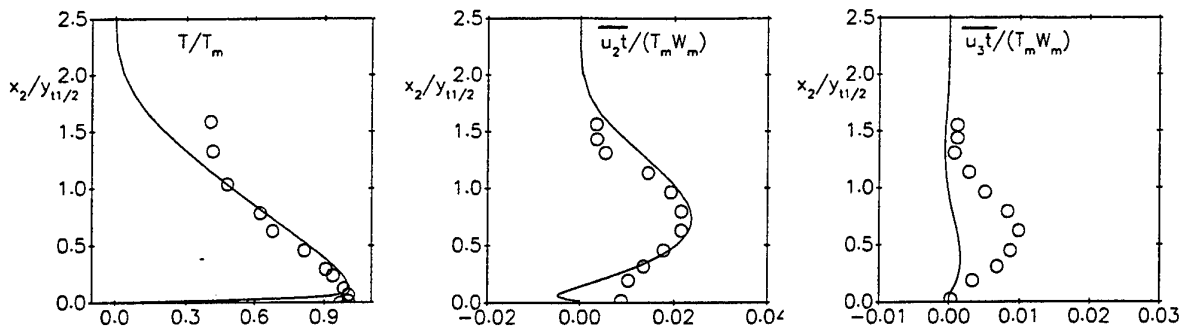


Figure 7: Mean temperature and heat flux profiles on the symmetry plane  $x_1 = 0$ .

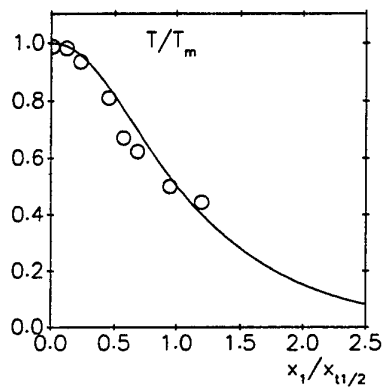


Figure 8: Temperature profile in the horizontal plane through the point of maximum temperature.

# APPLICATION OF THERMAL IMAGING TO DETERMINE THE HEAT TRANSFER CHARACTERISTICS OF THREE-DIMENSIONAL, TURBULENT WALL JETS

R Bridon, GP Hammond and GD Lock

Department of Mechanical Engineering  
Faculty of Engineering and Design  
University of Bath  
Bath, BA2 7AY, United Kingdom

## ABSTRACT

The heat transfer characteristics of a heated, three-dimensional, turbulent wall jet have been studied. This jet was formed by the ejection of a hot stream of air from a small-aspect-ratio (1:1.5), rectangular nozzle over a flat-plate test section. An infra-red thermal imaging camera has been used to measure the surface temperature beneath the wall jet in both steady-state and transient experiments. The one-dimensional heat-conduction equation is solved using specified thermal boundary conditions to yield the local wall-jet cooling effectiveness and heat transfer coefficient. The experiments are supported by steady-state temperature and aerodynamic measurements within the jet, using a simple thermocouple and Pitot-static probe. The jet Reynolds number was held constant at about 60,000, for which the mean flowfield was found to coincide with earlier studies.

## 1. INTRODUCTION

Wall jets of various types are widely used for industrial applications such as gas turbine film cooling and aircraft blown flaps, as well as in heating and air-conditioning practice (1). Such jets occur whenever a fluid is discharged from an aperture or nozzle, and then flows over an adjacent surface that is initially parallel to the nozzle axis. The critical Reynolds number for jet flows is of the order 10, while wall jets are normally considered "fully turbulent" at aperture Reynolds numbers greater than about  $3.5 \times 10^3$  and are self-similar for Reynolds numbers about  $3.4 \times 10^5$ . In most practical situations, wall jets typically operate with Reynolds numbers closer to the latter values, and their far field may be regarded as composed of two interacting turbulent shear layers: an inner (or boundary) layer and an outer (or mixing) layer. Launder and Rodi (2) produced a comprehensive review of experiments pertaining to turbulent wall jets. At the time of this review, and since, there has been a lack of experimental heat transfer data for three-dimensional wall jets. Such data is required particularly for CFD code validation.

A three-dimensional wall jet is defined as one emanating from an orifice of finite width, as illustrated in Figure 1. The flow characteristics must be considered both along and across the jet.

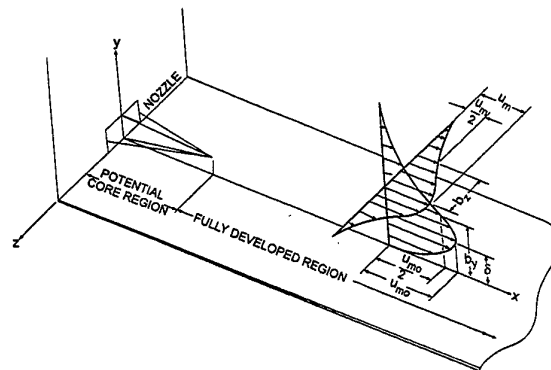


Fig.1. Schematic Representation of Three-dimensional Wall Jets [adapted from Rajaratnam and Pani (15)]

Three regions may be identified where, in each, the maximum velocity ( $u_m$ ) decays at different rates in the axial ( $x$ ) direction. These regions are the *Potential Core Region (I)*, where  $u_m$  remains constant; the *Characteristic Decay Region (II)*, where the geometry of the nozzle has an influence on the decay of  $u_m$ ; and the *Radial Decay Region (III)*, where  $u_m$  decays as a radial jet irrespective of the nozzle geometry.

Launder and Rodi (2) have reviewed three-dimensional wall-jet data obtained using a variety of nozzle geometries. In the work reported here a simple, rectangular nozzle is used with a heated wall jet efflux at a nominal

Reynolds number of  $6 \times 10^4$ . The measured aerodynamic flow field is shown to exhibit the classic characteristics expected of a three-dimensional wall jet. Thermal image techniques are used to measure the heat transfer characteristics of this jet in both transient and steady-state experiments, and the focus of this paper is on the practical issues concerning these measurements. Data has been obtained on the mean flow and thermal field, and surface cooling effectiveness and heat transfer coefficient (or Stanton number).

## 2. WALL JET THERMAL BOUNDARY CONDITIONS

The thermal boundary conditions for a heated jet are  $T_{mo} > T_w = T_\infty$  where the suffices denote maximum, wall and free-stream conditions respectively (see Figure 2). In this case, the thermal conditioning of the supply air takes place before it is discharged over the test plate, and the are nominally the same;  $\delta = \delta_\theta$ . However, there is a lack of clarity in the literature between these boundary conditions and those for the heated plate case ( $T_{mo} = T_w > T_\infty$ ). Here, the thermal field grows from the jet slot, and its thickness is always less than that of the shear layer: that is  $\delta > \delta_\theta$ . This case applies when analogous surface mass transfer measurements are used, such as the naphthalene sublimation technique employed by Alamdari et al (3). Wall jet profile analysis by Hammond (4) can be used to illustrate the differences in the thermal field caused by these differing boundary conditions as shown in Figure 2. In practice, the heated wall jet will normally give

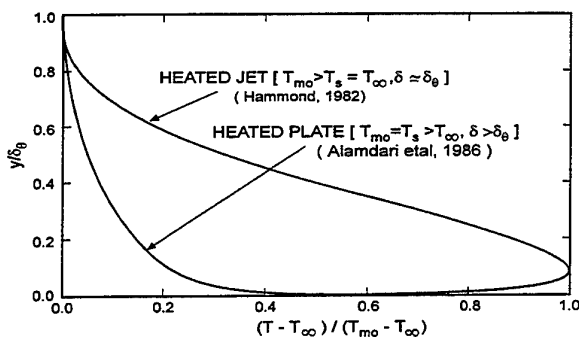


Fig. 2 Idealised Wall Jet Thermal Fields [after Alamdari et al (3)]

rise to a “three temperature problem” ( $T_{mo} > T_s > T_\infty$ ) unless the wall temperature is independently controlled.

## 3. COOLING EFFECTIVENESS AND HEAT TRANSFER COEFFICIENT

The thermal interaction of the heated wall jet with the wall and cooler ambient air will be considered in the same manner as a film cooling experiment. The main quantities of interest in film cooling experiments (5) are the convective heat transfer coefficient ( $h$ ) and the film cooling effectiveness ( $\eta$ ). The former is the constant of proportionality between the local heat flux ( $q$ ), and the difference between the surface temperature ( $T_s$ ) and convection driving temperature of the gas ( $T_{aw}$ , or *adiabatic wall temperature*) at that point:

$$q = h(T_s - T_{aw}) \quad (1)$$

The adiabatic wall temperature is chosen in common with film cooling practice since it is desirable to define, and measure, a heat transfer coefficient which is independent of the temperature boundary conditions and a function of the aerodynamic character of the flowfield alone. This is not strictly possible as there are well known and predictable differences between an isothermal wall situation and a constant heat flux boundary condition. However, for small streamwise gradients in temperature and constant fluid properties, a wall temperature variation has only a minor influence on local convective heat transfer. For the heated (or cooled) wall-jet experiment, with two gas temperatures present,  $T_{aw}$  is intermediate between the peak jet ( $T_{mo}$ ) and ambient ( $T_\infty$ ) total temperatures. It is argued in the film cooling literature that the consequent surface heat transfer coefficient depends only upon the nozzle geometry and degree of mixing (entrainment) between these gases upstream of the point of interest on the surface. In the light of the above discussion of the wall jet thermal boundary conditions, this assertion is open to question. To eliminate the temperature dependence a conventional dimensionless adiabatic film effectiveness is defined for constant-property, incompressible flow on an adiabatic surface:

$$\eta = \frac{T_{aw} - T_{\infty}}{T_e - T_{\infty}} \quad (2)$$

Only incompressible flows will be dealt with here and no distinction is made between the total and static temperatures, and no recovery effects are considered. The jet temperature ( $T_e$ ) is taken as the temperature at the nozzle exit.

For a three-dimensional wall jet, the cooling effectiveness and heat transfer coefficient at the wall are a function of the nozzle geometry, jet Reynolds number, and the ( $x, z$ ) co-ordinate location (see Figure 1). It is convenient to non-dimensionalise the heat transfer coefficient in terms of the Stanton number,

$$St = \frac{h}{\rho c u_e} \quad (3)$$

where  $\rho$ ,  $c$  and  $u_e$  are the incompressible fluid density, specific heat at constant pressure, and jet velocity at the nozzle exit respectively.

#### 4. TRANSIENT EXPERIMENTAL TECHNIQUE

Several different measurement techniques have been employed to obtain film cooling data. The heat-mass transfer analogy is used in the swollen polymer (6) and naphthalene sublimation (4, 7) techniques to determine heat transfer coefficient and effectiveness. Effectiveness alone may also be found using gas concentration techniques of which the Ammonia and Diazo (8) technique is an example.

The transient method employed here determines the convective heat transfer coefficient and effectiveness by measuring the transient response of surface temperature when an acrylic test plane is suddenly exposed to a fluid of known temperature. By assuming that uniform, semi-infinite flat-plate boundary conditions apply, it is possible to express the instantaneous heat flux as an analytical function of this transient surface temperature (9). Thin film gauges (10), wide-band thermochromic liquid crystals (11), or infra-red thermography (12) can be employed to measure the surface temperature history; the latter two methods have a great advantage over the former as they provide such temperature histories on the entire wetted surface visible to

the camera, rather than an average over the gauge width at fixed locations.

The local surface heat flux history is calculated from the temperature histories using the one-dimensional heat conduction equation:

$$\frac{\partial T_s}{\partial t} = \alpha \frac{\partial T_s}{\partial n^2} \quad (4)$$

where  $\alpha$  is the thermal diffusivity of the substrate,  $n$  is the distance into the substrate, and  $t$  is time. The assumption is made that the duration of the measurement is short enough that the penetration of the thermal pulse into the substrate is small when compared to the depth of the test plane. The boundary conditions are a uniform substrate temperature before the transient experiment begins and that the heat flux is proportional to the temperature gradient at the surface. The time variation of heat flux,  $q$ , may be evaluated by numerical integration (9, 13):

$$q_s = \frac{1}{\pi\alpha} \left[ \frac{T_i - T_s}{\sqrt{t}} + \right] \int_0^t \frac{T_i - T_s}{2(t-\tau)^{3/2}} d\tau \quad (5)$$

where  $T_i$  is the initial temperature of the substrate before the experiment, and  $\tau$  is the variable of integration. The convective heat transfer coefficient and adiabatic wall temperature can then be determined, by regression, using the heat flux and surface temperature histories in conjunction with Eq.1 during the time segment after the wall-jet flow has stabilised. Analytical solutions to the one-dimensional heat conduction equation exist for the specific case of a step-change in wall-jet temperature (9, 11), but the above integral is more general.

#### 5. EXPERIMENTAL APPARATUS

An experimental rig, similar to that described by Alamdari et al. (4) and specifically designed for the study of wall jets, was used and is shown in Figure 3. Dry, compressed air is passed through a British Standard orifice plate and 3 kW heater controlled by a variac. The heated air (typically 55 C) enters a large, insulated plenum chamber featuring an inclined baffle and perforated plate. The air exits the plenum chamber via an interior alignment nozzle which has a rectangular exit cross-section dimensions of 60 by 90 mm.

A second exit orifice of similar dimensions is employed to create a near-step change in thermal boundary conditions for the transient experiments. While waiting for thermal equilibrium to be established, the air flow bypasses the test section through the secondary

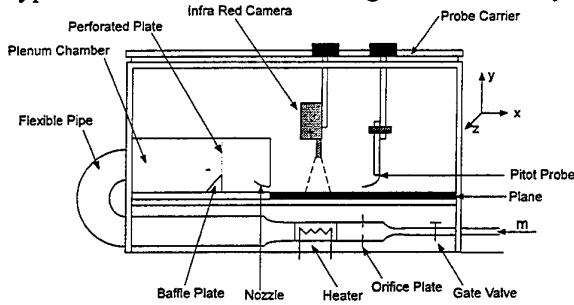


Fig. 3 Schematic Representation of the Wall Jet Test Facility

orifice with the main nozzle blocked. When ready to conduct the experiment, this secondary orifice is blocked and the main nozzle opened to create a sudden, and near step-change thermal boundary condition, for the heated wall-jet flow over the initially isothermal test surface.

The test plane is made of Perspex and the surface is painted with matt-black paint of known emissivity. A moving trolley holding an infra-red camera, flattened aerodynamic (Pitot) probe and thermocouple is located above the test plane.

The infra-red camera is part of an Agema Infra-Red Thermovision System, capable of acquiring images at a rate of 6.64 images per second for a maximum of 100 frames. Each image contains 140 by 140 pixels and the temperature resolution, if accurately calibrated, is 0.1 C. Each pixel is characterised by its intensity, which varies between 0 and 255. This intensity corresponds to a temperature dependent upon the level and range of temperature used by the infra-red camera. The images are captured onto computer disc and transferred to a Silicon-Graphics workstation where image processing occurs.

## 6. WALL-JET VELOCITY AND TEMPERATURE PROFILES

The experimental results are for a wall jet with a nozzle-exit Reynolds number of  $6 \times 10^5$ , exit jet temperature of 43 C, and ambient air temperature

18 C. The nomenclature used is described in Figure 1.

The nondimensional velocity distribution along the jet centre-plane (at  $x/\sqrt{A} = 6.1$ ) was obtained by traversing the Pitot probe in vertical ( $y$ ) direction at  $z = 0$ . This velocity profile was found to agree well with the semi-empirical relocation of Verhoff (14) for a plane wall jet, viz.,

$$\frac{u_m}{u_{m0}} = 1.48\phi^{1/7} [1 - \text{erf}(0.68\phi)] \quad (6)$$

where  $\phi = y/b_y$ , and erf is the error function. This correlation, which is close to that obtained by Hammond (1) using profile analysis, agrees well with the data despite the different geometry.

The nondimensional velocity distribution in the horizontal ( $z$ ) direction (at  $x/\sqrt{A} = 6.1$  and  $y = 4$  mm) agree well with the following empirical correlation for 3D wall jets from Rajaratnam and Pani (15):

$$\frac{u}{u_m} = \exp[-0.693\beta^2] \quad (7)$$

where  $\beta = z/b_z$ .

The maximum velocity ratio  $u_m/u_{m0}$  along the wall-jet centre-line agree well with data gathered by Rajaratnam and Pani (15) from a range of sources. The velocity ratio was found to remain nearly constant near the nozzle exit (potential core region) and then decays exponentially further downstream. In the characteristic decay region the velocity decays linearly on the logarithmic scale with a slope of -0.42; and the radial decay region where the velocity decays linearly but with a slope of -0.95, which compares well with previous research (15).

The growth of the length scales  $b_y$  and  $b_z$  have been measured and found to be:

$$\frac{db_y}{dx} = 0.046 \pm 0.002, \quad \frac{db_z}{dx} = 0.22 \pm 0.02$$

which agree well with those reported by Launder and Rodi (2) as  $db_y/dx$  and  $db_z/dx$  of 0.048 and 0.26 respectively.

The nondimensional temperature profile with height above the wall for the jet centre-line is shown in Figure 4. These measurements were made using a thermocouple traverse in the steady-state (at  $x/\sqrt{A} = 2.8$ ,  $z = 0$ ). The

temperature distribution spanwise ( $z$  direction) across the jet was found to be similar to the normal distribution exhibited by the velocity field. The decay of jet maximum (peak) temperature displayed the three characteristic regions again in an analogous way to the velocity field.

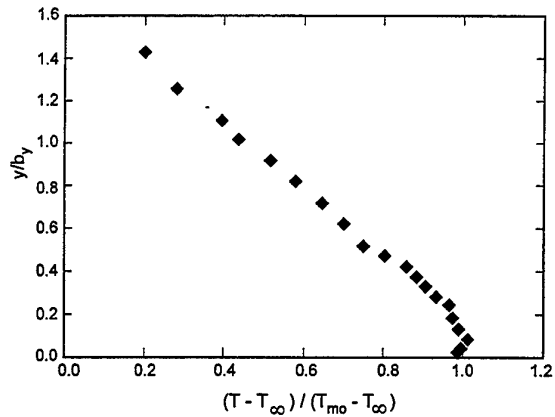


Fig. 4 3D Wall Jet Cross-stream Temperature Profile: Measurements on the Centreline ( $x/\sqrt{A} = 2.8, z = 0$ )

## 7. WALL JET HEAT TRANSFER AND EFFECTIVENESS

A typical surface temperature at a single point, obtained from approximately 90 images, is shown in Figure 5. The temperature rises from an initial value (at time zero) of about  $25^\circ\text{C}$  towards an adiabatic wall temperature of  $41^\circ\text{C}$ . A seventh-order polynomial has been fitted to the data. The heat flux is computed from Duhamel's integral and plotted against surface temperature in Figure 6. The slope of this line yields the heat transfer coefficient and the intercept, obtained by extrapolation to zero heat flux, yields the adiabatic wall temperature. The effectiveness can then be calculated from Eq. 2. The centreline variation of effectiveness is plotted against in Figure 7. As expected, the effectiveness is near unity at the exit of the aperture and decreases thereafter as cold ambient gas is entrained into the jet. The greatest rate of decrease in  $\eta$  occurs for  $x/\sqrt{A} < 5$ , which is in the potential core region. Far from the aperture, the effectiveness falls towards zero, as expected. Effectiveness data has also been obtained in a spanwise direction ( $z$ ), but is not shown here.

The Stanton number variation along the centreline is plotted against  $x/\sqrt{A}$  in Figure 8. Stanton number data is shown to reach a peak value near  $x/\sqrt{A} = 5$ , at the end of the potential core region. Thereafter, it decreases a typical uncertainty bar is shown.

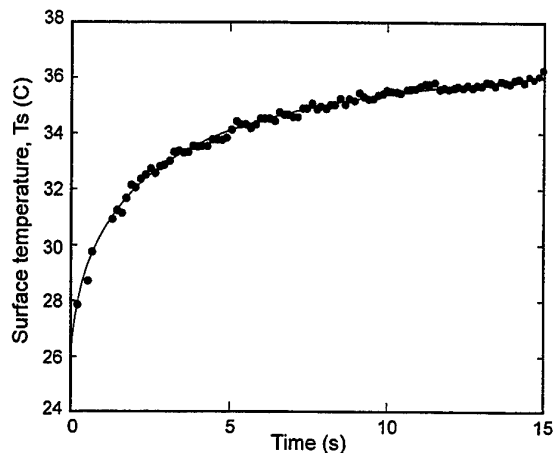


Fig. 5. Time History of the Surface Temperature and Smoothed Curve

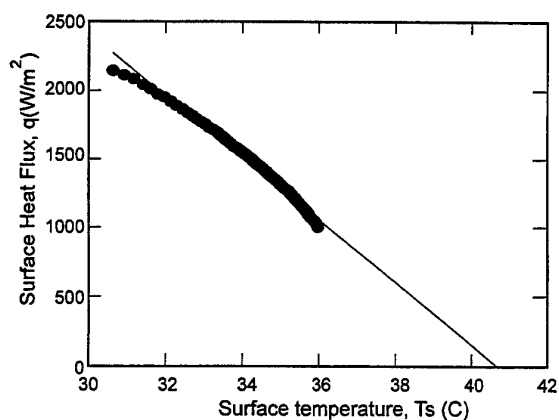


Fig. 6 Determination of the Convective Heat Transfer Coefficient

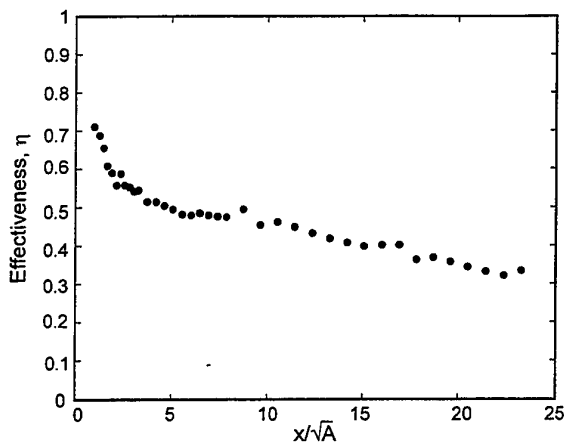


Fig. 7 Effectiveness Variation Along the 3D Wall Jet Centreline

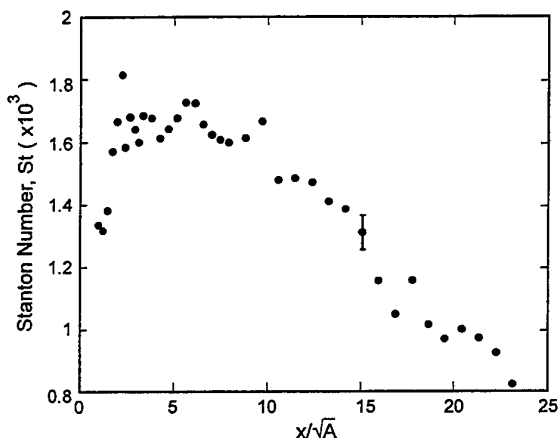


Fig. 8 Stanton Number Variation Along the 3D Wall Jet Centreline

## 8. CONCLUDING REMARKS

The main test criteria used by Launder and Rodi (2) in order to evaluate wall-jet measurements for the 1980-81 Stanford Conference on 'Complex Turbulent Rows' was compliance of data sets with the requirements of the momentum integral equation. However, there are several, alternative 'schools of thought' among thermo-fluid dynamicists as to the most appropriate measurable quantities for verifying calculation methods. These include measurements of time-averaged velocity and temperature distributions, and the use of turbulence data. The latter might be either turbulent stress and heat-flux

distributions or the measurements of the higher-order terms in the Reynolds-averaged 'transport equations' associated with turbulence models. Alternatively, Chieng and Launder (17) recommended using local heat transfer distributions on boundary surfaces, as these are sensitive to both outer flow and near-wall modelling. Most calculation methods used in computational fluid dynamics codes can be made to ensure reasonable agreement with the mean flow, while turbulence properties tend to be difficult to measure and/or are model dependent. Heat and mass transfer coefficients are more readily measured, and are therefore ideal candidates for refining and verifying calculation methods for complex, wall-bounded turbulent shear flows.

Experimental measurements have been reported here of the local heat transfer beneath a heated three-dimensional (3D) wall jet. This jet was formed by the ejection of a hot air stream from a small-aspect-ratio (1:1:5) rectangular nozzle over a flat test plate, at a jet exit Reynolds number held constant at about 60,000. Under these conditions the jet is self-similar, and indeed mean flow field measurements displayed agreement with earlier studies. Launder and Rodi (2) suggested that future wall jet research should be directed towards such 3D wall jets emanating from nozzles of finite width. These complex turbulent flows exhibit differential rates of jet spread observed between that in the lateral (or spanwise) direction and that normal to take the wall. The cause of this phenomenon is not well understood, partly due to the limited number of reliable data sets available. It is hoped that the surface heat transfer measurements beneath heated 3D wall jets, of the type reported here, will contribute to a better understanding of these flows. An infra-red thermal imaging camera has been used for the first time to conduct a series of transient experiments that yielded distributions of wall jet heat transfer and 'cooling effectiveness'. This data may in turn be employed to verify modern CFD codes for complex turbulent flows. It is through an interaction between measurements and computations that the underlining physics of these flows will become apparent.

The present study has highlighted the need to clarify the thermal boundary conditions in wall jet studies, and their possible influence on surface heat transfer. In the case of constant-



property boundary layer flows the heat free-stream and heated plate are thermally similar. That is, changing from one condition to the other simply alters the direction of the surface heat flux. However, this is not the situation in wall jet flows (see Figure 2), where the heated jet case constitutes a 'three-temperature' problem. In the current research, the thermal imaging technique gave rise to a near uniform heat flux wall boundary condition ( $q \simeq \text{constant}$ , and  $T_{\text{mo}} > T_s > T_{\infty}$ ) below the heated wall jet. Clear specification of those boundary conditions will enable computational modellers to more realistically stimulate these complex turbulent flows.

## 9. ACKNOWLEDGEMENTS

The research reported here was undertaken at Bath while the first author (RB) was on secondment from the Ecole Centrale de Nantes, France. Support for the construction of the wall-jet test rig was received from British Gas plc, who partially supported the Chair of the second author (GPH). The thermal imaging equipment was supported by a Royal Society research grant (G503/18296) awarded to the last author (GDL). All the authors are grateful for the care with which Mrs Heather Golland prepared the typescript and Mrs Gill Green prepared the figures.

The authors' names appear alphabetically.

## 10. NOMENCLATURE

$b$	Wall jet length scales
$c$	Specific heat at constant pressure
$h$	Surface heat transfer coefficient
$k$	Thermal conductivity
$q$	Convective heat flux
$u$	Mean velocity
$t$	Time
$T$	Temperature

### Greek Symbols

$\rho$	Density
$\eta$	Film cooling effectiveness

### Subscripts

$i$	Initial
$aw$	Adiabatic wall
$e$	Jet exit nozzle

$s$	Surface
$\infty$	Ambient
$\theta$	Thermal field

## 11. REFERENCES

- (1) Hammond, G.P., *Complete Velocity Profile and Optimum Skin Friction Formulas for a Plane Wall-Jet*, ASME J. Fluids Engg, 1982, (104), 59-66.
- (2) Launder, B.E. and Rodi, W., *The Turbulent Wall Jet*, Progress in Aerospace Science, 1982, (19), 81-123.
- (3) Alamdari, F., Hammond, G.P., Montazerin, N., *Heat/Mass Transfer Beneath a Two-dimensional Wall-jet Deflected by a Normal, Flat-plate Obstruction*, Heat Transfer 1986 : Proc. 8<sup>th</sup> Int. Heat Transfer Conf., San Francisco, 1986, (3), 1213-1218 (Hemisphere, Washington).
- (4) Hammond, G.P., *Profile Analysis of Heat/Mass transfer Across the Plane Wall-jet*, Heat Transfer 1982 : Proc. 7<sup>th</sup> Int. Heat Transfer Conf., Munich, 1982 (3), 349-355 (Hemisphere, Washington).
- (5) Goldstein, R.J., *Film Cooling*, Advances in Heat Transfer, 1971, (7), 321-379.
- (6) Hay, N., Lampard, D. and Saluja, C.L., *Effects of Cooling Films on the Heat Transfer Coefficient on a Flat Plate with Zero Mainstream Pressure Gradient*, 1984, ASME paper 84-GT-40.
- (7) Cho, H.H. and Goldstein, R.J., *Heat (Mass) Transfer and Film Cooling Effectiveness with Injection Through Discrete Holes: Part II - On the Exposed Surface*, 1995, ASME Journal of Turbomachinery, (117), 451-460.
- (8) Friedrichs, S., Hodson, H.P. and Dawes, W.N., *Distribution of Film-Cooling Effectiveness on a Turbine Endwall Measured Using the Ammonia and Diazo Technique*, 1995, ASME Paper 95-GT-1.
- (9) Schultz, D.L., and Jones, T.V., *Heat Transfer Measurements in Short-Duration Hypersonic Facilities*, 1973, AGARD AG-165.
- (10) Jones, T.V., *The Thin Film Heat Transfer Gauge - a History and New Developments*, 1995, Invited Lecture, 4th National UK Heat Transfer Conference, Manchester, IMechE Conference Transactions C510/150/95 1-12.

- (11) Ireland, P.T., Wang, Z.W. and Jones T.V., *Liquid Crystal Heat Transfer Measurements*, 1993, von Karman Institute for Fluid Dynamics 1992-1993 Lecture Series.
- (12) Wittig, S., Schulz, A., Gritsch, M. and Thole, K.A., *Transonic Film Cooling Investigations: Effects of Hole Shapes and Orientations*, 1996, ASME Paper 96-GT-222.
- (13) Myers, G.E., *Analytical Methods in Conduction Heat Transfer*, 1971, McGraw Hill, New York.
- (14) Verhoff, A., *The Two-dimensional Wall Jet With and Without an External Stream*, Princeton University Report 626, 1963.
- (15) Rajaratnum, N. and Pani, B.S., *Three-Dimensional Turbulent Wall Jets*, 1974, ASCE J. Hydraulics, HYL, (69).
- (16) Yevdjovich, *Diffusion of Slot Jets with Finite Orifice Length-width Ratios*, Colorado State University Hydraul. Pap. 2, 1966.
- (17) Chieng, C.C. and Launder, B.E., *On the Calculation of Turbulent Heat Transport Downstream from an Abrupt Pipe Expansion*, Numerical Heat Transfer, 1980, (3), 189-207.

# MATHEMATICAL MODELLING OF HEAT EXCHANGE BY TURBULENT FLOW OF SUSPENSION IN A PIPE

A.V.Starchenko, A.M.Bubenchikov, E.S.Burlutsky

Tomsk State University, Russia

## ABSTRACT

This paper is devoted to numerical modelling of turbulent heat transfer and gas - solids flows in pipes in frameworks of theory of interacting and interpenetrating continua. Collisions of particles with walls are modelled by division of monodispersed particulate phase on fractions of falling and reflected solids. This approach allows to use physical boundary conditions on the walls for dispersed phase. Processes of turbulent transfer are described by using modification of Kondratiev's model for turbulent correlations of solid phase. The developed model is tested on experimental data for turbulent gas- solids flows and heat transfer in pipes. Results of calculations have shown essential influence of contact heat exchange between particulate phase and walls of a pipe on intensity of heat transfer at turbulent gas- solids flow in a pipe.

## 1 INTRODUCTION

The gas- solids flows in pipes often happens in a technical systems of different purposes. In particular the work of dust separators and combustion chambers, the transfer of dispersed substance in pneumatic transport, catalytic creaking and so on are connected with these flows. While studying internal two- phase heterogeneous flows it is necessary to take into account the interaction between gas- solids flow and walls of a pipe along with such factors as mutual influence of carrying and particulate phases, the particles dynamic interaction between themselves, the presence of possible phase exchanges and so on. The certain difficulties of principle nature arise here. Apparently this is the basic reason at present time that the quantity of scientific publications on problems of free gas- solids flows essentially outstrips the number of theoretical researches of gas- solids flows in a pipe. At the turbulent regime of flow the complexity of mathematical modelling of gas- solids flow and heat exchange is essentially increased from the necessity to take into account mutual phase influence on the level of turbulent fluctuations.

A.Mulgi<sup>(1)</sup> offered the following classification of gas- solids turbulent flows by value of parameter  $\varphi_u$  on the basis of numerous experimental researches of isothermal gas- solids turbulent flows in round pipes:

$$\varphi_u = \left( \frac{\rho_p^0}{\rho_1^0} \right)^{-0,6} \left( \frac{2r_0}{d} \right) Re_D^{-0,4} Re_b^{0,12} (1+M)^{0,15} + 0,22 \quad (1)$$

Here  $\rho_p^0, \rho_1^0$  are the densities of particles and gas;  $r_0, d$  are radius of a pipe and diameter of particles;  $M$  is loading ratio of a gas-particles flow ( $M = G_p/G_1$  is ratio of the mass rates of phases);  $U_b$  is the velocity of gas in the inlet of a pipe;  $\mu_1$  is the dynamic viscosity of gas;  $\nu_b$

is the terminal velocity;  $\varphi_0$  is equal to 14,42+22,66 and depends of the material of a wall.

1. Values  $\varphi_u > 1,8$  correspond to diffusion regime of the turbulent flow or the regime of an equilibrium flow, at which the particles are sensitive to a turbulent fluctuations of gas and do not interact with the walls of a pipe. The distribution of the particle concentration is practically uniform in the cross section region of a pipe.

2. Values  $1 \leq \varphi_u \leq 1,8$  correspond to diffusion- migration regime of the gas-solid flow or to a locally nonequilibrium motion. The interaction of the particles with an internal surface of a pipe is weak, but nevertheless, the particles being reflected from the walls acquire sufficient rotation and under the action of Magnus force move to an axis of a pipe. The local velocities of sliding of the phases are small ( $u_1 - u_2 \approx 0,1u_1$ ). The exponential distribution of particles concentration with the maximum on the axis of a pipe and the absence of average sliding velocity are characteristic for a given regime of the gas-particle flow.

3. Values  $\varphi_u < 1$  correspond to jump-shaped regime or the regime of essentially nonequilibrium two-phase flow. The strong shock interaction between particulate phase and internal surface of a pipe takes place. The particles move in a flow and sharply change the direction of movement after collisions with the walls of a pipe. The particles are practically not sensitive to turbulent fluctuations of gas. The structure of particles velocities has about uniform distribution. The change of concentration of the particulate phase is described as exponential function from the radial co-ordinate.

Thus, to use this model in a wide range of change of main parameters of the flow in accordance with present ideas of turbulent gas- solids flow in pipes<sup>(1)-(3)</sup> the mathematical model of considered process should take into account both dynamic and thermal sliding of phases, interaction of particles with walls of a pipe and their rotation.

The review of the literature on problems of mathematical modelling of turbulent gas- solids flow and heat exchange in a pipe <sup>(4-6)</sup> shows that it is possible to distinguish the following approaches for the description of the investigated phenomena.

1. The combined of Eulerian- Lagrangian representation of turbulent gas- solids flow <sup>(7)</sup>. The flow and heat exchange of gas are described in the frameworks of Eulerian continual approach. The motion of particles in a flow is being modelled by using of Lagrangian approach enabling to control the change of dynamic and thermal properties of separate particles along their trajectories and to take into account their reverse influence on gas. The turbulent fluctuations of particles velocity are calculated on the basis of stochastic method of modelling <sup>(8)</sup>, which requires significant quantity of computing realisations to receive authentic averaging picture of flow. Nevertheless, such approach permits to simulate all features of interaction between particles and the walls of a pipe in detail.

2. The use of transport equation for probability density function of particles velocity and temperature in turbulent flow for obtaining closed equations of hydrodynamics and heat- and mass transfer of the particulate phase in Eulerian representation <sup>(9,10)</sup>. The problem of closure of conservation equations for average characteristics is being decided as a rule by attraction of transport equations for the second moments of velocity and temperature fluctuations. It permits to take into account anisotropic character of transfer processes in gas- solids turbulent flow in a pipe.

3. Application of Reynolds averaging procedure to the basic equations of the theory of interacting and interpenetrative continua <sup>(11)</sup> for obtaining of system of mass, quantity of motion and energy conservation equations for average values, describing turbulent gas- solids flow and heat exchange in a pipe <sup>(5,12,13)</sup>. Closing of this system is carried out with the use of semiempirical models which enter into consideration the differential transport equations for turbulent correlation moments.

At the present time within the third approach the mathematical model offered by L.V. Kondratiev <sup>(13,14)</sup> has built up quite a reputation for description of two-phase flow. Its application permits to predict reliable distributions of hydrodynamics and thermal values of gas and particles in the various models of nonisothermal turbulent gas- solids flow in a pipe and to simulate effects connected with rotation of particles and their interactions with walls of a pipe.

In this paper is offered the modification of Kondratiev model connected with some of its simplifications in modelling of turbulent moments of the particulate phase (the fluctuations of radial component of angular particles velocity were not taken into account and simple gradient hypothesis was used for correlations involving of fluctuations of transversal component of angular velocity), using of transport equation for gas heat turbulent flux, the application of physical

conditions for falling and reflected particles to simulate an interaction between solid particles and walls of a pipe.

The change of the particle velocity and temperature during collision is defined by the relations <sup>(5,12)</sup>:

$$\begin{aligned} u_p^{++} &= \frac{5+2a_\tau}{7} u_p^+ + \frac{1-a_\tau}{7} \omega_p^+ d; \\ v_p^{++} &= -a_n v_p^+; \\ \omega_p^{++} &= \frac{5a_\tau+2}{7} \omega_p^+ + \frac{10(1-a_\tau)u_p^+}{7d}; \\ T_p^{++} &= T_p^+ + a_T (T_w - T_p^+); \end{aligned} \quad (2)$$

where  $\omega_p$  is angular velocity of single particle; the superscripts “+”, “++” correspond to values of parameters before and after the collision between particle and solid surface;  $T_w$  is temperature of internal surface of the pipe wall;  $T_p$  is temperature of the particle;  $a_\tau, a_n$  are restitution coefficients for longitudinal and normal components of particle velocity after the collision with the wall of pipe;  $a_T$  is coefficient temperature change after collision.

## 2 MATHEMATICAL MODEL

This paper is devoted to gas-solid axisymmetric steady nonisothermal turbulent flow in the pipe. We'll take into consideration that the particles have the same size and sphere shape. The density of the particulate phase is much more bigger to that one of the fluid phase(gas). The interaction between particles is not taken into account because the particulate phase is diluted ( $\alpha_p \ll 1$ ). The modelling interactions of particles with the wall of the pipe is realised on the basis of the theory of interaction and interpenetrating continua <sup>(1)</sup> by dividing the particulate phase into fractions of falling and reflected particles <sup>(11)</sup> with mass exchange between fractions and by using the boundary conditions describing the character of the recovery of the velocity of particles and their additional rotation after collision with the walls. Dynamic interaction between phases is determined by friction force and by force of Magnus only.

### 2.1 Governing equations

We can write down the following mathematical model of process <sup>(12,13)</sup> after application of Reynolds averaging procedure to a system of equations which determine the flow heat exchange of interacting continua <sup>(11)</sup> and use the assumptions characteristic for boundary layer approximation:

Carrying phase:

$$\frac{\partial(\rho_1 u_1)}{\partial x} + \frac{1}{r} \frac{\partial(r \rho_1 v_1)}{\partial r} = 0; \quad (3)$$

$$\begin{aligned} \rho_1 u_1 \frac{\partial u_1}{\partial x} + \rho_1 v_1 \frac{\partial u_1}{\partial r} = \\ = -\frac{\partial p}{\partial x} + \frac{1}{r} \frac{\partial}{\partial r} \left[ r \left( \mu_1 \frac{\partial u_1}{\partial r} - \rho_1 \overline{u_1' v_1'} \right) \right] - \sum_{i=2}^3 F_{xi} - \rho_1 g_x; \end{aligned} \quad (4)$$

$$\frac{\partial p}{\partial r} = 0; \quad (5)$$

$$\begin{aligned} \rho_1 u_1 \frac{\partial T_1}{\partial x} + \rho_1 v_1 \frac{\partial T_1}{\partial r} = \\ = \frac{1}{r} \frac{\partial}{\partial r} \left[ r \left( \frac{\mu_1}{Pr} \frac{\partial T_1}{\partial r} - \rho_1 \overline{v_1' T_1'} \right) \right] + \frac{u_1}{C_1} \frac{\partial p}{\partial x} - \\ - \frac{1}{C_1} \sum_{i=2}^3 Q_i + \frac{1}{C_1} \sum_{i=2}^3 [F_{xi}(u_1 - u_i) + F_{ri}(v_1 - v_i)]; \end{aligned} \quad (6)$$

$$\rho_1 = \frac{(1 - \alpha_2 - \alpha_3)p}{R_g T_1}; \quad (7)$$

Dispersed phase: (i = 2,3)

$$\frac{\partial(\rho_i u_i)}{\partial x} + \frac{1}{r} \frac{\partial}{\partial r} [r(\rho_i v_i + \overline{\rho_i' v_i'})] = J_i; \quad (8)$$

$$\begin{aligned} \rho_i u_i \frac{\partial u_i}{\partial x} + (\rho_i v_i + \overline{\rho_i' v_i'}) \frac{\partial u_i}{\partial r} = -\frac{1}{r} \frac{\partial}{\partial r} (r \rho_i \overline{u_i' v_i'}) + \\ + F_{xi} - \rho_i g_x + J_i(u_3 - u_i); \end{aligned} \quad (9)$$

$$\begin{aligned} \rho_i u_i \frac{\partial v_i}{\partial x} + (\rho_i v_i + \overline{\rho_i' v_i'}) \frac{\partial v_i}{\partial r} = \\ = -\frac{1}{r} \frac{\partial}{\partial r} [r(\rho_i \overline{v_i'^2} + \overline{\rho_i' v_i' v_i'})] + \frac{\rho_i \overline{w_i'^2}}{r} + \\ + F_{ri} + J_i(v_3 - v_i); \end{aligned} \quad (10)$$

$$\begin{aligned} \rho_i u_i \frac{\partial \omega_i}{\partial x} + (\rho_i v_i + \overline{\rho_i' v_i'}) \frac{\partial \omega_i}{\partial r} = \\ = -\frac{1}{r} \frac{\partial}{\partial r} (r \rho_i \overline{\omega_i' v_i'}) - \frac{\rho_i}{\tau_\omega} \left( \omega_i + \frac{1}{2} \frac{\partial u_1}{\partial r} \right) + \\ + J_i(\omega_3 - \omega_i); \end{aligned} \quad (11)$$

$$\begin{aligned} \rho_i u_i \frac{\partial T_i}{\partial x} + (\rho_i v_i + \overline{\rho_i' v_i'}) \frac{\partial T_i}{\partial r} = \\ = -\frac{1}{r} \frac{\partial}{\partial r} (r \rho_i \overline{v_i' T_i'}) + \frac{Q_i}{C_2} + J_i(T_3 - T_i) + \\ + \frac{J_i}{2C_2} [(u_3 - u_i)^2 + (v_3 - v_i)^2]; \end{aligned} \quad (12)$$

where  $u, v, p, T$  are components of velocity vector, pressure and temperature;  $\rho_i = \rho_p^0 \alpha_i$ ;  $\rho_p^0$  is density of particles;  $\alpha_i$  is volumetric share of  $i$ th fraction of particles: value  $i=2$  corresponds to fraction of particles falling on the wall and  $i=3$  correspond to fraction of reflected particles;  $C_1, C_2$  are specific heat capacities of gas and particles;  $g_x$  is projection of the gravity acceleration into the  $Ox$  axis (It allows to apply this model (3)-(12) for nonvertical flows if the axial symmetry of the flow is not infringed<sup>(13)</sup>);  $\mu_1, Pr$  are dynamic viscosity and molecular Prandtl number of gas;  $F_{xi}, F_{ri}, Q_i$  are components of dynamic interaction force and intensity of heat exchange between gas and  $i$ th fraction of particles;  $\omega_i$  is angular velocity of rotation of  $i$ th fraction of particles;  $J_i$  is mass rate of particles transition from the fraction of reflected particles ( $i=3$ ) into fraction of falling particles ( $i=2$ );  $\overline{u_i' v_i'}, \overline{v_i' T_i'}, \overline{\rho_i' v_i'}, \overline{u_i' v_i'^2}, \overline{v_i'^2}, \overline{w_i'^2}, \overline{\omega_i' v_i'}, \overline{v_i' T_i'}$  are correlation moments arising in transport equations as a result of application of Reynolds averaging procedure and describing turbulent transfer of mass, impulse and energy of phases and fractions;  $d$  is diameter of particles;  $\tau_\omega = \rho_p^0 d^2 / 60 \mu_1$ .

As it was already marked above, the intensity of force interaction between gas and particles is determined by aerodynamic friction force and Magnus force<sup>(12,13)</sup>:

$$F_{xi} = \frac{\rho_i f_{Di}(u_1 - u_i)}{\tau_p} - \frac{c_m \rho_p^0 \rho_i}{\rho_p^0} \left[ \overline{\omega_i' v_i'} - (v_1 - v_i) \left( \omega_i + \frac{1}{2} \frac{\partial u_1}{\partial r} \right) \right]; \quad (13)$$

$$F_{ri} = \frac{\rho_i f_{Di}(v_1 - v_i)}{\tau_p} + \frac{c_m \rho_p^0 \rho_i}{\rho_p^0} \left[ \overline{\omega_i' u_i'} - (u_1 - u_i) \left( \omega_i + \frac{1}{2} \frac{\partial u_1}{\partial r} \right) \right]; \quad (14)$$

$$\tau_p = \frac{\rho_p^0 d^2}{18 \mu_1}; \quad \tau_{pi} = \frac{\tau_p}{f_{Di}};$$

$$f_{Di}(Re_i) = \begin{cases} 1 + 0,15 Re_i^{0,687} & , Re_i \leq 1000 \\ 0,44 Re_i / 24 & , Re_i > 1000 \end{cases};$$

$$Re_i = \frac{\rho_1^0 \sqrt{(u_1 - u_i)^2 + (v_1 - v_i)^2} d}{\mu_1} \quad (i = 2,3);$$

$\rho_1^0$  is gas density;  $c_m = 0,75$ .

The convective heat exchange between phases is described by following dependence:

$$Q_i = \frac{6\rho_i\lambda_i(T_i - T_i)Nu_i}{\rho_p^0 d^2}; \quad (15)$$

$$Nu_i = 2,0 + 0,459 Re_i^{0,55} Pr_i^{0,33} \quad (i = 2,3);$$

$\lambda_i$  is a coefficient of heat conductivity of gas.

The expression which is used for calculation of mass exchange intensity between fractions of falling and reflected particles is <sup>(11)</sup>:

$$J_i = (-1)^j \chi_j \frac{\rho_2 \rho_3 \sqrt{(u_2 - u_3)^2 + (v_2 - v_3)^2}}{\rho_p^0 d} \quad (16)$$

$$(i = 2,3); \chi_j = 100,0.$$

## 2.2 Turbulence model

Turbulent structure of gaseous phase is modelled with the usage of Boussinesq hypothesis for  $\overline{u_i'v_i'}$  correlation, of Vasiliev-Kvon<sup>(15,16)</sup> one-equation turbulent model, having modified for a case of the presence of the particles in the flow and transport equation for turbulent moments  $\overline{v_i'^2}$  and  $\overline{v_i'T_i'}$ :

$$\begin{aligned} \rho_1 u_1 \frac{\partial k}{\partial x} + \rho_1 v_1 \frac{\partial k}{\partial r} &= \frac{1}{r} \frac{\partial}{\partial r} \left[ r(\mu_{t1} + \kappa \mu_{t1}) \frac{\partial k}{\partial r} \right] + \\ &+ \mu_{t1} \left( \frac{\partial u_1}{\partial r} \right)^2 - \frac{3,93(\mu_{t1} + \kappa \mu_{t1})k}{L^2} - \\ &- 2k \sum_{i=2}^3 \frac{\rho_i [1 - f(\psi_i)]}{\tau_{pi}}, \end{aligned} \quad (17)$$

$$-\rho_1 \overline{u_i'v_i'} = \mu_{t1} \frac{\partial u_1}{\partial r};$$

$$\frac{L(r)}{r_0} = 0,37 - 0,24 \left( \frac{r}{r_0} \right)^2 - 0,13 \left( \frac{r}{r_0} \right)^4; \quad (18)$$

$$\mu_{t1} = 0,2\rho_1 \sqrt{k} L f_\mu; \quad (19)$$

$$f_\mu = 1 - \exp(-\sigma_1 Re_t^2) + \sigma_3 \sqrt{Re_t} \exp(-\sigma_2 Re_t^2);$$

$$\begin{aligned} \rho_1 u_1 \frac{\partial \overline{v_i'^2}}{\partial x} + \rho_1 v_1 \frac{\partial \overline{v_i'^2}}{\partial r} &= \frac{1}{r} \frac{\partial}{\partial r} \left[ r(\mu_{t1} + \kappa \mu_{t1}) \frac{\partial \overline{v_i'^2}}{\partial r} \right] + \\ &+ 0,7 \frac{\rho_1 k^{3/2}}{L} - 1,4 \frac{\rho_1 \overline{v_i'^2} \sqrt{k}}{L} - 140,0 \frac{\mu_{t1} \overline{v_i'^2}}{L^2} - \\ &- \frac{2\mu_{t1} \overline{v_i'^2}}{r^2} - 2\rho_1 \overline{v_i'^2} \frac{\partial v_1}{\partial r} - 2\overline{v_i'^2} \sum_{i=2}^3 \frac{\rho_i [1 - f(\psi_i)]}{\tau_{pi}} - \end{aligned} \quad (20)$$

$$-4\overline{v_i'^2} \frac{c_m \rho_1^0}{\rho_p^0} \overline{u_i'v_i'} \sum_{i=2}^3 \rho_i \left( \omega_i + \frac{1}{2} \frac{\partial u_1}{\partial r} \right) [1 - f(\psi_i)];$$

$$\begin{aligned} \rho_1 u_1 \frac{\partial \overline{v_i'T_i'}}{\partial x} + \rho_1 v_1 \frac{\partial \overline{v_i'T_i'}}{\partial r} &= -\rho_1 \overline{v_i'T_i'} \frac{\partial v_1}{\partial r} + \\ &+ \frac{1}{r} \frac{\partial}{\partial r} \left[ r \left( \mu_{t1} + \frac{\mu_{t1}}{Pr} \right) \frac{\partial \overline{v_i'T_i'}}{\partial r} \right] - \rho_1 \overline{v_i'^2} \frac{\partial T_1}{\partial r} - \frac{\mu_{t1} \overline{v_i'T_i'}}{r^2} - \\ &- 1,5\rho_1 \overline{v_i'T_i'} \frac{\sqrt{k}}{L} - 10,0 \left( \mu_{t1} + \frac{\mu_{t1}}{Pr} \right) \frac{\overline{v_i'T_i'}}{\left[ L \left( 1 + \frac{0,871}{\sqrt{Pr}} \right) \right]^2} - \end{aligned} \quad (21)$$

$$-\overline{v_i'T_i'} \sum_{i=2}^3 \left\{ \frac{\rho_i [1 - f(\psi_i)]}{\tau_{pi}} + \frac{6\rho_i \lambda_i Nu_i [1 - f(\Theta_i)]}{\rho_p^0 d^2 C_1} \right\};$$

where  $k$  is the energy of turbulence of gas;  $\mu_{t1}$  is a coefficient of turbulent viscosity of gas;  $L$  is scale of turbulence;  $r_0$  is radius of a pipe;

$$f(\psi_i) = \exp(\psi_i^2 / \pi) \operatorname{erfc}(\psi_i / \sqrt{\pi}) \psi_i;$$

$$\psi_i = L / \left( \sqrt{\overline{v_i'^2}} + |u_1 - u_i| \right) \tau_{pi};$$

$$\Theta_i = \psi_i \tau_{pi} / (\rho_p^0 d^2 C_2 / 6\lambda_i Nu_i); \quad i = 2,3;$$

$$Re_t = \rho_1 \sqrt{k} L / \mu_{t1};$$

$$\kappa = 0,4; \sigma_1 = 2,1 \cdot 10^{-4}; \sigma_2 = 4 \cdot 10^{-4}; \sigma_3 = 0,02$$

The use of the transport equation (21) for  $\overline{v_i'T_i'}$  permits not to attract Boussinesq hypothesis for turbulent heat flow and not to apply the idea of turbulent analogue of Prandtl number for turbulent carrying phase loaded by solid particles.

The following assumptions were used for closing of system of averaging transport equations of the particulate phase (8)-(12) ( $i=2,3$ ):

$$-\overline{u_i'v_i'} = -f(\psi_i) \overline{u_i'v_i'} + \frac{\tau_{pi} \overline{v_i'^2}}{2} \frac{\partial u_1}{\partial r}; \quad (22)$$

$$-\rho_i \overline{v_i'} = D_i \frac{\partial \rho_i}{\partial r}; \quad D_i = \frac{1}{\rho_1} f(\psi_i) \mu_{t1} + \frac{\tau_{pi} \overline{v_i'^2}}{2}; \quad (23)$$

$$-\overline{\omega_i'v_i'} = \frac{\tau_{pi} \tau_\omega \overline{v_i'^2}}{\tau_{pi} + \tau_\omega} \frac{\partial \omega_i}{\partial r}; \quad (24)$$

$$-\overline{\omega_i'u_i'} = \frac{\tau_{pi} \tau_\omega \overline{u_i'v_i'}}{\tau_{pi} + \tau_\omega} \frac{\partial \omega_i}{\partial r}; \quad (25)$$

$$\begin{aligned} \rho_i u_i \frac{\partial \overline{v_i'^2}}{\partial x} + (\rho_i v_i + \overline{\rho_i v_i'}) \frac{\partial \overline{v_i'^2}}{\partial r} &= \frac{1}{r} \frac{\partial}{\partial r} \left( r \rho_i D_i \frac{\partial \overline{v_i'^2}}{\partial r} \right) - \\ - 2 \rho_i \overline{v_i'^2} \frac{\partial v_i}{\partial r} + \frac{2 \rho_i \overline{v_i' w_i'^2}}{r} + \frac{2 \rho_i \left[ f(\psi_i) \overline{v_i'^2} - \overline{v_i'^2} \right]}{\tau_{pi}} &= (26) \\ - \frac{2 c_m \rho_i^0}{\rho_p^0} \left[ \frac{\rho_i \tau_{pi} \overline{v_i'^2}}{2} \left( \omega_i + \frac{1}{2} \frac{\partial u_i}{\partial r} \right) \frac{\partial u_i}{\partial r} + \rho_i (u_i - u_i) \overline{\omega_i' v_i'} \right] + \\ + 2 J_i \left( \overline{v_3'^2} - \overline{v_i'^2} \right); \end{aligned}$$

$$\begin{aligned} \rho_i u_i \frac{\partial \overline{w_i'^2}}{\partial x} + (\rho_i v_i + \overline{\rho_i v_i'}) \frac{\partial \overline{w_i'^2}}{\partial r} &= - \frac{1}{r} \frac{\partial}{\partial r} \left( r \rho_i v_i' w_i'^2 \right) \\ - \frac{2 \rho_i \left( \overline{v_i' w_i'^2} + \overline{w_i'^2} v_i \right)}{r} + \frac{2 \rho_i \left[ f(\psi_i) \overline{v_i'^2} - \overline{w_i'^2} \right]}{\tau_{pi}} + &= (27) \\ + 2 J_i \left( \overline{w_3'^2} - \overline{w_i'^2} \right); \end{aligned}$$

$$-\overline{v_i' w_i'^2} = \frac{D_i}{3} \frac{\partial \overline{w_i'^2}}{\partial r}; \quad (28)$$

$$\begin{aligned} \rho_i u_i \frac{\partial \overline{v_i' T_i'}}{\partial x} + (\rho_i v_i + \overline{\rho_i v_i'}) \frac{\partial \overline{v_i' T_i'}}{\partial r} &= \\ = \frac{1}{r} \frac{\partial}{\partial r} \left( r \rho_i D_i \frac{\partial \overline{v_i' T_i'}}{\partial r} \right) - \rho_i \overline{v_i'^2} \frac{\partial T_i}{\partial r} - \\ - \rho_i \overline{v_i' T_i'} \frac{\partial v_i}{\partial r} + \frac{\rho_i \left[ f(\Theta_i) \overline{v_i' T_i'} - \overline{v_i' T_i'} \right]}{\tau_{pi}} + &= (29) \\ + \frac{6 \rho_i \lambda_1 N u_i}{\rho_p^0 d^2 C_2} \left[ f(\psi_i) \overline{v_i' T_i'} - \overline{v_i' T_i'} \right] + \\ + 2 J_i \left( \overline{v_3' T_3'} - \overline{v_i' T_i'} \right). \end{aligned}$$

The relation (22) expresses balance of "generation-dissipation" terms in corresponding differential transport equation for correlation  $\overline{u_i' v_i'}$ . It partially takes into account prehistory of particles flow development <sup>(5)</sup> because  $\overline{v_i'^2}$  is determined by a transport equation (26). The ratio (23) determines a turbulent diffusion of particles for a concrete fraction. The validity of use of these assumptions at the description processes of turbulent transport of mass and impulse of the particles has been confirmed by the results of comparison of calculated and experimental data showed in <sup>(13)</sup>. The necessity of attraction of differential equation for  $\overline{w_i'^2}$  is stipulated by the fact, that the solving of equation (10) which enables to find the radial component of particles velocity appears highly sensitive to modelling of term

$\rho_i \frac{\overline{w_i'^2}}{r}$  ( $i=2,3$ ). Description quality of the particles distribution concentration character depends in a determining degree on the accuracy of modelling this term, which expresses the impact of centrifugal force (stipulated by the presence of particles fluctuation motion in a transversal direction).

### 2.3 Boundary conditions

The boundary conditions for system of equations (3)-(12), (17), (20), (21), (26), (27) and (29) were set up: with  $r=0$ :

- the symmetric conditions;

on the wall of the pipe with  $r = r_0$ :

- for carrying phase

$$\begin{aligned} u_1 = v_1 = k = \overline{v_1'^2} = \overline{v_1' T_1'} = 0; \\ -\lambda_1 \frac{\partial T_1}{\partial r} = q_w - \sum_{i=2}^3 (\rho_i v_i + \overline{\rho_i v_i'}) C_2 T_i; \end{aligned} \quad (30)$$

- for fraction of the falling particles ( $i = 2$ )

$$\frac{\partial u_2}{\partial r} = \frac{\partial \omega_2}{\partial r} = \frac{\partial \overline{v_2'^2}}{\partial r} = \frac{\partial \overline{w_2'^2}}{\partial r} = 0, \quad \overline{\rho_2 v_2'} = \rho_2 \sqrt{\overline{v_2'^2}}, \quad (31)$$

- for fraction of the reflected particles ( $i = 3$ )

$$\begin{aligned} u_3 = \frac{5 + 2a_\tau}{7} u_2 + \frac{1 - a_\tau}{7} \omega_2 d; \\ \omega_3 = \frac{5a_\tau + 2}{7} \omega_2 + \frac{10(1 - a_\tau)}{7} \frac{u_2}{d}; \\ v_3 = -a_n v_2; \overline{v_3'^2} = a_n^2 \overline{v_2'^2}; \overline{w_3'^2} = \overline{v_3'^2} / 4; \\ T_3 = T_2 + a_T (T_w - T_2); \\ \rho_3 v_3 + \overline{\rho_3 v_3'} = -(\rho_2 v_2 + \overline{\rho_2 v_2'}); \\ \overline{v_3' T_3'} = -a_n \overline{v_2' T_2'} + a_T a_n \sqrt{\overline{v_2'^2}} (T_2 - T_w); \end{aligned} \quad (32)$$

on the inlet of the pipe with  $x = 0$  were set up the uniform distributions for all characteristics in agreement with the considering conditions of turbulent flow and heat exchange of particles.

### 3 SOLUTION PROCEDURE

The problem has been solving numerically using staggered grids thicken to the wall of the pipe in such a way that not more than 5-10 grid nodes should find in viscous sublayer. There are using a staggered grids for radial component of velocity  $v_i$  ( $i=1,2,3$ ) and turbulent heat fluxes  $\overline{v_i' T_i'}$  ( $i=1,2,3$ ) of gas and particulate phase. The grids is differ from main by that nodes in which the

values  $v_i$ ,  $\overline{v_i^2}$  ( $i=1,2,3$ ) were calculated lie in the middle between nodes of main grid. Discreet analogies of the differential equations having got after using the method of control volume <sup>(5)</sup> and implicit finite-differential schemes and they were solved by the effective method of TDMA. The additional global iterations were organised on each step of integration along  $x$  because the main equations of mathematical model is non-linear and interconnected. Offered numerical algorithm was tested on a well known analytical and experimental distributions concerned with laminar and turbulent one-phase flows in a round pipe. All calculations presented in this paper were executed on the grids contains of 40 or 50 nodes in a cross direction. Besides the systematic calculations were executed on the enclosed grids regards of basic grids (80,100 nodes in a radial direction). Here, for example, the results were different on a value of (0,5÷1)% for the friction stress on the wall. The calculation step of the longitudinal co-ordinate was determined according to requirements of the stability of algorithm.

#### 4 RESULTS

The proof of possibility to use offered mathematical model for predicting of turbulent flow and heat exchange characteristics of gas- solids flow in a pipe was carried out on the basis of comparative analysis of calculated results with experimental data in a wide range of change for determining parameters.

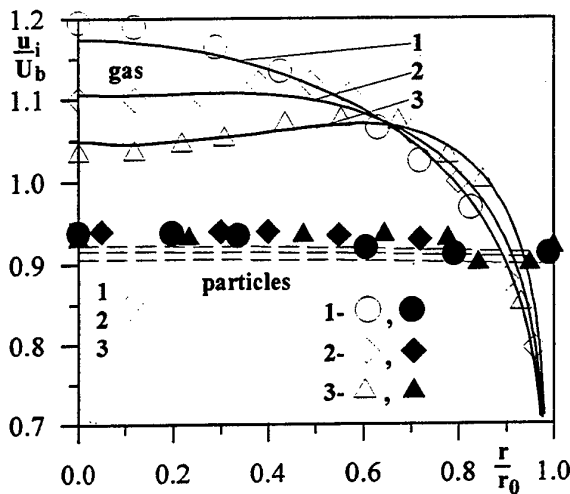


Figure 1

Calculated (curves) and measured <sup>(18)</sup> (symbols) velocities of carrying ( $i=1$ ) and dispersed phase ( $i=p$ ) in developed turbulent gas-solid flows in a pipe; 1-  $M=1,92$ ; 2-  $M=6,1$ ; 3-  $M=14,4$ ;  $Stk=446,5$ ;  $Re_D=36250$ ;  $a_r=0,85$ ;  $a_n=0,92$ .

The calculated and measured <sup>(18)</sup> values of longitudinal component of gas and particles velocity

$u_p = (\alpha_2 u_2 + \alpha_3 u_3) / (\alpha_2 + \alpha_3)$  are offered on fig.1 for developed turbulent gas- solids flow in a pipe. The conditions for conducting of experiment <sup>(18)</sup> correspond to the following values of determining parameters:  $Re_D=36250$ ;  $Stk=446,5$ ;  $Fr=0,009$  and by classification <sup>(1)</sup> refer into a regime of essentially nonequilibrium turbulent gas- solids flow ( $\varphi_u \approx 0,58 \div 0,68$ ). In that case the turbulent structure of the particulate phase practically does not respond to turbulent fluctuations of carrying phase ( $\psi_i \ll 1$ ,  $f(\psi_i) \rightarrow 0$ ) and the longitudinal velocity of particles by the radial coordinate is changed feebly. The profile of gas velocity in a centre of flow becomes more flat with the increase of loading parameter  $M$ , which is connected with different influence character of aerodynamical friction force within different parts of cross sectional region of a pipe. The concentration of particle phase has a high values (Fig.2,  $\rho_p = \rho_2 + \rho_3$ ) in an axis region of a pipe and its influence on a gaseous phase more considerably then in nearwall region of a pipe. The further increasing of values  $M$  results that under influence of its mechanism the maximum of velocity is displaced from the axis of flow into the nearwall region of pipe and the distribution  $u_1(r)$  acquires the shape of a saddle. This character of gas and inertial particles velocity distributions and theirs concentrations was obtained numerically by L.V. Kondratiev <sup>(13)</sup>.

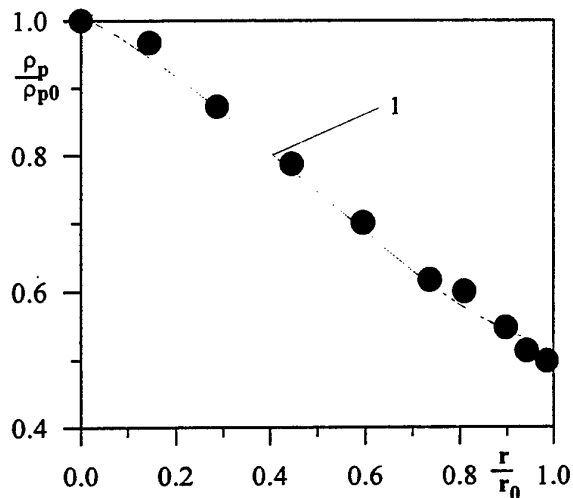


Figure 2

Distribution of relative particle concentration in developed turbulent gas-inertial particles flow in pipe.  $\rho_{p0}$  is value of particle concentration at  $r=0$ ; the other markings correspond to ones of Figure 1.

Figures 3 and 4 show the influence of particles concentration in a flow on the hydro-resistance and heat exchange at a developed turbulent gas-solids flow in a vertical pipe ( $\varphi_u \approx 0,7 \div 0,8$ ;  $Re_D = 20000$ ;  $Pr = 0,7$ ;  $Stk = 296$ ;  $C_2/C_1 = 1,17$ ;  $Fr = 0,027$ ). Here  $\Delta p_0$ ,  $Nu_0$  are pressure drop on a fixing part of a pipe and nondimensional coefficient of heat transfer (Nusselt



number) for one-phase flow,  $\Delta p$  is a pressure drop of gas-solids flow in the same part of a pipe, stipulated by gas friction and by interaction between particulate phase and walls of a pipe.

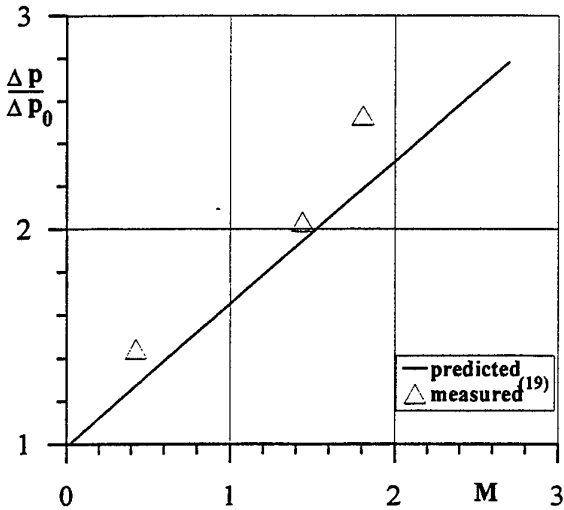


Figure 3

Undimensional pressure drop via loading ratio M.  
 $Re_D=20000$ ;  $Stk=296$ ;  $Fr=0,027$ ;  $a_r=0,0$ ;  $a_n=0,2$ .

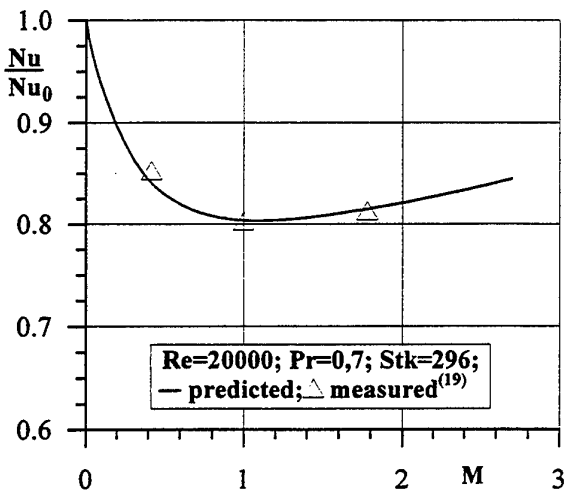


Figure 4

Comparison of calculated and experimental<sup>(19)</sup> values of Nusselt number.  $a_r=0,0015$ .

The predicted value of undimensional coefficient of heat transfer is determined by the following expressions:

$$Nu = \frac{q_w D}{\lambda_1 (T_w - T_b)}; \quad T_b = \frac{\int_0^{r_0} (\rho_1 u_1 T_1 + \rho_p u_p T_p) r dr}{\int_0^{r_0} (\rho_1 u_1 + \rho_p u_p) r dr}$$

here  $q_w = \text{const}$  is heat flux to suspension;  $T_w(x)$ ,  $T_b(x)$  are temperature of wall and mean expenditure temperature of suspension in considered cross sectional region of a pipe. The presence of the inertial particles in a flow, which highly interact with walls of a pipe, essentially increases hydro friction of gas-solids flow, as it follows from figure 3. It is known that the influence of loading ratio on the relative coefficient of hydro resistance is described by linear dependence. Here change the worsening of heat transfer takes place in comparison with free gas flow (Fig.4 and fig.5,  $Re=30000$ ;  $C_2/C_1=0,75$ ;  $Pr=0,7$ ;  $Fr=0,005$ ) at small values of loading ratio M ( $M < 5$ ). There is observed

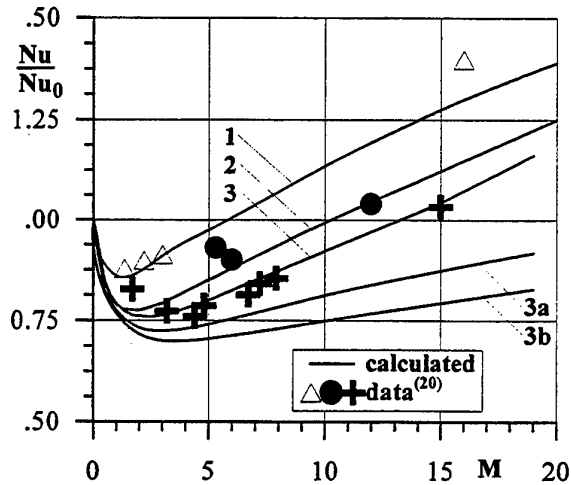


Figure 5

Relative heat transfer coefficient via loading ratio M.  
 $Re_D=30000$ ;  $Pr=0,7$ ;  $C_2/C_1=0,75$ ; 1- $Stk=386$ ;  $a_r=0,9$ ;  $a_n=0,99$ ; 2- $Stk=1565$ ;  $a_r=0,8$ ;  $a_n=0,99$ ; 3- $Stk=3002$ ;  $a_r=0,05$ ;  $a_n=0,99$ ;  $a_r=0,0038$ .

the monotonous increasing of heat transfer intensity with the loading ratio M growing at values of loading ratio  $M > 1 \div 2$ . This character of heat transfer change dependent on the particles concentration in a flow was observed in experiments<sup>(19)-(21)</sup>.

The distributions of heat transfer intensity according to loading ratio M, obtained for  $Stk=3002,0$  with the assumption that the temperature of particles does not change when they interact with the walls of a pipe are presented for comparison on figure 5 ( $a_r = 0,0$ ; curve 3a is calculated for conditions of nonideal collisions:  $a_r = 0,05$ ;  $a_n = 0,99$ ; curve 3b corresponds to conditions of ideal collisions:  $a_r = a_n = 1,0$ ). As the results of comparisons show (curves 3, 3a, 3b in the fig.5) not taking into account of contact heat transfer gives essentially decreased values of heat transfer coefficient at turbulent gas-inertial solids flow in a pipe. The divergence between curves 3 and 3a is increasing while the particles concentration is growing. The influence of dynamic interaction character between inertial particles and the walls of a pipe upon the heat

transfer intensity is less important. But nevertheless particles acquire the additional rotation at nonideal collision between particles and walls of a pipe. The influence of Magnus force on a nature of average and fluctuation flow of particulate phase becomes essential. There is an increase of the level of turbulent fluctuation of particles ensemble in the nearwall region of a pipe at insignificant decreasing of turbulent heat transfer that results into heat transfer intensification.

The calculations were made by using this model for studying influence of intensity of the collisions between the particles and the walls of the pipe on heat transfer at turbulent gas- solids flow in a pipe with the following value of parameters:  $Re_D=30000$ ;  $Pr=0,7$ ;  $C_2/C_1=0,75$ ;  $Fr=0,01$ ;  $Stk=150, 300, 500$ ;  $M<20$ ;  $a_\tau = 0,95$ ;  $a_n = 0,97$ ;  $a_T = 0,0015$  <sup>(22)</sup>. The distribution of intensity of the collisions between particles and inside surface of the pipe  $J_w = (\rho_2 v_2 + \rho_2' v_2')|_{r=r_0}$  and the relative Nusselt number through dependence of the loading ratio of flow were shown on fig.6,7.

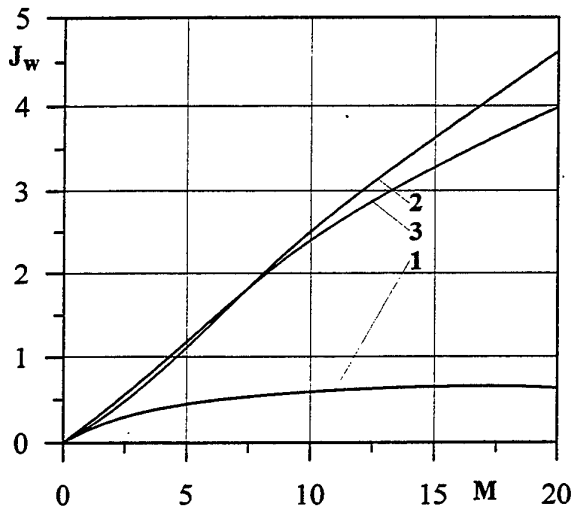


Figure 6

Intensity of collisions of dispersed phase with pipe wall via loading ratio  $M$ . 1- $Stk=150$ ; 2- $Stk=300$ ; 3- $Stk=500$ .

It is visible that by low value of  $J_w$  ( $0 < M < 4$  for  $Stk \leq 500$  and  $M \leq 20$  for  $Stk = 150$ ) its observed the worsening of heat transfer in comparison with nondusted flow. The essential temperature sliding of phases showing for the most part for inertial particles is the reason of that (Fig.4,  $0 < M < 4$ ). The increasing of heat transfer for account of additional heat transport of reflected particles goes by the growing up of the collision between the particles and the wall of the pipe ( $M > 5$ ,  $Stk \geq 300$ ) that is supported by the experimental data of A.Sukomel and et al <sup>(20,21)</sup>.

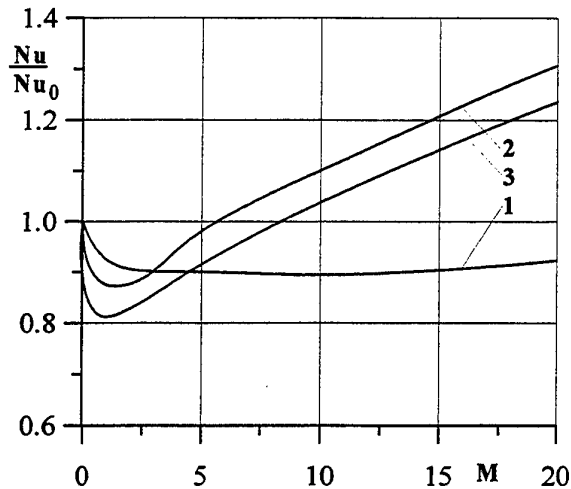


Figure 7

Influence of particle concentration on a heat transfer of turbulent gas-inertial solids flow in pipe.  $Re_D=30000$ ;  $Pr=0,7$ ;  $Fr=0,01$ ; 1- $Stk=150$ ; 2- $Stk=300$ ; 3- $Stk=500$ ;  $a_\tau=0,95$ ;  $a_n=0,97$ ;  $a_T=0,0015$ .

## 5 CONCLUSIONS

This paper offers the mathematical model for research of nonisothermal turbulent gas- inertial solids particles flow in a pipe which permits to determine average characteristics of flow and heat exchange, such as turbulent structure of phases and intensity of collisions between particles and walls of a pipe within the theory of interaction and interpenetrating continua. The results of numerical calculations executed on its basis are satisfactory conformed with the experimental data and calculations of others authors. It was theoretically determined that the proportional increasing of hydro resistance takes place, when loading ratio  $M$  is growing, as well as intensification of heat transfer at  $0 < M < 1$  and its intensification at  $M > 1$ . The last fact is connected with growing contribution of contact heat exchange, which is displayed at collisions between particles and walls of a pipe, into the general process of heat transfer at turbulent gas- inertial solids flows in pipes.

## 6 ACKNOWLEDGEMENTS

The work presented in this paper is a part of research programme funded by Russian Foundation for Basic Researches, grant 97-01-00471a.

## 7 NOMENCLATURE

$a_\tau, a_n, a_T$       restitution coefficients of longitudinal and normal components of particles velocity after the

	collision with the wall of pipe and coefficient of particle temperature change;
C	specific heat capacity;
d	particle diameter;
D	pipe diameter;
$F_x, F_r$	components of dynamic interaction force;
g	gravitational acceleration;
$J_i$	mass rate of particles transition 3-2;
k	turbulent energy of gas;
L	scale of turbulence;
M	loading ratio;
Nu	Nusselt number;
p	mean static pressure;
$\Delta p$	pressure drop;
Pr	molecular Prandtl number of gas;
$Q_i$	intensity of heat exchange between gas and $i$ th fraction of particles;
$r_0$	pipe radius;
$Re_b$	Reynolds number based on terminal velocity of particles and d;
$Re_D$	Reynolds number based on mean velocity $U_b$ and pipe diameter D;
T	temperature;
Stk	Stocks number;
$u, v, w$	velocity components;
$v_b$	terminal velocity of particles;
$U_b$	velocity of gas in the inlet of a pipe;
$x, r$	co-ordinates

#### Greek symbols

$\alpha$	volume fraction of particles;
$\lambda$	coefficient of heat conductivity of gas;
$\mu$	dynamic viscosity of a gas;
$\rho$	density;
$\tau$	response time;
$\omega$	angular velocity of rotation of particles

#### Subscripts

b	inlet;
$i=2$	fraction of falling on the pipe wall particles;
$i=3$	fraction of reflected particles;
p	particulate phase;
t	turbulent;
1	gas

#### 8 REFERENCES

(1) Mulgi, A.S. The basic regularity of transfer processes in a flow with a small particles in a pipe,

Turbulent Two-Phase Flow and Technique of Experimentation, Tallinn, 1985, pp.161-167 (in Russian).

(2) Boothroyd, R.G. Flowing Gas-Solids Suspensions, 1975, 378p. (Chapmann & Hall).

(3) Soo, S.L. Fluid Dynamics of Multiphase Systems, 1971.- 533p. (Blaisdell Pub. Co.).

(4) Andreeva, I.V., Bubenchikov, A.M., Starchenko, A.V. Mathematical modelling of turbulent gas-solids flows in a pipes (a review), Aerogasdynamics, Tomsk, 1992, pp.26-37 (Trans. of NIIPMM of TSU) (in Russian).

(5) Naumov, V.A., Podvysotsky, A.M., Shraiber, A.A. The theory of two-phase turbulent polydisperse flows in channels, Proceedings of the First International Symposium on Two-Phase Flow Modelling and Experimentation, Rome, Italy, 9-11 October, 1995, 1995, V.1, pp.109-116.

(6) Zaichik, L.I., Pershukov, V.A. Problems in modelling of turbulent gas-solids flow, Proceedings of III International Minsk Forum "Heat and Mass Exchange - MMF-96", 1996, V.5, pp.123-129 (in Russian).

(7) Sommerfield, M. Modelling of particle-wall collisions in confined gas-particle flow, Journal of Multiphase Flow, 1992, V.18, No.6, pp.905-926.

(8) Mostafa, A.A., Mongia, H.C., McDonell, V.G., Samuelsen, G.S. Spreading of dust jet flows. Theoretical and experimental research, AAIA Journal, 1989, No.2, pp.167- 183.

(9) Zaichik, L.I. Models of turbulent heat and impulse transfer in a particulate phase bases on equations for second and third pulsation moments of particles velocity and temperature, Journal of Engineering Physics and Thermophysics, 1992, V.63, No.4, pp.404-413 (in Russian).

(10) Derevich, I.V. Statistical description and calculation of hydrodynamics and mass transfer of turbulent gas- solids flow in a pipes, Proceedings of III International Minsk Forum "Heat and Mass-exchange - MMF- 96", 1996, V.5, pp.134-141(in Russian).

(11) Nigmatulin, R.I. The Dynamics of Multiphase Media, V.1, 1987.464 p. (Moscow, Nauka).

(12) Shraiber, A.A., Gavin, L.B., Naumov, V.A., Jatsenko, V.P. Turbulent Flows in Gas Suspensions, 1987, 239 p. (Hemisphere).

(13) Kondratiev, L.V., Shor, V.V. Research of turbulent flow of suspension in pipe with take into account the collisions with wall and particles rotation, Proceedings of the USSR Acad. Sci., Ser. Mechanics of Liquids and Gases, 1990, No.1, pp.56-64 (in Russian).

(14) Kondratiev, L.V. Mathematical modelling of turbulent nonisothermal gas-solids flow in a vertical pipe, Modelling in Mechanics, 1988, V.2(19), No.6, pp.55-61 (in Russian).

(15) Vasiliev, O.F., Kvon, V.I. Nonsteady turbulent flow in a pipe, Journal of Applied Mechanics and Technical Physics, 1971, No.6, pp.132-140 (in Russian).

- (16) Starchenko, A.V. Numerical research of nonisothermal gas-solid turbulent flow in the inlet of pipe, Proceedings of III International Minsk Forum "Heat and Mass Exchange-MMF-96", 1996, V.5, pp.64-68 (in Russian).
- (17) Patankar, S. Numerical Heat Transfer and Fluid Flow, 1980, 150p. (Hemisphere).
- (18) Mulgi, A.S. Experimental research of gas flow with homogeneous sphere particles in pipe, Turbulent Two-Phase Flow, Tallin, 1979, pp.47-59 (in Russian).
- (19) Shimizu, A., Hasegawa, S., Tanaka, H. Flow and heat transfer characteristics of gaseous solid suspension medium within circular riser tubes, JSME International Journal, 1988, Series II, Vol.31, No.3, pp.451-460.
- (20) Sukomel, A.S., Tsvetkov, F.F., Kerimov, R.V. Investigation of local heat transfer from the wall of pipe into the turbulent gas flow carrying particles, Thermal Engineering, 1967, No.2, pp.77-80 (in Russian).
- (21) Sukomel, A.S., Tsvetkov, F.F., Kerimov, R.V. Heat Exchange and Hydraulic Resistance in Gas-Solids Flow in a Pipe, 1977, 192p. (Moscow, Energy) (in Russian).
- (22) Ztirkunov, Yu.M., Panfilov, S.V., Klychnikov, M.B. A semiempirical model of shock interaction of a solid particle with a surface streamlined by gas-particle flow, Journal of Engineering Physics and Thermophysics, 1994, V.67, No.5-6. pp.379-386 (in Russian).

# A VISUALISATION STUDY OF THE FLOW PATTERNS OF LONGITUDINAL VORTICES GENERATED BY WINGLETS IN A CHANNEL

V. Vasanta Ram, S. Lau\* and M. Kaniewski\*\*

Institut fuer Thermo- und Fluidodynamik  
Ruhr University, Bochum, Germany

\* presently at GHH Borsig Turbomaschinen GmbH,  
Oberhausen, Germany

\*\* presently at SAMSON, Warsaw, Poland

## ABSTRACT

Winglets are commonly employed devices to enhance heat transfer by suitable control of the flow. They generate longitudinal vortices in the shear flow which in turn exert a decisive influence on the other quantity of engineering interest in these devices, viz. the power required to drive the flow. The heat-transfer characteristics and the power requirement of the device are both governed by the size and strength of the longitudinal vortices as well as the paths and locations they take up in the flow. These are decided by details of the winglet geometry and the operating Reynolds number. The present paper is a visualisation study of the flow patterns with longitudinal vortices generated by three different but related geometrical configurations of winglets in a channel. The parameter range for flow visualisation covers a Reynolds number range from the onset of transition onwards, which, for this flow, is around 300 up to around 7000. The experiments have been conducted in a specially built channel-flow facility which operates with water as the flowing medium and in which the flow is visualised by seeded particles. The video recording of the visualised flow shows the different stages of vortex formation and development. It brings out the similarities and differences between the patterns of formation and interaction of the vortices in the three winglet configurations.

## 1 INTRODUCTION

The shear flow with embedded longitudinal vortices is a type of flow encountered in many engineering applications. Some examples are: aircraft wings, diffusers and compact heat exchangers. In these and other such applications, surface mounted winglets generate embedded longitudinal vortices that exert a dominant influence on the flow character and on quantities of engineering interest like heat transfer. Some of these effects have been studied earlier, but much details that are as important to applications as from a point of view of fundamentals yet remain to be investigated. The need for a deeper understanding is more urgent in the transition and turbulent flow regimes. An essential step to this end is visualisation of the flow patterns. Flow visualisation is thus an indispensable tool that helps to gain an insight into the myriad of phenomena that occur during transition and affect flow and heat transfer, and this motivated the present study.

In an earlier work Lau, Meiritz and Vasanta Ram (1) conducted detailed probe surveys of the velocity and temperature fields in the heated channel flow with embedded longitudinal vortices. The longitudinal vortices in their work were generated by an array of winglets that were placed in a certain geometrical configuration characterised by regular intervals in both the streamwise and spanwise directions. The winglet array was on one of the channel walls and the individual winglets of the array extended half way through the channel height. The measurements were conducted by

quadruple-hot-wire sensors. This study brought out the need for supplementing the probe measurements through visualisation of the flow in question, since otherwise, there was found to be room for uncertainty in interpreting probe signals. Visualisation is therefore an essential link in interpreting probe measured data for understanding structural features of the complex turbulent flow with embedded longitudinal vortices, and this has been the motivation for the present work. We present in this paper visualisation studies of the unheated channel flow with embedded longitudinal vortices in the Reynolds number regime starting from the onset of transition, which is around 300 for this flow, up to around 7000. The longitudinal vortices were generated by several geometrical configurations of winglets one of which is the configuration for the above probe measurements.

## 2 THE EXPERIMENTAL FACILITY AND THE METHOD FOR FLOW VISUALISATION

In fig. 1a,b are shown a schematic diagram and a photograph respectively of the water channel facility specially built for the purpose of the present flow visualisation studies. The facility is of the closed circuit type with no exposure of either the flow visualisation section or its neighbourhood to any free surface. The channel walls are made out of plexiglas to enable visualisation of the flow. In its cross section the channel is rectangular with dimensions 10mm x 200mm.

Denoting the spacing between the channel walls as  $2H$  ( $=10\text{mm}$ ), the salient dimensions of the test section are  $2H \times 40H \times 120H$ . Upstream of the test section it is a channel with the same cross section dimensions as the test section with a length of  $800\text{mm}$  ( $160H$ ). The contraction ratio ahead of this section is 6:1. The long uniform channel upstream of the test section and its large aspect ratio of 1:20 assures two-dimensionality of the oncoming flow in the channel section upstream of the winglets.

Water is pumped up from the lower level against the steady head maintained in the reservoir at the top. The circulating water leaves the reservoir into the return piping, flowing over V-notches that are calibrated to measure the volume flow rate. The flow rate through the channel is regulated by a frequency divider, throttle valve and a bypass. The pump in this system could maintain a steady flow rate through the channel in the range from 0.02 up to 4 l/s, which corresponds to an average through flow velocity in the test section of  $1\text{cm/s}$ - $2\text{m/s}$ . For further details of the facility the reader is referred to Lau and Vasanta Ram (2).

Longitudinal vortices embedded in the channel flow are generated by winglets mounted on the rear channel wall. The individual winglets are thin ( $0.1H$ ) rectangularly shaped sharp edged plates with dimensions  $1H \times 4H$  placed at an angle of  $30^\circ$  to the main flow direction, see fig. 2. The winglets were arranged in three different geometrical configurations denoted configuration 1, 2 and 3 respectively. Configuration 1 is the isolated winglet pair shown in fig. 2. Configuration 2 is a single row of the winglet pairs of Configuration 1 arranged in a regular interval in the spanwise direction only, see fig. 3. The planes G, H, J, K and L shown in this figure are locations where probe measurements were done in this winglet configuration and reported in Lau and Vasanta Ram (2). Configuration 3 consists of the single winglet row of Configuration 2 repeated at regular intervals in the streamwise direction, see fig. 4. The probe measurements in the heated channel flow reported in Lau, Meiritz and Vasanta Ram (1) were done in this winglet configuration. For further details of the probe measurements the reader is referred to Lau (3).

The means for flow visualisation is seeding the flowing water with Iridin® 120 particles. These are saucer-shaped particles roughly  $10\text{-}25\ \mu\text{m}$  in diameter and  $3\text{-}4\ \mu\text{m}$  thick. Due to their saucer shape they align themselves with the axes of the strain rate tensor in the flow. When illuminated from a certain direction, differences in light reflection produces a light intensity distribution that renders the main structure of the flow visible. In our facility the test section could be illuminated by two alternative light sources. One is flood lighting by conventional bulbs. This illuminates the flow in the test section over the entire channel height. The other is by a laser light sheet generated by a helium-neon laser together with a cylindrical lens. This light source illuminates only a relatively thin (ca.  $2\text{mm}$ ) sheet in the flow. With this sheet parallel to the channel walls,

this technique of illumination provides additional information regarding the position of the illuminated particles, and hence of the vortex, relative to the channel wall.

### 3 VISUALISATION STUDIES

The visualised flow patterns were photographed and recorded on video over a Reynolds number range of  $Re_H=300$  up to 7000, where the reference length for the Reynolds number has been chosen as the semi-channel height  $H$  ( $=5\text{mm}$ ). The exposure time for the photographs was  $1/120\text{s}$  on a 400 ASA (black and white). The video camera was a Sony video Hi8 Handycam. The recordings were done for three different geometrical configurations of the vortex generators. Quadruple hot-wire probe measurements of the velocity field in the flow with Configuration 2 are reported in Lau and Vasanta Ram (2) and Lau (3).

### 4 RESULTS

Over the entire Reynolds number range except at the higher end the oncoming flow in the channel section upstream of the winglets was steady and laminar. However there were occasional "bursts" observed in this section from a Reynolds number of around 900 onwards. These were possibly caused by disturbances due to screens and the honeycomb not having decayed sufficiently.

A selection of photographs of the visualised flow at various Reynolds numbers for the 3 winglet configurations is presented in figs. 5-10. At the lower end of the Reynolds number range the flow in the section with winglets was also steady as it in the oncoming flow. Unsteadiness of the flow over the winglet section started in all the three configurations studied at a Reynolds number of just over 300, although no unsteadiness was observable the flow in the upstream section. The unsteadiness was followed by the formation of regular structures which increased in complexity. At different levels of increasing Reynolds number the beginning of unsteadiness followed in turn by the formation of structures at different levels of scales at different locations could be observed.

Table 1 gives a selected overview on the flow patterns for Configuration 1 together with approximate Reynolds numbers at which the patterns form. At a Reynolds number of about 300 both the surrounding channel flow and longitudinal vortices are steady. From the Reynolds number of about 320 onwards structures appear in the vortices. These structures are periodic both in time and space and their frequency depends on the Reynolds number. At  $Re_H=600$  the visualised flow region far behind the vortex generators has the same appearance as a turbulent wake in a free stream. However, the two vortices are still discernible and

parallel. Additional vortex types are visible e.g. vortices similar to "horseshoe" vortices. From  $Re_H=900$  onwards first turbulent spots appear in the channel flow and up to  $Re_H=1500$  the entire channel flow becomes turbulent with still relatively coarse structures in it. With increasing Reynolds number the structures become finer and finer and at  $Re_H=6700$  they cannot any longer be registered by the human eye. Yet the longitudinal vortices behind the two vortex generators are visible over the entire Reynolds number range.

Configuration 2 generates a spanwise row of longitudinal vortices. Our visualisation studies indicate that the effects described for Configuration 1 are all present in Configuration 2 also, and that they appear at the same Reynolds number. A qualitative comparison of the visualised flow pattern for the winglet configuration 2 with the corresponding quadruple hot-wire probe measurements may be carried out with the help of fig. 11 taken from Lau and Vasanta Ram (2) showing the streamwise development of the v- (normal to the channel wall) and w- (spanwise) velocity components in this flow.

In Configuration 3 vortices generated by the upstream winglet interact with those generated downstream. Fig. 9a, b shows the visualised flow pattern at some instant of time at  $Re_H=320$  at upstream locations and over the whole test section.

## ACKNOWLEDGEMENTS

This work has been supported financially by the Deutsche Forschungsgemeinschaft (DFG).

## REFERENCES

- (1) S. Lau, K. Meiritz and V. Vasanta Ram (1996) Measurement of momentum and heat transport in the turbulent channel flow with embedded longitudinal vortices. Paper presented at the Engineering Foundation Conference "Turbulent Heat Transfer", San Diego, March 10-15, 1996.
- (2) S. Lau and V. Vasanta Ram (1998) Measurement and analysis of the turbulent flow quantities in a channel with embedded longitudinal vortices. To appear in Notes on Numerical Fluid Mechanics No. 63, Verlag Vieweg.
- (3) S. Lau (1996) Messung und Analyse der Transportgroessen in der turbulenten Kanalstroemung mit eingebetteten Laengswirbeln. Dr.-Ing. Dissertation, Fakultae fuer Maschinenbau, Ruhr University, Bochum, Germany

$Re_H$	Characteristic patterns
300	laminar channel flow, laminar and steady vortices
320	laminar channel flow, in time and space periodic structures in the vortices generated at the front edge of the winglets
370	several periodic structures in the vortices generated at the front and at the rear edge of the winglets
670	periodic structures in the vortices; far field in shape of a turbulent wake with slightly visible vortices
890	wake with "embedded" vortices; first turbulent spots in the channel flow
1180	only few "laminar" areas in the whole channel area, vortices better visible
1550	turbulent channel flow with coarse structures; well visible vortices
3400	turbulent channel flow with fine structures; well visible vortices
6700	turbulent channel flow with very fine structures; well visible vortices

Table 1 Characteristic patterns in the channel flow with embedded longitudinal vortices for configuration 1.

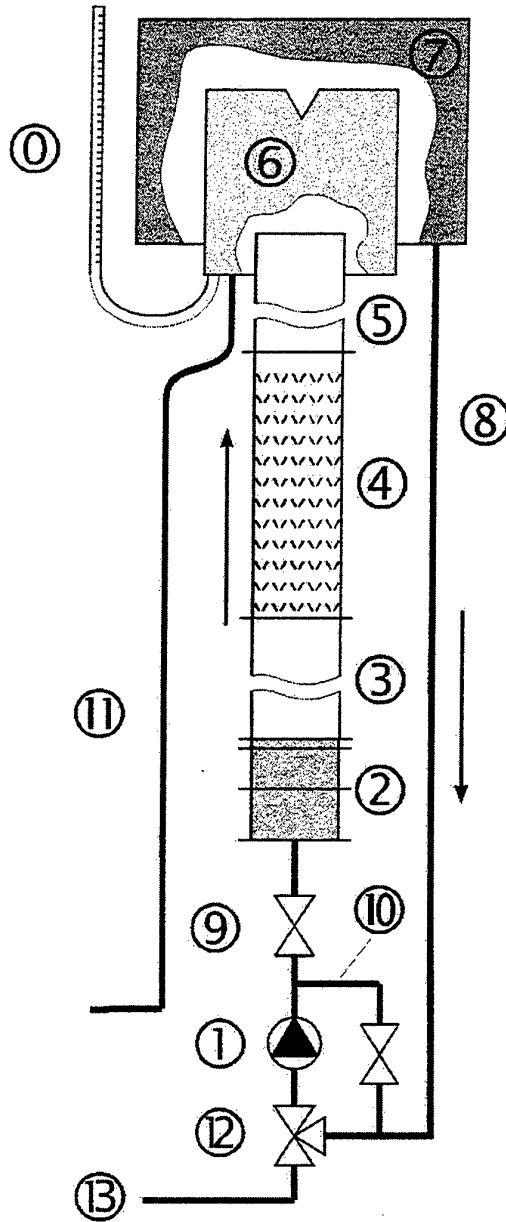


Figure 1a Flow visualisation facility: schematic diagram  
 (1) pump, (2) settling chamber, (3) channel section for developing flow,  
 (4) channel section for flow visualisation, (5) channel section for outflow,  
 (6) trough with glass tube (0) to read, (7) overflow trough, (8) return piping,  
 (9) valve, (10) bypass, (11), (13) pipings for emptying the facility,  
 (12) three-way valve for filling the facility



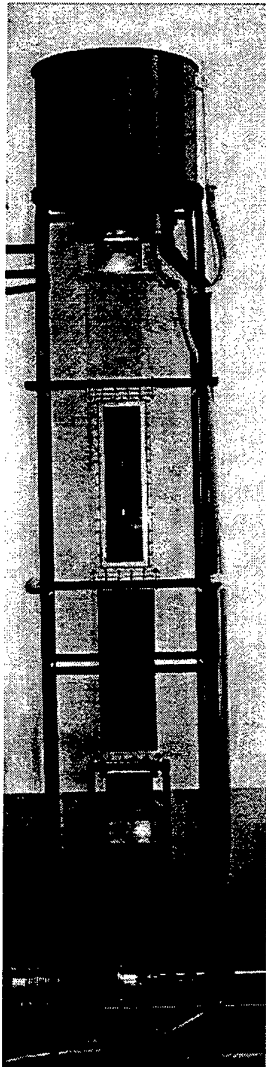


Figure 1b Flow visualisation facility: photograph.

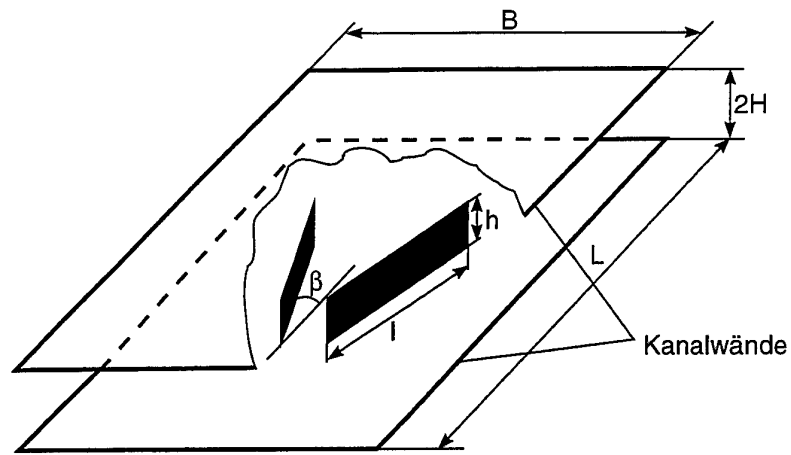


Figure 2 Winglet configuration 1:  $2H=40\text{mm}=2h$ ,  $L=200\text{mm}=10h$ ,  $l=80\text{mm}=4h$ ,  $B=160\text{mm}=8h$ ,  $\beta=30^\circ$ , thickness of the winglets  $s=1\text{mm}$ .

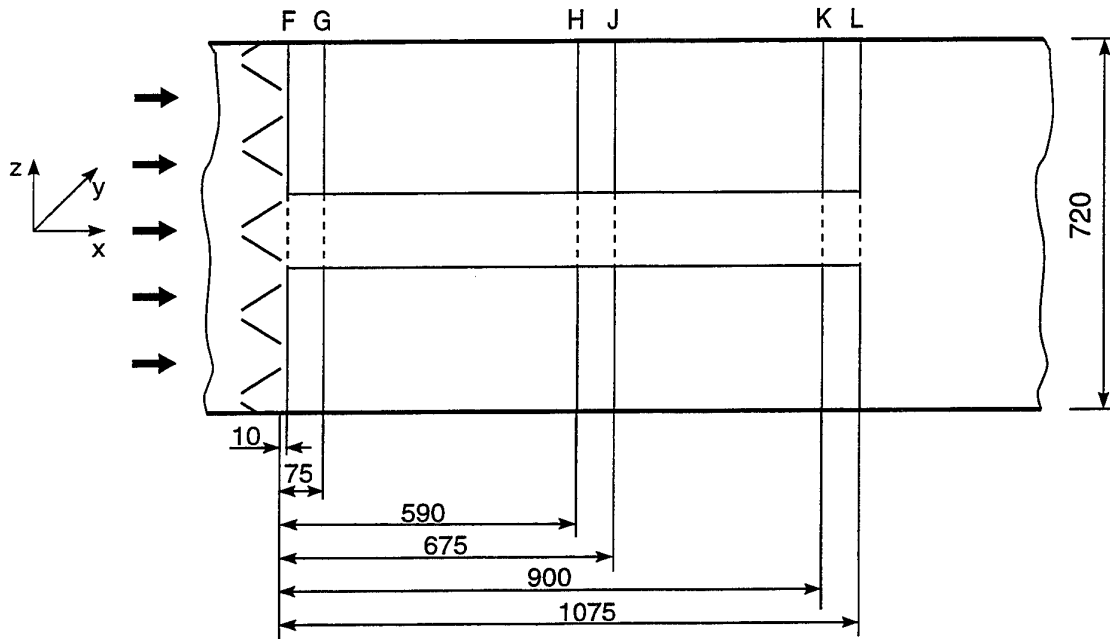


Figure 3 Winglet configuration 2: G, H, J, K and L are planes of probe measurement.

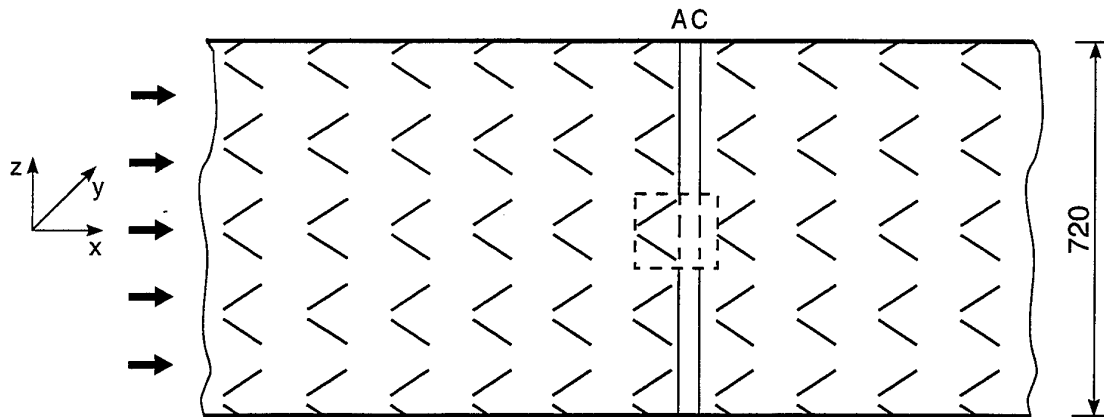


Figure 4 Winglet configuration 3: A and C are planes of measurement.

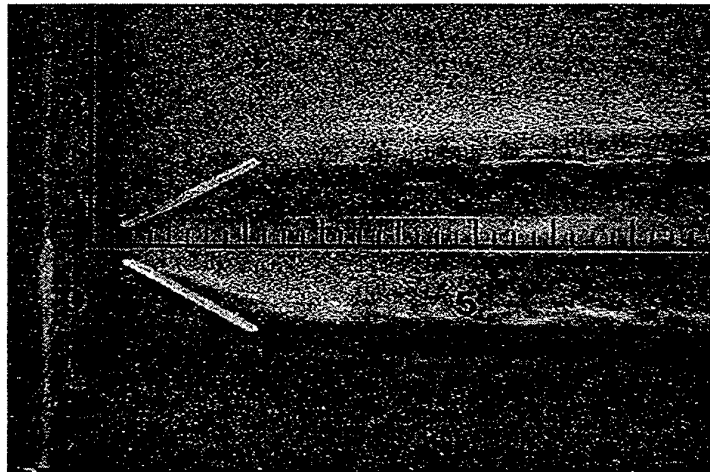


Figure 5 Visualised flow for configuration 1,  $Re_H=320$ .

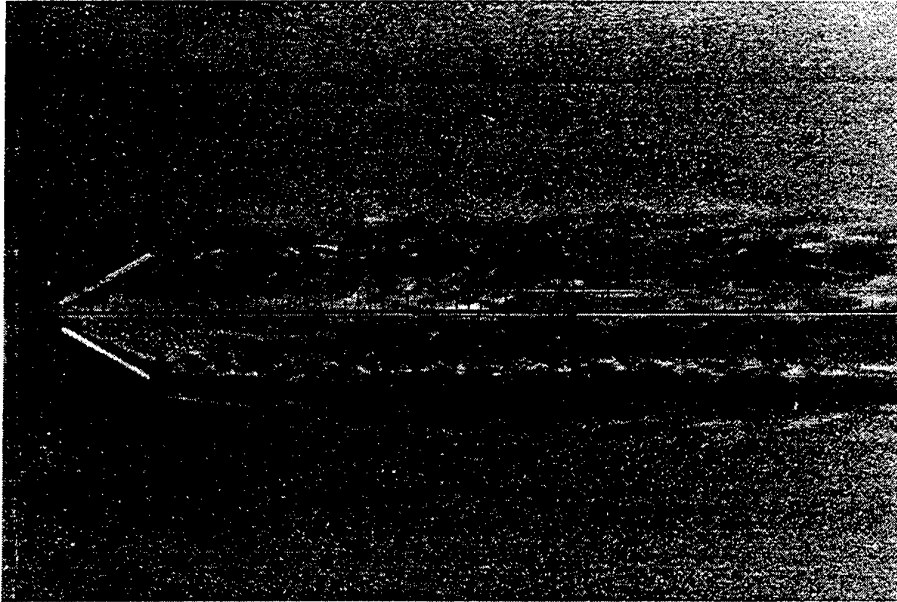


Figure 6 Visualised flow for configuration 1,  $Re_H=370$ .



Figure 7 Visualised flow for configuration 2,  $Re_H=370$ .

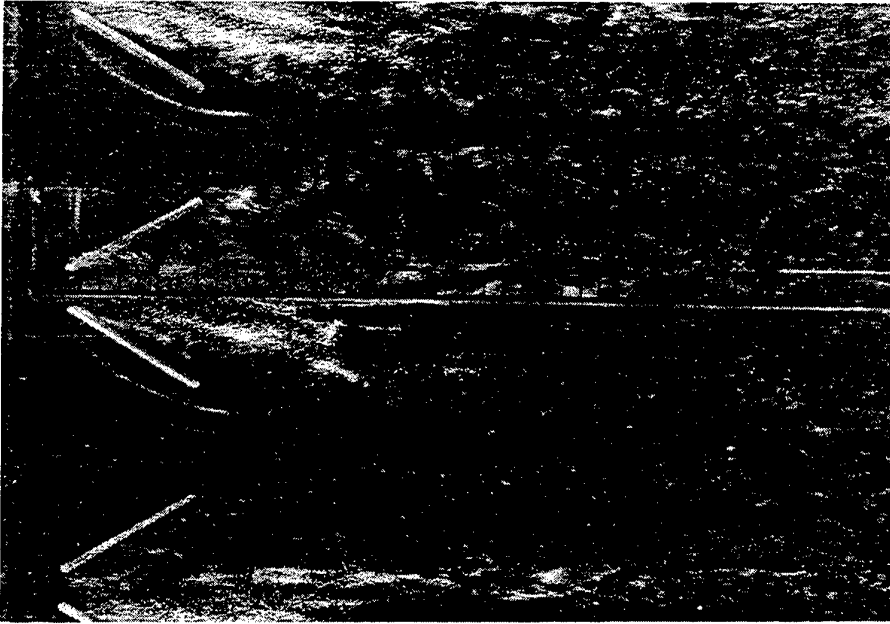


Figure 8 Visualised flow for configuration 2,  $Re_H=670$ .

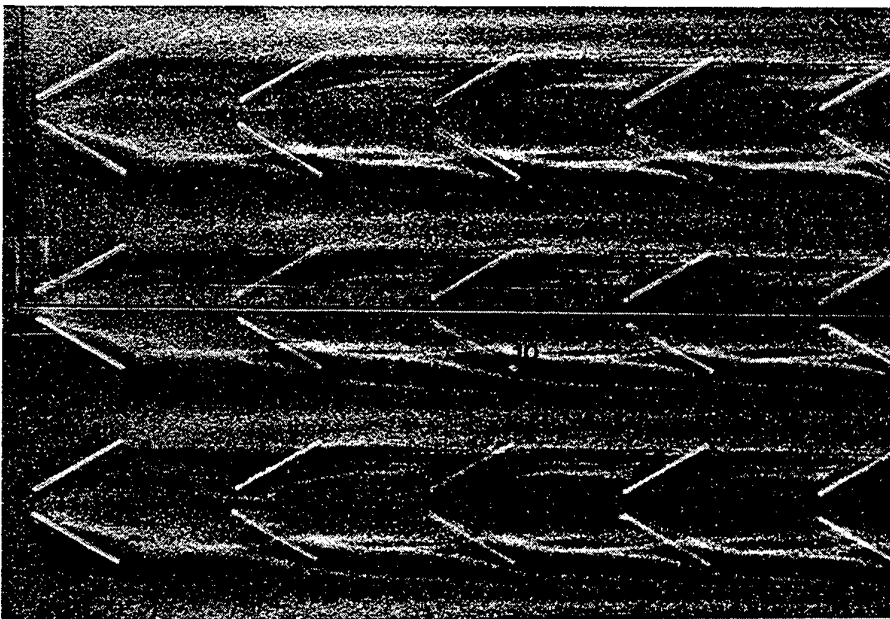


Figure 9a Visualised flow for configuration 3,  $Re_H=320$ .

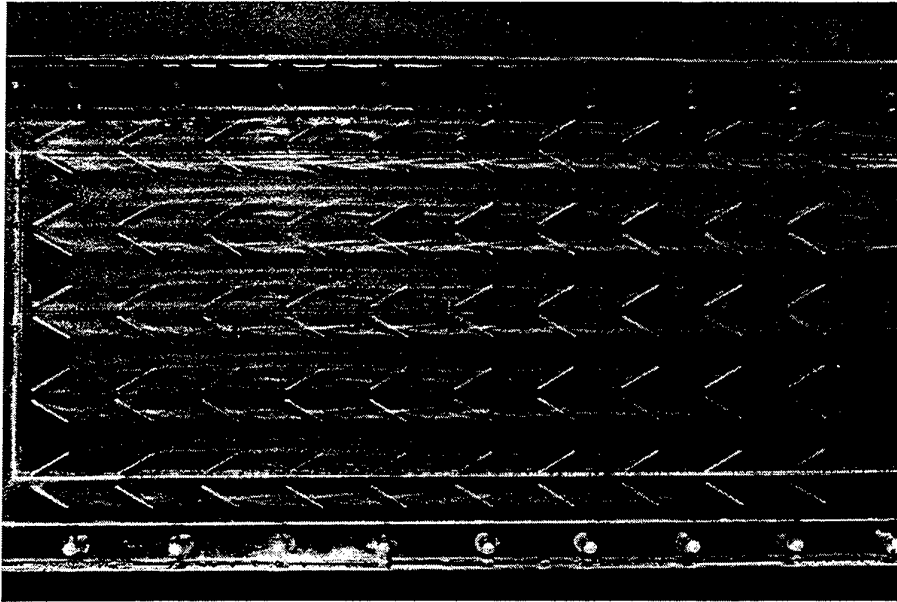


Figure 9b Visualised flow for configuration 3,  $Re_H=320$ .

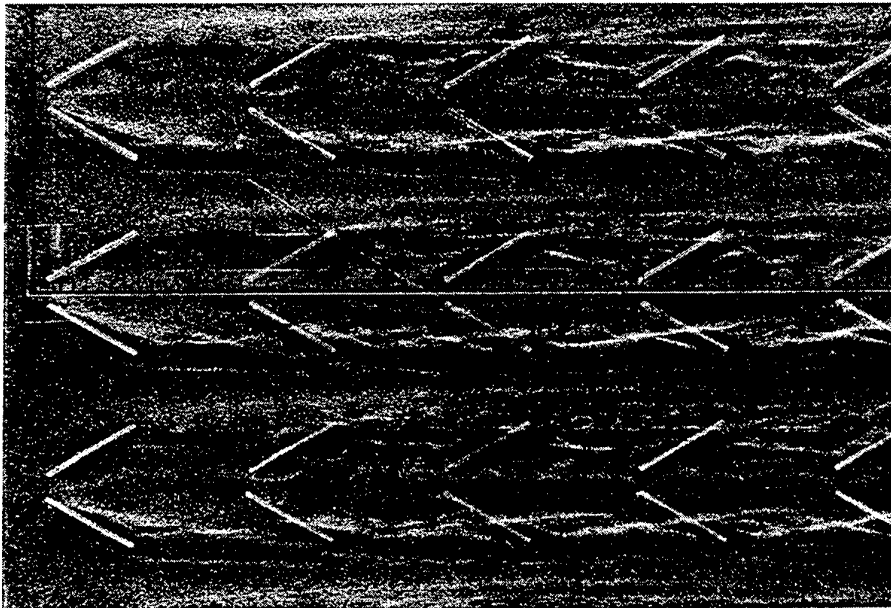


Figure 10 Visualised flow for configuration 3,  $Re_H=370$ .

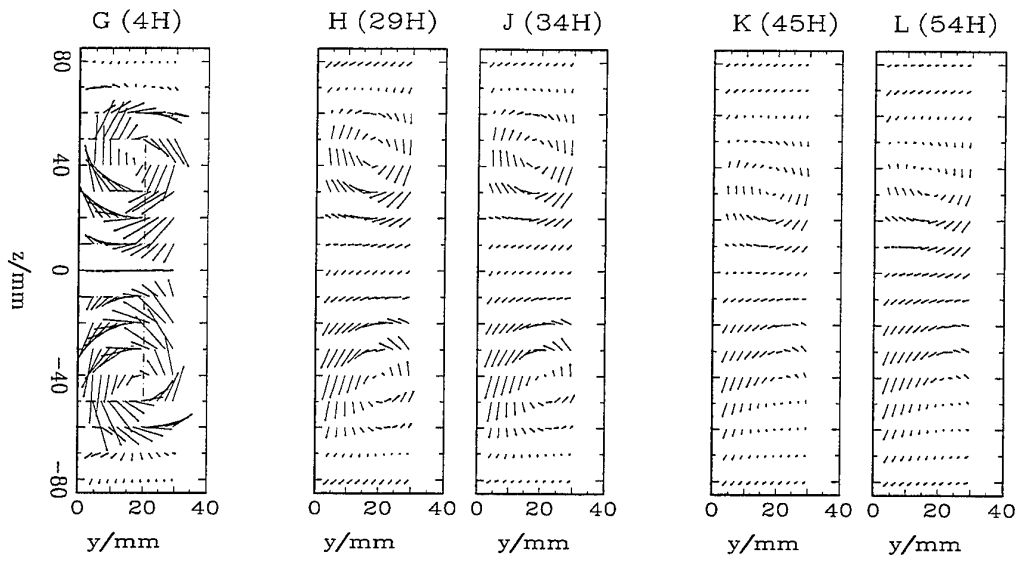


Figure 11 Secondary velocity components behind a spanwise row of winglets (configuration 2).  
 The locations of the planes G, H, J, K and L are given from the trailing edge of the winglet row.

# DISSIPATIVE PROPERTIES OF A DYNAMIC AND THERMAL FLAT WAKE WITH NEGATIVE NET EXCESSIVE MOMENTUM IN STRATIFIED FLOW.

P.Ya. Cherepanov and V.A. Babenko

The Luikov Heat and Mass Transfer Institute  
National Academy of Sciences, Belarus

## ABSTRACT

In the paper a complex experimental and theoretical study of a turbulent wake with negative net excessive momentum in a temperature-stratified medium with steady linear stratification has been carried out. The experimental investigation has been made in air wind tunnel with a velocity of upstream flow  $U_{1\infty} = 14$  m/s for three values of mean temperature gradient ( $\Gamma = dT_{\infty}/dx_2 = 65, 130, 220$  K/m). The results show a complex transformation of various characteristics of thermal wake. Numerical simulation made with Reynolds stress model was able to predict the main features of the dynamic and thermal wake development.

## 1 INTRODUCTION

The first investigations of thermal turbulence can be dated to the end of forties, Hinze & Zijnen (1) and Corrsin & Uberoi (2). Later in seventies, Townsend (3), Freymuth & Uberoi (4), and Fabris (5) studied the thermal wake behind the heated cylinder, and Freymuth & Uberoi (6) behind the heated sphere. In the paper by Antonia & Browne (7) the dynamic and thermal turbulent wake of a heated cylinder was investigated in more detail. In particular, the longitudinal  $\langle u_1 t \rangle$  and transverse  $\langle u_2 t \rangle$  turbulent heat fluxes were measured. Using the results of these measurements and the time scale based on dispersion and mean dissipation rate of temperature fluctuation, Antonia & Browne (7) suggested numerical values for some constants entering the modern models of interaction between the correlations of temperature and pressure gradients. Except for the regions close to the external boundary of the wake, the vertical turbulent heat flux  $\langle u_2 t \rangle$  was in simple correlation with the Reynolds shear stress.

Alexsopoulos & Keffer (8) also studied a thermal wake of a cross-flowed cylinder, but in their case the cylinder was not heated; instead, a linear thermal stratification of the main stream was created with the electrically heated grid located at some upstream distance from the cylinder. For three different cylinder sizes Alexsopoulos & Keffer (8) measured the profiles of mean temperature defect and temperature fluctuations together with the wake's widening laws. In these experiments a noticeable asymmetry of mean temperature profile was observed. The attention is also drawn to the unusual form of temperature fluctuation profile with large ratio  $(\Theta_{\max} / \Theta_0)^{1/2} \approx 1.7$ . The mean temperature defect in paper (8) grew with the distance from the flowed body. For the cylinder of outer diameter  $d = 12.7$  mm the growth of temperature

defect lasted up to the coordinate  $x_1 / d = 228$ . The ratio of  $\Delta T_{\max} / \Gamma \delta_T$  decreased reaching the constant value of about 0.38 at  $x_1 / d = 120$

Bolonov et.al. (9) investigated experimentally the development of a flat wake behind cross flowed cylinder in stratified water stream with constant mean velocity. The stratification was created with two or three water layers of different density. These experiments covered a relatively wide range of Froude and Reynolds numbers ( $Fr = 5 \dots 1400$ ,  $Re = 500 \dots 1800$ ) and demonstrated an essential influence of stratification to evolution laws of a flat turbulent wake.

A common drawback of the cited above and some other works was that the almost no data on dissipation were obtained. The lack of such data prevents the testing of modern numerical simulation methods and their further development.

The present paper is an extension of work (10), where the wake generated by a wing profile in air stream has been considered. As against (10), here the basic emphasis is given to study of dissipative properties of a dynamic and thermal wake.

## 2. EXPERIMENTAL INSTALLATION

### 2.1 Experimental setup

The experimental investigation was made in the wind tunnel of an open-closed type with a velocity of upwind air flow  $U_{1\infty} = 14$  m/s and three values of mean temperature gradient ( $\Gamma = dT_{\infty}/dx_2 = 65, 130, 220$  K/m). In the investigated range of distances from the flowed body ( $x_1 / d \leq 100$ ,  $d = 0.01$  m) it corresponded to a case of weak temperature



stratification ( $N = (g\Gamma / T_{\infty 0})^{1/2} = 1.6, 2.2, 2.9 \text{ s}^{-1}$ ), where  $N$  is the Brunt-Vaissala frequency.

Temperature stratification of air flow was produced by twenty electrically heated tubes (diameter 5mm, step 15mm) placed in a stream near inlet contraction. This heating system let us to reach a linear temperature stratification of the flow in a range of temperature gradient within  $\Gamma = 30 \div 300 \text{ K/m}$ . The majority of experiments was performed at  $\Gamma = 65 \text{ K/m}$ .

The flowed model was a hollow symmetrical airfoil with the two razor edges at the rear. It was made of polished duralumin. The maximum thickness of the wing cross section,  $d$ , was equal to 0.01 m, the chord was 0.1m, and the span was 0.074m. The wing was set at zero incidence in a horizontal symmetry plane at the beginning of the test section of tunnel. The air, injected from a flat slot in the rear of the body was supplied from a special pneumatic installation, having cooling and heating devices to maintain the jet temperature at a desired level. The schedules of experimental setup and the flowed model were described in (10) and (11).

## 2.2 Experimental procedures

The DISA equipment was used to measure the statistical parameters of turbulent velocity and scalar fields. Dynamic turbulence characteristics were measured according to known standard procedures (Cherepanov & Dmitrenko (12), Dmitrenko *et al.* (13)).

Probes for measuring the velocity fluctuation had wires with the diameter  $5\mu\text{m}$  and the sensible part 1.2mm long, temperature probes  $1\mu\text{m}$  and 0.4mm, accordingly. The probes were positioned in three-coordinate device moving in a space accurately to 0.01mm.

Mean temperature of upstream flow and the wake behind the body was registered with a comb consisting of 40 differential chromel-constantan thermocouples having diameter 0.1mm and sensibility  $59.3\mu\text{V/K}$ . The comb was made of a plastic and occupied vertically nearly all the channel's cross section. Working sides of thermocouples were set in vertical symmetry plane, the reference side being common and placed in upstream flow. To control the measurement of mean temperature a single movable differential thermocouple was also used. The temperature profiles determined by the both methods proved to be the same.

Mean temperature and temperature fluctuations were measured by the special homemade thermoresistor unit TR-2. The probe of the unit was a tungsten wire with the diameter  $1\mu\text{m}$  and 0.4mm long, through which the current of 0.7mA was passed. The output signal from TR-2, which was proportional to temperature fluctuation, passed through the special correction block and then through low frequency Butterworth filter of the third order with cut-off frequency of 5kHz. After

extending the bandwidth of the probe by a factor of ten with this correction block, the resulting frequency bandwidth of temperature fluctuation was 1-4kHz.

The measured dispersion of temperature fluctuations was corrected by subtracting the dispersions of background and apparatus noises. The resolution at measuring the main temperature was 0.05K. Velocity and temperature microscales were determined with the known Taylor's "frozen turbulence" hypothesis by formula

$$\lambda_w = U_1 K_{\text{exp}} \tau_{\text{exp}} e_w / \dot{e}_w$$

where  $U_1$  is the longitudinal velocity component, m/s;  $K_{\text{exp}}$  the magnification of differentiator,  $K_{\text{exp}}=1$ ;  $\tau_{\text{exp}}$  the characteristic time of differentiator,  $\tau_{\text{exp}}=0.6369\text{ms}$ ;  $e_w$  the voltage which was proportional to longitudinal velocity or temperature fluctuation;  $\dot{e}_w$  the time derivative of the voltage  $e_w$ ;  $e_w = (\overline{e^2} - \overline{e_b^2})^{1/2}$ ;  $\dot{e}_w = (\dot{\overline{e^2}} - \dot{\overline{e_b^2}})^{1/2}$ . Here  $\overline{e^2}$  is the measured mean square voltage proportional to  $\langle u_1^2 \rangle$  or  $\langle t^2 \rangle$ ;  $\overline{e_b^2}$  is the measured mean square voltage in background.

Microscale determined by the above formula was corrected for a limited resolution of velocity probe 55P01 by Wingaard procedure (14), and for temperature probe 55P31 by Larsen procedure (15).

Dissipation of turbulence energy was calculated by isotropic relation  $\varepsilon_u = 15\nu \langle u_1^2 \rangle / \langle \lambda_{u1}^2 \rangle$ , where  $\lambda_{u1}$  was the Taylor's velocity microscale; and dissipation of temperature by relation  $\varepsilon_t = 6\kappa \langle t^2 \rangle / \langle \lambda_t^2 \rangle$ , where  $\kappa$  was the thermal diffusivity coefficient,  $\lambda_t$  the Taylor's temperature microscale.

Mixed correlations of velocity and temperature fluctuations were measured with a three-wire probe, which was made from standard X-form probe 55P51, and one-wire probe 55P31 by DISA (with the diameter  $1\mu\text{m}$ , 0.4mm long). The both probes were installed with a simple tiny device in such a way that the wire of probe 55P31 was at 0.8mm from the symmetry plane of crossing wires of 55P51 probe. Wires mutual position was adjusted under microscope.

Inclined wires of the probe were switched to DISA thermoanemometers of constant temperature 55D01 and operated at overheating extent 0.8. Temperature wire was switched to thermoanemometer 55D01 in a direct current mode. Through the wire with the diameter  $1\mu\text{m}$  the current of 0.7mA passed, so far the wire was practically insensible to velocity fluctuations. Extending the bandwidth of temperature test channel was done with the blocks of wires' heat inertia compensation. The characteristic time of compensation

scheme was adjusted to a transient process arising when pulsed current passed through the wire. For the wire with the diameter of 1μm at the flow velocity 14m/s and minimal correction the bandwidth of test channel was about 20kHz. At the correction block output there were the low frequency Battersworth filters of the third order (with attenuation of 18db per octave) with cut-off frequencies of 5, 10, and 20kHz. Filtration of constant temperature anemometer signals was made by the same filters of DISA blocks 55D26.

Fluctuation components of signals from the three wires (with the frequencies from 1Hz and above) were magnified by multi-channel amplifier and sent to the input of automatic processing system, where they were transformed to digital form by analog-digital transformer and downloaded to PC. At any tested point the arrays of about  $2 \cdot 10^5$  samples were accumulated. These arrays then were processed by special computer program accounting for the graduation curves of wires and the mean voltages at thermoanemometers outputs, obtained during testing with digital voltmeter and integrator. The procedure of measuring the mixed velocity-temperature correlations is detailed in (16).

During the experiments the following characteristics were measured: mean temperature profiles, temperature fluctuation intensity, Taylor's velocity and temperature microscales, second order mixed moments (transverse and longitudinal heat fluxes), third mixed moments, third and fourth central moments (skewness, excess), and some other one-point turbulence parameters of velocity and scalar fields. A diversified information on various parameters in the wake, obtained within the framework of our experiment, offers some insight into development of more adequate and exact theoretical turbulence models of free stratified flows.

### 3 NUMERICAL INVESTIGATION

#### 3.1 Reynolds stress turbulence model

For numerical simulation we used the nearly homogeneous "Reynolds stress - vorticity" model from refs. (17), (18) which consists of the two blocks of equations. The first or hydrodynamic one is written for the Reynolds stresses  $\langle u_i u_j \rangle$  and the vorticity  $\epsilon_u$  which is defined through Laplace operator from a double point velocity correlation taken in a space of two closely located points,

$$\epsilon_u = \sqrt{-\partial^2 \langle u_i u_j \rangle / \partial x_k^2} \Big|_{\vec{x} \rightarrow 0}.$$

The vorticity can

be expressed through the dissipation rate of turbulence kinetic energy,  $\epsilon_u$  as  $\epsilon_u = \epsilon_u - (\nu/4) \partial^2 q^2 / \partial x_k^2$ , where  $q^2 = \langle u_i u_i \rangle$  is the doubled kinetic energy. Since the difference between  $\epsilon_u$  and  $\epsilon_u$  is mainly rendered at very long distances from a turbulence

source, in this paper we shall consider the two values to be equal. With this remark the hydrodynamic block of equation from (17) looks like this

$$\begin{aligned} D \langle u_i u_j \rangle / D\tau - P_{ij} + 2 \left( d_u \langle u_i u_j \rangle / q^2 + (1 - d_u) \delta_{ij} / 3 \right) \epsilon_u \\ + a_u (1 - d_u) a_{ij} \epsilon_u + b_u \left( \alpha_u q^2 S_{ij} + (\beta_u b_{ij} + \gamma_u c_{ij}) P_{kk} \right) + \\ + \beta (g_i \langle u_j t \rangle + g_j \langle u_i t \rangle) = (\nu/2) \partial^2 \langle u_i u_j \rangle / \partial x_k^2 \\ D \epsilon_u / D\tau + (F_u^{**} - 3 \bar{P}_u) \epsilon_u^2 / q^2 - \\ - \frac{\partial}{\partial x_k} \left[ \alpha_{\epsilon_u} \left( \frac{q^2}{\epsilon_u} \right) \langle u_k u_l \rangle \frac{\partial \epsilon_u}{\partial x_l} \right] = (\nu/2) \partial^2 \epsilon_u / \partial x_k^2 \end{aligned} \quad (1)$$

where  $g_i$  is the gravity vector,  $\beta = \frac{1}{\rho_0} \left( \frac{\partial \rho}{\partial T} \right)_0$  is the

thermal expansion coefficient of medium,  $\delta_{ij}$  is the

Kronecker delta,  $P_{ij} = - \left( \langle u_i u_k \rangle \frac{\partial U_j}{\partial x_k} + \langle u_j u_k \rangle \frac{\partial U_i}{\partial x_k} \right)$  is

the production rate tensor of the Reynolds stresses,

$S_{ij} = \frac{1}{2} \left( \frac{dU_i}{dx_j} + \frac{dU_j}{dx_i} \right)$  is the tensor of mean

velocity strain,  $a_{ij}$ ,  $b_{ij}$ ,  $c_{ij}$  are the deviatric tensors of the tensors  $\langle u_i u_j \rangle$ ,  $P_{ij}$  and

$$D_{ij} = - \left( \langle u_i u_k \rangle \frac{\partial U_k}{\partial x_j} + \langle u_j u_k \rangle \frac{\partial U_k}{\partial x_i} \right);$$

$$a_{ij} = 3 \langle u_i u_j \rangle / q^2 - \delta_{ij}, \quad b_{ij} = 3 P_{ij} / P_{kk} - \delta_{ij},$$

$$c_{ij} = 3 D_{ij} / P_{kk} - \delta_{ij}; \quad \bar{P}_u = - \frac{P_{kk}}{2 \epsilon_u}$$

is the doubled turbulence kinetic energy production to dissipation rate ratio.

The variable coefficients  $a_u$ ,  $b_u$ ,  $\alpha_u$ ,  $\beta_u$ ,  $\gamma_u$ ,  $F_u^{**}$  are obtained from approximation of unknown terms proposed in refs. (17),(18):

$$\begin{aligned} a_u = 3, \quad b_u = 2 / \left\{ 1 + \bar{P}_u \left[ (1 - d_u) / (F_{us}^{**} - 2) + 0.5 d_u / (F_{uw}^{**} - 2) \right] \right\} \\ F_{us}^{**} = F_{us}^{**} (1 - d_u) + F_{uw}^{**} d_u, \quad F_{us}^{**} = 14 / 5 \\ F_{uw}^{**} = 11 / 3, \quad \alpha_u = 2 (d_u / 11 - 1 / 11), \\ \beta_u = 4 d_u / 33, \quad \gamma_u = d_u / 33 \end{aligned}$$

where  $d_u(R_\lambda^2) = 1 - 2 / (1 + \sqrt{1 + 2800 / R_\lambda^2})$ ,  $d_u \in (0,1)$  is the parameter used in paper (17) to parametrize some unknown terms,  $R_\lambda^2 = \lambda_u^2 q^2 / \nu^2$  - the squared turbulence Reynolds number, built on

squared velocity fluctuation and the Taylor microscale  $\lambda_u$ , defined as  $\lambda_u^2 = 5\nu q^2 / \varepsilon_u$ .

The second block of equations is written for the squared temperature fluctuation  $\langle t^2 \rangle$ , velocity-scalar correlation tensor  $\langle u_i t \rangle$ , and the rate of dissipation of a scalar fluctuations  $\varepsilon_t = \kappa \langle (\partial t / \partial x_k)^2 \rangle$ . The equations for these functions are the following:

$$\begin{aligned} D \langle t^2 \rangle / D\tau + 2(1 - \bar{P}_t) \varepsilon_t &= 0, \\ D \langle u_i t \rangle / D\tau - P_{it} + \varepsilon_{it} - \Phi_{it} &= -\beta g_i \langle t^2 \rangle, \\ D \varepsilon_u / D\tau + (F_u^{**} - 3\bar{P}_u) \varepsilon_u^2 / q^2 &= \\ = -2d_u \beta g_i \frac{\sigma}{1 + \sigma} \tau_{uw}^{-1} \langle u_i t \rangle &\quad (2) \end{aligned}$$

where

$$\begin{aligned} \bar{P}_t &= P_{tt} / 2\varepsilon_t, \quad P_{tt} = -2 \langle u_k t \rangle \partial T / \partial x_k, \\ P_{it} &= -(\langle u_i u_k \rangle dT / dx_k + \langle u_k t \rangle dU_i / dx_k), \\ \tau_{uw}^{-1} &= \tau_u^{-1} [2(\sigma_{sw} + 3/5)R / R_{sw} - \bar{P}_u], \\ \Phi_{it} &= \frac{1}{\rho} \langle p \frac{\partial t}{\partial x_k} \rangle. \end{aligned}$$

Here  $\tau_u = q^2 / \varepsilon_u$ ,  $\tau_t = \langle t^2 \rangle / \varepsilon_t$ ,  $R = \tau_u / \tau_t$  are time scales for velocity and scalar turbulent fields together with their ratio,

$$\begin{aligned} R_{sw} &= \frac{1}{5\sigma} \left[ 1 - 2 \left( \frac{2\sigma}{1+\sigma} \right)^{3/2} + \sigma^{3/2} \right] \left[ 1 - 2 \left( \frac{2\sigma}{1+\sigma} \right)^{1/2} + \sigma^{1/2} \right]^{-1}, \\ \sigma_{sw} &= \frac{3}{10} \frac{1-\sigma}{\sigma} \left[ 1 - \left( \frac{2\sigma}{1+\sigma} \right)^{3/2} \right]^{-1/2} \end{aligned}$$

are the asymptotic values of time scale ratio  $R$  and turbulent Prandtl number  $\sigma_T$  in a final stage of decay from exact solution made by Dunn & Reid (19) in a passive scalar case.

The tensor  $\Phi_{it}$  in (2) was estimated to be the following

$$\begin{aligned} \Phi_{it} &= -[1/3 + 10 \langle u_i^2 \rangle / q^2] R - \bar{P}_u \tau_u^{-1} (1 - d_u) \langle u_i t \rangle + \\ &+ \left( \frac{4}{5} \frac{dU_i}{dx_k} - \frac{1}{5} \frac{dU_k}{dx_i} \right) \langle u_i t \rangle + \frac{1}{3} \beta g_k (d_u a_{ik} + \delta_{ik}) \langle t^2 \rangle \end{aligned}$$

### 3.2 Mathematical formulation of the problem.

In the present work we investigate the turbulence in a wake propagated horizontally into a medium with a mean temperature distributed linearly in vertical direction across the main flow,  $T_\infty = T_{\infty 0} + \Gamma x_2$ ,

where  $T_{\infty 0}$  is the axial value of mean temperature. The gravity vector in this case is opposite to the vertical coordinate  $x_2$ :  $g_i = \{0, -g, 0\}$ .

In view of turbulent mixing the initial linear distribution of mean temperature  $T_\infty(x_2)$  is disturbed in a wake, so far the mean temperature profile attains the characteristic S-form.

Based on the above second-order model, eqs. (1)-(2), being applied to this special case, the steady state turbulence in the wake is described by the set of the following parabolic differential equations written in a non-dimensional form:

for continuity

$$\frac{\partial}{\partial x}(U) + \frac{\partial}{\partial y}(V) = 0,$$

for axial momentum

$$(1+U) \frac{\partial U}{\partial x} + V \frac{\partial U}{\partial y} - \frac{\partial}{\partial y} \left( \frac{1}{\text{Re}} \frac{\partial U}{\partial y} + R_{12} \right) = 0,$$

for shear stress  $R_{12}$

$$\begin{aligned} (1+U) \frac{\partial R_{12}}{\partial x} + V \frac{\partial R_{12}}{\partial y} - R_{22} \frac{\partial U}{\partial y} + \\ + b_u \left[ \alpha_u E \frac{\partial U}{\partial y} + 2R_{12} \frac{\partial U}{\partial y} (\beta_u b_{12} + \gamma_u c_{12}) \right] + \\ + [2d_u + 3a_u(1-d_u)] \frac{D_u}{E} R_{12} + \frac{7}{10} F^2 R_{11} - \\ - \frac{\partial}{\partial y} \left[ \frac{1}{2\text{Re}} \frac{\partial R_{12}}{\partial y} + \alpha_q \frac{E}{D_u} \left( 2R_{22} \frac{\partial R_{12}}{\partial y} + R_{12} \frac{\partial R_{22}}{\partial y} \right) \right] = 0, \end{aligned}$$

for normal Reynolds stresses  $R_{11}$  and  $R_{22}$

$$\begin{aligned} (1+U) \frac{\partial}{\partial x} R_{11} + V \frac{\partial}{\partial y} R_{11} + [2d_u + 3a_u(1-d_u)] \left( \frac{R_{11}}{E} - \frac{1}{3} \right) D_u + \\ + \frac{2}{3} D_u - 2(1-b_u \frac{3}{11} d_u) R_{12} \frac{\partial U}{\partial y} - \frac{1}{5} F^2 R_{21} - \\ - \frac{\partial}{\partial y} \left\{ \left[ \frac{1}{2\text{Re}} + \alpha_q \frac{E}{D_u} R_{11} \right] \frac{\partial R_{11}}{\partial y} + 2\alpha_q R_{12} \frac{E}{D_u} \frac{\partial R_{12}}{\partial y} \right\} = 0, \\ (1+U) \frac{\partial R_{22}}{\partial x} + V \frac{\partial R_{22}}{\partial y} + [2d_u + 3a_u(1-d_u)] \left( \frac{R_{22}}{E} - \frac{1}{3} \right) D_u - \\ - \frac{4}{11} d_u b_u R_{12} \frac{\partial U}{\partial y} + \frac{2}{3} D_u - \frac{8}{5} F^2 R_{21} - \\ - \frac{\partial}{\partial y} \left\{ \left[ \frac{1}{2\text{Re}} + 3\alpha_q \frac{E}{D_u} R_{22} \right] \frac{\partial R_{22}}{\partial y} \right\} = 0, \end{aligned}$$

for doubled turbulence kinetic energy  $E = R_{11} + R_{22} + R_{33}$

$$(1+U)\frac{\partial E}{\partial x} + V\frac{\partial E}{\partial y} - 2R_{12}\frac{\partial U}{\partial y} + 2D_u - 2F^2 R_{2t} - \frac{\partial}{\partial y} \left[ \left( \frac{1}{2\text{Re}} + \alpha_q \frac{E}{D_u} R_{22} \right) \frac{\partial E}{\partial y} + 2\alpha_q \frac{E}{D_u} \left( R_{12} \frac{\partial R_{12}}{\partial y} + R_{22} \frac{\partial R_{22}}{\partial y} \right) \right] = 0,$$

for dissipation rate of turbulence kinetic energy  $D_u$

$$(1+U)\frac{\partial D_u}{\partial x} + V\frac{\partial D_u}{\partial y} + (F_u^{**} - 3\overline{P_u})\frac{D_u^2}{E} - d_u F^2 R_{2t} \frac{D_u}{E} \frac{2\sigma}{\sigma+1} \left( 2(\sigma_{sw} + 3/5) \frac{R}{R_{sw}} - \frac{R_{12}}{D_u} \frac{dU}{dy} \right) - \frac{\partial}{\partial y} \left\{ \left[ \frac{1}{2\text{Re}} + \alpha_{eu} \frac{E}{D_u} \left( R_{22} + 2 \frac{R_{12}^2 + R_{22}^2}{E} \right) \right] \frac{\partial D_u}{\partial y} \right\} = 0,$$

for mean temperature defect  $C$

$$(1+U)\frac{\partial C}{\partial x} + V\left(\frac{\partial C}{\partial y} + 1\right) = \frac{\partial}{\partial y} \left( \frac{1}{\sigma \text{Re}} \frac{\partial C}{\partial y} + R_{2t} \right),$$

for vertical turbulent heat flux  $R_{2t}$

$$(1+U)\frac{\partial R_{2t}}{\partial x} + V\frac{\partial R_{2t}}{\partial y} - R_{22} \left( \frac{\partial C}{\partial y} + 1 \right) + F_w R_{2t} \frac{D_u}{E} + \frac{1}{5} R_{1t} \frac{\partial U}{\partial y} = F^2 d_u \frac{\Theta}{E} \frac{1}{5} \tau_w R_{1t} - F^2 \left( \frac{2}{3} - d_u \left( \frac{R_{22}}{E} - \frac{1}{3} \right) \Theta \right) + \frac{\partial}{\partial y} \left[ \left( \frac{\sigma+1}{2\sigma} \frac{1}{\text{Re}} + 2\alpha_{uw} R_{22} \frac{E}{D_u} \right) \frac{\partial R_{2t}}{\partial y} + \alpha_{ut} R_{2t} \frac{E}{D_u} \frac{\partial E}{\partial y} \right],$$

for the intensity of temperature fluctuations  $\Theta$

$$(1+U)\frac{\partial \Theta}{\partial x} + V\frac{\partial \Theta}{\partial y} + 2D_t - 2R_{2t} \left( \frac{\partial C}{\partial y} + 1 \right) = \frac{\partial}{\partial y} \left[ \left( \frac{1}{2\sigma \text{Re}} + \alpha_{ut} R_{2t} \frac{\Theta}{D_t} \right) \frac{\partial \Theta}{\partial y} + 2\alpha_{ut} R_{2t} \frac{\Theta}{D_t} \frac{\partial R_{2t}}{\partial y} \right],$$

for the rate of temperature fluctuations smearing  $D_t$

$$(1+U)\frac{\partial D_t}{\partial x} + V\frac{\partial D_t}{\partial y} - R_{12} \frac{D_t}{E} \frac{\partial U}{\partial y} - 2R_{2t} \frac{D_t}{\Theta} \left( \frac{\partial C}{\partial y} + 1 \right) + F_{t1}^{**} \frac{D_u}{E} D_t + F_{t2}^{**} \frac{D_t}{\Theta} D_t - \frac{4}{3} d_u \left( 1 - \frac{3}{5} \frac{1}{R_{sw}} \right) \frac{D_t}{\Theta} D_t = \frac{\partial}{\partial y} \left\{ \left[ \frac{1}{2\sigma \text{Re}} + \alpha_{et} \frac{\Theta}{D_t} \left( R_{22} + 2 \frac{R_{2t}^2}{\Theta} \right) \right] \frac{\partial D_t}{\partial y} \right\}, \quad (3)$$

where the following dimensionless variables and coordinates were introduced

$$x = x_1/d, \quad y = x_2/d, \quad U = (U_1 - U_{1\infty})/U_{1\infty}, \quad V = U_2/U_{1\infty}, \\ R_{11} = \langle u_1^2 \rangle / U_{1\infty}^2, \quad R_{12} = -\langle u_1 u_2 \rangle / U_{1\infty}^2, \quad R_{22} = \langle u_2^2 \rangle / U_{1\infty}^2, \\ E = q^2 / U_{1\infty}^2, \quad D_u = \varepsilon_u d / U_{1\infty}^3, \quad \Theta = \langle t^2 \rangle / (\Gamma d)^2, \\ C = (T - T_{\infty}) / \Gamma d = (T - T_{\infty 0}) / \Gamma d - y, \quad D_t = \varepsilon_t / \Gamma^2 d U_{1\infty}, \\ R_{it} = -\langle u_i t \rangle / (\Gamma d U_{1\infty}), \quad i = 1, 2$$

The rest of designations made in equations (3) is:

$$F_{t1}^{**} = F_u^{**} - 2 - \frac{4}{5} d_u, \quad F_{t2}^{**} = 2 + \frac{4}{5} d_u$$

are empirical functions similar to the function  $F_u^{**}$  in "dynamic" part of the problem;

$$F_{ut} = (1 - d_u) \left[ \frac{1}{3} + 10 \left( 1 + \frac{9}{5} \frac{R_{12}}{D_u} \frac{\partial U}{\partial y} \right) \frac{R_{22}}{E} R - \frac{R_{12}}{D_u} \frac{\partial U}{\partial y} \right] + d_u \left[ 2 \left( \sigma_{sw} + \frac{3}{5} \right) \frac{R}{R_{sw}} - \frac{R_{12}}{D_u} \frac{\partial U}{\partial y} \right], \quad \tau_{ut}^{-1} = \tau_u^{-1} F_{ut}$$

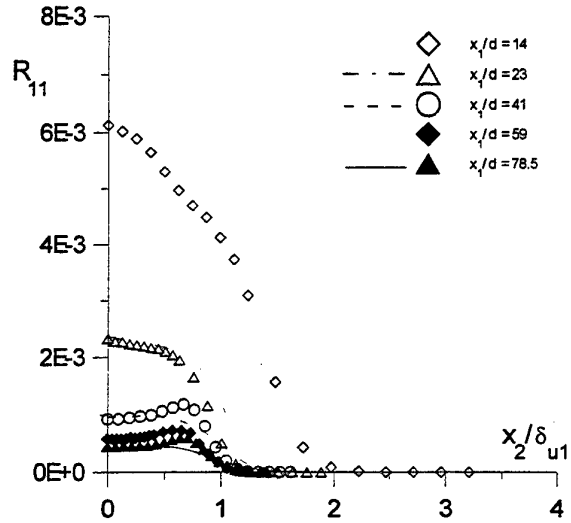


Figure 1 The development of vertical profiles of normal Reynolds stress  $R_{11}$ . Symbols - in experiment, lines - in simulation: dotted  $x_1/d=23$ , dashed -  $x_1/d=41$ , solid -  $x_1/d=78.5$

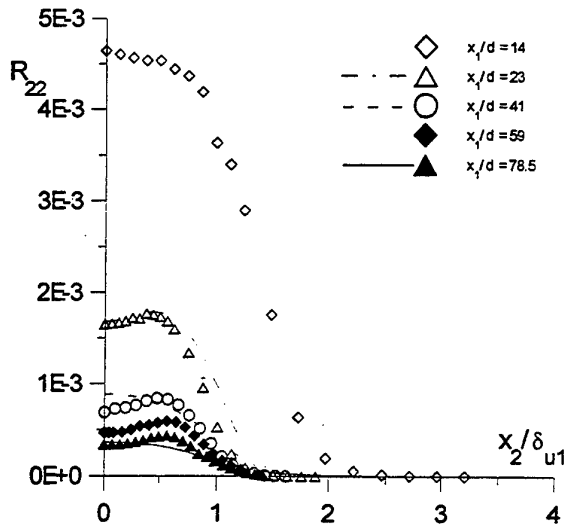


Figure 2 The development of vertical profiles of normal Reynolds stress  $R_{22}$  (for notation see figure 1).

Longitudinal turbulent heat flux,  $R_{1t}$ , in system (3) is determined from the algebraic relation

$$R_{1t} = \left[ \frac{1}{5} R_{2t} \frac{\partial U}{\partial y} + R_{12} \left( \frac{\partial C}{\partial y} + 1 \right) \right] \frac{E}{D_u} \frac{1}{F_{ut}} + d_u \frac{R_{12}}{E} \Theta F^2, \quad (4)$$

which is the consequence of differential equation for  $R_{1t}$ , if neglecting convection and diffusion of this parameter.

The influence of temperature stratification in system (3) is represented by the terms proportional to the squared inverse Froude number  $F = (Nd) / U_{1\infty}$ .

Comparing experimental and calculated results regarding to the extension rates of velocity and thermal wakes, the diffusion coefficients in the model were found to be equal to  $a_q=0.13$ ,  $a_{eu}=0.04$ ,  $a_{uc}=0.03$ ,  $a_{cc}=0.11$ ,  $a_{Dc}=0.1$ .

### 3.3 Boundary and initial conditions

Boundary conditions account for symmetry of the wake:

$$\begin{aligned} \partial U / \partial y(x, 0) &= 0, \quad R_{12}(x, 0) = 0, \\ \partial R_{ii} / \partial y(x, 0) &= \partial E / \partial y(x, 0) = \partial D_u / \partial y(x, 0) = 0, \\ C(x, 0) &= \frac{\partial R_{2t}}{\partial y}(x, 0) = \frac{\partial \Theta}{\partial y}(x, 0) = \frac{\partial D_t}{\partial y}(x, 0) = 0. \end{aligned}$$

At the external boundary of the wake the parameters of turbulence are the functions of a turbulence state in surrounding medium (functions with asterisk), where the

turbulence is homogeneous with uniform mean velocity and a constant gradient of mean temperature  $dT / dx_2 = \Gamma$ .

$$\begin{aligned} U(x, \infty) &= 0, \quad R_{12}(x, \infty) = 0, \quad R_{11}(x, \infty) = E^* / 3, \\ R_{22}(x, \infty) &= E^* / 3, \quad E(x, \infty) = E^*, \quad D_u(x, \infty) = D_u^* \\ C(x, \infty) &= 0, \quad R_{2t}(x, \infty) = R_{2t}^*, \\ \Theta(x, \infty) &= \Theta^*, \quad D_t(x, \infty) = D_t^* \end{aligned}$$

These functions are to be found from the corresponding Cauchy problem for the ordinary differential equations, obtained from system (3) if omitting all the terms with the first and second  $y$ -derivatives. This system was numerically solved by Gear's method in parallel with solution of partial differential equations (3) by Patankar's method (20) described in (10) in more detail. Initial conditions were ordered from the experimental data in appropriate cross sections.

## 4 RESULTS

### 4.1 Reynolds stresses

The main purpose of the paper is the investigation of thermal wake. This wake evolves at the background of the turbulent dynamic wake, so we start describing the results from some figures showing evolution the Reynolds stresses in the flow.

In figures 1 and 2 we correlated our measurements of normal Reynolds stresses with the data of numerical simulation according to the model described in the previous section. Numerical simulation started from the wake's cross-section where all the necessary profiles for specifying initial conditions were known from the experiment (typically at  $x_1 / d = 14$ ). Thus, for the beginning cross section the experimental and numerical cross profiles coincided. The difference between the two grew with the distance but as a whole the correlation stayed to be rather good. As judged from the distribution of normal Reynolds stresses, self-similar state was reached at  $x_1 / d = 80$ . In near span  $x_1 / d < 15$  the characteristic profiles were close to parabolic form, later at  $x_1 / d > 20$  they attained a  $\Pi$ -type distribution, afterwards the form of the both distributions became non monotone, with two maxima located at  $x_2 / \delta_{u1} = \pm 0.6$ . In numerical simulation all the cross profiles considered to be symmetric, but in experiment we observed slight but noticeable asymmetry of these two components of velocity fluctuations.

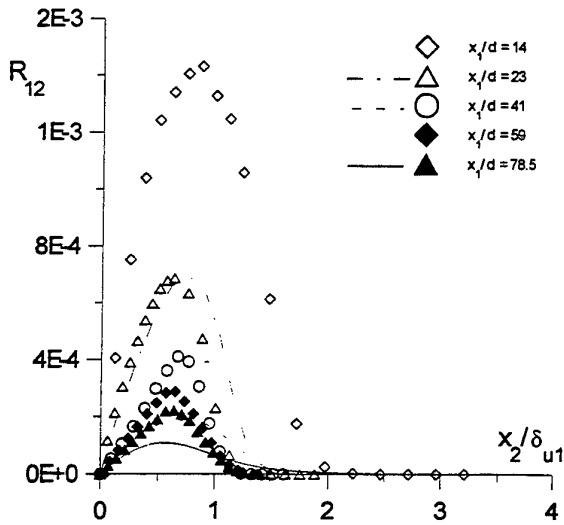


Figure 3 Decreasing the shear stresses  $R_{12}$  in the wake (for notation see figure 1)

Normalized distributions of shear stress  $R_{12}$  are shown in figure 3. Again, we can see a satisfactory fit of experimentally obtained and numerically predicted data. These distribution being divided by squared mean axial velocity defect  $U_0$  showed non monotone trend. Up to the axial coordinate  $x_1/d = 14$  the experimental profiles of  $R_{12}/U_0^2$  grew, then began to decline, and after  $x_1/d = 80$  the experimental ratio  $R_{12}/U_0^2$  attained nearly constant value of 0.044.

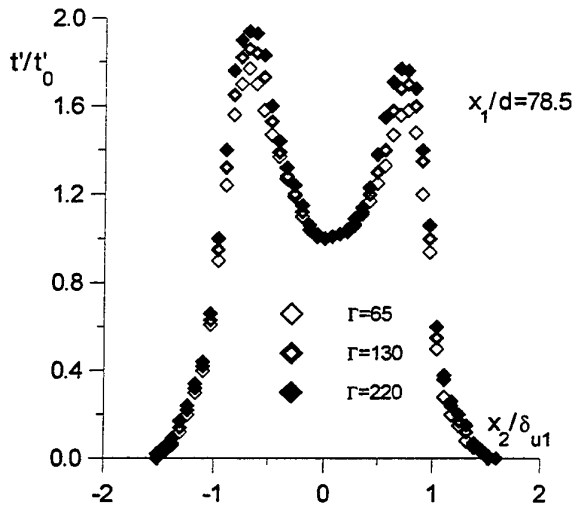


Figure 4 Asymmetry of temperature fluctuation profile at various temperature gradients.

#### 4.2 Temperature fluctuations

Figure 4 represents the vertical distribution of r.m.s. temperature fluctuations  $t'$  normalized by its value at the central plane. Left part of these curves refers to the

under side of the wake and the right one to the upper side. This plot shows a noticeable influence of stratification and asymmetry of fluctuation profile near the end of test section ( $x_1/d = 78.5$ ). The difference between upper and lower parts of the profile became more significant with approaching to the end of test section and increasing temperature gradient. This irregularity of temperature fluctuations is probably associated to slight non uniformity of lower and upper parts of mean temperature defect profile detected in our measurements as well as earlier in the work by Alexopolous & Keffer (8), where the temperature defect profile was more filled in a lower half-plane. It may be related to a non-local contragradiant heat transfer observed also in other anisotropic flows (Morel *et.al.* (21) in a wake of an asymmetrically heated plate, Beguier *et.al.* (22) in mixing layers).

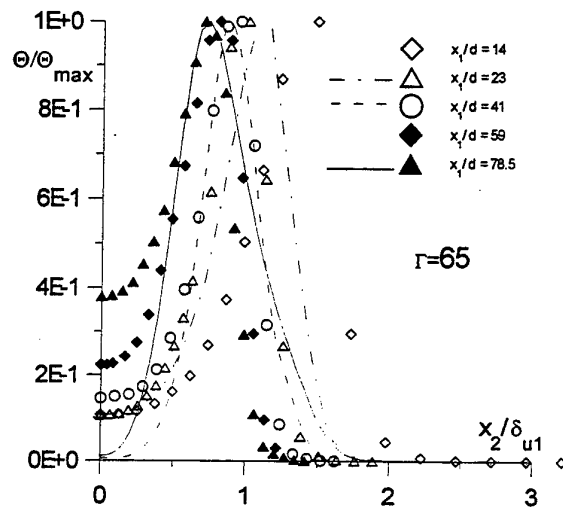


Figure 5 The development of temperature fluctuation profile (for notation see figure 1).

It is interesting to compare the maximum ratio of  $t'/t'_0$  in a wake cross section for the present experiment, where it was  $t'/t'_0 = 1.6 \dots 1.9$ , and for Alexopolous & Keffer work (8) with  $t'/t'_0 = 1.7$ . In our experiment the maximum thermal fluctuation intensity exceeds the corresponding axial value by a factor of about 10 at  $x_1/d = 14$  (see figure 5). In numerical simulation the distribution is even more sharp, because of axial  $\Theta$  being very small in the interval  $15 < x_1/d < 50$ . Later numerical predicted value of  $\Theta_0$  increased and caught up the experimental points (see authors' paper (10), where a total trend of  $\Theta_0$  growing with the distance was demonstrated).

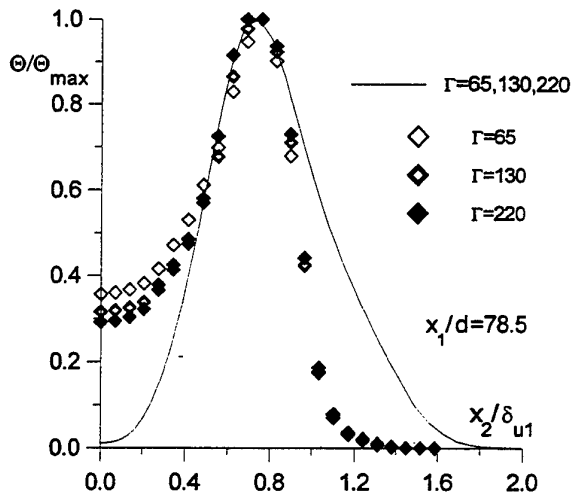


Figure 6 Stratification of temperature fluctuation intensity averaged over lower and upper half-planes.

Figure 5 and all subsequent figures except for figure 6 refers to minimal value from investigated range of temperature gradients,  $\Gamma = 65\text{K/m}$ . For such a small stratification there were only small differences (about 5-7%) between lower and upper half-planes. The influence of stratification grew with the distance from the flowed body and the temperature gradient, but in the investigated range it was relatively weak and most markedly noticed by the mentioned above asymmetry of temperature fluctuation profile. Being averaged over lower and upper half-planes (Figure 6) the influence of stratification was less evident even at relatively long distances from the body. As a whole, the influence of stratification is more noticeable in distributions of temperature fluctuations rather than in mean temperature profiles. As to simulation where deflections from symmetry was not taken into account, the numerically predicted curves reveal negligible splitting with temperature gradients in this range.

#### 4.3 Mutual correlations of velocity and temperature

In the course of experiment the following mutual velocity-temperature correlations were measured:  $\langle u_1 t \rangle$ ,  $\langle u_2 t \rangle$ ,  $\langle u_2 t^2 \rangle$ ,  $\langle u_2^2 t \rangle$ ,  $\langle u_1 u_2 t \rangle$ , but here we shall discuss only turbulent heat fluxes  $\langle u_1 t \rangle$  and  $\langle u_2 t \rangle$ . These fluxes were found from relation  $\langle u_i t \rangle = \rho_{ii} u_i' t'$ , where  $\rho_{ii}, i=1,2$  are the correlation coefficients between appropriate velocity components and temperature. All multipliers in right hand side of this relation were determined independently.

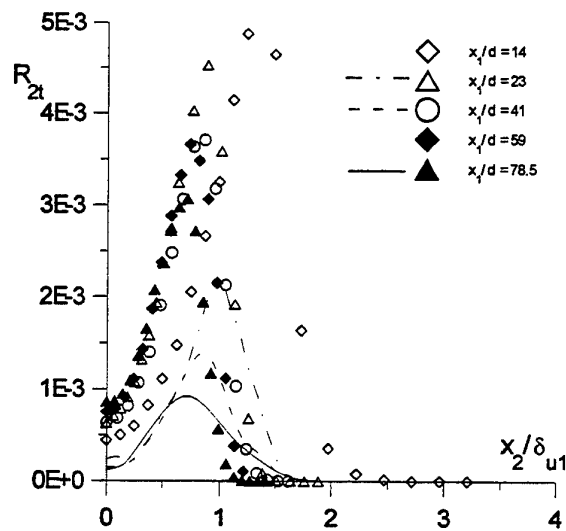


Figure 7 Cross distribution of turbulent heat flux  $\langle u_2 t \rangle$  (for notation see figure 1).

Figure 7 shows vertical distribution of normalized heat flux  $\langle u_2 t \rangle$ . Turbulent wake produces disturbances which are anti-symmetrical as to central plane, so that the longitudinal turbulent heat flux  $\langle u_1 t \rangle$  is zero at the axis, while the transverse one  $\langle u_2 t \rangle$  is finite; the situation being contrast to that arising at symmetrical distribution of mean temperature. Numerically predicted evolution of vertical heat flux is principally the same as in the experiment but scaled by a factor of about 0.5.

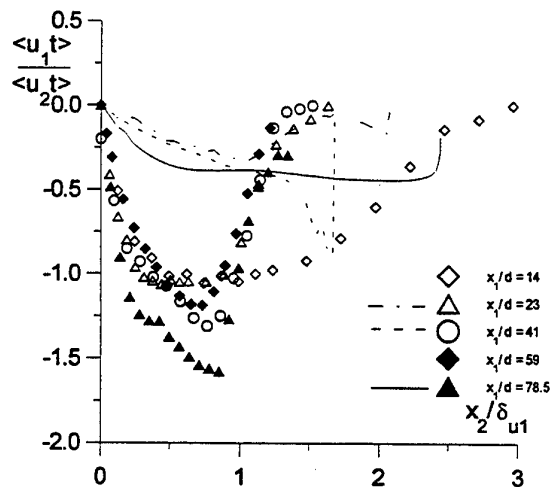


Figure 8 Cross profiles of the ratio of longitudinal to transverse turbulent heat fluxes

The ratio of heat fluxes  $\langle u_1 t \rangle$  and  $\langle u_2 t \rangle$  is not constant and varies non monotonously across the wake's cross section. In experiment the maximal ratio  $\langle u_1 t \rangle / \langle u_2 t \rangle$  was in the range of 1...1.5 and grew with the axial coordinate. For comparison, in Antonia & Browne work (7) this ratio was about 1.7, and in

experiment by Fabris 1.4. Only at short distances ( $x_1/d \leq 14$ ) from the turbulence source we observed the parity between the two fluxes. In simulation this ratio was less,  $\langle u_1 t \rangle / \langle u_2 t \rangle_{\max} \approx 0.4$ , and distributed more uniformly. The strange behaviour of the ratio near outer boundary in numerical curves is explained by accuracy loss in computation according to formula (4), produced by dividing two small magnitudes. Of course, there were no such artefacts in the plots of the main variables, those entering directly in system (3).

The calculated and measured ratio of two correlation coefficients,  $\rho_{2t}$  and  $\rho_{12}$ , is given in figure 9. In our case this ratio is also non monotone across the wake. The singularity near axis is caused by difference in boundary conditions for  $R_{2t}$  and  $R_{12}$  when heat flux  $R_{2t}$  stays finite and  $R_{12}$  is zero. Both in the experiment and simulation there is a nearly constant part at the centre of the curves. In this region the values of the measured ratio  $\rho_{2t}/\rho_{12}$  in our experiment grouped near 1.17. In a wake behind heated cylinder Antonia & Browne (7) determined this ratio to be 1.1, in the work by Fabris (5) the ratio of  $\rho_{2t}/\rho_{12}=1.0$  was pointed out. Our simulation also predicted correctly the change of trends in outer region of the wake ( $x_2/\delta_{u1} > 1$ ) with the distance. It is seen from figure 9, that after  $x_2/d > 70$  the ratio  $\rho_{2t}/\rho_{12}$  tends to zero at outer boundary of the wake both in experiment and numerically predicted data.

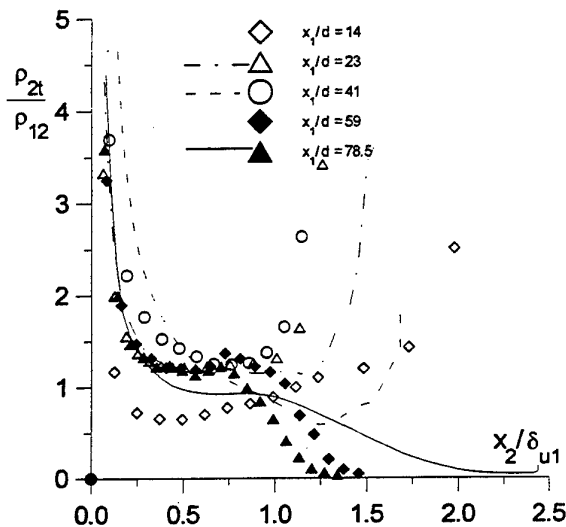


Figure 9 The ratio of correlation coefficients  $\rho_{2t}$  and  $\rho_{12}$ .

In figures 10 and 11 the distributions of two characteristic coefficients  $a_\theta$  and  $b_\theta$  are plotted. These coefficients are often used in closure of theoretical models for turbulent heat flux  $\langle u_2 t \rangle$ . The coefficients are defined by relations

$$a_\theta = \frac{|\langle u_2 t \rangle|}{\langle t^2 \rangle^{1/2} |\langle u_1 u_2 \rangle|^{1/2}} = \frac{|\rho_{2t}| \langle u_2^2 \rangle^{1/4}}{\rho_{12} \langle u_1^2 \rangle^{1/4}},$$

$$b_\theta = \frac{|\langle u_2 t \rangle| \langle u_1^2 \rangle^{1/2}}{|\langle u_1 u_2 \rangle| \langle t^2 \rangle^{1/2}} \quad (5)$$

The value  $b_\theta$  was used by Sætran (23) at modeling heat and momentum transfer in turbulent flow, parameter  $a_\theta$  links together transverse heat flux, fluctuations of scalar and Reynolds shear stress entering in equation for  $\langle u_2 t \rangle$ . Sætran (23) determined the parameter  $a_\theta$  in a thermal wake and parameter  $b_\theta$  in boundary layer. They were equal to  $a_\theta \approx 1.0$  and  $b_\theta \approx 1.15$ . Fabris (24) showed that  $a_\theta = 0.65$  in a thermal wake behind cylinder. Antonia & Browne found parameter  $a_\theta$  to be  $a_\theta = 0.61$ , also in a wake of heated cylinder. In the present experiment at  $0.2 < x_2/\delta_{u1} < 1.0$  the following values are characteristic  $a_\theta \approx 0.67$   $b_\theta \approx 1.2$  (see figures 10 and 11). These data correlate well with the cited above results by Fabris (24), Antonia & Browne (7) and Sætran (23) works.

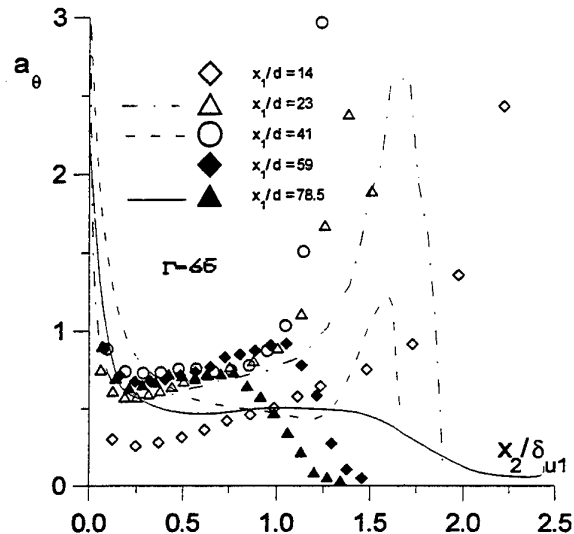


Figure 10 Measured and calculated cross profiles of parameter  $a_\theta$  in various sections of the wake.



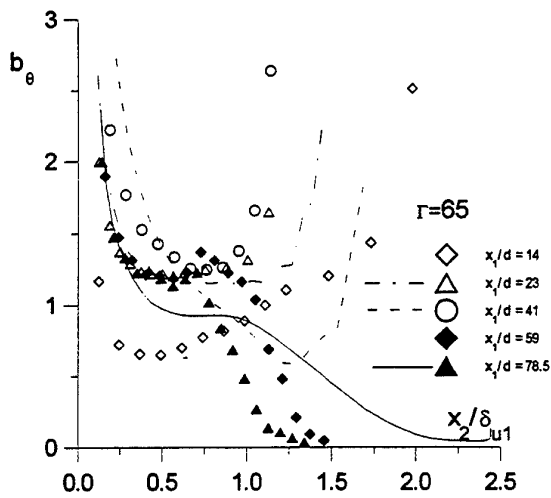


Figure 11 Measured and calculated cross profiles of parameter  $b_\theta$  in various sections of the wake.

Numerically predicted data for parameters  $a_\theta$  and  $b_\theta$  almost completely repeat all experimentally observed trends except for simulated profiles were wider a bit. It is related to discussed in the next paragraph differences in calculated and measured wake's half-width.

#### 4.4 Dissipative microscales of velocity and scalar fields, time scale ratio, scalar dissipation and wake's width

Normalized cross distributions of dynamic and thermal Taylor microscales are represented in figures 12 and 13.

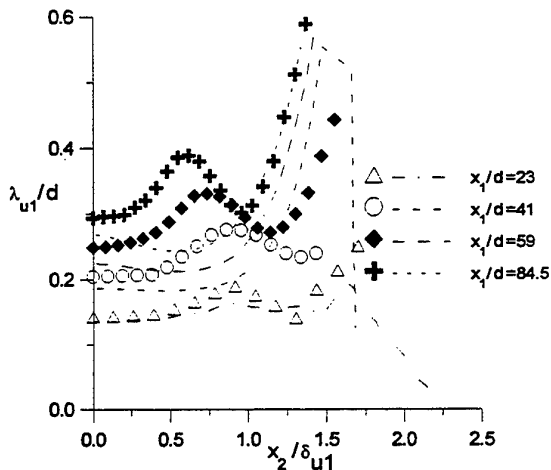


Figure 12 The cross profiles of the Taylor's dynamic microscale in various cuts of a wake.

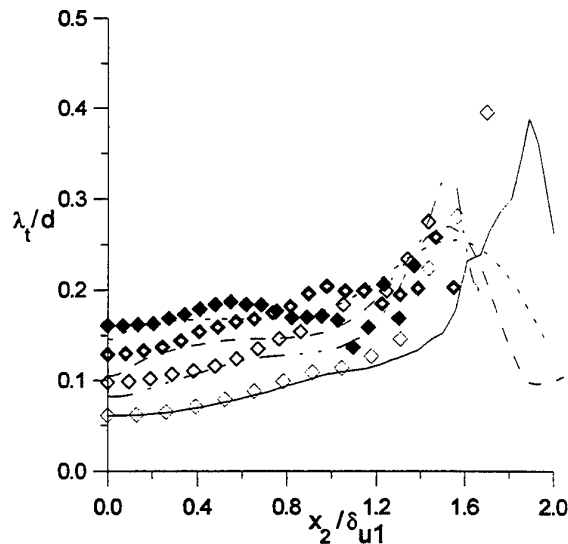


Figure 13 The cross profiles of the Taylor's temperature microscale in the various cuts of wake. (For notations see fig. 12.)

Figure 14 represents the growth of the Taylor's dynamic and thermal microscales  $\lambda_{u1}/d$  and  $\lambda_t/d$  at the axis of a wake. It is seen that the computation correctly describes the complex behaviour of the both microscales, as in vertical direction as the axial transformation. The both microscales are non monotone across the wake.

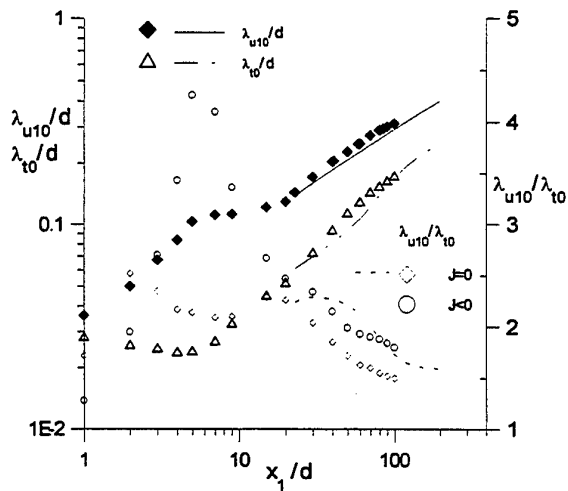


Figure 14 The growth of the Taylor's dynamic and temperature microscales at the wake axis. The right axes is for ratio of microscales.

The axial velocity microscale is larger than temperature microscale, the ratio of microscales decreases up to 1.8 at the distance  $x_1/d = 100$  from the body, but not yet reaches a constant value characteristic of self-similar behaviour. This essentially differs from a similar ratio in case of zero net momentum ( $J = 0$ ), where the ratio attains a known self-similar value

$\lambda_{u10}/\lambda_{t0}=1.5$  at  $x_1/d=100$  (see figure 14). For comparison, Beguier et.al. (22) determined self-similar ratio  $\lambda_{u10}/\lambda_{t0}$  to be equal 1.53 in asymmetrically heated mixing layer, that correlates well with the data of present experiment. The value of  $\lambda_{u10}/\lambda_{t0}=1.7$  was found in experiment by Sreenivasan et.al (25) in a wake of heated grid, but in their case a constant self-similar value seemed not to be reached at the end of test section. At the initial span  $x_1/d < 10$  the value of dynamic scale  $\lambda_{u1}$  exceeds the corresponding thermal scale  $\lambda_t$  by a factor of about 5, as the dynamic scale grows while the thermal one stays nearly constant.

Figure 15 plots the distribution of time scale ratio in a dynamic and thermal wake,  $R_\tau$ . Here, time scale ratio  $R_\tau$  was defined with accordance to formula  $R_\tau = 5\sigma(\langle u_1 u_1 \rangle / q^2) (\lambda_t / \lambda_{u1})^2$ . As in numerical simulation as in experiment the given parameter is not constant and behaves by a complex way, the predicted curves being in a rather good correlation with experimental data. In the investigated longitudinal coordinate range the axial and maximum value in a given cross section grew with the distance from the flowed body.

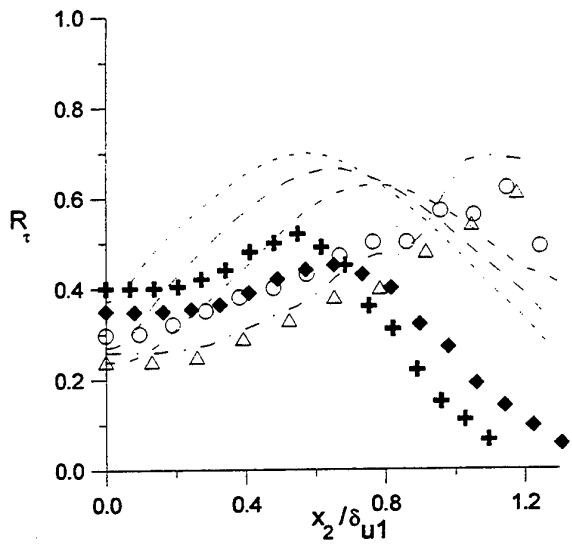


Figure 15. The profiles of radial distribution of a ratio of time scales. (For notations see fig. 12).

The axial variance of dimensionless thermal dissipation rate,  $D_t = \varepsilon_t / (\Gamma^2 dU_\infty)$ , is shown in fig. 16 together with the variance of maximum dissipation rate taken in a cross distribution.

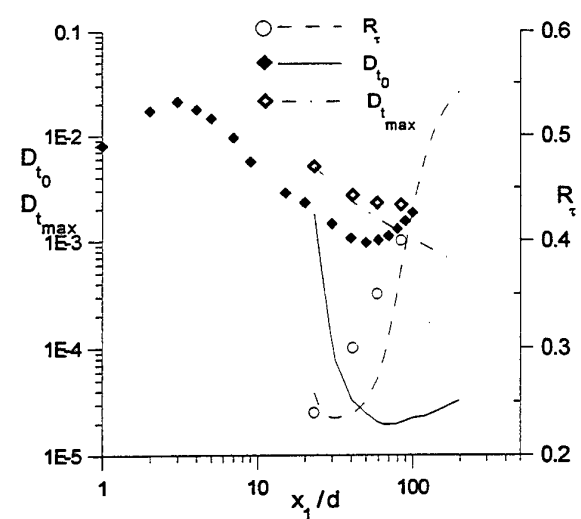


Figure 16. The variation of dissipation rate of temperature fluctuations along the axis. A right axes is for the axial ratio of time scales  $R_\tau$ .

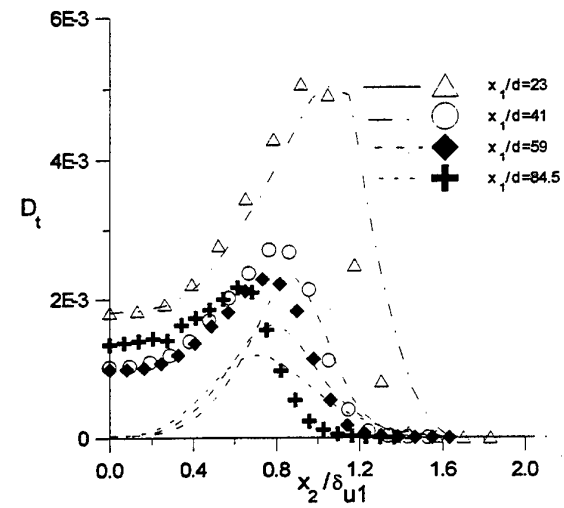


Figure 17 The profiles of a dimensionless dissipation rate of temperature fluctuations.

Figure 17 plots the transverse profiles of this value in various cross sections of the wake. The attention in figures 16 and 17 is drawn to significant divergence of computational results and experiments in the area near the wake axis while maximum calculated values of  $D_t$  in cross profiles fit the experimental data satisfactorily. The radial distributions of temperature dissipation differ from experiment in an interior part of wake, but are close to it in the peripheral part.

The various behaviour of  $\langle t^2 \rangle$  and  $\lambda_t$  causes non monotone dependencies of  $\varepsilon_t = 6\kappa \langle t^2 \rangle / \lambda_t^2$  and its normalized value,  $D_t$ , with both longitudinal and transverse coordinate. In a span  $x_1/d \ge 50$  the axial fluctuation of temperatures,  $\langle t^2 \rangle$ , grows with the

exponent 0.7-0.8, and the microscale  $\lambda_t$  with the exponent  $n \approx 0.5$ . Axial time scale ratio  $R_r$  also reveals a noticeable deflection from experimental points (see figure 17, left axis). The mentioned distinction accords with pointed above divergence of temperature fluctuation intensity near central symmetry plane (see figures 5 and 6). It is probably caused by mentioned above asymmetry of radial profiles of temperature fluctuations (figure 4). Calculated and measured maximal values of the temperature fluctuation dissipation rate fit each other more closely, see figure 17.

$Pr_t = \delta_U / \delta_T$  was close to unity. For comparison, at  $x_1/d = 2$  this number was twice less,  $Pr_t \approx 0.5$ . On a whole, in a span  $2 \leq x_1/d < 20$  a turbulent heat transfer prevails over transfer of momentum, later they matches.

The majority of thermal wake characteristic features, observed in experiment by Alexopolous & Keffer (8) were supported by the present more complete investigation. It is pertinent to note that experiment (8) and such a flow as a whole was mentioned in the past (see Launder (26)) as an excellent tool for developing and testing new turbulence models.

## 5. CONCLUSION

1. The carried out investigation showed that the development of thermal wake falling behind the dynamic wake, thus causing many interesting effects.
2. In temperature-stratified wake flow a strong radial non homogeneity of temperature fluctuations is observed. So, at small relative distances from a turbulence source,  $x_1/d \approx 10 \div 20$ , the maximum intensity of temperature fluctuations exceeds the corresponding axial value by a factor of about ten in experiment and even more in numerical simulation.
3. Asymmetry of mean temperature defect profiles results in asymmetrical distributions of temperature fluctuations, thus leading to appearance of non-local (contragradiant) turbulent heat transfer.
4. A non monotone growth of axial temperature fluctuation intensity was pointed out both in experiment and numerical simulation (see also authors' work (10)). It has a consequence of the growth of turbulent heat fluxes  $\langle u_1 t \rangle$  and  $\langle u_2 t \rangle$  with the distance from flowed body.
5. The dynamic and thermal Taylor microscales grow with axial distance. There is a non uniform distribution of Taylor microscales over cross section of the wake. The axial ratio of Taylor microscales  $\lambda_{u10} / \lambda_{t10}$  in self similar region of the wake tends to a constant value  $\lambda_{u10} / \lambda_{t10} = 1.5$ .
6. Non uniformity of cross distributions of Taylor microscales results in non monotone behaviour of time scale ratio,  $R_r$ . This ratio is not constant across the wake. The value of  $R_r$  grows along the axis of the flow. Its asymptotic value seems to be equal 0.5..0.6.
7. The temperature fluctuation wake is more than two times wider than the wake of mean temperature and velocity.
8. As a whole, the used Reynolds stress - vorticity model from (17),(18) let us to obtain satisfactorily description of almost all interesting features of the flow, except for axial behaviour of temperature fluctuation intensity and its dissipation rate.

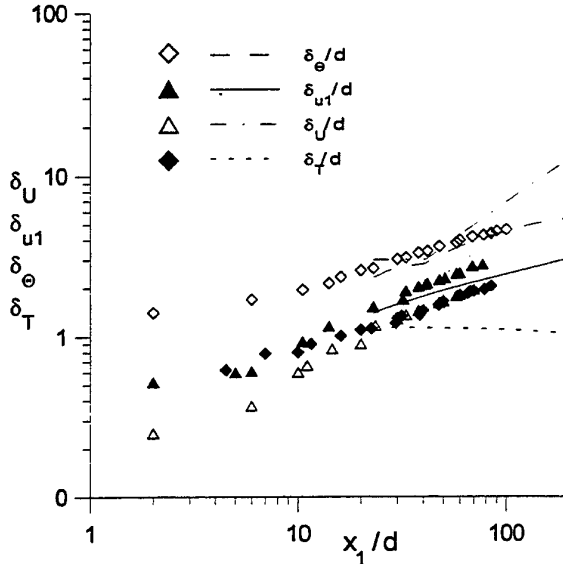


Figure 18. The variance of a half-widths of dynamic and thermal wakes.

In figure 18 the growth of various wake's half-widths is compared. Here, these half-widths were determined alternatively by temperature fluctuation profile (according to condition  $\Theta / \Theta_{\max} = 1/4$ ),  $\delta_{\theta}/d$ ; by mean temperature profile (position of maximum in temperature defect profile),  $\delta_T/d$ ; by longitudinal velocity profile (by condition  $\Delta U / \Delta U_0 = 1/2$ ),  $\delta_U/d$ ; and by longitudinal fluctuation profile ( $R_{11} / R_{11\max} = 1/4$ ). In experiment, the dynamic and thermal wakes extended with an identical exponent after  $x_1/d = 30$ . The wake determined by temperature fluctuations was the widest. Its width exceeded the one determined by mean temperature defect by a factor of about 2.2. A special feature of maximum temperature defect  $\Delta T_{\max}$  position in computations was the practical constancy of this value in a range  $x_1/d < 100$ , given the common expansion of temperature wake. In experiment there was a strict coincidence of two widths,  $\delta_U$  and  $\delta_T$  at  $x_1/d > 20$ , so, in this region the mean value of turbulent Prandtl number, determined as

## LIST OF SYMBOLS

### Dimensional variables

#### Latin letters:

$d$  - maximal thickness of the flowed body  
 $x_1, x_2$  - longitudinal and transverse coordinates  
 $U_1, U_2$  - longitudinal and vertical velocity components  
 $U_{1\infty}$  - upstream flow velocity  
 $\Delta U = U_1 - U_{1\infty}$  - velocity defect  
 $u_1, u_2$  - turbulent velocity fluctuations  
 $q^2 = \langle u_i u_i \rangle$  - doubled turbulence kinetic energy  
 $T$  - temperature  
 $t$  - turbulent temperature fluctuation  
 $J$  - net excessive momentum  
 $p$  - pressure

#### Greek letters:

$\tau$  - time,  
 $\delta_{u1}$  - wake's half width determined by the profile of longitudinal velocity fluctuation,  
 $\delta_U$  - wake's half width determined by the profile of mean velocity defect,  
 $\rho$  - density,  
 $\nu$  - kinematic viscosity coefficient,  
 $\kappa$  - thermal diffusivity coefficient  
 $\varepsilon_u = \nu \langle \partial u_i / \partial x_k \rangle^2$  - turbulence kinetic energy dissipation rate,  
 $\lambda_{u1}$  - Taylor's microscale measured by the profile of longitudinal velocity fluctuation,  
 $\lambda_u = (10 \nu q^2 / \varepsilon_u)^{1/2}$  - Taylor's microscale determined by the profile of turbulence kinetic energy,  
 $\lambda_t$  - Taylor's microscale measured by the profile of temperature fluctuation  
 $\varepsilon_t = \kappa \langle \partial t / \partial x_k \rangle^2$  - dissipation rate of temperature fluctuation,  
 $\Gamma = dT_\infty / dx_2$  - mean temperature gradient in upstream flow,

### Non dimensional variables

#### Latin letters:

$x = x_1 / d, y = x_2 / d, U = (U_1 - U_{1\infty}) / U_{1\infty}$ ,  
 $V = U_2 / U_{1\infty}, R_{12} = - \langle u_1 u_2 \rangle / U_{1\infty}^2$ ,  
 $R_{11} = \langle u_1^2 \rangle / U_{1\infty}^2, R_{22} = \langle u_2^2 \rangle / U_{1\infty}^2$ ,  
 $E = q^2 / U_{1\infty}^2, C = (T - T_\infty) / (\Gamma d)$ ,  
 $D_u = \varepsilon_u d / U_{1\infty}^3, \Theta = \langle t^2 \rangle / (\Gamma d)^2$ ,  
 $D_t = \varepsilon_t / (d U_{1\infty} \Gamma^2), R_{tt} = - \langle u_i t \rangle / (U_{1\infty} \Gamma d)$ ,  
 $F_u^{**} = F_{us}^{**} (1 - d_u) + F_{uw}^{**} d_u$  - the empirical function of vortex interaction,  
 $Re = U_{1\infty} d / \nu$  - mean flow Reynolds number,  
 $R_{\lambda_{u1}} = u_1' \lambda_{u1} / \nu, R_\lambda = \lambda_u (q^2)^{1/2} / \nu$  - turbulence Reynolds numbers,  
 $Fr = U_{1\infty} / Nd$  - Froude number,  
 $F = Fr^{-1}$  - inverse Froude number

#### Greek letters:

$\eta = \delta_{u1} / d$  - wake's half width  
 $\eta_1 = x_2 / \delta_{u1}$  - normalised vertical coordinate  
 $\sigma = \nu / \kappa$  - molecular Prandtl number

### Indexes

1, 2 - in directions of orts  $x_1, x_2$   
0 - at a symmetry plane  
 $\infty$  - conditions of upstream flow  
max - maximum value in this cross section  
prime - r.m.s. value

## REFERENCES

- (1) J.O. Hinze, B. Van der Zijnen, Transfer of heat and matter in the turbulent mixing zone of an axially symmetric jet, Appl. Sci. Res., 1949, 1A, p. 435
- (2) S. Corrsin, M.S. Uberoi, Further experiments on the flow and heat transfer in a heated turbulent air jet. 1950, NACA, Rept. N 998
- (3) A.A. Townsend, The Structure of Turbulent Shear Flows, 1976, (Cambridge University Press)
- (4) P. Freymuth, M.S. Uberoi, Structure of temperature fluctuations in the turbulent wake behind a heated cylinder, Physics of Fluids, 1971, v.14, pp. 2574-2580
- (5) G. Fabris, Turbulent temperature and flow characteristics in the wake behind a cylinder, J. of Fluid Mech., 1979, v. 94, pp. 673-709
- (6) P. Freymuth, M.S. Uberoi, Temperature fluctuations in the turbulent wake behind an optically heated sphere, Physics of Fluids, 1973, v.16, pp. 161-168
- (7) R.A. Antonia, L.W.R. Browne, Heat transfer in a turbulent plane wake, Int. J of Heat and Mass Transfer, 1986, v. 29, N 10, pp. 1585-1592

- (8) C.C. Alexopoulos, J.F. Keffer, Turbulent wake in passively stratified fluid, *Physics of Fluids*, 1971, v.14, p. 216
- (9) N.I. Bolonov, V.G. Lobachev, V.V. Chechula, Schedules of turbulent wake evolution in temperature stratified media (in Russian). in *Transfer Processes in Turbulent Flows*, 1988, pp. 138-148, (Minsk, Luikov Heat & Mass Transfer Inst.)
- (10) P.Ya. Cherepanov, V.A. Babenko, Flat turbulent wake in temperature stratified media, *International Conference on Turbulent Heat Transfer*, San Diego, CA, USA, March 10-15, 1996
- (11) P.Ya. Cherepanov, V.A. Babenko, Experimental and numerical study of flat momentumless wake, *Int. J. of Heat and Fluid Flows* (to be published)
- (12) P.Ya. Cherepanov, Yu.M. Dmitrenko, The influence of the body shape on self-similar parameters of a turbulent two-dimensional wake. *Journal of Engineering Physics*, 1988, v.54, pp. 912-919
- (13) Yu.M. Dmitrenko, I.I. Kovalev, N.N. Luchko, P.Ya. Cherepanov, Study of a two-dimensional turbulent momentumless wake, *Journal of Engineering Physics*, 1987, v.52, pp. 743-751
- (14) J.C. Wyngaard, Spatial resolution of the vorticity meter and other hot-wire arrays, *J. Sci. Instr.*, 1969, v2, Ser 2, pp. 983-987
- (15) S. Larsen, J. Hojstrup, Spatial and temporal resolution of a thin-wire resistance thermometer, *J. Phys. Exp.: Scientific Instruments*, 1982, v.15, N4, pp. 471-477
- (16) Yu.M. Dmitrenko, Measurement of mutual correlations of velocity and temperature fluctuations in non-isothermic flows (in Russian). in *Structure of turbulent flows*, 1982, pp. 82-90, (Minsk, Luikov Heat & Mass Transfer Inst.)
- (17) B.A. Kolovandin, Modeling the dynamics of turbulent transport processes, *Advances in heat transfer*, 1991, v.21, pp. 185-237
- (18) B.A. Kolovandin, I.A. Vatutin, V.U. Bondarchuk, Modeling of homogeneous turbulence of stratified fluid flows (in Russian), 1997, 204 p. (Minsk, FTI ANB)
- (19) D.W. Dunn, W.H. Reid, Heat transfer in isotropic turbulence during final period of decay, 1956, NACA Technical Notes, TN4186
- (20) S.V. Patankar, D.B. Spalding, A finite-difference procedure for solving the equations of the two-dimensional boundary layer, *Int. J. of Heat and Mass Transfer*, 1967, v.10, pp. 1389-1411
- (21) R. Morel, M. Awad, J.P. Schon, J. Mathieu, Experimental study of asymmetrical thermal wake, *Lecture Notes Phys.*, 1978, v.76, pp. 36-43
- (22) C. Beguier, I. Dekeyser, B.E. Launder, Ratio of scalar and density dissipation time scales in shear flow turbulence, *Phys. of Fluids*, 1978, v.21, N3, pp. 307-310
- (23) L.R. Sætran, Experimental investigation and mathematical modeling of momentum, heat and mass transfer in some turbulent flows., Ph. D. thesis, Univ. of Trondheim, 1984
- (24) G. Fabris, Turbulent temperature and thermal flux characteristics in the wake of a cylinder, in *Turbulent shear flows 1*, 1979, pp. 59-70 (ed. by F. Durst, B.E. Launder, F.W. Schmidt, and J.H. Whitelaw, Springer-Verlag, Berlin,)
- (25) K.R. Sreenivasan, S. Tavoularis, R. Henry, S. Corrsin, Temperature fluctuations and scales in grid generated turbulence, *J. of Fluid Mech.*, 1980, v.100, Pt.3, pp. 597-621.
- (26) B.E. Launder, Heat and Mass transfer, in book *Turbulence*, 1978 (ed. by Bradshaw, Springer-Verlag)

## AUTHOR INDEX

- |                     |             |  |
|---------------------|-------------|--|
| Abe, H.             | 1-15        |  |
| Abe, K.             | 8-15        |  |
| Agnew, N.D.         | 4-26        |  |
| Al-Dini, S.         | P-54        |  |
| Al-Farayedhi, A.    | P-54        |  |
| Angelis V.De        | 3-3         |  |
| Armitage, C.A.      | 5-36        |  |
| Asgar, A.           | P-54        |  |
| Axcell, B.P.        | 7-72        |  |
| Babenko, V.A.       | P-152       |  |
| Ball, K.S.          | P-83        |  |
| Banerjee, S.        | 3-3         |  |
| Bergstrom, D.J.     | P-3         |  |
| Bogusławski, L.     | P-15        |  |
| Bölcs, A.           | 7-29        |  |
| Bergeles, G.        | P-99        |  |
| Bonhoff, B.         | 7-29        |  |
| Bouris, D.          | P-99        |  |
| Bremhorst, K.       | 4-26        |  |
| Bridon, R.          | P-123       |  |
| Bubenchikov, A.M.   | P-131       |  |
| Burlutsky, E.S.     | P-131       |  |
| Byrne, J.E.         | 7-72        |  |
| Castaing, B.        | 5-3         |  |
| Chaubaud, B.        | 5-3         |  |
| Chavanne, X.        | 5-3         |  |
| Cherepanov, P. Ya.  | P-152       |  |
| Cheng, X.           | 7-3         |  |
| Chieng, C.C.        | 4-39        |  |
| Chillà, F.          | 5-3         |  |
| Chumakov, Y. S.     | 2-9         |  |
| Cotton, M.A.        | 2-20        |  |
| Craft, T.J.         | 4-15, P-115 |  |
| Daisaka, H.         | P-21        |  |
| Davidson, L.        | 5-24        |  |
| De Angelis, V.      | 3-3         |  |
| Diamessis, P.       | P-99        |  |
| Epik, E.Ya.         | 4-49        |  |
| Fu, S.              | 6-52        |  |
| Gbadebo, S.A.       | P-54        |  |
| Giebert, D.         | 6-30        |  |
| Gorin, A.V.         | P-63        |  |
| Grötzbach, G.       | 8-31        |  |
| Habib, M.           | P-54        |  |
| Hagiwara, Y.        | 1-48        |  |
| Hammond, G.P.       | P-123       |  |
| Hanjalić, K.        | 5-9, 7-58   |  |
| Hanratty, T.J.      | 1-3         |  |
| He S.S.             | 4-59        |  |
| Hébral, B.          | 5-3         |  |
| Hill, R. W.         | P-83        |  |
| Hishida, K.         | P-21        |  |
| Hopfinger, E.       | P-39        |  |
| Huang, X.           | P-3         |  |
| Hwang, C.B.         | 6-9         |  |
| Iida, O.            | 5-58        |  |
| Ilyushin, B.B.      | 5-48        |  |
| Iacovides, H.       | 7-14, 7-42  |  |
| Inaoka, K.          | 4-3         |  |
| Ismael, J.O.        | 2-20        |  |
| Jackson D.C.        | 7-14        |  |
| Jackson J.D.        | 2-31, 4-59  |  |
| Jazbutis, B.        | 2-3         |  |
| Johansson, A.V.     | 6-46        |  |
| Johnson, B.V.       | 7-29        |  |
| Jones, T.V.         | 6-22        |  |
| Kaniewski, M.       | P-141       |  |
| Karayianis, T.G.    | P-30        |  |
| Kawaguchi, Y.       | P-21        |  |
| Kawamura, H.        | 1-15        |  |
| Kelemenis G.        | 7-14        |  |
| Kenjereš, S.        | 5-9         |  |
| Kirwin, P.J.        | 2-20        |  |
| Koch, R.            | 6-30        |  |
| Kobayashi, M.       | 1-23        |  |
| Kunugi, T.          | 1-33        |  |
| Kurbatski, A.F.     | P-46        |  |
| Lauder, B.E.        | 5-36, 7-14  |  |
| Lau, S.             | P-141       |  |
| Lee, C.B.           | 1-54        |  |
| Leschziner, M. A.   | 5-36        |  |
| Leusch, J.          | 7-29        |  |
| Li J.               | 2-31        |  |
| Li, P.W.            | P-21        |  |
| Lin, C.A.           | 6-9         |  |
| Lin, W.W.           | 4-39        |  |
| Lock, G.D.          | P-123       |  |
| McEligot, D. M.     | 1-33        |  |
| Matsubara, K.       | 1-23        |  |
| M. Maeda            | P-21        |  |
| Maekawa, H.         | 1-23        |  |
| Meinders, E.R.      | 7-58        |  |
| Moro, J-P.          | P-39        |  |
| Mohsen Shehata, A.  | 1-33        |  |
| Musiellak, D.E.     | 6-3         |  |
| Murai, S.           | 1-48        |  |
| Na, Y.              | 1-3         |  |
| Nagano, Y.          | 5-58        |  |
| Neitzel, H.J.       | 7-3         |  |
| Nikolskaja, S.B.    | 2-9         |  |
| Okuda, T.           | 1-48        |  |
| Papavassiliou, D.V. | 1-3         |  |
| Parneix, S.         | 7-29        |  |
| Peng, S.H.          | 5-24        |  |

Poroseva, S.V. P-46  
Pořkas, P. 2-3  
Ram. A. V. P-141  
Raisee, M. 7-42  
Razuvanov, N.G. P-73  
Roche, P. 5-3  
Saez, M. P-39  
Said, S.A.M. P-54  
Schabacker, S. 7-29  
Schulz, A. 6-30  
Sikovsky, D.Ph. P-63  
Starchenko, A.V. P-131  
Suprun, T.T. 4-49  
Suga, K. 8-15  
Suzuki, K. 1-23, 4-3  
Sviridov, V.G. P-73  
Tanaka, M. 1-48  
Tian, Y.S. P-30  
Tsai, W.B. 4-39  
Thianpong, C. 7-72  
Tsumimura, S. 5-58  
Ustinov, A.V. P-73  
Voke, P.R. 8-3  
Wang, C. 6-52  
Wikström, P.M. 6-46  
Wittig, S. 6-30  
Wörner, M. 8-31  
Xu, Z. 4-59  
Yabe, A. P-21  
Yamamoto, J. 4-3  
Yuan Y-M 7-14  
Yurchenko, N.F. P-77  
Yushyna, L.E. 4-49